Physics of the Solid State, Vol. 47, No. 1, 2005, pp. 1–4. Translated from Fizika Tverdogo Tela, Vol. 47, No. 1, 2005, pp. 5–8.
Original Russian Text Copyright © 2005 by Batalov, Bayazitov, Khusnullin, Terukov, Kudoyarova, Mosina, Andreev, Kryzhkov.

PROCEEDINGS OF THE CONFERENCE "NANOPHOTONICS 2004"
(Nizhni Novgorod, Russia, May 2–6, 2004)

Structure, Impurity Composition, and Photoluminescence of Mechanically Polished Layers of Single-Crystal Silicon

R. I. Batalov*, R. M. Bayazitov*, N. M. Khusnullin, E. I. Terukov***, V. Kh. Kudoyarova***, G. N. Mosina***, B. A. Andreev****, and D. I. Kryzhkov******

** Zavoĭskiĭ Physicotechnical Institute, Russian Academy of Sciences, Sibirskiĭ trakt 10/7, Kazan, 420029 Tatarstan, Russia*
e-mail: bayaz@kfti.knc.ru
*** Kazan State University, ul. Kremlevskaya 18, Kazan, 420008 Tatarstan, Russia*
****Ioffe Physicotechnical Institute, Russian Academy of Sciences, Politekhnicheskaya ul. 26, St. Petersburg, 194021 Russia*
*****Institute of the Physics of Microstructures, Russian Academy of Sciences, Nizhni Novgorod, 603950 Russia*

Abstract—The introduction of optically active defects (such as atomic clusters, dislocations, precipitates) into a silicon single crystal using irradiation, plastic deformation, or heat treatment has been considered a possible approach to the design of silicon-based light-emitting structures in the near infrared region. Defects were introduced into silicon plates by traditional mechanical polishing. The changes in the defect structure and the impurity composition of damaged silicon layers during thermal annealing (TA) of a crystal were examined using transmission electronic microscopy and x-ray fluorescence. Optical properties of the defects were studied at 77 K using photoluminescence (PL) in the near infrared region. It has been shown that the defects generated by mechanical polishing transform into dislocations and dislocation loops and that SiO_2 precipitates also form as a result of annealing at temperatures of 850 to 1000°C. Depending on the annealing temperature, either oxide precipitates or dislocations decorated by copper atoms, which are gettered from the crystal bulk, make the predominant contribution to PL spectra. © *2005 Pleiades Publishing, Inc.*

1. INTRODUCTION

Single-crystal silicon is one of the main materials used in microelectronics, but it is of little use in light-emitting structures because of its indirect band structure and low probability of radiative transitions. Over the past 10–15 years, prospects for integrating both micro- and optoelectronic devices on a Si single-crystal wafer have encouraged intense development of a new line of studies (silicon-based optoelectronics) whose aim is to produce Si-based light-emitting structures in the visible and near-infrared regions and to integrate them with existing microelectronic devices [1].

One approach to the formation of silicon-based structures emitting at communication wavelengths (1.3 and 1.55 μm) is the introduction of various types of defects (point, linear, and bulk) into Si crystals. Point defects are centers consisting of silicon and impurity atoms (oxygen, carbon) formed as a result of Si crystals being irradiated by high-energy particles (γ rays, electrons, neutrons) [2]. Examples of optically active radiation-induced defects are complexes of interstitial (*i*) and substitutional (*s*) atoms of carbon (C_iC_s) and oxygen (C_iO_i) radiating in the region of 1.3 and 1.6 μm, respectively. The first silicon light-emitting diode using defects as radiative recombination centers was reported in [3].

In the mid-1990s, information was reported about the fabrication of silicon light-emitting diodes in which extended defects (dislocations) were introduced by plastic deformation or laser melting of a Si crystal [4, 5]. It has also been shown that the introduction of bulk defects into silicon (precipitates of silicon dioxide SiO_2) during multistage and long-term heat treatment is accompanied by the generation of photoluminescence (PL) in the near-infrared region (0.78–0.86 eV) [6, 7].

In spite of the variety of methods developed for introducing defects into silicon, the conventional mechanical treatment of silicon plates (lapping and polishing) has not been applied so far to introduce extended defects or to study their luminescent properties during subsequent heat treatments. We recently reported the observation of an intense PL signal with a peak at 0.83 eV (1.5 μm) arising after heat treatment of an *n*-Si (100) plate whose nonoperating backside was preliminary mechanically polished [8].

It was believed that this PL signal could be due to extended defects, generated by mechanical treatment, being decorated either by transition-metal (Cu, Ni, Fe) or oxygen atoms present in the initial Si crystals at a concentration level of less than 10^{14} and approximately 10^{18} cm^{-3}, respectively. Earlier, the effect of defects decorating metal impurities on dislocation PL spectra

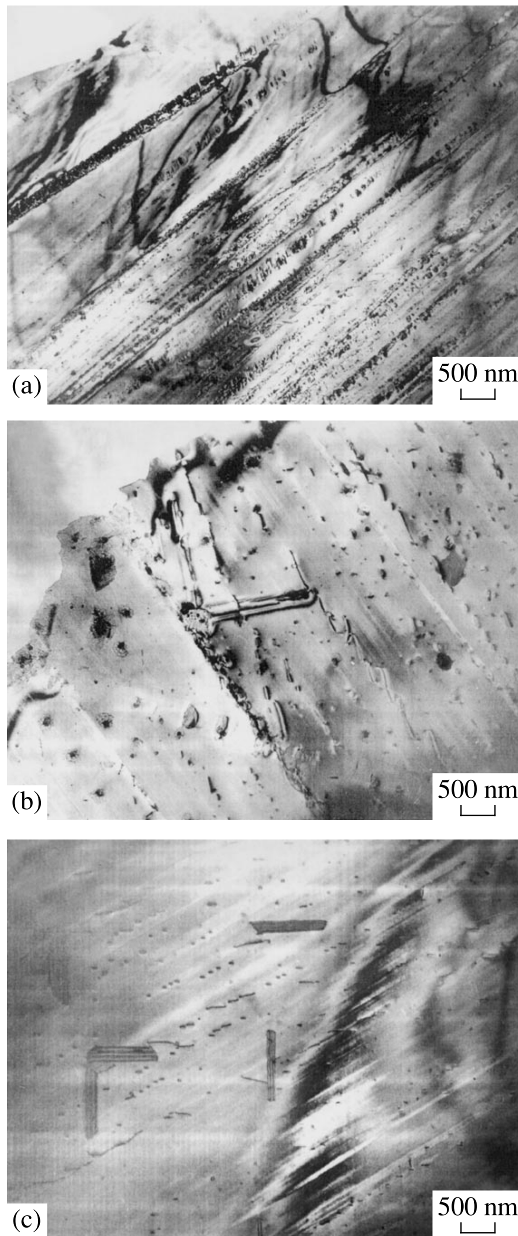

Fig. 1. Bright-field TEM images (horizontal section) of a Si surface layer (a) subject to mechanical polishing and (b, c) subsequent thermal annealing for 20 min at (b) 850 and (c) 1000°C.

(lines *D*1–*D*4) was reported [9, 10]. Therefore, in this work, a relationship was studied between the PL of mechanically polished and thermally annealed Si layers on one hand and the structure and impurity composition of damaged layers on the other.

2. EXPERIMENTAL

In the present work, *n*-Cz-Si (100) plates with mechanically polished backsides and an electrical resistance of 4 to 5 Ω cm were used. Thermal annealing (TA) of crystals was carried out in a nitrogen atmosphere at temperatures $T_1 = 850°C$ and $T_2 = 1000°C$ for 20 to 60 min, followed by slow cooling. The structure of damaged layers before and after TA was examined, using transmission electron microscopy (TEM), both near the silicon surface and at a depth of about 7 μm after chemical removal of a layer. The impurity composition of Si surface layers for atoms with $Z > 20$ was examined using x-ray fluorescence (XRF). The photoluminescence of damaged layers before and after TA was measured at 77 K with a BOMEM Fourier spectrometer equipped with a cooled germanium detector.

3. RESULTS AND DISCUSSION

Figure 1a shows a TEM image of the microstructure of a damaged Si layer on the backside of a plate near the surface. One can see that the Si surface is covered with bands and scratches about 0.5 μm in width, induced by the finishing mechanical polishing by micropowders of chromium oxide with similar grain fineness. The thickness of a damaged Si layer is 1 to 1.5 μm. According to the results of TEM studies, after etch removal of a Si layer about 7-μm thick, no marks of mechanical damages caused by polishing were found at this depth (not shown in the figure). There were only square etch pits associated with dislocations, whose density was about 10^3 cm^{-2} in the initial crystal.

Heat treatment of a Si crystal at temperature $T_1 =$ 850°C produced considerable changes in the defect structure of the damaged layer (Fig. 1b). In the places where scratches were before, their traces are observed to contain dislocations of different lengths (100 to 450 nm) and dislocation loops 40 to 50 nm in size. The density of loops and dislocations is about 4×10^8 and 3×10^8 cm^{-2}, respectively. Deeper scratches serve as sources of higher concentrations of dislocations.

In addition to dislocation structures, round-shaped particles about 0.2 μm in size form at the points where there are scratches; these particles are precipitates of a second phase. Electron microdiffraction data show that additional point reflections appear in the diffraction pattern, which were interpreted as belonging to α-SiO_2 (cristobalite). Precipitation of oxygen in the form of SiO_2 particles in silicon during heat treatments at an elevated temperature (above 800°C) is caused by its supersaturation due to the concentration of oxygen in Si (~10^{18} cm^{-3}) considerably exceeding its equilibrium solubility (~10^{16} cm^{-3}) at such temperatures. The density of SiO_2 particles in the silicon surface layer is about 10^8 cm^{-2}. In deeper layers of a crystal (~7 μm from the surface), the density of SiO_2 particles is much higher (~10^9 cm^{-2}) and they are slightly smaller in size (50 to 150 nm).

Annealing of a Si crystal at temperature $T_2 =$ 1000°C (Fig. 1c) resulted in further improvement of the structural state of the damaged layer (the traces of

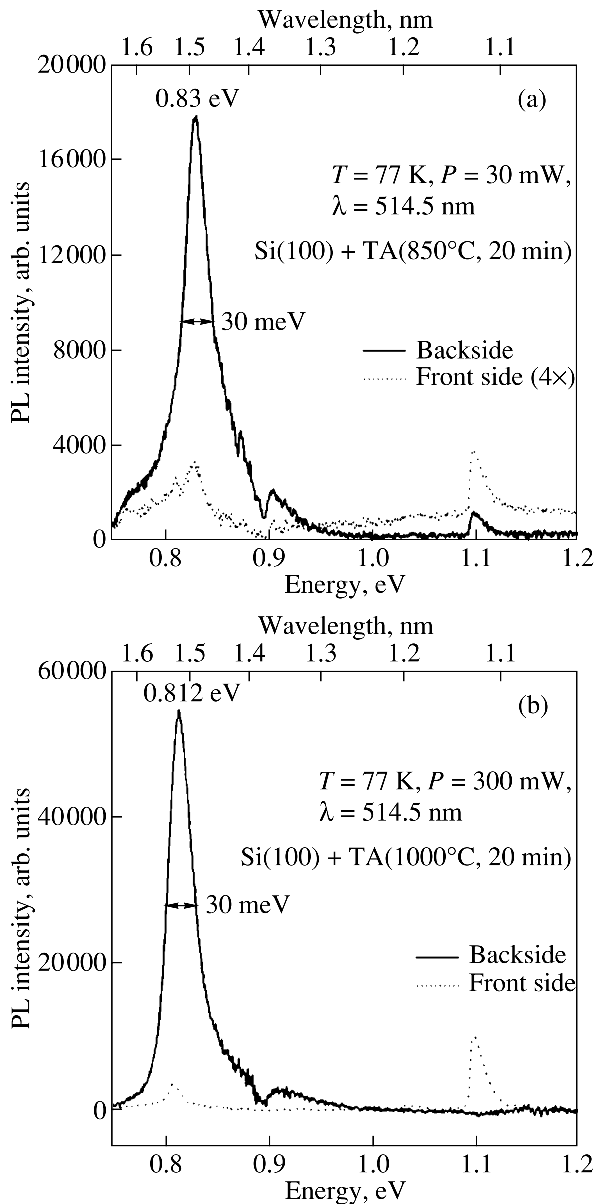

Fig. 2. Photoluminescence spectrum of Si subject to mechanical polishing and thermal annealing for 20 min at temperatures of (a) 850 and (b) 1000°C. The spectra are detected both from the front side and the backside of the plate. The dip in the spectrum at 0.9 eV is caused by radiation absorption by the quartz window of the Dewar vessel.

scratches became less noticeable). The densities of loops and dislocations decreased slightly to 3×10^8 and 10^8 cm^{-2}, respectively, while the size of loops themselves increased up to 0.2 μm. The generation of stacking faults was also observed with a density of about 10^7 cm^{-2}, which is typical of decomposition of a supersaturated solid solution of oxygen in a Czochralski-grown silicon. It should be noted that almost no SiO_2 particles are seen in Fig. 1c, though in deeper layers their density remains the same (~10^9 cm^{-2}) as their sizes reduce further down to 30–50 nm. This fact can be explained as resulting from the oxygen depletion of Si surface layers, which is observed at elevated annealing temperatures (≥1000°C) [11].

Examination of the impurity composition of silicon before and after TA using the XRF method revealed an excess copper concentration in damaged layers after TA. The characteristic spectral line of copper (CuK_α, E = 8 keV) was not detected at either Si surface before TA. After annealing at T_1 = 850°C, XRF spectra (not cited in the present work) exhibit the CuK_α line, with its intensity being higher on the backside (damaged) surface of the plate. After annealing at T_2 = 1000°C, the CuK_α line intensity increased on the damaged side. The excess concentration of copper in the defected Si layer is explained by copper gettering from the bulk of the crystal during TA. The extraction of technological impurities (Cu, Ni, Fe) from the active (device) areas of a Si crystal by mechanically damaging its backside and the formation of oxide precipitates in the crystal bulk during heat treatment are widely used practical methods of background impurity gettering [12].

Figure 2 shows PL spectra of mechanically polished and thermally annealed Si layers taken from the front side and from the backside of the plate. After TA at T_1 = 850°C (Fig. 2a), a PL line with a peak at 0.83 eV (1.5 μm) is visible in both spectra; however, its intensity is much higher for the backside of the plate. In addition, the above spectra exhibit an intrinsic emission signal of Si at 1.1 eV, whose intensity is higher when taken from the front (chemically polished) side of the plate. Annealing of Si at T_2 = 1000°C (Fig. 2b) shifts the maximum of the defect line to 0.808–0.812 eV, i.e., to the position of the dislocation line $D1$ at cryogenic temperatures [4, 5]; the line shape becomes nonsymmetric, with a tail on the short-wavelength side. The intensity of the signal taken from the backside increases considerably, and the signal from Si at 1.1 eV disappears.

4. CONCLUSIONS

The transformation of the defect structure of damaged layers during heat treatment of a Si crystal has been shown to be accompanied by the formation of both dislocation structures and oxides precipitates, which are decorated by copper atoms from the bulk of the crystal. The transformation of defects during annealing has an effect on the PL spectra, with the contribution from either SiO_2 particles or dislocations to these spectra becoming predominant depending on the temperature of annealing. Intense PL from the backside of the plate is essentially due to the decorating of defects with copper atoms, whose concentration is related to the concentration of defects produced by mechanical polishing.

ACKNOWLEDGMENTS

This work was supported by the program of the Department of Physical Sciences of the Russian Academy of Sciences "New Materials and Structures" and the program "Basic Research and Higher Education" (no. BRHE REC-007).

REFERENCES

1. L. Pavesi, J. Phys.: Condens. Matter **15**, R1169 (2003).
2. M. V. Bortnik, V. D. Tkachev, and A. V. Yukhnevich, Fiz. Tekh. Poluprovodn. (Leningrad) **1**, 353 (1967) [Sov. Phys. Semicond. **1**, 290 (1967)].
3. L. T. Canham, K. G. Barraclough, and D. J. Robbins, Appl. Phys. Lett. **51**, 1509 (1987).
4. V. V. Kveder, E. A. Steinman, S. A. Shevchenko, and H. G. Grimmeiss, Phys. Rev. B **51**, 10520 (1995).
5. E. O. Sveinbjorsson and J. Weber, Appl. Phys. Lett. **69**, 2686 (1996).
6. S. Binetti, S. Pizzini, E. Leoni, R. Somaschini, A. Castaldini, and A. Cavallini, J. Appl. Phys. **92**, 2437 (2002).
7. A. J. Kenyon, E. A. Steinman, C. W. Pitt, D. E. Hole, and V. I. Vdovin, J. Phys.: Condens. Matter **15**, S2843 (2003).
8. R. I. Batalov, R. M. Bayazitov, B. A. Andreev, D. I. Kryzhkov, E. I. Terukov, and V. Kh. Kudoyarova, Fiz. Tekh. Poluprovodn. (St. Petersburg) **37**, 1427 (2003) [Semiconductors **37**, 1380 (2003)].
9. V. Higgs, E. C. Lightowlers, G. Davies, F. Schaffler, and E. Kasper, Semicond. Sci. Technol. **4**, 593 (1989).
10. V. Higgs, M. Goulding, A. Brinklow, and P. Kightley, Appl. Phys. Lett. **60**, 1369 (1992).
11. T. J. Magee, C. Leung, H. Kawayoshi, B. K. Furman, and C. A. Evans, Jr., Appl. Phys. Lett. **39**, 631 (1981).
12. A. A. Istratov, H. Hieslmair, and E. R. Weber, Appl. Phys. A **70**, 489 (2000).

Translated by E. Borisenko

Physics of the Solid State, Vol. 47, No. 1, 2005, pp. 102–105. Translated from Fizika Tverdogo Tela, Vol. 47, No. 1, 2005, pp. 99–101.
Original Russian Text Copyright © 2005 by Kuznetsov, Rubtsova, Shabanov, Kasatkin, Sedova, Maksimov, Krasil'nik, Demidov.

PROCEEDINGS OF THE CONFERENCE "NANOPHOTONICS 2004"
(Nizhni Novgorod, Russia, May 2–6, 2004)

Crystal Lattice Defects and Hall Mobility of Electrons in Si : Er/Si Layers Grown by Sublimation Molecular-Beam Epitaxy

V. P. Kuznetsov*, R. A. Rubtsova*, V. N. Shabanov*, A. P. Kasatkin*, S. V. Sedova*, G. A. Maksimov*, Z. F. Krasil'nik, and E. V. Demidov****

** Research Physicotechnical Institute, Nizhni Novgorod State University, pr. Gagarina 23/5, Nizhni Novgorod, 603950 Russia*
*** Institute for Physics of Microstructures, Russian Academy of Sciences, Nizhni Novgorod, 603950 Russia*
e-mail: lab10@phys.unn.runet.ru

Abstract—The density of crystal lattice defects in Si : Er layers grown through sublimation molecular-beam epitaxy at temperatures ranging from 520 to 580°C is investigated by a metallographic method, and the Hall mobility of electrons in these layers is determined. It is found that the introduction of erbium at a concentration of up to $\sim 5 \times 10^{18}$ cm^{-3} into silicon layers is not accompanied by an increase in the density of crystal lattice defects but leads to a considerable decrease in the electron mobility. © *2005 Pleiades Publishing, Inc.*

1. INTRODUCTION

The discovery of luminescence phenomena, such as photoluminescence and electroluminescence, in Si : Er/Si structures in the wavelength range 1.5–1.6 μm has given impetus to more comprehensive investigation into the properties of these structures and has stimulated the development of various methods for their preparation.

Implantation of erbium ions into silicon layers [1–4] is the most extensively employed method for producing luminescent silicon structures. Moreover, these structures have often been prepared by molecular-beam epitaxy [5, 6] and sublimation molecular-beam epitaxy [7, 8].

The density of lattice defects is an important characteristic of crystal quality. It can be expected that crystal layers implanted with high-energy ions of erbium contain defects of different types in rather large amounts, in particular, dislocations at a density of 10^8–10^{10} cm^{-2} [3]. One of the purposes of the present work was to investigate defects involved in silicon layers grown by sublimation molecular-beam epitaxy.

As was shown earlier by Franzo *et al.* [3] and Coffa *et al.* [4], erbium ions are excited in a reverse-biased *p–n* junction through collisions with hot electrons. In this work, collisions of electrons with erbium complexes in Si : Er layers grown through sublimation molecular-beam epitaxy were studied by analyzing the Hall mobility μ_H in the layers. To the best of our knowledge, the Hall mobility μ_H has never been examined in Si : Er structures prepared by molecular-beam epitaxy. In a recent work, Aleksandrov *et al.* [9] obtained a dependence of the Hall mobility μ_H on the donor impurity concentration in silicon layers implanted with erbium ions; however, the level of erbium doping (2.5×10^{17} cm^{-3}) was relatively low as compared to the optimum value for electroluminescence ($N_{Er} \approx 1 \times 10^{19}$ cm^{-3}). Apparently, this light doping of the silicon layers could be the reason why those authors did not reveal a change in the Hall mobility μ_H after the erbium doping. The second purpose of the present study was to analyze the Hall mobility μ_H in Si : Er layers grown through sublimation molecular-beam epitaxy.

2. SAMPLE PREPARATION AND EXPERIMENTAL TECHNIQUE

For our measurements, Si : Er epitaxial layers up to 3 μm thick were grown through sublimation molecular-beam epitaxy at a rate of 1.0–1.5 μm/h under vacuum at a residual pressure of $(2–8) \times 10^{-7}$ mbar and at temperatures ranging from 520 to 580°C on Si(100) substrates doped with boron (10 Ω cm). The growth method and its potential were described in greater detail in [7, 8].

The concentration n and the Hall mobility μ_H of electrons in Si : Er epitaxial layers were measured using the van der Pauw method, the distribution of charge carriers over the layer thickness was determined by the electrochemical capacitance–voltage technique, and the distributions of impurities (specifically of erbium and oxygen) were obtained using secondary ion mass spectrometry. An important advantage of sublimation molecular-beam epitaxy is that this method provides for growing sufficiently thick layers. In turn, this made it possible to employ a simple reliable technique for revealing defects, namely, selective etching with subsequent observation of defects with the use of an MII-4 optical microscope ($300^{\times}$).

1063-7834/05/4701-0102$26.00 © 2005 Pleiades Publishing, Inc.

Erbium was uniformly distributed over the thickness of the epitaxial layers. The erbium concentration N_{Er} in the epitaxial layers was equal to (2–5) × 10^{18} cm^{-3}. The Si : Er layers had *n*-type conductivity. In all the structures grown through sublimation molecular-beam epitaxy, photoluminescence was observed at a temperature T = 77 K. As was shown in [10], back-biased diodes fabricated from these structures exhibited electroluminescence at 300 K.

3. CRYSTAL LATTICE DEFECTS

In this work, we studied defects in *p–n* structures. Here, *p* stands for a silicon substrate and *n* denotes a Si : Er layer. The electron concentration in Si : Er layers was estimated as n = (1.5–2.0) × 10^{16} cm^{-3}. The main defects observed with an optical microscope after etching of the samples were dislocations. As a rule, the density of dislocations in Si : Er layers (10^2–10^4 cm^{-2}) coincided with that observed in the silicon substrate. This gave grounds to believe that dislocations grew from the silicon substrate into a Si : Er layer.

After weak selective etching, the layer–substrate boundary was observed with an optical microscope in the form of a thin line on the (111) cleavage surface. In some cases, prolonged selective etching revealed dislocation pits on the (111) cleavage surface. The density of dislocation etch pits in our layers also did not exceed 10^4 cm^{-2}; however, these pits as a rule were not observed on the cleavage surface.

In diode structures prepared by implantation of erbium ions, the electron concentration at an optimum erbium concentration N_{Er} ~ 10^{19} cm^{-3} is sufficiently high: n ~ 10^{18} cm^{-3}. It is assumed that, in these structures, the erbium complexes serve as donors. In the Si : Er layers grown through sublimation molecular-beam epitaxy, the above electron concentration (10^{18} cm^{-3}) was reached by additional doping with phosphorus and antimony during growth of the layers [8]. After selective etching, the Si : Er epitaxial layers at an electron concentration of 10^{18} cm^{-3} did not contain dislocation pits. It should be noted that the disappearance of dislocation etch pits at a higher electron concentration (≥10^{18} cm^{-3}) has been observed both in heavily doped erbium-free layers grown through sublimation molecular-beam epitaxy [11] and in heavily doped bulk silicon [12].

4. HALL MOBILITY OF ELECTRONS

The Hall mobility μ_H of electrons was investigated in *n*-Si : Er layers isolated from the substrate by a *p–n* junction. These layers were grown using plates cut out from different Si : Er ingots serving as sources of erbium atoms. The electron concentration in the *n*-Si : Er layers varied from 3 × 10^{15} to 6 × 10^{17} cm^{-3}.

The dependence of the Hall mobility on the electron concentration $\mu_H(n)$ for Si : Er layers grown through sublimation molecular-beam epitaxy is depicted in the figure. For comparison, this figure shows the dependences $\mu_H(n)$ for bulk *n*-Si and Si : P, Si : Sb, and Si : As layers grown through sublimation molecular-beam epitaxy but not doped with erbium. Let us now explain the choice of the dependence $\mu_H(n)$ for bulk *n*-Si. According to Glowinke and Wagner [13], the Hall mobility μ_H of electrons in bulk *n*-Si depends on the oxygen concentration N_O and reaches a maximum value of 1850 cm^2/(V s) for N_O ~ 10^{18} cm^{-3} in the case when the donor concentration is less than 10^{13} cm^{-3}. In all the layers grown through sublimation molecular-beam epitaxy in our experiments, the oxygen concentration N_O falls in the range from 10^{19} to 10^{20} cm^{-3}. On this basis, the dependence $\mu_H(n)$ for bulk silicon (see figure) was constructed from the data reported by Debye and Kohane [14], according to which the maximum mobility of electrons is identical to that obtained in [13]. The same values of μ_H were obtained in our study of *n*-Si crystals grown by the Czochralski method with a high oxygen content.

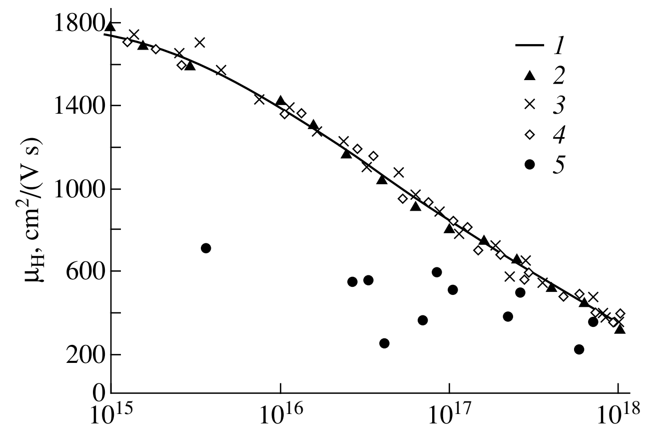

Dependences of the Hall mobility on the electron concentration at a temperature of 300 K for samples of (*1*) bulk silicon and (*2*) Si : P, (*3*) Si : Sb, (*4*) Si : As, and (*5*) Si : Er layers.

From analyzing the dependences $\mu_H(n)$ shown in the figure, we can draw the following conclusions: (i) the Hall mobility of electrons in an *n*-Si epitaxial layer free from erbium coincides with the value of μ_H for *n*-Si single crystals over the entire range of electron concentrations; and (ii) at the same electron concentrations, the Hall mobilities of electrons in Si : Er layers are 1.5–3.0 times lower than those observed in bulk silicon and in silicon layers not doped with erbium. The decrease in the Hall mobility μ_H of electrons in the Si : Er layers cannot be explained in terms of scattering by ionized impurities, because, in this case, the concentrations of donors and acceptors should be several tens of times higher than the measured concentration of electrons. However, this assumption disagrees with the results of analyzing the temperature dependence of the electron

concentration $n(T)$. Furthermore, the decrease in the Hall mobility μ_H of electrons in the Si : Er epitaxial layers also cannot be explained as resulting from the presence of defects in the crystal structure, because, as was shown above, the defect density is not very high.

In our opinion, the observed decrease in the Hall mobility μ_H of electrons in the Si : Er epitaxial layers is more logically explained in terms of electron scattering by erbium complexes. In what follows, the term "erbium complex" will be used in reference to a three-dimensional cluster that contains an erbium atom surrounded by impurity atoms. The electron mobilityμ_{Er}, which is associated with the electron scattering only by erbium complexes at a temperature of 300 K, can be determined from the expression

$$\frac{1}{\mu_{Er}} = \frac{1}{\mu_{exp}} - \frac{1}{\mu_b}, \quad (1)$$

where μ_{exp} is the measured mobility of electrons in the Si : Er layers and μ_b is the mobility of electrons in bulk silicon at the same electron concentration. The value of μ_{Er} at an erbium concentration $N_{Er} = 4 \times 10^{18}$ cm^{-3} is approximately equal to 500 cm^2/(V s).

The mechanism of electron scattering by erbium complexes was analyzed in the framework of two models. According to the first model, an erbium impurity complex is considered a sphere of radius r and the electron scattering is assumed to be elastic in nature. Within this approximation [15], the electron mobility μ_{Er} can be represented in the form

$$\mu_{Er} = \frac{4eL}{3\sqrt{2\pi m_c^* kT}}, \quad (2)$$

$$L = \frac{1}{\pi r_0^2 N_{Er}}. \quad (3)$$

Here, L is the mean free path of electrons upon scattering by erbium complexes, e is the elementary charge, and $m_c^* = 0.26m_0$ is the effective conductivity mass (where m_0 is the electron mass) [16]. For $N_{Er} = 4 \times 10^{18}$ cm^{-3} and $\mu_{Er} = 500$ cm^2/(V s), the first model of electron scattering by erbium complexes gives $L = 18$ nm and $r_0 = 2.1$ nm. The obtained value of r_0 considerably exceeds the minimum distance at which the oxygen impurity atoms surrounding the erbium atom are located in the structure of the complex. This value of r_0 can be explained either by a local distortion of the crystal lattice around the erbium complex or in terms of the fact that the impurity atoms are separated from the erbium atom by a distance that is substantially longer than the interatomic distance.

When analyzing the mechanism of electron scattering by erbium complexes in the framework of the second model, we used the Erginsoy formula for the relaxation time upon scattering of electrons by a neutral impurity [17]. Taking into account this formula, the electron mobility μ_{Er} can be written in the form

$$\mu_{Er} = \frac{e^3 m_0}{20\varepsilon(h/2\pi)^3 N_{Er}}\left(\frac{m^*}{m_0}\right)^2 \frac{m_0}{m_c^*}. \quad (4)$$

Here, $m^* = 3(m_\parallel m_\perp^2)^{1/3}/(m_\parallel^{-1} + 2m_\perp^{-1})m_0$ (where $m_\parallel$ is the longitudinal effective electron mass and $m_\perp$ is the transverse effective electron mass) [15], h is the Planck constant, and ε is the permittivity. Within this model, it is assumed that the scattering center is a hydrogen-like neutral atom immersed in a medium with permittivity ε. By substituting the erbium concentration $N_{Er} = 4 \times 10^{18}$ cm^{-3} into relationship (4), we obtain the electron mobility $\mu_{Er} = 810$ cm^2/(V s), which is in satisfactory agreement with the electron mobility μ_{Er} = 500 cm^2/(V s) determined from expression (1). According to relationship (4), the mean free path of electrons upon scattering by erbium complexes has the form

$$L = 3.4 \times 10^{-9}\sqrt{\frac{T}{300\text{ K}}}\mu_{Er}. \quad (5)$$

Here, μ_{Er} and L are expressed in cm^2/(V s) and cm, respectively. For $\mu_{Er} = 500$ cm^2/(V s) at $T = 300$ K, we obtain $L = 17$ nm. This value of L is close to the mean free path determined in the framework of the first model. It is difficult at this point to decide between the two above mechanisms of electron scattering. This problem calls for further investigation.

5. CONCLUSIONS

Thus, we investigated the density of crystal lattice defects and the Hall mobility of electrons in Si : Er layers grown through sublimation molecular-beam epitaxy. The erbium concentration in these layers was as high as 5×10^{18} cm^{-3}.

It was found that the introduction of erbium into silicon layers is not accompanied by an increase in the density of crystal lattice defects. The observed density of defects (dislocations) was not very high (10^2–10^4 cm^{-2}) and coincided with the density of dislocations in silicon substrates.

It was revealed that the Hall mobility of electrons in Si : Er epitaxial layers is considerably less than that observed in erbium-free silicon layers at the same electron concentration.

ACKNOWLEDGMENTS

This work was supported by the Russian Foundation for Basic Research (project nos. 01-02-16439, 02-02-16773) and the Ministry of Industry, Science, and Technology of the Russian Federation (state contract nos. 40.020.I.I.II61, 40.020.I.I.II59).

The secondary ion mass spectrometric measurements were performed at the Ioffe Physicotechnical Institute, Russian Academy of Sciences (St. Petersburg), and at the Institute for Physics of Microstructures, Russian Academy of Sciences (Nizhni Novgorod).

REFERENCES

1. H. Ennen, J. Schneider, G. Pomrenke, and A. Axmann, Appl. Phys. Lett. **43** (10), 943 (1983).
2. N. A. Sobolev, Fiz. Tekh. Poluprovodn. (St. Petersburg) **29**, 1153 (1995) [Semiconductors **29**, 595 (1995)].
3. G. Franzo, S. Coffa, F. Priolo, and C. Spinella, J. Appl. Phys. **81** (6), 2784 (1997).
4. S. Coffa, J. Franzo, F. Priolo, A. Pacelli, and A. Lacaita, Appl. Phys. Lett. **73** (1), 93 (1998).
5. J. Stimmer, A. Reittinger, J. F. Nutzel, G. Abstreiter, H. Holzbrecher, and Ch. Buchal, Appl. Phys. Lett. **68** (23), 3290 (1996).
6. K. Serna, Jung H. Shin, M. Lohmeier, E. Vlieg, A. Polman, and P. F. Alkemade, J. Appl. Phys. **79** (5), 2658 (1996).
7. V. P. Kuznetsov and R. A. Rubtsova, Fiz. Tekh. Poluprovodn. (St. Petersburg) **34** (5), 519 (2000) [Semiconductors **34**, 502 (2000)].
8. E. N. Morozova, V. B. Shmagin, Z. F. Krasil'nik, A. V. Antonov, V. P. Kuznetsov, and R. A. Rubtsova, Izv. Ross. Akad. Nauk, Ser. Fiz. **67** (2), 283 (2003).
9. O. V. Aleksandrov, A. O Zakhar'in, N. A. Sobolev, and Yu. A. Nikolaev, Fiz. Tekh. Poluprovodn. (St. Petersburg) **36** (3), 379 (2002) [Semiconductors **36**, 358 (2002)].
10. M. Stepikhova, B. Andreev, V. Shmagin, Z. Krasil'nik, N. Alyabina, V. Chalkov, V. Kuznetsov, V. Shabanov, V. Shengurov, S. Svetlov, E. Uskova, N. Sobolev, A. Emel'yanov, O. Gusev, and P. Pak, in *Proceedings of Meeting on Nanophotonics* (Inst. Fiziki Mikrostruktur Ross. Akad. Nauk, Nizhni Novgorod, 2001), p. 265.
11. V. P. Kuznetsov, R. A. Rubtsova, T. N. Sergievskaya, and V. V. Postnikov, Kristallografiya **16** (2), 432 (1971) [Sov. Phys. Crystallogr. **16**, 357 (1971)].
12. M. G. Mil'vidskiĭ, O. G. Stolyarov, and A. V. Berkova, Fiz. Tverd. Tela (Leningrad) **6** (12), 3259 (1964) [Sov. Phys. Solid State **6**, 2606 (1964)].
13. T. S. Glowinke and J. B. Wagner, J. Phys. Chem. Solids **38** (9), 963 (1977).
14. P. P. Debye and T. Kohane, Phys. Rev. **94** (3), 724 (1954).
15. A. I. Ansel'm, *Introduction to the Theory of Semiconductors* (Fizmatlit, Moscow, 1962), p. 305 [in Russian].
16. P. I. Baranskiĭ, V. P. Klochkov, and I. V. Potykevich, *Semiconductor Electronics: A Handbook* (Naukova Dumka, Kiev, 1975), pp. 157, 243 [in Russian].
17. C. Erginsoy, Phys. Rev. **79** (6), 1013 (1950).

Translated by O. Borovik-Romanova

Physics of the Solid State, Vol. 47, No. 1, 2005, pp. 106–109. Translated from Fizika Tverdogo Tela, Vol. 47, No. 1, 2005, pp. 102–104.
Original Russian Text Copyright © 2005 by Teterukov, Lisachenko, Shalygina, Zhigunov, Timoshenko, Kashkarov.

PROCEEDINGS OF THE CONFERENCE "NANOPHOTONICS 2004"
(Nizhni Novgorod, Russia, May 2–6, 2004)

Effect of Nonuniform Permittivity of a Solid-State Matrix on the Spectral Width of Erbium Ion Luminescence

S. A. Teterukov, M. G. Lisachenko, O. A. Shalygina, D. M. Zhigunov, V. Yu. Timoshenko, and P. K. Kashkarov

Moscow State University, Vorob'evy gory, Moscow, 119992 Russia
e-mail: vtim@vega.phys.msu.su

Abstract—The Stark splitting of the energy levels of Er^{3+} ions implanted in a structure made up of alternating layers of silicon dioxide and quasi-ordered silicon nanocrystals is calculated. The level splitting is caused by the electric field of the image charges induced at the interfaces between layers with different permittivities. The splitting was established to increase as the contrast in permittivity between the silicon dioxide and silicon nanocrystal layers increases, as well as when the erbium ions approach the layer interface. The results obtained offer an adequate explanation of the experimentally observed additional broadening of the erbium photoluminescence band (0.8 eV) with increasing characteristic size of the silicon nanocrystals. © *2005 Pleiades Publishing, Inc.*

1. INTRODUCTION

The recent interest in the luminescence of Er^{3+} ions in various silicon structures stems from the need to develop devices capable of efficient emission at a wavelength of 1.5 μm, which corresponds to the minimum absorption in fiber-optic communication lines [1]. A system that has alternating layers of quasi-ordered silicon nanocrystals and erbium-doped silicon dioxide (denoted subsequently as nc-Si/SiO_2 : Er) is a structure with application potential [2, 3].

The presence in nc-Si/SiO_2 : Er structures of regions with different values of permittivity inevitably gives rise to nonuniform polarization of the medium in electric fields. In such a system, at the interfaces between regions with different permittivities, Er^{3+} ions induce image charges, whose electric fields, in turn, act on the ions themselves and bring about an additional energy level splitting. As a consequence, the luminescence line undergoes additional broadening as compared to systems in which Er^{3+} resides in a dielectrically homogeneous matrix.

In this work, we studied the photoluminescence (PL) spectra of Er^{3+} ions in a silicon oxide matrix containing silicon nanocrystals (nc-Si) of various sizes. A model was constructed to account for the experimentally observed broadening of the Er^{3+} PL line with increasing nanocrystal dimensions.

2. SAMPLES AND EXPERIMENTAL RESULTS

The nc-Si/SiO_2 : Er samples used in the study were prepared by reactive cosputtering (with SiO and SiO_2 layers deposited successively on a *c*-Si substrate) [4] followed by annealing, which favored the formation of nanocrystals. Nanocrystals in each sample had a spread in size *d* to within 0.5 nm, and their size varied from one sample to another from 2 to 6 nm. After this, Er^{3+} ions were implanted into the samples to a dose of $\sim 2 \times 10^{15}$ cm^{-2} (average concentration $N_{Er} \sim 10^{20}$ cm^{-3}).

Figure 1 shows the PL spectra of Er^{3+} ions for three different nc-Si/SiO_2 : Er samples. The excitation was effected by nanosecond-range N_2-laser pulses (photon energy $\hbar\omega = 3.7$ eV, pulse length $\tau \sim 10$ ns, pulse energy $E \leq 1$ μJ, pulse repetition frequency $\nu \sim 100$ Hz). We

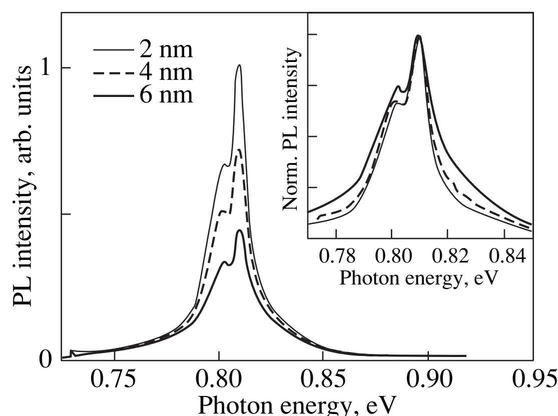

Fig. 1. PL spectra of Er^{3+} ions in nc-Si/SiO_2 : Er samples with nc-Si substrates of different dimensions. N_2 laser pumping: $E_{exe} = 3.7$ eV, $T = 300$ K. Inset: normalized PL spectra of Er^{3+} ions.

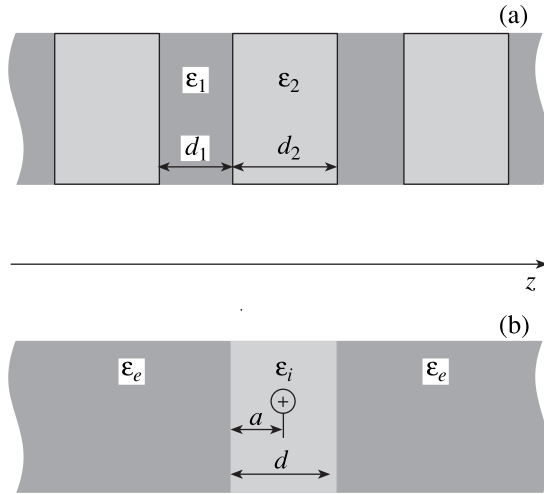

Fig. 2. (a) nc-Si/SiO_2 : Er structure in one-dimensional approximation (schematic) and (b) the model employed in the calculations.

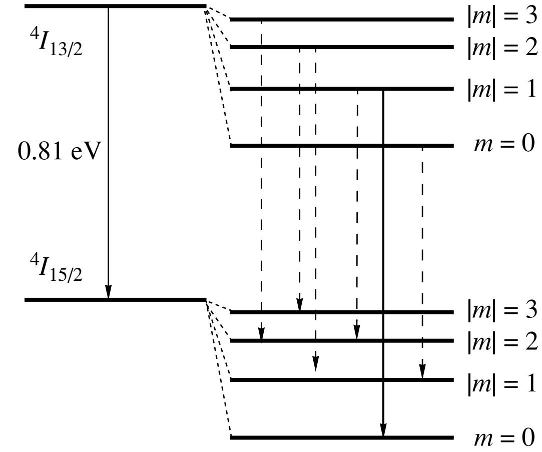

Fig. 3. Energy level splitting of the ground and first excited states of the Er^{3+} ion in an additional electric field. Vertical arrows identify possible optical transitions. The solid arrow indicates the optical transition used to estimate the splitting energy.

can see that, as the silicon nanocrystals grow in size (SiO layer thickness increases), the Er^{3+} PL intensity decreases and the spectral width of the line increases (see inset to Fig. 1). In addition, the Er^{3+} PL line in these structures is also noticeably broadened (FWHM ~ 20 meV) as compared to the analogous band in the samples where erbium is contained in a homogeneous silicon dioxide matrix [5]. This property could be employed to advantage in the development of various optoelectronics devices in which the transmission band, spectral width, etc., have to be varied. The next section deals with a model explaining the behavior of the Er^{3+} PL linewidth in nc-Si/SiO_2 : Er structures.

3. MODEL AND METHODS OF CALCULATION

The symmetry of the nc-Si/SiO_2 : Er structure allows us to approximate it with an infinite sequence of alternating layers of nanocrystals of silicon and silicon dioxide with dielectric constants ε_1 and ε_2, respectively (Fig. 2). Because nanocrystals form a close-packed array within each layer [2, 3], consideration may be limited to a one-dimensional problem. The thickness of the nanocrystalline layer d_2 in different samples can be varied purposefully from 1 to 6 nm [2]. The SiO_2 layer thickness (d_1) is usually 1–4 nm. Because the solubility of erbium in SiO_2 exceeds that in Si by several orders of magnitude, it can be maintained that erbium ions reside primarily in the SiO_2 layers.

To calculate the additional electric fields acting on the Er^{3+} ion in a nc-Si/SiO_2 structure, we have to solve the Poisson equation subject to the corresponding boundary conditions. The image charge potential $V(z)$ in the layer where the ion resides can be written in the form [6]

$$V(z, a) = \frac{1}{\varepsilon}\int_0^{\infty} J_0(ka)(\Psi(k)e^{kz} + \Phi(k)e^{-kz})dk, \quad (1)$$

where $J_0(ka)$ is the zero-order Bessel function and a is the distance from the ion to the layer boundary (Fig. 2). The origin coincides with the ion position. The explicit form of the functions $\Psi(k)$ and $\Phi(k)$ was found by solving the coupled equations from the continuity of the potential and electric induction at the interfaces. Expression (1) remains finite within the layer d. The problem was simplified by assuming that the layer containing the ion is surrounded by a medium with an effective dielectric constant ε_e (effective-medium approximation), depending on the thicknesses $d_{1,2}$ and dielectric constants $\varepsilon_{1,2}$ (Fig. 2). The dielectric constant ε_e is given by [7]

$$\varepsilon_e = \frac{(d_2 + d_1)\varepsilon_1\varepsilon_2}{d_1\varepsilon_2 + d_2\varepsilon_1}. \quad (2)$$

Using Eq. (2), we can find the dependence of ε_e on the thickness of the nanocrystalline layer for several values of its dielectric constant. In doing this, we take into account the dependence of ε_2 on the size of the nanocrystals and their concentration in the layer.

The strength of the additional electric field F, found by differentiating the integrand in Eq. (1) with respect to z, was subsequently used to estimate the Stark effect through perturbation theory. In the system at hand, the Stark effect is quadratic [8], because the Er^{3+} ion does not have a noticeable dipole moment in a zero field. To

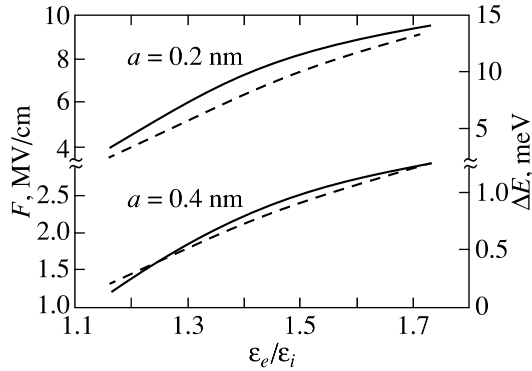

Fig. 4. Additional field (solid lines) and level-splitting energies (dashed lines) plotted vs. dielectric contrast for an Er^{3+} ion located at different distances from the interface between the media.

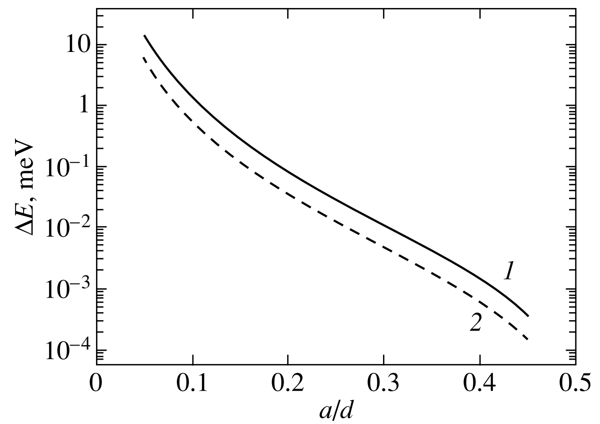

Fig. 5. Dependence of splitting energy on Er^{3+} ion position for different values of the dielectric contrast $\varepsilon_e/\varepsilon_i$: (*1*) 1.7 and (*2*) 1.3.

simplify the problem, the one-electron approximation was employed. Figure 3 displays the level splitting pattern for this case. The additional energies of the split levels are given by [8]

$$\Delta E_{n,m} = -\frac{f^2}{16}n^4[17n^2 - 9m^2 + 19], \quad (3)$$

where $f = F/F_0$ is the perturbation parameter, F_0 is the intraatomic field, n is the principal quantum number ($n = 4$), and m is the magnetic quantum number (Fig. 3). We took for the splitting the largest difference in the transition energies (corresponding to a pair of levels) allowed by the selection rules in the magnetic quantum number ($\Delta m = \pm 1$):

$$\Delta E = \Delta E_{4,1} - \Delta E_{4,0}. \quad (4)$$

Figure 4 plots the additional electric field induced by image charges at the interface separating the media and the additional energy associated with splitting in this field versus the dielectric contrast calculated within the above model for $d = 4$ nm. The dielectric constants ε_1 and ε_2 were assumed to be 11.8 and 3.5, respectively. The calculations were carried out for an erbium ion located at a distance of 0.2 and 0.4 nm from the interface. The smaller distance was dictated by the Si–O bond length (~0.18 nm), because this length is the minimum distance to which an ion can approach the interface in a structure while still remaining in the silicon oxide. The relation displayed in Fig. 4 can be explained by the higher contrast generating a larger image charge and, hence, a higher electric field. The additional field and the energy splitting drop sharply as the separation of an ion from the interface increases.

Figure 5 illustrates the calculated splitting as a function of relative ion position in the structure for two values of the dielectric contrast. The splitting is the largest near the interface and becomes additionally enhanced with increasing dielectric contrast, in full agreement with the graph in Fig. 4. The sharp decrease in ΔE observed to occur in Fig. 5 as the parameter a/d approaches 0.5 is accounted for by the simultaneous influence exerted on the ion by the two interfaces, whose action cancel each other out in the middle of the layer.

4. CONCLUSIONS

The values $\Delta E = 10$–15 meV obtained for $a = 0.2$ nm, $d = 4$ nm, and $\varepsilon_e/\varepsilon_i = 1.5$–$1.7$ are close to the experimentally measured widths of erbium luminescence spectra in nc-Si/SiO_2 : Er structures with silicon nanocrystals ~4–6 nm in size (Fig. 1). In addition, the results obtained within the simple model considered here fit well the experimentally observed broadening of the PL line with an increase in the nanocrystal size, i.e., with an increase in the dielectric contrast in the nc-Si/SiO_2 structure.

ACKNOWLEDGMENTS

This study was supported by the Russian Foundation for Basic Research (project nos. 02-02-17259, 03-02-16647), CRDF (project no. RE2-2369), and INTAS (project no. 03-51-6486) and carried out at the Center for Collective Use, Moscow State University.

REFERENCES

1. G. S. Pomrenke, P. B. Klein, and D. W. Langer, *Rare Earth Doped Semiconductors* (MRS, Pittsburgh, 1993), Mater. Res. Soc. Symp. Proc., Vol. 301.

2. M. Schmidt, M. Zacharias, S. Richter, P. Fisher, P. Veit, J. Bläsing, and B. Breeger, Thin Solid Films **397**, 211 (2001).
3. J. Heitmann, M. Schmidt, M. Zacharias, V. Yu. Timoshenko, M. G. Lisachenko, and P. K. Kashkarov, Mater. Sci. Eng. B **105**, 214 (2003).
4. P. K. Kashkarov, M. G. Lisachenko, O. A. Shalygina, V. Yu. Timoshenko, B. V. Kamenev, M. Schmidt, J. Heitmann, and M. Zacharias, Zh. Éksp. Teor. Fiz. **124** (6), 1255 (2003) [JETP **97**, 1123 (2003)].
5. A. Polman, J. Appl. Phys. **82** (1), 1 (1997).
6. W. R. Smythe, *Static and Dynamic Electricity*, 2nd ed. (McGraw-Hill, New York, 1950; Inostrannaya Literatura, Moscow, 1954).
7. M. Born and E. Wolf, *Principles of Optics*, 4th ed. (Pergamon, Oxford, 1969; Nauka, Moscow 1970).
8. P. Elyutin and V. D. Krivchenko, *Quantum Mechanics* (Nauka, Moscow, 1976) [in Russian].

Translated by G. Skrebtsov

Physics of the Solid State, Vol. 47, No. 1, 2005, pp. 110–112. Translated from Fizika Tverdogo Tela, Vol. 47, No. 1, 2005, pp. 105–107.
Original Russian Text Copyright © 2005 by Gusev, Wojdak, Klik, Forcales, Gregorkiewicz.

PROCEEDINGS OF THE CONFERENCE "NANOPHOTONICS 2004"
(Nizhni Novgorod, Russia, May 2–6, 2004)

Erbium Excitation in a SiO_2 : Si-nc Matrix under Pulsed Pumping

O. B. Gusev*, M. Wojdak, M. Klik**, M. Forcales**, and T. Gregorkiewicz****

**Ioffe Physicotechnical Institute, Russian Academy of Sciences, Politekhnicheskaya ul. 26, St. Petersburg, 194021 Russia*
e-mail: oleg.gusev@mail.ioffe.ru

***Van der Waals–Zeeman Institute, University of Amsterdam, Valckenierstaat 65, NL-1018 XE Amsterdam, The Netherlands*

Abstract—The photoluminescence of Er^{3+} ions in a SiO_2 matrix containing silicon nanocrystals 3.5 nm in diameter is studied under resonant and nonresonant pulsed pumping with pulses 5 ns in duration. The effective erbium excitation cross section under pulsed pumping, $\sigma_{eff} = 8.7 \times 10^{-17}$ cm^2, is close to that for nanocrystals. Comparison of the erbium photoluminescence intensity obtained for a SiO_2 matrix with and without nanocrystals made it possible to determine the absolute concentration of optically active nanocrystals capable of exciting erbium ions, the concentration of optically active erbium, and the average number of erbium ions excited by one nanocrystal. The study revealed that excitation transfer from one erbium ion to another is a relatively slow process, which accounts for the low efficiency of erbium ion excitation under pulsed pumping in a SiO_2 matrix containing silicon nanocrystals. © *2005 Pleiades Publishing, Inc.*

1. INTRODUCTION

Silicon undoubtedly is and obviously will remain in the future a basic material for use in modern electronics. A promising application of silicon in optoelectronics is closely connected with its doping by erbium, which emits in the transition from the first excited state to the ground state at a wavelength of 1.54 μm coinciding with the minimum of absorption in fiber-optic communication lines. The efficiency of erbium excitation in silicon is several orders of magnitude higher than that in dielectric matrices. Unlike the SiO_2 dielectric matrix, however, erbium luminescence in silicon suffers very strong temperature quenching. Intense research is presently under way on a new type of optical medium that combines the advantages of semiconducting and dielectric matrices [1–4]. This is a heterogeneous system in the form of a SiO_2 matrix doped by erbium and containing nanocrystals of silicon (Si-nc). In this case, the pump radiation is mainly absorbed by the silicon nanocrystals, which subsequently transfer energy with a high efficiency to the erbium ions present in SiO_2. Because nonradiative erbium de-excitation processes characteristic of silicon are absent in SiO_2, the photoluminescence (PL) intensity of erbium is practically independent of temperature.

The vast majority of studies on erbium excitation in heterogeneous SiO_2 : Si-nc matrices were made under cw pumping. By contrast, pulsed pumping performed with pulse lengths shorter than the characteristic erbium excitation and de-excitation times and the exciton lifetime in silicon nanocrystals allows deeper insight into the mechanism of electron transfer from nanocrystals to erbium ions and makes it possible to determine a number of parameters characterizing the SiO_2 : Si-nc matrix [5]. These are very important factors in the search for ways to increase the erbium luminescence efficiency in this matrix.

2. EXPERIMENTAL RESULTS

Three SiO_2 films 100-nm thick were PECVD-grown on SiO_2 substrates. Two of them contained silicon nanocrystals obtained by producing 8% supersaturation by silicon of stoichiometric composition from a SiO_x gas mixture. The diameter of the silicon nanocrystals, 3.5 nm, and their concentration, 5×10^{18} cm^{-3}, were determined with a planar transmission electron microscope (TEM). Erbium was implanted into one of the two SiO_2 : Si-nc samples and into the SiO_2 film at the same energies and to the same dose. The erbium concentration implanted in these samples was 2.2×10^{20} cm^{-3}. A detailed description of the sample preparation technology employed can be found in [2]. The characteristics of the samples studied in this work are listed in the table.

Photoluminescence measurements were performed under pulsed pumping using a tunable optical parametric oscillator (OPO) with 5-ns pulses at a repetition rate

Sample characteristics

Sample no.	Composition	[Si-nc], 10^{18} cm^{-3}	[Er], 10^{20} cm^{-3}
1	SiO_2 : Si-nc	5	
2	SiO_2 : Si-nc : Er	5	2.2
3	SiO_2 : Er		2.2

1063-7834/05/4701-0110$26.00 © 2005 Pleiades Publishing, Inc.

of 20 Hz. The OPO enable us to tune the pump wavelength in the range 500–560 nm for a spectral linewidth of 5 nm. The PL to be measured passed through a grating monochromator and was subsequently detected with a Hamamatsu NIR photomultiplier.

The PL spectra obtained in the 1.5-μm wavelength region on samples 2 and 3 containing erbium had approximately the same shape and spectral position of the maximum (Fig. 1). The luminescence in this region derives from radiative transitions of the Er^{3+} ion from the first excited state, $^4I_{13/2}$, to the ground state, $^4I_{15/2}$. Resonant excitation of erbium in sample 3 was effected by an OPO tuned to a wavelength of 520 nm, which corresponds to the $^4I_{15/2}$–$^2H_{11/2}$ transition. An identical spectrum was obtained on sample 2 within a broad region of spectral excitation. Figure 2 shows the PL excitation spectra of samples 2 and 3 measured at a wavelength of 1.54 μm, which corresponds to the maximum of the erbium PL spectral line.

Figure 3 sums up the main experimental results obtained. Curve *a* relates to sample 2 excited at a wavelength of 510 nm, at which erbium can be pumped via nanocrystals only; curve *b* refers to sample 2 excited at 520 nm, a wavelength permitting both direct erbium excitation and excitation mediated by silicon nanocrystals; curve *c* identifies sample 3 excited at 520 nm (resonant excitation of erbium in a SiO_2 matrix); and curve *d* plots the difference between data *b* and *a*; i.e., it reflects direct excitation of erbium in the presence of nanocrystals.

The PL spectrum of silicon nanocrystals (sample 1) was a fairly broad spectral line peaking at about 900 nm. The excitation cross section of silicon nanocrystals in this sample, 1.08×10^{-16} cm^2, and the exciton lifetime in the nanocrystals, 100 μs, were measured in [2].

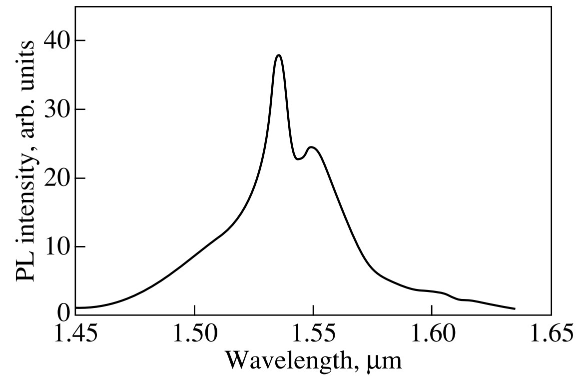

Fig. 1. Typical PL spectrum of samples 2 and 3 taken at T = 300 K.

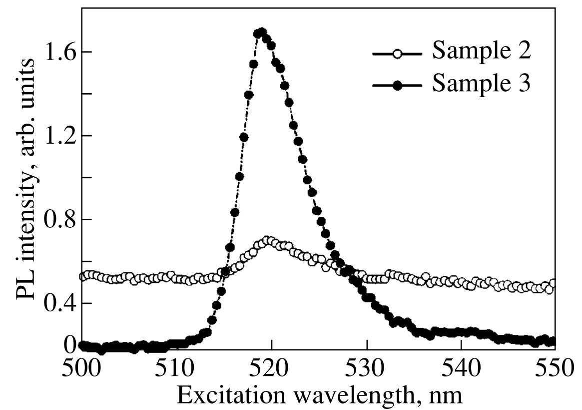

Fig. 2. Excitation spectra of samples 2 and 3 obtained at a wavelength of 1.54 μm at T = 300 K.

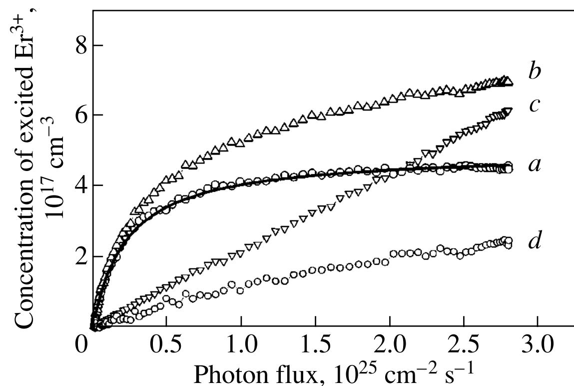

Fig. 3. Excited-erbium concentration plotted vs. photon flux density for sample 2 pumped with radiation at wavelengths of 510 and 520 nm (curves *a*, *b*, respectively) and sample 3 pumped resonantly at a wavelength of 520 nm (curve *c*); curve *d* is the difference between curves *b* and *a*. T = 300 K.

3. DISCUSSION OF THE RESULTS

An essential feature of the results displayed in Fig. 3 is their calibration against the absolute concentration of excited erbium for both samples. For this purpose, we used a simple two-level model of erbium excitation in which photons are directly absorbed by erbium ions. In this case, the concentration of excited erbium is described by the rate equation

$$\frac{dN^*_{\mathrm{Er}}}{dt} = \sigma\Phi(N_{\mathrm{Er}} - N^*_{\mathrm{Er}}) - \frac{N^*_{\mathrm{Er}}}{\tau}, \quad (1)$$

where σ is the photon absorption cross section by erbium ions, Φ is the pump photon flux, N_{Er} is the total concentration of erbium ions, N^*_{Er} is the concentration of excited erbium ions, and τ is the erbium ion lifetime in the first excited state $^4I_{13/2}$. In our case, because the OPO pulse length (5 ns) is substantially shorter than the characteristic erbium lifetime in the excited state, Eq. (1) can be solved to yield

$$N^*_{\mathrm{Er}} = N_{\mathrm{Er}}(1 - \exp(-\sigma\Phi\Delta t)), \quad (2)$$

where Δt is the OPO pulse duration and σ is the erbium absorption cross section in the SiO_2 matrix, which is 2×10^{-20} cm^2 at a wavelength of 520 nm corresponding to the $^4I_{15/2}$–$^2H_{11/2}$ transition in the inner erbium ion

shell [6]. Thus, using the concentration of implanted erbium and Eq. (2), we could determine the excited-erbium concentration in sample 3 as a function of the pumping level.

As is evident from Fig. 3, the excited-erbium concentration in sample 2 due to direct photon absorption by erbium ions (curve *d*) depends linearly on the photon flux, as is the case for the excited erbium concentration in sample 3, but with a substantially smaller slope. Assuming the photon absorption cross section of erbium ions to be the same in these two samples, we found that the concentration of optically active erbium ions in sample 2 is about 40% of that in sample 3.

At photon energies in excess of the band-gap width of silicon nanocrystals, the erbium contained in the SiO_2 : Si-nc matrix is excited primarily through excitation transfer from the nanocrystals to erbium ions. In this case, the first to be excited are the erbium ions located near the nanocrystals, after which the excitation can be transferred from one erbium ion to another. As seen from Fig. 3 (curve *a*), in the presence of nanocrystals, the concentration of excited erbium saturates rapidly at a level substantially lower than the concentration of optically active erbium ions found for sample 2. This implies that excitation transfer from an erbium ion in the vicinity of a nanocrystal to other erbium ions is a slow process and can be disregarded in our case of pulsed pumping. Therefore, the concentration of excited erbium ions under interband pump absorption by nanocrystals can be presented in a form similar to Eq. (2),

$$N_{Er}^{*} = nN_{nc}(1-\exp(-\sigma_{eff}\Phi\Delta t)), \qquad (3)$$

where σ_{eff} is the effective erbium excitation cross section under pump absorption by nanocrystals, n is the number of erbium ions that can be excited by one silicon nanocrystal, and N_{nc} is the concentration of the nanocrystals capable of exciting erbium. Thus, the product nN_{nc} is actually the total concentration of erbium that can be excited via nanocrystals. The solid line in Fig. 3 displays the results of processing the experimental data presented by curve *a* in Fig. 3 with $\sigma_{eff} = 8.7 \times 10^{-17}$ cm^2. The effective cross section σ_{eff} under pulsed erbium excitation mediated by nanocrystals is close in magnitude to the excitation cross section of nanocrystals, $\approx 1 \times 10^{-16}$ cm^2, which suggests that this process is highly efficient. The concentration of erbium that can be pumped through nanocrystals in sample 2 saturates at a level of $\approx 4.5 \times 10^{17}$ cm^{-3}.

The saturated concentration of excited erbium thus obtained is noticeably lower than the concentration of nanocrystals in sample 2 (5×10^{18} cm^{-3}). This suggests that, under pulsed pumping, one nanocrystal is capable of directly exciting one erbium ion only. Thus, the saturated concentration of excited erbium we have obtained corresponds to the concentration of nanocrystals capable of transferring energy to erbium ions. The concentration of excited erbium in sample 2 generated under cw pumping (where the excitation is transferred from one erbium ion to another) saturates at a level of $\approx 1 \times 10^{19}$ cm^{-3}, which is considerably higher than that under pulsed pumping.

4. CONCLUSIONS

Thus, we have studied the excitation of erbium ions in a SiO_2 matrix containing silicon nanocrystals under resonant and nonresonant pulsed pumping with a pulse length of 5 ns. The effective erbium excitation cross section under pulsed pumping, $\sigma_{eff} = 8.7 \times 10^{-17}$ cm^2, is close to the excitation cross section of nanocrystals.

Our results suggest that, although loading the SiO_2 matrix with nanocrystals does strongly increase the efficiency of erbium excitation, the concentration of optically active erbium decreases noticeably. In addition, the silicon nanocrystals in the SiO_2 matrix are by no means all optically active, i.e., capable of exciting erbium. As follows from our estimates, the time needed to transfer excitation from one erbium ion to another is substantially longer than that from Si-nc to an erbium ion and the exciton lifetime in nanocrystals.

ACKNOWLEDGMENTS

This study was supported by the Russian Foundation for Basic Research, INTAS (project no. 03-51-6486), and the RAS program “New Materials.”

REFERENCES

1. G. Franzo, F. Priolo, and V. Vinciguerra, Appl. Phys. A **69**, 3 (1999).
2. F. Priolo, G. Franzo, D. Pacifici, V. Vinciguerra, F. Iacona, and A. Irrera, J. Appl. Phys. **89** (1), 264 (2001).
3. P. G. Kik and A. Polman, J. Appl. Phys. **88** (4), 1992 (2000).
4. D. Pacifici, G. Franzo, F. Priolo, F. Iacona, and L. D. Negro, Phys. Rev. B **67**, 245301 (2003).
5. M. Forcales, M. Wojdak, M. A. Klik, T. Gregorkiewicz, O. B. Gusev, G. Franzo, D. Pacifici, F. Priolo, and F. Iacona, Mater. Res. Soc. Symp. Proc. **770**, 16.9.1 (2003).
6. W. J. Miniscalco, J. Lightwave Technol. **9**, 234 (1991).

Translated by G. Skrebtsov

Physics of the Solid State, Vol. 47, No. 1, 2005, pp. 113–116. Translated from Fizika Tverdogo Tela, Vol. 47, No. 1, 2005, pp. 108–111.
Original Russian Text Copyright © 2005 by Sobolev, Denisov, Emel'yanov, Shek, Ber, Kovarskiĭ, Sakharov, Serenkov, Ustinov, Cirlin, Kotereva.

PROCEEDINGS OF THE CONFERENCE "NANOPHOTONICS 2004"
(Nizhni Novgorod, Russia, May 2–6, 2004)

MBE-Grown Si : Er Light-Emitting Structures: Effect of Epitaxial Growth Conditions on Impurity Concentration and Photoluminescence

N. A. Sobolev*, D. V. Denisov*, A. M. Emel'yanov*, E. I. Shek*, B. Ya. Ber*, A. P. Kovarskiĭ*, V. I. Sakharov*, I. T. Serenkov*, V. M. Ustinov*, G. E. Cirlin*, and T. V. Kotereva**

**Ioffe Physicotechnical Institute, Russian Academy of Sciences, Politekhnicheskaya ul. 26, St. Petersburg, 194021 Russia*
e-mail: nick@sobolev.ioffe.rssi.ru
***Institute of Chemistry of High-Purity Substances, Russian Academy of Sciences, ul. Tropinina 49, Nizhni Novgorod, 603600 Russia*

Abstract—The technology and properties of light-emitting structures based on silicon layers doped by erbium during epitaxial MBE growth are studied. The epitaxial layer forming on substrates prepared from Czochralski-grown silicon becomes doped by oxygen and carbon impurities in the process. This permits simplification of the Si : Er layer doping by luminescence-activating impurities, thus eliminating the need to make a special capillary for introducing them into the growth chamber from the vapor phase. The photoluminescence spectra of all the structures studied at 78 K are dominated by an Er-containing center whose emission line peaks at 1.542 μm. The intensity of this line measured as a function of the substrate and erbium dopant source temperatures over the ranges 400–700°C and 740–800°C, respectively, exhibits maxima. The edge luminescence and the *P* line observed in the PL spectra are excited predominantly in the substrate. The erbium atom concentration in the epitaxial layers grown at a substrate temperature of 600°C was studied by Rutherford proton backscattering and exhibits an exponential dependence on the erbium source temperature with an activation energy of ~2.2 eV. © *2005 Pleiades Publishing, Inc.*

1. INTRODUCTION

Ion implantation and molecular beam epitaxy (MBE) are widely employed in the development of light-emitting structures based on single-crystal Si : Er layers [1]. MBE technology has a major asset in that it makes it possible to control the concentration profiles of various impurities with a high precision. However, the high complexity of various design realizations of the MBE techniques gives rise to specific properties of the light-emitting structures fabricated. The present communication reports on a study of the effect that the various epitaxial growth conditions exert on the impurity concentration in a growing Si : Er MBE layer and on photoluminescence (PL) spectra at low oxygen and carbon impurity concentrations as compared to that of erbium.

2. EXPERIMENTAL

MBE-grown Si : Er layers were produced with a SUPRA-32 (RIBER) apparatus. A Si flux was obtained with an electron beam evaporator bombarding a target of *n*-type silicon grown through floating-zone melting (*n*-FZ-Si) with an electrical resistivity $\rho = 2\ \Omega$ cm. A flux of rare-earth atoms was produced by an effusion cell containing metallic Er. The substrates used were polished *n*-Cz-Si plates with a (100)-oriented surface and $\rho = 4.5\ \Omega$ cm. The epitaxial growth proceeded at a constant substrate temperature $T_{Si} = 400$–700°C, a deposition rate of 0.26–0.70 Å/s, and a residual gas pressure in the growth chamber not exceeding 8×10^{-9} Torr. To make the original surface as smooth as possible, a thin (100–300 Å thick) buffer layer of undoped Si was preliminarily grown on it. The Er concentration in an MBE layer could be varied by properly controlling the operating Er source temperature (T_{Er}) from 740 to 800°C. Analysis of the dynamics of the reflection high-energy electron diffraction patterns revealed that, in the technological conditions chosen, the growth of Si : Er layers follows a two-dimensional pattern. The layer thickness was as high as 1.3 μm. The MBE-grown layers were *n*-type.

The concentrations of the oxygen impurity in interstitial positions (O_i) and of carbon in lattice sites (C_s) in the silicon source plate for MBE growth and in the substrate plate prior to epitaxial growth were derived from the maximum of the lines at 1107 and 605 cm^{-1} in IR absorption spectra measured with a resolution of 1 cm^{-1} on an IFS-113 Fourier spectrometer (Bruker) with a $Cd_xHg_{1-x}Te$ detector in the range 500–1600 cm^{-1} at room temperature. The calibration coefficients for oxygen and carbon were 3.14×10^{17} [2] and 8.2×10^{16} cm^{-2} [3], respectively. It was found that $[O_i] < 8 \times 10^{15}$ cm^{-3} and $[C_s] < 5 \times 10^{16}$ cm^{-3} in FZ-Si and $[O_i] = (1.1 \pm 0.3) \times 10^{18}$ cm^{-3} and $[C_s] = (5 \pm 3) \times 10^{16}$ cm^{-3} in Cz-Si. The

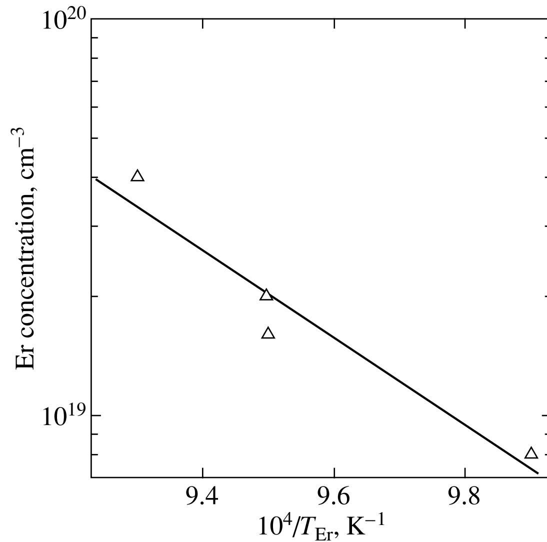

Fig. 1. Er concentration plotted vs. effusion cell temperature.

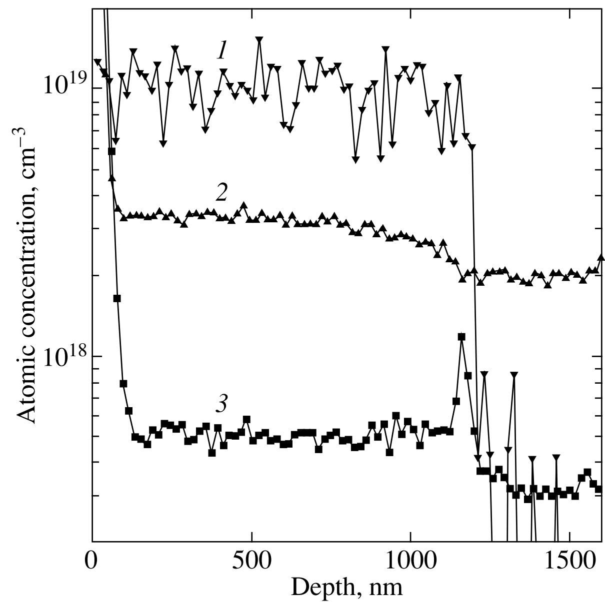

Fig. 2. Concentration profiles of (*1*) Er, (*2*) O, and (*3*) C impurities measured by SIMS.

concentration profiles of the Er, C, and O impurities were measured by secondary-ion mass spectrometry (SIMS) on a Cameca IMF 4F. Rutherford backscattering (RBS) of 231-keV protons in the random and channeling regimes was used to study the structural perfection of the epitaxial layers and the Er atom concentration. PL spectra were measured with a resolution of 7 nm at a temperature of 78 K. The visible radiation from a ~50-mW halogen lamp used to excite PL was mechanically chopped at a frequency of 36 Hz. The radiation emitted by a sample was collected by a lens and, on passing through an MDR-23 monochromator, detected by an InGaAs photodetector operating at 300 K.

3. RESULTS AND DISCUSSION

High structural perfection of the MBE-grown layers is indicated by the RBS data; indeed, the relative yield of scattered protons (the ratio between the numbers of counts in the channeling and random RBS operation modes for the channels beyond the surface peak) is at a level typical of Si single crystals. The dependence of the erbium atom concentration (measured using RBS) in MBE layers grown at a substrate temperature of 600°C on the effusion cell temperature is presented graphically in Fig. 1. The calculated activation energy derived from this dependence was ~2.2 eV. A similar value for the activation energy was found in [4], where MBE growth of Si : Er layers was performed at a substantially higher effusion cell temperature (800–1200°C).

Figure 2 displays SIMS concentration profiles of the Er, C, and O impurities in sample 167, which was MBE-grown at T_{Si} = 600°C and T_{Er} = 785°C. Note that the impurity concentrations [O] ≅ 2.0 × 10^{18} cm^{-3} and [C] ≅ 3.0 × 10^{17} cm^{-3} in the substrate are slightly higher than those accepted in the microelectronics industry. It is no wonder that the oxygen and carbon concentrations in substrates measured using SIMS and IR absorption are different, because the SIMS method determines the total concentration of an impurity, whereas IR absorption determines only the concentration of impurities in the silicon interstitial (O_i) and lattice site (C_s) positions. Oxygen and carbon could enter the epitaxial layer both from the gas medium in the growth chamber and from the silicon substrate. The factors responsible for the approximate 1.6-time increase in the concentration of these impurities in the Si : Er epitaxial layer as compared to the substrate are yet to be established.

Figure 3 (curve *1*) presents a PL spectrum of MBE-grown Si : Er sample 189 prepared at T_{Si} = 600°C and T_{Er} = 785°C. The PL spectrum is seen to be dominated by three peaks, namely, a peak at the wavelength of maximum intensity λ_m ≅ 1.542 μm deriving from Er^{3+} radiative transitions from the first excited state $^4I_{13/2}$ to the ground state $^4I_{15/2}$, a peak at λ_m ≅ 1.62 μm, and an edge luminescence peak with λ_m ≅ 1.13 μm. The maximum PL intensity in all our MBE-grown samples is observed to fall on the lines with λ_m = 1.542 μm. Similar Er-related spectra were produced by samples with implanted erbium and carbon ions [5, 6] or grown by sublimation MBE [7]. Note that the spectra of samples with implanted erbium and oxygen ions usually reveal Er–O-containing centers with λ_m = 1.537 μm [1]. The above SIMS data corroborate the formation of Er–C-containing optically active centers in the MBE-grown layers under study here.

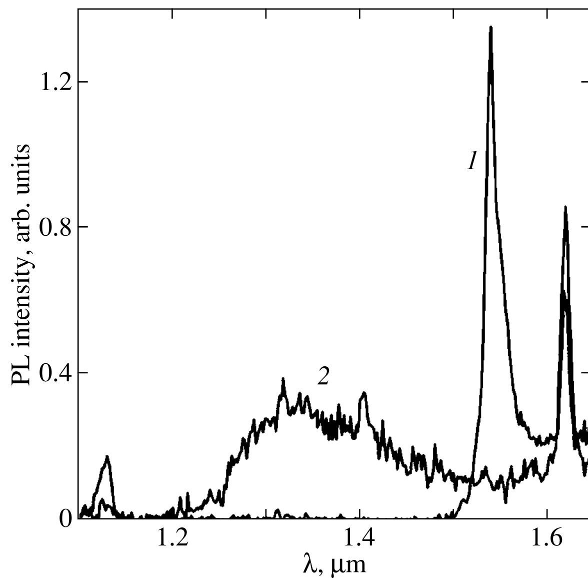

Fig. 3. PL spectra (*1*) of an MBE-grown Si : Er structure (T_{Si} = 600°C, T_{Er} = 785°C) and (*2*) of a Si : Ho implantation structure.

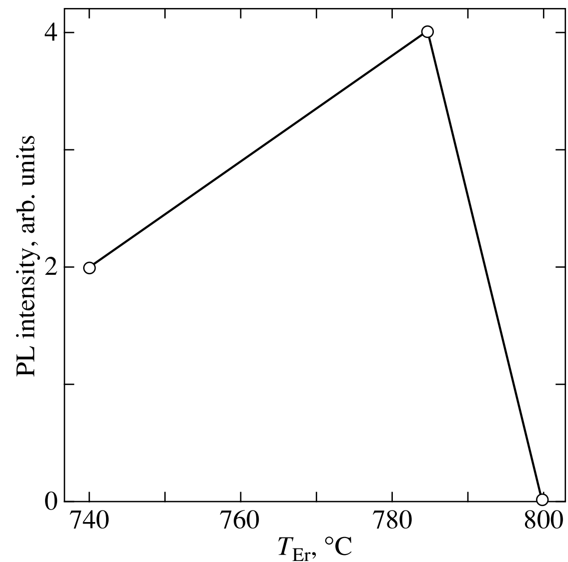

Fig. 4. Er-related PL line intensity plotted vs. erbium source temperature at fixed T_{Si} = 600°C.

The dependence of the PL intensity of the Er-related line on the erbium source temperature measured at a fixed substrate temperature T_{Si} = 600°C is displayed in Fig. 4. The intensity grows with the concentration of the rare-earth element to reach a maximum value at [Er] ~ 2×10^{19} cm^{-3} (T_{Er} = 785°C). As the erbium concentration is increased even further, no lines related to Er-containing centers or edge luminescence are observed in the PL spectrum. A TEM study of these samples revealed defects of a fairly unusual shape whose nature still remains to be established. The PL intensity of an Er-containing center in MBE-grown layers is comparable to that of an Er–O-containing center in Er- and O-implanted samples.

Figure 5 shows graphs relating the intensities of the three dominant lines in the PL spectra of the samples under study to the substrate temperature at a fixed erbium source temperature T_{Er} = 785°C. The fact that the PL edge intensity is independent of substrate temperature during epitaxial growth implies that the luminescence excitation level is the same in MBE-grown layers. The line at $\lambda_m \cong 1.62$ μm, referred to in the literature as the *P* line (or the 0.767-eV line), belongs to a center containing carbon and oxygen that forms after silicon annealing at ~450°C [8, 9]. The observed correlation between the Er-related and *P*-line intensities is an additional argument for the carbon impurity being directly involved in the formation of these centers. The *P* line was observed by us earlier in *n*-Cz-Si after implantation of holmium ions with energies E = 2.0 and 1.6 MeV to a dose $D = 1 \times 10^{14}$ cm^{-2} and of oxygen with E = 290 and 230 keV to a dose $D = 1 \times 10^{15}$ cm^{-2} and subsequent annealing at 620°C for 1 h (curve *2* in Fig. 3). After the epitaxial layer in the structure exhibiting a strong edge PL and the intense Er-related and *P* lines was removed, the Er-related line was not observed and the intensities of the other two lines remained almost the same. This suggests that photoluminescence of these two lines is excited primarily in the substrate.

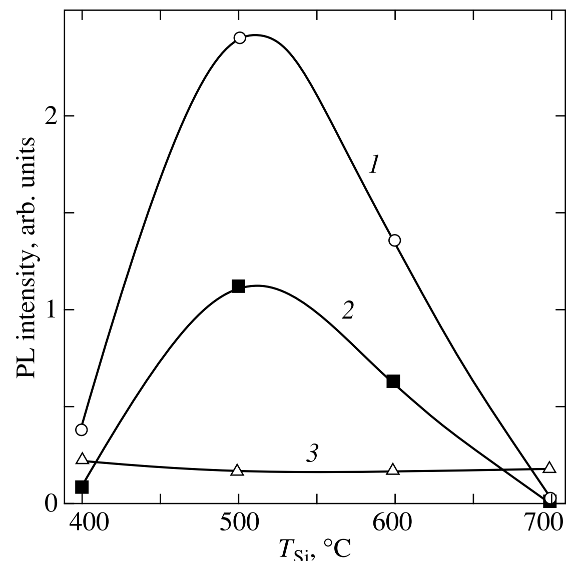

Fig. 5. PL line intensities at (*1*) $\lambda_m \cong 1.542$, (*2*) 1.62, and (*3*) 1.13 μm plotted vs. substrate temperature for fixed T_{Er} = 785°C.

4. CONCLUSIONS

A technique for fabricating light-emitting structures based on silicon layers doped by erbium in the course of MBE growth has been developed, and their properties have been studied. The activation energy as determined from the dependence of the erbium atom concentration in the epitaxial layer on the reciprocal temperature of the effusion cell containing metallic erbium was found to be ~2.2 eV. It was established that the epitaxial Si : Er layer becomes doped by carbon and oxygen impurities during MBE growth. This apparently favors the formation of Er-containing, optically active centers in the course of epitaxial growth of a Si : Er layer. The PL spectra of all samples are dominated by radiation of the Er-containing center peaking at a wavelength of 1.542 μm. The PL lines of edge luminescence and of the center containing carbon and oxygen impurities (the *P* line) are excited in the substrate.

ACKNOWLEDGMENTS

The authors are indebted to V.I. Vdovin for TEM studies of structural defects and to D.I. Kryzhkov for helpful discussions.

This study was supported in part by INTAS (project no. 2001-0194), the Russian Foundation for Basic Research (project nos. 02-02-16374, 04-02-16935), and the Department of Physical Sciences of the RAS (program “New Materials and Structures”).

REFERENCES

1. N. A. Sobolev, Fiz. Tekh. Poluprovodn. (St. Petersburg) **29**, 1153 (1995) [Semiconductors **29**, 595 (1995)].
2. DIN 50 438, Part 1 (1993).
3. ASTM F1391-92 (1992), p. 646.
4. H. Efeoglu, J. H. Evans, T. E. Jackman, B. Hamilton, D. C. Houghton, J. M. Langer, A. R. Peaker, D. Perovic, I. Poole, N. Ravel, P. Hemment, and C. W. Chen, Semicond. Sci. Technol. **8**, 236 (1993).
5. J. Michel, J. L. Benton, R. F. Ferrante, D. C. Jacobson, D. J. Eaglesham, E. A. Fitzgerald, Y.-H. Xie, J. M. Poate, and L. C. Kimerling, J. Appl. Phys. **70** (5), 2672 (1991).
6. F. Priolo, S. Coffa, G. Franzo, C. Spinella, A. Carnera, and B. Bellany, J. Appl. Phys. **74** (8), 4936 (1993).
7. V. G. Shengurov, S. P. Svetlov, V. Yu. Chalkov, E. A. Uskova, Z. F. Krasil’nik, B. A. Andreev, and M. V. Stepikhova, Izv. Ross. Akad. Nauk, Ser. Fiz. **64** (2), 353 (2000).
8. N. S. Minaev and A. V. Mudryi, Phys. Status Solidi A **68**, 561 (1981).
9. G. Davies, Phys. Rep. **176**, 176 (1989).

Translated by G. Skrebtsov

Physics of the Solid State, Vol. 47, No. 1, 2005, pp. 117–120. Translated from Fizika Tverdogo Tela, Vol. 47, No. 1, 2005, pp. 112–115.
Original Russian Text Copyright © 2005 by Sobolev, Denisov, Emel'yanov, Shek, Parshin.

PROCEEDINGS OF THE CONFERENCE "NANOPHOTONICS 2004"
(Nizhni Novgorod, Russia, May 2–6, 2004)

MBE-Grown Si : Er Light-Emitting Structures: Effect of Implantation and Annealing on the Luminescence Properties

N. A. Sobolev*, D. V. Denisov*, A. M. Emel'yanov*, E. I. Shek*, and E. O. Parshin**

**Ioffe Physicotechnical Institute, Russian Academy of Sciences, Politekhnicheskaya ul. 26, St. Petersburg, 194021 Russia*
e-mail: nick@sobolev.ioffe.rssi.ru
***Institute of Microelectronics and Automation, Russian Academy of Sciences, ul. Universitetskaya 21, Yaroslavl, 150007 Russia*

Abstract—Features appearing in the photo- and electroluminescence spectra of light-emitting structures based on MBE-grown Si : Er layers are studied. The luminescence properties of Si layers implanted by Er and O ions were used as a reference. The temperature quenching of the photoluminescence intensity of Er-containing centers in MBE-grown and implanted layers can be approximated adequately by the same functional relationships with equal activation energies but with preexponential factors differing by more than two orders of magnitude. It is shown that the electroluminescence of Er^{3+} ions can be increased by additional coimplantation of erbium and oxygen ions into MBE-grown light-emitting diode structures and subsequent annealing. After this treatment, the Er-containing centers continue to dominate the luminescence spectrum. © *2005 Pleiades Publishing, Inc.*

1. INTRODUCTION

Light-emitting structures based on Si : Er single-crystal structures are prepared using various modifications of the technology of molecular-beam epitaxy (MBE). The luminescence intensity of Er^{3+} ions can be increased if activators of optically active centers, namely, oxygen, carbon, or fluorine, are introduced into a layer during MBE. These impurities are usually introduced from the gas phase through a capillary built into the growth chamber. Earlier, we observed the effect of doping of the MBE layer by oxygen and carbon impurities without their purposeful admission into the growth chamber [1]. The goal of this work was to study the effect of implantation of oxygen and erbium ions and subsequent annealing on the luminescence properties of light-emitting structures based on Si : Er MBE-grown layers and to compare their properties with the characteristics of structures based on implanted Si : (Er,O) layers.

2. EXPERIMENTAL CONDITIONS

Si : Er layers were prepared by MBE in a SUPRA-32 (RIBER) setup on polished plates of Czochralski-grown *n*-Si (*n*-Cz-Si) with a (100)-oriented surface and an electrical resistivity $\rho = 4.5\ \Omega$ cm. A Si flux was obtained with an electron beam evaporator bombarding a target of *n*-type silicon grown through floating-zone melting (*n*-FZ-Si) with an electrical resistivity $\rho = 2\ \Omega$ cm. A flux of rare-earth atoms was produced by an effusion cell containing metallic Er. The epitaxial growth proceeded at a constant substrate temperature of 600°C, a deposition rate of 0.6 Å/s, and a residual gas pressure in the growth chamber of no greater than 8×10^{-9} Torr. To make the original surface as smooth as possible, a thin (100-Å-thick) buffer layer of undoped Si was preliminarily grown on it. The erbium source temperature was 785°C, which provided an erbium concentration of $\approx 1 \times 10^{19}$ cm^{-3}. Analyzing the dynamics of the reflection high-energy electron diffraction patterns revealed that, in the technological conditions chosen, the growth of Si : Er layers follows a two-dimensional pattern [1]. The layer thickness was 1.1 μm. The MBE-grown layers were *n*-type.

The *p*–*n* junctions were obtained by implanting boron ions with an energy $E = 40$ keV into Si : Er epitaxial layers to a dose $D = 5 \times 10^{15}$ cm^{-2}. Phosphorus ions with an energy $E = 80$ keV were implanted to a dose $D = 1 \times 10^{15}$ cm^{-2} into the rear side of the *n*-type substrates to produce a heavily doped n^+ layer. To anneal implantation defects and stimulate electrically active centers, the samples were subjected to heat treatment at 950°C for 0.5 h in a chlorine-containing atmosphere (CCA), which was actually a flow of oxygen with an admixture of 1 mol % carbon tetrachloride. Light-emitting diode mesa structures with an operating area of 3 mm^2 were fabricated by photolithography, aluminum deposition, and chemical etching of the *p*–*n* junction surface.

We studied the effect of additional implantation of oxygen ions with $E = 100$ keV and $D = 3 \times 10^{15}$ cm^{-2} into MBE-grown Si : Er layers and of subsequent isochronous annealing (for 0.5 h) at 600–800°C in argon

1063-7834/05/4701-0117$26.00 © 2005 Pleiades Publishing, Inc.

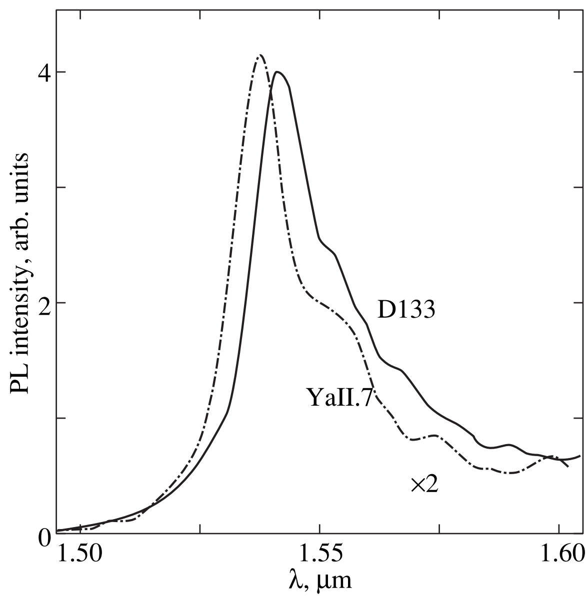

Fig. 1. PL spectra obtained with implanted (YaII.7) and MBE-grown (D133) Si : Er structures.

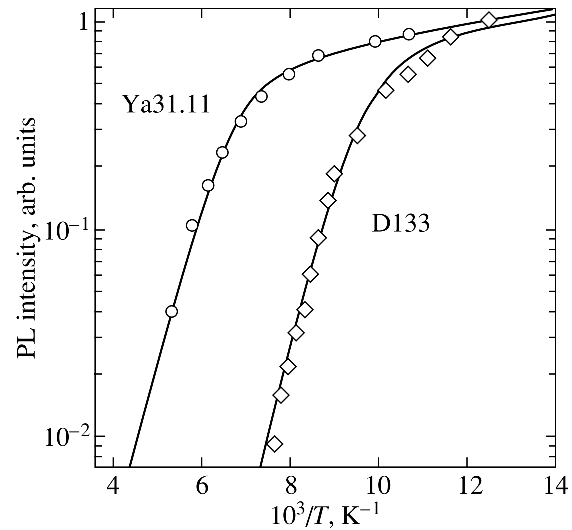

Fig. 2. Temperature dependence of the Er^{3+} ion PL intensity in implanted (Ya31.11) and MBE-grown (D133) samples.

on the photoluminescence (PL). We also studied the effect of additional implantation of erbium ions with $E = 2$ and 1.6 MeV and $D = 1 \times 10^{13}$ cm^{-2} and of oxygen with $E = 280$ and 220 keV and $D = 1 \times 10^{14}$ cm^{-2} into MBE-grown Er^{3+} layers of light-emitting diode structures and subsequent two-stage annealing (at 650 and 900°C) for 0.5 h in CCA on the electroluminescence (EL).

To better understand the processes involved in the formation of optically and electrically active centers and the mechanisms responsible for the excitation–de-excitation of rare-earth ions in MBE-grown layers, the properties of Er^{3+} layers prepared by MBE and ion implantation were compared. The Er^{3+}-implanted layers were grown on (100)-oriented p-Cz-Si substrates. Erbium ions with energy $E = 1.0$ MeV and dose $D = 1 \times 10^{14}$ cm^{-2} and with $E = 0.8$ MeV and $D = 1 \times 10^{13}$ cm^{-2} were implanted on a K2MV High-Voltage Engineering Europe setup at 300 K into substrates with $\rho = 1$ and 4.5 Ω cm, respectively. The implanted samples were annealed at 620–900°C for 0.5 h in CCA. After the annealing, the conduction in the implanted layers was observed to undergo $p \longrightarrow n$ conversion. The electron concentration in them was about an order of magnitude lower than the concentration of the introduced erbium ions.

PL and EL measurements were conducted at 78 and 80 K, respectively. The visible radiation from a ~50-mW halogen lamp used to excite PL was chopped mechanically at a frequency of 36 Hz. The injection EL was excited by current pulses applied at a frequency of 33 Hz, an amplitude of up to 500 mA, and a duration of 5 ms. The radiation from the sample was collected by a lens and, on passing through an MDR-23 monochromator, was measured with an InGaAs photodetector operating at 300 K.

3. RESULTS AND DISCUSSION

Figure 1 shows PL spectra obtained on implanted (YaII.7) and MBE-grown (D133) Er^{3+} structures. The YaII.7 sample was prepared on a (100)-oriented p-Si substrate with $\rho = 1$ Ω cm by implanting erbium ions with $E = 1$ MeV and $D = 1 \times 10^{14}$ cm^{-2} and annealing in CCA at 620°C over 0.5 h and then at 900°C over 0.5 h. The D133 sample was studied following epitaxial growth with no additional annealing. The structure of the optically active centers is seen to be different; indeed, the implanted sample is dominated by Er–O-containing centers with a peak in radiation at λ_m = 1.537 μm [2], and the MBE-grown sample, by Er–C-containing centers with λ_m = 1.542 μm [3, 4]. It is customarily accepted that the dominant lines derive from Er^{3+} transitions from the first excited state, $^4I_{13/2}$, to the ground state, $^4I_{15/2}$. The PL intensities of the Er-containing centers in the structures prepared by both methods were of about the same order of magnitude.

Figure 2 displays the temperature dependences of the PL intensity of Er-containing centers in the implanted (Ya31.11)) and MBE-grown (D133) samples. The Ya31.11 sample was prepared on a (100)-oriented p-Si substrate with $\rho = 4.5$ Ω cm by implanting erbium ions with $E = 0.8$ MeV and $D = 1 \times 10^{13}$ cm^{-2} and annealing in CCA at 900°C over 0.5 h. The temperature quenching of the PL intensity of Er-containing centers in the implanted and MBE structures can be fitted well by the following respective functional relations, which have equal activation energies but have

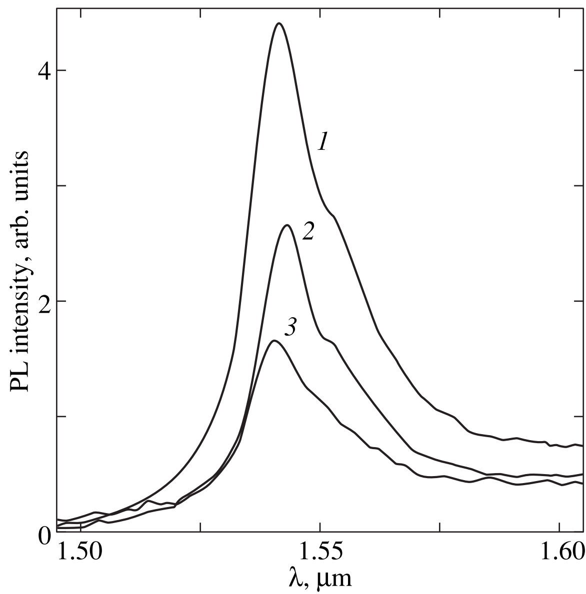

Fig. 3. PL spectra of MBE-grown Si : Er structures taken after implantation of oxygen ions and annealing at (*1*) 600, (*2*) 700, and (*3*) 800°C.

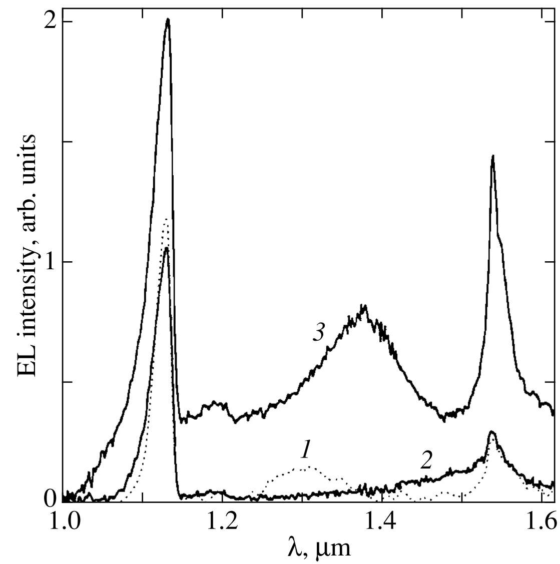

Fig. 4. EL spectrum of MBE-grown diode structures taken (*1*) before and (*2*, *3*) after implantation of Er and O ions and subsequent annealing at (*2*) 650 and (*3*) 900°C.

preexponential factors that differ by more than two orders of magnitude:

$$PL_{\text{impl}} = 1.4/[1 + 12\exp(-E_1/kT) + 1.3 \times 10^6 \exp(-E_2/kT)], \quad (1)$$

$$PL_{\text{MBE}} = 1.6/[1 + 18\exp(-E_1/kT) + 5.0 \times 10^8 \exp(-E_2/kT)], \quad (2)$$

where $E_1 = 22$ meV and $E_2 = 170$ meV. Similar relations for the temperature quenching of the PL intensity of Er-containing centers in Si : Er implanted and MBE-grown samples, as well as the PL intensity of Ho-containing centers in Si : Ho samples, were reported in [5–7].

Additional implantation of oxygen ions into MBE-grown Si : Er layers and annealing neither increase the PL intensity of Er-containing centers nor modify their structure (Fig. 3). Annealing at 600°C has almost no influence on the PL spectrum, including on the maximum line intensity. Increasing the annealing temperature brings about a decrease in the PL intensity (curves *2*, *3* in Fig. 3). A similar effect for MBE-grown structures was observed in [6], whereas additional implantation of oxygen ions into the Si : Er implanted layers followed by annealing was accompanied by an increase in the PL intensity of Er-containing centers [8].

Despite the rectifying pattern of the *I–V* characteristics, no well-developed breakdown of *p–n* junctions in MBE-grown light-emitting diodes could be reached (as opposed to the implanted structures). Therefore, Er^{3+} EL in MBE light-emitting diodes was observed only under forward bias (curve *1* in Fig. 4). Additional implantation of Er and O ions and two-stage annealing (at 650°C for 0.5 h and at 900°C for 0.5 h) are accompanied by an increase in the EL intensity of Er^{3+} ions and a change in the EL spectrum originating from the defects thus introduced but do not cause any modification in the structure of Er–C-containing centers (curves *2*, *3* in Fig. 4). Curve *1* was obtained at a current of 300 mA, and curves *2* and *3*, at 500 mA. In these conditions, saturation of the PL intensity of Er^{3+} ions is already observed.

4. CONCLUSIONS

The specific features of the luminescence spectra of MBE-grown Si : Er light-emitting structures have been studied. It was established that additional implantation of Er and O ions into MBE-grown light-emitting diode structures and annealing permit one to increase the Er^{3+} EL intensity while not affecting the structure of the dominant Er–C-containing centers.

ACKNOWLEDGMENTS

The authors are indebted to V.I. Vdovin, Yu.A. Nikolaev, and R.V. Tarakanova for their TEM study of structural defects, for performing post-implantation annealings, and for their assistance in forming the light-emitting structures.

This study was supported in part by INTAS (project no. 2001-0194), the Russian Foundation for Basic Research (project nos. 02-02-16374, 04-02-16935), and the Department of Physical Sciences of the RAS (program “New Materials and Structures”).

REFERENCES

1. N. A. Sobolev, D. V. Denisov, A. M. Emel'yanov, E. I. Shek, B. Ya. Ber, A. P. Kovarskiĭ, V. I. Sakharov, I. T. Serenkov, V. M. Ustinov, G. E. Cirlin, and T. V. Kotereva, Fiz. Tverd. Tela (St. Petersburg) **47** (1), 108 (2005) [Phys. Solid State **47**, 113 (2005)].
2. N. A. Sobolev, Fiz. Tekh. Poluprovodn. (St. Petersburg) **29**, 1153 (1995) [Semiconductors **29**, 595 (1995)].
3. F. Priolo, S. Coffa, G. Franzo, C. Spinella, A. Carnera, and B. Bellany, J. Appl. Phys. **74** (8), 4936 (1993).
4. V. G. Shengurov, S. P. Svetlov, V. Yu. Chalkov, E. A. Uskova, Z. F. Krasil'nik, B. A. Andreev, and M. V. Stepikhova, Izv. Ross. Akad. Nauk, Ser. Fiz. **64** (2), 353 (2000).
5. J. Palm, F. Gan, B. Zheng, J. Michel, and L. C. Kimerling, Phys. Rev. B **54** (24), 17603 (1996).
6. H. Efeoglu, J. H. Evans, T. E. Jackman, B. Hamilton, D. C. Houghton, J. M. Langer, A. R. Peaker, D. Perovic, I. Poole, N. Ravel, P. Hemment, and C. W. Chen, Semicond. Sci. Technol. **8**, 236 (1993).
7. N. A. Sobolev, A. M. Emel'yanov, R. N. Kyutt, and Yu. A. Nikolaev, Solid State Phenom. **69–70**, 371 (1999).
8. N. A. Sobolev, A. M. Emel'yanov, Yu. A. Kudryavtsev, R. N. Kyutt, M. I. Makovijchuk, Yu. A. Nikolaev, E. O. Parshin, V. I. Sakharov, I. T. Serenkov, E. I. Shek, and K. F. Shtel'makh, Solid State Phenom. **57–58**, 213 (1997).

Translated by G. Skrebtsov

Physics of the Solid State, Vol. 47, No. 1, 2005, pp. 121–124. Translated from Fizika Tverdogo Tela, Vol. 47, No. 1, 2005, pp. 116–119.
Original Russian Text Copyright © 2005 by Timoshenko, Shalygina, Lisachenko, Zhigunov, Teterukov, Kashkarov, Kovalev, Zacharias, Imakita, Fujii.

PROCEEDINGS OF THE CONFERENCE "NANOPHOTONICS 2004"
(Nizhni Novgorod, Russia, May 2–6, 2004)

Erbium Ion Luminescence of Silicon Nanocrystal Layers in a Silicon Dioxide Matrix Measured under Strong Optical Excitation

V. Yu. Timoshenko*, O. A. Shalygina*, M. G. Lisachenko*, D. M. Zhigunov*, S. A. Teterukov*, P. K. Kashkarov*, D. Kovalev, M. Zacharias***, K. Imakita****, and M. Fujii******

**Moscow State University, Vorob'evy gory, Moscow, 119992 Russia*
e-mail: vtim@vega.phys.msu.su
***Munich Technical University, Physics Department E16, Garching, 85747 Germany*
****Max-Planck-Institut für Mikrostrukturphysik, Halle, 06120 Germany*
*****Kobe University, Department of EEE, Kobe, 657-8501 Japan*

Abstract—The photoluminescence (PL) spectra and kinetics of erbium-doped layers of silicon nanocrystals dispersed in a silicon dioxide matrix (nc-Si/SiO_2) are studied. It was found that optical excitation of nc-Si can be transferred with a high efficiency to Er^{3+} ions present in the surrounding oxide. The efficiency of energy transfer increases with increasing pumping photon energy and intensity. The process of Er^{3+} excitation is shown to compete successfully with nonradiative recombination in the nc-Si/SiO_2 structures. The Er^{3+} PL lifetime was found to decrease under intense optical pumping, which implies the establishment of inverse population in the Er^{3+} system. The results obtained demonstrate the very high potential of erbium-doped nc-Si/SiO_2 structures when used as active media for optical amplifiers and light-emitting devices operating at a wavelength of 1.5 μm. © *2005 Pleiades Publishing, Inc.*

1. INTRODUCTION

Interest in the photoluminescence (PL) of the Er^{3+} erbium ion in silicon matrices can be traced to the need to develop silicon optoelectronic devices capable of operating at a wavelength of 1.5 μm (the $^4I_{13/2} \longrightarrow {}^4I_{15/2}$ transitions in the inner Er^{3+} 4*f* shell), which falls at the minimum of absorption in fiber-optic communication lines [1, 2]. A number of related problems remain, however, unsolved. For instance, if crystalline silicon (*c*-Si) is employed as a matrix, the PL of Er^{3+} ions is observed to undergo strong temperature quenching caused by their nonradiative de-excitation through reverse energy transfer to the matrix [3]. As a result, the PL quantum yield of *c*-Si : Er at room temperature turns out to be very low. The temperature quenching of the PL of erbium-doped amorphous hydrogenated silicon (*a*-Si : H) at a wavelength of 1.5 μm is substantially weaker [4]. Analysis of the Er^{3+} PL kinetics in *a*-Si : H revealed that the energy of electron–hole pairs is transferred to ions in sufficiently short times (submicrosecond scale), which provides a high efficiency of excitation [5–7]. Because of nonradiative energy losses, however, the PL intensity of Er^{3+} ions in *a*-Si : H(Er) is still not high enough to warrant application of this material in light-emitting devices.

Among the promising approaches to overcoming these difficulties is to use erbium to dope the insulating matrix containing layers of silicon nanocrystals (nc-Si) [8–11]. It should be noted that, although the wavelength of erbium PL is practically independent of the nature of the matrix (because the "operating" 4*f* shell of the Er^{3+} ion is screened by outer electronic shells), the ion excitation efficiency can be controlled by properly varying the properties of the matrix, for instance, its band-gap width and/or the density of electronic states of the defects and impurities it contains [1, 3]. This control can easily be reached in nc-Si structures, because the effective band-gap width of nanocrystals increases with a decrease in their size [12, 13]. In addition, Si nanocrystals favor simultaneously high carrier localization in small spatial regions near the Er^{3+} ions and sufficiently long lifetimes (hundreds of microseconds) of electronic excitation [12, 13]. In this case, the energy of a photoexcited electron–hole pair can efficiently be transferred to the Er^{3+} ion. Indeed, erbium-doped nc-Si layers in the SiO_2 matrix reveal intense and stable PL of the Er^{3+} ions even at room temperature [9, 10]. This suggests as the most promising candidates layers of quasi-ordered silicon nanocrystals in multilayered nc-Si/SiO_2 structures, which are characterized by a high controllability of the size of the nanocrystals and their separation [11].

This communication reports on a study of the PL spectra and kinetics of erbium-doped samples containing silicon nanocrystals in the silicon oxide matrix at different excitation levels and temperatures. The data obtained enabled us to gauge the possibility of reaching an inverse population in the system of erbium ions in such structures.

1063-7834/05/4701-0121$26.00 © 2005 Pleiades Publishing, Inc.

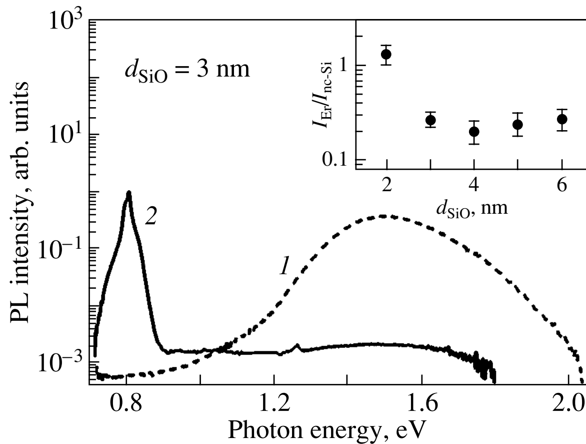

Fig. 1. PL spectra of undoped (*1*) and Er-doped (*2*) samples of series 1 with nc-Si size $d = 3$ nm. Inset: the ratio of integrated intensities of Er^{3+} PL in doped samples to excitonic PL in undoped structures plotted vs. nanocrystal size. Excitation: $E_{exc} = 3.6$ eV, $T = 300$ K.

2. SAMPLES AND EXPERIMENTAL TECHNIQUES

The nc-Si/SiO_2 samples studied by us were obtained by reactive evaporation (with SiO and SiO_2 layers deposited successively on a *c*-Si substrate) [14] (series 1) and by rf magnetron sputtering of solid targets [15] (series 2). The samples were thermally annealed to form nanocrystals. The nanocrystals in each sample had a spread in size d to within 0.5 nm, and their size varied from one sample to another from 2 to 6 nm. Er^{3+} ions were implanted in some samples of series 1 to a dose of $\sim 2 \times 10^{15}$ cm^{-2} (average concentration $N_{Er} \sim 10^{20}$ cm^{-3}). The samples of series 2 contained 0.1 at. % Er ($N_{Er} \sim 10^{19}$ cm^{-3}).

The PL was excited by a cw He–Cd laser (photon energy $\hbar\omega = 2.8$ eV), a pulsed N_2 laser ($\hbar\omega = 3.7$ eV, pulse duration $\tau \sim 10$ ns, pulse energy $E \leq 1$ μJ, pulse repetition frequency $\nu \sim 100$ Hz), and a pulsed copper-vapor laser ($\hbar\omega = 2.4$ and 2.1 eV, $\tau \sim 20$ ns, $E \leq 10$ μJ, $\nu \sim 12$ kHz). The laser beams were focused on a sample to a spot 1.5 mm in diameter. The PL spectra and kinetics were measured with computerized spectrometers equipped with a PM tube, a CCD camera, and an InGaAs photodiode with a time constant of ~0.5 ms. The spectra were corrected to allow for the spectral response of the system.

3. EXPERIMENTAL RESULTS AND DISCUSSION

Figure 1 displays typical PL spectra of undoped and Er-doped samples of series 1. The excitonic PL spectrum of undoped structures is a broad band (with an FWHM of ~0.3 eV) peaking at 1.3–1.6 eV [14]. Note that the PL quantum yield of the samples under study reached as high as 1%, which indicates a fairly low efficiency of nonradiative recombination as compared to that typical of other kinds of silicon structures [16]. Incorporation of Er^{3+} ions into the samples under study brought about suppression of the excitonic PL (by a factor of $\sim 10^2$) and the appearance of a strong PL band near 0.8 eV characteristic of the $^4I_{13/2} \longrightarrow {}^4I_{15/2}$ intracenter transitions in Er^{3+}. At the same time, the PL efficiency of Er^{3+} ions in the matrix of homogeneous amorphous SiO_2 was extremely low for the nonresonant excitation employed [14]. Thus, the Er^{3+} ions in our samples are excited not in a direct optical process but rather through energy transfer from excitons in nc-Si to the Er ion. The quantum yield ratio of the Er^{3+} to excitonic PL may serve as a quantitative characteristic of this transfer. The inset to Fig. 1 plots the dependence of this ratio on the nc-Si size. We can see that this ratio is 0.3–0.4 for structures with $d = 3$–6 nm and increases to 2 for $d = 2$ nm. In the latter case, the number of photons emitted by a nc-Si/SiO_2 : Er sample is twice that emitted by an undoped structure. This suggests partial suppression of the nonradiative recombination channel in nc-Si as a result of competition with the transfer of optical excitation to the Er^{3+} ions. This process is more likely to occur in samples with smaller nanocrystals because the high-energy Er^{3+} states become involved [17].

Note that, as follows from low-temperature PL spectra [17], suppression of the excitonic PL originating from phonon-mediated energy transfer from nc-Si to Er^{3+} ions is less than 0.1% of the total level of suppression of the excitonic PL caused by incorporation of the Er^{3+} ions. This suggests the operation of a substantially stronger energy transfer mechanism, for instance, of resonant Coulomb interaction between excitons in nc-Si and nearby Er^{3+} ions in SiO_2.

We studied the dependence of the PL intensity of nc-Si/SiO_2 : Er structures on the intensity of optical pumping by pulsed and cw laser radiation. Figure 2 displays such dependences obtained under excitation by nanosecond-scale pulses of a N_2 laser. The intensity of excitonic PL in undoped samples is seen to deviate from a linear relationship with increasing pump power, which may be assigned to an enhanced probability of Auger recombination in nc-Si at high pumping levels. In doped samples, however, this dependence remains linear, which suggests a weakened Auger recombination rate. The latter is most likely due to an interplay with a competing process of energy transfer from nanocrystals to the Er^{3+} ions. Note that, under the excitation conditions used, the PL intensity of Er^{3+} ions also follows a linear course.

Figure 3 displays the intensity of the excitonic and erbium PL as functions of cw pump intensity in the form of a graph. The excitonic PL in undoped samples exhibits a sublinear dependence for $I_{exc} > 0.1$ W/cm^2. However, in Er^{3+}-doped samples, the excitonic PL does not saturate and even becomes superlinear for $I_{exc} > 0.02$ W/cm^2, which suggests suppression of nonradia-

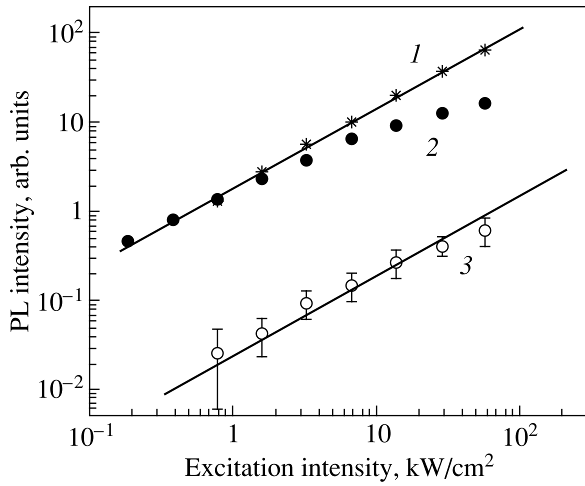

Fig. 2. PL intensities of Er^{3+} ions (*1*) and of silicon nanocrystals in nc-Si/SiO_2 (*2*) and nc-Si/SiO_2 : Er samples (*3*) (series 1) plotted vs. N_2 laser pumping level (E_{exc} = 3.6 eV, τ_{exc} = 10 ns). Solid lines show linear relations.

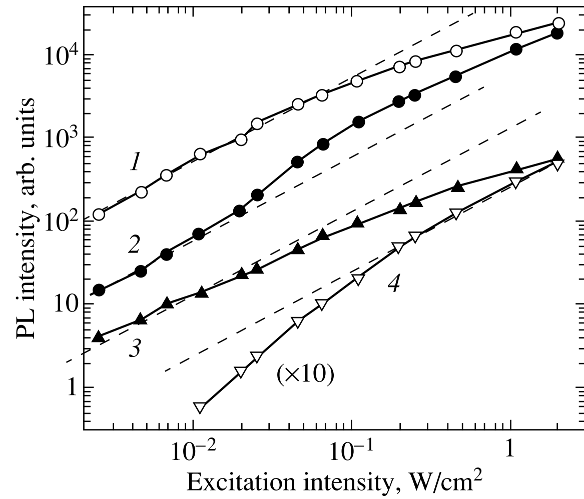

Fig. 3. PL intensity of a sample of series 1 (d = 3 nm) plotted vs. pump intensity of a He–Cd laser (E_{exc} = 2.8 eV): *1*—nc-Si (1.6 eV), *2*—nc-Si : Er (1.6 eV), *3*—nc-Si : Er (0.8 eV), *4*—nc-Si : Er (1.26 eV). Dashed lines are linear relations. T = 10 K.

tive processes for excitons (Auger recombination and energy transfer to the Er^{3+} ions). As for the PL intensity at 0.8 eV, it exhibits a tendency toward saturation. This behavior of the erbium PL may be caused by two factors. First of all, an increase in the number of excited ions enhances the probability of cooperative upconversion [18], which gives rise to a sublinear dependence of the PL intensity deriving from the $^4I_{13/2} \longrightarrow {}^4I_{15/2}$ transitions and superlinear behavior for the $^4I_{11/2} \longrightarrow {}^4I_{15/2}$ transitions. As is evident from Fig. 3 (curve *4*), the PL intensity for transitions from the second excited state, $^4I_{11/2} \longrightarrow {}^4I_{15/2}$ (1.26 eV), is linear in the pump intensity region of interest to us here. Thus, upconversion in our samples cannot bring about saturation of the Er^{3+} PL intensity.

A more probable cause of erbium PL saturation could be transition of most of the Er^{3+} ions to an excited state, i.e., the onset of inverse population in this system. To test this assumption, we calculated the ratio of the concentration of Er^{3+} ions in the first excited state, N_1, to their total concentration, N_{Er}. To do this, we measured the kinetics of the rise and decay in Er^{3+} PL intensity in a nc-Si/SiO_2 : Er sample (series 2) pumped by a square pulse from a quasi-cw copper-vapor laser (Fig. 4). Fitting the PL rise and decay curves by single-exponential functions permitted us to determine the corresponding times for different pump intensity levels (inset to Fig. 4). Using coupled rate equations (see, e.g., [18]), one can express the relative ion concentration in the first excited state as

$$N_1/N_{Er} = 1 - \tau_{rise}/\tau_{decay}, \quad (1)$$

where τ_{rise} and τ_{decay} are the PL rise and decay times, respectively. Figure 5 plots the dependence of the relative concentration N_1/N_{Er} calculated from Eq. (1) on excitation intensity. We can see that inverse population ($N_1/N_{Er} > 0.5$) is attained at excitation intensities in excess of 0.1 W/cm². Note that a higher pump intensity is required to establish inverse population in samples of series 1 because of the higher values of N_{Er}. The pumping level needed to attain inverse population decreased with increasing pump photon energy and decreasing sample temperature. The establishment of inverse population was paralleled by a shortening of the time τ_{decay}, which may be attributed to the ion lifetime in the

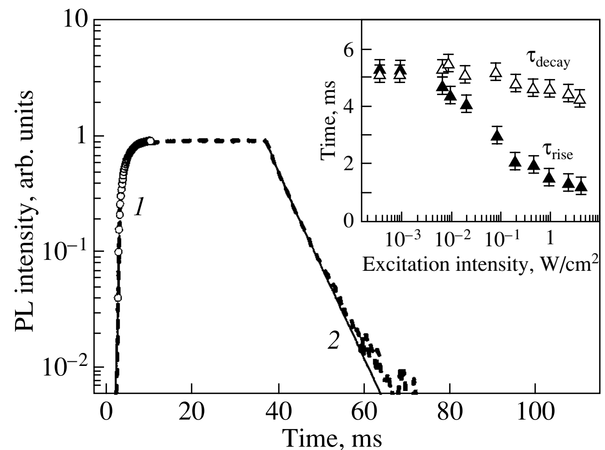

Fig. 4. Erbium PL kinetics (0.8 eV) of nc-Si/SiO_2 : Er structures of series 2 obtained under copper-vapor laser excitation with 40-ms pulses (dashed line), with the pulse rise and decay fitted by the functions $1 - \exp(-t/\tau_{rise})$ (*1*) and $\exp(-t/\tau_{decay})$ (*2*), respectively. The inset gives the dependences of the PL rise and decay times on pumping intensity. E_{exc} = 2.14 and 2.43 eV, T = 300 K.

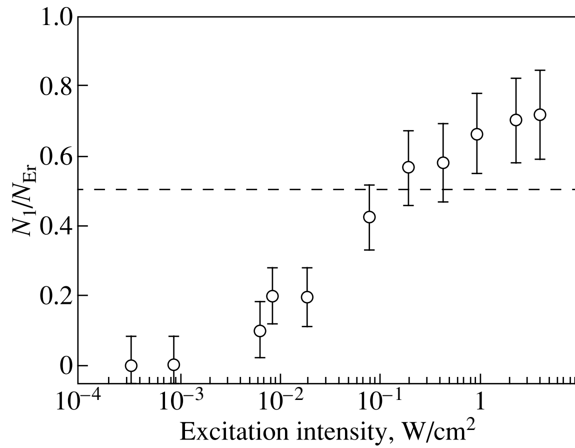

Fig. 5. Relative concentration of excited Er^{3+} ions (N_1/N_{Er}) in a nc-Si/SiO_2 : Er sample (series 2) plotted vs. pumping intensity. E_{exc} = 2.14 and 2.43 eV, T = 300 K. Dashed line identifies the N_1/N_{Er} = 0.5 level (establishment of erbium inverse population).

excited state decreasing because of the increasing contribution of induced optical transitions. Another cause of the shortening of the time τ_{decay} could be reverse energy transfer from Er^{3+} to nc-Si, a process that becomes possible when an ion transfers to an upper excited state due to double excitation. Further studies are needed to shed light on the nature of this effect. We note, however, that the contribution of induced transitions in Er^{3+} can obviously be increased by properly optimizing the sample parameters, as well as by forming waveguide structures.

4. CONCLUSIONS

To sum up, our studies have shown that undoped nc-Si/SiO_2 structures have a fairly high quantum yield of excitonic PL in the visible and near IR spectral regions. Erbium-doped structures exhibit strong PL at 1.5 μm due to efficient energy transfer from excitons in nc-Si to the Er^{3+} ions in SiO_2. At high optical excitation levels, the process of energy transfer can compete successfully with nonradiative Auger recombination in nc-Si. It has been established that inverse population can be attained in the Er^{3+} system under strong optical pumping, which, combined with the high efficiency of the Er^{3+} PL, may stimulate considerable interest in the development of optical amplifiers and light-emitting devices intended for operation at a wavelength of 1.5 μm.

ACKNOWLEDGMENTS

This study was supported by the Russian Foundation for Basic Research (project nos. 02-02-17259, 03-02-16647), CRDF (project no. RE2-2369), and INTAS (project no. 03-51-6486) and was conducted at the Center of Collective Use, Moscow State University.

REFERENCES

1. G. S. Pomrenke, P. B. Klein, and D. W. Langer, *Rare Earth Doped Semiconductors* (MRS, Pittsburgh, 1993), Mater. Res. Soc. Symp. Proc., Vol. 301.
2. K. Iga and S. Kinoshita, *Progress Technology for Semiconductors Lasers* (Springer, Berlin, 1996), Springer Ser. Mater. Sci., Vol. 30.
3. F. Priolo, G. Franzo, S. Coffa, A. Polman, S. Libertino, and D. Carey, J. Appl. Phys. **78** (6), 3874 (1995).
4. W. Fuhs, I. Ulber, G. Weiser, M. S. Bresler, O. Guseva, A. N. Kuznetsov, V. Kh. Kudoyarova, E. I. Terukov, and I. N. Yassievich, Phys. Rev. B **56** (15), 9545 (1997).
5. E. A. Konstantinova, B. V. Kamenev, P. K. Kashkarov, V. Yu. Timoshenko, V. Kh. Kudoyarova, and E. I. Terukov, J. Non-Cryst. Solids **282** (2–3), 321 (2001).
6. B. V. Kamenev, V. Yu. Timoshenko, E. A. Konstantinova, V. Kh. Kudoyarova, E. I. Terukov, and P. K. Kashkarov, J. Non-Cryst. Solids **299–302**, 668 (2002).
7. B. V. Kamenev, V. I. Emel'yanov, E. A. Konstantinova, P. K. Kashkarov, V. Yu. Timoshenko, C. Chao, V. Kh. Kudoyarova, and E. I. Terukov, Appl. Phys. B **74** (2), 151 (2002).
8. A. J. Kenyon, C. E. Chryssou, C. W. Pitt, T. Shimizu-Iwayama, D. E. Hole, N. Sharma, and C. J. Humphreys, J. Appl. Phys. **91** (1), 367 (2002).
9. K. Watanabe, M. Fujii, and S. Hayashi, J. Appl. Phys. **90** (9), 4761 (2001).
10. M. Schmidt, M. Zacharias, S. Richter, P. Fisher, P. Veit, J. Bläsing, and B. Breeger, Thin Solid Films **397**, 211 (2001).
11. M. Zacharias, J. Heitmann, R. Shcholz, U. Kahler, M. Schmidt, and J. Bläsing, Appl. Phys. Lett. **80** (4), 661 (2002).
12. D. J. Lockwood, Z. H. Liu, and J. M. Baribeau, Phys. Rev. Lett. **76** (3), 539 (1996).
13. A. G. Cullis, L. T. Canham, and P. D. J. Calcott, J. Appl. Phys. **82** (3), 909 (1997).
14. P. K. Kashkarov, M. G. Lisachenko, O. A. Shalygina, V. Yu. Timoshenko, B. V. Kamenev, M. Schmidt, J. Heitmann, and M. Zacharias, Zh. Éksp. Teor. Fiz. **124** (6), 1255 (2003) [JETP **97**, 1123 (2003)].
15. S. Takeoka, M. Fujii, and S. Hayashi, Phys. Rev. B **62** (24), 16820 (2000).
16. S. Coffa, G. Franzo, and F. Priolo, MRS Bull. **23** (4), 25 (1998).
17. V. Yu. Timoshenko, M. G. Lisachenko, O. A. Shalygina, P. K. Kashkarov, J. Heitmann, M. Schmidt, and M. Zacharias, Appl. Phys. Lett. **84** (14), 2512 (2004).
18. D. Pacifici, G. Franzo, F. Priolo, F. Iacona, and L. Dal Negr, Phys. Rev. B **67**, 245301 (2003).

Translated by G. Skrebtsov

Physics of the Solid State, Vol. 47, No. 1, 2005, pp. 125–128. Translated from Fizika Tverdogo Tela, Vol. 47, No. 1, 2005, pp. 120–123.
Original Russian Text Copyright © 2005 by Shmagin, Remizov, Obolenskiĭ, Kryzhkov, Drozdov, Krasil'nik.

PROCEEDINGS OF THE CONFERENCE "NANOPHOTONICS 2004"

(Nizhni Novgorod, Russia, May 2–6, 2004)

Er^{3+} Ion Electroluminescence of p^+-Si/n-Si : Er/n^+-Si Diode Structure under Breakdown Conditions

V. B. Shmagin, D. Yu. Remizov, S. V. Obolenskiĭ, D. I. Kryzhkov, M. N. Drozdov, and Z. F. Krasil'nik

Institute of the Physics of Microstructures, Russian Academy of Sciences, Nizhni Novgorod, 603950 Russia

e-mail: shm@ipm.sci-nnov.ru

Abstract—The electroluminescence (EL) of p^+-Si/n-Si : Er/n^+-Si light-emitting diode structures in which a thin lightly doped n-Si : Er layer ($N_D \sim 10^{16}$ cm^{-3}) is sandwiched between heavily doped silicon layers is studied. It is shown that the Er^{3+} ion EL intensity reaches a maximum in structures operating in a regime of mixed-type breakdown in the space-charge region. The dark-region width is determined ($d_{dark} \sim 0.015$–0.020 μm) within which the electrons attain an energy sufficient to excite Er^{3+} ions. © *2005 Pleiades Publishing, Inc.*

1. INTRODUCTION

Impact excitation of Er^{3+} ions realized in Si : Er/Si light-emitting diode (LED) structures operating under the conditions of p–n junction breakdown has made it possible to significantly suppress nonradiative Auger relaxation of excited Er^{3+} ions involving free carriers and to obtain intense electroluminescence (EL) at wavelengths $\lambda \sim 1.5$ μm (the ${}^4I_{13/2} \longrightarrow {}^4I_{15/2}$ transition in the Er^{3+}-ion 4f shell) at room temperature [1, 2].

Earlier, we showed that, in diode structures with a "thick" base (p^+-Si/n^+-Si : Er-type structures in which the thickness of the diode base, i.e., the n^+-Si : Er layer, exceeds the width of the space-charge region (SCR) under the breakdown conditions), the intensity and excitation efficiency of the Er^{3+} ion EL reach a maximum in the regime of mixed-type SCR breakdown. If either the tunneling- or avalanche breakdown mechanism becomes dominant, the EL intensity and excitation efficiency decrease at a fixed drive current [3]. In this work, we study another type of Si : Er-based LED structures, so-called diode structures with a punctured base. These are structures of the p^+-Si/n-Si : Er/n^+-Si type in which a thin, lightly doped n-Si : Er layer is sandwiched between heavily doped silicon layers. In such structures, as the reverse bias voltage increases, the SCR edge will have reached the n-Si : Er/n^+-Si interface before the p–n junction breakdown occurs. The breakdown voltage for such structures is determined to a greater extent by the base thickness than by the impurity concentration [4]. These structures are of interest because the p–n junction breakdown conditions in them can be controlled by varying the thickness of the lightly doped n layer, which makes it possible to vary (via the breakdown conditions) the EL properties of the structures.

2. EXPERIMENTAL TECHNIQUE

The LED structures studied in this work were grown on p-Si : B (100) substrates with a resistivity of 10 Ω cm using the sublimation molecular-beam epitaxy [5]. The free-carrier concentration in the n-Si : Er layer was $\sim 1 \times 10^{16}$ cm^{-3}, the layer thickness was varied from 0.01 to 0.5 μm, the growth temperature was ~580°C, and the Er concentration was $\sim 2 \times 10^{18}$ cm^{-3}. The carrier concentrations in the p^+-Si and n^+-Si layers were 5×10^{18} and 1×10^{20} cm^{-3}, respectively. LEDs were fabricated using the conventional mesa technology; the mesa area was ~2.5 mm^2, with 70% of this area being transparent to the generated light. Note that all diode structures under study were grown in the same growth experiment. The technique used to grow epitaxial structures (including Si : Er/Si LED structures) in which the epitaxial-layer thickness and the carrier concentration vary smoothly along the length of the structure was described in [6].

The EL spectra were taken in the range 1.0–1.6 μm with a resolution of 6 nm by using an MDR-23 grating monochromator and an infrared InGaAs photodetector cooled to liquid-nitrogen temperature. EL spectra were excited and detected using pulsed drive-current modulation (pulse duration, 4 ms; repetition frequency, ~40 Hz; amplitude up to 500 mA) and a lock-in technique. The current–voltage (I–U) characteristics of the diodes were measured in pulsed mode. The breakdown voltage U_{br} was determined by extrapolating the linear portion of the I–U curve at reverse bias to its intersection with the voltage axis.

3. EXPERIMENTAL RESULTS AND DISCUSSION

Figure 1 shows the evolution of the voltage U_{br} (and the breakdown mode) with the n-Si : Er layer thickness d for p^+-Si/n-Si : Er/n^+-Si LEDs. As expected, a

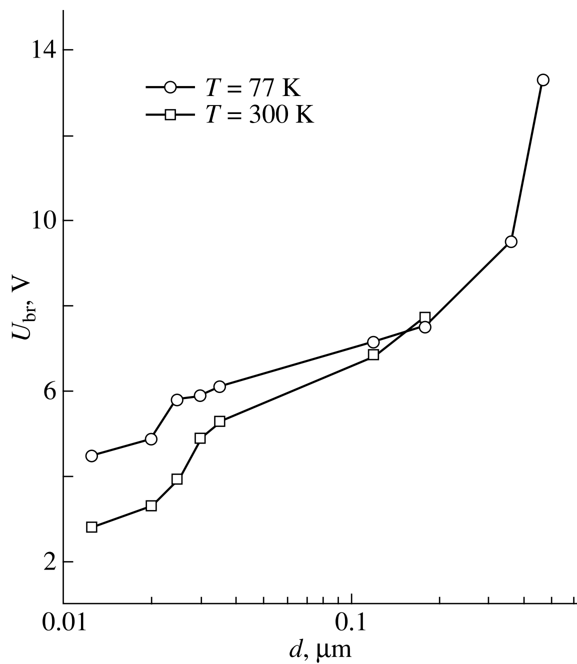

Fig. 1. Breakdown voltages of p^+-Si/n-Si : Er/n^+-Si LEDs as a function of n-Si : Er layer thickness at temperatures of 77 and 300 K.

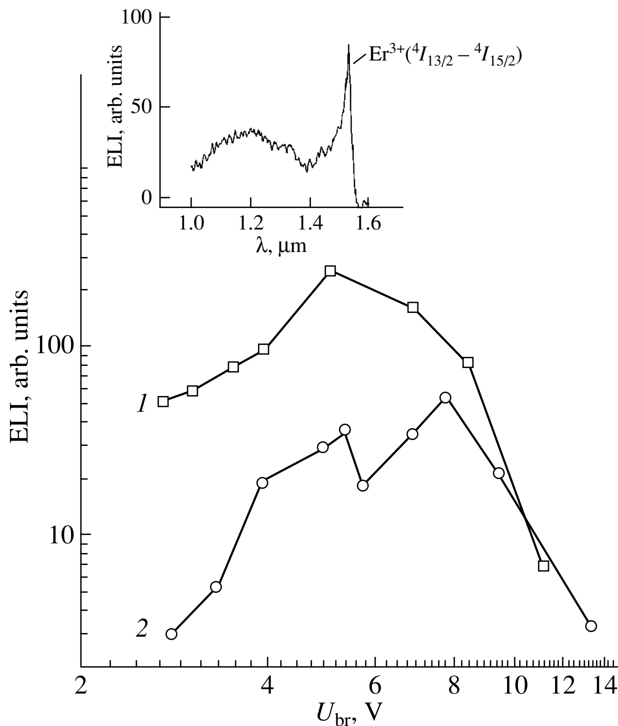

Fig. 2. Er^{3+} ion EL intensity as a function of breakdown voltage for LEDs of the (*1*) p^+-Si/n^+-Si : Er and (*2*) p^+-Si/n-Si : Er/n^+-Si types. The inset shows the EL spectrum of a p^+-Si/n-Si : Er/n^+-Si LED with the mixed breakdown mechanism taken at 300 K. The drive current density is ~8 A/cm^2.

decrease in the n-Si: Er layer thickness at a fixed carrier concentration in the layer causes the breakdown voltages U_{br}^{77} and U_{br}^{300} to decrease. Furthermore, the relationship between U_{br}^{77} and U_{br}^{300} indicates that the breakdown mechanism changes as the n-Si : Er layer thickness decreases. We note that, even for such a low donor concentration in the diode base ($N_D \sim 10^{16}$ cm^{-3}), the tunneling breakdown mode dominates ($U_{br}^{77} > U_{br}^{300}$) at a diode base of a few tens of nanometers. As the diode base increases to 0.1 μm, a change from the tunneling to a mixed-type breakdown mode ($U_{br}^{77} \approx U_{br}^{300}$) occurs. This change can be explained by the fact that the probability of avalanche development and, hence, the avalanche contribution to the breakdown current increase with the base thickness.

Based on the relationship between the values of U_{br}^{77} and U_{br}^{300}, we did not detect a pronounced avalanche breakdown in the LEDs under study with maximum n-Si : Er layer thicknesses (Fig. 1). However, we observed the formation of separate microplasmas on the LED surface in the breakdown regime, whose number increased with the n-Si : Er layer thickness and the breakdown voltage U_{br} in LEDs exhibiting a mixed breakdown. This behavior suggests that the avalanche component of the diode breakdown current gradually increases with the n-Si : Er layer thickness.

The EL spectrum of an LED with the mixed breakdown mechanism is shown in the inset to Fig. 2. This spectrum is typical of LEDs exhibiting a mixed breakdown and consists of a fairly narrow Er EL line (the $^4I_{13/2} \longrightarrow {^4I_{15/2}}$ transition in the Er^{3+}-ion 4f shell) and a wide band of so-called hot EL, which is associated with radiative relaxation of carriers accelerated by the electric field in the SCR. Figure 2 also shows the dependences of the Er EL intensity (ELI) on breakdown voltage U_{br} for a p^+-Si/n-Si : Er/n^+-Si LED studied in this work and a p^+-Si/n^+-Si : Er LED studied by us earlier [3]. The ELI(U_{br}) dependences for both types of LEDs are similar in character. In both cases, as U_{br} increases and the change from the tunneling to the mixed breakdown mechanism occurs, the EL intensity increases, which is due to an increase in the EL excitation efficiency and in the emitting volume determined by the product of the mesa area times the SCR thickness (in p^+-Si/n-Si : Er/n^+-Si structures, the SCR thickness is dictated by the thickness of the n-Si : Er layer). In the case of a mixed breakdown, ELI(U_{br}) reaches a maximum and then decreases noticeably with increasing U_{br}, which we associate with the development of a microplasma breakdown.

Note that the Er EL intensity in p^+-Si/n-Si : Er/n^+-Si structures is noticeably lower than that in p^+-Si/n^+-Si : Er structures. In our opinion, the reason for this distinction is as follows. An electron accelerated by the electric

field in the SCR of the reverse-biased diode interacts most efficiently with the optically active Er^{3+} ions if its kinetic energy satisfies the condition $W_{th1} < W < W_{th2}$, where $W_{th1} \approx 0.8$ eV is the Er excitation energy (the ${}^4I_{13/2} \longrightarrow {}^4I_{15/2}$ transition in the Er^{3+}-ion $4f$ shell) and $W_{th2} \sim 1.5E_G$ (E_G is the band-gap width in silicon) is the energy at which intense avalanching begins in the SCR of the p–n junction. At $W < W_{th1}$, the electron energy is not sufficiently high to excite an Er^{3+} ion, and at $W > W_{th2}$ the interaction between the electron and the silicon lattice becomes essentially inelastic, because the electron loses its energy by generating electron–hole pairs. Since the Si atomic concentration is five to six orders of magnitude greater than that of optically active erbium centers, the silicon crystal lattice becomes an efficient sink for hot electrons at $W > W_{th2}$ and the excitation efficiency of Er ions decreases.

Preliminary calculations show that the flow of carriers with energies in the range $W_{th1} < W < W_{th2}$ forms mainly in the weak-field region; this region is absent in p^+-Si/n-Si : Er/n^+-Si structures (Fig. 3) but is present in p^+-Si/n^+-Si : Er structures, though fairly narrow. The interaction between hot carriers and an array of Er ions is more efficient in so-called tunneling transit-time structures of the p^+-Si/n^+-Si/n-Si : Er type, in which the electric field strength and the thicknesses of the strong- and weak-field regions can be varied separately over wide limits (Fig. 3c). The narrow p^+-Si/n^+-Si junction (the strong-field region) operates in the tunneling breakdown mode and acts as an injector of hot carriers with energies within the range $W_{th1} < W < W_{th2}$. The n-Si : Er layer is a weak-field region, which is needed to excite Er ions and compensate for the energy loss due to scattering by optical phonons.

An important characteristic for the impact excitation of Er^{3+} ions is the thickness d_{dark} of the "dark" region, where the carriers are accelerated by the field of the reverse-biased p–n junction and attain an energy W_{th1}. In this work, we determined d_{dark} in the p^+-Si/n-Si : Er/n^+-Si structure as the minimum thickness of the n-Si : Er layer for which the Er^{3+} ion EL is still observed. In Fig. 4, the thick line corresponds to the range where the erbium EL intensity decreases with a decrease in the n-Si : Er layer thickness. By extrapolating this line to zero erbium EL intensity, one can estimate d_{dark}. For the p^+-Si/n-Si : Er/n^+-Si structures studied in this work, we obtained $d_{dark} \sim 0.015$–0.02 μm.

The thickness d_{dark} for the structures studied was also estimated theoretically to be approximately 0.01 μm, which agrees fairly well with the experimental data. In the calculations, the carriers were assumed to be generated (with a zero initial velocity) at the plane of the metallurgic p–n junction. The critical field in the SCR for the onset of tunneling breakdown was taken to be $\sim 8 \times 10^5$ V/cm [7]. Allowance was also made for inelas-

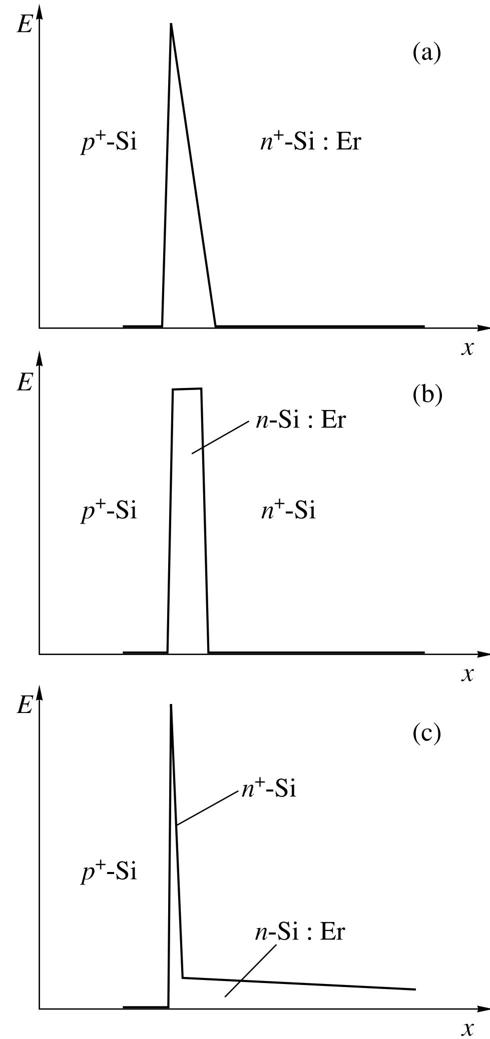

Fig. 3. Electric-field distribution over the space-charge region in LEDs of the (a) p^+-Si/n^+-Si : Er, (b) p^+-Si/n-Si : Er/n^+-Si, and (c) p^+-Si/n^+-Si/n-Si : Er types.

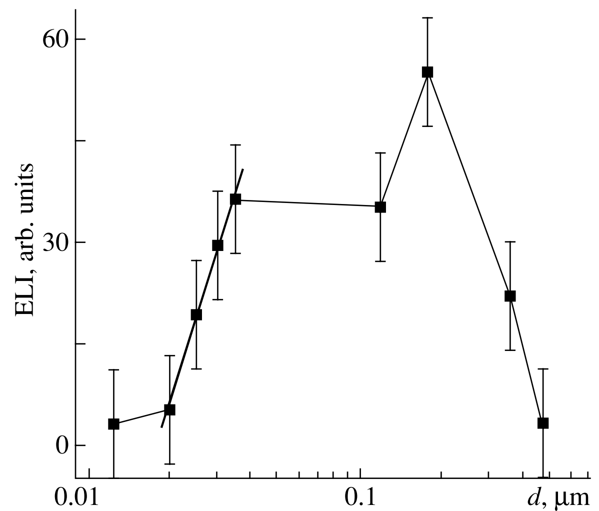

Fig. 4. Er^{3+} ion EL intensity as a function of n-Si : Er layer thickness for a LED of the p^+-Si/n-Si : Er/n^+-Si type measured at 300 K. The drive current density is ~8 A/cm^2.

tic scattering of the accelerated carriers by acoustic and optical phonons.

Note that our estimate of d_{dark} differs from that obtained in [8] for p^+-Si/n^+-Si : Er structures (~0.045 μm). In our opinion, this discrepancy is due to the different field distributions in the active region of the structures (Fig. 3). Indeed, the almost uniform field in the p^+-Si/n-Si : Er/n^+-Si structures studied in this work accelerates the carriers more effectively than the linearly decreasing field in the p^+-Si/n^+-Si : Er structures studied in [8].

4. CONCLUSIONS

The breakdown mode in a p^+-Si/n-Si : Er/n^+-Si structure with a pronounced puncture of the lightly doped n-Si : Er base ($N_D \sim 10^{16}$ cm^{-3}) is determined by the base thickness. As the base thickness increases from 0.01 to 0.1 μm, a change from the tunneling ($U_{br}^{77} > U_{br}^{300}$) to the mixed breakdown mechanism ($U_{br}^{77} \approx U_{br}^{300}$) is observed. The Er^{3+} ion EL intensity reaches a maximum in structures operating under the conditions of a mixed breakdown. The thickness of the dark region within which the electrons attain a energy sufficient to excite Er^{3+} ions has been estimated to be $d_{dark} \sim 0.015$–0.02 μm.

ACKNOWLEDGMENTS

The authors are grateful to V.P. Kuznetsov and V.N. Shabanov (RPTI, NNSU, Nizhni Novgorod) for helpful discussions and V.P. Kuznetsov for preparing the light-emitting structures.

This study was supported by the Russian Foundation for Basic Research (project nos. 02-02-16773, 04-02-17120) and INTAS (grant nos. 01-0194, 03-51-6486).

REFERENCES

1. G. Franzo, F. Priolo, S. Coffa, A. Polman, and A. Carnera, Appl. Phys. Lett. **64** (17), 2235 (1994).
2. N. A. Sobolev, A. M. Emel'yanov, and K. F. Shtel'makh, Appl. Phys. Lett. **71** (14), 1930 (1997).
3. V. B. Shmagin, D. Yu. Remizov, Z. F. Krasil'nik, V. P. Kuznetsov, V. N. Shabanov, L. V. Krasil'nikova, D. I. Kryzhkov, and M. N. Drozdov, Fiz. Tverd. Tela (St. Petersburg) **46** (1), 110 (2004) [Phys. Solid State **46**, 109 (2004)].
4. S. Sze, *Physics of Semiconductor Devices*, 2nd ed. (Wiley, New York, 1981; Mir, Moscow, 1984), Chap. 1.
5. V. P. Kuznetsov and R. A. Rubtsova, Fiz. Tekh. Poluprovodn. (St. Petersburg) **34** (5), 519 (2000) [Semiconductors **34**, 502 (2000)].
6. E. N. Morozova, V. B. Shmagin, Z. F. Krasil'nik, A. V. Antonov, V. P. Kuznetsov, and R. A. Rubtsova, Izv. Ross. Akad. Nauk, Ser. Fiz. **67** (2), 283 (2003).
7. V. I. Gaman, *Physics of Semiconductor Devices* (Tomsk. Gos. Univ., Tomsk, 1989) [in Russian].
8. M. Markmann, E. Neufeld, A. Sticht, K. Brunner, and G. Abstreiter, Appl. Phys. Lett. **78** (2), 210 (2001).

Translated by Yu. Epifanov

Physics of the Solid State, Vol. 47, No. 1, 2005, pp. 129–132. Translated from Fizika Tverdogo Tela, Vol. 47, No. 1, 2005, pp. 124–127.
Original Russian Text Copyright © 2005 by Yurasova, Antipov, Ermolaev, Cherkasov, Lopatina, Chesnokov, Ilyina.

PROCEEDINGS OF THE CONFERENCE "NANOPHOTONICS 2004"
(Nizhni Novgorod, Russia, May 2–6, 2004)

Novel Polymer Nanocomposites with Giant Dynamical Optical Nonlinearity

I. V. Yurasova*, O. L. Antipov, N. L. Ermolaev**, V. K. Cherkasov***, T. I. Lopatina***, S. A. Chesnokov***, and I. G. Ilyina******

** Nizhni Novgorod State University, pr. Gagarina 23, Nizhni Novgorod, 603950 Russia*
e-mail: irene_yurasova@mail.ru
*** Institute of Applied Physics, Russian Academy of Sciences, ul. Ul'yanova 46, Nizhni Novgorod, 603950 Russia*
**** Razuvaev Institute of Organometallic Chemistry, Russian Academy of Sciences, ul. Tropinina 49, Nizhni Novgorod, 603950 Russia*
***** Moscow State University, Vorob'evy gory, Moscow, 119992 Russia*

Abstract—The giant optical nonlinearity of a novel organic nanocomposite based on a conducting polymer, namely, poly(9-vinylcarbazole), and quinone derivatives as a charge photogenerator is investigated. The change in the refractive index of a thin polymer film (60 μm thick) is determined to be $\Delta n = -7.3 \times 10^{-3}$. The inference is made that the origin of the optical nonlinearity is associated with the difference between the polarizabilities of the quinone molecule and the quinone radical anion formed under exposure to laser radiation. The optical nonlinearity is examined using two methods: (i) the self-action of a Gaussian beam in a layer of the material and (ii) *Z*-scan measurements of a thin film at a wavelength of 633 nm. These nanocomposite materials can serve as active media in diverse applications, including image processing, high-density optical information storage, and phase conjugation. *© 2005 Pleiades Publishing, Inc.*

1. INTRODUCTION

In recent years, increased interest has been expressed by researchers in the nonlinear optical properties of organic polymer nanocomposites, because these materials hold considerable promise, in particular, for use in the storage and processing of optical information and in many other fields of engineering [1–3]. Organic materials are characterized by a number of attractive and unique features, such as a high nonlinear optical susceptibility, structural flexibility, simplicity of treatment, and a relatively low cost. Furthermore, owing to their significant advantages over inorganic media, organic materials are very promising and quite competitive from the standpoint of application in modern systems of optical communication. In this respect, the design and study of novel polymer nanocomposites that will exhibit nonlinear optical and electro-optical properties and be suitable for a wide range of practical applications are important problems in nonlinear optics.

In our previous work [4], we investigated the inertial optical nonlinearity of photorefractive polymer nanocomposites based on a conducting polymer, namely, poly(9-vinylcarbazole), and fullerenes C_{70} and C_{60}. An explanation was offered for the mechanism responsible for the observed nonlinear variation in the refractive index of these materials. According to this mechanism, the optical nonlinearity is associated with the dynamical transformation of fullerene molecules into radical anions under exposure to optical beams from a helium–neon laser operating at a wavelength of 633 nm. Moreover, a number of optical experiments were performed with the aim of determining the magnitude and sign of the optical nonlinearity.

The purpose of this work was to investigate the optical nonlinearity of organic polymer nanocomposite materials with a similar composition in which molecules belonging to the quinone class (rather than fullerene molecules) act as a photosensitive component. The optical nonlinear response was examined using a standard *Z*-scan technique and self-action of a Gaussian laser beam in a layer of the material.

2. EXPERIMENTAL INVESTIGATION INTO THE SELF-ACTION OF LASER BEAMS IN FILMS

According to the mechanism of self-focusing of laser radiation, which was proposed earlier in [4], an organic polymer nanocomposite material should contain a photosensitive donor–acceptor pair with specific properties. Irradiation of the organic polymer nanocomposite material should result in efficient electron transfer from the donor component to the acceptor component. Moreover, the photointeraction between components of the donor–acceptor pair should lead only to electron transfer without subsequent chemical reaction between the components of this pair or the quantum yield of the chemical reaction should be minimum. Let us now consider a donor–acceptor pair con-

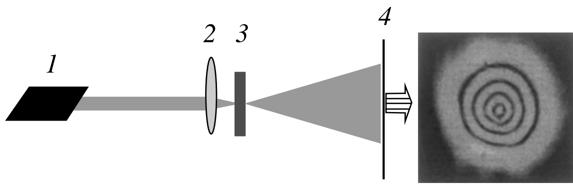

Fig. 1. Schematic diagram illustrating the observation of the interaction of a laser beam with a layer of the material: (*1*) helium–neon laser, (*2*) lens with a focal distance F = 5.5 cm, (*3*) cell, and (*4*) screen.

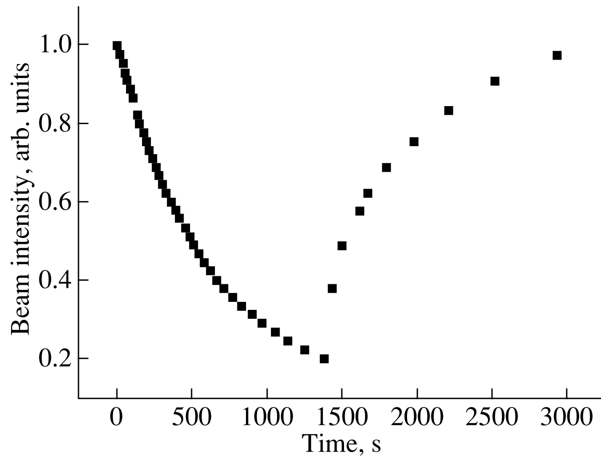

Fig. 2. Characteristic kinetics of the formation and relaxation of a nonlinear lens. The optical field is switched off at an instant of time t = 1380 s.

sisting of *p*-chloranil and poly(9-vinylcarbazole) under the above conditions. In principle, these compounds can enter into the photochemical reaction of hydrogen transfer with the formation of new compounds and, correspondingly, with a decrease in the content of the components of the initial pair. The hydrogen phototransfer reaction involves two stages, namely, (i) electron transfer and (ii) proton transfer. The free energy of electron transfer ΔG_e [5] for this pair of reactants was estimated as $\Delta G_e \sim -0.77$ eV (in the calculation, the electrochemical oxidation potential of poly(9-vinylcarbazole) was taken to be equal to that of ethylcarbazole, i.e., 1.12 V [6]). It is known that, in this case, the rate constant of electron phototransfer between reactants is maximum [5, 7]. On the other hand, the rate constant for the reaction of photoreduction of *p*-chloranil at this value of the free energy ΔG_e should be insignificant [8]. In other words, the photointeraction between *p*-chloranil and poly(9-vinylcarbazole), for the most part, should be reduced to reversible electron transfer without subsequent chemical reaction and these compounds can be used as the main components of the desired nanocomposite.

The organic nanocomposite material studied in this work consisted of the following components: poly(9-vinylcarbazole) serving as a conducting matrix, *p*-chloranil serving as a photosensitizer, and a mixture of ethylcarbazole with phenyltrimethoxysilane serving as plasticizers (in a percentage ratio of 41.5 : 3.0 : 55.5%, respectively). For experiments, samples in the form of 60- to 100-μm-thick films were prepared from a solution in toluene. These films were placed between two glass plates.

The self-defocusing effect in the nonlinear films under investigation was observed using a weakly focused Gaussian beam from a continuous-wave helium–neon laser operating at wavelength λ = 633 nm and at an initial power of 15 mW (Fig. 1). The propagation of the Gaussian laser beam under conditions of strong focusing brought about the formation of an aberration nonlinear lens in the far-field region; to put it differently, there arose a characteristic distribution of the optical field intensity in the form of alternating bright and dark fringes (see Fig. 1). This fact is decisive evidence that the organic polymer nanocomposite studied is characterized by a nonlinear response. In our case, a stable pattern consisting of thirteen fringes was observed when the laser beam was focused by a lens with focal distance F = 5.5 cm. The characteristic time required for the formation of a nonlinear lens was found to be inversely proportional to the intensity of the writing beam. This is a distinguishing feature of the optical nonlinearity which is governed primarily by a photoexcitation mechanism. Figure 2 illustrates the kinetics of the formation and relaxation of the optical nonlinearity in the organic polymer nanocomposite under investigation. The experimental results demonstrate that the lens observed in our case is not a thermal lens, because the time of its relaxation is considerably longer than the thermal diffusion time τ_T of the polymer in a film of thickness l. The thermal diffusion time τ_T is defined by the following relationship: $\tau_T = l^2/4\chi$, where χ is the thermal diffusivity of the polymer matrix. This time was estimated as $\tau_T \approx 25$ ms for $l \approx 0.1$ mm and $\chi \approx 10^{-3}$ cm^2/s.

3. *Z*-SCAN MEASUREMENTS OF THE OPTICAL NONLINEARITY OF A FILM

The magnitude and sign of the optical nonlinearity were determined by a standard *Z*-scan method using a thin film. This experimental technique consists in determining the constant of optical nonlinearity from the dependence of the intensity of a laser beam passed through a nonlinear film on the position of the film (or cell) with respect to the focal point of the lens [9].

In our experiments, the polymer film was moved in the *Z* direction along the focal waist (Fig. 3) and the beam intensity was measured in the far-field region at the axis as a function of the film position with respect to the focal point of the lens (Fig. 4).

The nonlinear response of the organic nanocomposite was evaluated under the assumption that the optical nonlinearity of the film is related to the optical field and, hence, obeys the relationship $\Delta n = n_2 I$. Moreover,

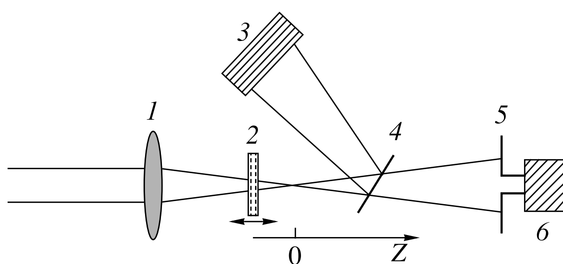

Fig. 3. Schematic diagram of a *Z*-scan experimental setup: (*1*) lens with a focal distance $F = 11$ cm, (*2*) cell, (*3*, *6*) photodetectors, (*4*) beam splitter, and (*5*) pinhole.

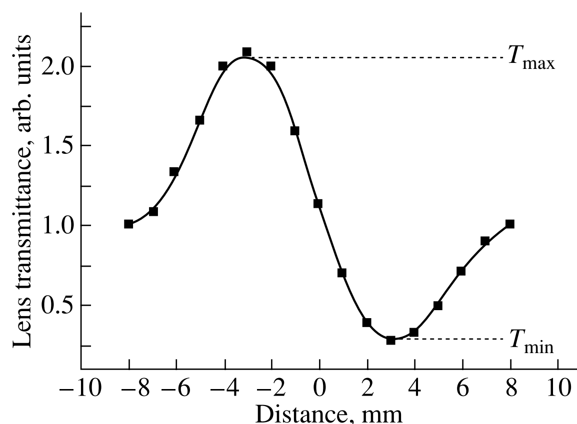

Fig. 4. Experimental *Z*-scan curve.

we ignored the small change in the absorption coefficient $\Delta\alpha$ of the medium, even though this change could lead to an additional modulation of the amplitude over the cross section of the optical beam (it is easy to demonstrate that the contribution from this effect to the nonlinear refraction of the optical beam is insignificant as compared to the contribution from the nonlinear change in the refractive index of the material under the condition $\Delta\alpha \ll \Delta nk$, where k is the wave number). For a local nonlinearity of this type, the *Z*-scan data are adequately described in terms of the self-focusing theory. Therefore, the small change in the refractive index Δn of the medium can be determined from the relationship

$$\Delta n = \Delta T/(0.4(1-S)^{0.27} k L_{\text{eff}}). \tag{1}$$

Here, S is the transmittance of the recording aperture (i.e., the ratio between the total radius of the limiting aperture at the axis and the radius of the optical beam), $L_{\text{eff}} = [1 - \exp(-\alpha l)]/\alpha$ is the effective length of the nonlinear interaction, α is the absorption coefficient of the medium, and $\Delta T = T_{max} - T_{min}$ is the change in the normalized transparency of the lens. The quantity ΔT is defined as the difference between the transmittances (the ratios between the powers of the optical beam passed through the pinhole at the axis and the total power of the beam passed through the nonlinear film) at the extreme points in the experimental *Z*-scan curve. With knowledge of the beam intensity at the axis and the experimentally measured quantity ΔT, it is possible to determine the nonlinear refractive index n_2.

The estimate obtained from relationship (1) for the maximum change in the refractive index of the studied sample with the use of the parameters known from our experiment was found to be $\Delta n = -7.3 \times 10^{-3}$. The negative sign of Δn indicates that the organic polymer nanocomposite is characterized by a defocusing nonlinearity.

4. CONCLUSIONS

The experimentally observed self-defocusing of the laser beam in the polymer film allows us to make the inference that the nanocomposite containing poly(9-vinylcarbazole), plasticizers, and sensitizing *p*-chloranil possesses strong optical nonlinearity. The revealed effect has defied explanation in terms of both the photorefractive nonlinearity (because the mixture used does not contain components characterized by an electro-optical response) and the thermal nonlinearity (the relaxation time of the lens is substantially longer than the thermal diffusion time of the polymer in a film of specified thickness). No nonlinear change in the refractive index of the sample due to photochemical processes occurred during measurements, because the formation of new stable chemical compounds was not revealed in the course of our experiments. Therefore, from analyzing the results of the above investigation, we can conclude that the strong optical nonlinearity found in similar polymer nanocomposites has a photochromic nature and can be associated with the difference between the polarizabilities of the *p*-chloranil molecule and the *p*-chloranil radical anion formed under exposure to laser radiation.

The mechanism of the optical nonlinearity can be described as follows. The introduction of *p*-chloranil into a poly(9-vinylcarbazole) solution in toluene leads to a drastic change in the color of the solution. The absorption spectra of the mixture exhibit a broad band that is extended over the entire visible range and has a maximum at wavelength $\lambda = 530$ nm. A similar band is not observed in the absorption spectra of individual solutions of *p*-chloranil and poly(9-vinylcarbazole). This band can be attributed to the charge-transfer complex formed by *p*-chloranil and poly(9-vinylcarbazole). Irradiation in the wavelength range corresponding to the band of the charge-transfer complex results in the formation of a radical ion pair that consists of a quinone radical anion and a poly(9-vinylcarbazole) radical cation. It should be noted that the change observed in the refractive index of various compounds upon excitation of molecules with different polarizabilities in the ground and excited states is a well-known effect (see, for example, [10]).

The magnitude of the optical nonlinearity of the photosensitive quinone-containing polymer composites under investigation is no less than that of the majority of similar media [11]. Undeniably, the main disadvantage of the aforementioned materials is the degradation of the polymer film. This process can be precluded only by careful hermetic sealing. At the same time, the quinone-containing polymer nanocomposites with a giant nonlinear optical susceptibility seem to be very promising materials for use in devices of optical data processing (for example, for isolating a signal against the background of random fluctuating noise).

REFERENCES

1. N. Peyghambarian, S. Marder, Y. Koike, and A. Persoons, IEEE J. Sel. Top. Quantum Electron. **7** (5), 757 (2001).
2. A. Kost, L. Tutt, M. B. Klein, T. K. Dougherty, and W. E. Elias, Opt. Lett. **18**, 334 (1993).
3. Y. Zhang, T. Wada, and H. J. Sasabe, Mater. Chem. **8**, 809 (1998).
4. I. V. Yurasova and O. L. Antipov, Opt. Commun. **224** (4–6), 329 (2003).
5. H. Leonhardt and A. Weller, Ber. Bunsenges. Phys. Chem. **67**, 791 (1963).
6. C. K. Mann and K. K. Barnes, *Electrochemical Reactions in Nonaqueous Systems* (Marcel Dekker, New York, 1970; Khimiya, Moscow, 1974).
7. P. P. Levin and V. A. Kuz'min, Usp. Khim. **56** (4), 527 (1987).
8. S. A. Chesnokov, G. A. Abakumov, V. K. Cherkasov, and M. P. Shulygina, Dokl. Akad. Nauk **385** (6), 780 (2002).
9. A. P. Sukhorukov, Soros. Obraz. Zh. **5**, 85 (1996).
10. V. S. Butylkin, A. E. Kaplan, Yu. G. Khronopulo, and E. I. Yakubovich, *Resonance Interactions of Light with a Substance* (Nauka, Moscow, 1977) [in Russian].
11. *Nonlinear Optical Properties of Organic Molecules and Crystals*, Ed. by D. S. Chemla and J. Zyss (Academic, New York, 1987).

Translated by O. Borovik-Romanova

Physics of the Solid State, Vol. 47, No. 1, 2005, pp. 13–17. Translated from Fizika Tverdogo Tela, Vol. 47, No. 1, 2005, pp. 17–21.
Original Russian Text Copyright © 2005 by Tetelbaum, Gorshkov, Kasatkin, Mikhaylov, Belov, Gaponova, Morozov.

PROCEEDINGS OF THE CONFERENCE "NANOPHOTONICS 2004"
(Nizhni Novgorod, Russia, May 2–6, 2004)

Effect of Coalescence and of the Character of the Initial Oxide on the Photoluminescence of Ion-Synthesized Si Nanocrystals in SiO_2

D. I. Tetelbaum*, O. N. Gorshkov*, A. P. Kasatkin*, A. N. Mikhaylov*, A. I. Belov*, D. M. Gaponova, and S. V. Morozov****

** Physico-Technical Research Institute, Nizhni Novgorod State University, pr. Gagarina 23/3, Nizhni Novgorod, 603950 Russia*
e-mail: Tetelbaum@phys.unn.ru

*** Institute for Physics of Microstructures, Russian Academy of Sciences, Nizhni Novgorod, 603950 Russia*
e-mail: dmg@ipm.sci-nnov.ru

Abstract—The photoluminescence intensity (PLI) related to Si nanocrystals in a SiO_2 : nc-Si system synthesized by ion implantation is studied experimentally and theoretically as a function of the Si+ ion dose at various annealing temperatures T_{ann} (1000–1200°C). The dose corresponding to the maximum PLI is found to decrease with increasing T_{ann}. These data are explained in terms of a model taking into account the coalescence of neighboring nanocrystals and the dependence of the probability of radiative recombination of quantum dots on their size. It is found that, when silicon oxide is grown in a wet atmosphere, the photoluminescence spectrum contains an additional band (near 850 nm), which is related to shells around the nanocrystals. This band weakens abrupily after high-temperature annealing in an oxidizing atmosphere (air). *© 2005 Pleiades Publishing, Inc.*

1. INTRODUCTION

The system of Si nanocrystals (NCs) in a SiO_2 matrix (SiO_2:nc-Si) has been extensively studied, since it is promising for the creation of next-generation light-emitting and memory devices based on silicon quantum dots. Ion implantation is one of the most convenient methods for making such a system. Although numerous studies have been performed that deal with this system, a number of questions related to the physics of its formation and operation remain open. One of these questions is the dependence of the photoluminescence intensity (PLI) on the silicon dose Φ and the postimplantation annealing temperature T_{ann}. The authors of [1, 2] found that, at fixed T_{ann}, the PLI depends nonmonotonically on Φ; more specifically, the PLI first increases and then drops as the dose increases. At relatively low T_{ann} (~1000°C), this dependence was explained as follows: the NC concentration increases with the excess-silicon density; at a high NC concentration, NCs partially overlap, the mean inclusion size increases, and (according to theory) the probability of radiative transitions (oscillator strength) decreases. However, at higher values of T_{ann} that intensify silicon diffusion in SiO_2, coalescence (Ostwald ripening, OR) rather than mechanical overlapping of the inclusions is dominant [3]. In this case, small inclusions decompose to feed larger ones.

As applied to the evolution of the SiO_2 : nc-Si system during annealing, OR was theoretically considered in [4]. However, that work does not contain a quantitative analysis of the effect of OR on the dose dependences of PLI at various values of T_{ann}. Moreover, the calculations were based on certain assumptions. For example, the authors of [4] assumed that the excess Si was entirely in the form of Si–Si dimers even before annealing and that the attachment of Si atoms to nanocrystals and their "evaporation" into the matrix are quasi-steady-state processes. These assumptions are disputable.

Another important question is the effect of the character of the initial SiO_2 matrix on the photoluminescence (PL) spectra. Ordinarily, thermal oxide films grown in a dry–wet–dry or wet–dry cycle are applied. In this case, a PL band with a single maximum at 800 ± 50 nm forms upon annealing at $T_{ann} \geq 1000$°C. However, a comprehensive analysis of the spectra indicates that this band is asymmetric (see, e.g., [5]); the band decomposition reveals a long-wavelength peak near 900 ± 50 nm. This peak has not been discussed in the literature. In [1, 6, 7], we also detected similar PL bands when studying SiO_2 films grown in a dry–wet–dry cycle. However, in the case of SiO_2 grown in a wet atmosphere, we revealed a pronounced two-mode PL structure and the long-wavelength peak (850–900 nm) was comparable to or even higher in intensity than the peak in the region 750–800 nm.

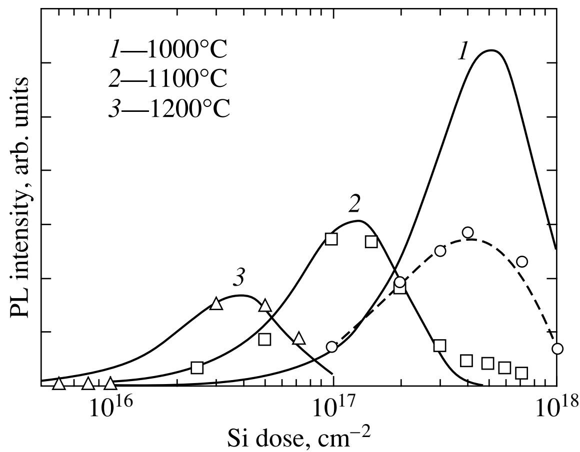

Fig. 1. Dose dependences of the PLI of the SiO_2 : nc-Si system for different temperatures of annealing in N_2. Points represent experimental data, and lines show calculated data (the dashed line is borrowed from [1]).

In this work, we study the effects of Φ and T_{ann} and the character of the SiO_2 thermal film on PL spectra. The Φ and T_{ann} dependences are analyzed in terms of a model taking into account OR and the oscillator strength. A model is proposed to explain the two-mode structure of the PL spectra.

2. EXPERIMENTAL

Oxidized silicon samples of two types were studied. Samples of the first type were oxidized in a dry–wet–dry cycle at a temperature of 1100°C, and the SiO_2 thickness was 0.3 μm. Samples of the second type were oxidized in a wet atmosphere also at 1100°C to an oxide thickness of 0.52 μm. The dose dependence of PL was studied on first-type samples only.

Si^+ ion implantation was performed on an ILU-200 implanter at an energy $E = 150$ keV and an ion-current density $j \leq 5$ μA/cm^2. Postimplantation annealings were carried out for 2 h in a dried-nitrogen flow. Some samples were air-annealed either after implantation or before it (see below). PL spectra were recorded at room temperature using an MDR-23 monochromator and Ar-laser excitation (at wavelength $\lambda_{ex} = 488$ nm).

3. RESULTS AND DISCUSSION

Figure 1 shows maximum PLIs at various values of Φ and T_{ann}. It is seen that the curves are bell-shaped at all values of T_{ann}. The higher the T_{ann}, the larger the shift in the optimum dose toward low values. Earlier [1, 8], we observed this type of behavior for $T_{ann} = 1100$ and 1000°C. For $T_{ann} = 1100$°C, the position of the maximum in the Φ axis coincides with the data from [2], which were obtained under similar conditions.

To account for these dependences, we consider the growth of NCs during the first-order phase transition in a Si-SiO_2 supersaturated solid solution by making allowance for OR [3]. Let us point out the main assumptions of our model.

(1) NCs are formed during annealing via homogeneous nucleation.

(2) NC nucleation centers are two-atom complexes, which form during random meeting of diffusing Si atoms.

(3) NCs grow in the form of spherical particles of radius r due to diffusion of individual Si atoms from the supersaturated solid solution to them.

(4) The spatial distribution of NCs is a Poisson distribution.

(5) OR is taken into account as follows: as soon as the distances between the centers of two or more NCs in a certain volume become smaller than the double diffusion length for a given annealing temperature and a given annealing time, the thermoemission decomposition of smaller inclusions (with $r < r_0$, where r_0 is the critical radius) and the related growth of coarse NCs (with $r > r_0$) begin. As in the Lifshitz–Slezov theory [9], we assume that inclusions with a mean size of about r_0 are involved in coalescence from the very beginning.

(6) NCs contribute to photoluminescence according to the probability of radiative recombination, which depends on the resulting NC size.

In the first stage, the thermoemission detachment and attachment of diffusing atoms to a nucleation center occur irrespective of other nucleation centers in a small surrounding region (diffusion sphere) with a radius of the order of the diffusion length $(Dt)^{1/2}$. Here, D is the diffusion coefficient and t is the time. It is obvious that such regions must overlap to provide an atomic flux from one inclusion to another. Thus, the mean center distance is a coalescence control parameter.

The nucleation rate is directly proportional to the probability of random meeting of two silicon atoms and depends exponentially on the annealing temperature T_{ann}. Therefore, the concentration of nucleation centers formed by a time $t = t_{ann}$ (where t_{ann} is the annealing time) can be written as

$$\begin{aligned} N_c &= 8\pi r_c D n_s^2 t_{ann} \exp\left(-\frac{E_b}{kT_{ann}}\right) \\ &= 8\pi r_c D t_{ann} \exp\left(-\frac{E_b}{kT_{ann}}\right)\frac{\Phi^2}{d^2}, \end{aligned} \quad (1)$$

where r_c is the capture sphere radius, which is approximately equal to the average interatomic distance in silicon in our case; E_b is the energy barrier to the joining of two atoms; n_s is the average concentration of excess silicon introduced into the matrix (for simplicity, this concentration is assumed to be independent of depth in the layer); and d is the layer thickness ($d \approx R_p + \Delta R_p$, where R_p is the mean projected range and ΔR_p is the ion straggling). In Eq. (1), N_c is the nucleation-center con-

centration that would be by the end of the annealing time (t_{ann}) if the coalescence were to be insignificant. However, if the average distance between nucleation centers is shorter than $2(Dt_{ann})^{1/2}$, their diffusion spheres overlap upon annealing and the coalescence efficiency increases sharply. As the dose increases, the distance between nucleation centers decreases and the number of inclusions involved in coalescence increases. When these inclusions decompose, coarser inclusions form, which make a smaller contribution to the PL because of the smaller probability of radiative recombination; therefore, the PL intensity decreases at high doses. Thus, the problem is to find the fraction of Si inclusions located within spheres of volume $(4/3)\pi(Dt_{ann})^{3/2}$ (diffusion cells) at each dose. We divide the whole volume into cells each of volume $(4/3)\pi(Dt_{ann})^{3/2}$. The concentration N_{cell} of such cells is

$$N_{cell} = \frac{1}{V_{cell}} = \frac{3}{4\pi(Dt_{ann})^{3/2}}, \tag{2}$$

and the average number of nucleation centers per cell $N_c^{\text{per cell}}$ is

$$N_c^{\text{per cell}} = N_c V_{cell}. \tag{3}$$

We apply the Poisson equation to determine the probability of m centers being present in a diffusion cell

$$W(m, N_c^{\text{per cell}}) = \exp(-N_c^{\text{per cell}})\frac{(N_c^{\text{per cell}})^m}{m!}. \tag{4}$$

The number of diffusion cells in which m centers are present and are involved in coalescence is obviously equal to

$$N_{cell}^{coal}(m) = N_{cell}W(m). \tag{5}$$

We assume that, as a result of OR, one inclusion eventually forms in each cell; in this case, the partial concentration of inclusions formed during the decomposition of the m initial particles is equal to $N_{cell}^{coal}(m)$. The resulting inclusion concentration is the total concentration of cells with $m = 1, 2, 3, \ldots$ interacting particles.

In general, coarse inclusions forming due to the coalescence of fine nucleation centers take part in luminescence; however, their contribution is specified by the probability of a radiative transition, which depends strongly on the NC size. To take this contribution into account, we use the following model. Let the PL be caused by electron transitions between the ground states of NCs. In this case, with allowance for phonon absorption or emission, the time τ of radiative recombination in a silicon quantum dot is given by [10]

$$\tau^{-1} = \frac{C}{\nu}\left(\frac{a_0}{r}\right)^3 \coth\left(\frac{\hbar\nu}{2k_B T}\right), \tag{6}$$

where $a_0 = 0.543$ nm is the silicon lattice parameter, ν is the frequency of transverse optical phonons (with an energy of about 57.5 meV), and C is a dimension parameter that is independent of T and r (only transitions between the ground states in a quantum dot are taken into account). The size of an NC that forms as a result of the coalescence of m inclusions of radius r_0 within a diffusion cell is $r(m) = r_0 m^{1/3}$. Therefore, the dependence of the transition probability on the number m is given by

$$\tau^{-1}(m) \sim \frac{1}{m}. \tag{7}$$

Finally, the PL intensity is expressed as

$$I_{PL}(\Phi, T_{ann}) \sim N_{cell}(T_{ann}) \sum_{m=0}^{M} W(\Phi, T_{ann}, m)\tau^{-1}(m). \tag{8}$$

Here, the main fitting parameters are the activation energy E_b and D. By fitting the calculated dependences to the experimental data for three annealing temperatures (Fig. 1), we obtain $E_b = 2.31$ eV and $D(\text{cm}^2/\text{s}) = 1.9 \times 10^{-13}\exp\left(-\frac{0.68\text{eV}}{kT_{ann}}\right)$. The sum of activation energies $E_b + E_d = 3.0$ eV is close to a value of 2.8 eV, which was attributed in [4] to the sum of the diffusion activation energy and the energy of detachment of a Si atom from an NC.

The deviation of the calculated dose dependence from the experimental one at $T_{ann} = 1000°C$ (Fig. 1) is likely due to the fact that the predominant factor at this T_{ann} is not OR but rather the mechanical joining of NCs because of their high density (bringing about the formation of a continuous Si layer), which was described by us in [1]. The discrepancy at the highest doses for T_{ann} = 1100°C may also be expected, since we did not take into account dimer formation during implantation at high Si concentrations, which is highly probable even without annealing [11].

Let us consider the effect of the character of the initial silicon dioxide on the PL spectra. As noted above, apart from the maximum at 750–800 nm, the PL spectrum of the SiO_2 : nc-Si system sometimes exhibits signs of a second long-wavelength band, which manifests itself as asymmetry of the main band or as a weakly pronounced shoulder. However, researchers have not mentioned this feature. Moreover, since the spectral sensitivity range of the measuring apparatus is usually not given in the literature, we may assume that the long-wavelength portion of the spectrum (at $\lambda \geq$ 800 nm) was cut off in some cases. The authors of [12] observed a second peak in the PL spectra of porous Si at ~900 nm. Therefore, we aimed to reveal whether the appearance of the long-wavelength band and its different intensity are related to the character (growing conditions) of thermal silicon oxide.

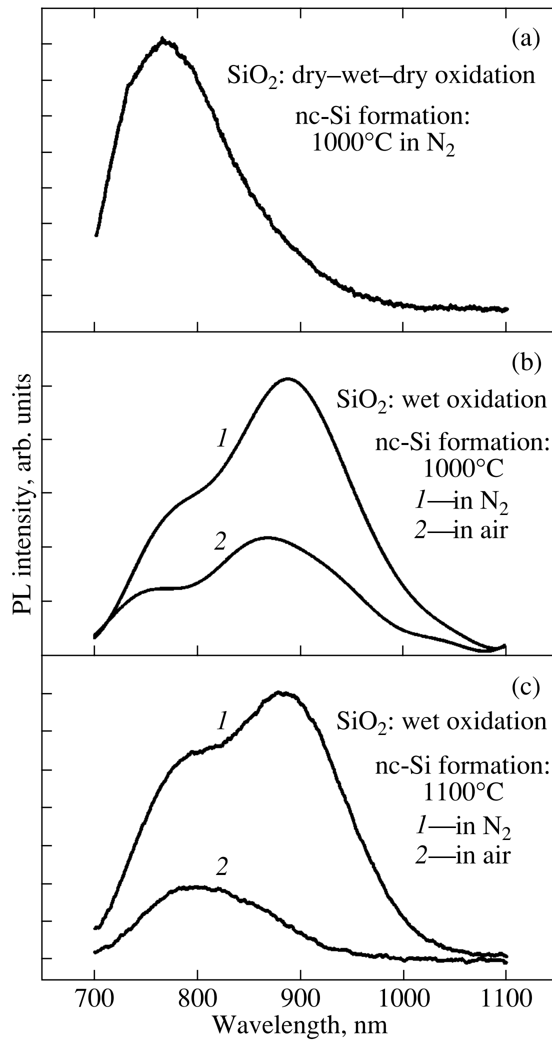

Fig. 2. PL spectra of the SiO_2 : nc-Si system for different conditions of SiO_2 thermal growth and Si NC formation ($\Phi = 10^{17}$ cm^{-2}).

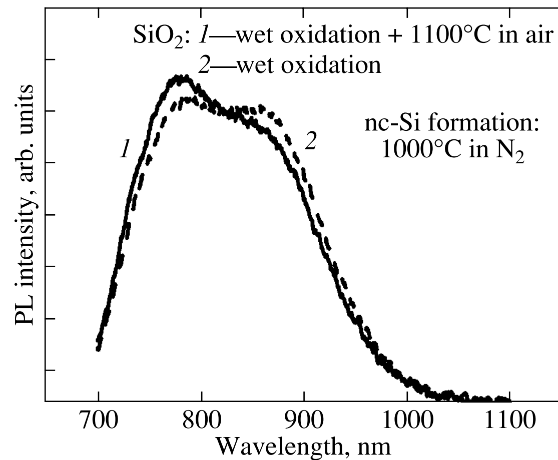

Fig. 3. Effect of preliminary annealing of the initial oxide in air on the experimental PL spectrum of the SiO_2 : nc-Si system ($\Phi = 10^{17}$ cm^{-2}). Postimplantation annealing was performed in an N_2 atmosphere.

Indeed, for the first-type samples, where SiO_2 was grown in the dry–wet–dry cycle, the PL spectrum does not exhibit an additional peak and has a usual shape (Fig. 2a). However, the second-type samples (where SiO_2 was grown in a wet atmosphere) exhibit a clearly pronounced two-mode spectrum structure after annealing at 1000°C in N_2 or air (Fig. 2b): two bands are visible, with their maxima located near 770 and 880 nm, respectively. As compared to annealing in N_2, annealing in air decreases the total PLI and shifts the spectrum somewhat toward the blue side. Annealing at a higher temperature (1100°C) in an inert atmosphere (Fig. 2c) changes the PLI ratio only slightly in favor of the short-wavelength band, whereas annealing in air at this temperature almost quenches the band at ~880 nm (and decreases the total PLI).

These results indicate that the two-mode structure of the PL spectrum is not accidental and depends strongly on the annealing conditions. In discussing this structure, we have to take into account the PL mechanisms proposed in the literature for the SiO_2 : nc-Si system. The authors of [2, 13] believe that the band at ~750–800 nm is related to an interband transition inside an NC (quantum dot). However, another point of view is more widely accepted (see, e.g., [5, 14, 15]). According to this point of view, excitons form in a quantum dot, whereas radiative recombination occurs through the levels localized in the interface region near the NC, although the nature of these levels is still unknown (the transition region is usually supposed to be nonstoichiometric). Currently, we cannot reliably state which of the two standpoints regarding the band at ~750–800 nm is right. Apparently, both mechanisms can be operative depending on the experimental conditions. Our experiments show that the band near ~880 nm is most likely due to the interface states related to the presence of water vapor in the oxidizing atmosphere; however, these states are not associated with the main band (at ~750–800 nm). It is natural to assume that the centers that are responsible for the ~880-nm band contain hydrogen or OH groups. This interpretation is supported by the fact that this band disappears after annealing in an oxidizing atmosphere at a sufficiently high temperature, which obviously occurs because of oxidation of the interface region and/or hydrogen removal. A relative decrease in the intensity of this band also took place when the second-type samples were subjected to annealing in air for 3 h (SiO_2 dehydrogenation) before Si implantation (Fig. 3).

Figure 4 shows a possible PL model in the case where the above-mentioned interface region exists around an NC. During excitation, an exciton forms in the NC; the exciton can recombine directly (interband transition) or through the interface region states (this

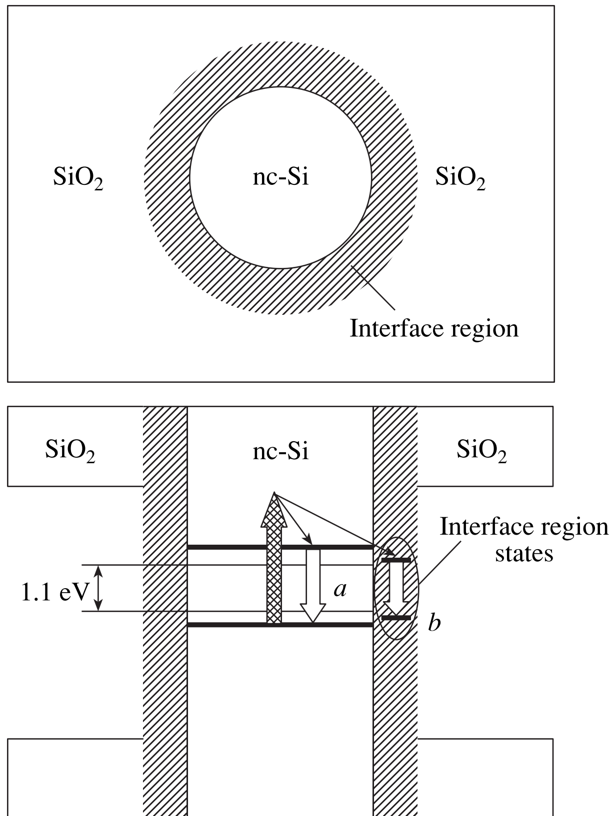

Fig. 4. Probable band structure of the SiO_2 : nc-Si system and possible radiative transitions: (a) transitions through states in a quantum dot (at a wavelength of ~770 nm) and (b) through states at the interface (at a wavelength of ~880 nm).

case is not shown in Fig. 4). In the case of wet oxidation, this region contains additional centers that capture an electron and a hole from the NC. Their radiative recombination gives the 880-nm band. The interface region states can also be excited due to the Auger process during the interband recombination of the NC.

4. CONCLUSIONS

The character of the PL spectra of SiO_2 : nc-Si layers has been shown to be dependent in a complicated manner on the dose, annealing temperature, and the character of silicon oxide. The dependences obtained can be explained by OR, if we take into account the influence of the NC sizes on the probability of radiative recombination, and by the effect of hydrogen-containing impurities on the interface regions of NCs, if we assume that these regions, in addition to the NCs, are involved in PL. It should be noted that the interpretation of the spectra differs from the traditional one [5, 14, 15], where the PL band near ~750–800 nm is attributed to the interface regions. Conclusively revealing the nature of the two-mode structure would require further investigations.

ACKNOWLEDGMENTS

This work was supported by the program of the Ministry of Education of the Russian Federation “Higher School Research in Priority Directions of Science and Engineering” (subprogram no. 205), the joint program of the Ministry of Education of the Russian Federation and the CRDF BRHE Foundation (project no. NN-001-01), the program FP6 STREP (no. 505285-1), and INTAS (project no. 00-0064).

REFERENCES

1. D. I. Tetelbaum, O. N. Gorshkov, S. A. Trushin, D. G. Revin, D. M. Gaponova, and W. Eckstein, Nanotechnology **11**, 295 (2000).
2. B. Garrido Fernandez, M. Lopez, C. Garcia, A. Perez-Rodriguez, J. R. Morante, C. Bonafos, M. Carrada, and A. Claverie, J. Appl. Phys. **91** (2), 798 (2002).
3. W. Ostwald, Z. Phys. Chem. **34**, 495 (1900).
4. C. Bonafos, B. Colombeau, A. Altibelli, M. Carrada, G. Ben Assayag, B. Carrido, M. Lopez, A. Perez-Rodriguez, J. R. Morante, and A. Claverie, Nucl. Instrum. Methods Phys. Res. B **178**, 17 (2001).
5. K. S. Zhuravlev, A. M. Gilinsky, and A. Yu. Kobitsky, Appl. Phys. Lett. **73** (20), 2962 (1998).
6. D. I. Tetelbaum, S. A. Trushin, V. A. Burdov, A. I. Golovanov, D. G. Revin, and D. M. Gaponova, Nucl. Instrum. Methods Phys. Res. B **174**, 123 (2001).
7. D. I. Tetelbaum, S. A. Trushin, A. N. Mikhaylov, V. K. Vasil’ev, G. A. Kachurin, S. G. Yanovskaya, and D. M. Gaponova, Physica E (Amsterdam) **16** (3–4), 410 (2003).
8. S. A. Trushin, A. N. Mikhaylov, D. I. Tetelbaum, O. N. Gorshkov, D. G. Revin, and D. M. Gaponova, Surf. Coat. Technol. **158–159**, 717 (2002).
9. I. M. Lifshitz and V. V. Slezov, Zh. Éksp. Teor. Fiz. **35**, 479 (1958) [Sov. Phys. JETP **8**, 331 (1959)].
10. V. A. Belyakov, V. A. Burdov, D. M. Gaponova, A. N. Mikhaĭlov, D. I. Tetelbaum, and S. A. Trushin, Fiz. Tverd. Tela (St. Petersburg) **46** (1), 31 (2004) [Phys. Solid State **46**, 27 (2004)].
11. G. A. Kachurin, I. E. Tischenko, K. S. Zhuravlev, N. A. Pazdnikov, V. A. Volodin, A. K. Gutakovsky, A. F. Leiser, W. Skorupa, and R. A. Yankov, Nucl. Instrum. Methods Phys. Res. B **122**, 571 (1997).
12. L. A. Balagurov, B. M. Leiferov, E. A. Petrova, A. F. Orlov, and E. M. Panasenko, J. Appl. Phys. **79**, 7143 (1996).
13. K. S. Min, K. V. Scheglov, C. M. Yang, H. A. Atwater, M. L. Brongersma, and A. Polman, Appl. Phys. Lett. **69**, 2033 (1996).
14. T. Shimizu-Iwayama, K. Fujita, S. Nakao, K. Saitoh, R. Fujita, and N. Itoh, J. Appl. Phys. **75**, 7779 (1994).
15. Y. Kanemitsu and S. Okamoto, Phys. Rev. B **58**, 9652 (1998).

Translated by K. Shakhlevich

Physics of the Solid State, Vol. 47, No. 1, 2005, pp. 133–140. Translated from Fizika Tverdogo Tela, Vol. 47, No. 1, 2005, pp. 128–135.
Original Russian Text Copyright © 2005 by Germanenko, Min'kov, Rut, Larionova, Zvonkov, Shashkin, Khrykin, Filatov.

PROCEEDINGS OF THE CONFERENCE "NANOPHOTONICS 2004"
(Nizhni Novgorod, Russia, May 2–6, 2004)

Effect of Roughness of Two-Dimensional Heterostructures on Weak Localization

A. V. Germanenko*, G. M. Min'kov*, O. É. Rut*, V. A. Larionova*, B. N. Zvonkov, V. I. Shashkin***, O. I. Khrykin***, and D. O. Filatov******

** Institute of Physics and Applied Mathematics, Ural State University, Yekaterinburg, 620083 Russia*
e-mail: Alexander.Germanenko@usu.ru
***Research Physicotechnical Institute, Lobachevskiĭ State University, pr. Gagarina 23/5, Nizhni Novgorod, 603950 Russia*
**** Institute for Physics of Microstructures, Russian Academy of Sciences, Nizhni Novgorod, 603950 Russia*
***** Research Center for Physics of Solid-State Nanostructures, Nizhni Novgorod, 603600 Russia*

Abstract—The effect that a longitudinal magnetic field exerts on the transverse negative magnetoresistance by suppressing the interference quantum correction is studied in $GaAs/In_xGa_{1-x}As/GaAs$ structures with a single quantum well. It is shown that the variation in the shape of the transverse magnetoresistance curve caused by a longitudinal magnetic field depends strongly on the relation between the mean free path, the phase-breaking length, and the correlation length characterizing the roughness of the two-dimensional layer. It is shown that the experimental results allow one to estimate the parameters of large-scale and small-scale roughness of the two-dimensional layer in the structures under study. The results obtained are in good agreement with the data of probe microscopy. © *2005 Pleiades Publishing, Inc.*

1. INTRODUCTION

The temperature and magnetic field dependences of the conductivity of disordered two-dimensional systems are substantially determined by the interference quantum correction. It is known that only a magnetic field normal to the plane of the system ($B_\perp$) destroys the interference of electronic waves and gives rise to a negative magnetoresistance in the case of an ideally flat two-dimensional system [1]. In real two-dimensional systems, the effect of a magnetic field is more complicated [2]. Among the reasons giving rise to a longitudinal magnetoresistance in two-dimensional systems with one filled confinement subband, the most important is the roughness of the interfaces forming a quantum well (QW). Moreover, due to roughness, the application of a longitudinal field ($B_\parallel$) changes the transverse magnetoresistance. The first studies of the effect of a longitudinal magnetic field on magnetoresistance in the presence of a transverse magnetic field were performed on silicon MOS transistors [3]. It has been shown that, in the presence of small-scale roughness (such that $L < l_p$, where L is the correlation length characterizing the roughness in the sample plane and l_p is the mean free path), the change in the shape of the transverse-magnetoresistance curve caused by the application of an additional longitudinal magnetic field can be described assuming that the phase-breaking time τ_φ decreases with increasing $B_\parallel$. Theoretical analysis [4, 5] has shown that such an effect of the longitudinal magnetic field is not universal and is actually determined by the relation between the characteristic lengths L, l_p, and $l_\varphi = \sqrt{D\tau_\varphi}$, where D is the diffusion coefficient. Thus, by studying the quantum interference correction in crossed magnetic fields, one can obtain information on the roughness and nonplanarity of a two-dimensional layer.

2. EXPERIMENTAL DETAILS

Studies were performed on $GaAs/In_xGa_{1-x}As/GaAs$ semiconductor heterostructures with a single QW, grown on a semi-insulating GaAs substrate by gas phase epitaxy from organometallic compounds. Two structures of different design were studied. Heterostructure 3512 was a series of epitaxial layers forming an 8-nm-wide $In_{0.2}Ga_{0.8}As$ QW with barriers of undoped GaAs. Doping was performed by introducing Sn δ layers into the barriers on both sides of the QW at a distance of 9 nm. On the upper side, a 300-nm-thick covering layer of pure GaAs was grown. In the other structure, H5610, a thin InAs layer was grown instead of the $In_{0.2}Ga_{0.8}As$ QW. In this case, a strong mismatch in the lattice parameters of GaAs and InAs resulted in the formation of nanoclusters on the InAs wetting layer, which had a thickness of several monolayers and represented a deep QW for electrons. Several field-effect transistors in the form of a Hall bar were fabricated from each structure, which allowed us to perform measurements at different electron concentrations in the QW. Aluminum was thermally sputtered in vacuum through a mask and was used as a field electrode. It was shown in [6] that, for electron concentrations exceeding 7×10^{11} cm^{-2} for structure 3512 and 9×10^{11} cm^{-2} for structure H5610, the states in the doping δ layers are

1063-7834/05/4701-0133$26.00 © 2005 Pleiades Publishing, Inc.

Parameters of the investigated structures

Structure	V_g, V	n, 10^{12} cm^{-2}	σ^a, G_0	σ_0, G_0	τ_p, 10^{-13} s	B_{tr}, T
3512	–0.5	0.88	123.0	127.6	3.8	0.011
	–0.75	0.69	83.6	88.7	3.4	0.018
	–1.0	0.67	70.4	75.5	3.0	0.024
	–1.5	0.47	20.4	26.4	1.47	0.138
	–2.5	0.32	4.27	9.3	0.76	0.76
H5610#1[b]	–1.0	0.91	38.8	45.3	1.31	0.091
	–2.5	0.73	22.9	29.5	1.06	0.172
	–3.5	0.59	10.3	16.4	0.73	0.45

[a] $T = 1.45$ K.

[b] The parameters of samples #1 and #2 are close.

populated, which gives rise to additional effects in the magnetoresistance. In this study, we restrict ourselves to the case where δ layers are not populated. The sample parameters for various values of the gate voltage V_g are given in the table. The method of finding the Drude conductivity σ_0, the transport momentum relaxation time τ_p, and the transport magnetic field ($B_{tr} = \hbar/2el_p^2$) is described in [7]. In this study, we denote by G_0 the quantity $e^2/2\pi^2\hbar \simeq 1.23 \times 10^{-5}\ \Omega^{-1}$.

Measurements were performed in the temperature range from 1.4 to 4.2 K. The magnetic system of the experimental setup consisted of two superconducting solenoids: the main one (creating a longitudinal magnetic field of up to 6 T) and an additional split solenoid with an axis oriented normally to the axis of the main solenoid. The additional solenoid created a field of up to 0.5 T. The solenoids were fed from independent current sources, which allowed us to scan one of the magnetic fields continuously, whereas the other was kept constant. Magnetic fields were measured using two normally oriented Hall sensors.

3. RESULTS AND DISCUSSION

Figure 1 shows the conductivity as a function of the transverse magnetic field, measured on structures 3512 and H5610 at a fixed longitudinal magnetic field. The gate voltage was chosen such that the conductivities in both cases were similar in magnitude. It is seen that the longitudinal magnetic field affects the shape of the transverse magnetoresistance curves in different ways. For structure 3512, the shape of the magnetoresistance curves changes in a wide range of magnetic fields. For the samples fabricated on the basis of structure H5610, the main changes occur in the region of low magnetic fields, $B_\perp < 0.2B_{tr}$, whereas for high magnetic fields, $B_\perp > 0.2B_{tr}$, the $\sigma(B_\perp)$ curves are only displaced

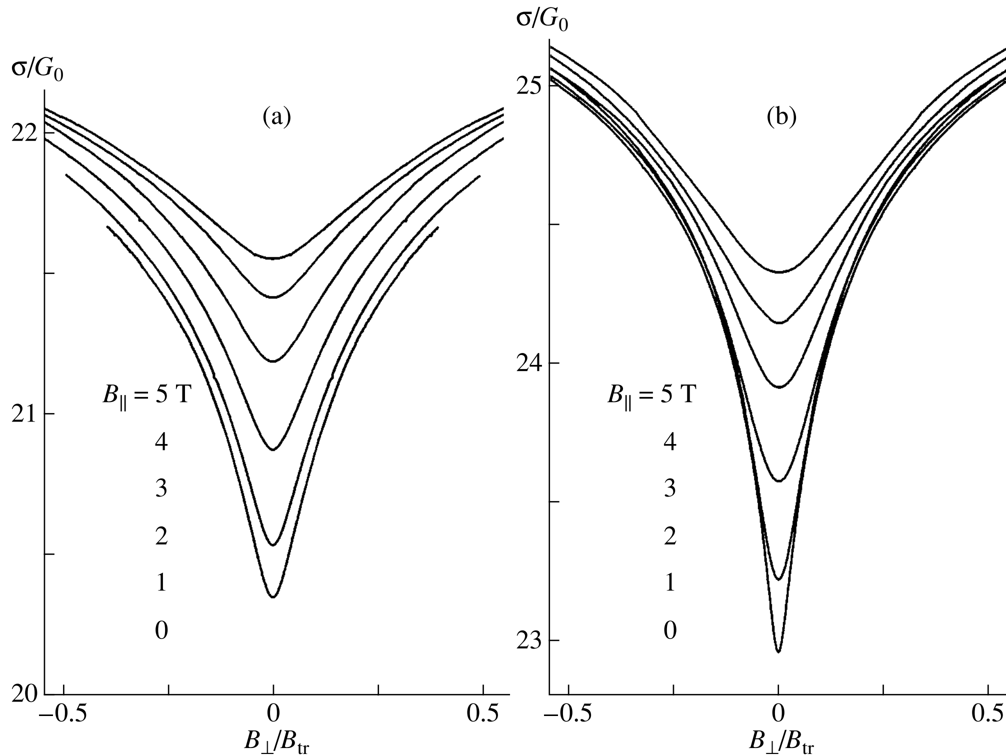

Fig. 1. Conductivity as a function of $B_\perp$ measured at $T = 1.45$ K for different values of $B_\parallel$. (a) Structure 3512, $V_g = -1.5$ V; (b) structure H5610#1, $V_g = -2.5$ V.

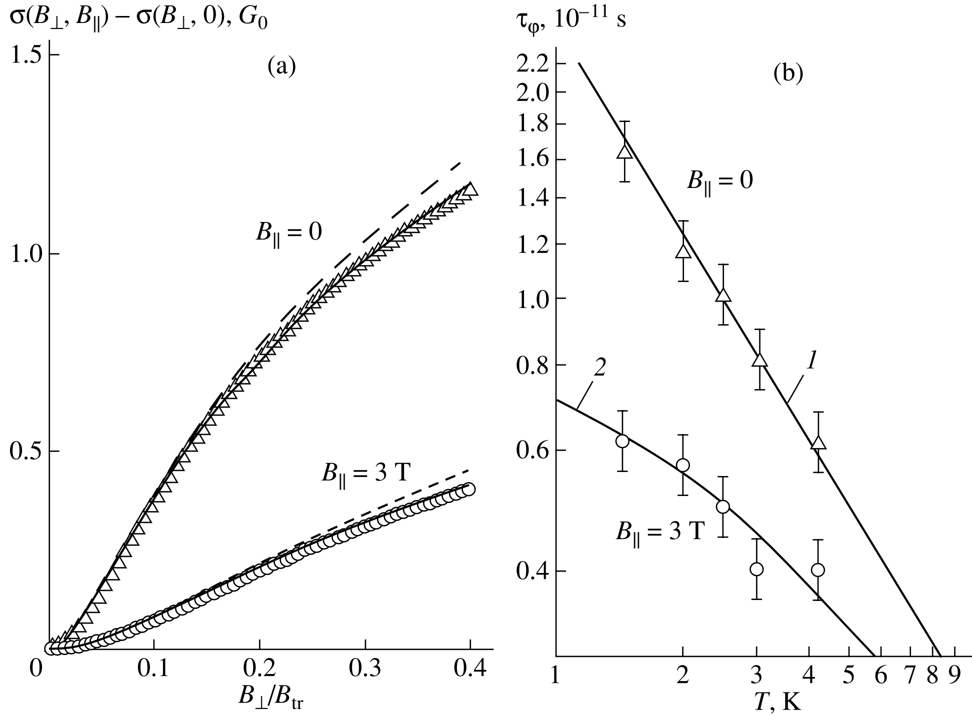

Fig. 2. (a) Transverse magnetoconductivity $\sigma(B_\perp, B_\parallel) - \sigma(B_\perp, 0)$ as a function of the transverse magnetic field for structure 3512 at $B_\parallel = 0$ and 3 T, $T = 1.45$ K, and $V_g = -1$ V. Symbols represent experimental data, and curves are the result of fitting using Eq. (1) with the following fitting parameters: $B_\parallel = 0$; $\alpha = 0.98$ and $\tau_\varphi = 1.5 \times 10^{-11}$ s (dashed curve); $\alpha = 0.87$ and $\tau_\varphi = 1.65 \times 10^{-11}$ s (solid curve); $B_\parallel = 3$ T; $\alpha = 0.75$ and $\tau_\varphi^* = 0.56 \times 10^{-11}$ s (dashed curve); and $\alpha = 0.62$ and $\tau_\varphi^* = 0.63 \times 10^{-11}$ s (solid curve). Dashed and solid curves correspond to different ranges of magnetic fields in which the fitting was made: dashed curves correspond to $B_\perp = (0\text{–}0.1)B_{tr}$, and solid curves to $B_\perp = (0\text{–}0.2)B_{tr}$. (b) Temperature dependence of the phase relaxation time at $B_\parallel = 0$ and 3 T for structure 3512. Symbols represent experimental data. Curve *1* corresponds to the T^{-1} law, and curve *2* is plotted as described in the text.

upwards with increasing $B_\parallel$. As will be shown below, this difference in behavior is related to the difference in the scales of interface roughness in the structures under study.

3.1. The Role of Small-Scale Roughness

We consider the results obtained for structure 3512. Analysis shows that the dependence of the conductivity on the transverse magnetic field, as well as the temperature dependence of the conductivity measured at $B_\parallel = 0$, is in good agreement with the theory of weak localization. The transverse magnetoconductivity $\Delta\sigma(B) = \rho_{xx}^{-1}(B) - \rho_{xx}^{-1}(0)$ is well described by the known expression [8]

$$\frac{\Delta\sigma(B)}{G_0} = \alpha\left\{\psi\left(\frac{1}{2} + \frac{\tau_p}{\tau_\varphi}\frac{B_{tr}}{B}\right) - \psi\left(\frac{1}{2} + \frac{B_{tr}}{B}\right) - \ln\left(\frac{\tau_p}{\tau_\varphi}\right)\right\}, \quad (1)$$

where α and τ_φ are fitting parameters (Fig. 2a). In Eq. (1), $\psi(x)$ is the digamma function. It is seen in Fig. 2b that the temperature dependence of the parameter τ_φ closely obeys the T^{-1} law. Finally, the temperature dependence of the conductivity at $B = 0$ is logarithmic and its slope in $(\ln T, \sigma/G_0)$ coordinates is equal to 1.45 ± 0.05. The above value of the slope is determined by the quantum interference correction, whose contribution is approximately equal to unity, and by the correction related to the electron–electron interaction.

Let us consider the results obtained in the presence of a longitudinal magnetic field. In this case, the magnetoconductivity $\sigma(B_\perp, B_\parallel) - \sigma(0, B_\parallel)$ is also well described by Eq. (1) and the parameters α and τ_φ^* (here and in what follows, the asterisk denotes a parameter obtained at $B_\parallel \neq 0$) are very negligibly sensitive to the range of magnetic fields in which the data were processed (Fig. 2a). It is seen in Fig. 3a that the parameter τ_φ^* decreases rapidly with increasing $B_\parallel$ and is well described by the law $1/\tau_\varphi^* \propto B_\parallel^2$. Thus, the application of a longitudinal magnetic field results in an effective increase in the inelastic phase relaxation rate.

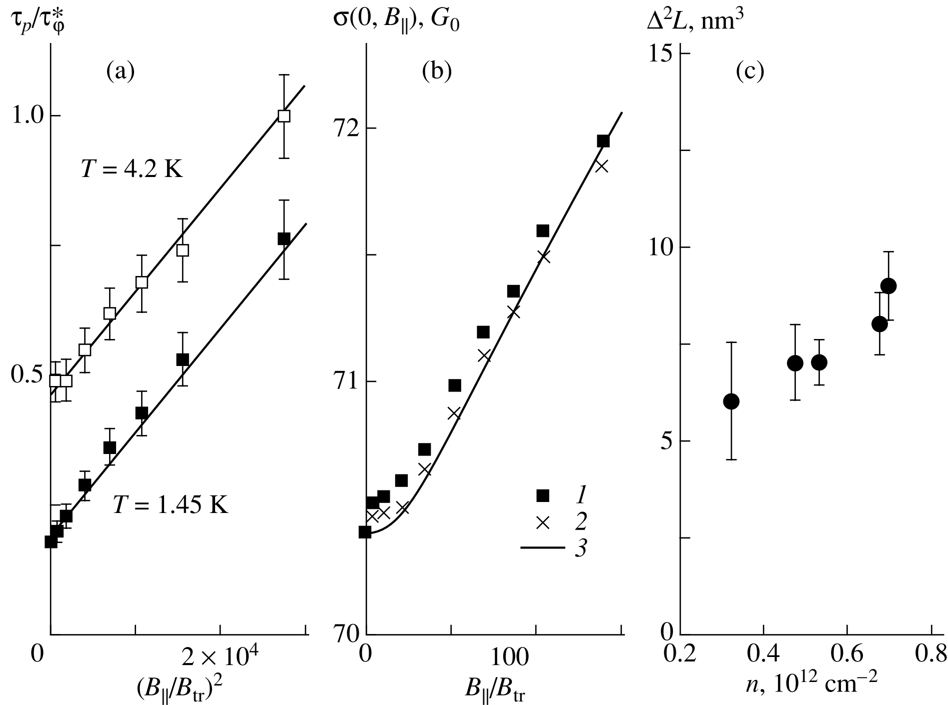

Fig. 3. (a) Ratio τ_p/τ_φ^* as a function of $B_\parallel^2$ for structure 3512 at T = 1.45 and 4.2 K, V_g = –1 V. Symbols represent experimental data, and curves are calculated from Eqs. (2) and (3) with $\Delta^2 L$ = 7.2 nm^3, l_p = 117 nm, and τ_p/τ_φ = 0.018 (T = 1.45 K) and 0.048 (T = 4.2 K). (b) Conductivity as a function of $B_\parallel$ for structure 3512 at T = 1.45 K and V_g = –1 V; (*1*) experimental results; (*2*) dependence given by Eq. (4a), where τ_φ and τ_φ^* are obtained by processing the experimental $\Delta\sigma(B_\perp)$ curves for $B_\parallel = 0$ and $B_\parallel \neq 0$, respectively; and (*3*) Eq. (4b) with $\Delta^2 L$ = 7.2 nm^3 and l_p = 117 nm. (c) Dependence of the roughness parameter $\Delta^2 L$ on the electron concentration for structure 3512.

Qualitatively, we may interpret this effect as follows. The interference quantum correction to the conductivity is related to the interference of electronic waves propagating along closed trajectories in opposite directions and produces an effective increase in the backscattering cross section and, hence, a decrease in the classical conductivity. A magnetic field produces a phase shift between these trajectories, thereby destroying this interference and giving rise to a negative magnetoresistance. An ideal two-dimensional system does not experience a longitudinal magnetic field, since all closed trajectories lie in one plane and the magnetic field flux through them is zero. In real two-dimensional structures, because of the interface roughness, the electron motion is accompanied by a variation in the position of the electronic wave function in the direction perpendicular to the growth plane and, therefore, the flux of the longitudinal magnetic field through closed trajectories is nonzero. Thus, the application of a longitudinal magnetic field results in an additional phase shift and, therefore, should affect the shape of the magnetoresistance curves measured in a transverse magnetic field. A theoretical analysis of this phenomenon [3, 5, 9] shows that, in the case of small-scale roughness, the role of a longitudinal magnetic field is indeed reduced to an increase in the phase relaxation rate and the $\sigma(B_\perp)$ dependence measured at $B_\parallel \neq 0$ should be described by Eq. (1), with the effective phase relaxation rate given by

$$\frac{1}{\tau_\varphi^*} = \frac{1}{\tau_\varphi} + \frac{1}{\tau_\parallel}, \tag{2}$$

where $1/\tau_\parallel$ is determined by the roughness parameters and by $B_\parallel$ [5]:

$$\frac{1}{\tau_\parallel} \simeq \frac{1}{\tau_p}\frac{\sqrt{\pi}}{4}\frac{\Delta^2 L}{l_p^3}\left(\frac{B_\parallel}{B_{tr}}\right)^2. \tag{3}$$

Here, Δ is the root-mean-square roughness amplitude.

Let us discuss to what extent the results obtained for sample 3512 agree with the model described above. As noted above, τ_p/τ_φ^* indeed increases quadratically with $B_\parallel$ (Fig. 3a) and the slope of the function $\tau_p/\tau_\varphi^*(B_\parallel^2)$ is temperature-independent, in complete agreement with Eqs. (2) and (3). In the context of this model, the temperature dependence of τ_φ^* in the presence of a longitudinal magnetic field is predicted to be saturated to $\tau_\parallel$ with decreasing temperature. In Fig. 2b, we see that the

experimental $\tau_\varphi^*(T)$ dependence obtained at $B_\parallel = 3$ T tends to saturation as $T \longrightarrow 0$. In the same figure, curve *2* shows the $\tau_\varphi^*(T)$ dependence calculated using Eq. (2). We used the expression $2.5 \times 10^{-11}/T$ for $\tau_\varphi(T)$, which provides a good interpolation for the case $B_\parallel = 0$ (curve *1* in Fig. 2b); the value of $\tau_\parallel^{-1}$ equal to 1×10^{11} s^{-1} was obtained as the difference between $(\tau_\varphi^*)^{-1}$ and τ_φ^{-1} at $T = 1.45$ K. Apparently, good agreement between the calculated curve and experimental points is observed in the entire temperature range.

This model also predicts that, as the longitudinal magnetic field increases (in the absence of a transverse field), the conductivity increases according to the law

$$\sigma(0, B_\parallel) = \sigma(0, 0) + G_0 \ln\frac{\tau_\varphi}{\tau_\varphi^*} \quad (4a)$$

$$\simeq \sigma(0, 0) + G_0 \ln\left[1 + \frac{\tau_\varphi}{\tau_p}\frac{\sqrt{\pi}}{4}\frac{\Delta^2 L}{l_p^3}\left(\frac{B_\parallel}{B_{\mathrm{tr}}}\right)^2\right]. \quad (4b)$$

In Fig. 3b, we see that the experimental $\sigma(B_\parallel)$ dependence is well described by the formula (4a) if we use the $\tau_\varphi^*(B_\parallel)$ dependence shown in Fig. 3a.

Thus, for structure 3512, all theoretical predictions are confirmed experimentally and, therefore, we may assume that the slope of the dependence of τ_p/τ_φ^* on $(B/B_{\mathrm{tr}})^2$ gives the quantity $\Delta^2 L$, in accordance with Eq. (3). Using the data from Fig. 3a, we can easily find that the roughness parameter $\Delta^2 L$ is 7.2 nm^3 at $V_g = -1$ V. Naturally, Eq. (4b) with this value of $\Delta^2 L$ also describes well the experimental $\sigma(B_\parallel)$ dependence measured in the absence of a transverse magnetic field (cf. data *1* and curve *3* in Fig. 3b).

This type of detailed analysis was performed for experimental results obtained at different gate voltages. Figure 3c shows the dependence of the parameter $\Delta^2 L$ on the electron concentration in the QW. We see that the quantity $\Delta^2 L$ increases with electron concentration. This behavior may be interpreted if we assume that the outer interface forming the QW is rougher than the inner interface. With decreasing gate voltage, i.e., with decreasing electron concentration, the electronic wave function is displaced away from the rough outer interface, thus reducing its role in weak localization. The fact that the outer interface is rougher than the inner one is natural for GaAs/$In_xGa_{1-x}As$/GaAs heterostructures [10]. Similar results were reported in [3] for silicon field-effect transistors with a surface QW.

3.2. Effect of Nanoclusters on Weak Localization

We consider now the results obtained for the H5610 structure with nanoclusters. As in the previous case, the magnetoconductivity measured in the absence of a longitudinal magnetic field is described well by Eq. (1). However, if we try to use this formula for the case of $B_\parallel \neq 0$, reasonable agreement will be impossible to achieve. Indeed, in contrast to structure 3512, the fitting parameters α and τ_φ^* appear to be strongly dependent on the magnetic-field range in which the fitting is made (Fig. 4a). Moreover, it becomes unclear how to account for the prefactor values that are substantially greater than unity ($\alpha = 1.4$–2.2). As far as we know, only the valley degeneracy or the presence of several filled confinement subbands can result in $\alpha > 1$. Obviously, this is not the case in the situation considered. All this indicates that Eq. (1) cannot adequately describe our experimental results and that the effect of a longitudinal magnetic field does not reduce to an effective increase in the phase relaxation rate as in the case of structure 3512. Below, we show that the experimental results can be quantitatively described with allowance for the existence of large-scale roughness arising due to the presence of nanoclusters in the H5610 structure. Actually, due to the existence of nanoclusters, the motion of an electron along the plane of the structure is no longer two-dimensional; the electron position in the QW is subjected to fluctuations, as shown in the inset to Fig. 4a.

The effect of a longitudinal magnetic field on the shape of the transverse magnetoresistance curves for the case $L > l_{\mathrm{p}}$ was studied theoretically in [5]. However, the final expressions for the magnetoconductivity appear to be rather involved and inconvenient for practical use. From the physical point of view, the limiting case of $L > l_\varphi$ is simpler. In this case, we may assume that all closed trajectories of interest lie in the flat elements with a characteristic size exceeding l_φ and that these elements form small random angles β with the plane of the ideal structure. The magnetoresistance of such a system is given by the sum of the contributions from each of these regions. If we write the contribution of each element as $\delta\sigma(B_n, \tau_\varphi) \simeq \delta\sigma(B_\perp + \beta B_\parallel, \tau_\varphi)$, where B_n is the projection of the total magnetic field onto a normal to the plane of the element, the total magnetoresistance can be written as

$$\sigma(B_\perp, B_\parallel, \tau_\varphi) = \int d\beta F(\beta)\delta\sigma(B_\perp + \beta B_\parallel, \tau_\varphi), \quad (5)$$

where $F(\beta)$ is the slope-angle distribution function. In order to use Eq. (5) to process experimental results, we must specify the function $F(\beta)$. We assumed that the slope angles are distributed under a normal law with standard deviation Δ_β. For $\delta\sigma(B_\perp + \beta B_\parallel, \tau_\varphi)$, we used the experimental $\sigma(B_\perp)$ curve measured at $B_\parallel = 0$. In this approach, there is only one fitting parameter, Δ_β; this substantially facilitates the processing of the results. The results of the fitting procedure for $\sigma(B_\perp, B_\parallel) - \sigma(0, B_\parallel)$ are shown in Fig. 4b. We see that the shape of the experimental curves is described well by this simple model down to $B_\parallel = 2$ T and, moreover, the magnitude

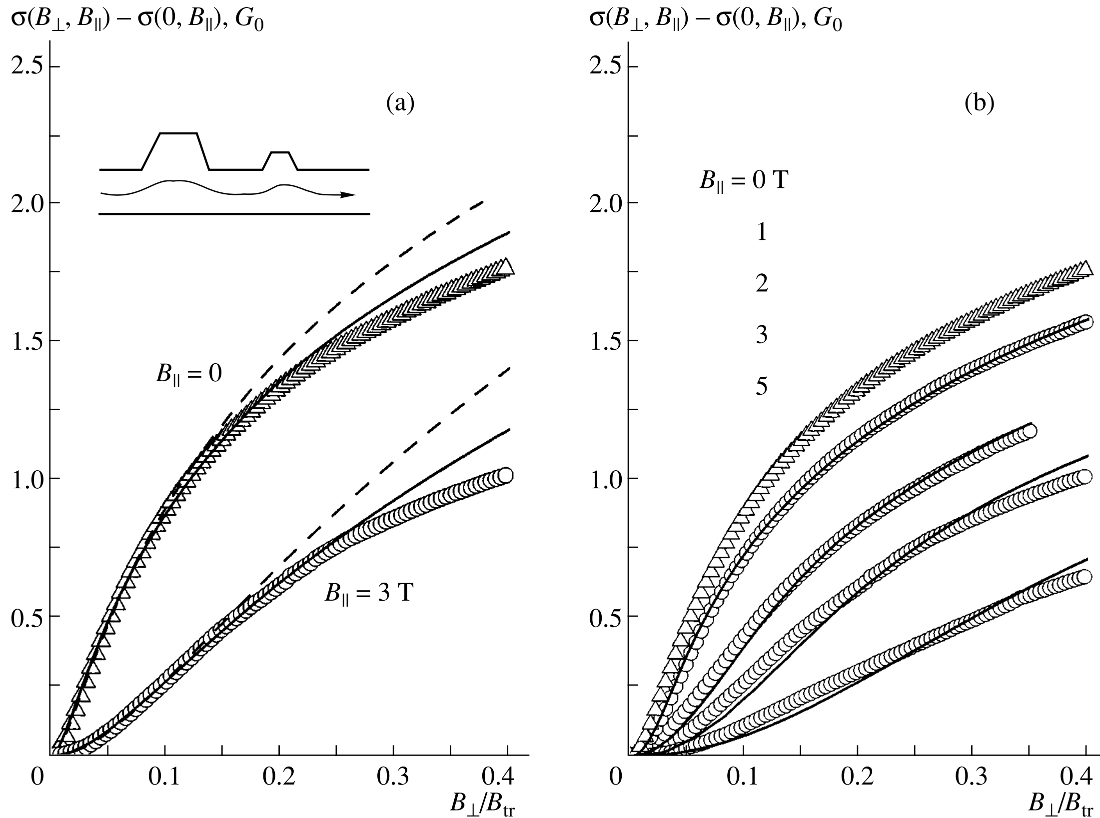

Fig. 4. Transverse magnetoconductivity $\sigma(B_\perp, B_\parallel) - \sigma(0, B_\parallel)$ as a function of $B_\perp$ measured at different values of $B_\parallel$ for sample H5610#2 at $T = 1.45$ K and $V_g = -2.5$ V. Symbols correspond to experimental results. Curves in panel (a) are the results of fitting by Eq. (1) with the following parameters: $B_\parallel = 0$: $\alpha = 1.0$, $\tau_\varphi = 1.2 \times 10^{-11}$ s (dashed curves) and $\alpha = 0.9$, and $\tau_\varphi = 1.45 \times 10^{-11}$ s (solid curves); $B_\parallel = 3$ T: $\alpha = 2.2$, $\tau_\varphi = 2.3 \times 10^{-12}$ s (dashed curves) and $\alpha = 1.4$, and $\tau_\varphi = 2.9 \times 10^{-12}$ s (solid curves). Dashed and solid curves correspond to different ranges of magnetic fields in which the fitting procedure was made: the dashed curve corresponds to $B_\perp = (0\text{–}0.1)B_{tr}$, and the solid curve to $B_\perp = (0\text{–}0.2)B_{tr}$. Curves in panel (b) are the result of fitting by Eq. (5). The values of parameter Δ_β are 0.34°, 0.41°, 0.47°, and 0.52° for $B_\parallel$ changing from 1 to 5 T. The inset illustrates the motion of an electron along the QW with one rough interface.

of the parameter Δ_β indeed appears to be small, $\Delta_\beta \simeq$ 0.3°–0.4°.

For high magnetic fields, $B_\parallel > 3$T, the curves calculated in this model deviate appreciably from the experimental curves. We believe that this disagreement is related to the fact that, in our approach, we disregarded small-scale roughness, which obviously exists in the H5610 structure in addition to large-scale roughness. As shown above, small-scale roughness is the reason for the decrease in τ_φ after the application of a magnetic field. Thus, when processing the experimental results obtained for high $B_\parallel$, the substitution of the experimental $\sigma(B_\perp)$ curve measured at $B_\parallel = 0$ into Eq. (5) is not justified.

3.3. Results of Microscopic Studies

To obtain direct information on the characteristic roughness scale, we measured the profile of the QW surface in the structures under study. After transport measurements, the covering GaAs layer was removed using selective etching [11–13]. Then, the surface was studied using a TopoMetrix Accurex TMX-2100 atomic-force microscope (AFM). The results obtained for both structures are shown in Fig. 5. It is clearly seen that the roughness scale widely differs for different structures. Indeed, the amplitude of roughness with lateral size $\mathcal{L} > l_\varphi$ is much greater for structure H5610 (the length l_φ determined at $T = 1.5$ K is equal to 870 and 490 nm for structures 3512 and H5610, respectively). To obtain quantitative information related to the information obtained from transport measurements, mathematical scan processing was performed.

First, we consider the results of the analysis of large-scale roughness. The correlation analysis performed for structure H5610 showed that the correlation length, $L \simeq$ 1 μm, is indeed greater than the phase-breaking length l_φ, which is approximately equal to 300–500 nm at $T =$ 1.5 K (for different voltages at the gate electrode). Therefore, the approach used above in analyzing the

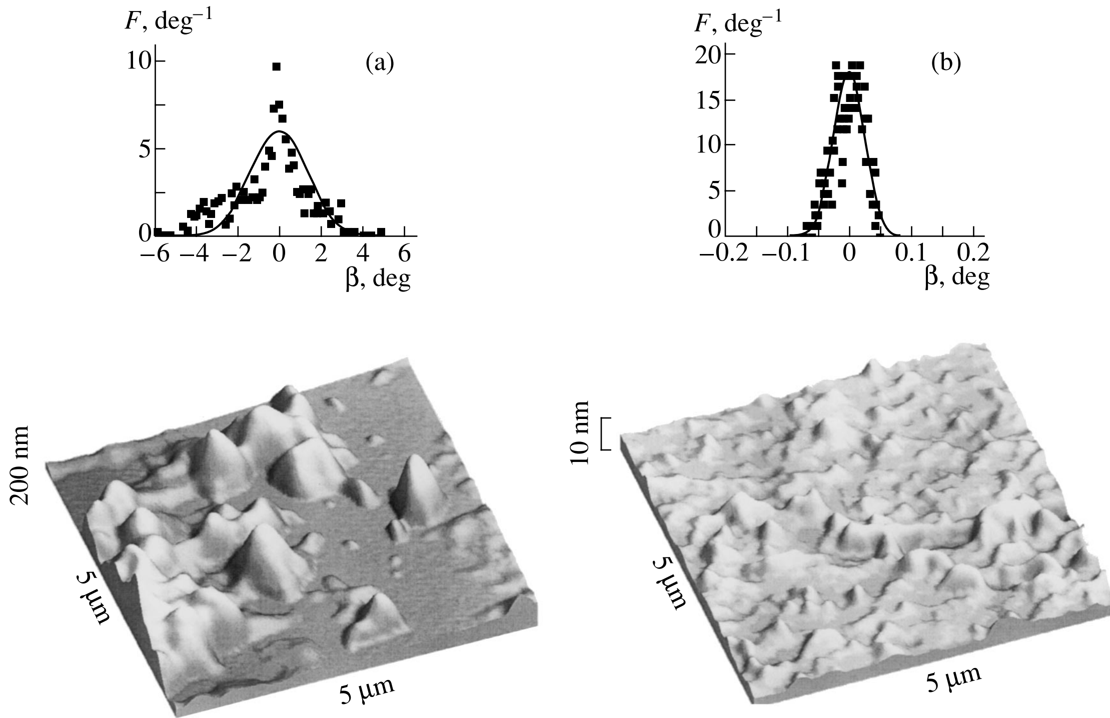

Fig. 5. Results of AFM studies for structures (a) H5610 and (b) 3512. The insets show the angle distribution function $F(\beta)$ obtained for $\mathcal{L} = 2l_\varphi$.

transverse magnetoconductivity of structure H5610 is justified. Next, according to the model used in the previous subsection, the surface was approximated by a set of flat fragments of fixed size $\mathcal{L} > l_\varphi$. Then, we found the slope-angle distribution function $F(\beta)$ involved in Eq. (5). For structure H5610, the result is shown in the inset to Fig. 5a. If the distribution obtained in this way is fitted by a Gaussian function, then it appears that the standard deviation Δ_β is approximately equal to 2° and differs by no more than 30% for different sizes of the approximating fragments, $\mathcal{L} = 2l_\varphi$ and $3l_\varphi$. This value of Δ_β is approximately six times greater than the value obtained from studying the interference quantum correction. Qualitatively, this can be understood if we take into account that the electron actually moves not along the surface, whose profile is obtained from AFM studies, but rather in the QW, which is located under this surface. Therefore, the deviations of the trajectory of electron motion in the growth direction of the structure appear to be smaller than the deviations of the surface from an ideal plane.

Similar processing performed for structure 3512 shows that, in this case, the standard deviation Δ_β is only 0.035° (see inset to Fig. 5b); it follows that there is virtually no large-scale roughness in this structure. This conclusion completely agrees with the results of the transport measurements.

To estimate the parameter $\Delta^2 L$ describing the contribution of small-scale roughness to weak localization, we studied selectively etched surfaces of the structures with a high resolution. Mathematical processing showed that the magnitude of this parameter for structure 3512 is approximately 8 nm^3, in good agreement with the results shown in Fig. 3c.

4. CONCLUSIONS

We have experimentally studied the effect that a longitudinal magnetic field exerts on the transverse negative magnetoresistance by suppressing the interference quantum correction. We have shown that this effect depends substantially on the relation between the mean free path and the characteristic lateral roughness size. An analysis of the shape of the transverse magnetoresistance curves measured at different values of $B_\parallel$ has allowed us to estimate the characteristic roughness size. The results obtained are in good agreement with the results of atomic force microscopy studies.

ACKNOWLEDGMENTS

This study was supported by the Russian Foundation for Basic Research (projects nos. 03-02-16150, 03-02-06025, 04-02-16626), RESC (grants EK-005-X1, Y1-P-05-11), and the program "Physics of Solid State Nanostructures."

REFERENCES

1. J. S. Meyer, A. Altland, and B. L. Altshuler, Phys. Rev. Lett. **89**, 206601 (2002).
2. J. S. Meyer, V. I. Fal'ko, and B. L. Altshuler, in *Proceedings of the NATO ASI: Field Theory of Strongly Correlated Fermions and Bosons in Low-Dimensional Disordered System, Windsor, 2001*, Ed. by I. V. Lerner, B. L. Altshuler, V. I. Fal'ko, and T. Giamarchi (Kluwer Academic, Dordrecht, 2002), NATO Sci. Ser. II, Vol. 72, p. 117.
3. P. M. Mensz and R. G. Wheeler, Phys. Rev. B **35**, 2844 (1987).
4. A. G. Malshukov, K. A. Chao, and M. Willander, Phys. Rev. B **56**, 6436 (1997).
5. H. Mathur and H. U. Baranger, Phys. Rev. B **64**, 235325 (2001).
6. G. M. Minkov, A. V. Germanenko, O. E. Rut, A. A. Sherstobitov, B. N. Zvonkov, E. A. Uskova, and A. A. Birukov, Phys. Rev. B **64**, 193309 (2001).
7. G. M. Minkov, O. E. Rut, A. V. Germanenko, A. A. Sherstobitov, B. N. Zvonkov, E. A. Uskova, and A. A. Birukov, Phys. Rev. B **65**, 235322 (2002).
8. S. Hikami, A. Larkin, and Y. Nagaoka, Prog. Theor. Phys. **63**, 707 (1980).
9. A. G. Malshukov, V. A. Froltsov, and K. A. Chao, Phys. Rev. B **59**, 5702 (1999).
10. Kuo-Jen Chao, Ning Liu, Chin-Kang Shin, D. W. Gotthold, and B. G. Streetman, Appl. Phys. Lett. **75**, 1703 (1999).
11. R. Retting and W. Stolz, Physica E (Amsterdam) **2**, 277 (1998).
12. I. A. Karpovich, N. V. Baidus, B. N. Zvonkov, D. O. Filatov, S. B. Levichev, A. V. Zdoroveishev, and V. A. Perevoshikov, Phys. Low-Dimens. Semicond. Struct., No. 3/4, 341 (2001).
13. I. A. Karpovich, A. V. Zdoroveishev, A. P. Gorshkov, D. O. Filatov, and R. N. Skvortsov, Phys. Low-Dimens. Semicond. Struct., No. 3/4, 191 (2003).

Translated by I. Zvyagin

Physics of the Solid State, Vol. 47, No. 1, 2005, pp. 141–144. Translated from Fizika Tverdogo Tela, Vol. 47, No. 1, 2005, pp. 136–138.
Original Russian Text Copyright © 2005 by Demidov, Karzanov, Demidova, Belorunova, Gorshkov, Stepikhova, Sharonov.

PROCEEDINGS OF THE CONFERENCE "NANOPHOTONICS 2004"
(Nizhni Novgorod, Russia, May 2–6, 2004)

Properties of Magnesium Silicate Doped with Chromium in Porous Silicon

E. S. Demidov*, V. V. Karzanov*, N. E. Demidova*, I. S. Belorunova*, O. N. Gorshkov*, M. V. Stepikhova, and A. M. Sharonov****

** Nizhni Novgorod State University, pr. Gagarina 23/3, Nizhni Novgorod, 603950 Russia*
e-mail: demidov@phys.unn.runnet.ru
*** Institute for Physics of Microstructures, Russian Academy of Sciences, Nizhni Novgorod, 603950 Russia*

Abstract—Forsterite doped with Cr^{4+} ions is prepared in silicon-based structures according to a simple technique. These structures are of interest due to the characteristic luminescence in the near-IR range. Forsterite is synthesized by impregnation of porous silicon layers on n^+-Si and p^+-Si substrates with subsequent annealing in air. A photoluminescence response at a wavelength of 1.15 μm is observed at room temperature in porous silicon layers doped with magnesium and chromium for which the optimum annealing temperature is close to 700°C. The photoluminescence spectrum of porous silicon on the p^+-Si substrate contains a broad band at a wavelength of approximately 1.2 μm. This band does not depend on the annealing temperature and the magnesium and chromium content and is most likely associated with the presence of dislocations in silicon. The experimental EPR data and electrical properties of the structures are discussed. It is found that layers of pure porous silicon and chromium-doped porous silicon on n^+-Si substrates exhibit indications of discrete electron tunneling. *© 2005 Pleiades Publishing, Inc.*

1. INTRODUCTION

It is known that crystalline magnesium silicate (forsterite) doped with tetravalent chromium Mg_2SiO_4 : Cr is characterized by the maximum photoluminescence quantum efficiency (38%) in the range of the highest transparency in systems of quartz fiber optics at a wavelength of approximately 1.3 μm [1]. In the present work, we synthesized and studied a similar phase in thin layers of porous silicon. This system is of interest for the development of technologies for fabricating highly efficient electroluminescent light sources that would be compatible with silicon microelectronics. The specific features of these multiphase structures are the photonic and electronic interactions of silicon nanocrystals with inclusions of a dielectric phase activated by transition elements. Similar structures are also of interest from the standpoint of investigating the discrete tunneling through atoms of transition elements [2].

Porous silicon is especially attractive for the synthesis of oxides with tetravalent chromium replacing silicon due to the use of a simple technique that involves impregnation of pores with aqueous salt solutions followed by oxidation annealing. The nanotopology of porous silicon favors rapid formation of oxides at temperatures substantially lower than the temperatures necessary for the growth of forsterite single crystals.

In this work, the photoluminescence, electron paramagnetic resonance (EPR), and transverse transport in porous silicon layers doped with magnesium and chromium and grown on n-Si and p-Si single crystals heavily doped with shallow-level impurities (up to approximately 10^{19} cm^{-3}) were investigated in order to elucidate how Group III and V dopant impurities affect both the Fermi level in porous silicon and the properties of the materials prepared by the proposed technique. Solving this problem with the use of Mg_2SiO_4 : Cr crystals grown by a traditional technique presents considerable difficulties. The high conductivity of the silicon substrate almost eliminates its contribution to the EPR spectra of porous silicon and the current–voltage characteristics of diode structures with porous silicon interlayers.

2. SAMPLE PREPARATION AND EXPERIMENTAL TECHNIQUE

Porous silicon layers were grown through a standard anodic dissolution of Si(110) single-crystal plates in a 50% hydrofluoric acid solution in ethanol for 10 min at a current density of 10 mA/cm^2. A layer 2.7 μm thick was grown on a KÉS 0.01 n-Si substrate, and a layer approximately 1 μm thick was formed on a KDB 0.005 p-Si substrate. Porous silicon was saturated either with chromium or with chromium and magnesium by impregnation with $MgCl_2$ and CrO_3 aqueous solutions, followed by drying and oxidation annealing in a furnace at temperatures of 700 and 1000°C for 10 min in air. In the case when porous silicon was doped with both magnesium and chromium, these elements were taken in an atomic ratio of 200 : 1 (i.e., at approximately the same ratio used for Mg_2SiO_4 : Cr laser crystals [1]). When porous silicon was doped only with

1063-7834/05/4701-0141$26.00 © 2005 Pleiades Publishing, Inc.

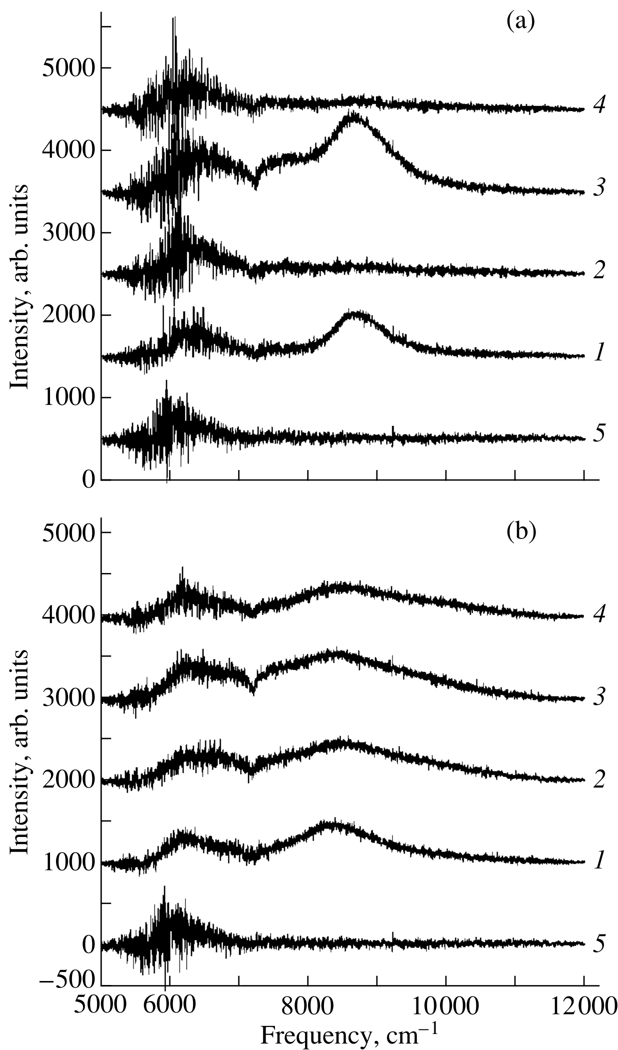

Fig. 1. Photoluminescence spectra of porous silicon layers on (a) KÉS 0.01 and (b) KDB 0.005 substrates at room temperature: (*1*) porous silicon with magnesium and chromium after annealing at 1000°C, (*2*) porous silicon with chromium after annealing at 700°C, (*3*) porous silicon with magnesium and chromium after annealing at 700°C, (*4*) pure porous silicon after annealing at 700°C, and (*5*) spectrometer noise.

chromium, the impregnation was carried out in a 10% CrO_3 aqueous solution. Our preliminary experiments showed that annealing of a dried $MgCl_2$ salt at a temperature of 700°C in air led to its transformation into MgO (this was revealed from the change in the hyperfine structure of the EPR spectra of the unavoidable manganese traces contained in magnesium compounds). Hexavalent chromium in CrO_3 readily transformed into a state with a lower valence, because this process occurs with a loss of oxygen upon heating of the oxide to temperatures above 200°C.

The photoluminescence spectra were measured at room temperature on a BOEM DAS Fourier spectrometer with a germanium detector cooled in liquid nitrogen. Optical pumping was performed with an argon laser at a wavelength of 514.5 nm and a radiation power of 250 mW. The EPR spectra were recorded at temperatures of 293 and 77 K on a spectrometer operating in the 3-cm band. The transverse transport was studied at room temperature by using the static current–voltage characteristics of diode structures containing porous silicon interlayers with indium metal contacts deposited on a silicon substrate and porous silicon (according to the procedure described in [3]).

3. RESULTS AND DISCUSSION

Our expectations regarding the formation of the forsterite phase doped with tetravalent chromium in porous silicon proved to be correct, at least, for silicon initially doped with antimony. It can be seen from Fig. 1a that the photoluminescence spectra of the porous silicon samples on the KÉS substrate after doping with magnesium and chromium (curves *1*, *3*) contain photoluminescence bands with maxima at a frequency of 8700 cm^{-1} (1.15 μm), which is close to the 1.17-μm photoluminescence band of Mg_2SiO_4 : Cr. Compared to the spectrum of the sample annealed at a temperature of 1000°C (curve *1*), the spectrum of the sample annealed at 700°C (curve *3*) contains a broader asymmetric photoluminescence band with a higher lying long-wavelength wing and an intensity that is higher by a factor of 2. No noticeable photoluminescence is observed for the porous silicon samples on the KÉS substrate without dopants or doped only with chromium (curves *2*, *4*). This implies that silicon is not replaced by chromium in SiO_2 at 700°C. It turned out that the porous silicon samples on the KDB 0.005 *p*-Si substrate exhibit a broad-band photoluminescence with the maximum at a frequency of 8400 cm^{-1} (1.2 μm). The manifestation of this photoluminescence is virtually independent of the presence of magnesium and chromium and the annealing temperature (Fig. 1b). It seems likely that this luminescence has a dislocation nature, as is the case with dislocation silicon containing boron [4].

The porous silicon samples on the KÉS 0.01 substrate after annealing at 700°C are characterized by an anisotropic EPR spectrum due to the presence of P_b centers at room temperature and 77 K (Fig. 2). According to the inferences drawn in our earlier work [5], this spectrum is associated with the dislocations involved in silicon nanograins in porous silicon. The intensities of the EPR spectra of pure porous silicon and porous silicon containing only chromium are rather high and comparable in magnitude. The intensity of the spectrum of magnesium-doped porous silicon is one order of magnitude lower. This can be caused by the decrease in the amount of silicon grains due to the formation of the Mg_2SiO_4 : Cr phase. The spectrum disappears altogether after annealing at 1000°C (most likely, because

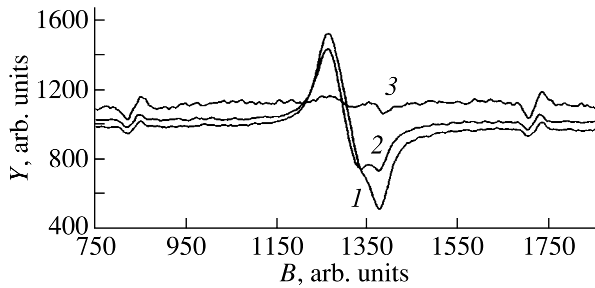

Fig. 2. EPR spectra of porous silicon samples at $T = 77$ K on the KÉS 0.01 substrate after annealing at 700°C: (*1*) pure porous silicon, (*2*) porous silicon with chromium, and (*3*) porous silicon with magnesium and chromium. The two extreme lines with reversed polarities in all the spectra correspond to the MgO : Mn reference sample.

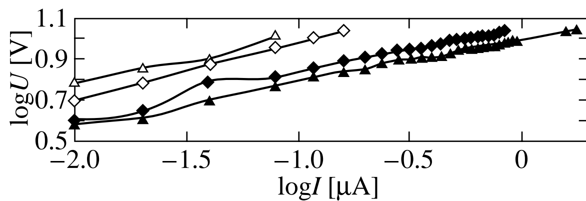

Fig. 3. Current–voltage characteristics of diode structures with interlayers formed by porous silicon on the KÉS 0.01 substrate without magnesium and chromium dopants after annealing at 700°C. The current–voltage curves for two junctions are depicted. Closed and open symbols indicate forward and reverse branches of the current–voltage characteristics, respectively.

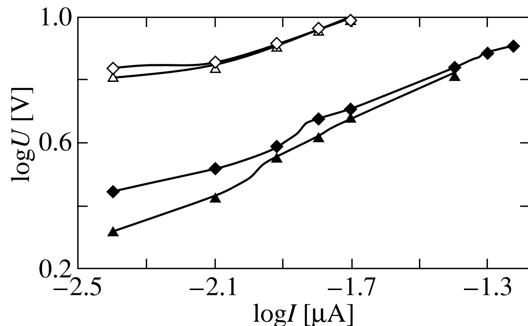

Fig. 4. The same as in Fig. 3 for diode structures with interlayers formed by porous silicon doped with chromium.

porous silicon almost completely transforms into forsterite and silicon oxide). As can be judged from the lower intensity of photoluminescence spectrum *3* as compared to the intensity of spectrum *1* (Fig. 1a), the amount of silicon transformed into SiO_2 at 1000°C is larger than that transformed at 700°C. It can be seen from Fig. 2 that the EPR spectrum of porous silicon doped with chromium (spectrum *2*) and the spectrum of porous silicon doped with chromium and magnesium (spectrum *3*) contain a narrow line. The *g* factor is equal to approximately 2. Possibly, this line can be attributed to tetravalent chromium. For the sample doped only with chromium (spectrum *2*), this can indicate that chromium is incorporated into SiO_2 in place of silicon. However, this hypothesis calls for additional verification. The EPR signal of porous silicon on the KDB 0.005 substrate, as in [5], cannot be distinguished against the background of noises induced by recharging of P_b centers due to the lowering of the Fermi level.

As should be expected, the annealing of porous silicon in air leads to a drastic decrease in the electrical conductivity due to the oxidation of silicon nanoparticles. The passage of an electric current before the breakdown was observed only in diode structures with interlayers formed by pure porous silicon and chromium-doped porous silicon on the KÉS 0.01 substrates after annealing at 700°C. The current–voltage characteristics of these diodes (Figs. 3, 4) are nonlinear and obey the power law $I \sim V^n$ with additional stepwise changes in the current, as was observed earlier in [6, 7]. As follows from the data presented in Fig. 3, the current–voltage characteristics for pure porous silicon are described by a power dependence with $n = 3$–5. In chromium-doped porous silicon (Fig. 4), the electrical conductivity at voltage $U = 10$ V decreases by a factor of 40, most likely, due to the chemical reaction of chromium oxide with silicon nanoparticles. However, the electric current in this diode varies more weakly: $n \approx 2$ (similar to the passage of injection currents in dielectrics). The current steps and large exponents n indicate discrete electron tunneling through silicon nanograins in porous silicon. The exponent $n \approx 2$ for chromium-doped porous silicon can be associated with the smaller band gap in the chromium oxide as compared to that in SiO_2 and the larger contribution of injection currents, because silicon grains in this sample (according to the data in Fig. 2) are almost identical to those in pure porous silicon.

4. CONCLUSIONS

Thus, forsterite doped with tetravalent chromium was prepared in porous silicon on an n^+-Si substrate. The characteristic photoluminescence band at a wavelength of 1.15 μm was observed at room temperature. It turned out that the oxidation annealing temperature of 700°C is closer to being an optimum temperature than 1000°C. The presence of shallow-level impurities in silicon at a concentration of 10^{19} cm^{-3} has a profound effect not only on the formation of porous silicon but also on its properties. The photoluminescence spectrum of porous silicon on a p^+-Si substrate contains a broad band at a wavelength of approximately 1.2 μm. This band does not depend on the annealing temperature and the magnesium and chromium content and is most likely associated with the presence of dislocations in silicon. It was demonstrated that the EPR technique is

a convenient tool for controlling the state of silicon nanoparticles in porous silicon on an n^+-Si substrate.

It was found that layers of pure porous silicon and chromium-doped porous silicon on a KÉS 0.01 substrate exhibit indications of discrete electron tunneling.

REFERENCES

1. K. Kück, Appl. Phys. B **72**, 515 (2001).
2. E. S. Demidov, Pis'ma Zh. Éksp. Teor. Fiz. **71**, 513 (2000) [JETP Lett. **71**, 351 (2000)].
3. E. S. Demidov, V. V. Karzanov, N. E. Demidova, and V. N. Shabanov, Pis'ma Zh. Éksp. Teor. Fiz. **75**, 673 (2002) [JETP Lett. **75**, 556 (2002)].
4. Wai Lek Ng, M. A. Lourenco, R. M. Gwilliam, S. Ledain, G. Shao, and K. P. Homewood, Nature **410**, 192 (2001).
5. E. S. Demidov, V. V. Karzanov, and N. E. Demidova, in *Proceedings of Meeting on Nanophotonics* (Inst. Fiziki Mikrostruktur Ross. Akad. Nauk, Nizhni Novgorod, 2003), Vol. 1, p. 38.
6. E. S. Demidov, V. V. Karzanov, and V. G. Shengurov, Pis'ma Zh. Éksp. Teor. Fiz. **67**, 794 (1998) [JETP Lett. **67**, 839 (1998)].
7. E. S. Demidov, V. V. Karzanov, N. E. Demidova, and D. A. Zhestin, in *Proceedings of V International Conference on Optics, Optoelectronics, and Technology* (Ul'yanov. Gos. Univ., Ul'yanovsk, 2003), p. 199.

Translated by O. Borovik-Romanova

Physics of the Solid State, Vol. 47, No. 1, 2005, pp. 145–149. Translated from Fizika Tverdogo Tela, Vol. 47, No. 1, 2005, pp. 139–143.
Original Russian Text Copyright © 2005 by Gippius, Tikhodeev, Christ, Kuhl, Giessen.

PROCEEDINGS OF THE CONFERENCE
"NANOPHOTONICS 2004"
(Nizhni Novgorod, Russia, May 2–6, 2004)

Waveguide Plasmon Polaritons in Metal–Dielectric Photonic Crystal Slabs

N. A. Gippius*, S. G. Tikhodeev*, A. Christ, J. Kuhl**, and H. Giessen*****

**Prokhorov Institute of General Physics, Russian Academy of Sciences, ul. Vavilova 38, Moscow, 117942 Russia*
e-mail: tikh@gpi.ru
***Max-Planck-Institut für Festkörperforschung, Stuttgart, Germany*
****Universität Bonn, Institut für Angewandte Physik, Germany*

Abstract—The optical properties of arrays of metallic (gold) nanowires deposited on dielectric substrates are studied both theoretically and experimentally. Depending on the substrate, Wood's anomalies of two types are observed in the transmission spectra of such planar metal–dielectric photonic crystals. One of them is diffraction (Rayleigh) anomalies associated with the opening of diffraction channels to the substrate or air with an increase in the frequency of the incident light. The other type of Wood's anomaly is resonance anomalies associated with excitation of surface quasi-guided modes in the substrate. Coupling of the quasi-guided modes with individual nanowire plasmons brings about the formation of waveguide plasmon polaritons. This effect is accompanied by a strong rearrangement of the optical spectrum and can be utilized to control the photonic bands of metal–dielectric photonic crystal slabs. *© 2005 Pleiades Publishing, Inc.*

Photonic crystals are structures whose permittivity varies periodically in space with a period of the order of the wavelength of light. An explosive growth in the number of studies of such structures began after publications [1, 2]. A characteristic feature of the optical spectra of photonic crystals is the presence of photonic band gaps (see, e.g., [3, 4]). In addition to three-dimensional (3D) photonic crystals, one- and two-dimensionally periodic layered photonic crystals with an arbitrary complex vertical geometry are also of interest [5–7]. Photonic crystal slabs can be prepared using modern layer-by-layer lithographic techniques. The optical properties of such structures are of practical interest because of their potential integrability with microelectronics.

It should be noted that studies on photonic crystals had begun long before the appearance of this term. For example, the influence of the photonic energy gap on the radiative atomic transition times had been investigated by Bykov [8]. Studies on photonic crystal slabs, which are in effect diffraction gratings, began even earlier. In particular, the main features of the optical spectra of diffraction gratings are called Wood's anomalies, because they were first studied in classical work [9].

In the presence of optically active electronic resonances, the pattern of the photonic-crystal behavior becomes richer, because electronic and photonic resonances are coupled to form polaritons. Such photonic crystals are commonly called polaritonic. In polaritonic crystals, the electronic and photonic resonances can be controlled simultaneously. Depending on the type of electronic resonance, the crystals are called exciton-polaritonic (with a semiconducting nanostructure) and plasmon-polaritonic (with a metallic nanostructure). Among the exciton-polaritonic crystals, the so-called Bragg superlattices (one-dimensionally periodic vertical-layered structures) were the first to be studied [10–12], followed by another modification of exciton-polaritonic crystals, photonic crystal slabs with a semiconducting nanostructure in the layer plane [13–16].

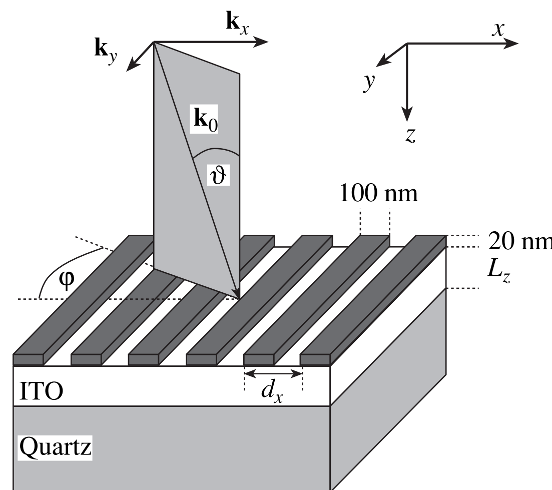

Fig. 1. Metal–dielectric photonic crystal consisting of an array of gold nanowires deposited on the surface of an indium–tin oxide (ITO) guide on a quartz substrate (schematic). The inclined arrow indicates the direction of incidence of light (in measuring the transmission spectrum) defined by the angle of incidence ϑ and the azimuth angle ϕ. The components of the wave vector $\mathbf{k}_0$ of the incident photon of frequency ω in vacuum ($k_0 = \omega/c$) in the horizontal plane are $k_x = k_0 \sin\vartheta\cos\phi$ (perpendicular to the nanowires) and $k_y = k_0 \sin\vartheta\cos\phi$ (along the wires).

1063-7834/05/4701-0145$26.00 © 2005 Pleiades Publishing, Inc.

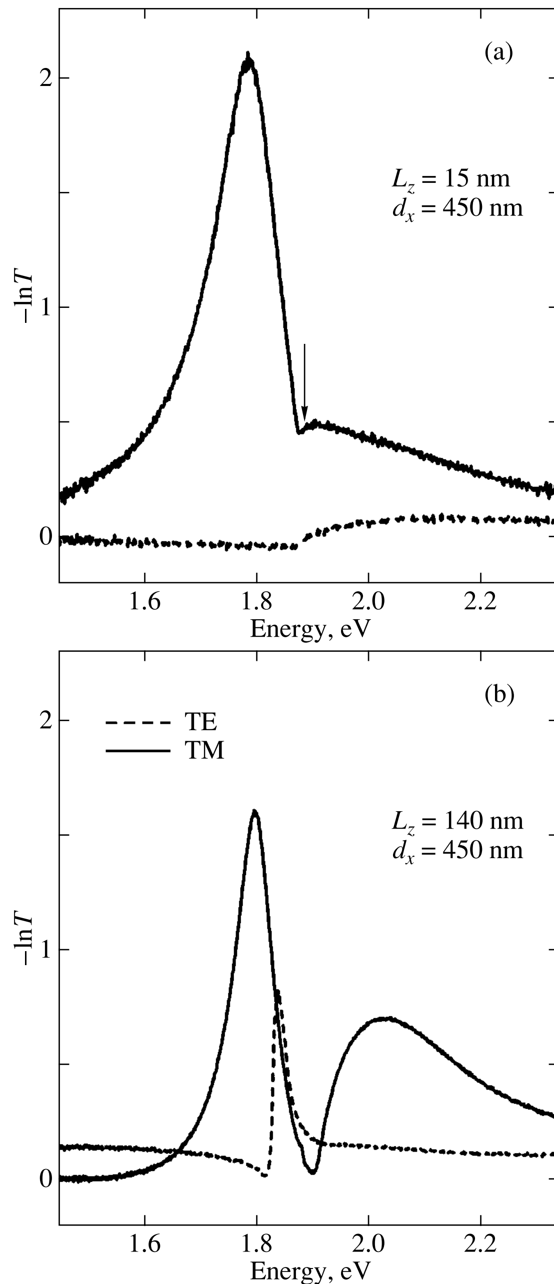

Fig. 2. Extinction spectra (–ln*T*, where *T* is the transmission) for structures with a period d_x = 450 nm deposited on (a) a thin and (b) a thick ITO layer, measured at normal incidence of light, $\vartheta = \phi = 0$. Solid and dashed curves correspond to the TM and TE polarizations (with the magnetic and electric fields directed along the nanowires), respectively. In panel (a), the arrow indicates the position of the diffraction (Rayleigh) anomaly.

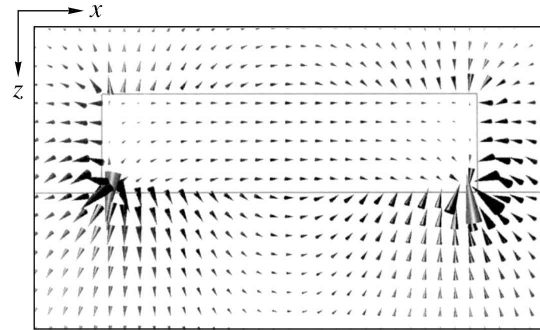

Fig. 3. Electric-field distribution over the region of a metallic nanowire near plasmon resonance. The plasmon is excited by a TM-polarized plane electromagnetic wave (with the electric field directed along the *x* axis perpendicular to the wire) incident from above (the angles of incidence are $\vartheta = \phi = 0$; see Fig. 1). The rectangle at the center corresponds to a cross section of the nanowire, and the region below the nanowire is an ITO waveguide. The length and orientation of a cone indicate the magnitude and direction of the electric field at the center of the cone.

One type of plasmon-polaritonic photonic crystals is a thin metallic film with an array of holes (or dielectric inclusions). Recently, an anomalously high transmittance of light was detected in such systems with holes whose diameter was smaller than the wavelength of light [17]. Physically, this effect is associated with the behavior of surface plasmons in a metal, which are excited due to Bragg resonances with the array of holes. In fact, in order to observe the resonant transmission, holes are not necessary; it will suffice to have a metallic layer with periodically modulated thickness such that the thickness in certain places is small in comparison with the skin depth [18]. Recently, the possible application of surface plasmons in high-resolution nanooptics, nanophotolithography, and other areas has been discussed (see, e.g., [19]).

Another type of polaritonic photonic crystals is an array of metallic nanodots [20] or nanowires [21]. However, in contrast to the surface plasmons in continuous metallic layers with periodically distributed dielectric inclusions considered above (or in arrays of closely spaced metallic particles), we have plasmons localized in metallic nanoparticles that are much smaller in size than the wavelength of light. Since the polarizability of localized plasmons is high, resonance phenomena in this case are more pronounced.

A metal–dielectric structure consisting of an array of metallic (gold) nanowires on a dielectric substrate is shown schematically in Fig. 1. Gold nanowires are deposited on an indium–tin oxide (ITO) layer on a quartz substrate. Experimental extinction spectra (–ln*T*), where *T* is the transmission coefficient) for a system with a period d_x = 450 nm for normal incidence of light with polarization parallel (TE) and perpendicular (TM) to the nanowires are shown in Fig. 2. Figures 2a and 2b show extinction spectra measured for systems supporting and not supporting waveguide modes, respectively, in the spectral region covered. The broad maximum observed in the TM polarization at a photon energy of 1.8 eV corresponds to excitation of a plasmon localized within a nanowire. The typical distribution of the electric field of a localized plasmon in the region of a

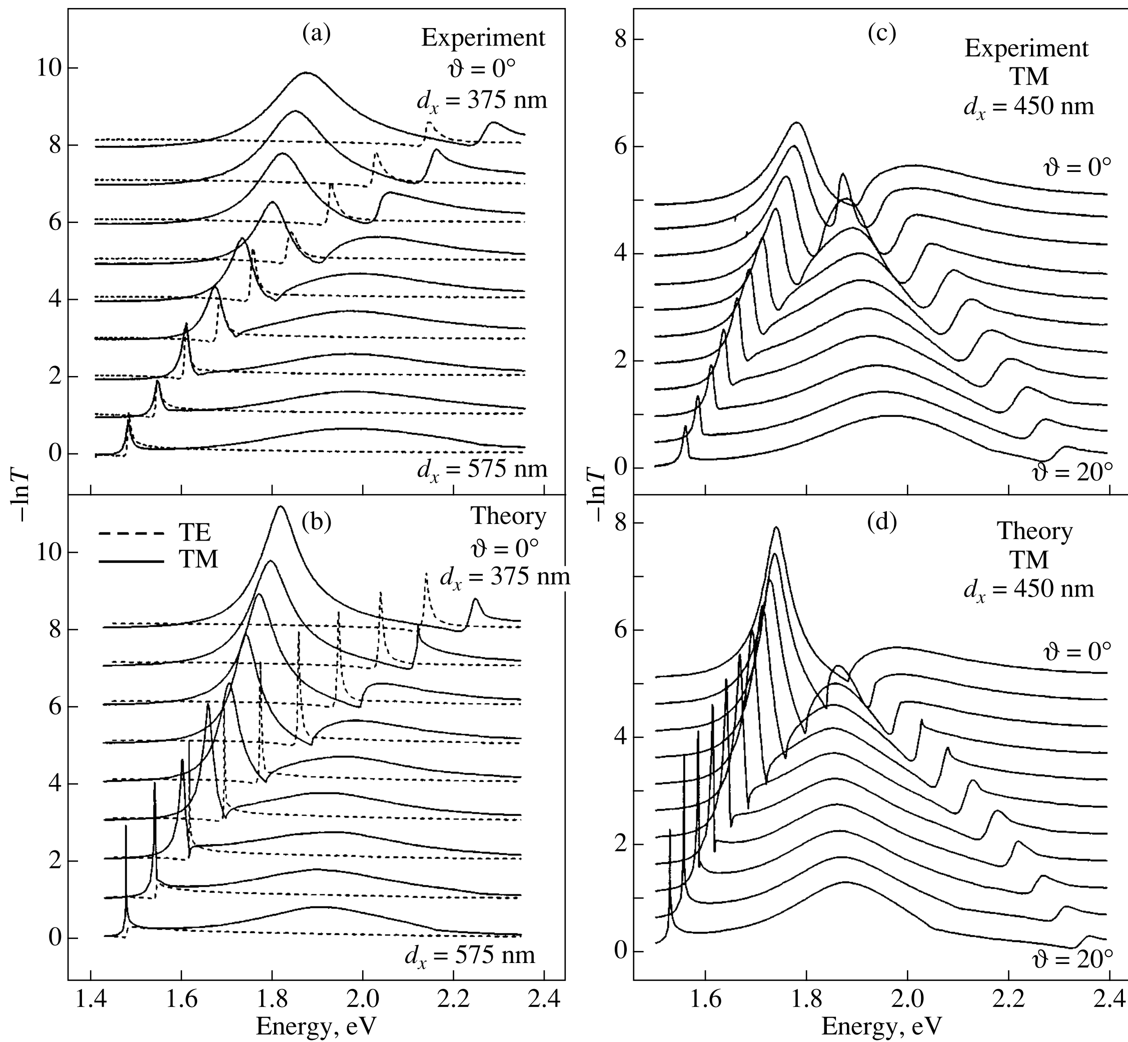

Fig. 4. Extinction spectra (–ln*T*, where *T* is the transmission) (a, c) measured and (b, d) calculated using the scattering-matrix method for the case where the plane of incidence of light is perpendicular to the nanowires ($\varphi = 0$). Also shown are (a, b) the dependences on the structure period d_x, varied from 375 to 575 nm in steps of 25 nm, for normal incidence of light, $\vartheta = 0°$, and (c, d) the dependences on the angle of incidence ϑ, varied from 0° to 20° in steps of 2°, for a structure with a period d_x = 450 nm. Solid and dashed curves correspond to the TM and TE polarizations (with the magnetic and electric fields directed along the nanowires), respectively. The bottom spectra in each panel are shown on the correct scale. All other spectra are shifted equidistantly upward.

nanowire is shown in Fig. 3. A characteristic feature of the localized plasmon is the pronounced dipolar character of the field distribution in the near wave zone outside the nanowire, whereas the field is approximately uniform over the nanowire. The significant enhancement of the field near the nanowire corners is also worth noting. Localized plasmons are not excited in the TE polarization (i.e., in the case where the electric field is directed along the nanowire). In the high-frequency wing of the plasmon resonance, we see Wood's anomaly (indicated by an arrow in Fig. 2a) associated with the opening of a diffraction channel to the substrate, which occurs as the frequency of the incident light increases. Such square root singularities commonly manifest themselves as a cusp in the spectral dependences.

If substrates support waveguide modes, the extinction spectra change significantly (Fig. 2b). In the TE polarization, the changes are simpler: in the case of normal incidence, a narrow peak appears, which shifts to lower frequencies as the period of the structure is increased. This behavior is clearly shown in Figs. 4a and 4b (dashed lines). The narrow peak is associated with the resonant excitation of a standing wave formed by TE_0 waveguide modes with Bragg wave vectors $\pm 2\pi/d_x$ in the waveguide. Therefore, this peak is a so-called resonance Wood anomaly associated with an incident quasi-waveguide-mode wave in the photonic crystal slab. A more detailed analysis of the behavior of quasi-waveguide modes in photonic crystal slabs can be found in [22] (see also references therein).

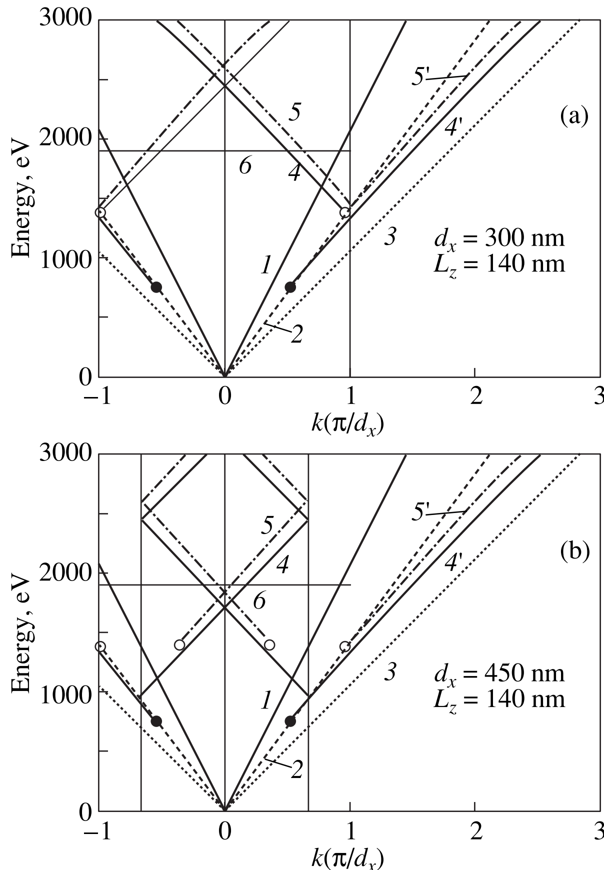

Fig. 5. Empty-lattice approximation for a system with a period d_x equal to (a) 300 and (b) 450 nm. Lines *1–3* represent cones of light in air, quartz, and ITO, respectively; lines *4*' and *5*' are dispersion curves of the TE_0 and TM_0 waveguide modes, respectively, in an ITO waveguide of thickness L_z = 140 nm; and lines *4* and *5* are dispersion curves of the TE_0 and TM_0 waveguide modes, respectively, folded into the first Brillouin zone of the corresponding lattice. Solid and open circles indicate the energy cutoffs of the TE_0 and TM_0 modes. Horizontal line *6* corresponds to the energy of the localized plasmon in a nanowire.

The behavior of such standing waves with variations in the structure period can be explained in terms of the empty-lattice approximation for the 1D photonic crystal slab (Fig. 5). By folding the dispersion curves of the TE_0 mode into the first Brillouin zone (lines *4*', *4* in Fig. 5), it can be seen that there is Bragg resonance at the Γ point, which shifts to lower energies as the period increases, that is, as the first Brillouin zone decreases in size (Figs. 5a, 5b for d_x = 300, 450 nm, respectively).

The behavior of TM-polarized spectra is much more complicated and relates to the coupling of the TM_0 quasi-waveguide modes (lines *5*', *5* in Fig. 5) with localized plasmons in nanowires (horizontal lines *6*). In the empty-lattice approximation, it can be seen that such resonance can occur in a structure with a period $d_x \sim 450$ nm if the localized-plasmon frequency is of the order of 1.8 eV. Indeed, the anticrossing of the two resonances is clearly seen from Fig. 4 to occur at $d_x \sim 450$ nm and is accompanied by the formation of a waveguide plasmon polariton [21].

For oblique incidence of light, the behavior of the extinction curves is more complex because of a third resonance (Figs. 4c, 4d). This resonance is associated with the excitation of a mode that is antisymmetric at the center of the Brillouin zone and, hence, does not manifest itself at normal incidence of light.

Thus, if the dielectric substrate supports waveguide modes, second-type Wood anomalies can arise, which are resonance anomalies associated with the excitation of surface quasi-waveguide modes in the substrate. Resonance coupling of these surface modes with localized plasmon excitations brings about the formation of waveguide plasmon polaritons [21]. This effect is accompanied by a significant rearrangement of the optical spectrum and can be used to control the photon energy bands in photonic crystal slabs. For example, photon stop bands overlapping for all polarizations can be formed. Due to the high optical oscillator strength of nanowire plasmons, the Rabi splitting in the waveguide plasmon polariton can be extremely large (up to 250–300 meV).

The theoretical extinction spectra in Figs. 4b and 4d were calculated using the scattering-matrix method [22] without fitting parameters; the geometrical dimensions of the system were measured experimentally, and the frequency-dependent permittivities were taken from the literature (see discussion in [21]). It can be seen that the scattering-matrix method reproduces all qualitative features of the behavior of optical spectra fairly well. Furthermore, this method enables one to calculate the distribution of electromagnetic fields in the near wave zone, which is essential to understanding the physics of the processes occurring in a photonic crystal slab and to describing possible nonlinear optical effects. The electric-field distribution in the region of a metallic nanowire presented in Fig. 3 was calculated using the scattering-matrix method.

The scattering-matrix method has significant advantages over the direct method of the finite difference on time domain (FDTD) used to solve Maxwell's equations in photonic-crystal physics. Since the former method is directly based on the general scattering theory, it is advantageous to use general properties, such as the unitarity (for transparent media) and reciprocity of scattering channels coupled via the time-reversal operation [23]. Using the scattering-matrix method, a resonance approximation has been developed for describing the optical properties of photonic crystal slabs in terms of resonant photonic modes, which are calculated with inclusion of the actual geometry and composition of a particular structure [23]. Furthermore, the method does not require large computational resources, in contrast to the FDTD method, and a personal computer will suffice in many cases. This method also allows one to include the frequency dispersion of the permittivity of

the various photonic-crystal constituents, which is particularly important in the case of metals. Using this method, one can also directly calculate losses due to radiation. A disadvantage of this method is its poor convergence when applied to metals.

ACKNOWLEDGMENTS

This study was supported in part by the Russian Foundation for Basic Research, the Ministry of Industry and Science of the Russian Federation, and the Presidium of the RAS.

REFERENCES

1. E. Yablonovitch, Phys. Rev. Lett. **58**, 2059 (1987).
2. S. John, Phys. Rev. Lett. **58**, 2486 (1987).
3. J. D. Joannopoulos, R. D. Meade, and J. D. Winn, *Photonic Crystals* (Princeton Univ. Press, Princeton, N.J., 1995).
4. K. Sakoda, *Optical Properties of Photonic Crystals* (Springer, Berlin, 2001).
5. R. Zengerle, J. Mod. Opt. **34**, 1589 (1987).
6. D. Labilloy, H. Benisty, C. Weisbuch, T. E. Krauss, R. M. De La Rue, V. Bardinal, R. Houdré, U. Oesterle, D. Cassagne, and C. Jouanin, Phys. Rev. Lett. **79**, 4147 (1997).
7. V. N. Astratov, D. M. Whittaker, I. S. Culshaw, R. M. Stevenson, M. S. Skolnick, T. F. Krauss, and R. M. De La Rue, Phys. Rev. B **60**, R16255 (1999).
8. V. P. Bykov, Zh. Éksp. Teor. Fiz. **62**, 505 (1972) [Sov. Phys. JETP **35**, 269 (1972)].
9. R. W. Wood, Philos. Mag. **4**, 396 (1902).
10. E. L. Ivchenko, A. I. Nesvizhskiĭ, and S. Jorda, Fiz. Tverd. Tela (St. Petersburg) **36**, 2118 (1994) [Phys. Solid State **36**, 1156 (1994)].
11. V. P. Kochereshko, G. R. Pozina, E. L. Ivchenko, D. R. Yakovlev, A. Waag, W. Ossau, G. Landwehr, R. Hellmann, and E. O. Göbel, Superlattices Microstruct. **15**, 471 (1994).
12. M. Hübner, J. Kuhl, T. Stroucken, A. Knorr, S. W. Koch, R. Hey, and K. Ploog, Phys. Rev. Lett. **76**, 4199 (1996).
13. L. Pilozzi, A. D'Andrea, and R. Del Sole, Phys. Rev. B **54**, 10763 (1996).
14. T. Fujita, Y. Sato, T. Kuitani, and T. Ishihara, Phys. Rev. B **57**, 12428 (1998).
15. A. L. Yablonskii, E. A. Muljarov, N. A. Gippius, S. G. Tikhodeev, T. Fujita, and T. Ishihara, J. Phys. Soc. Jpn. **70**, 1137 (2001).
16. R. Shimada, A. L. Yablonskii, S. G. Tikhodeev, and T. Ishihara, IEEE J. Quantum Electron. **38**, 872 (2002).
17. T. W. Ebbesen, H. J. Lezec, H. F. Ghaemi, T. Thio, and P. A. Wolff, Nature **391**, 667 (1998).
18. I. Avrutsky, Y. Zhao, and V. Kochergin, Opt. Lett. **25**, 595 (2000).
19. W. L. Barnes, A. Dereux, and T. W. Ebbsen, Nature **424**, 824 (2003).
20. S. Linden, J. Kuhl, and H. Giessen, Phys. Rev. Lett. **86**, 4688 (2001).
21. A. Christ, S. G. Tikhodeev, N. A. Gippius, J. Kuhl, and H. Giessen, Phys. Rev. Lett. **91**, 183901 (2003).
22. S. G. Tikhodeev, A. L. Yablonskii, E. A. Muljarov, N. A. Gippius, and T. Ishihara, Phys. Rev. B **66**, 045102 (2002).
23. N. A. Gippius, S. G. Tikhodeev, and T. Ishihara, cond-mat/0403010 (2004).

Translated by Yu. Epifanov

Physics of the Solid State, Vol. 47, No. 1, 2005, pp. 150–152. Translated from Fizika Tverdogo Tela, Vol. 47, No. 1, 2005, pp. 144–146.
Original Russian Text Copyright © 2005 by Sychev, Murzina, Kim, Aktsipetrov.

PROCEEDINGS OF THE CONFERENCE "NANOPHOTONICS 2004"
(Nizhni Novgorod, Russia, May 2–6, 2004)

Ferroelectric Photonic Crystals Based on Nanostructured Lead Zirconate Titanate

F. Yu. Sychev, T. V. Murzina, E. M. Kim, and O. A. Aktsipetrov
Department of Physics, Moscow State University, Vorob'evy gory, Moscow, 119992 Russia
e-mail: fsychev@shg.ru

Abstract—The first results obtained in the synthesis of one-dimensional ferroelectric photonic crystals based on nanostructured lead zirconate titanate and porous silicon are reported. The samples synthesized are studied using linear reflection and second optical harmonic spectroscopy. © *2005 Pleiades Publishing, Inc.*

1. INTRODUCTION

Photonic crystals and microcavities based on these crystals have been intensively studied in recent years. Great interest has been expressed by researchers in these structures due to their unique optical properties associated with the existence of the so-called photonic band gap. The presence of the photonic band gap in photonic crystals renders them promising for use in optoelectronic devices [1, 2] and, moreover, makes it possible to observe novel optical and nonlinear optical effects in these structures [3, 4].

Porous silicon is a material that has been widely used for producing photonic crystals [5, 6]. One-dimensional photonic crystals can be prepared by periodic variations in the porosity. This results in spatial modulation of the refractive index of porous silicon and in the formation of a photonic band gap in a frequency–angular range [6]. Moreover, the possibility exists of filling pores with various materials and, thus, of producing photonic crystals with different properties on the basis of porous silicon matrices. In this work, we present the first results obtained in the design and synthesis of one-dimensional ferroelectric photonic crystals and microcavities based on nanostructured lead zirconate titanate introduced into a photonic crystal matrix prepared from porous silicon.

The considerable research attention given to ferroelectric photonic crystals is mainly caused by the fact that the crystal structure of ferroelectrics in the ferroelectric phase has no inversion symmetry. As a result, these materials possess a volume dipolar quadratic susceptibility, which can be used, for example, for the generation of second optical harmonics. A photonic crystal or microcavity prepared from a ferroelectric material can significantly amplify the second optical harmonic signal due to the field localization and the fulfillment of the phase synchronism conditions. It is also of interest to analyze the possibility of controlling the properties of photonic crystals and microcavities. The permittivity and, correspondingly, the refractive index of ferroelectrics depend on the temperature and the external electrostatic field. Therefore, the location of the photonic band gap and the allowed microcavity mode of the ferroelectric photonic crystal can be controlled by varying the temperature and the magnitude of the applied electrostatic field.

2. SAMPLE PREPARATION AND EXPERIMENTAL TECHNIQUE

Photonic crystals based on lead zirconate titanate were synthesized according to the following procedure. At the first stage, samples of photonic crystals or microcavities were prepared by electrochemical etching of *p*- or *n*-type crystalline silicon with (001) orientation, which brought about the formation of pores in the direction perpendicular to the surface of the plate. According to atomic force microscopy, the mean diameter of the pores was approximately equal to 10 nm in *p*-type silicon and 100 nm in *n*-type silicon. Then, the samples were annealed at a temperature of 900°C. At the second stage, the sol of lead zirconate titanate was introduced into the photonic crystal samples in order to provide partial filling of the pores in the photonic crystals or microcavities. Thereafter, the samples were subjected to heat treatment under the following temperature–time conditions accepted for the sol–gel synthesis of polycrystalline lead zirconate titanate films: the first heat treatment was performed for 10 min at 180°C; the second heat treatment, for 30 min at 450°C; and the third heat treatment, for 60 min at 900°C. For the samples thus prepared, we analyzed the linear reflection spectra and the spectra of the intensity of the reflected second harmonics. In the nonlinear optical experiments, light from an optical parametric oscillator operating in the wavelength range 700–1200 nm with a pulse duration of 10 ns and a peak power of approximately 1 MW/cm^2 was used as probe radiation.

1063-7834/05/4701-0150$26.00 © 2005 Pleiades Publishing, Inc.

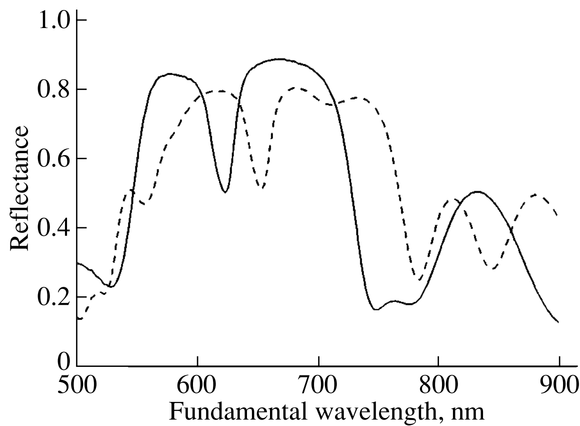

Fig. 1. Linear reflection spectra of the microcavities based on *p*-type silicon. The solid line represents the spectrum of the sample free of lead zirconate titanate. The dashed line indicates the spectrum of the sample with the introduced lead zirconate titanate sol.

3. RESULTS AND DISCUSSION

The photonic band gap of the photonic crystals and the mode of the microcavities are shifted because the pores in the matrices are partially filled with the lead zirconate titanate sol. Figure 1 shows the linear reflection spectra for two samples of the microcavities based on *p*-type silicon with the introduced lead zirconate titanate sol and without it. Both samples were subjected to heat treatment. The magnitude of the spectral shift is approximately equal to 50 nm. According to estimates, this value corresponds to the degree of filling of the porous structure with crystalline lead zirconate titanate, which falls in the range 10–15%. Moreover, the spectral width of the photonic band gap increases.

The linear reflection spectra of the annealed photonic crystals based on *n*-type silicon with the introduced lead zirconate titanate sol and without it are shown in Fig. 2a. The spectral shift of the photonic band gap is approximately equal to 50 nm. The spectrum of the unannealed sample free of lead zirconate titanate is also shown in this figure. Figure 2b displays the spectra of the intensity of reflected second harmonics for the same samples. The ferroelectric ordering of lead zirconate titanate in the porous silicon structure can be judged from the significant increase in the signal of the second harmonics for the sample containing lead zirconate titanate and subjected to high-temperature annealing. This increase in the signal of the second harmonics is caused by the formation of the polar phase in the form of lead zirconate titanate nanocrystallites in the porous structure. The intensity of the second harmonics at a maximum for the annealed sample containing lead zirconate titanate is more than 20 times higher than that for the annealed sample free of lead zirconate titanate. For comparison, Fig. 2b shows the spectrum of the intensity of the second harmonics for the unannealed sample free of lead zirconate titanate. The intensity of

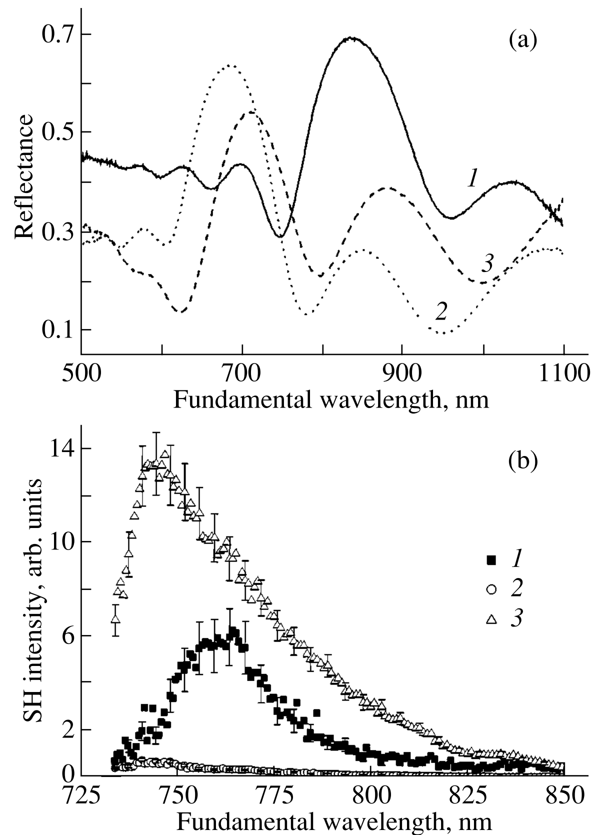

Fig. 2. (a) Linear reflection spectra and (b) the spectra of the second-harmonic intensity for photonic crystals based on *n*-type silicon: (*1*) unannealed sample free of lead zirconate titanate, (*2*) annealed sample free of lead zirconate titanate, and (*3*) annealed sample with the introduced lead zirconate titanate sol.

the second harmonics for this sample is approximately three times lower than that for the sample containing lead zirconate titanate. The intensity of the second harmonics increases in the case when the phase synchronism conditions are satisfied at the edges of the photonic band gap [2]. For the unannealed sample free of lead zirconate titanate, this increase is observed at the short-wavelength edge of the photonic band gap but is almost completely absent at the long-wavelength edge. For the annealed samples with the introduced lead zirconate titanate and without it, the increase in the intensity of the second harmonics is observed at the long-wavelength edge of the photonic band gap. Whether or not the intensity of the second harmonics increases at the short-wavelength edge of the photonic band gap for these samples cannot be conclusively established in this case, because their photonic band gaps lie outside the wavelength range of the optical parametric oscillator used in our experiments.

Figure 3 shows the linear reflection spectra and the spectra of the intensity of the reflected second harmonics for the annealed photonic crystal with the introduced lead zirconate titanate at different angles of inci-

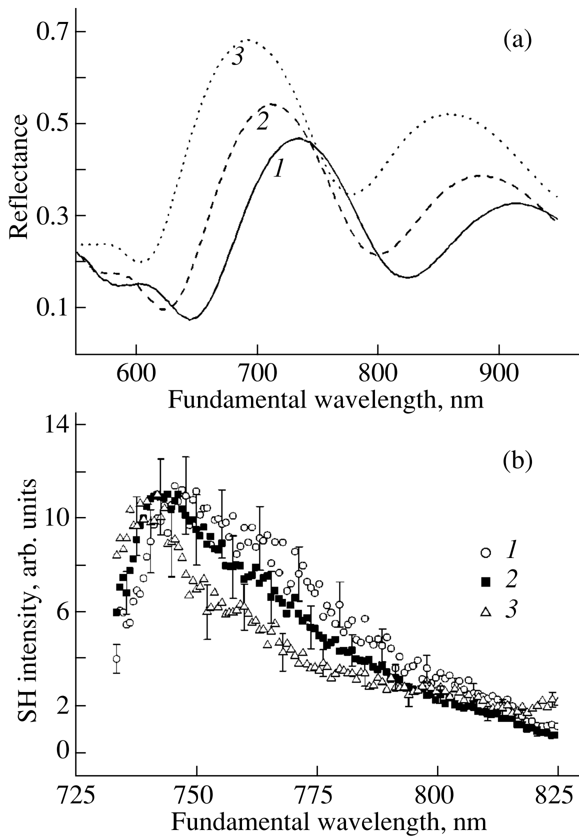

Fig. 3. (a) Linear reflection spectra and (b) the spectra of the second-harmonic intensity for the annealed photonic crystal based on *n*-type silicon with the introduced lead zirconate titanate sol at different angles of incidence of radiation θ = (*1*) 30°, (*2*) 45°, and (*3*) 60°.

dence of radiation θ = 30°, 45°, and 60°. An increase in the angle of incidence leads to a shift of the photonic band gap of the photonic crystal toward the short-wavelength range (Fig. 3a). For angles θ = 30°, 45°, and 60°, the center of the photonic band gap lies at wavelengths of 735, 715, and 695 nm, respectively. This behavior of the photonic band gap is characteristic of one-dimensional photonic crystals. As can be seen from the spectra of the second-harmonic intensity at the same angles of incidence of radiation, the maximum of the intensity also shifts with a change in the angle of incidence: it is located at wavelengths of approximately 748, 743, and 739 nm for angle θ = 30°, 45°, and 60°, respectively (Fig. 3b).

4. CONCLUSIONS

In this work, we developed a method for introducing lead zirconate titanate into a porous structure of photonic crystals and microcavities based on porous silicon. It was found that the intensity of the second harmonics in the ferroelectric photonic crystal based on nanostructured lead zirconate titanate increases by a factor of 20. The photonic band gap and the maximum of the intensity of the second harmonics in the ferroelectric photonic crystal are shifted when the angle of incidence of radiation on the structure is changed.

ACKNOWLEDGMENTS

This work was supported by the International Association of Assistance for the Promotion of Cooperation with Scientists from the New Independent States of the Former Soviet Union (project no. INTAS 03-51-3784) and the Russian Foundation for Basic Research (project nos. 04-02-16847, 03-02-39011).

REFERENCES

1. S. G. Johnson and J. D. Joannopolous, Acta Mater. **51**, 5823 (2003).
2. C. Weisbuch, H. Benisty, and R. Houdre, Int. J. High Speed Electron. Syst. **10**, 339 (2000).
3. T. V. Dolgova, A. I. Maidykovski, M. G. Martemyanov, A. A. Fedyanin, O. A. Aktsipetrov, G. Marowsky, V. A. Yakovlev, and G. Mattei, Appl. Phys. Lett. **81**, 2725 (2002).
4. A. Fainstein, B. Jusserand, and V. Thierry-Mieg, Phys. Rev. Lett. **75**, 3764 (1995).
5. L. Pavesi, Microelectron. J. **27**, 437 (1996).
6. F. Muller, A. Birner, U. Gösele, V. Lehmann, S. Ottow, and H. Foll, J. Porous Mater. **7**, 201 (2000).

Translated by I. Volkov

Physics of the Solid State, Vol. 47, No. 1, 2005, pp. 153–155. Translated from Fizika Tverdogo Tela, Vol. 47, No. 1, 2005, pp. 147–149.
Original Russian Text Copyright © 2005 by Murzina, Kim, Kapra, Aktsipetrov, Ivanchenko, Lifshits, Kuznetsova, Kravets.

PROCEEDINGS OF THE CONFERENCE
"NANOPHOTONICS 2004"
(Nizhni Novgorod, Russia, May 2–6, 2004)

Magnetization-Induced Third-Harmonic Generation in Nanostructures and Thin Films

T. V. Murzina*, E. M. Kim*, R. V. Kapra*, O. A. Aktsipetrov*, M. V. Ivanchenko, V. G. Lifshits**, S. V. Kuznetsova***, and A. F. Kravets******

** Department of Physics, Moscow State University, Vorob'evy gory, Moscow, 119992 Russia*
e-mail: mur@shr.shg.ru, aktsip@shg.ru
*** Institute of Automatics and Control Processes, Far East Division, Russian Academy of Sciences, ul. Radio 5, Vladivostok, 690041 Russia*
**** Institute of Physics and Information Technologies, Far East State University, ul. Sukhanova 8, Vladivostok, 690600 Russia*
***** Institute of Magnetism, National Academy of Sciences of Ukraine, Kiev, 03680 Ukraine*

Abstract—This paper reports on the results of research into low-dimensional magnetic structures that have been intensively studied over previous decades due to the discovery of novel effects that are exhibited by these structures but not observed in bulk magnetic materials. A nonlinear optical analog of the magnetooptical Kerr effect is revealed in the optical third-harmonic generation in thin magnetic metallic films and nanogranular structures. It is shown that the magnetic nonlinear optical Kerr effect observed in the third harmonic exceeds the magnetooptical analog by more than one order of magnitude. © *2005 Pleiades Publishing, Inc.*

1. INTRODUCTION

Magnetic nanostructures have attracted considerable research attention owing to the discovery of novel physical phenomena (such as spin-dependent scattering and tunneling, giant magnetoresistance, oscillations of exchange interaction between magnetic and nonmagnetic layers, etc. [1, 2]) that are observed in these structures but are absent in bulk magnetic materials. It has been demonstrated that magnetic nanostructures can exhibit new nonlinear optical and magnetooptical effects. In particular, recent studies have revealed that, under the conditions of optical second-harmonic generation (SHG), multilayer magnetic structures and magnetic nanoparticles are characterized by a giant nonlinear magnetooptical Kerr effect, which is a nonlinear optical analog of the magnetooptical Kerr effect [3, 4]. It should be noted that the revealed effects exceed the magnetooptical analogs by no less than one order of magnitude. However, up to now, investigation into the magnetic nonlinear optical effects has been limited only to the second-order processes and magnetization-induced optical third-harmonic generation (THG) in nanostructures has not been observed.

In this work, we revealed magnetization-induced optical third-harmonic generation, i.e., a nonlinear magnetooptical Kerr effect in the third-harmonic generation in magnetic nanoparticles and thin films. It was found experimentally that the magnetic nonlinear optical effect in the third harmonic has the same order of magnitude as in the second harmonic and exceeds the analogous linear magnetooptical effect by no less than one order of magnitude.

2. SAMPLE PREPARATION AND EXPERIMENTAL TECHNIQUE

Samples of iron and cobalt epitaxial films 200 nm thick and magnetic nanogranular films served as the objects of our investigation. The iron films were deposited under vacuum at a residual pressure of 1×10^{-9} to 2×10^{-9} Torr in a Riber LAS-600 apparatus equipped for diagnostics using low-energy electron diffraction and Auger electron spectroscopy. Single-crystal *n*-Si(111) with a resistivity of 4.5 Ω cm was used as a substrate. Granular films of composition Co_xAg_{1-x} were prepared through electron-beam evaporation from two sources under high vacuum. The mean size of cobalt grains in the films reached several nanometers at a cobalt content $x < 0.5$. Magnetization-induced third-harmonic generation was observed in the case when the surface of the samples was exposed to radiation from a YAG : Nd^{3+} laser at a wavelength of 1064 nm. The pulse duration was 15 ns, and the peak power was approximately equal to 1 MW/cm^2. The reflection of the radiation at the frequency of the third or second harmonics was separated out using suitable interference and color filters and was then recorded with a photomultiplier and an electronic gated recording system. The magnetization-induced changes in the phase of the second- or third-harmonic waves were measured using interferometry of the second and third harmonics, which is based on the interference between the second- and third-harmonic waves from a standard nonlinear source (a 30-nm-thick ITO film) and from the sample. The interference pattern is determined by the phase difference between the second-harmonic signals from the sample

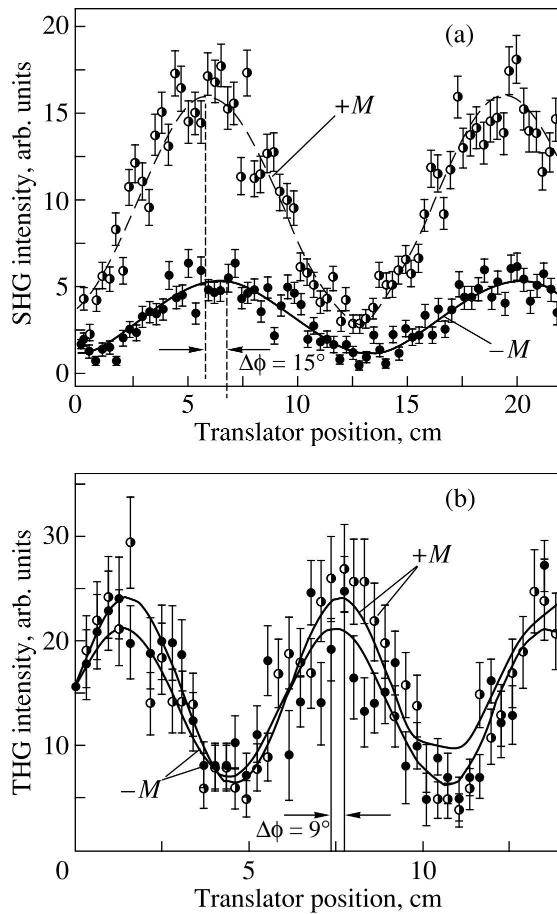

Fig. 1. Interferograms of the intensity of the (a) second and (b) third harmonics for iron films.

and the standard source and, consequently, can be described by a periodic function of the distance between these sources of the second and third harmonics (due to the dispersion of air).

3. RESULTS AND DISCUSSION

Magnetization-induced third-harmonic generation was revealed for all the studied samples. This effect manifests itself both in changes in the third-harmonic intensity and phase and in the polarization of the third-harmonic wave under application of a static magnetic field to the sample. Basic measurements were performed for the equatorial magnetooptical Kerr effect, for which the magnetic field is aligned parallel to the plane of the sample surface and is perpendicular to the plane of incidence of probe radiation. In this case, for both the linear and nonlinear magnetooptical Kerr effects, one can expect magnetization-induced changes in the intensity and phase of the second- and third-harmonic waves with no rotation of the plane of polarization [5]. For this reason, we measured both the magnetic contrast of the second- and third-harmonic intensity and the interference of the second and third harmonics in an external magnetic field, which made it possible to estimate the relative magnitude of the effective magnetization-induced components of the cubic susceptibility.

Figures 1a and 1b show the interferograms of the intensity of the second and third harmonics reflected from the iron film, which were measured for opposite directions of the magnetic field applied according to the scheme of the equatorial magnetooptical Kerr effect. It can be seen from these dependences that the change in the direction of the magnetic field leads to noticeable changes in both the intensity and the phase of the second- and third-harmonic waves.

In order to analyze the observed effects, the quadratic and cubic nonlinear susceptibility can be conveniently represented as the sum of the even component χ^{even} (which does not depend on the direction of the applied magnetic field) and the odd component χ^{odd} (which reverses sign when the direction of the magnetic field changes): $\hat{\chi} = e^{i\varphi}\hat{\chi}^{\text{odd}}(\mathbf{M}) + \chi^{\text{even}}$, where φ is the phase shift between the even and odd components and $\mathbf{M}$ is the magnetization of the medium. Therefore, the change in the direction of the magnetic field can lead to an odd (with respect to the magnetic field) change in the intensity of the second and third harmonics due to interference of the even and odd (with respect to the magnetization) fields of the second and third harmonics:

$$I \propto (e^{i\varphi}E^{\text{odd}} + E^{\text{even}})^2 \approx (\chi^{\text{even}})^2 \pm 2e^{i\varphi}\chi^{\text{odd}}(\pm M)\chi^{\text{even}}.$$

The magnetic contrast can serve as a measure of the magnetization-induced change in the intensity of the second or third harmonics:

$$\rho = (I(M) - I(-M))/(I(M) + I(-M)) \approx 2\chi^{\text{odd}}\cos\varphi/\chi^{\text{even}}.$$

The magnitude of the magnetic contrast is determined by both the relative magnitude of the odd (with respect to the magnetization) component of the nonlinear susceptibility and the phase shift φ. From the measurements of the magnetic contrast and the interferograms, we can estimate the relative magnitudes of the odd and even (with respect to the magnetic field) components of the susceptibility for cobalt. Taking into account the magnetization-induced phase shift, we obtain $\hat{\chi}^{(2)\text{odd}}(M)/\hat{\chi}^{(2)\text{even}} \approx 0.18$ for the quadratic susceptibility and $\hat{\chi}^{(3)\text{odd}}(M)/\hat{\chi}^{(3)\text{even}} \approx 0.09$ for the cubic susceptibility. For comparison, the maximum values for the linear magnetooptical Kerr effect do not exceed 1%.

The magnetization-induced effects observed in the third-harmonic generation were investigated in nanogranular films of composition Co_xAg_{1-x}. These films exhibit a giant magnetoresistance (up to 20% in a magnetic field of ~8 kOe at room temperature). The dependence of the magnetoresistance on the cobalt content in the films is shown in Fig. 2. A change in the intensity of

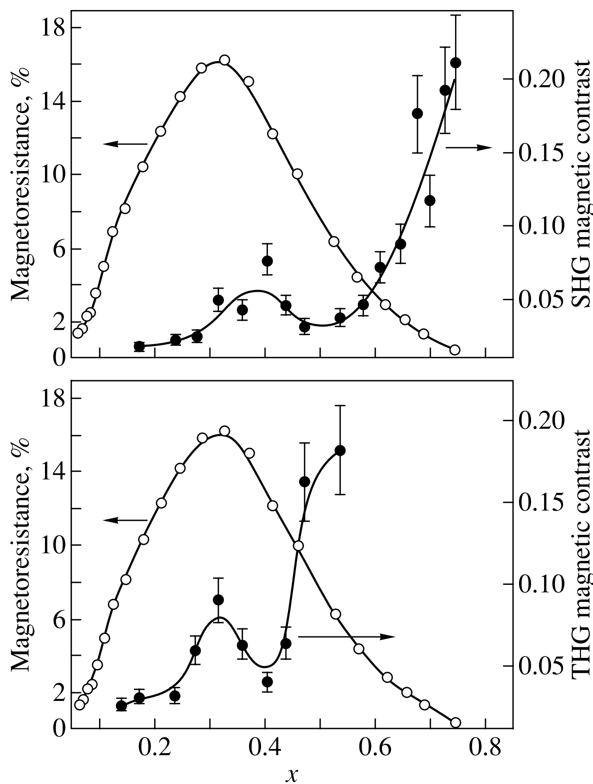

Fig. 2. Dependences of the magnetoresistance and the magnetic contrast of the second and third harmonics on the cobalt content x in the Co_xAg_{1-x} granular films.

both the second and third harmonics is observed in the geometry of the equatorial magnetooptical Kerr effect induced by the magnetic field. According to interferometry of the second and third harmonics, the magnetization-induced phase shift of the second- and third-harmonic wave in nanogranular films is insignificant (no more than 15°); hence, the magnetic contrast can be determined to a high accuracy from the ratio $\hat{\chi}^{(2,3)\text{odd}}(M)/\hat{\chi}^{(2,3)\text{even}}$.

The revealed magnetic contrast of the third-harmonic intensity has the same order of magnitude as that for the second harmonic and exceeds the contrast of the magnetooptical Kerr effect by at least one order of magnitude, as is the case with homogeneous thin films. The increase observed in the magnetic contrast for films with $x > 0.5$ is associated with both the increase in the cobalt content and the ferromagnetic ordering in the films. At the same time, the films with a cobalt content $x < 0.5$ are characterized by a nonmonotonic dependence of the magnetic contrast of the second and third harmonics. Note that the maximum in the magnetic contrast and the maximum in the magnetoresistance are observed in the same range of concentrations x of the magnetic material. In this range of concentrations, there exists a nanogranular structure in the films. It seems likely that the increase in the magnetic contrast in the second and third harmonics is due to the increase in the magnetic component of the nonlinear susceptibility in magnetic nanoparticles. The second mechanism responsible for the increase in the magnetic contrast of the second and third harmonics in the Co_xAg_{1-x} films can be the excitation of local surface plasmons in metallic nanoparticles and its related decrease in the nonmagnetic component of the nonlinear susceptibility for films of the given composition.

4. CONCLUSIONS

Thus, we revealed magnetization-induced effects under conditions of the third-harmonic generation in thin metallic films and nanogranular structures. It was demonstrated that the magnetic nonlinear optical Kerr effect in the third harmonic exceeds the magnetooptical analog by more than one order of magnitude.

ACKNOWLEDGMENTS

This work was supported by the International Association of Assistance for the Promotion of Cooperation with Scientists from the New Independent States of the Former Soviet Union (project no. INTAS 03-51-3784) and by the Russian Foundation for Basic Research (project no. 04-02-17059).

REFERENCES

1. S. S. Parkin, R. Bhadra, and K. P. Roche, Phys. Rev. Lett. **66**, 2152 (1991).
2. M. N. Baibich, J. M. Broto, A. Fert, F. Nguyen van Dau, F. Petroff, P. Etienne, G. Creuset, A. Freiederich, and J. Chazellas, Phys. Rev. Lett. **61**, 2472 (1988).
3. H. A. Wierenga, W. de Jong, M. W. J. Prins, Th. Rasing, R. Vollmer, A. Kirilyuk, H. Schwabe, and J. Kirshner, Phys. Rev. Lett. **74**, 1462 (1995).
4. T. V. Murzina, A. A. Nikulin, O. A. Aktsipetrov, J. W. Ostrander, A. A. Mamedov, N. A. Kotov, M. A. C. Devillers, and J. Roark, Appl. Phys. Lett. **79**, 1309 (2001).
5. T. V. Murzina, R. V. Kapra, A. A. Rassudov, O. A. Aktsipetrov, K. Nishimura, H. Uchida, and M. Inoue, Pis'ma Zh. Éksp. Teor. Fiz. **77**, 639 (2003) [JETP Lett. **77**, 537 (2003)].

Translated by O. Moskalev

Physics of the Solid State, Vol. 47, No. 1, 2005, pp. 156–158. Translated from Fizika Tverdogo Tela, Vol. 47, No. 1, 2005, pp. 150–152.
Original Russian Text Copyright © 2005 by Aktsipetrov, Dolgova, Soboleva, Fedyanin.

PROCEEDINGS OF THE CONFERENCE "NANOPHOTONICS 2004"
(Nizhni Novgorod, Russia, May 2–6, 2004)

Anisotropic Photonic Crystals and Microcavities Based on Mesoporous Silicon

O. A. Aktsipetrov, T. V. Dolgova, I. V. Soboleva, and A. A. Fedyanin

Moscow State University, Vorob'evy gory, Moscow, 119992 Russia
e-mail: fedyanin@shg.ru

Abstract—A technique to prepare one-dimensional anisotropic photonic crystals and microcavities based on anisotropic porous silicon exhibiting optical birefringence has been developed. Reflectance spectra demonstrate the existence of a photonic band gap and of an allowed microcavity mode at the photonic band gap center. The spectral position of these bands changes under rotation of the sample about its normal and/or under rotation of the plane of polarization of the incident radiation. The dependence of the shift of the spectral position of the photonic band gap edges and of the microcavity mode on the orientation of the polarization vector of incident electromagnetic wave with respect to the optical axis of the photonic crystals and microcavities was studied. © *2005 Pleiades Publishing, Inc.*

The interest in the development of microstructures with a photonic band gap, namely, photonic crystals and microcavities [1] based on silicon, stems from the possibility they provide to control the optical response of silicon and to purposefully enhance the intensity of photoluminescence [2] or Raman scattering [3] within a certain spectral interval, as well as to increase the efficiency of the nonlinear optical response of silicon, for instance, the efficiency of second- [4] and third-harmonic generation [5]. The application potential of silicon-based photonic crystals is accounted for by their possible use to construct modern photonics and optoelectronics devices, such as optical transistors, switches, and multiplexers. Techniques are presently available to fabricate one-, two-, and three-dimensional (1D, 2D, and 3D, respectively) silicon-based photonic crystals, i.e., structures with dielectric function varying with a period of the order of one wavelength in the visible or IR spectral regions in one, two, or three directions. One-dimensional photonic crystals (Bragg mirrors) are made of mesoporous silicon [6], 2D photonic crystals are made of macroporous silicon [7], and 3D devices are based on opal–silicon composites [8]. A promising aspect of this problem is the development of anisotropic photonic crystals based on anisotropic mesoporous silicon, which possesses optical birefringence [9].

The present communication reports on the development of 1D photonic crystals and microcavities based on anisotropic mesoporous silicon and a study of the spectral position of the photonic band gap and of the microcavity mode as a function of orientation of the polarization vector with respect to the optical axis of a sample.

Samples were prepared from heavily doped silicon with a (110)-oriented surface and a resistivity of 50 mΩ cm using electrochemical etching [6, 10] in a 22%-aqueous solution of hydrofluoric acid with ethanol. Ordinarily, silicon is stable against hydrofluoric acid. However, application of an electric voltage initiates electrochemical etching, which is accompanied by a release of SiF_4 and hydrogen and produces pits in the near-surface layer of single-crystal silicon, with the pits evolving subsequently into channels (pores). The hydrogen released in the reaction passivates the pore walls, with only the pore bottom left active. As a result, the pore diameter remains practically constant across the sample thickness. The density of the current flowing through the silicon surface determines the porosity of the silicon and, accordingly, its effective refractive index, while the etching time governs the thickness of the porous silicon layer. Thus, by periodically varying the etching parameters, namely, the current density and etch time of each layer, one can produce 1D photonic crystals and microcavities with the spectral positions of the photonic band gap and of the microcavity mode determined by the optical thicknesses of the layers. The pore size in mesoporous silicon produced from plates of heavily doped silicon varies from 10 to 100 nm. The highest etching rate and pore growth rate are attained in {100}-type directions, which brings about directed growth of the pores. In silicon with surface crystallographic orientation (110), the [100] and [010] directions make an angle of 45° with the surface. In this case, the pores are also oriented at 45° to the surface, which accounts for anisotropy in the sample refractive index both in the plane of incidence and in the sample surface plane [11].

Photonic crystals consist of 25 pairs of alternating layers of mesoporous silicon with effective refractive indices $n_1 = 1.39$ and $n_2 = 1.58$ and an optical thickness equal to $\lambda_0/4$, where $\lambda_0 = 850$ nm coincides with the

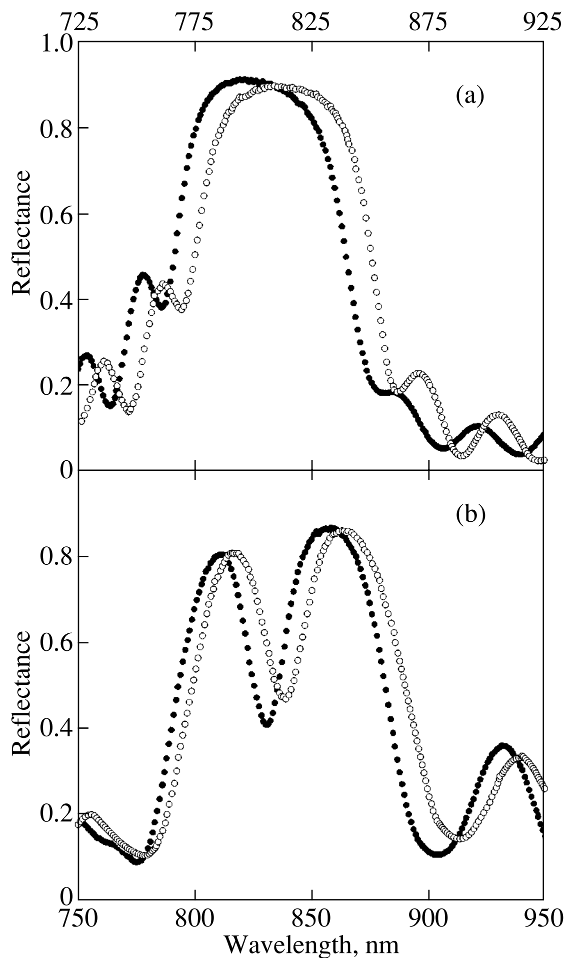

Fig. 1. Reflectance spectra of (a) a photonic crystal and (b) a microcavity measured with *s*-polarized radiation at an angle of incidence of 20° for sample azimuthal angles $\psi = 0°$ (open circles) and $\psi = 90°$ (filled circles).

center of the photonic band gap under normal incidence. The layer porosities are about 0.7 and 0.8, respectively. Microresonators are made up of two photonic crystals, each formed by 12 pairs of mesoporous silicon layers separated by a microcavity layer with an optical thickness $\lambda_0/2$. The anisotropy of the refractive indices found by approximating the reflectance spectra of single anisotropic mesoporous silicon layers was found to be $\Delta n_1 = 0.07$ and $\Delta n_2 = 0.08$ at a wavelength of 800 nm.

Figure 1 displays reflectance spectra of *s*-polarized light from a photonic crystal (Fig. 1a) and a microcavity (Fig. 1b) measured at an angle of incidence of 20° for two values of the sample azimuthal angle, which is actually the angle between the plane of incidence and the (001) plane. The reflectance spectra demonstrate the existence of a photonic band gap with a reflectance of about 0.9 in the wavelength region of 770–850 nm for the photonic crystal, as well as of a photonic band gap with a reflectance of about 0.85 in the wavelength region of 780–900 nm and of a microcavity mode at the wavelength $\lambda_0 = 830$ nm for the microcavity. The spectra also reveal a shift in the photonic band gap spectral position with variation of the azimuthal angle. The largest shift, about 20 nm, is observed with the sample rotation from 0° to 90°.

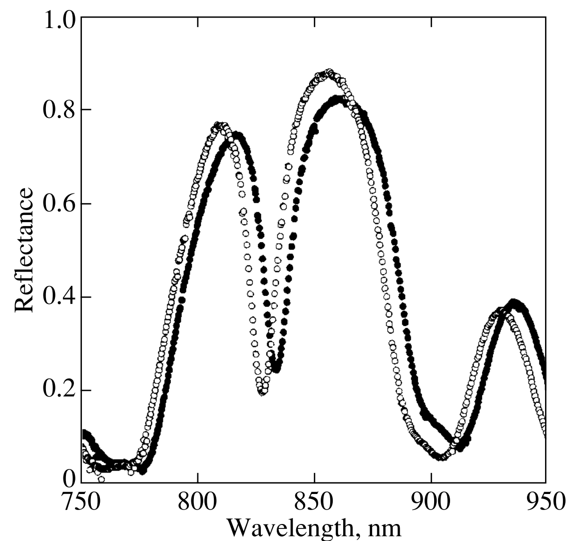

Fig. 2. Reflectance spectra of a microcavity measured with *p*- (open circles) and *s*-polarized (filled circles) radiation at an angle of incidence of 20° for the sample azimuthal angle $\psi = 0°$.

Figure 2 presents reflectance spectra of a microcavity for *s*- and *p*-polarized light. The spectra show the presence of a photonic band gap and of a microcavity mode for both polarizations. The spectral position of the microcavity mode is observed to change when the polarization of the incident light is switched, with the shift exceeding the mode half-width. With *p*-polarized light and large angles of incidence (about 55°), the shift of the microcavity mode increases to 30 nm.

Another manifestation of the anisotropy is a spectral shift of the microcavity mode observed when the incident polarization is changed. Figure 3 plots the spectral shift of the microcavity modes (measured at an angle of incidence of 20°) for *p*- and *s*-polarized light, $\Delta\lambda = \lambda_p - \lambda_s$, related to the mode half-width Δ as a function of the microcavity azimuthal angle ψ. This dependence is seen to have two maxima, at $\psi = 0°$ and 180°, and two minima, at $\psi = 90°$ and 270°. The spectral positions of the modes for the *s*- and *p*-polarized light measured at the azimuthal angles $\psi = 45°$, 135°, 225°, and 315° coincide.

To sum up, we have prepared 1D photonic crystals and microcavities based on anisotropic mesoporous silicon. Their reflectance spectra reveal the existence of a photonic band gap and of an allowed microcavity mode whose wavelength positions can be varied by properly rotating the sample about the normal to its surface. We also have studied the dependence of the shift in the

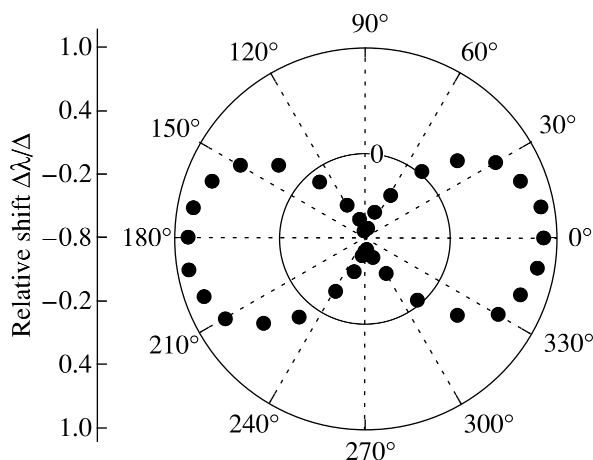

Fig. 3. Relative spectral shift of microcavity modes Δλ/Δ (see text) plotted vs. microcavity azimuthal angle. Angle of incidence 20°.

mode spectral position on the parameters determining the mutual orientation of the vector of electromagnetic wave polarization and of the optical axis of the photonic crystal, more specifically, the angle of incidence of light, the azimuthal angle of the sample, and the angle of rotation of the plane of incident polarization.

ACKNOWLEDGMENTS

This study was supported by the federal program of support for leading scientific schools (project no. 1604.2003.2) and the program "Universities of Russia."

REFERENCES

1. K. Sakoda, *Optical Properties of Photonic Crystals* (Springer, Berlin, 2001).
2. V. Pellegrini, A. Tredicucci, C. Mazzoleni, and L. Pavesi, Phys. Rev. B **52**, R14328 (1995).
3. L. A. Kuzik, V. A. Yakovlev, and G. Mattei, Appl. Phys. Lett. **75**, 1830 (1999).
4. T. V. Dolgova, A. I. Maidykovski, M. G. Martemyanov, A. A. Fedyanin, O. A. Aktsipetrov, G. Marowsky, V. A. Yakovlev, and G. Mattei, Appl. Phys. Lett. **81**, 2725 (2002).
5. T. V. Dolgova, A. I. Maĭdykovskiĭ, M. G. Martem'yanov, A. A. Fedyanin, and O. A. Aktsipetrov, Pis'ma Zh. Éksp. Teor. Fiz. **75**, 17 (2002) [JETP Lett. **75**, 15 (2002)].
6. O. Bisi, S. Ossicini, and L. Pavesi, Surf. Sci. Rep. **38**, 1 (2000).
7. S. W. Leonard, J. P. Mondia, H. M. van Driel, O. Toader, S. John, K. Busch, A. Birner, U. Gösele, and V. Lehmann, Phys. Rev. B **61**, R2389 (2000).
8. V. G. Golubev, V. A. Kosobukin, D. A. Kurdyukov, A. V. Medvedev, and A. B. Pevtsov, Fiz. Tekh. Poluprovodn. (St. Petersburg) **35**, 710 (2001) [Semiconductors **35**, 680 (2001)].
9. P. K. Kashkarov, L. A. Golovan, A. B. Fedotov, A. I. Efimova, L. P. Kuznetsova, V. Yu. Timoshenko, D. A. Sidorov-Biryukov, A. M. Zheltikov, and J. W. Haus, J. Opt. Soc. Am. B **19**, 2273 (2002).
10. W. Theiss, Surf. Sci. Rep. **29**, 91 (1997).
11. D. Kovalev, G. Polisski, J. Diener, H. Heckler, N. Kunzner, V. Yu. Timoshenko, and F. Koch, Appl. Phys. Lett. **78**, 916 (2001).

Translated by G. Skrebtsov

Physics of the Solid State, Vol. 47, No. 1, 2005, pp. 159–165. Translated from Fizika Tverdogo Tela, Vol. 47, No. 1, 2005, pp. 153–159.
Original Russian Text Copyright © 2005 by Kashkarov, Golovan, Zabotnov, Mel'nikov, Krutkova, Konorov, Fedotov, Bestem'yanov, Gordienko, Timoshenko, Zheltikov, Petrov, Yakovlev.

PROCEEDINGS OF THE CONFERENCE "NANOPHOTONICS 2004"

(Nizhni Novgorod, Russia, May 2–6, 2004)

Methods for Increasing the Efficiency of Nonlinear Optical Interactions in Nanostructured Semiconductors

P. K. Kashkarov*, L. A. Golovan*, S. V. Zabotnov*, V. A. Mel'nikov*, E. Yu. Krutkova*, S. O. Konorov*, A. B. Fedotov*, K. P. Bestem'yanov*, V. M. Gordienko*, V. Yu. Timoshenko*, A. M. Zheltikov*, G. I. Petrov, and V. V. Yakovlev****

** Moscow State University, Vorob'evy gory, Moscow, 119992 Russia*

e-mail: leo@vega.phys.msu.ru

*** University of Wisconsin–Milwaukee, Milwaukee, Wl 53211 USA*

Abstract—Methods for increasing the efficiency of the optical second- and third-harmonic generation in gallium phosphide and silicon nanostructures formed by electrochemical etching of crystalline semiconductors are discussed. The efficiency of nonlinear optical interactions can be increased by using phase matching in anisotropic nanostructured semiconductors that exhibit form birefringence or by increasing the local field, as in scattering in macroporous semiconductors. The efficiencies of third-harmonic generation in porous silicon and of second-harmonic generation in porous gallium phosphide are found to increase by more than an order of magnitude. *© 2005 Pleiades Publishing, Inc.*

1. INTRODUCTION

Electrochemical etching of solids, which results in a growth of nanopores and nanocrystals, has become a method for creating semiconductor media with new optical, including nonlinear optical, properties. The advantages of this technique for producing nanostructures are the rapidity, controllability, and low cost of the process. In the case where the characteristic sizes of pores and nanocrystals are much smaller than wavelengths of light, a nanostructured semiconductor can be considered a uniform optical medium with a certain effective refractive index differing from the refractive indices of the substances making up the nanostructure.

Nanostructured materials can be used to increase the efficiency of optical frequency conversion. The harmonic generation efficiency is determined, first, by optical anisotropy of the porous semiconductors induced by anisotropic electrochemical etching and, second, by light localization in ensembles of nanoparticles. In this work, these two factors are used in nanostructured semiconductors such as porous silicon (por-Si) [1] and porous gallium phosphide (por-GaP) [2, 3]. Note that both factors are combined in photonic-crystal structures based on porous semiconductors [1, 3], for which both the inherent dispersion law and locally increased field strength are important.

In the final analysis, both factors are associated with the effect of local fields in nanostructures on their macroscopic optical properties. As is known, the local fields control the magnitude and symmetry of effective nonlinear susceptibilities [4, 5]. An increase in the efficiency of nonlinear optical interactions (both parametric and nonparametric) due to an increase in the local field was predicted and observed for optical composite media containing metallic inclusions [6] or, in a more general case, inclusions that exhibit resonance at frequencies close to the frequencies of interacting waves [7, 8]. Increased efficiency was also observed in cases where an inclusion with optical nonlinearity was surrounded by a medium with a higher refractive index [9, 10]. However, the recently detected increase in the efficiency of nonlinear optical processes in por-Si [11–14] and por-GaP [15–17] consisting of semiconductor nanocrystals separated by nanopores is a new phenomenon that merits detailed consideration. In this work, we obtain and discuss experimental results.

2. EXPERIMENTAL

Por-Si films were fabricated by electrochemical etching of single-crystal (110) silicon wafers with resistivities of 1.5 and 3 mΩ cm in an HF (48 vol %) : C_2H_5OH (1 : 1) solution. The etching current densities were 50 and 100 mA/cm^2. The etching time was varied from 2.5 to 20 min, and the layer thicknesses ranged from 10 to 80 μm. To remove a film from the substrate, the current density was sharply increased to 700 mA/cm^2 over a period of a few seconds. The treatment conditions resulted in mesoporous silicon with pores and silicon nanocrystals about 10 nm in size.

Por-GaP layers were formed using electrochemical etching of (110) and (111) n-GaP doped with Te to a concentration of 3×10^{17} cm^{-3} in a 0.5 M aqueous solution of H_2SO_4 and an HF (48 vol %) : C_2H_5OH (1 : 1) solution, respectively. Both free-standing por-GaP films and por-GaP layers on substrates were studied. The thicknesses of the porous layers ranged from 4 to 40 μm. As seen from atomic-force microscopy images

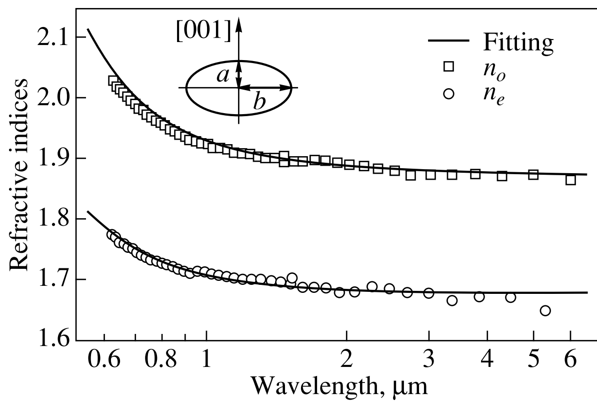

Fig. 1. Dispersion of the refractive indices of birefringent por-Si for ordinary (n_o) and extraordinary (n_e) waves. Solid lines show the results of fitting using a generalized Bruggeman model, Eq. (1). The inset shows an ellipsoid of revolution with semiaxes a and b and the axial-symmetry axis coinciding with the [001] crystallographic direction.

of the por-GaP surfaces [16, 17], the inhomogeneities (pores and nanocrystals) were about 0.5 μm in size.

Transmission spectra of por-Si films and scattering spectra of por-GaP layers were recorded in the visible and near-infrared (IR) regions (0.47 to 1.6 μm) with an incandescent lamp, an MDR-12 monochromator, silicon (for the range 0.47–1.0 μm) and germanium (for 1.0–1.6 μm) photodiodes, and a computer-aided recording system. The IR spectra in the range 1.6–8.0 μm were recorded with a Perkin Elmer Spectrum RX I FT-IR spectrometer.

Second- (SH) and third-harmonic (TH) generation was performed with laser systems based on a Nd : YAG crystal (1.064 μm, 35 ps, pulse energy of up to 3 mJ), a Cr : forsterite crystal (1.250 μm, 50 fs, repetition frequency of 25 MHz, pulse energy of 6 nJ), and a parametric light oscillator (with the idler wave smoothly tuned from 1.0 to 2.0 μm, a pulse duration of 3 ns, and a pulse energy of 10 mJ). The use of the parametric light oscillator allowed us to satisfy the phase-matched conditions for third-harmonic generation (THG) in por-Si and vary the ratio of the wavelength to the nanocrystal size; the latter gave information on the effect of light scattering on second-harmonic generation (SHG) in por-GaP.

3. SHAPE ANISOTROPY AND ITS APPLICATION FOR PHASE MATCHING

3.1. Form Birefringence in Por-Si

As shown in [18–21], mesoporous silicon layers (with pore and nanocrystal sizes of about 10–30 nm) created on a substrate of single-crystal silicon with a low surface symmetry have the properties of an optically uniaxial crystal with a negative birefringence $\Delta n = n_o - n_e$ reaching 0.24 (n_o and n_e are the refractive indices of ordinary and extraordinary waves, respectively). The optical axis of birefringent por-Si on a (110) substrate lies in the surface plane and coincides with the [001] crystallographic direction.

To check the applicability of an effective-medium model to the refractive indices measured, it is fruitful to study their dispersion. Figure 1 shows the wavelength dependences of n_o and n_e determined from the transmission spectra of a por-Si film under normal incidence of linearly polarized light onto the sample surface [22]. To describe the dispersion of the por-Si refractive indices, we used a generalized Bruggeman effective-medium model taking into account the shapes of silicon nanocrystals and pores [23]. This model relates the effective permittivity ε_{eff} of such a system to the silicon permittivity ε_{Si} and the permittivity ε_d of the dielectric filling the pores. In the case of pores filled with air, $\varepsilon_d = 1$ and we have

$$p\frac{\varepsilon_d - \varepsilon_{\text{eff}}}{\varepsilon_{\text{eff}} + L(\varepsilon_d - \varepsilon_{\text{eff}})} + (1-p)\frac{\varepsilon_{\text{Si}} - \varepsilon_{\text{eff}}}{\varepsilon_{\text{eff}} + L(\varepsilon_{\text{Si}} - \varepsilon_{\text{eff}})} = 0. \quad (1)$$

where p is the porosity of the material and L is the depolarization factor, which is specified by the shapes of the nanocrystals and pores and depends on the direction of polarization of the light-wave electric field. For ellipsoids of revolution, L is determined by the ratio of the ellipsoid semiaxes. By comparing the experimental and calculated data, we see that the generalized Bruggeman model in which silicon nanocrystals and pores are ellipsoids of revolution turns out to be a good approximation. However, in the long- and short-wavelength regions, differences between the calculated and experimental refractive indices become noticeable. In the former region, these differences are caused by the fact that absorption by free carriers was not taken into account in the calculations, and in the latter region the differences are due to the wavelength approaching nanocrystal size, in which case the effective-medium theory becomes inapplicable.

3.2. Phase Matching for Harmonics Generation

The high value of birefringence in por-Si, which is comparable to the dispersion of this material, allows us to satisfy the conditions of phase matching for SHG and THG. The phase matching of a harmonic and the corresponding nonlinear-polarization wave can be attained by varying the effective refractive index for an extraordinary wave. This variation can be realized by varying the angle of incidence of light, by filling pores with dielectric liquids, or by changing the fundamental radiation wavelength.

When a SH is generated by pumping with picosecond pulses of light from a Nd : YAG laser, the SH intensity is observed to increase by two orders of magnitude in the above-mentioned samples at a certain angle of incidence of the fundamental wave. Calculations show

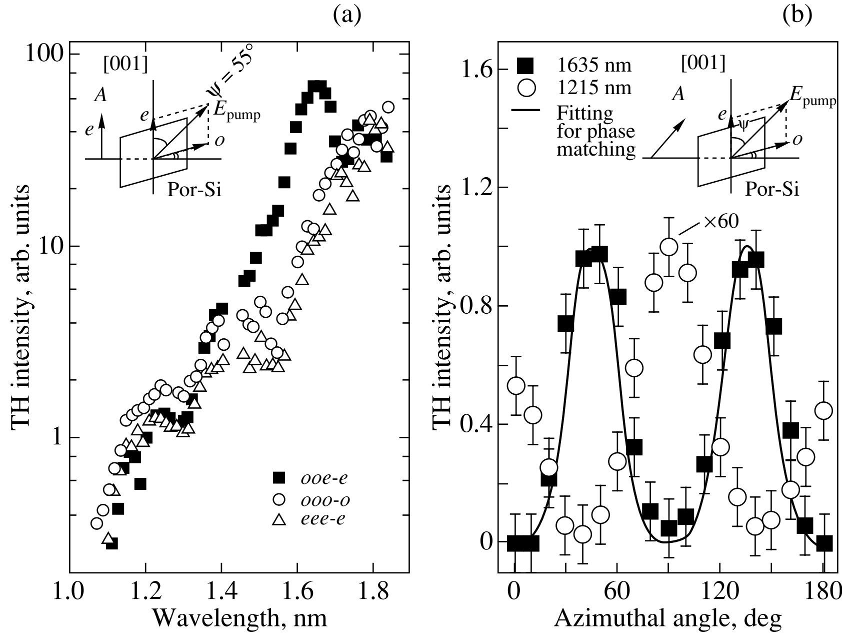

Fig. 2. THG in a birefringent por-Si film. (a) Dependence of the TH intensity on the fundamental wavelength for various geometries; the inset shows the scheme of sample arrangement in the THG experiment in the *ooe-e* geometry; letter *A* designates a Glan prism used as an analyzer. (b) Orientation dependences for fundamental wavelengths of 1635 and 1215 nm; zero in the coordinate axis corresponds to the orientation of the [001] axis along the fundamental-wave polarization; the solid line illustrates the orientation dependence under phase-matched conditions; the inset shows the scheme of sample arrangement for measuring the orientation dependences; and letter *A* designates a Glan prism that transmits TH radiation in the fundamental-wave polarization direction.

that the conditions of phase matching are satisfied for this angle [4, 5].

The magnitude of birefringence also turns out to be sufficient for achieving phase-matched THG. Figure 2a shows the dependence of the TH intensity in the *ooe-e* geometry on the fundamental wavelength (Fig. 2a, inset). The clearly visible maximum at a wavelength of 1.635 μm corresponds to phase matching. We also obtained spectral dependences of the TH intensity in other geometries. Noticeable TH signals were also detected in cases where both the TH and the fundamental wave were polarized along the direction of polarization of either an ordinary or extraordinary wave (the *ooo-o* or *eee-e* geometry, respectively). However, for other geometries (*ooo-e*, *oee-e*), the TH signal was lower than the experimental noise level. As is seen from Fig. 2a, the dependences for the *ooo-o* and *eee-e* geometries do not have pronounced extrema. This result is obvious, since the dispersion of the refractive indices of the materials hinders the phase matching of THG for these geometries. The increase in the TH intensity with wavelength for all the geometries shown in Fig. 2a is explained by the decreased absorption at the TH frequency.

The orientation dependences of the TH intensity in the presence and in the absence of phase matching are given in Fig. 2b. These dependences are substantially different. In the case of phase matching, the dependence of the TH intensity I_3 on the rotation angle ψ of the sample (Fig. 2b, inset) is predominantly determined by phase-matched THG:

$$I_3 \propto (\sin^2\psi\cos^2\psi)^2 \propto \sin^4 2\psi. \quad (2)$$

Far from phase matching, the $I_3(\psi)$ dependence is mainly specified by *ooo-o* and *eee-e* interactions, for which phase matching is impossible in a medium with normal dispersion, and the maxima of the orientation dependence coincide with the extrema of the $\sin^4(2\psi)$ and $\cos^4(2\psi)$ functions.

3.3. Modification of the Cubic Nonlinear Susceptibility Tensor

Just as the anisotropic local field changes the linear properties of nanostructured silicon, we may also expect changes in the symmetry properties of the cubic nonlinear susceptibility tensor $\chi^{(3)}(3\omega; \omega, \omega, \omega)$. Following [24] and taking into account the effect of the local field in the effective-medium approximation, we obtain [25]

$$\chi^{(3)}_{\mathrm{eff},\,ijkl} = (1-p)\mathfrak{L}_i(3\omega)\mathfrak{L}_j(\omega)\mathfrak{L}_k(\omega)\mathfrak{L}_l(\omega)\chi^{(3)}_{c\text{-Si},\,ijkl}, \quad (3)$$

where, with allowance for the effective-medium anisotropy, the local-field factor $\mathfrak{L}_i$ relates the fields outside

($\mathbf{E}_{out}$) and inside ($\mathbf{E}_{in}$) an ellipsoid to each other as follows:

$$\mathbf{E}_{in,\,i} = \mathfrak{L}_i \mathbf{E}_{out,\,i} = \frac{1}{1 + \{(\varepsilon_{Si} - \varepsilon_{eff,\,i})/\varepsilon_{eff,\,i}\} L_i} \mathbf{E}_{out,\,i}. \quad (4)$$

It is known [26] that crystalline silicon belongs to the symmetry group $m3m$ and its cubic nonlinear susceptibility tensor has two independent elements, $\chi^{(3)}_{1111} = \chi^{(3)}_{2222} = \chi^{(3)}_{3333}$ and $\chi^{(3)}_{1212} = \chi^{(3)}_{1122} = \chi^{(3)}_{1221}$. Therefore, for the effective medium formed by silicon and vacuum ellipsoids, the following five elements of the tensor $\chi^{(3)}(3\omega; \omega, \omega, \omega)$ are independent: $\chi^{(3)}_{1111}$, $\chi^{(3)}_{1122}$, $\chi^{(3)}_{1133}$, $\chi^{(3)}_{3311}$, and $\chi^{(3)}_{3333}$. Here,

$$\chi^{(3)}_{3333} < \chi^{(3)}_{1111} \quad (5)$$

(subscript 3 corresponds to the optical axis of birefringent por-Si).

The orientation dependences of the TH intensity obtained far from phase matching (Fig. 2b) allow us to find the following relation between the elements of the tensor $\chi^{(3)}(3\omega; \omega, \omega, \omega)$:

$$r = \frac{\chi^{(3)}_{1111} + 3\chi^{(3)}_{1122}}{\chi^{(3)}_{3333}} = 2\sqrt{\frac{I_3(\psi = \pi/2)}{I_3(\psi = 0)}} \left|\frac{3k^o_1 - k^o_3}{3k^e_1 - k^e_3}\right|, \quad (6)$$

where $k^{o,\,e}_{1,\,3}$ are the wave vectors of the ordinary and extraordinary waves at the fundamental and TH frequencies. For birefringent por-Si, r is found to be 3.3 ± 0.2, whereas for crystalline silicon the value of $(\chi^{(3)}_{1111} + \chi^{(3)}_{1122})/\chi^{(3)}_{1111}$ is 2.35 ± 0.15. The different values of the ratio between the elements of the tensor $\chi^{(3)}(3\omega; \omega, \omega, \omega)$ are caused by inequality (5), which agrees qualitatively with our analysis of the effect of a nanostructure on this ratio.

3.4. Increased THG Efficiency in Mesoporous Silicon

The effective-medium model predicts a decrease in the THG efficiency for mesoporous silicon. In our experiments, however, the TH intensity in the mesoporous silicon was more than an order of magnitude higher than that in the corresponding crystalline material [14]. Note that, for microporous silicon with the same porosity and a nanocrystal size of 1–2 nm, the THG efficiency was, on the contrary, lower than in the crystalline silicon. The latter fact agrees well with the effective-medium model predictions. Thus, we can state that the nanocrystal size in por-Si is a decisive factor that limits the applicability of this model. Although the nanocrystal sizes (a few tens of nanometers) in the mesoporous silicon are even smaller than the TH wavelength in this material (~200 nm), the electrostatic approximation becomes invalid and the effects of interaction and localization of light waves should be taken into account.

4. INCREASED HARMONIC-GENERATION EFFICIENCY DUE TO LOCALIZATION OF LIGHT

The efficiency of nonlinear optical processes can be increased using the phenomenon of light localization in scattering media. This method was realized in the case of por-GaP. This material has a wider band gap and, therefore, could be used in the visible region (at wavelengths higher than 0.55 μm). Furthermore, por-GaP is a noncentrosymmetric medium whose quadratic dipole susceptibility is two orders of magnitude greater than that for most crystals applied for frequency doubling. The inhomogeneities (pores and nanocrystals) in por-GaP were about 0.5 μm in size, which is close to the SH wavelength. The samples exhibited significant scattering of light. The recorded scattering spectra indicate non-Rayleigh scattering, and the detected wavelength dependence of the scattered light intensity is characteristic of Mie scattering [17].

The measured orientation dependences of SH are shown in Fig. 3. For crystalline GaP (c-GaP), these dependences have certain distinguishing characteristics. In contrast, the orientation dependence for por-GaP is isotropic: the SH intensity is independent of the mutual orientation of the polarizer and the sample. The SH intensity is higher by an order of magnitude for por-GaP produced on the (110) surface (Fig. 3a) and by nearly two orders of magnitude for por-GaP produced on the (111) surface (Fig. 3b) than that for c-GaP.

The results obtained demonstrate the key role of scattering in SHG in por-GaP. Scattering can be the reason for the depolarization of the SH signal. The increased SHG efficiency can be due to light localization effects [27] associated with scattering. The possible light localization effects are indicated by the non-Rayleigh character of scattering. The relation

$$kl = 2\pi nl/\lambda \sim 1 \quad (7)$$

(where k is the wave vector in the medium, n is the effective refractive index of the medium, l is the photon mean free path) is the criterion for the Anderson localization of light in random media, which is characterized by a substantial deceleration of light propagation. Using the photon mean free paths given in [27], we find kl = 5–20. However, a direct indication of the light localization effects could be obtained by directly measuring the photon lifetime in a scattering medium. To understand the role of these effects in SHG, it is instructive to find the wavelength dependence of the SHG efficiency in por-GaP.

The photon lifetime was measured using an optical-heterodyning scheme [28] with a Michelson interferometer and a Cr : forsterite crystal–based femtosecond laser

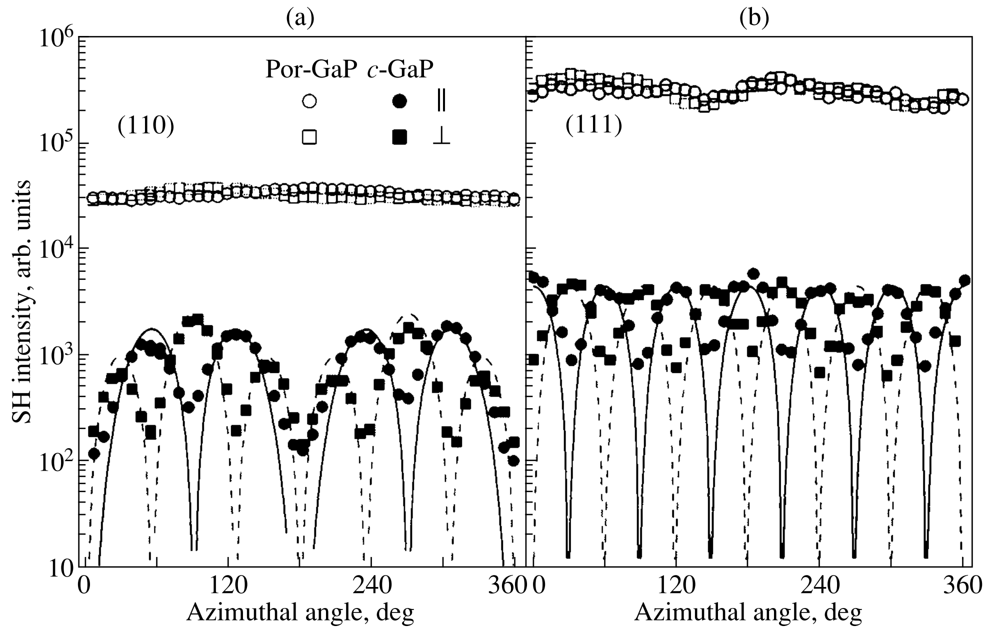

Fig. 3. Orientation dependences of the SH signal of por-GaP and *c*-GaP for the (a) (110) and (b) (111) surface orientations. The SH is polarized either parallel or normal to the fundamental-wave polarization.

system. In this scheme, a cross-correlation function is measured for the wave scattered by por-GaP [29]:

$$C(\tau) = \int_{-\infty}^{\infty} A(t-\tau)S(t)dt, \quad (8)$$

where τ is the delay time, $A(t)$ is the field of the incident light wave, and $S(t)$ is the field of the light wave scattered by por-GaP. The experimentally obtained function $C(\tau)$ is shown in Fig. 4. As is seen from Fig. 4, this function is nonzero for a much longer time than the laser pulse duration (50 fs). Analysis indicates that the lifetime of scattered fundamental-frequency photons is 0.7 ps in this case. Simple estimations show that, within this time, a photon travels about 100 μm and undergoes about one hundred scattering acts.

Figure 5 shows the SH intensities generated in por-GaP and *c*-GaP as functions of the fundamental wavelength. It is seen that, for fundamental wavelengths longer than 1.5 μm, the SH signal from the crystalline sample is higher in intensity than the SH signal from por-GaP. This result agrees qualitatively with the predictions from the effective-medium model. However, at fundamental wavelengths shorter than 1.5 μm, the SH

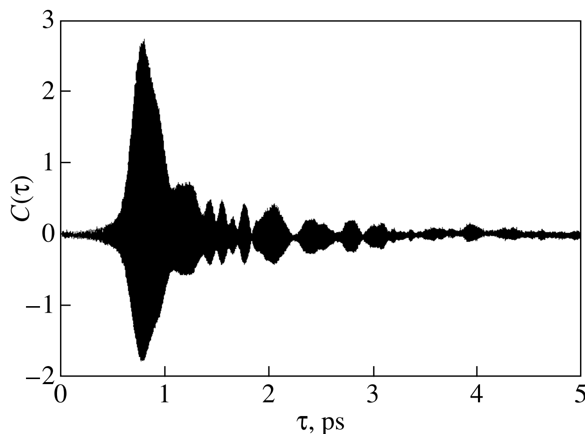

Fig. 4. Correlation function for the field of the fundamental wave scattered by por-GaP.

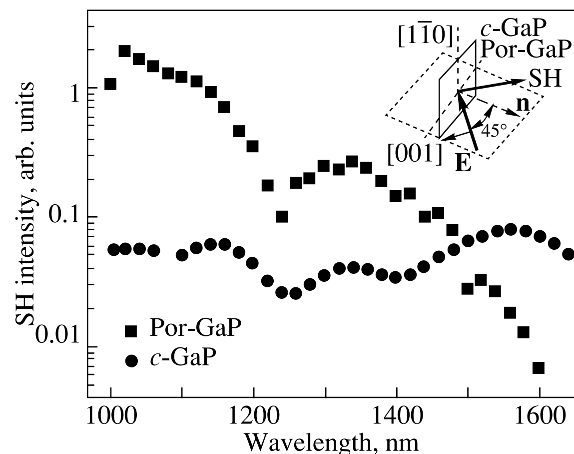

Fig. 5. Intensity of the SH signal (in the direction normal to the incident wave) upon scattering by por-GaP and *c*-GaP as a function of the fundamental wavelength. The inset shows the experimental scheme.

intensity in por-GaP exceeds that in *c*-GaP. As the fundamental wavelength decreases, the SH intensity in *c*-GaP remains virtually unchanged, whereas the SH intensity in por-GaP increases and exceeds the intensity in *c*-GaP by a factor of 35 at a wavelength of 1.02 μm. This result is explained by the drop in the mean free path with decreasing fundamental and SH wavelengths and indicates that the light localization is of importance in SHG in por-GaP.

Like in photonic-crystal structures, the increase in the SHG efficiency in por-GaP is caused by two interrelated factors: first, a local increase in the field of light waves due to constructive interference of scattered waves and, second, an increase in the interaction length between fundamental and nonlinear-polarization waves because of partial phase-mismatch compensation during the propagation of light in a heterogeneous structure. The idea behind the first factor can be formulated as follows: at a point with a coordinate **r**, the field can be written as

$$\mathbf{E}(\mathbf{r}) = [1 + \delta(\mathbf{r})]\mathbf{E}_a, \quad (9)$$

where $\mathbf{E}_a$ is the average field in the medium and $\delta(\mathbf{r})$ is an **r**-dependent field variation. By averaging, we obviously obtain $\langle\delta(\mathbf{r})\rangle = 0$. In this case, the averaged nonlinear polarization at the SH frequency is proportional to the average square of the field at the fundamental frequency:

$$\langle\mathbf{E}^2\rangle = \langle[1 + \delta(\mathbf{r})]^2\rangle\mathbf{E}_a^2 = [1 + \langle\delta^2(\mathbf{r})\rangle]\mathbf{E}_a^2. \quad (10)$$

Thus, the higher the field nonuniformity, the higher the average nonlinear polarization. The second factor is an analog of quasi-phase matching in polar periodic structures [24] and of phase matching in photonic crystals [30], where an effective increase in the coherent length of the nonlinear optical process is observed.

5. CONCLUSIONS

We have analyzed methods for increasing the efficiency of the optical second- and third-harmonic generation in nanostructured semiconductors. One method for increasing the efficiency of these processes is to use nanostructured structures with artificial anisotropy in which phase-matched harmonic generation becomes possible. Another method is based on light-wave localization effects, which lead to an increase in the photon lifetime in a nanostructure and to a local increase in the field of light.

ACKNOWLEDGMENTS

This work was performed at the Center of Equipment Collective Use, Moscow State University, and was supported by a grant of the President of the Russian Federation (project MD-42.2003.02), the Russian Foundation for Basic Research (project nos. 02-02-17259, 03-02-16929, 02-02-17098), CRDF (project nos. RE2-2369, RP2-2558), NSF (project no. 9984225), NIH (project no. R21RR16282), and programs of the Ministry of Industry, Science, and Technology of the Russian Federation.

REFERENCES

1. O. Bisi, S. Ossicini, and L. Pavesi, Surf. Sci. Rep. **38** (1–3), 1 (2000).
2. F. J. P. Schuurmans, D. Vanmaekelbergh, J. van de Lagemaat, and A. Lagendijk, Science **284**, 141 (1999).
3. R. W. Tjerkstra, J. Gömez Rivas, D. Vanmaekelbergh, and J. J. Kelly, Electrochem. Solid-State Lett. **5** (5), G32 (2002).
4. P. M. Hui and D. Stroud, J. Appl. Phys. **82** (10), 4740 (1997).
5. P. M. Hui, P. Cheung, and D. Stroud, J. Appl. Phys. **84** (7), 3451 (1998).
6. D. Ricard, Ph. Roussignol, and C. Flytzanis, Opt. Lett. **10**, 511 (1985).
7. J. J. Maki, M. S. Malcuit, J. E. Sipe, and R. W. Boyd, Phys. Rev. Lett. **67** (8), 972 (1991).
8. D. Stroud, Phys. Rev. B **54** (51), 3295 (1996).
9. G. L. Fisher, R. W. Boyd, R. J. Gehr, S. A. Jenekhe, J. A. Osaheni, J. E. Sipe, and L. A. Weller-Brophy, Phys. Rev. Lett. **74** (10), 1871 (1995).
10. *Properties of Nanostructured Random Media*, Ed. by V. M. Shalaev (Springer, New York, 2002).
11. L. A. Golovan, A. M. Zheltikov, P. K. Kashkarov, N. I. Koroteev, M. G. Lisachenko, A. N. Naumov, D. A. Sidorov-Biryukov, V. Yu. Timoshenko, and A. B. Fedotov, Pis'ma Zh. Éksp. Teor. Fiz. **69** (4), 274 (1999) [JETP Lett. **69**, 300 (1999)].
12. L. A. Golovan, V. Yu. Timoshenko, A. B. Fedotov, L. P. Kuznetsova, D. A. Sidorov-Biryukov, P. K. Kashkarov, A. M. Zheltikov, D. Kovalev, N. Künzner, E. Gross, J. Diener, G. Polisski, and F. Koch, Appl. Phys. B **73** (1), 31 (2001).
13. P. K. Kashkarov, L. A. Golovan, A. B. Fedotov, A. I. Efimova, L. P. Kuznetsova, V. Yu. Timoshenko, D. A. Sidorov-Biryukov, A. M. Zheltikov, and J. W. Haus, J. Opt. Soc. Am. B **19** (9), 2273 (2002).
14. L. A. Golovan, L. P. Kuznetsova, A. B. Fedotov, S. O. Konorov, D. A. Sidorov-Biryukov, V. Yu. Timoshenko, A. M. Zheltikov, and P. K. Kashkarov, Appl. Phys. B **76** (4), 429 (2003).
15. I. M. Tiginyanu, I. V. Kravetsky, J. Monecke, W. Cordts, G. Marowsky, and H. L. Hartnagel, Appl. Phys. Lett. **77** (15), 2415 (2000).
16. L. A. Golovan, V. A. Mel'nikov, S. O. Konorov, A. B. Fedotov, S. A. Gavrilov, A. M. Zheltikov, P. K. Kashkarov, V. Yu. Timoshenko, G. I. Petrov, L. Li, and V. V. Yakovlev, Pis'ma Zh. Éksp. Teor. Fiz. **78** (3–4), 229 (2003) [JETP Lett. **78**, 193 (2003)].
17. V. A. Mel'nikov, L. A. Golovan, S. O. Konorov, D. A. Muzychenko, A. B. Fedotov, A. M. Zheltikov, V. Yu. Timoshenko, and P. K. Kashkarov, Appl. Phys. B **79** (2), 225 (2004).
18. O. G. Sarbeĭ, E. K. Frolova, R. D. Fedorovich, and D. B. Dan'ko, Fiz. Tverd. Tela (St. Petersburg) **42** (7), 1205 (2000) [Phys. Solid State **42**, 1240 (2000)].

19. D. Kovalev, G. Polisski, J. Diener, H. Heckler, N. Künzner, V. Yu. Timoshenko, and F. Koch, Appl. Phys. Lett. **78** (7), 916 (2001).

20. N. Künzner, D. Kovalev, J. Diener, E. Gross, V. Yu. Timoshenko, G. Polisski, F. Koch, and M. Fujii, Opt. Lett. **26** (16), 1265 (2001).

21. L. P. Kuznetsova, A. I. Efimova, L. A. Osminkina, L. A. Golovan, V. Yu. Timoshenko, and P. K. Kashkarov, Fiz. Tverd. Tela (St. Petersburg) **44** (5), 780 (2002) [Phys. Solid State **44**, 811 (2002)].

22. L. A. Golovan, A. F. Konstantinova, K. B. Imangazieva, E. Yu. Krutkova, V. Yu. Timoshenko, and P. K. Kashkarov, Kristallografiya **49** (1), 151 (2004) [Crystallogr. Rep. **49**, 143 (2004)].

23. J. E. Spanier and I. P. Herman, Phys. Rev. B **61** (15), 10437 (2000).

24. N. Bloembergen, *Nonlinear Optics* (Benjamin, New York, 1965; Mir, Moscow, 1966).

25. J. W. Haus, R. Inguva, and C. M. Bowden, Phys. Rev. A **40** (10), 5729 (1989).

26. Yu. I. Sirotin and M. P. Shaskol'kaya, *Fundamentals of Crystal Physics*, 2nd ed. (Nauka, Moscow, 1979) [in Russian].

27. A. Lagendijk, J. Gómez Rivas, A. Imhof, F. J. P. Schuurmans, and R. Sprik, in *Photonic Crystals and Light Localization in the 21st Century*, Ed. by C. M. Soukoulis (Kluwer Academic, Dordrecht, 2001), p. 447.

28. V. M. Gordienko, A. N. Konovalov, S. A. Magnitskiĭ, and Zh. S. Tursynov, Kvantovaya Élektron. (Moscow) **31** (1), 83 (2001) [Quantum Electronics **31** (1), 83 (2001)].

29. P. M. Johnson, A. Imhof, B. P. J. Bret, J. Gómez Rivas, and A. Lagendijk, Phys. Rev. E **68** (1), 016604 (2003).

30. M. Scalora, M. Bloemer, A. Manka, J. Dowling, C. Bowden, R. Vismanatan, and J. W. Haus, Phys. Rev. A **56**, 3166 (1997).

Translated by K. Shakhlevich

Physics of the Solid State, Vol. 47, No. 1, 2005, pp. 166–169. Translated from Fizika Tverdogo Tela, Vol. 47, No. 1, 2005, pp. 160–163.
Original Russian Text Copyright © 2005 by Akimov, Bogoyavlenskiĭ, Vasil'kov, Ryabova, Khokhlov.

PROCEEDINGS OF THE CONFERENCE "NANOPHOTONICS 2004"
(Nizhni Novgorod, Russia, May 2–6, 2004)

Recombination at Mixed-Valence Impurity Centers in PbTe(Ga) Epitaxial Layers

B. A. Akimov, V. A. Bogoyavlenskiĭ, V. A. Vasil'kov, L. I. Ryabova, and D. R. Khokhlov
Moscow State University, Vorob'evy gory, Moscow, 119992 Russia
e-mail: khokhlov@mig.phys.msu.ru

Abstract—The photoconductivity kinetics in PbTe(Ga) epitaxial films prepared by the hot-wall method is studied. The recombination of nonequilibrium photoexcited electrons at low temperatures was found to proceed in two stages, with a period of relatively fast relaxation followed by delayed photoconductivity. The temperature at which delayed photoconductivity appears increases with decreasing film thickness. The relaxation rate over the period of fast relaxation depends on film thickness and is the lowest in the thinnest layers. In semi-insulating films, photoconductivity is always positive, whereas in samples with lower electrical resistivity positive and negative photoconductivities are observed to coexist. The data obtained are discussed in terms of a model in which the impurity gallium atom can be in more than one charged state. *© 2005 Pleiades Publishing, Inc.*

1. INTRODUCTION

Several dopants that have a mixed valence and stabilize the Fermi level in lead telluride are currently known (Ga, In, Yb, Cr). However, almost every one of these impurities exhibits specific features. Gallium is the only dopant that allows one to attain the semi-insulating state in PbTe. In PbTe(Ga) single crystals, delayed photoconductivity is observed to exist below $T_C \sim 80$ K, a temperature substantially in excess of T_C in samples doped by other mixed-valence impurities. Another remarkable feature of PbTe(Ga) is the fairly narrow dopant concentration interval within which the Fermi level can be stabilized. An increase in gallium concentration in single-crystal samples initiates a sharp growth in the electron concentration, which may be caused by the excess gallium starting to behave as an active donor.

The properties of single-crystal PbTe(Ga) samples have been studied in considerable detail [1, 2]. The present communication reports on an investigation of the electrophysical and photoelectric properties of epitaxial PbTe(Ga) layers with variation of the layer thickness, substrate type, and dopant concentration.

2. SAMPLES

Samples were prepared by a modified hot-wall technique. By properly varying the substrate temperature T_{sub}, the film conductivity could be controlled over a broad range. For $T_{sub} < 200$°C, films with *p* conduction formed. At substrate temperatures near 200°C, reversal of the conduction type was observed, and the films prepared at T_{sub} lying in the interval from 210 to 240°C were *n*-type and semi-insulating at low temperatures. A subsequent increase in T_{sub} to 250°C or higher brought about destruction of the semi-insulating state, which was accompanied by an increase in electron concentration in the layers. Thus, by properly varying the substrate temperature, we succeeded in reconstructing the pattern corresponding to variation of the properties of single-crystal samples under a successive increase in gallium content. In the case of films, however, it turned out possible to achieve a substantially smoother variation of the impurity concentration and to prepare a series of samples corresponding to an intermediate state between the stabilized Fermi level position and *n*-type metallic conduction. Substrates were primarily made of ⟨111⟩-oriented barium fluoride, which favored epitaxial growth with good adhesion and with no visible signs of mechanical strains. Silicon with a SiO_2 buffer layer was also employed to obtain semi-insulating layers. In this case, the adhesion was poor.

The temperature dependences of the conductivity and relaxation kinetics were measured in the temperature range 4.2–300 K in a chamber that screened the samples from background illumination. A miniature incandescent lamp and a light-emitting diode operating at wavelength $\lambda = 1$ μm served as IR sources.

3. PHOTOCONDUCTIVITY IN SEMI-INSULATING PbTe(Ga)

Figure 1 displays temperature dependences of the electrical resistivity ρ of semi-insulating films deposited on various substrates. The film thickness was 2 μm. We can see that the qualitative pattern of the $\rho(10^2/T)$ graphs does not depend on substrate type. When illuminated, photoconductivity is observed at temperatures $T < T_C \sim 100$ K, which is 20 K above the corresponding temperature for single-crystal samples. Significantly, the trend toward an increase in T_C with decreasing epitaxial-layer thickness is well pronounced. Indeed, in

1063-7834/05/4701-0166$26.00 © 2005 Pleiades Publishing, Inc.

films 0.2-μm thick, T_C reaches as high as 140 K. The amplitude of the photoresponse was found to be slightly higher in layers grown on a BaF_2 substrate. Figure 2 displays photoconductivity kinetics measured at several temperatures for the same film under pulsed illumination by a light-emitting diode. Just as in single-crystal samples, the photoconductivity signal decay kinetics observed after the illumination is removed has a period of relatively fast decay followed by delayed photoconductivity. The rapidly relaxing signal is dominant under pulsed illumination. By properly varying the experimental conditions (pulse duration, type of radiation source, temperature, etc.), one can obtain various amplitude ratios of the rapidly relaxing to delayed photoconductivity signal. However, both in single crystals and in films with a thickness of a few microns, the photoconductivity falls off nonexponentially. The situation in sufficiently thin films with $d \sim 0.2$ μm is qualitatively different. Practically immediately after the termination of the illumination pulse, signal decay reveals exponential kinetics, $\Delta\sigma(t) \propto \exp(-t/\tau)$. At $T = 4.2$ K, the fast-relaxation time τ is 13 ms. It is important to note that, in thin films, the relaxation occurs more slowly than in thicker ones.

The specific features of the kinetics of nonequilibrium processes occurring in bulk samples and films with different thicknesses can be assigned to the gallium in lead telluride having mixed valence. The recombination of nonequilibrium carriers is actually a sum of the processes involved in the carrier capture to impurity centers residing in different charge states. Therefore, the recombination rate is determined not only by the concentration and spatial distribution of nonequilibrium carriers but also by the number of impurity centers in different charge states and their distribution over the sample volume. Nonuniform carrier distribution over the volume, combined with a nonuniform distribution of impurity centers in different charge states, may give rise to nonequivalent conditions for the recombination of different carrier groups and to a substantial modification of the kinetic processes involved. Spatial uniformity in the distribution of nonequilibrium carriers and of charged impurity centers apparently takes place only in sufficiently thin layers with $d \leq 0.2$ μm. The relaxation process is described in this case by an exponential relation.

4. PHOTOCONDUCTIVITY IN PbTe(Ga) WITH ENHANCED Ga CONTENT

The photoconductivity in comparatively low-resistivity samples characterized by an enhanced gallium content differs qualitatively from that found for semi-insulating layers. Figure 3 shows the temperature dependence of electrical resistivity of a low-Ohmic film ($d = 2$ μm). In addition to dark-conductivity curve *1*, Fig. 3 gives dependences measured at different levels of illumination (curves *2*, *3*). In the low-temperature region, illumination initiates an increase in film resis-

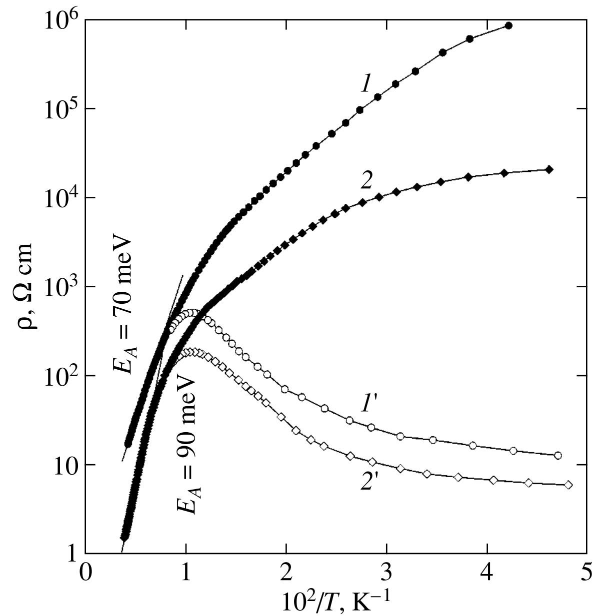

Fig. 1. Temperature dependences of the electrical resistivity ρ of *n*-PbTe(Ga) epitaxial films grown (*1*, *1'*) on ⟨111⟩-BaF_2 and (*2*, *2'*) on Si–SiO_2 substrates. Curves *1* and *2* were obtained in the dark, and curves *1'* and *2'*, under continuous illumination by a miniature incandescent lamp.

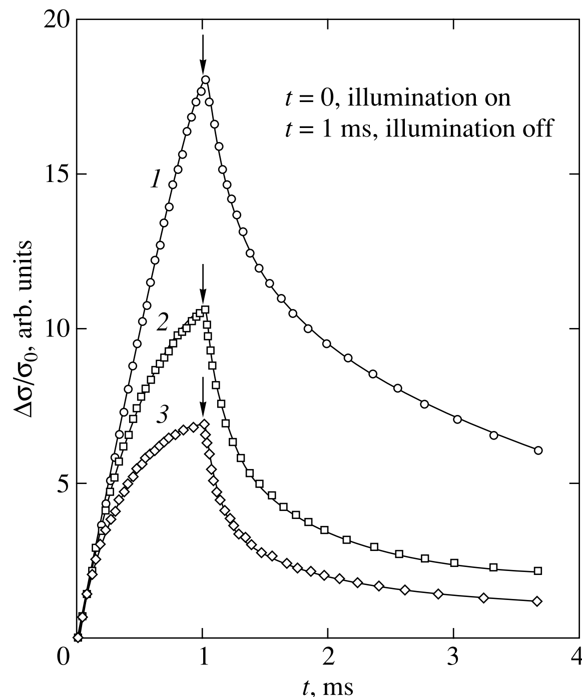

Fig. 2. Photoconductivity kinetics, $\Delta\sigma(t)$, obtained under pulsed illumination by a light-emitting diode (wavelength $\lambda = 1$ μm) from an *n*-PbTe(Ga) film on a ⟨111⟩-BaF_2 substrate at (*1*) 4.2, (*2*) 13, and (*3*) 30 K; IR pulse duration, 1 ms. Arrows indicate the instant illumination was removed.

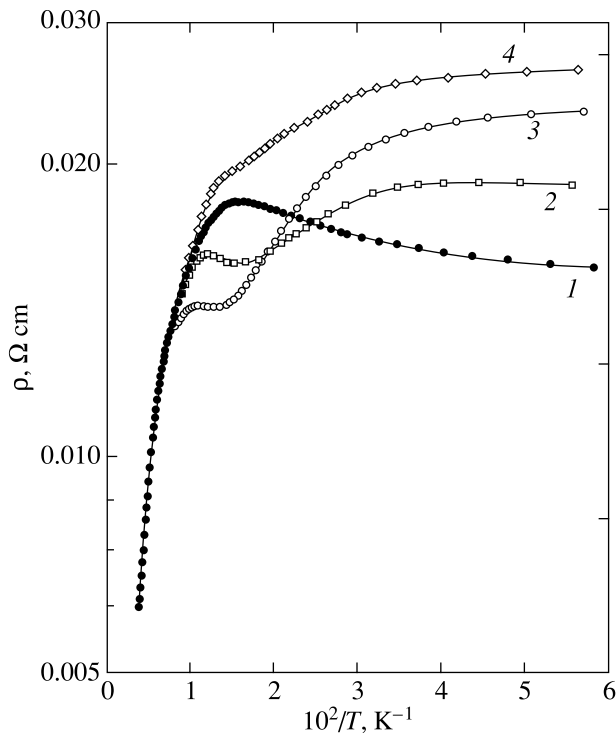

Fig. 3. Temperature dependence of the electrical resistivity ρ of an *n*-PbTe(Ga) sample. Relation *1* was obtained in the dark; *2* and *3*, under continuous illumination (by a miniature incandescent lamp) with different (but increasing) intensities; and *4*, under heating in the dark after removal of the IR source at $T = 4.2$ K.

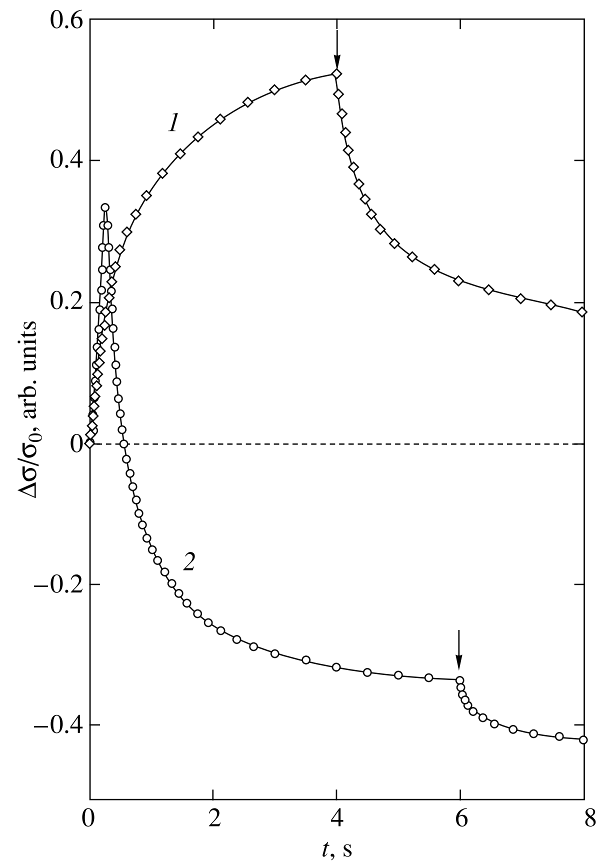

Fig. 4. Photoconductivity kinetics, $\Delta\sigma(t)$, measured under illumination of an *n*-PbTe(Ga) sample with a miniature incandescent lamp (see Fig. 3) at (*1*) 77 and (*2*) 4.2 K. Arrows indicate the instant illumination was removed.

tivity, i.e., negative photoconductivity. As the temperature increases, the amplitude of negative photoconductivity decreases and photoconductivity vanishes (at the point where curves *1* and *2* or *1* and *3* intersect), with positive photoconductivity setting in as T is increased further. Actually, the positive and negative photoconductivity components also coexist at low temperatures, but the negative photoconductivity dominates. This is demonstrated by the fact that, at $T = 4.2$ K, ρ reaches its maximum value after illumination is removed (curve *4* in Fig. 3). We see that delayed negative photoconductivity is observed up to $T \sim 100$ K.

Coexistence of the positive and negative photoconductivity contributions at low temperatures is even more revealing in studies of the photoconductivity kinetics (Fig. 4). At 77 K, only positive photoconductivity is seen to exist. As the temperature is lowered to 4.2 K, however, the original positive-photoconductivity signal reverses sign after approximately 0.5 s, with only delayed negative photoconductivity being observed thereafter; after the illumination is removed, part of the positive photoconductivity relaxes rapidly and the sample resistivity becomes even larger as compared to the dark level.

Note that delayed negative photoconductivity is in no way a unique phenomenon. It is observed in systems in which a recombination barrier forms for any reason. In particular, the recombination of spatially separated nonequilibrium electrons and holes in inhomogeneous semiconductors may be complicated by a modulation in the band relief; a similar situation may occur in quantum-well systems and polycrystalline samples. The fast component of negative photoconductivity observed under pulsed illumination is a more interesting phenomenon. Figure 5 displays the kinetics of decay of the photoconductivity signal, $\Delta\sigma(t)/\sigma_0$, measured at different temperatures. Under pulsed illumination, negative photoconductivity is dominant, with instantaneous relaxation times on the order of tens of microseconds, which is three orders of magnitude shorter than the corresponding positive photoconductivity times in semi-insulating PbTe(Ga) samples. This fast recombination defies explanation in models that assume a spatial separation of nonequilibrium carriers. The pattern of recombination should be determined by the band structure of the impurity states.

Thus, the photoconductivity signal observed in relatively low-resistivity PbTe(Ga) samples at low temper-

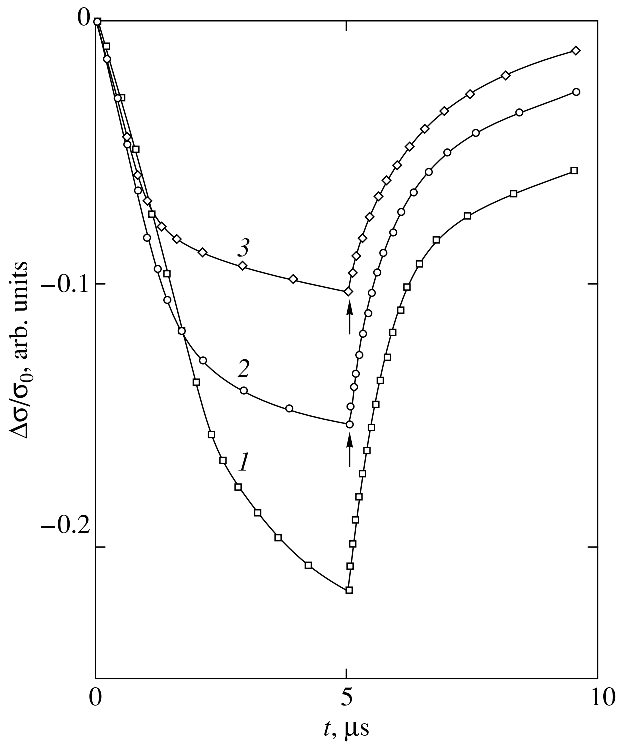

Fig. 5. Photoconductivity kinetics, $\Delta\sigma(t)$, measured under pulsed illumination by a light-emitting diode (wavelength 1 μm) from an *n*-PbTe(Ga) sample (see Fig. 3) at (*1*) 4.2, (*2*) 13, and (*3*) 30 K. IR radiation pulse 5 μs long. Arrows indicate the instant illumination was removed.

atures alternates in time, a feature associated with the coexistence of negative and positive photoconductivity, with each having a fast and a slow component that prevail at different instants of time.

5. DISCUSSION OF THE RESULTS

As a whole, the experimental data obtained can be best fitted by the model proposed in [3]. This model draws from the fact that the states of allowed bands in lead chalcogenides derive practically completely from the atomic *p* orbitals. The doping gallium atom substitutes for the lead atom in these materials. The stabilization of the Fermi level is conditioned by the negative correlation energy of electrons at the center. Hence, the charge state of the gallium atom Ga^{2+}, which is neutral relative to the lattice, is unstable and decays in the reaction $2Ga^{2+} \longrightarrow Ga^{+} + Ga^{3+}$. Thus, stabilization of the Fermi level rests upon a disproportionation of gallium atoms between the donor Ga^{3+} and acceptor Ga^{+} charge states. Treated in terms of atomic orbitals, the Ga^{2+} state can be identified with the s^1p^2 configuration; the Ga^{+} state, with the s^2p^1 configuration; and the Ga^{3+} state, with s^0p^3. The lead atom substituted for by gallium is in the s^2p^2 configuration. The allowed band states in lead chalcogenides evolve almost completely from the atomic *p* orbitals; therefore, for different charge states of the gallium atom, the electrons in the deep *s* shell are localized while the *p* electrons are delocalized. The stabilization of the Fermi level suggests that the *s* shell is empty in a sizable number of gallium atoms. The short-range attractive potential of this shell is capable of binding two *p* electrons with oppositely directed spins [4]. However, because of the large permittivity and the small effective mass of electrons in PbTe, a single impurity center with an empty *s* shell may not create a bound state at all. At the same time, the number of such centers is very large and a cluster of 10^3–10^4 impurity centers with an empty *s* shell may be capable of forming one *p*-electron bound state [5].

6. CONCLUSIONS

Thus, the generation and recombination of nonequilibrium carriers, both in PbTe(Ga) single crystals and in epitaxial films, are governed by electron transitions in a system of two allowed bands and three impurity levels. The density of states at the impurity levels can vary in the course of relaxation and be spatially nonuniform. In these conditions, one can observe intriguing phenomena, such as fast decay of the negative photoconductivity signal. The model from [3] can qualitatively describe all the main experimental findings revealed. Rigorous quantitative description is apparently unrealistic, because it would require the determination of many microscopic parameters and of their temporal and coordinate relationships. It should be noted, nevertheless, that experiments performed under identical conditions yield highly reproducible results.

ACKNOWLEDGMENTS

This study was supported in part by the Russian Foundation for Basic Research (project nos. 04-02-16497, 02-02-17057) and INTAS (project no. 2001-0184).

REFERENCES

1. B. A. Volkov, L. I. Ryabova, and D. R. Khokhlov, Usp. Fiz. Nauk **172**, 875 (2002) [Phys. Usp. **45**, 819 (2002)].
2. B. A. Akimov, A. V. Dmitriev, L. I. Ryabova, and D. R. Khokhlov, Phys. Status Solidi A **137**, 9 (1993).
3. A. I. Belogorokhov, B. A. Volkov, I. I. Ivanchik, and D. R. Khokhlov, Pis'ma Zh. Éksp. Teor. Fiz. **72**, 178 (2000) [JETP Lett. **72**, 123 (2000)].
4. B. A. Volkov and O. M. Ruchaĭskiĭ, Pis'ma Zh. Éksp. Teor. Fiz. **62**, 205 (1995) [JETP Lett. **62**, 217 (1995)].
5. A. I. Baz', Ya. B. Zel'dovich, and A. M. Perelomov, *Scattering, Reactions and Decays in Nonrelativistic Quantum Mechanics*, 2nd ed. (Israel Program for Scientific Translations, Jerusalem, 1966; Nauka, Moscow, 1971).

Translated by G. Skrebtsov

Physics of the Solid State, Vol. 47, No. 1, 2005, pp. 170–173. Translated from Fizika Tverdogo Tela, Vol. 47, No. 1, 2005, pp. 164–167.
Original Russian Text Copyright © 2005 by Pakhomov, Gaponova, Luk'yanov, Leonov.

PROCEEDINGS OF THE CONFERENCE
"NANOPHOTONICS 2004"
(Nizhni Novgorod, Russia, May 2–6, 2004)

Luminescence of Phthalocyanine Thin Films

G. L. Pakhomov, D. M. Gaponova, A. Yu. Luk'yanov, and E. S. Leonov

Institute for Physics of Microstructures, Russian Academy of Sciences, Nizhni Novgorod, 603950 Russia
e-mail: pakhomov@ipm.sci-nnov.ru

Abstract—The near-IR luminescence in thin films of metal-free phthalocyanine and phthalocyanine complexes is investigated at room temperature. It is shown that the intensity of the luminescence peaks depends on the polymorphic modification and the structure of the complexes, whereas the peak positions remain virtually unchanged. *© 2005 Pleiades Publishing, Inc.*

1. INTRODUCTION

Phthalocyanine metallocomplexes belong to one of the most important classes of low-molecular materials used in photovoltaics. For example, these compounds have been used in fabricating organic light-emitting diodes but, for the most part, as transport layers [1]. The intrinsic (weak) electroluminescence of phthalocyanine metallocomplexes in monolayer organic light-emitting diodes was observed in [2–5] for metal-free phthalocyanine H_2Pc (Fig. 1).

Although the quantum efficiency of the molecular photoluminescence in the red visible and near-IR ranges is greater than 0.5, the transition to the solid (crystalline) phase is accompanied by a strong quenching of luminescence (by three or four orders of magnitude) due to the intermolecular interaction [6]. This luminescence (usually measured in the wavelength range 700–1000 nm, i.e., below the absorption edge of the Q band; see Fig. 1) can be quenched by doping, for example, with C_{60}, which leads to an increase in the photoconductivity [7].

The position and intensity of the photoluminescence band depend on the polymorphic modification [8–10], i.e., on the molecular packing in the crystal, and the nature of the central metal atom (group) [6]. As is known, complexation leads to a change in the structure of molecular orbitals of phthalocyanine metallocomplexes and their coordination ability with respect to simple gas molecules (O_2, CO, H_2O) [11]. The aim of this work was to investigate the photoluminescence of metal-free phthalocyanine H_2Pc over a wide spectral range and its possible change in phthalocyanine metallocomplexes. Moreover, it was of interest to compare the effect of intermolecular and intramolecular interactions on the emission intensity in thin films.

2. SAMPLE PREPARATION AND EXPERIMENTAL TECHNIQUE

Metal-free phthalocyanine H_2Pc (99%) was obtained from Avocado Res. Chem. Phthalocyanines MgPc, AlFPc, and $SbCl_xPc$ were synthesized and purified at the Department of Fine Chemical Synthesis Technology (Ivanovo State University of Chemical Technology). Films of thickness ≤1 μm were prepared through thermal evaporation under vacuum (VUP-5) on R-cut sapphire plates. The samples were characterized by UV–VIS and IR spectroscopy (LOMO KSVU-12, LOMO IKS-29), atomic force microscopy (Solver P-4), and x-ray diffraction (DRON-4M). The deposition at rates of approximately 0.2–0.5 nm/s onto substrates at a temperature $T \leq 40°C$ resulted in the formation of fine-grain films of α-H_2Pc phthalocyanine [8]. The films had a texture determined by a preferred orientation of the molecular planes in stacks (with the closest packing along the b axis) aligned approximately parallel to the substrate surface. No similar orientation was observed in the MgPc films. After sublimation, the AlFPc complexes aggregated into a bridging μ-fluoropolymer [11], in which the large electric dipole stabilized a linear chain of uniaxial molecules oriented almost normally to the surface.

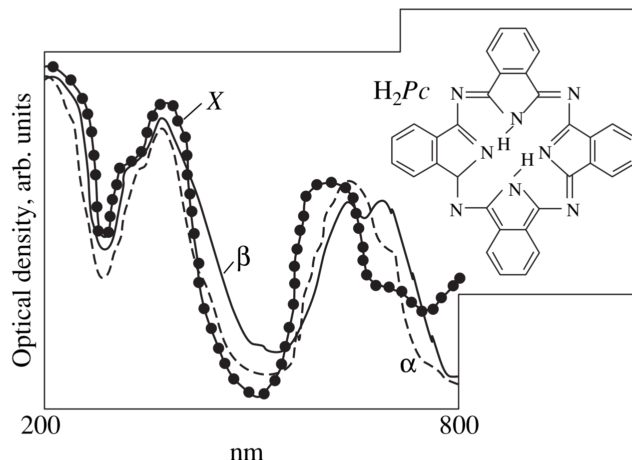

Fig. 1. Optical absorption spectra of H_2Pc films (α, β, X modifications) prepared under different conditions. The inset shows the structural formula of the H_2Pc molecule.

1063-7834/05/4701-0170$26.00 © 2005 Pleiades Publishing, Inc.

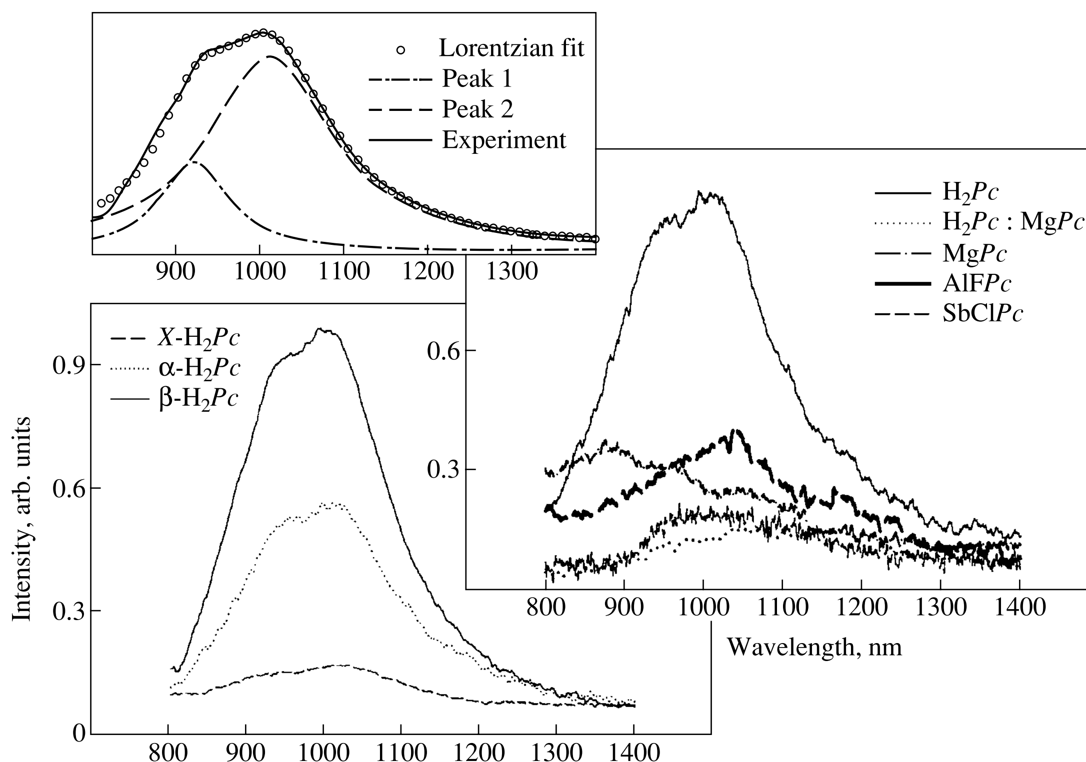

Fig. 2. Luminescence spectra of the H_2Pc films in three polymorphic states (at the left) and the films prepared from different phthalocyanines (at the right). The upper inset shows the approximation of the luminescence band of β-H_2Pc by two Lorentzian curves (see text).

All phthalocyanine metallocomplexes are intensely colored (bluish green). The spectra of these compounds contain several intense bands (extinction coefficient $\varepsilon \sim 10^5$) in the UV and visible ranges. The transition of a solution or a vapor phase to the crystalline state can lead to broadening, splitting, or shift of the bands; as a result, the absorption becomes nonzero even in dips between the maxima [12]. The typical absorption spectra of the H_2Pc films are shown in Fig. 1. The band with a lower intensity in the red visible spectral range (*Q* band) corresponds to the π–π* transition $a_{1u} \longrightarrow {}^2e_g$ in the *Pc* ring, i.e., the transition from the highest occupied molecular orbital (HOMO) to the lowest unoccupied molecular orbital (LUMO). The band in the range 300–350 nm (the Soret band) is associated with the mixed π–π* and *n*–π* transitions $a_{2u} \longrightarrow {}^2e_g$ and $b_{2u} \longrightarrow {}^2e_g$ [2, 13].

The luminescence spectra were excited with Ar^+ (λ = 514 nm, 50 mW), He : Cd (λ = 325 nm, 6 mW), and semiconductor (Mitsubishi ML 1016R-01, λ = 660 nm, 15 mW) lasers. The sample was in air at room temperature. The outgoing radiation was focused on an entrance slit of a monochromator (LOMO MDR-23; grating, 1200 or 600 groves/mm) and recorded at the exit (both slits, 1.2 mm) by a PEM-62 photomultiplier (600–1100 nm) or a germanium detector (Oxford Instrument, 800–1700 nm). It should be noted that, in the former case, the measured spectra were similar to those obtained in [6–8]. However, the increase in the spectral sensitivity of the receiver made it possible to reveal that the maximum of the broad luminescence band of H_2Pc is located in the IR range (approximately at 1 μm; see Fig. 2). This large Stokes shift between the absorption and emission bands is characteristic of α phases of phthalocyanine metallocomplexes [6].

3. RESULTS AND DISCUSSION

Excitation at a wavelength λ = 660 nm (corresponding to the HOMO ⟶ LUMO transition in H_2Pc molecules) and at λ = 514 nm, all other experimental conditions being the same, induces luminescence that is nearly identical in intensity. Most likely, this is associated with the compensation for different extinctions of the molecular layer at these wavelengths by the pumping power of the Ar^+ laser. In general, the position and shape of the peaks, including those in the spectra measured on another setup (MDR-4U with an InGaAs detector), coincide with each other. Upon illumination with light at λ = 325 nm (this corresponds to the excitation in the range of the Soret band; see Fig. 1), no luminescence peaks were observed in the spectral range under investigation.

The luminescence spectra excited with the Ar^+ laser and measured with the germanium detector (no notice-

able signals were observed in the ranges 600–800 and 1300–1700 nm) for the H_2Pc films are depicted in Fig. 2 (at the left). The smeared luminescence peak with a moderate intensity in the near-IR range is explained by the emission from the lowest (first) singlet exciton state [6, 7]. A closer examination performed in [9, 10] revealed the molecular luminescence ($S_1' \longrightarrow S_0$) and the existence of the excimer state ($S \longrightarrow S_0$), which is responsible for the long-wavelength peak. The deconvolution of the luminescence band of β-H_2Pc is shown in the upper inset to Fig. 2, which illustrates the true ratio between the peaks. As follows from [8–10], the shape of the luminescence band of H_2Pc in the near-IR range depends on the type of polymorphic modification, in particular, for the so-called α, β, and *X* forms. It is known that these modifications are formed under different conditions of synthesis or growth of crystallites [14]. In our case, the β modification was prepared by deposition on the substrate heated to 280–290°C [14] (according to [8, 15], this can be β_2 or τ form) and the *X* modification was produced using the procedure described in [15]. The differences in the x-ray diffraction patterns of the films with the thicknesses under investigation on the sapphire substrates are insufficient for reliable identification of the polymorphs. However, the optical spectra exhibit characteristic band splittings, predominantly, in the visible range (Fig. 1), which are well studied (see, for example, [16, 17]) and confirm the formation of the above phases. Note that the structures of the H_2Pc phases have been determined by different x-ray diffraction methods and have been continuously refined [18, 19]. For example, according to different data, the unit cell of the α modification consists of six, four, or two molecules [8–10, 14, 16–19].

As can be seen from Fig. 2, the positions of two peaks in the spectra of all three polymorphs differ insignificantly: 930 ± 5 and 1010 ± 5 nm (1032 nm for the *X* modification of H_2Pc). On the other hand, the luminescence intensity increases by approximately one order of magnitude in the series $X \longrightarrow \alpha \longrightarrow \beta$. These results were reproduced on different experimental setups. Possibly, in the works of other authors, the dependences of the peak shape on the packing were affected by the reabsorption of luminescence, which can be sufficiently strong in the range 800–900 nm due to the smeared absorption edge (or the presence of the fundamental absorption, as is the case with the *X* modification of H_2Pc; see Fig. 1). Furthermore, it is necessary to allow for different wavelengths of exciting radiation.

Figure 2 (at the right) shows the spectrum of the Mg*Pc* film. It is evident that this film does not emit in the spectral range under consideration (even though Sakakibara *et al.* [6] observed a weak peak at approximately 710 nm at room temperature). As is known, magnesium porphyrinates (phthalocyanines, chlorophylls) are able to interact selectively with molecular oxygen. Since H_2Pc and Mg*Pc* have a simpler structure of the molecular orbitals (there is no transition metal), the suppression of the radiative relaxation of the exciting state can be associated with this interaction. The quenching of luminescence of phthalocyanine metallocomplexes in the presence of O_2 was described by Amao *et al.* [20]. Moreover, van Faassen and Kerp [21] recently demonstrated that the diffusion coefficients and the volume concentration of O_2 in H_2Pc films are less than those in phthalocyanine metallocomplexes.

The luminescence spectrum of the composite film prepared by codeposition of H_2Pc and Mg*Pc* is depicted in Fig. 2 (at the right). Judging from the difference in the sublimation rates, the ratio between the contents of these compounds can be estimated at 3 : 1. It was shown earlier in [22] that codeposited polycrystalline films of structurally isomorphic planar phthalocyanine metallocomplexes can form solid solutions over a wide range of concentrations without disturbing the packing of stacks. It can be seen from Fig. 2 that the luminescence is almost completely quenched in the presence of Mg*Pc*. Since radiative transitions in stacking phthalocyanine metallocomplexes suggest a migration of excitons [6–8], we can assume that the introduction of even an insignificant amount of nonradiative-recombination centers (i.e., Mg*Pc* molecules) should lead to substantial quenching.

Owing to the chain geometry of the AlF*Pc* complex, the axial bonding of oxygen is hindered. However, we observed only a weak luminescence signal of this compound, whose position approximately coincides with that of the peak of H_2Pc (Fig. 2). It seems likely that, as in other chain polymers [11], the noncovalent bonding through the fluorine atom in the AlF*Pc* complex prevents the π interaction of *Pc* rings. On the other hand, this bonding is insufficient for achieving a high luminescence efficiency, as was shown in [6] for phthalocyanine chromophors separated by peripheral or axial bulky covalent substituents (groups). The films prepared from the SbCl*Pc* and $SbCl_3Pc$ complexes are characterized by a very weak luminescence (the most pronounced spectrum of SbCl*Pc* is depicted in Fig. 2). However, the luminescence spectra of these complexes differ substantially from each other. Indeed, the smeared luminescence band of SbCl*Pc* covers the range up to 1200 nm, most likely, due to the presence of peaks in the range of wavelengths longer than 1100 nm. More accurate assignment would require that measurements be made at low temperatures at which the luminescence (fluorescence) of phthalocyanine metallocomplexes becomes more intense [6, 9]. The broadening of luminescence bands (and their more complex structure) was also observed for peripherally substituted complexes, for example, for 4-Br_4Pc derivatives.

Unlike the solutions of phthalocyanine metallocomplexes, where luminescence has been well studied, no systematic data on the luminescence in solid compounds are available in the literature. Luminescence has been frequently observed as a side phenomenon

when measuring Raman spectra [8, 12]. Note that excitation at different wavelengths leads to several effects for phthalocyanine metallocomplexes. According to our data, the intensity of luminescence in phthalocyanine thin films is substantially affected by the intramolecular structure and the molecular packing in films. However, the positions of the peaks in the near-IR range vary insignificantly. It is possible that appropriate choice of the structure of the complexes, polymorphic modification, and experimental conditions (for example, in the absence of oxygen) will allow one to achieve a higher luminescence intensity in thin films. Moreover, investigating more composite phthalocyanine metallocomplexes (extradoped and sandwich complexes) that retain the typical advantages of the class of compounds under consideration will make it possible to reveal a luminescence peak in the IR or visible range.

ACKNOWLEDGMENTS

This work was supported by the Russian Foundation for Basic Research (project no. 03-02-17407) and the Presidium of the Russian Academy of Sciences within the program "Low-Dimensional Quantum Structures."

REFERENCES

1. D. Hohnholz, S. Steinbrecher, and M. Hanack, J. Mol. Struct. **521**, 231 (2000).
2. A. Fujii, M. Yoshida, Y. Ohmori, and K. Yoshino, Jpn. J. Appl. Phys., Part 2 **35**, L37 (1996).
3. M. Ottmar, D. Hohnholz, A. Wedel, and M. Hahack, Synth. Met. **105**, 145 (1999).
4. K. Shinbo *et al.*, Colloids Surf. A **198**, 905 (2002).
5. P. D. Hooper, M. I. Newton, G. McHale, and M. R. Willis, Int. J. Electron. **81**, 371 (1996).
6. Y. Sakakibara, R. N. Bera, T. Mizutani, K. Ishida, M. Tokumoto, and T. Tani, J. Phys. Chem. B **105**, 1547 (2001).
7. J. Morenzin, C. Schebusch, B. Kessler, and W. Eberhardt, Phys. Chem. Chem. Phys. **1**, 1765 (1999).
8. S. M. Bayliss, S. Heutz, G. Rumbles, and T. S. Jones, Phys. Chem. Chem. Phys. **1**, 3673 (1999).
9. K. Yoshino, M. Hikida, K. Tatsuno, K. Kaneto, and Y. Inuishi, J. Phys. Soc. Jpn. **34**, 441 (1973).
10. E. R. Menzel and K. J. Jordan, Chem. Phys. **32**, 223 (1978).
11. N. McKeown, J. Mater. Chem. **10**, 1979 (2000).
12. D. R. Tackley, G. Dent, and W. E. Smith, Phys. Chem. Chem. Phys. **3**, 1419 (2001).
13. M.-Sh. Liao and S. Scheiner, J. Chem. Phys. **114**, 9780 (2001).
14. J. Simon and J.-J. Andre, *Molecular Semiconductors* (Springer-Verlag, Berlin, 1985; Mir, Moscow, 1988), Chap. 1.
15. G. N. Meshkova, A. T. Vartanyan, and A. N. Sidorov, Opt. Spektrosk. **43**, 262 (1977) [Opt. Spectrosc. **43**, 151 (1977)].
16. Y. H. Sharp and M. Lardon, J. Phys. Chem. **72**, 3230 (1968).
17. S. Yim, S. Heutz, and T. S. Jones, J. Appl. Phys. **91**, 3632 (2002).
18. R. B. Hammond, K. J. Roberts, R. Docherty, M. Edmondson, and R. Gaims, J. Chem. Soc., Perkin Trans. 2, No. 8, 1527 (1996).
19. J. Janczak, Pol. J. Chem. **74**, 157 (2000).
20. Y. Amao, K. Asai, and I. Okura, Anal. Chim. Acta **407**, 41 (2000).
21. E. van Faassen and H. Kerp, Sens. Actuators B **88**, 329 (2003).
22. G. L. Pakhomov and Yu. N. Drozdov, Cryst. Eng. **6**, 23 (2003).

Translated by O. Borovik-Romanova

Physics of the Solid State, Vol. 47, No. 1, 2005, pp. 174–177. Translated from Fizika Tverdogo Tela, Vol. 47, No. 1, 2005, pp. 168–171.
Original Russian Text Copyright © 2005 by Bagaev, Onishchenko.

PROCEEDINGS OF THE CONFERENCE "NANOPHOTONICS 2004"
(Nizhni Novgorod, Russia, May 2–6, 2004)

Temperature Dependence of the Photoluminescence of CdTe/ZnTe Quantum-Dot Superlattices

V. S. Bagaev and E. E. Onishchenko

Lebedev Physical Institute, Russian Academy of Sciences, Leninskiĭ pr. 53, Moscow, 119991 Russia
e-mail: evgeny@lebedev.ru

Abstract—The temperature dependence of the luminescence of CdTe/ZnTe quantum-dot superlattices (self-assembled quantum-dot multilayers) with ZnTe spacers of various thicknesses was studied. Luminescence quenching observed to occur with increasing temperature is shown to depend substantially on the thickness of the ZnTe spacer. Particular attention is focused on the temperature dependence of the luminescence of a structure with the smallest ZnTe layer thickness, containing clusters of regularly arranged quantum dots. The luminescence line of tunneling-coupled quantum dots appearing in this structure exhibits an unusual temperature dependence, more specifically, an anomalously large shift of the peak position and fast luminescence quenching with increasing temperature. © *2005 Pleiades Publishing, Inc.*

1. Elastic strains play a crucial role in the spontaneous formation of semiconductor quantum dots (QDs) in highly lattice-mismatched systems. The strains created in the course of growth of multilayer structures initiate the formation of ordered QD arrays, and they affect the shape and electronic structure of the QDs. Of particular interest in this respect are the properties of CdTe/ZnTe multilayer QD structures. This heteropair is specific in that the jump in the potential in its valence band is determined almost entirely by the elastic strains generated by the lattice mismatch. Disregarding the strains, the valence-band offset is no greater than ten percent of the difference between the band-gap widths [1]. This offers the additional possibility of controlling the electronic spectrum of the structure (for instance, to change the type of the band diagram) by properly varying the elastic strain distribution through variation of the structure parameters (the buffer layer material, spacer layer thicknesses, etc.).

2. The CdTe/ZnTe quantum-dot superlattices (QDSLs) under study were grown by MBE on a (100)GaAs substrate. A CdTe buffer layer 4.5-μm thick was deposited on the substrate, and a QDSL was grown on this layer, which consisted of 200 CdTe layers with a nominal growth thickness of 2.5 monolayers separated by ZnTe spacers of a preset thickness (12, 25, and 75 monolayers, referred to subsequently as structures B12, B25, and B75, respectively). High-resolution transmission electron microscopy showed a QD layer in such structures to be actually a $Zn_{1-x}Cd_xTe$ solid-solution layer containing self-assembled QD regions (islands) with an enhanced cadmium concentration, measuring 6 to 10 nm in diameter and up to 2 nm in thickness. It was established that, in QDSLs with ZnTe spacers less than 25 monolayers thick, QD positions become correlated in the adjacent layers, as well as in the layer plane; correlated QD arrangement was observed to persist within six to seven layers in the growth direction and up to six islands in the lateral direction [2]. Such clusters of regularly arranged QDs are accompanied by regions where no correlation in QD arrangement is observed. The photoluminescence (PL) spectrum of QDSLs with thin enough spacers contains not only the emission line of "isolated" QDs (by which we mean CdTe islands having no close neighbors in adjacent QD layers) but also a longer wavelength emission line originating from the presence of quantum-mechanically coupled QDs.

3. PL spectra were measured at temperatures ranging from 5 to 200 K under cw pumping by an argon laser at wavelengths of 4880 and 5145 Å, as well as by a He–Cd laser (4416 Å). The pump power density was varied from 1 mW/cm^2 to 100 W/cm^2. We also measured PL spectra at room temperature. The spectra were analyzed with a DFS-24 double-grating monochromator with a limiting resolution no worse than 0.1 Å.

4. Unlike structures with isolated CdTe/ZnTe QD layers that have practically no lateral exciton migration [3], excitons in QDSLs migrate laterally, which becomes manifest in a broadening of the PL lines with increasing temperature. The shift of the emission line peak in the B75 and B25 structures, as well as in structure B12 with isolated QDs, follows the ZnTe band-gap shrinkage [4], which also takes place in structures with isolated QD layers studied earlier. The situation is completely different with the emission line of tunneling-coupled QDs in the B12 structure (Fig. 1), which reveals an anomalously large shift of the PL peak position with increasing temperature; indeed, as the temperature is raised from 5 to 50 K, the peak shift (15 meV) is 2.5 times larger than the ZnTe band-gap variation in this temperature range (6 meV).

1063-7834/05/4701-0174$26.00 © 2005 Pleiades Publishing, Inc.

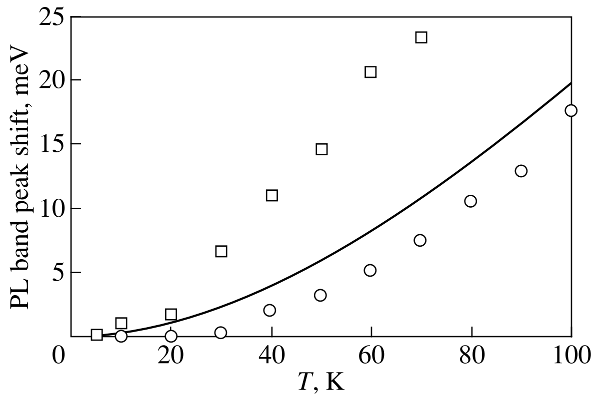

Fig. 1. Shift of the PL line maximum in isolated QDs (circles) and tunneling-coupled QDs (squares). Solid line plots the variation of the ZnTe band-gap width.

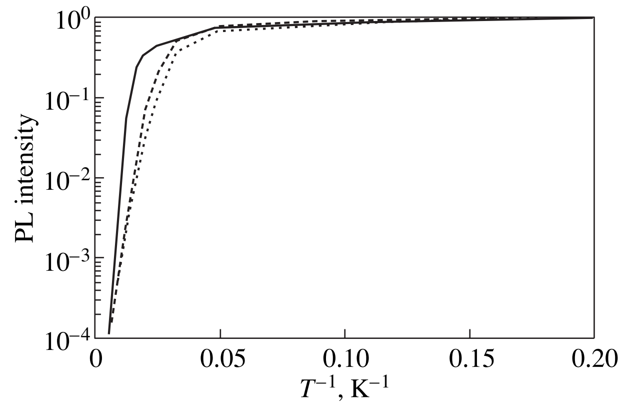

Fig. 2. Temperature dependence of the integrated PL intensity of the B75 (solid line) and B25 (dashed line) structures and of the emission line of isolated QDs in the B12 structure (points) (normalized to radiation intensity at 5 K).

An anomalous shift of the luminescence line peak in some temperature interval is frequently observed to occur in QD and quantum-well structures (see, e.g., [5, 6] and references therein). Excitons are capable of migrating in the QD layer plane (or in the plane of a quantum well exhibiting thickness fluctuations) via tunneling transitions between QDs (local potential minima in a quantum well). Such transitions are accompanied by the emission (absorption) of phonons; at low temperatures, migration entails primarily energy losses. As the temperature increases, excitons, in addition to the increasing probability of transferring directly to deeper states, also become capable of making this transition through an intermediate (higher energy) state, a process involving the absorption of a phonon. Thus, as the temperature is increased, it becomes possible for excitons to transfer from shallower to deeper localized states (for instance, from smaller to larger QDs).

Other mechanisms that could be responsible for the anomalous long-wavelength shift of the PL line peak position in QD structures with increasing temperature are also considered in the literature. For instance, in [7], where the temperature dependence of the CdSe/ZnSe QD luminescence was studied, it was assumed that the anomalous shift of the peak position is associated not with transitions between different QDs but rather with transitions between different states within a QD (island); such states can form as a result of the complex topological structure of the islands. Note that CdSe/ZnSe QDs resemble, in many respects, the CdTe/ZnTe QDs under study here: indeed, a QD layer is a layer of a $Zn_{1-x}Cd_xSe$ solid solution containing islands with an enhanced cadmium content, measuring 5 to 10 nm in the layer plane and 1.5- to 3-nm thick. As pointed out above, however, the QDSLs under study here do not exhibit any anomalous shift of the peak position (including the emission line of isolated QDs in the B12 structure), except for the PL line related to tunneling-coupled QDs. One may therefore assume that the anomalous shift originates from exciton migration among different QDs within clusters of self-assembled islands.

The onset of exciton redistribution among QDs at such low temperatures as 20–30 K is not typical of QD structures. The characteristic spread of exciton states in energy in clusters of self-assembled QDs is apparently small enough for thermally activated exciton transport among QDs to occur already at such low temperatures.

Studies of the temperature dependence of the integrated PL intensity of CdTe/ZnTe QDSLs reveal that PL quenching with increasing temperature depends substantially on the thickness of the ZnTe spacer. The behavior of the emission line of tunneling-coupled QDs in this case is also fairly unusual, and we will consider it in more detail below. The B75 structure exhibits noticeable luminescence even at room temperature, whereas the PL intensity of a QDSL with a thinner ZnTe spacer drops with increasing temperature substantially faster. The PL quenching activation energy, derived from the temperature dependence of the integrated QDSL PL intensity, decreases gradually with decreasing thickness of the ZnTe spacer from 60 meV in the B75 structure to less than 30 meV for the PL line of isolated QDs in B12 (Fig. 2). While the activation energy of 60 meV obtained for the B75 QDSL is comparable to the value observed earlier in structures with single CdTe/ZnTe QD layers having similar nominal growth thicknesses of the CdTe layer [3], activation energies on the order of 30 meV are certainly not typical of structures with single QD layers.

Such a pronounced decrease in the activation energy can be assigned to a variation of the elastic strain distribution pattern occurring in a QDSL with decreasing thickness of the ZnTe spacer. Our earlier analysis of IR reflectance spectra of the B12, B25, and B75 structures showed that, in the case of thick ZnTe spacers, the elastic strains are concentrated in the $Zn_{1-x}Cd_xTe$ layers,

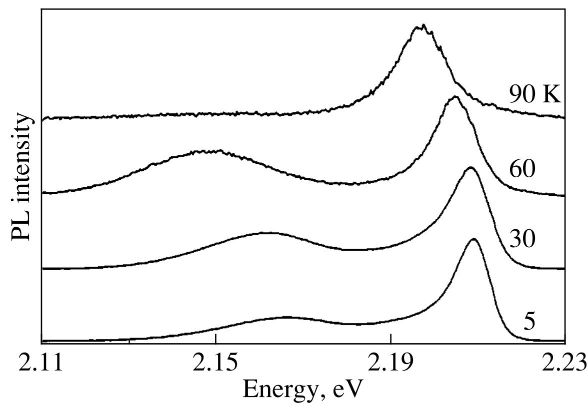

Fig. 3. PL spectra of the B12 structure measured at various temperatures. The spectra are normalized and translated vertically for clarity.

whereas in QDSLs with thin barriers the elastic strain distribution pattern is more complex [8]. In the B75 structure (as in structures with single QD layers), the CdTe/$Zn_{1-x}Cd_xTe$ layers (including the QDs themselves) undergo biaxial compression, whereas the ZnTe spacers are practically under zero stress; it is this that accounts for the relatively large depth of the potential well for the heavy hole in QDs. In the B25 and B12 structures, the ZnTe layers are distorted strongly by the thick CdTe buffer and the $Zn_{1-x}Cd_xTe$ layers, while the latter layers are less compressed, which substantially reduces the potential-well depth for the heavy hole. The QD luminescence quenching with increasing temperature is due to thermal ejection of carriers from the QDs, followed by their nonradiative recombination. Because the greater part of the difference between the band-gap widths of ZnTe and CdTe (0.8 eV) is, as already mentioned, caused by the conduction band offset, the magnitude of the activation energy is determined by the potential-well depth for the hole rather than for the electron.

PL spectra of the B12 structure obtained at various temperatures are displayed in Fig. 3. The relative intensity of the emission line of tunneling-coupled QDs grows with increasing temperature up to 40 K, to practically disappear in the spectrum at 80 K. Structures with isolated CdTe/ZnTe QD layers usually exhibit the reverse situation; namely, the larger the radiation wavelength (and, accordingly, the more strongly localized the carriers in the QDs), the more slowly the PL quenching begins with increasing temperature [3].

The observed anomaly can be explained in terms of the band diagram of the CdTe/ZnTe structures by taking into account the fact that the QDSLs under study were grown on a thick CdTe buffer layer. The band diagram of CdTe/ZnTe is such that the depth of the potential well for the electrons is determined primarily by the composition of the well and spacer materials and the potential-well depth for the holes, by the elastic strains. Therefore, a longer emission wavelength does not necessarily correspond to a deeper potential well for both carrier types. Under certain conditions, a situation may arise in CdTe- and ZnTe-based low-dimensional structures where an optical transition involving a spatially indirect electron–light-hole exciton has a lower energy than that involving a spatially direct electron–heavy-hole exciton. Indeed, for conventional CdTe/$Cd_{1-x}Zn_xTe$ superlattices, it was shown in [9] that, by properly varying the buffer layer composition so as to redistribute the strains between the CdTe and $Cd_{1-x}Zn_xTe$ layers, one can change the type of band diagram of the structure. The lowest energy can in this case have either the bound state of an electron and a heavy hole localized in the same CdTe layer (type-I superlattice) or the bound state of an electron and a light hole localized in two different layers, CdTe and $Cd_{1-x}Zn_xTe$ (type-II superlattice).

It was conjectured in [8] that, because of the presence of a thick CdTe buffer layer, the luminescence of tunneling-coupled QDs in the B12 structure may be due to spatially indirect excitons (the strains are maximum in the region between two CdTe islands in adjacent QD layers, which may bring about the formation of a potential well for light holes in these regions, with the electrons localized in CdTe islands). This conjecture is corroborated by photoreflectance spectroscopy data (to be published separately); indeed, in the photoreflectance spectra, the feature associated with tunneling-coupled islands is practically absent, whereas the feature deriving from isolated islands is distinct, thus showing the exciton oscillator strength to be substantially weaker in the former than in the latter case (as should be expected for indirect excitons).

Clusters of regularly arranged QDs contain an array of regularly arranged potential wells for the hole (between CdTe islands in adjacent QD layers). Since the depth of these potential wells is relatively small, the spread in the energy level positions for such wells should likewise be small. By slightly simplifying the situation, one can say that, within a cluster of regularly ordered QDs, a light hole can be bound to a certain QD only through Coulomb interaction with the electron localized in the deep potential well in the QD. The binding energy of a spatially indirect exciton is substantially smaller than that of a direct exciton, and the characteristic time of its radiative recombination noticeably exceeds that of a direct exciton. One may expect in these conditions that an increase in temperature will bring about a fairly fast luminescence quenching of the tunneling-coupled QDs, exactly what is observed in experiment. Even with a slight increase in temperature, intense exciton migration occurs in clusters of self-assembled QDs and gives rise to an increase in the number of excitons undergoing nonradiative recombination [10], which likewise favors quenching of the luminescence of tunneling-coupled QDs with increasing temperature.

5. To sum up, it has been shown that quenching of the CdTe/ZnTe QDSL luminescence observed to occur

with increasing temperature depends substantially on the ZnTe spacer thickness. The emission line of tunneling-coupled QDs that appears in QDSLs with the minimum ZnTe spacer thickness (12 monolayers) exhibits an unusual behavior; indeed, one observes an anomalously large shift of the line peak position and a fast drop in luminescence intensity with increasing temperature. This behavior can be accounted for by assuming that the luminescence of tunneling-coupled quantum dots derives from spatially indirect excitons and that excitons within regularly arranged quantum-dot clusters undergo intense migration even at low temperatures.

ACKNOWLEDGMENTS

The authors are indebted to G. Karchevskiĭ for preparing the samples.

This study was supported by the Russian Foundation for Basic Research (project nos. 03-02-16854, 02-02-17392), the program for support of leading scientific schools (project no. NSh-1923.2003.2), and the RAS Committee on Youth Support Activities.

REFERENCES

1. H. Mathie, A. Chatt, J. Allegre, and J. P. Faurie, Phys. Rev. B **41**, 6082 (1990).
2. S. Mackowski, G. Karczewski, T. Wojtowicz, J. Kossut, S. Kret, A. Szczepanska, P. Dluzewski, G. Prechtl, and W. Heiss, Appl. Phys. Lett. **78**, 3884 (2001).
3. V. V. Zaĭtsev, V. S. Bagaev, and E. E. Onishchenko, Fiz. Tverd. Tela (St. Petersburg) **41**, 717 (1999) [Phys. Solid State **41**, 647 (1999)].
4. B. Langen, H. Leiderer, W. Limmer, W. Gebhardt, M. Ruff, and U. Rossler, J. Cryst. Growth **101**, 718 (1990).
5. S. D. Baranowski, R. Eichmann, and P. Thomas, Phys. Rev. B **58**, 13 081 (1998).
6. A. Polimeni, A. Patane, M. Henini, L. Eaves, and P. C. Main, Phys. Rev. B **59**, 5064 (1999).
7. A. Klochikhin, A. Reznitsky, B Dal Don, H. Priller, H. Kalt, C. Klingshirn, S. Permogorov, and S. Ivanov, Phys. Rev. B **69**, 085 308 (2004).
8. V. S. Bagaev, L. K. Vodop'yanov, V. S. Vinogradov, V. V. Zaĭtsev, S. P. Kozyrev, N. N. Mel'nik, E. E. Onishchenko, and G. Karchevskiĭ, Fiz. Tverd. Tela (St. Petersburg) **46**, 171 (2004) [Phys. Solid State **46**, 173 (2004)].
9. H. Tuffigo, N. Magnea, H. Marriete, A. Wassiela, and Y. Merle d'Aubigne, Phys. Rev. B **43**, 14 629 (1991).
10. I. N. Krivorotov, T. Chang, G. D. Gillialand, L. P. Fu, K. K. Bajaj, and D. J. Wolford, Phys. Rev. B **58**, 10 687 (1998).

Translated by G. Skrebtsov

Physics of the Solid State, Vol. 47, No. 1, 2005, pp. 178–182. From Fizika Tverdogo Tela, Vol. 47, No. 1, 2005, pp. 172–175.
Original English Text Copyright © 2005 by Teperik, Popov, García de Abajo.

PROCEEDINGS OF THE CONFERENCE "NANOPHOTONICS 2004"
(Nizhni Novgorod, Russia, May 2–6, 2004)

Total Resonant Absorption of Light by Plasmons on the Nanoporous Surface of a Metal[1]

T. V. Teperik[1], V. V. Popov[1], and F. J. García de Abajo[2]

[1] *Institute of Radio Engineering and Electronics (Saratov Division), Russian Academy of Sciences, Saratov, 410019 Russia*
e-mail: teperik@ire.san.ru

[2] *Centra Mixto CSIC-UPV/EHU and Donostia International Physics Center, San Sebastian, 20080 Spain*

Abstract—We have calculated light absorption spectra of planar metal surfaces with a two-dimensional lattice of spherical nanovoids just beneath the surface. It is shown that nearly total absorption of light occurs at the plasma resonance in a void lattice in the visible range when the intervoid spacing and the void deepening into the metal are thinner than the skin depth, which ensures optimal coupling of void plasmons to external light. We conclude that the absorption and local-field properties of this type of nanoporous metal surface can be effectively tuned through nanoengineering of the spherical pores and that they constitute a very attractive system for various applications in future submicron light technology. *© 2005 Pleiades Publishing, Inc.*

1. INTRODUCTION

In general, planar metal surfaces absorb light very poorly. The reason for this is their high free-electron density, which reacts to the incident light by sustaining strong oscillating currents that, in turn, efficiently reradiate light back into the surrounding medium, whereas the light intensity inside the metal remains weak. Actually, the same phenomenon takes place when light excites plasma oscillations in metallic particles, and light absorption is inhibited as a result at the plasma resonances. In other words, the local-field enhancement inside or near the metallic particle appears to be quite moderate even at the plasma resonance. Local-field enhancement factors of up to 15 have been reported for spherical metallic nanoparticles [1, 2].

In apparent contradiction with the above arguments, sharp and deep (down to –20 dB) resonant dips in the reflectivity spectra of light from a nanoporous gold surface have been recently observed [3], which points to strong resonant light absorption on such a surface.

It was presumed in [3] that this phenomenon is related to the excitation of plasmon modes in spherical nanocavities inside the metal, which couple much more effectively to the light than those in metallic spheres. As an intuitive explanation of their observations, the authors of [3] employed a simple model of plasmon modes supported by a spherical void in an infinite metallic medium. Although that model gives eigenfrequency values that somehow can be fitted to the frequencies of the resonances in the measured reflectivity spectra, it cannot describe the coupling between plasmon modes in the nanocavity and the external radiation field. The reason for this is that the plasmon modes in a void are nonradiative, because their electromagnetic field cannot radiate into an infinite metal having a negative permittivity. However, the huge resonant dips in the reflectivity spectra observed in [3] suggest a strong coupling of nanocavity plasmons to the incident light. Therefore, gaining a better understanding of the effect of coupling between plasmons in metallic nanocavities and external radiation becomes of great importance.

On the other hand, it has been shown in [4–6] that the spectra of plasma oscillations in spherical metallic nanoparticles with inner voids (nanoshells) are much richer than those in metallic nanospheres. Both spherelike plasmons (those mainly bound to the outer surface of the shell) and voidlike plasmons (those mainly bound to the inner surface of the shell) can be excited in such a particle. The optical properties of a single metallic nanoshell and nanoshell clusters can be effectively tuned through nanoengineering of their geometry. As has been theoretically shown in [6], the local-field enhancement factor at the voidlike plasmon resonance can reach ultrahigh values for specific values of the metallic wall thickness in a nanoshell: local-field enhancement factors exceeding 60 and 150 in gold and silver nanoshells, respectively, have been predicted, and this field enhancement is accompanied by sharply enhanced light absorption at resonance.

In this paper, we study the optical properties of a nanoporous metal surface. We start with a simple model of the resonant surface in order to examine the essential physics underling strong light absorption on such a surface. Then, we calculate the reflection/absorption spectra of nanoporous metal surfaces in the framework of a rigorous electromagnetic scattering-matrix approach [7], taking into account the actual porous structure of the surface.

[1] This article was submitted by the authors in English.

1063-7834/05/4701-0178$26.00 © 2005 Pleiades Publishing, Inc.

2. MODEL OF A RESONANT SURFACE

Let us consider an electromagnetic plane wave incident from vacuum normally onto a planar surface of metal with a two-dimensional lattice of voids just underneath the surface (Fig. 1). In order to examine the essential physics of energy transformation in the system, we elaborate a simple equivalent model that describes the resonant surface in terms of its effective surface impedance Z_{eff} defined by the relation $\mathbf{E}_\tau = Z_{\text{eff}}(\mathbf{n} \times \mathbf{B}_\tau)$, where $\mathbf{E}_\tau$ and $\mathbf{B}_\tau$ are the tangential components of the total electric and magnetic fields, respectively, and $\mathbf{n}$ is the external normal to the planar metal surface. Making use of the impedance boundary condition [8] and solving Maxwell's equations in the surrounding medium, it is easy to obtain the complex amplitude reflection coefficient $r = (Z_{\text{eff}} - Z_0)/(Z_{\text{eff}} + Z_0)$, where Z_0 is the free-space impedance.

We describe plasma oscillations in the lattice of voids using an equivalent *RLC* circuit (Fig. 1) composed of the equivalent areal capacitance $C_l = |f_l|^2\delta\varepsilon_0$, where δ is the thickness of the nanoporous surface layer, ε_0 is the electrical constant, $|f_l|^2$ is the dimensionless phenomenological form factor characteristic of a given lth multipole plasmon mode, connected in parallel to $R_l - L_l$ series (Fig. 1). The equivalent areal electronic resistance and kinetic inductance are defined as $R_l = m\nu_l/(e^2\Delta_l N_e)$ and $L_l = m/(e^2\Delta_l N_e)$, respectively, where ν_l is the damping of the lth plasmon mode due to all dissipative processes except radiative damping, N_e is the total areal free-electron density in the surface skin layer, Δ_l is the fraction of free electrons participating in the plasma oscillations at the lth mode, and e and m are the electron charge and mass, respectively.

With these considerations, we can easily obtain the equivalent surface impedance in the form

$$Z_{\text{eff}} = \frac{m}{e^2 N_e}(\nu_e - i\omega) - i\frac{m}{2e^2}\sum_{l=1}^{\infty}\frac{|\beta_l|^2}{\Delta_l N_e}\frac{\omega_l^2}{\omega_l - \omega - i\nu_l}, \quad (1)$$

where

$$\omega_l = \sqrt{\frac{e^2\Delta_l N_e}{|f_l|^2\delta\varepsilon_0 m}} \quad (2)$$

is the frequency of the lth plasmon mode and $|\beta_l|^2 < 1$ is the phenomenological coefficient of coupling between the external light and the lth plasmon mode. The first term in Eq. (1), where ν_e is the free-electron scattering rate, describes the Drude response of a homogeneous metal surface within intervoid regions to incident light by the equivalent electronic resistance $R_e = m\nu_e/(e^2N_e)$ and kinetic inductance $L_e = m/(e^2N_e)$ (Fig. 1). In the vicinity of the lth plasma resonance, $\omega \simeq \omega_l$, the lth

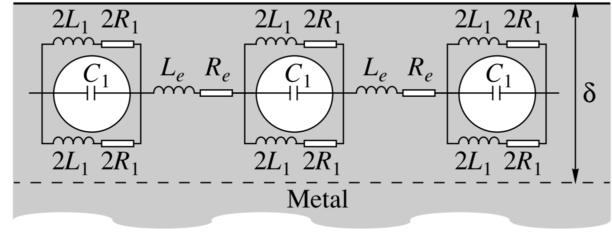

Fig. 1. Nanoporous surface of metal and its equivalent circuit.

term of the summation dominates the right-hand side of Eq. (1) and we have

$$Z_{\text{eff}} \approx -i\frac{m|\beta_l|^2}{2e^2\Delta_l N_e}\frac{\omega_l^2}{\omega_l - \omega - i\nu_l}. \quad (3)$$

The surface impedance given by Eq. (3) leads to the following expression for the absorbance of light in the neighborhood of the lth plasma resonance:

$$A = 1 - rr^* \approx \frac{4\nu_l\gamma_l}{(\omega_l - \omega)^2 + (\nu_l + \gamma_l)^2}, \quad (4)$$

where

$$\gamma_l = |\beta_l|^2\frac{m\omega_l^2}{2Z_0 e^2\Delta_l N_e} \quad (5)$$

is the radiative damping of the lth plasmon mode. It should be noted that the line of the absorption resonance given by Eq. (4) has a Lorentzian shape with a full width at half-maximum (FWHM) of $2(\nu_l + \gamma_l)$. Free parameters $|f_l|^2/\Delta_l$, and $|\beta_l|^2/\Delta_l$ can be obtained by fitting the resonance frequency and FWHM yielded by this simple model to those yielded by a rigorous electromagnetic modeling, which is done in the next section of this paper.

Finally, at resonance ($\omega = \omega_l$), one finds

$$A_{\text{res}} \approx \frac{4\nu_l\gamma_l}{(\nu_l + \gamma_l)^2}$$

and it is readily seen that nearly total light absorption by the lth plasmon mode (i.e., $A_{\text{res}} \approx 1$) occurs when $\gamma_l = \nu_l$. The radiative damping γ_l may be considered the coupling coefficient that controls the strength of interaction between the plasmon mode and light. For small γ_l (i.e., $\gamma_l \ll \nu_l$), the coupling is weak and the plasmon mode absorbs light only weakly. In the opposite limit, $\gamma_l \gg \nu_l$, the strong plasma oscillation currents flowing on the metal surface reradiate incident light back into the surrounding medium, which again reduces absorption drastically. Therefore, it is possible to realize the condition of total light absorption by plasmons on a nanoporous metal surface by varying the coupling coefficient $|\beta_l|^2$. The optimal value of $|\beta_l|^2$ can be easily real-

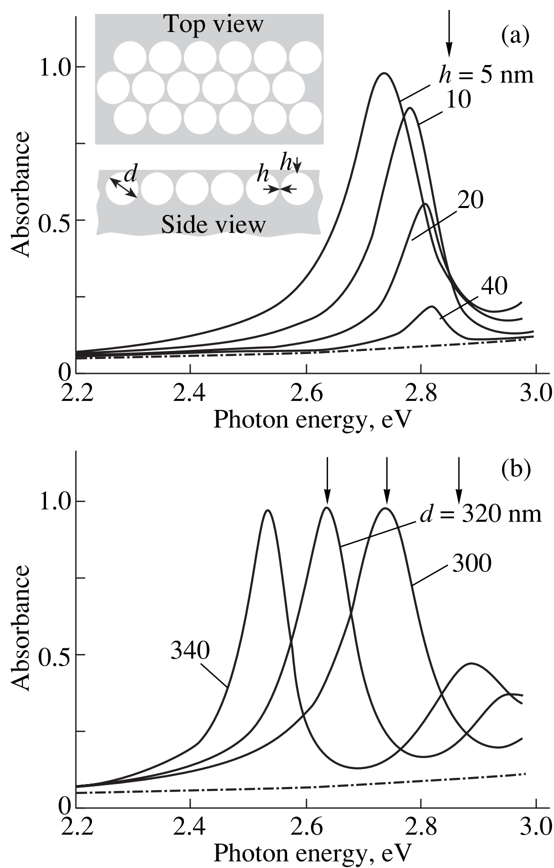

Fig. 2. Absorption spectra of light incident normally onto a planar silver surface with a lattice of spherical voids just beneath it (see inset). (a) Variation of the spectra with intervoid spacing h, chosen equal to the void deepening, for the void diameter $d = 300$ nm. (b) Variation of the spectra with void diameter for intervoid spacing $h = 5$ nm, also taken to be equal to the void deepening. The absorption of light on the surface of bulk silver is shown by a dash-dotted curve. Vertical arrows mark the energies of the fundamental plasmon modes ($l = 1$) of a single void in bulk silver.

ized for voidlike plasmon modes in the spherical voids buried in a metal substrate. For example, the condition $\gamma_l = \nu_l$ can be easily satisfied for voidlike plasmons in a nanoshell by choosing a specific value of the shell-layer thickness, as shown in [6].

3. SELF-CONSISTENT ELECTRODYNAMIC MODELING

Let us consider a periodic two-dimensional hexagonal lattice of spherical voids with the lattice vectors **a** and **b**, where $|\mathbf{a}| = |\mathbf{b}|$ and $\mathbf{a} \cdot \mathbf{b} = |\mathbf{a}|^2\cos\alpha$ with $\alpha = 60°$. We assume that the lattice of voids is buried inside a metal substrate at distance h from the planar metal surface to the top of the voids, therefore we call h the void deepening. We also assume that the intervoid spacing along the lattice vectors **a** and **b** is equal to the void deepening h (inset to Fig. 2a). We consider that external light shines normally onto the metal surface.

To calculate the light absorption on such a nanoporous surface of metal, we use a self-consistent rigorous electrodynamic method based on the scattering-matrix approach with the use of re-expansion of the plane-wave representation of electromagnetic fields in terms of the spherical harmonics [7]. This approach involves the following steps. First of all, we define a planar surface layer containing the periodic lattice of voids in such a way that the planar real surface of the metal and the imaginary plane located below the voids at a distance h from the void bottoms form the interfaces between the periodic surface layer and either the surrounding medium or metal substrate, respectively. The total fields in the surrounding medium and in the substrate result from the superposition of propagating and evanescent plane waves with in-plane wave vectors $\mathbf{G}_{pq} = p\mathbf{A} + q\mathbf{B}$, where $\mathbf{A} = 2\pi(\mathbf{b} \times \mathbf{n})/|\mathbf{a} \times \mathbf{b}|$ and $\mathbf{B} = 2\pi(\mathbf{n} \times \mathbf{a})/|\mathbf{a} \times \mathbf{b}|$ are the principal vectors of the reciprocal lattice and p and q are integers. It should be noted that, at frequencies below the bulk plasma frequency, every plane wave in the metal substrate is evanescent. The total field inside the periodic surface layer is represented as a superposition of the incoming plane waves (both propagating and evanescent) and the field scattered from every void. In this way, the multiple light scattering between all voids in the surface layer is self-consistently accounted for. The in-plane summations of fields scattered from different voids, performed in our case directly in real space, provide a quite fast convergence.

The interaction between the combined electromagnetic field incident upon a given single void and the electromagnetic field scattered from this void is determined by its scattering matrix [9, 10]. Because the scattering matrix of a single void is constructed in a spherical-harmonic representation, we decompose the combined field incident upon a given single void into spherical harmonics. Then, we transform the combined self-consistent field scattered from all voids into a plane-wave representation, expressed as a sum over in-plane wave vectors $\mathbf{G}_{pq}$, and apply the boundary conditions at the interfaces of the planar surface layer containing the lattice of voids with the surrounding medium and substrate. As a result, we construct the scattering matrix of the entire structure, which allows us to calculate the reflectance, R, and absorbance, $A = 1 - R$, of the porous metal surface. Note that this approach can be straightforwardly extended to model an arbitrary number of layers with periodically arranged spherical voids with the same period but having different void radii in different layers if one wishes. A detailed description of this method can be found in [7].

It is interesting to point out that the propagation of the electromagnetic field between voids is performed through the metal, so that each void interacts directly only with its nearest neighbors, unlike what happens in a dielectric environment. Accordingly, the Bragg resonances controlled by the periodicity of the system are

not exhibited in the calculated spectra. Therefore, only resonances originating from the excitation of Mie plasmon modes in every single void influenced by nearest void neighbors show up in the spectra.

Figure 2 shows the calculated absorption spectra of light incident normally onto a nanoporous silver surface for the case of a single periodic layer of closely packed voids buried inside the silver substrate (inset to Fig. 2a). We use experimental optical data [11] to describe the dielectric response of silver to an electric field in our calculations. The light absorption exhibits resonant enhancement at the frequencies of plasma resonances in nanovoids. Almost total resonant light absorption (the effect of "black silver") occurs when the lattice of voids is buried in the silver substrate at a distance smaller than the skin depth (the latter is about 23 nm for silver). Although the frequency of the plasma resonance on the porous metal surface is close to the frequency of the fundamental (with the orbital quantum number $l = 1$) Mie plasmon mode of a single spherical void in an infinite metallic medium, they do not coincide. As is clearly seen in Fig. 2a, the shift between these two frequencies grows as the intervoid spacing decreases, which shows that the reason for this shift is the coupling of plasmons in adjacent voids. Note that the spectra are independent of the polarization for normally incident light due to the symmetry of the void lattice, $|\mathbf{a}| = |\mathbf{b}|$.

Now, we can estimate free parameters $|f_l|^2/\Delta_l$ and $|\beta_l|^2/\Delta_l$ introduced in the previous section by fitting Eqs. (2) and (5) to the resonance frequency and FWHM in the case of total light absorption. In this case, the FWHM is equal to $4\gamma_l$ as shown in the previous section. We obtain free parameters $|f_l|^2/\Delta_l \approx 1$ and $|\beta_l|^2/\Delta_l \approx 0.1$ for every resonance shown in Fig. 2b.

Figure 2 depicts the resonant absorption caused by the excitation of the fundamental plasmon mode ($l = 1$) in voids. The frequencies of high-order plasma resonances fall within the interband absorption spectra (at frequencies higher than 3.5 eV for silver [11]), and, therefore, these resonances can hardly be observed in the reflectivity spectra. The frequencies of plasmon resonances on a nanoporous metal surface can be reduced by filling the pores with a dielectric material. Figure 3 shows the calculated absorption spectra of light incident normally onto a silver surface with filled spherical nanopores. In this case, the second and the third plasmon resonances along with the fundamental plasma resonance show up in the visible. Giant light absorption can also be achieved at high-order plasma resonances by choosing appropriate parameters of the porous layer (Fig. 3).

In conclusion, we have shown theoretically that nearly total light absorption on a nanoporous surface of metal can be achieved at the plasma resonance. This phenomenon occurs when the lattice of spherical voids is buried in the metal substrate at a specific distance from the metal surface, which ensures optimal coupling of plasmons in the voids to the external light. Based upon a simple model, later corroborated by detailed calculations, we have found a physical criterion for the optimal coupling, that the radiative broadening of the plasma resonance must be equal to its dissipative broadening in order to produce total light absorption at resonance. It is worth mentioning that the resonant light absorption must be accompanied by high local-field enhancement near or inside the voids, and this could be used to trigger nonlinear effects. The frequencies of absorption resonances can be easily tuned by varying the diameter of the voids or by filling them with dielectric materials. This makes this type of nanoporous metals very attractive for a variety of applications, from nanophotonics to biophysics.

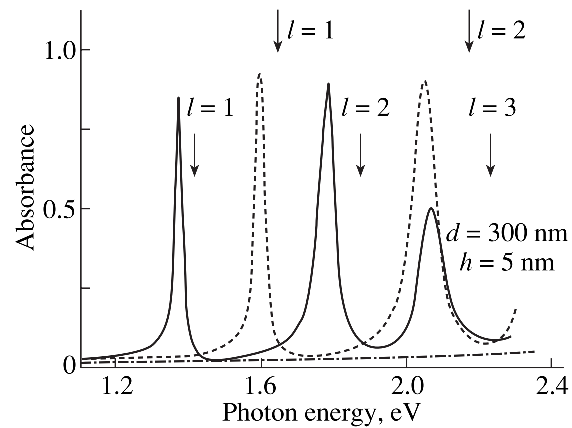

Fig. 3. Absorption spectra of light incident normally onto a silver surface with spherical inclusions of a material with dielectric constant $\varepsilon = 4.5$ (solid curve) and $\varepsilon = 3.3$ (dashed curve). The absorption of light on the surface of bulk silver is shown by a dash-dotted curve. Vertical arrows mark the energies of the fundamental ($l = 1$), second ($l = 2$), and third ($l = 3$) plasmon modes of a single void in bulk silver.

ACKNOWLEDGMENTS

We thank S.V. Gaponenko, V.G. Golubev, and S.G. Tikhodeev for inspiring conversations. Helpful discussions with A.N. Ponyavina and O. Stenzel are gratefully appreciated.

This work was supported by the Russian Foundation for Basic Research (grant no. 02-02-81031) and the Russian Academy of Sciences program "Low-Dimensional Quantum Nanostructures." T.V.T. acknowledges the support from the President of Russia through the grant for young scientists, MK-2314.2003.02, and from the National Foundation for the Promotion of Science. F.J.G.A. acknowledges help and support from the University of the Basque Country UPV/EHU (contract no. 00206.215-13639/2001) and the Spanish Ministerio de Ciencia y Tecnología (contract no. MAT2001-0946).

REFERENCES

1. T. Klar, M. Perner, S. Grosse, G. von Plessen, W. Spirkl, and J. Feldmann, Phys. Rev. Lett. **80**, 4249 (1998).
2. B. Lamprecht, J. R. Krenn, A. Leitner, and F. R. Aussenegg, Phys. Rev. Lett. **83**, 4421 (1999).
3. S. Coyle, M. C. Netti, J. J. Baumberg, M. A. Ghanem, P. R. Birkin, P. N. Bartlett, and D. M. Whittaker, Phys. Rev. Lett. **87**, 176801 (2001).
4. E. Prodan, P. Nordlander, and N. J. Halas, Chem. Phys. Lett. **368**, 94 (2003).
5. E. Prodan, C. Radloff, N. J. Halas, and P. Nordlander, Science **302**, 419 (2003).
6. T. V. Teperik, V. V. Popov, and F. J. García de Abajo, Phys. Rev. B **69**, 155402 (2004).
7. N. Stefanou, V. Yannopapas, and A. Modinos, Comput. Phys. Commun. **113**, 49 (1998); **132**, 189 (2000).
8. J. D. Jackson, *Classical Electrodynamics*, 2nd ed. (Wiley, New York, 1975; Inostrannaya Literatura, Moscow, 1965).
9. C. F. Bohren and D. R. Huffman, *Absorption and Scattering of Light by Small Particles* (Wiley, New York, 1998; Mir, Moscow, 1986).
10. F. J. García de Abajo, Phys. Rev. B **60**, 6086 (1999).
11. P. B. Johnson and R. W. Christy, Phys. Rev. B **6**, 4370 (1972).

Physics of the Solid State, Vol. 47, No. 1, 2005, pp. 18–21. Translated from Fizika Tverdogo Tela, Vol. 47, No. 1, 2005, pp. 22–25.
Original Russian Text Copyright © 2005 by Ezhevskiĭ, Lebedev, Morozov.

PROCEEDINGS OF THE CONFERENCE "NANOPHOTONICS 2004"
(Nizhni Novgorod, Russia, May 2–6, 2004)

Photoluminescence of Nanocrystalline Silicon Formed by Rare-Gas Ion Implantation

A. A. Ezhevskiĭ, M. Yu. Lebedev, and S. V. Morozov

Nizhni Novgorod State University, pr. Gagarina 23, Nizhni Novgorod, 603950 Russia

e-mail: ezhevski@phys.unn.ru

Abstract—A new method is suggested for fabricating nanocrystalline silicon by using high-dose ($D \gg D_a$) irradiation with rare-gas ions. In this case, a nanostructure is formed due to silicon self-assembling on the interface between amorphous layer and crystalline substrate. Two bands, at 720 and 930 nm, are found in the photoluminescence spectrum. These bands possibly originate from the quantum confinement effects in nanocrystals and may also be related to the regions of disordered silicon outside the amorphous layer containing nanocrystals. The intensity of the photoluminescence signal is studied as a function of duration of HF etching of samples and their subsequent exposure to atmosphere. The influence of thermal annealing on the photoluminescence spectrum is also studied. © *2005 Pleiades Publishing, Inc.*

1. INTRODUCTION

Silicon, the most abundant element in the earth's crust, has played an exceptional role in the development of the semiconductor industry. However, a new phase in the evolution of information technologies has recently posed a serious challenge to its dominance. Requirements for increasing speed in integrated circuits, advances in fiber-optic communication networks, and other factors have put optoelectronics forward as a substitute for traditional microelectronics. Indeed, increasing operational speeds can only be accomplished by replacing electrical links between active elements with optic ones. The development of fiber optics also demands designing new light-emitting and photoelectronic devices. Meanwhile, silicon, which is an indirect band gap semiconductor, has quite poor light-emitting properties. Hopes for it to keep its leading position have led to the expansion of both fundamental and applied research into silicon-related topics.

Recently, there has been a huge number of studies on the luminescence of silicon nanostructures. Most of them consider inclusions of silicon nanocrystallites (NCs) in a matrix of a wider band gap material, which, due to its large barrier, provides strong quantum confinement for electrons and holes motion. However, it is well known that intense luminescence at room temperature is also observed in amorphous–nanocrystalline compositions with much weaker confinement. In this case, luminescence bands are displaced significantly upward in energy. This type of composition can be produced, for example, by annealing either deposited hydrogenated amorphous silicon layers [1] or silicon layers made amorphous by ion beams with doses slightly less than the total amorphization dose [2].

In the present paper, we study the possible formation of nanocrystalline silicon by high-dose ($D \gg D_a$) irradiation with rare-gas ions. In this case, due to further modification of the amorphous layer by the appearance of inclusions of rare-gas atoms in the form of bubbles and blisters, nanostructure formation proceeds in several ways: by silicon self-assembling on the interface between the amorphous layer and the crystalline substrate, by a growth of silicon nanocrystallites from the interface towards the surface, and as a result of defect proliferation over the boundary.

2. EXPERIMENT

Samples of Si (111) with a resistivity of 2000 Ω cm were used as a raw material. Wafers were subjected to standard mechanochemical treatment, and a disrupted layer of about 20 μm was subsequently etched off. Samples were irradiated by Ne^+ ions using energies of 40 and 150 keV and doses of 6×10^{15}–6×10^{17} cm^{-2}. The ion current density never exceeded 5 μA/cm^2. Photoluminescence (PL) was measured at room temperature and at 77 K using argon laser excitation (λ = 488 nm). PL spectra were processed by frequency filtering. EPR was studied at liquid-nitrogen temperature using an RÉ-1306 spectrometer. In order to determine the concentration of centers with a g factor of 2.0055, differential curves were integrated twice. A Mn^{2+} : MgO standard was used to obtain a common scale. Samples were etched in a 40% HF solution. Surface topography was studied by means of a TopoMetrix TMX-2100 Accurex scanning probe microscope in the contacting operation mode (ACM) with silicon nitride probes. The

crystal structure was determined by reflection electron diffraction using an ÉRM-103 apparatus.

3. EXPERIMENTAL RESULTS AND DISCUSSION

High-dose irradiation ($D \gg D_a$) causes further reconstruction of a completely amorphous layer. The thickness of this layer can be estimated as $\Delta R = R_p + \Delta R_p + L_s$, where ΔR_p is the straggling length and L_s is the swelling. The swelling becomes comparable to R_p and ΔR_p when doses exceed D_a by an order of magnitude. For example, this quantity is between 10 and 100 nm for silicon irradiated by neon ions with an energy of 40 keV and doses of 6×10^{16}–6×10^{17} cm^{-2} [3]. The swelling is mainly related to the formation of neon bubbles and blisters in the irradiated layer. Sputtering of the silicon surface under neon irradiation may be neglected, because the thickness of the sputtered layer does not exceed 5–7 nm. It is clear that the formation of nanocrystalline silicon under high-dose irradiation cannot be related to the residual crystalline islands anywhere but in the transitional region between the amorphous layer and the single crystal. Possible reasons for the formation of the nanostructure are recrystallization of the amorphous regions in the vicinity of the interface between the amorphous layer and the single-crystal substrate and restructurization of the single crystal due to the propagation of defects and elastic stresses through the boundary of the amorphous layer into the depth of the crystal.

In order to study the internal structure of the layer and the nature of the radiating centers, we removed layers by etching irradiated silicon in HF. As is well known, HF reacts with SiO_2 and does not react with single-crystal silicon. However, the silicon surface damaged by ion bombardment can be etched by HF [4]. Highly selective action of HF (depending on the imperfection of the layer) causes the development of a nanoscale relief on the silicon surface, which is related to the nanocrystalline structure. The existence of such a structure is confirmed by the pyramid-shaped protuberances in the topograms (Fig. 1). Unfortunately, the probe radius was large in comparison with the lateral sizes of pyramids, which made it impossible to observe the actual shape of the NCs, because their shape is convoluted with the shape of the probe. These data are evidence of complex processes of recrystallization and self-assembling due to a nonuniform distribution of defects (rare-gas atoms, broken silicon bonds, self-interstitials) and elastic stresses originating from them.

PL spectra of such layers were found to contain two bands both at liquid-nitrogen and room temperature (Fig. 2). We tried to establish how the PL intensity varies as a result of HF etching. The data obtained are shown in Fig. 3. It turned out that the PL spectra depended on whether they were taken immediately

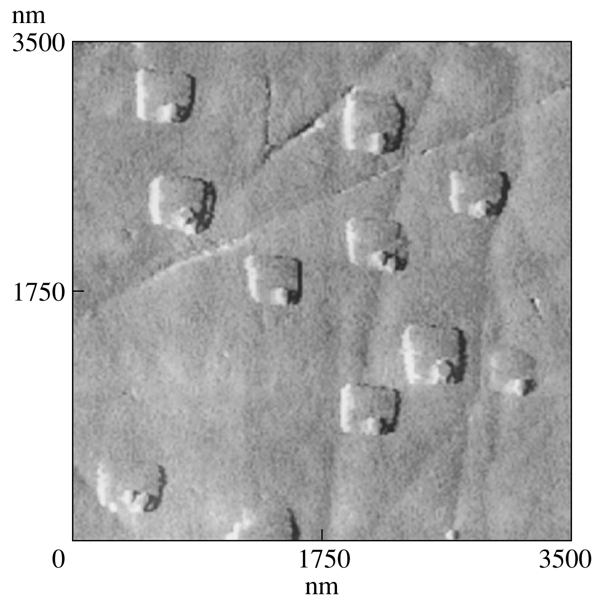

Fig. 1. Topogram of the surface of a Si sample irradiated by Ne^+ ions (40 keV) to a dose of 6×10^{16} cm^{-2} taken after processing with HF. The thickness of the etched-off layer is 150 nm.

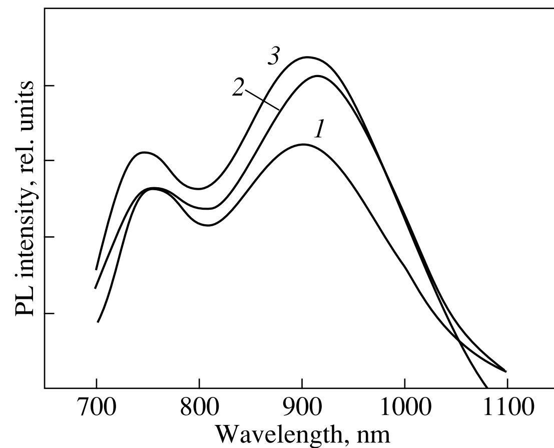

Fig. 2. PL spectra of Si samples irradiated with Ne^+ ions (40 keV) to doses of (*1*) 6×10^{16}, (*2*) 2×10^{17}, and (*3*) 6×10^{17} cm^{-2}.

after processing with HF or after long (several days) storage in air.

We measured PL spectra on the same sample immediately after 12-min etching, then after 50-min storage in air, and then after storage for several days. The PL spectra are shown in Fig. 4. It seems natural to assume that, as was the case in [5], storage leads to oxygenation of the layer, the formation of Si–O double bonds at the boundaries of NCs, and a growth in the intensity of the 720-nm transition, which, according to [6], corre-

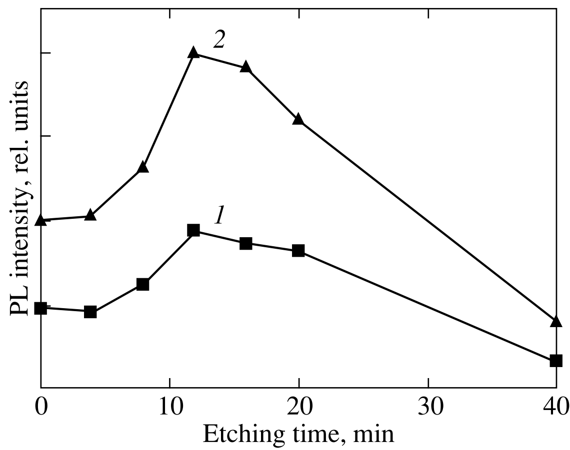

Fig. 3. PL peak intensities at (*1*) 720 and (*2*) 930 nm as a function of etching duration for Si samples irradiated by Ne^+ ions (40 keV) to a dose of 6×10^{16} cm^{-2}.

sponds to excitons localized on Si–O bonds. However, analysis of the PL spectra in Fig. 4 shows that the variation in the 720-nm band is smaller than that of the long-wavelength band. A study of PL spectra taken after long-term storage of samples as a function of the etching duration (Fig. 3) shows that the intensities of both bands increase after removal of the surface layer that is rich in neon and contains most of the broken bonds. The behaviors of the bands are correlated, which indicates that the two types of PL centers should be spatially linked. After 40-min HF etching, the amorphous layer is certainly removed (a layer about 450-nm thick is etched away, and there is no longer an EPR signal) but both PL bands are still observed. Hence, it is NCs formed due to the propagation of elastic stresses and defects beyond ΔR that are the PL centers in this case. As a result, reconstruction of the single-crystal lattice occurs and nanostructures form outside the above-mentioned boundary. The boundaries between crystallites apparently have a strongly imperfect structure and a wide spectrum of localized states in the band gap, since the PL bands are wide, especially in the long-wavelength range of the spectrum.

The development of both NCs and polycrystalline grains in the layer that was previously amorphous is due to crystallization of the amorphous layer. The remaining amorphous phase simultaneously provides quantum confinement and produces PL at about 900 nm. This PL band can be associated with interfacial states of NCs. The PL intensity in this case depends on the structure of the NC boundaries and adjoining external regions. The oxygen penetrating into the surface layers during prolonged storage in air plays an important role. Saturation of interfacial regions with oxygen enhances energy barriers at the NC boundaries and possibly reduces the nonradiative recombination rate, which leads to an increase in the PL intensity. In this case, the boundaries between NCs are not ordered dislocation boundaries; they are strongly disordered and close to *a*-Si or SiO_x in structure.

A sample irradiated to a dose of 6×10^{16} cm^{-2} was subjected to a series of annealings at temperatures in the range 100–800°C. As seen in Fig. 5, the variations in the intensities of both bands are correlated. After annealing at 600°C, the intensities of both bands pass through a maximum. EPR studies show that, at this temperature, reverse annealing takes place, which was previously observed in [7]. In the same temperature range, the highest yield of neon from a sample was observed in [8] and the most intense destruction of blisters took place, causing significant changes in the layer structure. As is well known, for samples irradiated to doses of the order of the amorphization dose, thermal annealing at a temperature of above 450°C leads to

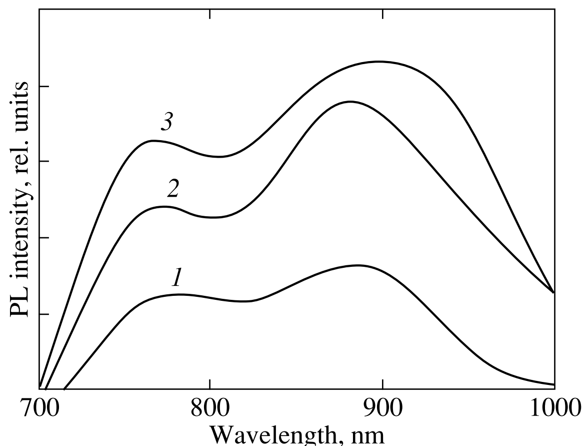

Fig. 4. PL spectra of a Si sample irradiated by Ne^+ ions (40 keV) to a dose of 6×10^{16} cm^{-2} and etched by HF for 12 min taken (*1*) immediately after the etching, (*2*) after 50-min storage in air, and (*3*) after 7 days of storage in air.

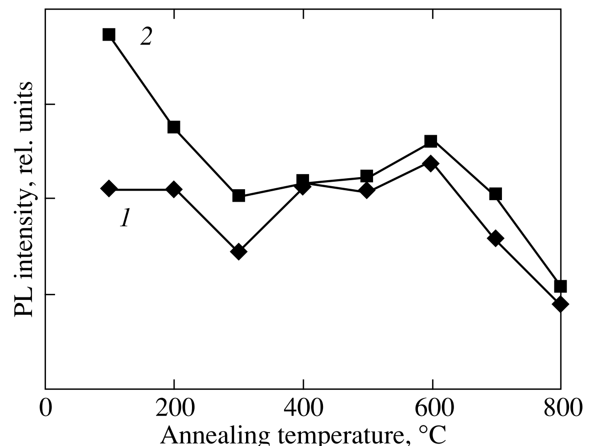

Fig. 5. PL peak intensities at (*1*) 720 and (*2*) 930 nm as a function of annealing temperature for a Si sample irradiated to a dose of 6×10^{16} cm^{-2}.

recrystallization of the damaged layer and to recovery of the single-crystal structure. However, for samples irradiated to a dose that is several orders of magnitude higher than the amorphization dose, the recovery of the single-crystal structure is incomplete, as shown by the reverse annealing phenomena. Probably, the layers modified by an ion beam still have damaged regions containing a large number of defects. These regions can contain NCs, which contribute to the increased PL signal.

4. CONCLUSIONS

Photoluminescence has been observed in the red and near infrared regions after ion bombardment of the silicon surface. The PL spectra are characterized by two bands, one at ~720 and one at ~930 nm. The spectra have been explained in terms of NCs surrounded by amorphous or strongly disordered regions whose structure and composition are similar to those of either *a*-Si or SiO_x. A study of PL spectra during successive etching of samples by HF has shown that the behaviors of the two bands are correlated, which means that the two types of PL centers are spatially linked. It has been demonstrated that the PL varies with the degree of sample oxygenation and the temperature of annealing performed after irradiation.

ACKNOWLEDGMENTS

The authors are grateful to V.K. Vasil'ev for performing the neon ion implantation into samples.

This work was supported by the program "Basic Research and Higher Education in Russia" (BRHE), the US Civilian Research and Development Fund (CRDF), the Ministry of Education of the Russian Federation (project no. REC-001), and the Russian Foundation for Basic Research (project no. 04-02-16493).

REFERENCES

1. V. G. Golubev, A. V. Medvedev, and A. B. Pevtsov, Fiz. Tverd. Tela (St. Petersburg) **41** (1), 153 (1999) [Phys. Solid State **41**, 137 (1999)].
2. D. I. Tetelbaum, S. A. Trushin, Z. F. Krasil'nik, D. M. Gaponova, and A. N. Mikhaylov, Opt. Mater. **17** (1–2), 57 (2001).
3. A. A. Ezhevskiĭ, A. F. Khokhlov, G. A. Maksimov, D. O. Filatov, and M. Yu. Lebedev, Vestn. Nizhegorod. Univ. im. N. I. Lobachevskogo, Fiz. Tverd. Tela **1** (3), 221 (2000).
4. A. A. Ezhevskiĭ, A. F. Khokhlov, G. A. Maksimov, D. O. Filatov, M. Yu. Lebedev, R. V. Kudryavtseva, and E. A. Pitirimova, Vestn. Nizhegorod. Univ. im. N. I. Lobachevskogo, Fiz. Tverd. Tela **1** (4), 124 (2001).
5. M. V. Wolkin, J. Jorne, P. M. Fauchet, G. Allan, and C. Delerue, Phys. Rev. Lett. **82** (1), 197 (1999).
6. Tsutomu Shimizu-Iwayamaa, Norihiro Kurumado, D. E. Hole, and P. D. Townsend, J. Appl. Phys. **83** (11), 6018 (1998).
7. A. V. Dvurechenskiĭ and I. A. Ryazantsev, Fiz. Tekh. Poluprovodn. (Leningrad) **12** (9), 1451 (1978) [Sov. Phys. Semicond. **12**, 860 (1978)].
8. A. F. Khokhlov, A. A. Ezhevskiĭ, A. I. Mashin, and D. A. Khokhlov, Fiz. Tekh. Poluprovodn. (St. Petersburg) **29**, 2113 (1995) [Semiconductors **29**, 1101 (1995)].

Translated by G. Tsydynzhapov

Physics of the Solid State, Vol. 47, No. 1, 2005, pp. 183–190. Translated from Fizika Tverdogo Tela, Vol. 47, No. 1, 2005, pp. 176–183.
Original Russian Text Copyright © 2005 by Balashova, Lemanov, Pankova.

Acoustic Properties of Glycine Phosphite Crystals with an Admixture of Glycine Phosphate

E. V. Balashova*, V. V. Lemanov*, and G. A. Pankova**

**Ioffe Physicotechnical Institute, Russian Academy of Sciences, Politekhnicheskaya ul. 26, St. Petersburg, 194021 Russia*
e-mail: Balashova@mail.ioffe.ru

***Institute of Macromolecular Compounds, Russian Academy of Sciences, Bol'shoĭ pr. 31, St. Petersburg, 199034 Russia*

Received May 25, 2004

Abstract—Acoustic and dielectric anomalies in the region of the ferroelectric phase transition in crystals of glycine phosphite (GPI) with a 2 mol % admixture of glycine phosphate (GP) are studied. The acoustic anomalies were found to differ strongly from those observed in nominally pure glycine phosphite crystals. A theoretical analysis of the acoustic and dielectric properties of the crystals was carried out within the model of a pseudoproper ferroelectric phase transition. It is shown that the acoustic anomalies, as well as the temperature dependences of the dielectric constant (for various external electric fields) and pyroelectric current observed in the vicinity of the phase transition in GPI–GP crystals, can be adequately described when the macroscopic polarization present in these crystals above the phase transition temperature is taken into account. The thermodynamic-potential parameters describing electrostriction and the biquadratic relation between the polarization and strain turned out to be close to those characterizing a nominally pure GPI crystal. An irreversible phase transition was observed to occur in GPI–GP crystals at $T = 240$ K, i.e., above the ferroelectric phase transition temperature. © *2005 Pleiades Publishing, Inc.*

1. INTRODUCTION

A large family of new crystals containing the aminoacid betaine and inorganic acids in a 1 : 1 ratio have been synthesized in recent years. These crystals revealed ferroelectric, antiferroelectric, and ferroelastic phase transitions, as well as transitions to incommensurate phases and glasslike states [1, 2]. Growth was reported of antiferroelectric crystals of betaine phosphate $(CH_3)_3NCH_2COO \cdot H_3PO_4$ (BP), ferroelectric crystals of betaine phosphite $(CH_3)_3NCH_2COO \cdot H_3PO_3$ (BPI), and crystals of BPI–BP solid solutions throughout the concentration range of the inorganic acids [1, 2]. The physical properties of these crystals and related solid solutions are described in [1–4].

A ferroelectric phase transition has recently been detected in crystals of glycine phosphite (GPI), $NH_3CH_2COO \cdot H_3PO_3$, which contains the glycine aminoacid $N^+H_3CH_2COO^-$ and phosphoric acid H_3PO_3 in 1 : 1 proportion [5]. At room temperature, these crystals have monoclinic symmetry $P2_1/a$ and a unit cell including four formula units [6]. At $T_c \cong 224$ K, they undergo a phase transition to the ferroelectric state with spontaneous polarization $\mathbf{P}_s$ oriented parallel to the twofold axis [5].

Nominally pure crystals of glycine phosphate (GP), $NH_3CH_2COO \cdot H_3PO_4$, which are actually a compound of the glycine aminoacid with phosphoric acid H_3PO_4 in a 1 : 1 ratio, have the same point group symmetry at room temperature as the glycine phosphite, but they do not reveal any phase transitions or the piezoelectric effect within the temperature region 120–294 K [7]. These crystals exhibit a low dielectric constant, $\varepsilon \sim 6$–9, in all crystallographic directions.

Preparation of glycine phosphite–phosphate (GPI–GP) solid solutions revealed that phosphoric acid enters the crystal composition in substantially smaller amounts than in solution [7]. These crystals were found to exhibit a pyroelectric response even at room temperature, which indicates the existence of the macroscopic polarization $\mathbf{P}_{int}$ in them. The polarization $\mathbf{P}_{int}$ is opposite in direction to the spontaneous polarization $\mathbf{P}$, which appears in these crystals at the ferroelectric phase transition. The presence of an impurity-induced macroscopic polarization in GPI–GP crystals is also corroborated by studies of the dielectric and piezoelectric properties of these crystals [7].

The ferroelectric phase transition in nominally pure glycine phosphite crystals is accompanied by an abrupt drop (by about 2%) in the velocities of longitudinal acoustic waves propagating both along the $X \parallel a$ and $Z \parallel c^*$ crystallographic axes and along the axis of spontaneous polarization $Y \parallel b \parallel C_2$ [8, 9]. Note that striction acoustic anomalies along the axis of spontaneous polarization in ferroelectrics are usually suppressed by long-range dipole–dipole interaction [10]. Quantitative estimation of the effect that long-range forces exert on the velocity anomalies [9] showed the acoustic anomalies along the polar axis in GPI to be only partially suppressed by the dipole–dipole interaction because of the relatively small Curie–Weiss constant (200–400 K) for

1063-7834/05/4701-0183$26.00 © 2005 Pleiades Publishing, Inc.

Table 1. Longitudinal-wave velocities and temperature coefficients of the room-temperature velocity measured in three crystallographic directions (*Y*, *X*, *Z*) for the GPI, GPI–GP, and GP crystals

Crystal	Velocity, 10^3 m/s			Temperature coefficient of velocity, 10^{-4} K^{-1}		
	Y	*X*	*Z*	*Y*	*X*	*Z*
GPI	5.3	4.0	3.7	–1.61	–2.77	–2.15
GPI–GP	5.6	3.9	3.7	–1.98	–2.91	–1.09
GP	3.63	5.04	5.14	–3.78		

a comparatively large electrostriction component d_{2222}, which determines the striction anomaly along the polar axis [9]. The presence of the polarization $\mathbf{P}_{int}$ in GPI–GP crystals within a broad temperature region, including temperatures above the phase transition point, may give rise to substantial changes in the acoustic anomalies at the phase transition as a result of a change in the order parameter describing the equilibrium state of the crystal. Acoustic studies also make it possible to determine the changes in the elastic moduli of the crystal and the relation between the strain and polarization originating from the presence of the impurity.

To study the effect of the glycine phosphate impurity in glycine phosphite crystals on the ferroelectric phase transition, we measured the temperature dependence of the velocities of longitudinal acoustic waves propagating along the three crystallographic axes, *X*, *Y*, and *Z*, in GPI–GP crystals, as well as in nominally pure GP and GPI crystals. We carried out a quantitative description of the acoustic anomalies in the vicinity of the ferroelectric phase transition in GPI–GP crystals in terms of a thermodynamic model including the macroscopic polarization, as well as the long-range dipole–dipole interaction for longitudinal waves moving along the *Y* polar axis. The results obtained for glycine phosphite crystals with an admixture of glycine phosphate are compared with data available on nominally pure glycine phosphite crystals.

2. CRYSTAL GROWTH AND MEASUREMENT TECHNIQUE

Single crystals of glycine phosphite with an admixture of glycine phosphate were grown from saturated aqueous solutions containing glycine and inorganic acids in a 1 : 1 ratio. The ratio of the H_3PO_3 to H_3PO_4 acids in aqueous solution was 75 : 25. Glycine phosphate single crystals were grown from a saturated solution containing glycine and H_3PO_4 in a 1 : 1 ratio. Crystals were grown by slow cooling from 25 to 8°C at a rate of 1°C/day. Earlier estimates [7] based on x-ray diffraction measurements suggested that the concentration of glycine phosphate in the grown GPI–GP crystals did not exceed 0.1–0.5 mol %. Here, we report the results of a chemical analysis of a GPI–GP solution in water. The H_3PO_4 concentration in the solution was found by weighing a residue precipitated in the form of double magnesium–ammonium phosphate. The analysis revealed that the molar concentration of glycine phosphate in the GPI–GP crystals is approximately 2%.

Acoustic measurements were performed on samples about 6 × 8 × 3.5 mm (GPI–GP) and 9 × 9 × 9 mm (GP) in size along the *X*, *Y*, and *Z* axes, respectively, where $X \parallel a$, $Y \parallel b$, and $Z \parallel (ab)$. Acoustic waves were excited by lithium niobate piezoelectric transducers at a fundamental frequency of 15 MHz. Relative velocity measurements were performed by the pulse superposition method (Papadakis method) with a sensitivity of about 10^{-4}. The absolute measurements of velocity were accurate to ~2–3%.

Dielectric measurements along the *X*, *Y*, and *Z* axes were carried out on GP samples 1-mm thick. The GPI–GP crystal on which acoustic measurements were carried out was also used to perform dielectric studies along the *Z* axis. The dielectric constant and $\tan\delta$ were measured at frequencies of 100 Hz and 1 kHz with an E7-15 immitance meter and at 1 MHz with an LCR E7-12 meter.

3. EXPERIMENTAL RESULTS

Table 1 lists the absolute velocities of longitudinal acoustic waves along three crystallographic directions, *X*, *Y*, and *Z*, of GPI, GPI–GP, and GP crystals, where the *Y* axis is parallel to the twofold axis and the axes *X* and *Z* were chosen as in [5]. Longitudinal waves propagate in different directions in GPI and GPI with a 2 mol % admixture of GP at practically the same velocity. Both in GPI and GPI–GP, acoustic waves moving along the twofold axis have the maximum velocity. By contrast, in GP crystals, the velocity of longitudinal acoustic waves along the twofold axis is the lowest.

Figure 1 shows the temperature-induced variations in the relative longitudinal-wave velocity along the twofold *Y* axis in GP crystals and along the *X* axis in GPI characterized by the largest temperature coefficient of velocity. The velocity of longitudinal acoustic waves in GP crystals is seen to grow linearly with decreasing temperature throughout the temperature interval of 120–300 K and to have no anomalies, whereas GPI crystals exhibit a velocity anomaly in the vicinity of the ferroelectric phase transition at T_c = 224 K. Note that the temperature coefficient of velocity along the twofold axis in GP crystals is substantially larger than that in GPI along the *Y* axis near room temperature (Table 1) and is close in magnitude to that along the *X* axis in the GPI crystal. The dielectric constant of GP crystals, which varies from 6 to 9 for different crystallographic directions, changes only slightly over the above temperature interval.

Figure 2 displays the temperature-induced variations in the dielectric constant ε_{c*} and loss tangent $\tan\delta$

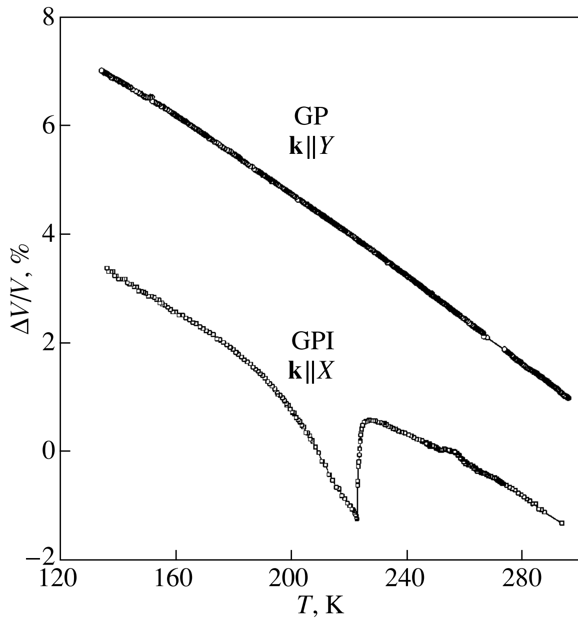

Fig. 1. Temperature dependences of the relative velocity variation of 15-MHz longitudinal acoustic waves propagating along the Y axis in the GP crystal and along the X axis in the GPI crystal.

for GPI–GP crystals during the first cooling and subsequent thermocycles performed in the temperature interval 300–100 K. We see that, during the first cooling (*I*), the dielectric constant and the loss tangent undergo an abrupt increase at frequencies of 100 and 1000 Hz at $T = 240$ K. The dielectric constant and $\tan\delta$ exhibit strong dispersion in the frequency range 100 Hz–1 MHz in this temperature region. After the temperature was increased to $T = 294$ K after the first cooling, the large values of ε_{c*} and $\tan\delta$ persist for several hours. In subsequent thermocycles (*II*), the temperature dependences of ε_{c*} and $\tan\delta$ become similar in character to that of the dielectric constant obtained in the same direction $c*(Z)$ in nominally pure GPI crystals [5] (Fig. 2). The jump in ε_{c*}, the frequency dispersion in the dielectric constant, and the losses practically disappear. Note that acoustic measurements on GPI–GP crystals were performed after they had been used in temperature studies of the dielectric constant and the loss tangent.

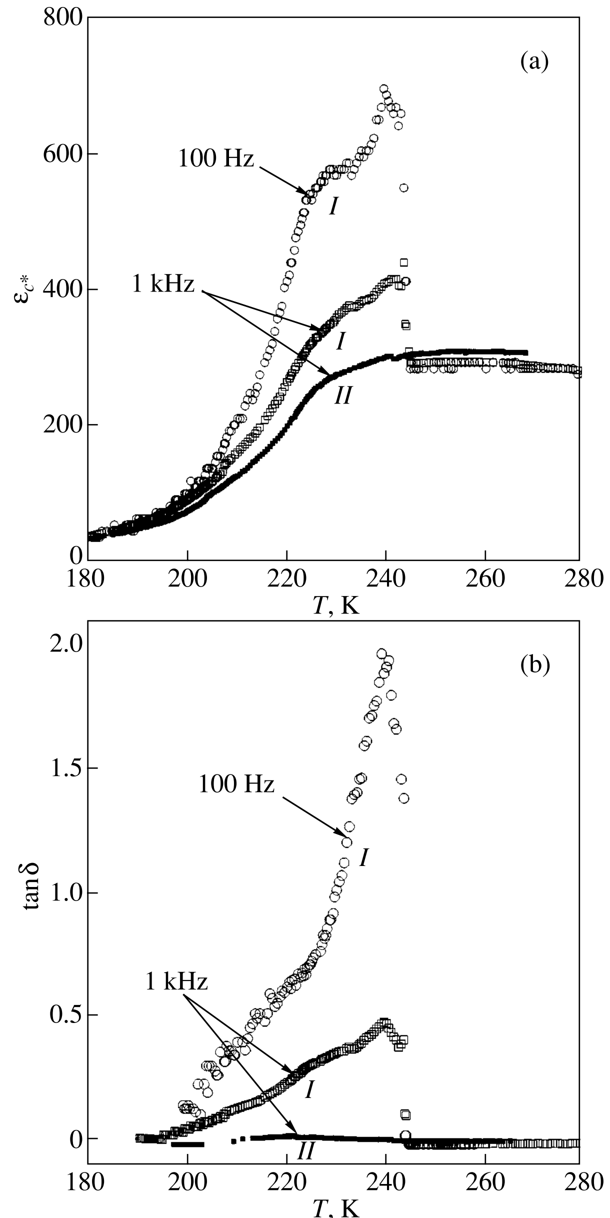

Fig. 2. Temperature dependences of (a) the dielectric constant ε_{c*} and (b) $\tan\delta$ at 100 and 1000 Hz obtained in the first cooling run of the GPI–GP crystal (curves *I*) and in subsequent thermocycles (curves *II*).

Figure 3 illustrates the temperature dependence of the velocity of longitudinal acoustic waves along the X, Y, and Z crystallographic directions in GPI crystals with a 2 mol % admixture of glycine phosphate and in the same directions in pure GPI crystals in the temperature interval, 160–300 K. We readily see that temperature-induced velocity variations in these two crystals are observed only in the region of the ferroelectric phase transition, whose temperature in GPI is $T_c \cong 224$ K. The velocity anomalies observed in different crystallographic directions of glycine phosphite with an admixture of glycine phosphate are smaller in magnitude, do not reveal distinct velocity jumps at the ferroelectric phase transition (unlike those in the glycine phosphite crystals), and instead resemble minima shifted slightly toward lower temperatures as compared to those in glycine phosphite. The temperatures of the minima in the longitudinal-wave velocity depend on the crystallographic direction. The temperature of the minimum is the lowest for longitudinal waves propagating along the twofold Y axis, which coincides with the direction of spontaneous polarization.

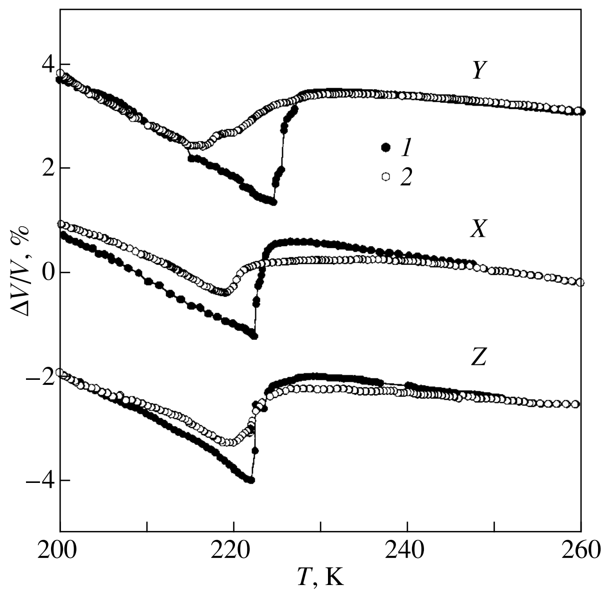

Fig. 3. Temperature dependences of the relative velocity variation of 15-MHz longitudinal acoustic waves propagating along the *Y*, *X*, and *Z* crystallographic axes in (*1*) the GPI and (*2*) GPI–GP crystals.

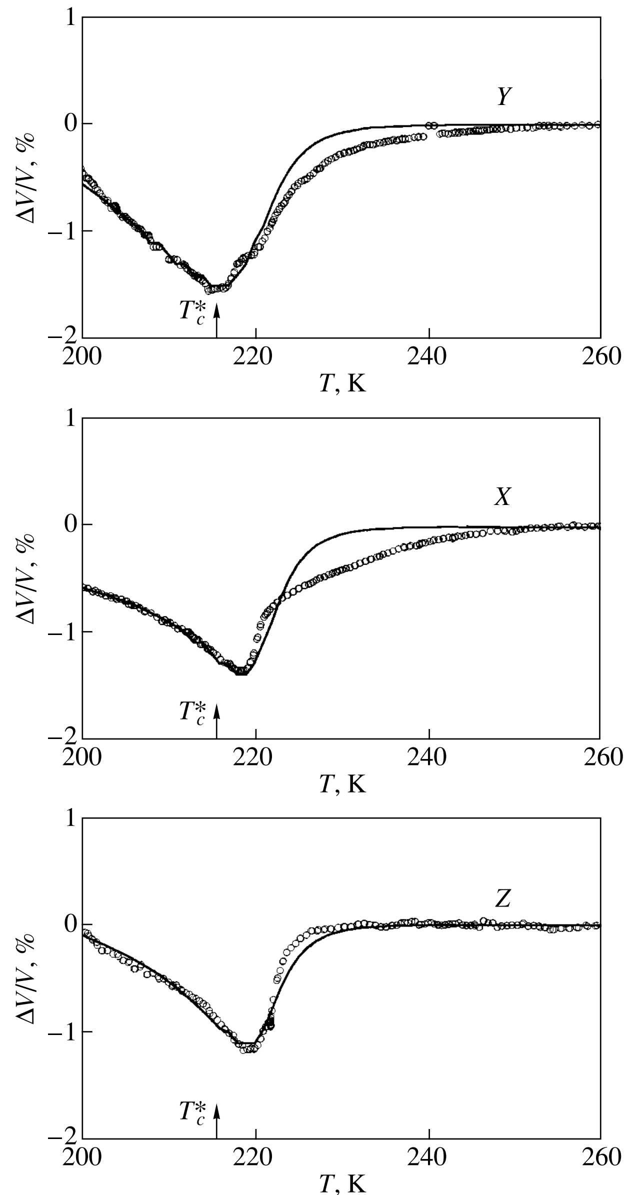

Fig. 4. Velocity anomalies of longitudinal acoustic waves propagating along the *Y*, *X*, and *Z* crystallographic directions in GPI–GP crystals in the vicinity of the ferroelectric phase transition, which were obtained by subtracting the linear velocity contribution extrapolated from the paraelectric phase. Solid lines: calculation with Eqs. (7) and (8) for **k** || *Y* and with Eqs. (6) and (8) for **k** || *X*, *Z*.

Figure 4 illustrates the temperature dependences of the velocity of longitudinal waves moving in crystals of glycine phosphite with an admixture of glycine phosphate along the *X*, *Y*, and *Z* axes in the region of the ferroelectric phase transition, which were obtained by subtracting the linear contribution to the velocity extrapolated from the paraelectric phase.

4. ANALYSIS OF THE EXPERIMENTAL DATA

The inorganic HPO_3 tetrahedra in glycine phosphite crystals form zigzag chains. One molecule of the aminoacid glycine is attached to each tetrahedron [5]. A similar structure with chains of inorganic tetrahedra connected with betaine aminoacid molecules is seen in a number of crystals, more specifically, in betaine phosphate (BP), betaine arsenate (BA), betaine phosphite (BPI), and their deuterated analogs. All these crystals possess monoclinic symmetry with point group $2/m$ (C_{2h}), but with the twofold axis oriented differently relative to the tetrahedron chain; indeed, in BP and BPI, this axis is parallel to the chains formed by the PO_4 and HPO_3 tetrahedra, respectively, and in BA crystals, it is perpendicular to the AsO_4 tetrahedron chains. Nevertheless, the longitudinal acoustic wave velocity in all the above nondeuterated crystals is the lowest along the chain of the inorganic tetrahedra. The elastic rigidity of crystals along the chains is almost the same in all these compounds. The situation is similar in GPI crystals, where, as seen from Table 1, the velocity is the lowest for longitudinal waves propagating along the *Z* axis, i.e., along the chains of HPO_3 tetrahedra arranged nearly parallel to the *Z* axis and perpendicular to the twofold *Y* axis [5]. In contrast to GPI, GP crystals exhibit elastic anisotropy of another kind; namely, the minimum velocity of longitudinal waves in these crystals is observed along the twofold axis. Furthermore, these crystals feature a noticeable difference between the temperature coefficients of velocity along the twofold axes. One may thus conclude that the tetrahedron chains in GP crystals are oriented parallel to the twofold axis (as is the case in the BP and BPI crystals). Therefore, the chains of inorganic tetrahedra in GPI and

GP crystals are differently oriented with respect to the twofold axis.

Note, however, that the difference in structure between the GPI and GP crystals cannot account for these compounds not forming solid solutions throughout the whole component concentration range. Indeed, the BP–BA system, whose components differ in chain orientation relative to the twofold axis, does form solid solutions. The phase diagram of this system drawn versus component concentration is separated into two parts, within one of which the structure of the mixed crystals is of the BA type and in the other, of the BP type [1, 4].

The sharp jump in the dielectric constant and $\tan\delta$ of GPI–GP crystals observed at various frequencies during the first cooling occurs at the same temperature of 240 K, below which the dielectric constant and $\tan\delta$ reveal strong dispersion (Fig. 2). This suggests long polarization relaxation times at this phase transition. The irreversible character of this transition indicates the formation of a metastable state during the crystal growth; in this state, the large glycine molecules that are associated with the impurity complex apparently enter sites corresponding to a relative rather than absolute minimum of energy. As the temperature decreases, the relative minimum becomes energetically unfavorable to the point where the system undergoes an irreversible first-order phase transition to an energetically preferable state, where it remains thereafter.

Studies of the acoustic properties of GPI and GPI + 2 mol % GP crystals reveal that introducing an admixture to glycine phosphite changes the character of the velocity anomalies in the region of the ferroelectric phase transition only. The absolute values of the longitudinal-wave velocity measured in different crystallographic directions and the temperature-induced variations in the velocity above and below the phase transition remain practically the same in both crystals. Admixture of GP to GPI was shown [7] to result in the appearance of a pyroelectric current along the Y axis even at room temperature, which is obviously due to the presence of a macroscopic polarization $\mathbf{P}_{\text{int}} \parallel Y$ in the crystal. It may be assumed that the variations in the acoustic anomalies near the ferroelectric phase transition observed when 2 mol % GP are introduced into GPI originate from the existence of the macroscopic polarization $\mathbf{P}_{\text{int}}$. The crystal symmetry lowers to point group 2 (C_2) in this case.

The acoustic anomalies observed at the ferroelectric phase transition in pure GPI crystals were quantitatively described within the framework of a pseudoproper model of ferroelectric phase transition, which includes long-range dipole–dipole interaction for longitudinal waves propagating along the polar axis [9]. The good agreement between the experimental and theoretical relations suggests that the phase transition occurs practically at the tricritical point and that the electrostriction tensor component d_{2222} (which accounts for the acoustic anomaly along the polar axis) is substantially larger than the other components of this tensor.

To describe the influence the polarization $\mathbf{P}_{\text{int}}$ exerts on the macroscopic crystal properties, we use the model of a pseudoproper ferroelectric phase transition [11] (employed in [9] to account for the properties of GPI crystals) and modify it to include the presence of polarization P_{int}. In this model, the thermodynamic potential is written in the form (here, the tensor notation is dropped)

$$F = \frac{1}{2}\alpha\eta^2 + \frac{1}{4}\beta\eta^4 + \frac{1}{6}\gamma\eta^6 + h\eta(P - P_{\text{int}}) + \frac{1}{2\chi_0}P^2 + d\eta^2 S + \frac{1}{2}c_0 S^2 + g\eta^2 S^2 - PE, \quad (1)$$

where $\alpha = \lambda(T - T_c)$; $\beta > 0$; η is a nonpolar order parameter transforming according to the same irreducible transformation as polarization P; h is the coupling coefficient between the order parameters η and P; χ_0 and c_0 are the background dielectric susceptibility and elastic modulus, respectively; and S is strain.

We reduce thermodynamic potential (1) to a dimensionless form,

$$f = \frac{1}{2}tq^2 + \frac{\beta}{2\beta^*}q^4 + \frac{1}{6}q^6 + \sqrt{\frac{\Delta T_1}{\Delta T}}q^2 s + \sqrt{\frac{\Delta T_1}{G}}q^2 s^2 + \frac{1}{2}\sqrt{\frac{\Delta T_1}{\Delta T}}s^2 + \frac{C_+}{(\varepsilon_\infty - 1)\Delta T}q(p - p_{\text{int}}) + \frac{1}{2}\frac{C_+}{(\varepsilon_\infty - 1)\Delta T}p^2 - \frac{C_+}{(\varepsilon_\infty - 1)\Delta T}pe, \quad (2)$$

where $t = (T - T_c)/\Delta T$ is the reduced temperature, $\Delta T = (\beta^*)^2/4\lambda\gamma$ determines the closeness of the second-order phase transition to the tricritical point, $\beta^* = \beta - 2d^2/c_0 > 0$, $C_+ = 4\pi h^2\chi_0^2/\lambda$ is the Curie–Weiss constant, and $\varepsilon_\infty = 4\pi\chi_0 + 1$ is the background dielectric constant. The parameters $\Delta T_1 = d^4/c_0^2\lambda\gamma$ and $G = c_0^2\gamma/g^2\lambda$ define the striction coupling and the biquadratic (in order parameter and strain) interaction, respectively; $f = F(8\gamma^2/(\beta^*)^3)$, $q^2 = \eta^2(2\gamma/\beta^*)$, $p^2 = P^2(2\gamma/\beta^* h^2\chi_0^2)$, $s = S(2\gamma c_0/\beta^* d)$, and $e = E(\sqrt{2\gamma}/h\sqrt{\beta^*})$.

The equilibrium values of the order parameters q and p are defined by the conditions $\partial f/\partial q = \partial f/\partial p = \partial f/\partial s = 0$ (disregarding the invariant q^2s^2). From here, one obtains the relations

$$p = e - q, \quad s = -q^2 \quad (3)$$

Table 2. Parameters $\Delta T_1 = d^4/c_0^2\lambda\gamma$ and $G = c_0^2\gamma/g^2\lambda$ describing the contributions from striction energy ($d\eta^2S$) and from the energy that is quadratic in order parameter and strain ($g\eta^2S^2$) to the velocity anomalies of longitudinal acoustic waves propagating along the *Y*, *X*, and *Z* axes of the GPI and GPI–GP crystals

Direction	GPI Tricritical point ($\Delta T = 0$)		GPI–GP Second-order phase transition ($\Delta T = 0.01$ K)	
	$\sqrt{\Delta T_1}$, $K^{1/2}$	$\sqrt{G}$, 10^3 $K^{1/2}$	$\sqrt{\Delta T_1}$, $K^{1/2}$	$\sqrt{G}$, 10^3 $K^{1/2}$
Y	0.29	0.27	0.25	0.29
X	0.10	1.10	0.074	2.27
Z	0.12	0.83	0.068	0.71

and the equation of state

$$\left(t - \frac{C_+}{(\varepsilon_\infty - 1)\Delta T}\right)q + 2q^3 + q^5 + \frac{C_+}{(\varepsilon_\infty - 1)\Delta T}(e - p_{\text{int}}) = 0. \tag{4}$$

The relation for the dielectric constant derived from Eqs. (3), as well as the expression for the relative velocity changes induced by the striction coupling of the order parameter to strain (using the equation of Thomas–Slonczewski [12] with due account of the relaxation factor), which is derived from Eqs. (2) and (3), can be cast as

$$\varepsilon = \varepsilon_\infty + \frac{C_+}{(T - T_c^*) + 6\Delta T q^2 + 5\Delta T q^4}, \tag{5}$$

$$\Delta V/V = -\frac{2\sqrt{\Delta T_1 \Delta T}q^2}{(T - T_c^*) + 6\left(\Delta T + \frac{1}{3}\sqrt{\Delta T_1\Delta T}\right)q^2 + 5\Delta T q^4} \times \frac{1}{1 + \omega^2\tau^2}. \tag{6}$$

In the case of longitudinal waves propagating along the *Y* polar axis, Eq. (6) can be transformed to the following form by taking into account the long-range dipole–dipole interaction:

$$\Delta V/V = -\frac{2\sqrt{\Delta T_1 \Delta T}q^2}{(T - T_c^*) + 6\left(\Delta T + \frac{1}{3}\sqrt{\Delta T_1\Delta T}\right)q^2 + 5\Delta T q^4 + \frac{C_+}{\varepsilon_\infty}} \times \frac{1}{1 + \omega^2\tau^2}, \tag{7}$$

where $T_c^* = T_c + C_+/(\varepsilon_\infty - 1)$ is the ferroelectric phase transition temperature, ω is the circular frequency of the acoustic wave, and $\tau = \tau_0/(\partial^2 f/\partial q^2)$.

The static contribution to the temperature-induced velocity variation coming from the biquadratic interaction of the order parameter with strain can be written as

$$\Delta V/V = \sqrt{\frac{\Delta T}{G}}q^2. \tag{8}$$

To describe the temperature-induced variations of the dielectric constant and acoustic wave velocity, we substitute the equilibrium values of the order parameter q obtained numerically from Eq. (4) into Eqs. (5)–(8). Figure 4 plots the temperature dependences of the velocity of longitudinal waves propagating both along the *X* and *Z* crystallographic axes and parallel to the *Y* polar axis; these dependences were calculated from Eqs. (6)–(8). The equilibrium values of the order parameter q were obtained numerically from the equation of state (4) assuming no external bias field ($e = 0$) and a constant polarization p_{int}, which was a fitting parameter. The values of the other parameters, ΔT_1 and G, turned out to be close to those obtained for pure GPI crystals (Table 2). The values of $T_c^* = 215$ K and of the ratio $C_+/\varepsilon_\infty = 20$ K for GPI–GP crystals were determined from the temperature dependences of the dielectric constant measured in the presence of an external electric field compensating for the polarization p_{int} [7]. The experimental curves are fitted well by theoretical relations with these parameters for longitudinal waves propagating both along the *Y* polar axis, where the long-range dipole–dipole interaction was included, and in the *X* and *Z* directions perpendicular to the polar axis. The temperatures of the velocity minima are direction-dependent, because the electrostriction coefficients and the velocity component that is biquadratic in order parameter and strain are anisotropic and because the long-range dipole–dipole interaction is included for longitudinal waves moving along the axis of spontaneous polarization. Above the ferroelectric phase transition point, the calculations made for longitudinal waves propagating along the *X* axis in the range 240–220 K disagree markedly with experiment. The experimental values of the velocity were found to be smaller than the predicted figures. Note that the temperature at which this disagreement is observed coincides with that of the irreversible first-order phase transition.

The values of the parameters ΔT, ΔT_1, and G for the GPI and GPI–GP crystals are listed in Table 2. It is seen that the ferroelectric phase transition in GPI–GP remains very close to the tricritical point and that the ΔT_1 and G parameters are close to those for the pure GPI crystal. The ferroelectric phase transition temperatures ($T_c^* \cong 224$ K in GPI and $\cong 215$ K in GPI–GP) and the dielectric parameters of the crystals, namely, the ratio of the Curie–Weiss constant to the background

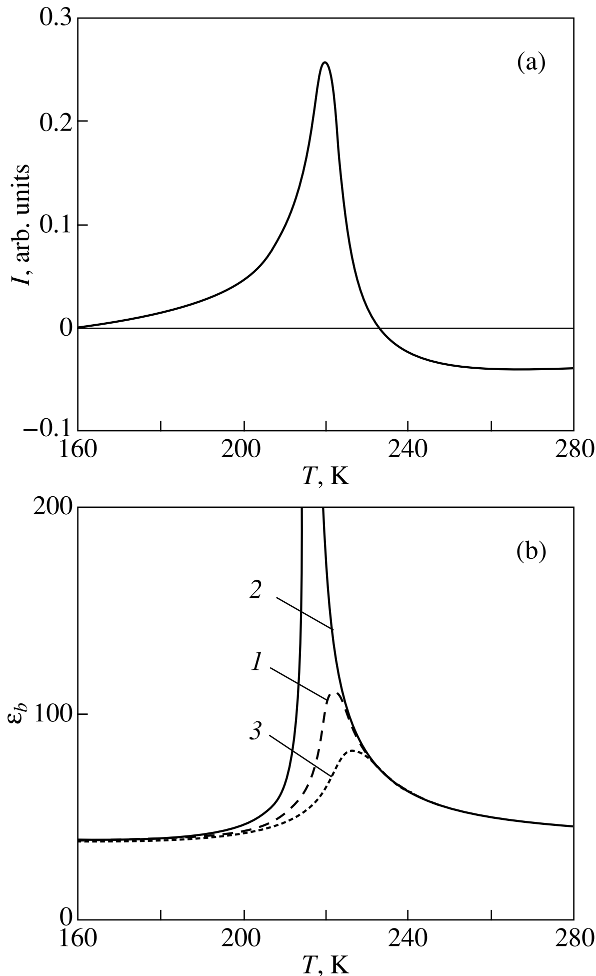

Fig. 5. Temperature dependences (a) of the pyroelectric current $I = \partial(p - p_{int})\partial T$ calculated assuming linear variation of the polarization p_{int} and using the temperature dependences of the equilibrium spontaneous polarization p as derived from Eq. (4) and (b) of the dielectric constant ε_b along the polar axis calculated from Eq. (5) for an external bias field (*1*) $E = 0$, (*2*) $\mathbf{E} \parallel -\mathbf{p}_{int}$, and (*3*) $\mathbf{E} \parallel \mathbf{p}_{int}$.

dielectric constant C_+/ε_∞, are different ($C_+/\varepsilon_\infty = 28$ K for GPI and 20 K for GPI–GP).

The acoustic properties of the crystal were considered above assuming the polarization p_{int} to be constant. The polarization p_{int} is, however, temperature-dependent, which accounts for the appearance of a pyroelectric current [7] even near room temperature; this current grows slightly with decreasing temperature and reverses sign at the onset of spontaneous polarization p near the phase transition. Let us assume that p_{int} varies with decreasing temperature approximately linearly, which corresponds to a constant pyroelectric current under temperature variation for $T > T_c$. As reported in [7], the piezoelectric effect near room temperature is weak compared to that near the phase transition point; therefore, we will assume p_{int} to be zero at room temperature and will find p_{int} in the interval near the phase transition by looking for the best fit of the theoretical curves to experimental temperature dependences of the velocity of longitudinal waves propagating in three crystallographic directions. Analysis shows that the temperature dependence of the velocity calculated under the assumption of constant p_{int} (Fig. 4) practically coincides with the relations obtained assuming a linear growth of p_{int} with decreasing temperature, provided the value of p_{int} at the phase transition point (about 220 K) is approximately equal to that found assuming the polarization p_{int} to be constant. The ratio of the spontaneous polarization p to p_{int} calculated for 160 K assuming a linear dependence of p_{int} on temperature is $p/p_{int} \approx 3$, which agrees with the experimental data quoted in [7].

Figure 5a displays the temperature dependences of the pyroelectric current $I = \partial(p - p_{int})\partial T$ in arbitrary units calculated under the assumption of a linear variation of the polarization p_{int} and by using the calculated temperature dependences of equilibrium spontaneous polarization p. Figure 5b plots the temperature dependences of the dielectric constant ε_b along the polar axis, calculated from Eq. (5) for the cases of both zero external bias and a nonzero bias field compensating for the polarization p_{int} or enhancing it. The theoretical $\partial(p - p_{int})\partial T$ and $\varepsilon_b(T)$ relations are in agreement with the experimental data reported in [7].

4. CONCLUSIONS

Our studies have shown that the acoustic anomalies observed in the GPI–GP crystals can be approximated well in the model of a pseudoproper ferroelectric phase transition if one includes the polarization p_{int}, which brings about broadening of the phase transition and, hence, of the acoustic and dielectric anomalies. Introduction of the impurity manifests itself in a change in the phase transition temperature T_c and in the dielectric parameters of the crystal, namely, the Curie–Weiss constant and the background dielectric constant. The ferroelectric phase transition remains very close to the tricritical point. The parameters describing striction interaction in GPI–GP are close to those observed in nominally pure GPI crystals. The model under consideration, in which the macroscopic polarization p_{int} and its temperature dependence are taken into account, also allows satisfactory description of the temperature dependence of the dielectric constant in an external field and of the pyroelectric response in GPI–GP crystals.

ACKNOWLEDGMENTS

The authors are indebted to Ya.S. Kamentsev for chemical characterization of the samples and to N.V. Zaĭtseva and N.F. Kartenko for x-ray diffraction measurements.

This study was supported by the Russian Foundation for Basic Research (project no. 04-02-17667), the federal program of support for leading scientific schools (NSh-2168.2003.2), and the program of the Department of Physical Sciences of the RAS.

REFERENCES

1. J. Albers, Ferroelectrics **78**, 3 (1988).
2. J. Albers, A. Klöpperpieper, H. J. Rother, and S. Haussühl, Ferroelectrics **81**, 27 (1988).
3. E. V. Balashova, V. V. Lemanov, A. K. Tagantsev, A. B. Sherman, and Sh. H. Shomuradov, Phys. Rev. B **51**, 8747 (1995).
4. S. Lanceros-Méndez, Diploma Thesis (Univ. of Würzburg, Würzburg, 1995).
5. S. Dacko, Z. Czapla, J. Baran, and N. Drozd, Phys. Lett. A **223**, 217 (1996).
6. M.-Th. Averbuch-Pouchot, Acta Crystallogr. C **49**, 85 (1993).
7. V. V. Lemanov, S. G. Shul'man, V. K. Yarmarkin, S. N. Popov, and G. A. Pankova, Fiz. Tverd. Tela (St. Petersburg) **46** (7), 1246 (2004) [Phys. Solid State **46**, 1285 (2004)].
8. J. Furtak, Z. Czapla, and A. V. Kityk, Z. Naturforsch. A **52**, 778 (1997).
9. E. V. Balashova, V. V. Lemanov, and G. A. Pankova, Fiz. Tverd. Tela (St. Petersburg) **43** (7), 1275 (2001) [Phys. Solid State **43**, 1328 (2001)].
10. S. Ya. Geguzina and M. A. Krivoglaz, Fiz. Tverd. Tela (Leningrad) **9** (11), 3095 (1967) [Sov. Phys. Solid State **9**, 2441 (1967)].
11. B. A. Strukov and A. P. Levanyuk, *Ferroelectric Phenomena in Crystals* (Nauka, Moscow, 1995; Springer, Berlin, 1998).
12. J. C. Slonczewski and H. Thomas, Phys. Rev. B **1**, 3599 (1970).

Translated by G. Skrebtsov

Physics of the Solid State, Vol. 47, No. 1, 2005, pp. 191–198. Translated from Fizika Tverdogo Tela, Vol. 47, No. 1, 2005, pp. 184–190.
Original Russian Text Copyright © 2005 by Chistyakov, Stankevich, Korlyukov.

FULLERENES
AND ATOMIC CLUSTERS

A New Allotropic Form of Carbon $[C_{28}]_n$ Based on Fullerene C_{20} and Cubic Cluster C_8 and Si and Ge Analogs of This Form: Computer Simulation

A. L. Chistyakov, I. V. Stankevich, and A. A. Korlyukov

Nesmeyanov Institute of Elementorganic Compounds, Russian Academy of Sciences, ul. Vavilova 28, Moscow, 119991 Russia

Received April 27, 2004

Abstract—The structure of a new allotropic form of carbon $[C_{28}]_n$ having a simple cubic lattice and space group $Pm\bar{3}$ is proposed. The geometrical parameters of the building block of such a hypothetic crystal are preliminarily determined from DFT–PBE calculations of the cluster $C_8@(C_{20})_8$ and the polyhedral hydrocarbon molecule $C_8@(C_{20}H_{13})_8$, in which the centers of the cubic clusters C_8 coincide with the centers of the cluster $C_8@(C_{20})_8$ and of the molecule $C_8@(C_{20}H_{13})_8$, respectively, and dodecahedral C_{20} carbon cages are located at the vertices of a cube. The energy of dissociation of the cluster $C_8@(C_{20})_8$ into a cubic cluster C_8 and eight dodecahedral clusters C_{20} is calculated to be 1482 kcal/mol, and the energy of each C_8–C_{20} bond is equal to 74.2 kcal/mol. The structure of the $[C_{28}]_n$ crystal is refined using the DFT–PBE96/FLAPW method and optimized geometry. Calculations show that the crystal is a dielectric with an energy gap of 3.3 eV. The lattice parameter a of the crystal is equal to 5.6 Å, and its density is 3.0 g/cm^3. The possible existence of analogous allotropic forms of elements Si and Ge is discussed. A method is proposed for designing a hypothetic allotropic form $[C_{28}]_n$ from $C_{20}(CH_3)_8$ molecules with T_h symmetry. © *2005 Pleiades Publishing, Inc.*

1. INTRODUCTION

The possible existence of an infinite number of carbon crystalline modifications was first theoretically grounded in review [1], which generalized earlier works dealing with the construction of new periodic forms of carbon and prediction of their properties [2–7]. According to [1] (see also [8–10]), different forms of carbon can consist of isolated carbon chains, joined carbon chains, polyhedral carbon clusters (fullerenes), fragments of graphite layers rolled into cylindrical structures (tubulenes), etc. These theoretical conclusions have been supported by the experimental synthesis of polyhedral carbon clusters, their polymer forms, tubular graphite forms, etc. [9].

In polymeric forms of fullerenes, monomers are linked by four-membered cycles, which are formed as a result of [2 + 2] cycloaddition along two double bonds of neighboring fullerenes. The C_{60} fullerene has six such bonds, whose centers are located at the vertices of an octahedron. Therefore, C_{60} fullerenes can form quasi-one-dimensional, quasi-two-dimensional, and three-dimensional structures. In particular, structures with a simple cubic lattice can form.

Fullerene C_{20} was synthesized in 2000 [11] by a purely chemical method, but its derivatives $C_{20}H_{20}$ and $C_{20}H_{18}Me_2$—hydrocarbon molecules with a dodecahedral carbon cage [12, 13]—were produced well before the discovery of fullerenes. Like fullerene C_{60}, the dodecahedral C_{20} fullerene formally contains six C–C bonds, whose centers are located at the vertices of an octahedron. In Fig. 1, the atoms involved in these bonds are represented by gray balls. Therefore, like fullerene C_{60}, the C_{20} fullerene can be used to construct quasi-one-dimensional, quasi-two-dimensional, and three-dimensional structures in which two neighboring clusters are linked by four-membered cycles.

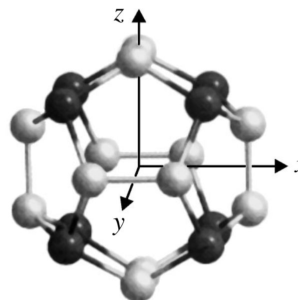

Fig. 1. Fullerene C_{20}: black balls are atoms located at the vertices of a cube; the C–C bonds along which [2 + 2] cycloaddition of the same fullerenes can occur are parallel to the cube faces. The coordinate axes are directed from the cube center through the midpoints of these bonds.

1063-7834/05/4701-0191$26.00 © 2005 Pleiades Publishing, Inc.

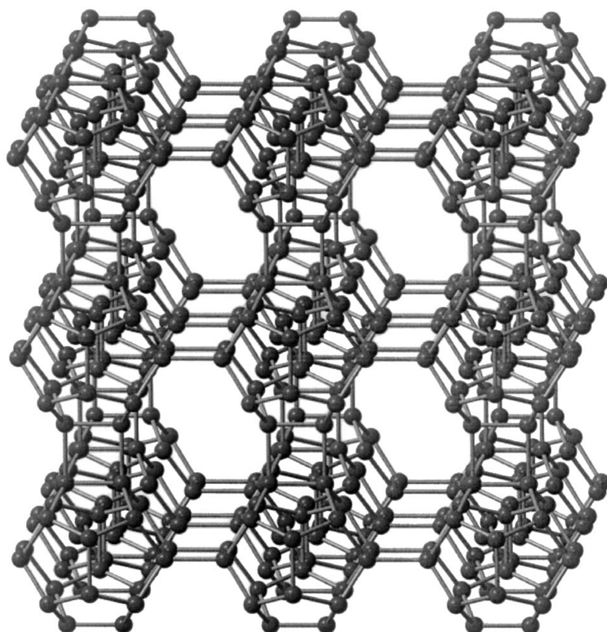

Fig. 2. Hypothetic structure of the $[C_{20}]_n$ crystal (structure **1**).

This method for modeling new forms of carbon having a simple cubic lattice was used in [14, 15]. The authors of [14] constructed two structures $[C_{20}]_n$ with a simple cubic lattice (Fig. 2).[1] Structure **1** was calculated using LDA and incompletely optimized geometry (the lattice parameter was fixed) and contains eight carbon atoms per fullerene with formal sp^2 hybridization in addition to saturated carbon atoms. The former atoms are radical centers located at the vertices of a cube. The second structure was calculated using completely optimized geometry, and it was found that the fullerene bonds involved in the formation of the four-corner cycles that link two neighboring fullerenes are broken. As a result, all the atoms of crystal **1'** turned out to have formal sp^2 hybridization. Therefore, this crystal should have metallic properties. The possible existence of two extra fullerene C_{20}–based crystal structures having denser (orthorhombic and tetragonal) packing was theoretically grounded in [15]. In these structures, only four atoms in each monomer are three-coordinated and the rest of the atoms are four-coordinated. In this work, we disclosed a modification $[C_{28}]_n$ (**2**) of carbon crystalline form **1** consisting of saturated carbon atoms only.

[1] Structure **1'** is not shown in Fig. 2, since the only difference between it and structure **1** is that the bonds in the four-membered cycles belonging to fullerenes are broken. All atoms in structure **1'** have sp^2 hybridization.

2. SIMULATION PROCEDURE

Local energy minima in the potential-energy surfaces of the clusters under study were calculated using completely optimized geometry by the DFT method with a Perdew–Burke–Ernzerhof exchange-correlation potential [16] (DFT–PBE), two-exponent DZ bases, and the PRIRODA computer program [17]. The geometry was optimized using the BFGS algorithm [18]. The total energies of the systems described above were also estimated with inclusion of zero-point nuclear energies. The character of the stationary points found was checked by analyzing the spectrum of the Hessian matrix. Crystal **2** was calculated by the full-potential linear augmented-plane-wave (FLAPW) method [19] using the WIEN2K computer program [20] with complete geometry optimization. Electron-correlation effects were taken into account in terms of the density functional theory (PBE96 functional). The basis set used for the calculations contained 7524 linearized plane waves and nine Gaussian functions; the muffin-tin sphere radius of a carbon atom was 0.72 Å, and the independent portion of the Brillouin zone was approximated using 76 k points.

3. RESULTS AND DISCUSSION

3.1. $[C_{28}]_n$ *Crystal*

A comprehensive analysis of structure **1** showed that this crystal had voids 5.76 Å in diameter, which can accommodate cubic C_8 carbon clusters. Each atom in a C_8 cluster has a covalent bond to one of the eight dodecahedral clusters located at the vertices of a cube, which, combined with one of the C_{20} fullerenes, forms a unit cell of structure **1**. The $[C_{28}]_n$ carbon crystal modification **2** (Fig. 3) consists only of saturated four-coordinated carbon atoms.[2] To estimate the possible existence of carbon crystal modification **2**, we first performed DFT–PBE calculations with complete geometry optimization of the $C_8\underline{@}(C_{20})_8$ cluster (Fig. 4, structure **2a**). This cluster consists of eight dodecahedral C_{20} fullerenes, which are located at the vertices of the cube described above and are linked by the four-membered cycles, and of a cubic cluster C_8 located inside this cube. We introduce the symbol $\underline{@}$ in order to distinguish the designations of the system under analysis from the notation that uses the symbol @ for endohedral fullerene complexes.

Calculations performed for cluster C_8 showed that there is a local minimum corresponding to a cubic structure. The energy of dissociation of cluster **2a** into a cubic cluster C_8 and eight clusters C_{20} is calculated to be 1482 kcal/mol, and the binding energy between a

[2] The proposed new allotropic form is called cubeful20, since it is constructed from cubic fragments C_8 and fullerenes C_{20}.

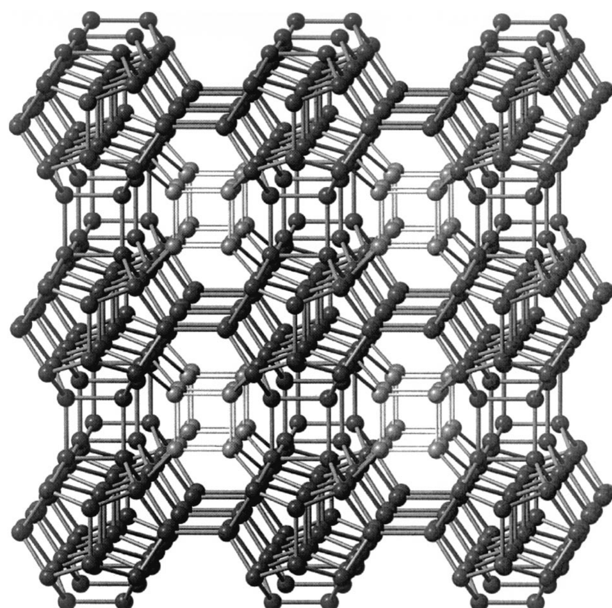

Fig. 3. Structure of $[X_{28}]_n$ crystals (X = C, Si, Ge). The atoms of fragments X_8 are represented by gray balls.

cluster C_8 and a cluster $[C_{20}]_8$ is 593 kcal/mol. Thus, the introduction of cubic cluster C_8 into the void in cluster **1a** is energetically favorable. Each C_{20}–C_8 bond is 1.456-Å long, and its energy is $[E(C_8) + E(\mathbf{1a}) - E(\mathbf{2a})]/8 = 74.2$ kcal/mol (here, $E(X)$ is the energy of particle X). The formation of the C_{20}–C_8 bonds is accompanied by elongation of the bonds in the cube (from 1.482 to 1.533 Å) and of the neighboring bonds in the C_{20} fragment (from 1.508 to 1.572 Å). However, the C_{20} fullerene bonds involved in [2 + 2] cycloaddition shorten from 1.603 to 1.592 Å. The atomization energy per atom of cluster **2a** is equal to 212.4 kcal/mol, which is higher than that in cluster **1a** (210.6 kcal/mol) and in fullerene C_{20} (205.0 kcal/mol) but lower than that in fullerene C_{60} (223.0 kcal/mol). The C–C bond lengths in the four-membered cycles linking two adjacent fullerenes are 1.58 Å (for the bond between atoms of the same fullerene) and 1.59 Å (for the bond between monomers). The C_8–C_{20} bond length between the atoms of the cubic cluster and the corresponding dodecahedron is 1.48 Å.

Since crystal **2** consists only of sp^3-hybridized atoms, we attached hydrogen atoms to unsaturated (three-coordinated) carbon atoms located on the external side of cluster **2a** to form a hydrocarbon molecule $C_8@(C_{20}H_{13})_8$ in order to determine the geometrical

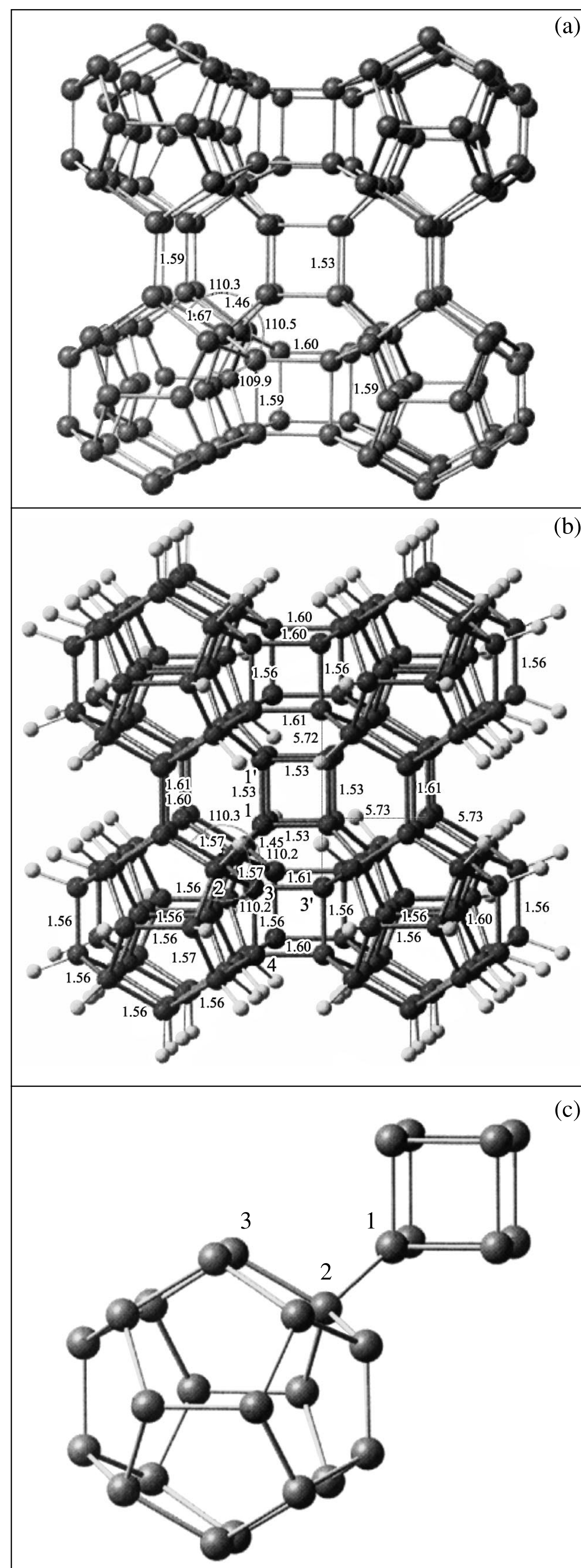

Fig. 4. Hypothetical structures: (a) cluster $C_8@[C_{20}]_8$ (structure **2a**), (b) hydrocarbon molecule $C_8@[C_{20}H_{13}]_8$ (structure **2b**), and (c) building block C_{20}–C_8 of crystal **2** (structure **2c**).

Table 1. Geometrical parameters of crystal **2** calculated by the DFT–PBE96/FLAPW method

Bond lengths in fragment C_{20}: the six (C3–C4) bonds between the monomers are 1.565-Å long; the other 24 (C2–C4) bonds are 1.553-Å long. (C1–C1') bond lengths in fragment C_8: all 12 bonds are 1.596-Å long.	C1–C2=C(C_{20})–C(C_8) = 1.456 Å C3–C3'=C(C_{20})–C(C_{20}) = 1.535 Å $Tx = Ty = Tz = 5.60$ Å

Note: Atom numbering is given in structure **2b** (Fig. 4); Tx, Ty, and Tz are the spatial periods along the corresponding coordinate axes.

parameters of the building block of the crystal lattice more exactly (Fig. 4, structure **2b**). The geometric parameters of this molecule are given in Table 1. It is seen that the C_8–C_{20} bond length is shorter and the C_{20}–C_{20} bond length is longer than the respective lengths in cluster **2a**. Moreover, the length of C3–C4 bonds (Fig. 4) involved in [2 + 2] cycloaddition decreases. The radical $(C_{20}H_{13})_8$ (**1b**) is also stable, and the C_8–C_{20} binding energy in molecule **2b**, which was calculated as $[E(C_8) + E(\mathbf{1b}) - E(\mathbf{2b})]/8$, is equal to 82.1 kcal/mol. The structure of the building block C_{20}–C_8 (**2c**) of crystal **2** is shown in Fig. 4.

In order to estimate the structure of covalent crystal **2** and its electrical properties more accurately, we performed FLAPW calculations with geometry optimization. Analysis of the calculated geometrical parameters of crystal **2** shows that they are close to those given in Table 1. This crystal is cubic ($a = 5.7$ Å) and belongs to space group $Pm\bar{3}$. The total number of atoms in the unit cell is 28, the number of independent atoms is equal to 3 (C1, C2, C3; see Fig. 4, structure **2c**), and the packing density of the crystal is 3.0 g/cm^3. As follows from the calculated density of states (Fig. 5), the electronic spectrum of the crystal has an energy gap of 3.3 eV, which indicates that crystal **2** is an insulator. The high density of states near the valence band top is due to the p electrons of the atoms in a cubic fragment C_8 (Fig. 6).

3.2. Possible Method for Designing the Cubeful20 Structure and Quasi-One- and Quasi-Two-Dimensional Polymers Based on the Derivates $C_{20}(CR_3)_8$ *of Fullerene* C_{20}

A rich variety of derivatives of fullerene C_{20} have been synthesized, among them the η^2 complexes of transition metals [12, 13, 21]. Apparently, $C_{20}(CR_3)_8$-type molecules with T_h symmetry in which methyl groups or their derivatives CR_3 are added to the C_{20} fullerene atoms located at the vertices of the cube (Fig. 1, black balls) can also be synthesized.

We propose a qualitative approach to illustrate one possible way to form and grow quasi-one-dimensional, quasi-two-dimensional, and three-dimensional structures using $C_{20}(CR_3)_8$ molecules. For the sake of simplicity, we consider the case where R = H. It was found that the molecule $C_{20}(CH_3)_8$ is stable and its ground state is a singlet (Fig. 7). The C–C bonds that are parallel to the faces of the cube can be used to form four-membered cycles linking neighboring fullerenes as a result of [2 + 2] cycloaddition reactions. We choose a Cartesian coordinate system with its origin at the cen-

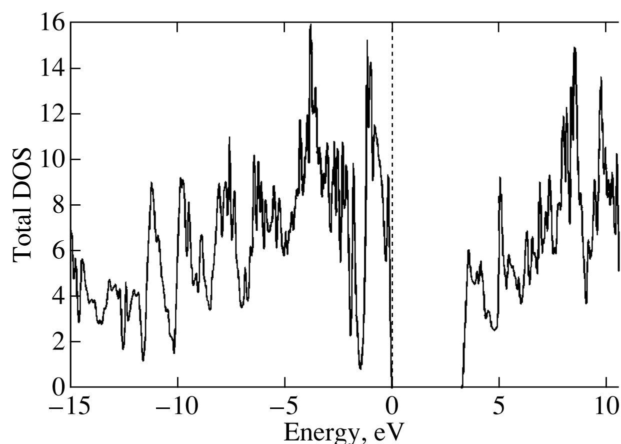

Fig. 5. Total density of states determined by the DFT–PBE96/FLAPW (full-potential linear augmented-plane-wave) method.

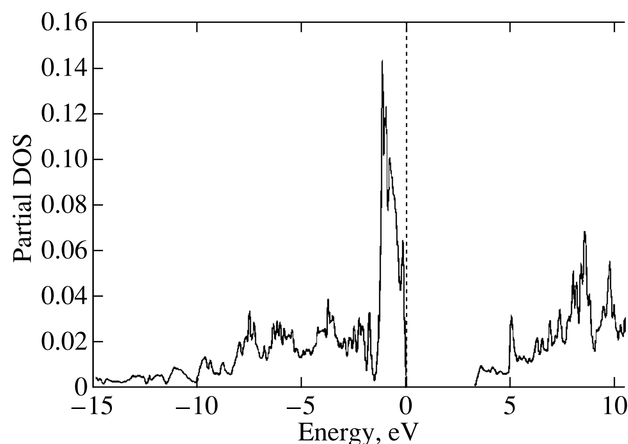

Fig. 6. Partial density of states of p electrons in fragment C_8.

ter of symmetry of the dodecahedron and the coordinate axes passing through the midpoints of these bonds (Fig. 7).

When two molecules **3** approach each other along the x axis and have an appropriate orientation, their interaction can result in cage molecule **4** with D_{2h} symmetry (Fig. 8). The left- and right-hand parts of this molecule are linked by six C–C bonds intersecting the x–y plane. Two of them, C20–C21 and C9–C22, can be interpreted as resulting from [2 + 2] cycloaddition. The other four bonds (C55–C56, C50–C53, C52–C51, C49–C54) result from the interaction of methyl groups. This interaction brings about the formation of four bridging bonds –CH_2–CH_2– or –CH=CH– and the separation of eight and sixteen H radicals, respectively, which can form four or eight H_2 molecules. Hereafter, we assume that only the latter case is realized under certain conditions (high temperature, high pressure, and the presence of a catalyst). The right- and left-hand parts of the lateral surface of molecule **4**, which is approximately parallelepiped-shaped, have the same atomic structure as the left and right parts of the lateral surface of molecule **3**. Therefore, if molecules **3** and **4** approach each other along the x axis and have an appropriate orientation, their interaction can result in a cage molecule $(C_{20})_3(CH_3)_8(C_2H_4)_4$ of D_{2h} symmetry with the symmetry axis coinciding with the x axis. When this interaction occurs, eight H_2 molecules are separated. This procedure of molecule growth along the x axis can continue infinitely. As a result, we have a quasi-one-dimensional periodic $[C_{24}H_4]_n$ structure translationally symmetric along the x axis. The spatial period is estimated to be ≈5.64 Å.

Let us consider other schemes of assembling polymeric molecule **3**–based structures, which make it possible to form either hydrocarbon quasi-two-dimensional periodic structures or crystalline carbon modification **2**.

When two molecules **4** approach each other along the y axis and have an appropriate orientation (in this case, it is convenient to place the origin of coordinates at the center of symmetry of molecule **4**), their interaction can result in a molecule **5** (Fig. 9), which is a derivative of oligomer $(C_{20})_4$ with monomers located at the vertices of a square. In this system, two fragments of molecule **4** are linked by two four-membered cycles, C16–C17–C75–C74 and C32–C34–C91–C89, formed through [2 + 2] cycloaddition and two cyclobutane-type four-membered cycles resulting from the interaction of bridging bonds –CH=CH–. In this case, eight H_2 molecules are separated. Similarly, another molecule **4** can be added to molecule **5**, and so on. The oligomers and polymers thus assembled can serve as a basis for assembling quasi-two-dimensional periodic structures

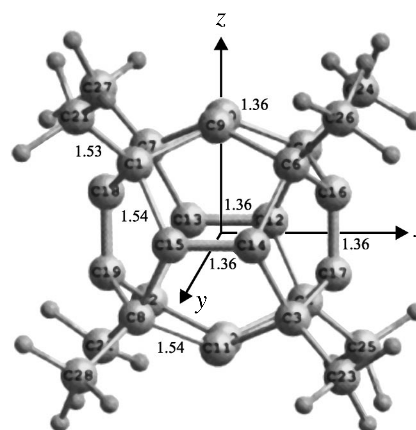

Fig. 7. Structure of molecule **3** with T_h symmetry.

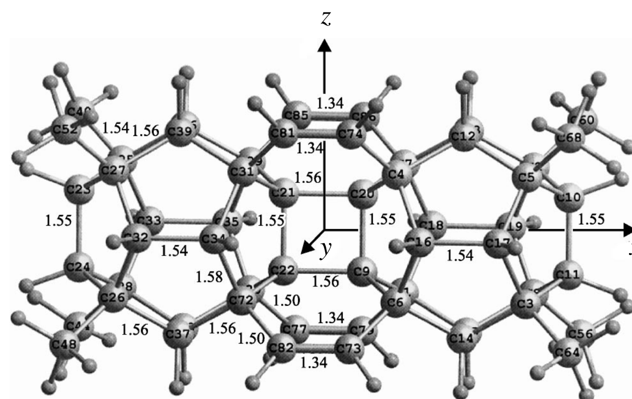

Fig. 8. Molecule $H_{32}C_{56}$ with D_{2h} symmetry (structure **4**).

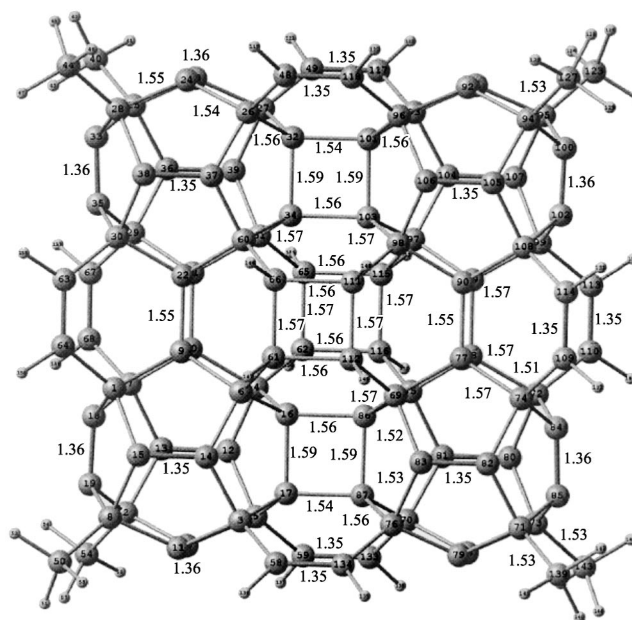

Fig. 9. Structure **5** with D_{2h} symmetry.

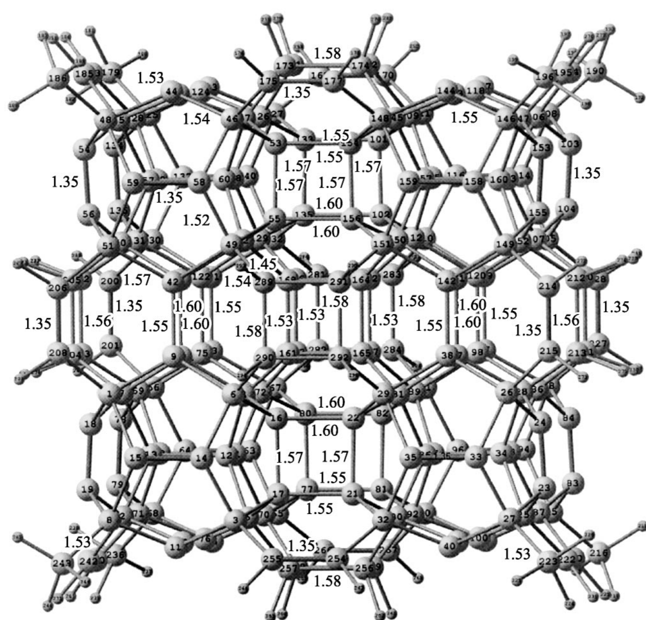

Fig. 10. Structure **6** with D_{2h} symmetry.

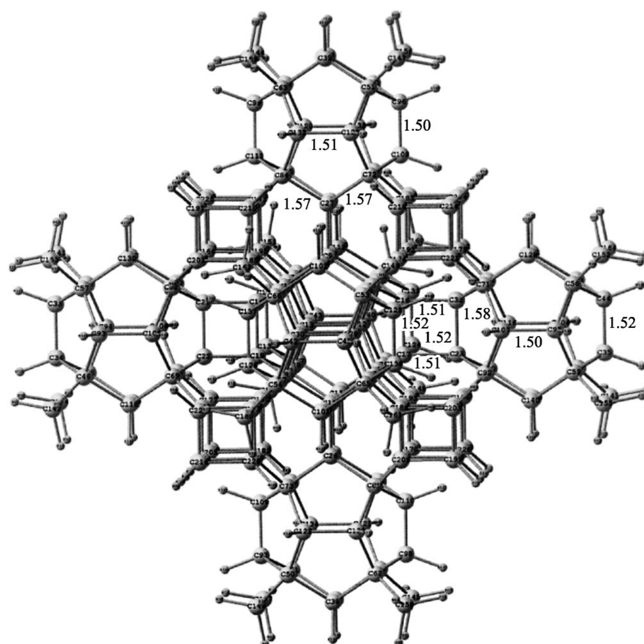

Fig. 11. Structure **7** with D_{2h} symmetry.

$[C_{26}H_2]_n$ having a square lattice with a lattice parameter of ≈5.66 Å.

We now explain how crystal **2** can be assembled. Molecule **5** has the shape of an oblate rectangular parallelepiped with a square base. The atomic structure of the top and bottom parts of the lateral surfaces of molecule **5** consists of four methyl groups, four –C–C– bonds of sp^3 carbon atoms, four bridging groups –CH=CH–, and one cyclobutane-type four-membered cycle. If the orientation of two molecules **5** approaching each other along the *z* axis is appropriate, their interaction can bring about the formation of a molecule **6** (Fig. 10). In this case, twelve hydrogen molecules are separated and 24 C–C bonds form. These are the bonds that intersect the equatorial plane of the formed molecule: eight bonds of the C9–C42 type between the monomers; four bonds of the C161–C168 type, which complete the formation of the cubic central fragment C_8; four double bonds of the C200=C206 and C214=C215 type; and eight single bonds in fragments HC–CH (e.g., C212–C213). Molecule **6** contains a cubic cluster C_8, each of whose atoms is linked to a dodecahedron. This cluster results from the interaction of two cyclobutane-type four-membered cycles. This procedure can continue infinitely. As a result, a quasi-one-dimensional system translationally invariant with respect to the *z* axis is formed. By assembling molecule **3**–based molecular systems along different directions of the coordinate axes simultaneously, we can produce crystal **2**.

To estimate the energetics of the initial stages of the procedures described above, we calculated the heats of the following reactions:

$$\mathbf{3} + \mathbf{3} \longrightarrow \mathbf{4} + 8H_2, \quad (1)$$

$$\mathbf{4} + \mathbf{4} \longrightarrow \mathbf{5} + 8H_2, \quad (2)$$

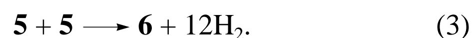

$$\mathbf{5} + \mathbf{5} \longrightarrow \mathbf{6} + 12H_2. \quad (3)$$

Table 2. Geometrical parameters of the building blocks of $[X_{28}]_n$ crystals obtained from calculations of molecules $X_8@(X_{20}H_{13})_8$ (the numbering is given in Fig. 4)

Element *X*	Basic parameters				Additional parameters		
	1–2	2–3	1–2–3	*a*	3–3'	1–1'	3–4
C	1.454	1.566	110.2	5.695–5.732	1.614	1.533	1.561–1.562
Si	2.307–2.308	2.386–2.388	107.9–108.1	8.802–8.808	2.420–2.443	2.370–2.371	2.400–2.402
Ge	2.412	2.505	108.1–108.2	9.226–9.245	2.568–2.570	2.489–2.490	2.513–2.514

Note: The bond lengths are in angstroms, and the bond angles, in degrees.

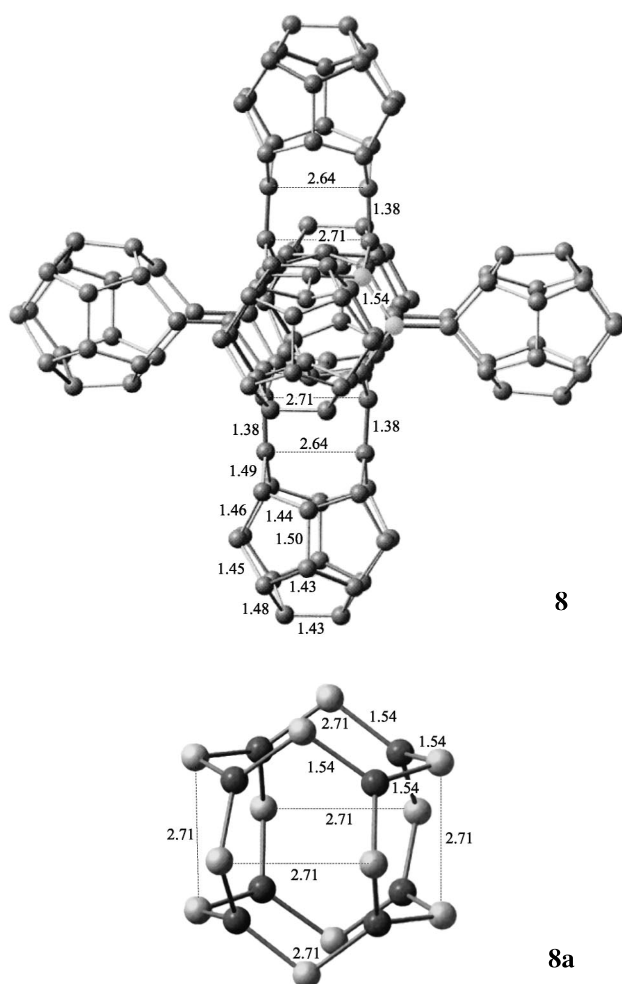

Fig. 12. Structure **8** with D_{2h} symmetry and building block **8a** of crystal **1**'.

The first reaction is found to be endothermic and to occur with heat absorption (≈102 kcal/mol). Reactions (2) and (3) are exothermic and should be accompanied by a release of 18 and 57 kcal/mol, respectively.

Note that the presence of cubic clusters in crystal **2** makes it possible to conserve the fullerene structure of clusters C_{20}, which is seen from comparing calculations of molecule **7** (Fig. 11) and oligomer $(C_{20})_7$ (Fig. 12, structure **8**). In molecule **7**, eight H_4C_{28} fragments, each of which contains a cubic cluster C_8, hinder rupture of the C–C bonds involved in [2 + 2] cycloaddition. In oligomer **8**, such bonds are broken. The central fragment C_{20} (Fig. 12, structure **8a**) ceases to be a fullerene, and its geometry characterizes the building block of crystal **1**'.

Thus, we have described a possible method of assembling quasi-one-dimensional, quasi-two-dimensional, and three-dimensional periodic structures based on octamethyl dodecahedron $C_{20}(CH_3)_8$ and its derivatives $C_{20}(CR_3)_8$. However, realization of this method requires special conditions, such as a high temperature, a high pressure, and, presumably, a catalyst. Note that the synthesis conditions can depend substantially on the nature of the substituent R and the strength of the C–R bond. For example, it is wise to take R = Br, since the C–Br bond is relatively weak. A similar approach was applied to synthesize a C_{20} cluster, which was formed from molecules $C_{20}HBr_{13}$ and $C_{20}HBr_9$ as a result of their debromation and dehydration [21].

4. CONCLUSIONS

We note that allotropic forms similar to crystal **2** should also exist for other Group IV elements (e.g., Si, Ge). To determine the geometry of the building blocks of such crystals (Fig. 3), we calculated clusters $X_8@(X_{20})_8$ and polyhedral molecules $X_8@(X_{20}H_{13})_8$ (X = Si, Ge) (their structures are analogous to structures **2a** and **2b** in Fig. 4). The calculated geometrical parameters of crystals $[Si_{28}]_n$ and $[Ge_{28}]_n$ are given in Table 2. The calculated densities of these crystals are 1.92 and 4.33 g/cm^3, respectively. Studying the electronic structures of such systems in the PBE96/FLAPW approximation requires large computational resources, which are not currently available to us.

The results obtained were reported on the 2nd International Conference "Carbon: Fundamental Problems of Science, Materials Science, and Technology" [22].

ACKNOWLEDGMENTS

We thank L.A. Chernozatonskiĭ for useful discussions of the results.

This work was supported by the Russian Foundation for Basic Research (project nos. 02-07-90169, 03-03-32214) and the Ministry of Science and Education of the Russian Federation.

REFERENCES

1. I. V. Stankevich, M. V. Nikerov, and D. A. Bochvar, Usp. Khim. **53** (7), 1101 (1984).
2. A. T. Balaban, C. C. Rentia, and E. Ciupitu, Rev. Roum. Chem. **13** (2), 231 (1968).
3. D. A. Bochvar and E. G. Gal'pern, Dokl. Akad. Nauk SSSR **209**, 610 (1973) [Sov. Phys. Dokl. **18**, 239 (1973)].
4. M. V. Nikerov, D. A. Bochvar, and I. V. Stankevich, Zh. Strukt. Khim. **23**, 177 (1982).
5. V. V. Korshak, Yu. P. Kudryavtsev, and A. M. Sladkov, Vestn. Akad. Nauk SSSR **1**, 70 (1978).
6. V. M. Mel'nichenko, Yu. I. Nikulin, and A. M. Sladkov, Dokl. Akad. Nauk SSSR **267**, 1150 (1982).
7. R. Hoffmann, T. Hughbanks, M. Kertesz, and P. H. Bird, J. Am. Chem. Soc. **105**, 4831 (1983).
8. F. Diedrich and Y. Rubin, Angew. Chem. Int. Ed. Engl. **39** (9), 1101 (1992).

9. V. I. Sokolov and I. V. Stankevich, Usp. Khim. **62** (5), 455 (1993).
10. I. V. Stankevich, Chem. Rev. **20**, 1 (1994).
11. H. Prinzbach, A. Weller, P. Landerberger, F. Wahl, J. Wörth, L. T. Scott, M. Gelmont, D. Olevaro, and B. V. Issendorff, Nature **407**, 60 (2000).
12. L. A. Paquette, D. W. Balogh, R. Usha, and D. Koutz, Science **211**, 575 (1981).
13. L. A. Paquette, R. J. Ternansky, D. W. Balogh, and G. J. Kentgen, J. Am. Chem. Soc. **105**, 5446 (1983).
14. Y. Miyamoto and M. Saito, Phys. Rev. B **63**, 161401(R) (2001).
15. S. Okada, Y. Miyamoto, and M. Saito, Phys. Rev. B **64**, 245405 (2001).
16. J. P. Perdew, K. Burke, and M. Ernzerhof, Phys. Rev. Lett. **77**, 3865 (1996).
17. D. N. Laikov, Chem. Phys. Lett. **281**, 151 (1997).
18. W. H. Press, S. A. Teukolsky, W. T. Vetterling, and B. P. Flannery, *Numerical Recipes in C: the Art of Scientific Computing* (Cambridge Univ. Press, Cambridge, MA, 1992).
19. P. Blaha, K. Schwarz, G. Madsen, D. Kvasnicka, and J. Luits, *Wien2k Userguide* (Vienna Univ. of Technology, Vienna, 2001).
20. P. Blaha, K. Schwarz, G. Madsen, D. Kvasnicka, and J. Luits, *Wien2k* (Vienna Univ. of Technology, Vienna, 2001).
21. T. Obwald, M. Keller, G. Janiak, M. Kolm, and H. Prinzbach, Tetrahedron Lett. **41**, 1631 (2000).
22. A. L. Chistyakov and I. V. Stankevich, in *Abstracts of 2nd International Conference on Carbon: Fundamental Problems of Science, Materials Science, and Technology* (Mosk. Gos. Univ., Moscow, 2003), p. 221.

Translated by K. Shakhlevich

Physics of the Solid State, Vol. 47, No. 1, 2005, pp. 22–25. Translated from Fizika Tverdogo Tela, Vol. 47, No. 1, 2005, pp. 26–28.
Original Russian Text Copyright © 2005 by Maksimov, Krasil'nik, Filatov, Kruglova, Morozov, Remizov, Nikolichev, Shengurov.

PROCEEDINGS OF THE CONFERENCE "NANOPHOTONICS 2004"
(Nizhni Novgorod, Russia, May 2–6, 2004)

Photoelectric Properties and Electroluminescence of *p–i–n* Diodes Based on GeSi/Si Heterostructures with Self-Assembled Nanoclusters

G. A. Maksimov*, Z. F. Krasil'nik, D. O. Filatov*, M. V. Kruglova*, S. V. Morozov**, D. Yu. Remizov**, D. E. Nikolichev*, and V. G. Shengurov***

** Research and Educational Center for Physics of Solid State Nanostructures, Nizhni Novgorod State University, pr. Gagarina 23/5, Nizhni Novgorod, 603950 Russia*

e-mail: Filatov@phys.unn.ru

*** Institute for Physics of Microstructures, Russian Academy of Sciences, Nizhni Novgorod, 603950 Russia*

Abstract—This paper reports on the results of investigations into the photoelectric properties and electroluminescence of *p–i–n* diodes based on GeSi/Si heterostructures with GeSi self-assembled nanoclusters embedded in the *i* region. The *p–i–n* diodes are grown through sublimation molecular-beam epitaxy using a vapor-phase source of germanium. The photovoltage spectra of the *p–i–n* diodes measured at a temperature of 300 K exhibit a photosensitivity band attributed to interband optical transitions in the GeSi nanoclusters. A new approach to analyzing the photosensitivity spectra of the heterostructures containing GeSi thin layers is proposed, and the energy at the edge of the photosensitivity bands assigned to these layers is determined. The electroluminescence observed in the *p–i–n* diodes at 77 K is associated with the radiative interband optical transitions in GeSi nanoclusters. *© 2005 Pleiades Publishing, Inc.*

1. INTRODUCTION

Over the last ten years, GeSi/Si heterostructures with nanoclusters prepared using self-assembled growth methods have been a subject of intensive study in the field of physics and the engineering of semiconductors [1]. The considerable interest expressed by researchers in these heterostructures stems from the possibility of designing integrated optoelectronic devices on the basis of silicon technology (for example, light-emitting diodes operating in the wavelength range 1.3–2.0 μm, which is of great practical importance) and prospective injection lasers [2]. Another important branch of research, namely, investigation into the photoconductivity of GeSi structures in the wavelength range 1–2 μm, is aimed at extending the spectral range of operation of silicon-based photodetectors to the infrared range.

As a rule, GeSi/Si heterostructures with GeSi self-assembled nanoclusters have been grown by molecular-beam epitaxy [3]. In the present work, we investigated the photoelectric properties and electroluminescence of *p–i–n* diodes based on GeSi/Si heterostructures with GeSi self-assembled nanoclusters that were grown through sublimation molecular-beam epitaxy using a vapor-phase source of germanium [4].

2. SAMPLE PREPARATION AND EXPERIMENTAL TECHNIQUE

In our experiments, we used three types of samples grown on Si(001) substrates (KDB-0.005). The deposition of silicon layers in samples of all three types was performed with a sublimation source as follows. First, a 0.6-μm-thick p^+-Si layer doped with boron at a concentration of $\sim 10^{18}$ cm^{-3} was grown on the substrate. Second, a 0.8-μm-thick *n*-Si layer lightly doped with phosphorus at a concentration of $\sim 10^{16}$ cm^{-3} was deposited on the first layer. Third, a 0.2-μm-thick n^+-Si layer with a donor concentration of $\sim 10^{18}$ cm^{-3} was grown on the second layer. In samples of the first type, a GeSi structure with a germanium layer whose nominal thickness was equal to 20 nm was embedded in the central region of the *n*-Si base layer. In order to provide deposition of germanium, GeH_4 was allowed to bleed into the growth chamber through a leak until the partial pressure of 5×10^{-5} Torr was reached. The substrate temperature during deposition of germanium was equal to 800°C. The other layers of the heterostructure were grown at a temperature of 600°C. Samples of the second type consisted of *p–i–n* structures that had the same parameters of the silicon layers but were prepared without deposition of germanium. These structures served as references samples. Examination of the morphology and composition of the nanoclusters was performed using samples of the third type with surface nanoclusters. In this case, germanium was deposited on the sur-

1063-7834/05/4701-0022$26.00 © 2005 Pleiades Publishing, Inc.

face of a 0.5-μm-thick heavily doped (~10^{18} cm^{-3}) p^+-Si buffer layer under conditions identical to those used for the deposition of germanium in the *p–i–n* structures.

The surface morphology of the samples of the third type was examined with a TopoMetrix® TMX-2100 Accurex™ atomic force microscope (AFM) operating in a contact mode in air. The composition of the self-assembled nanoclusters was studied using scanning Auger microscopy on an Omicron®MultiProbe S™ ultrahigh-vacuum apparatus. The electron probe diameter was approximately equal to 10 nm, the electron energy was 25 keV, and the electron beam current was 10 nA. The Auger spectra were recorded on a hemispherical energy analyzer. Since the samples were exposed to atmospheric air during transfer from the growth apparatus to the scanning Auger microscope, the sample surface was covered with an oxide layer ~2 nm thick. Prior to examination with the scanning Auger microscope, the surface oxide was removed by etching with Ar^+ ions (ion energy, 1 keV; ion beam current, 5 μA; beam diameter, 18 mm). Complete removal of the oxide from the surface of the structure was judged from the absence of the oxygen line in the Auger spectrum of the samples.

The *p–i–n* structures were used to produce mesa photodiodes (mesa diameter, 250 μm) with a window 150 μm in diameter in the top contact. The photoelectric properties of the photodiodes were investigated on a KSVU-23 spectrometric complex using a standard selective technique with modulated excitation and lock-in detection. In the experiments, we measured the spectral dependence of the open-circuit photovoltage $V_{ph}(h\nu)$, which was then normalized to the spectral distribution of the intensity of the exciting light $L_{ph}(h\nu)$. As a result, we obtained the photosensitivity spectra of the *p–i–n* photodiodes $S(h\nu) = V_{ph}(h\nu)/L_{ph}(h\nu)$.

The electroluminescence spectra of the diodes were measured at temperatures of 77 and 300 K in a pulsed mode. The duration of current pulses was equal to 4 ms, and the pulse-repetition frequency was 40 Hz. The luminescence spectra were recorded using an InGaAs photodetector with an MDR-23 monochromator.

3. RESULTS AND DISCUSSION

The AFM image of the GeSi/Si heterostructure with surface nanoclusters is displayed in Fig. 1. This heterostructure is characterized by a system of self-assembled nanoclusters with a surface density of ~10^8 cm^{-2}, a height of ~120 nm, and a diameter of ~800 nm.

According to scanning Auger microscopy, the composition of self-assembled nanoclusters corresponds to a Ge_xSi_{1-x} solid solution. The germanium content in the bulk of nanoclusters amounts to 30 ± 5 at. %. In the measurements with scanning Auger microscopy, the electron probe was directed at a nanocluster vertex. The high silicon content in the bulk of nanoclusters can be explained by the diffusion of silicon from the substrate into the bulk of nanoclusters in the course of growth [1].

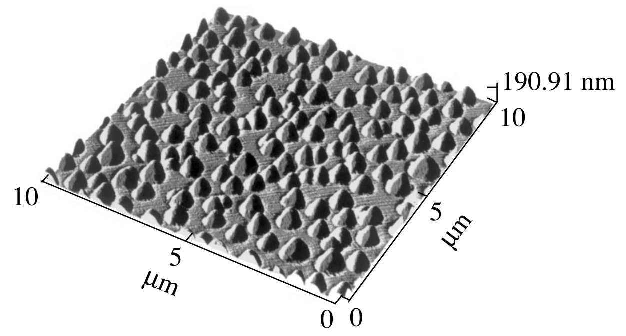

Fig. 1. AFM image of the GeSi/Si heterostructure with surface nanoclusters.

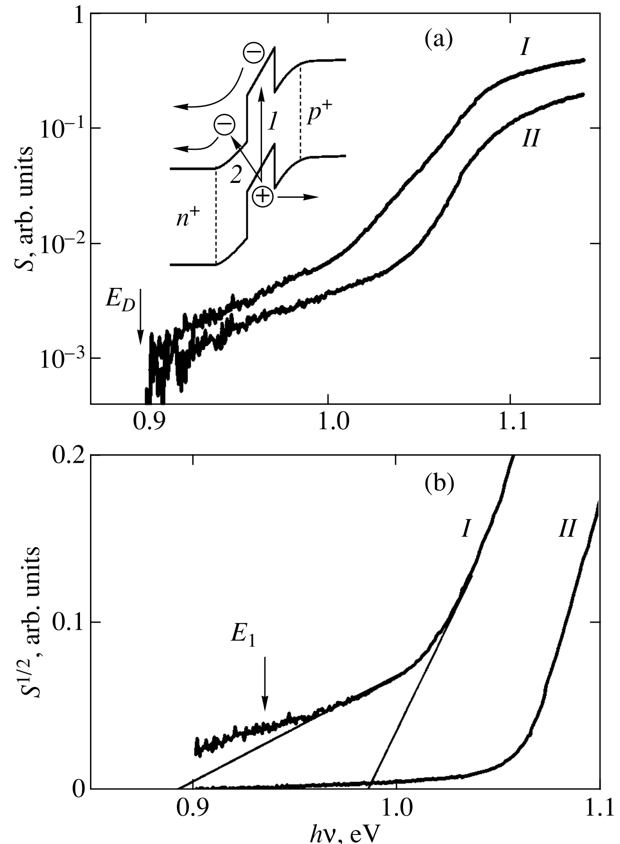

Fig. 2. (a) Photosensitivity spectra of (*I*) the *p–i–n* diode with GeSi self-assembled nanoclusters in the *i* region and (*II*) the *p–i–n* diode free of GeSi nanoclusters. (b) The same spectra in the $h\nu$–$S^{1/2}$ coordinates. $T = 300$ K.

The photosensitivity spectra of the *p–i–n* diodes with GeSi self-assembled nanoclusters in the *i* region and the spectra of the *p–i–n* diodes free of nanoclusters at a temperature of 300 K are shown in Fig. 2a. The photosensitivity edge of the *p–i–n* diode with GeSi self-

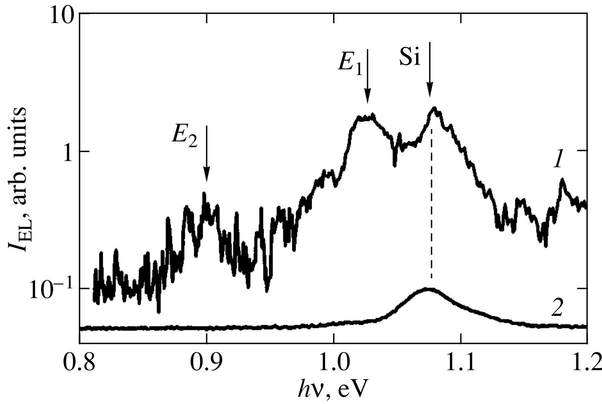

Fig. 3. Electroluminescence spectra of (*1*) the *p–i–n* diode with GeSi self-assembled nanoclusters in the *i* region and (*2*) the *p–i–n* diode free of GeSi nanoclusters. $T = 77$ K.

assembled nanoclusters (curve *I*) is shifted to the long-wavelength range with respect to the photosensitivity spectrum of the diode containing no GeSi nanoclusters (curve *II*). This shift is most likely associated with the optical absorption in GeSi nanoclusters.

The spectral dependence of the photosensitivity of *p–n* silicon-based junctions in the vicinity of the fundamental optical absorption edge can be described by the relationship [5]

$$S(h\nu) \sim \frac{\alpha(h\nu)L_n}{1+\alpha(h\nu)L_n}, \quad (1)$$

where $\alpha(h\nu)$ is the spectral dependence of the fundamental absorption coefficient and L_n is the diffusion length of minority carriers (in our case, electrons). The interband optical absorption coefficient of silicon near the fundamental optical absorption edge is sufficiently small; as a result, a large portion of light is absorbed deep in the interior of the structure outside the *p–n* junction. Therefore, the diffusion of minority carriers from a quasi-neutral region (in which they are generated) to the *p–n* junction plays a significant role in the mechanism of photovoltage.

In the case when the optical absorption occurs in a GeSi thin layer embedded in the *p–n* junction, charge carriers are generated in this layer, which can be treated as a δ-like source of electron–hole pairs. The diffusion of minority carriers toward the *p–n* junction is absent; hence, the photosensitivity can be considered to be proportional to the absorption coefficient:

$$S_{\text{ph}}(h\nu) \sim \alpha(h\nu). \quad (2)$$

Therefore, the technique used for examining the shape of the fundamental absorption edge can be applied to the analysis of the photosensitivity spectra of heterostructures containing self-assembled nanoclusters. For phonon-assisted indirect optical transitions, the spectral dependence $\alpha(h\nu)$ in the vicinity of the fundamental optical absorption edge can be described by the relationship [6]

$$\alpha(h\nu) \propto (h\nu - \Delta E_g \pm \hbar\Omega)^2, \quad (3)$$

where $\hbar\Omega$ is the phonon energy. In the $h\nu$–$\alpha^{1/2}$ coordinates, the spectral dependence described by relationship (3) is represented by two straight lines intersecting the abscissa axis at the points $\Delta E_g + \hbar\Omega$ and $\Delta E_g - \hbar\Omega$. It can be seen from Fig. 2b that, in the $h\nu$–$S^{1/2}$ coordinates, the edge of the photosensitivity band attributed to the optical absorption in GeSi self-assembled nanoclusters is also represented by two straight lines. This corresponds to indirect optical transitions with absorption and emission of phonons. On this basis, the energy of the optical transition was determined to be $E_1 \approx 0.94$ eV and the phonon energy was estimated as $\hbar\Omega \approx 46$ meV. The phonon energy thus obtained is slightly less than the energy of LO phonons in silicon (52.1 meV).

The electroluminescence spectrum of the *p–i–n* diode with GeSi self-assembled nanoclusters in the *i* region and the spectrum of the *p–i–n* diode free of nanoclusters at a temperature of 77 K are depicted in Fig. 3. Both spectra contain a peak with the maximum at a photon energy of ~1.07 eV due to phonon-assisted interband optical transitions in silicon. Spectrum *1* also contains peaks with maxima at photon energies of ~1.02 and ~0.9 eV. These peaks are associated with the optical transitions in GeSi self-assembled nanoclusters (i.e., with the transitions reverse to transition *1* shown in the inset to Fig. 2a) and with the transitions from the conduction band of the material (silicon) surrounding the self-assembled nanoclusters to the states of the valence band in GeSi (i.e., with the transitions reverse to transition *2* shown in the inset to Fig. 2a). This inference was made from the results of calculating the optical transition energies in the nanoclusters according to the model proposed by Aleshkin and Bekin [7]. Under the assumption that both transitions occurring in the GeSi self-assembled nanoclusters are phonon-assisted optical transitions, the germanium fractions in the nanoclusters were calculated to be 0.25 and 0.28 for transitions *1* and *2*, respectively. These results are in agreement with the data obtained from scanning Auger microscopy for the germanium content in nanoclusters.

The electroluminescence associated with the germanium and GeSi nanoclusters was observed earlier in structures grown through molecular-beam epitaxy [8, 9]. The results obtained in the present work demonstrate that the heterostructures with GeSi self-assembled nanoclusters grown through sublimation molecular-beam epitaxy with a vapor-phase source of germanium can also exhibit electroluminescence. This indicates that sublimation molecular-beam epitaxy can be applied in practice to the growth of device structures used in silicon optoelectronics.

As follows from the foregoing, the photosensitivity band with an energy $E_0 = 0.94$ eV at the band edge (Fig. 3) can be assigned to the interband optical transi-

tion in the GeSi self-assembled nanoclusters (transition *1* in the inset to Fig. 2a) with due regard for the temperature shift. The photovoltage spectra do not exhibit photosensitivity bands attributed to transitions from states of the valence band of the GeSi self-assembled nanoclusters to the conduction band of silicon. Possibly, these transitions do not manifest themselves against the background of the photosensitivity band with an energy $E_D \approx 0.9$ eV at the band edge at a temperature of 300 K (shown by an arrow in Fig. 2a). These bands are observed in the photovoltage spectra of both the diodes containing GeSi self-assembled nanoclusters and the diodes free of nanoclusters and, most likely, can be associated with dislocations.

ACKNOWLEDGMENTS

This work was supported by the Russian–American program "Basic Research and Higher Education" of the Ministry of Education of the Russian Federation and the US Civilian Research and Development Foundation for the Independent States of the Former Soviet Union (CRDF) (project no. REC-NN-001), the Russian Foundation for Basic Research (project no. 03-02-17085), and the Ministry of Education of the Russian Federation (project nos. E02-3.4-238, A03-2.9-473).

REFERENCES

1. Z. F. Krasil'nik and A. V. Novikov, Usp. Fiz. Nauk **170**, 3 (2000) [Phys. Usp. **43**, 1 (2000)].
2. G. Abstreiter, P. Schittenhelm, C. Engel, E. Silveira, A. Zrenner, D. Meertens, and W. Jäger, Semicond. Sci. Technol. **11**, 1525 (1996).
3. O. P. Pchelyakov, Yu. B. Bolkhovityanov, A. V. Dvurechenskiĭ, L. V. Sokolov, A. I. Nikiforov, A. I. Yakimov, and B. Voigtländer, Fiz. Tekh. Poluprovodn. (St. Petersburg) **34** (11), 1281 (2000) [Semiconductors **34**, 1229 (2000)].
4. S. P. Svetlov, V. G. Shengurov, V. Yu. Chalkov, Z. F. Krasil'nik, B. A. Andreev, and Yu. N. Drozdov, Izv. Ross. Akad. Nauk, Ser. Fiz. **65** (2), 204 (2001).
5. L. P. Pavlov, *Methods for Determining the Basic Parameters of Semiconductor Materials* (Vysshaya Shkola, Moscow, 1975), p. 112 [in Russian].
6. V. P. Gribkovskiĭ, *The Theory of Emission and Absorption of Light in Semiconductors* (Nauka i Tekhnika, Minsk, 1975), p. 86 [in Russian].
7. V. Ya. Aleshkin and N. A. Bekin, Fiz. Tekh. Poluprovodn. (St. Petersburg) **31**, 171 (1997) [Semiconductors **31**, 132 (1997)].
8. M. Stoffel, U. Denker, and O. G. Schmidt, Appl. Phys. Lett. **82**, 3236 (2003).
9. R. Apetz, L. Vescan, C. Dieker, and H. Luth, Appl. Phys. Lett. **66**, 445 (1995).

Translated by O. Borovik-Romanova

Physics of the Solid State, Vol. 47, No. 1, 2005, pp. 26–29. Translated from Fizika Tverdogo Tela, Vol. 47, No. 1, 2005, pp. 29–32.
Original Russian Text Copyright © 2005 by Vostokov, Drozdov, Krasil'nik, Lobanov, Novikov, Yablonskiĭ, Stoffel, Denker, Schmidt, Gorbenko, Soshnikov.

PROCEEDINGS OF THE CONFERENCE "NANOPHOTONICS 2004"
(Nizhni Novgorod, Russia, May 2–6, 2004)

Influence of a Predeposited $Si_{1-x}Ge_x$ Layer on the Growth of Self-Assembled SiGe/Si(001) Islands

N. V. Vostokov*, Yu. N. Drozdov*, Z. F. Krasil'nik*, D. N. Lobanov*, A. V. Novikov*, A. N. Yablonskiĭ*, M. Stoffel, U. Denker**, O. G. Schmidt***, O. M. Gorbenko***, and I. P. Soshnikov*****

**Institute of the Physics of Microstructures, Russian Academy of Sciences, Nizhni Novgorod, 603950 Russia*
e-mail: dima@ipm.sci-nnov.ru
*** Max-Planck-lnstitut für Festkörperforschung, Stuttgart, D-70569 Germany*
**** Ioffe Physicotechnical Institute, Russian Academy of Sciences, Politekhnicheskaya ul. 26, St. Petersburg, 194021 Russia*
*****Institute of Analytical Instrument Making, Russian Academy of Sciences, Rizhskiĭ pr. 26, St. Petersburg, 190103 Russia*

Abstract—The growth of self-assembled Ge(Si) islands on a strained $Si_{1-x}Ge_x$ layer (0% < x < 20%) is studied. The size and the surface density of islands are found to increase with Ge content in the $Si_{1-x}Ge_x$ layer. The increased surface density is related to augmentation of the surface roughness after deposition of the SiGe layer. The enlargement of islands is accounted for by the decrease of the wetting layer in thickness due to the additional elastic energy accumulated in the SiGe layer and to enhanced Si diffusion from the $Si_{1-x}Ge_x$ layer into the islands. The increase in the fraction of the surface occupied by islands leads to a greater order in the island arrangement. *© 2005 Pleiades Publishing, Inc.*

1. INTRODUCTION

Epitaxial self-assembled Ge nanosized islands on Si(001) have been actively studied for over a decade. The reason for this interest is that the Ge/Si(001) heteropair is a model system for studying the physics of heteroepitaxial growth (see [1] and reference therein). In addition, Ge islands in a Si matrix may be useful for development of a new generation of electronic and optoelectronic devices.

Among the various parameters of island growth, the surface density is the most important for the intensity of luminescence [2]. The surface density can be enhanced by raising the Ge deposition rate or by reducing the growth temperature, but in these cases the size of islands would simultaneously decrease, precluding the formation of densely packed arrays of islands [3], which are important for many applications. Nevertheless, dense packing may be achieved by using predeposited, highly strained $Si_{1-x}Ge_x$ layers with a low Ge content.

2. EXPERIMENTAL DETAILS

This paper presents the results of a study of the influence of predeposition of a $Si_{1-x}Ge_x$ layer (0% < x < 20%) on the subsequent growth of self-assembled Ge islands. The structures studied were grown on Si(001) substrates using molecular-beam epitaxy from solid sources at a substrate temperature of 700°C. The structures with self-assembled nanoislands consisted of a 100-nm-thick buffer Si layer and a 10-nm layer of $Si_{1-x}Ge_x$ with $0 \le x \le 20\%$, on which a Ge layer was deposited with an equivalent thickness of 3.8 to 12 ML. Structures intended for photoluminescence (PL) measurements were covered by a Si layer grown at 700°C. Surface morphology of the structures was studied *ex situ* by atomic force microscopy (AFM) in the semicontact mode. X-ray diffraction studies were performed using a DRON-4 diffractometer. PL spectra of GeSi heterostructures were measured using a BOMEM DA3.36 Fourier spectrometer and a cooled Ge detector. PL spectra were excited by an Ar^+ laser (514.5 nm).

3. RESULTS AND DISCUSSION

An analysis of AFM images of samples grown on a buffer Si layer and predeposited $Si_{1-x}Ge_x$ layers with different Ge content showed that the surface density of islands increases with Ge content in the $Si_{1-x}Ge_x$ layer (Fig. 1). We suggested that augmentation of the surface roughness resulting from deposition of an elastically strained SiGe layer onto Si(00l) (reported in the literature [4]) leads to a decreased diffusion length of adatoms and, hence, to an increased surface density of islands. It is found that the rms roughness of the SiGe layer surface calculated from the AFM images increases with Ge content in $Si_{1-x}Ge_x$. The increase is more than twofold (from 1.05 to 2.2 Å) after deposition

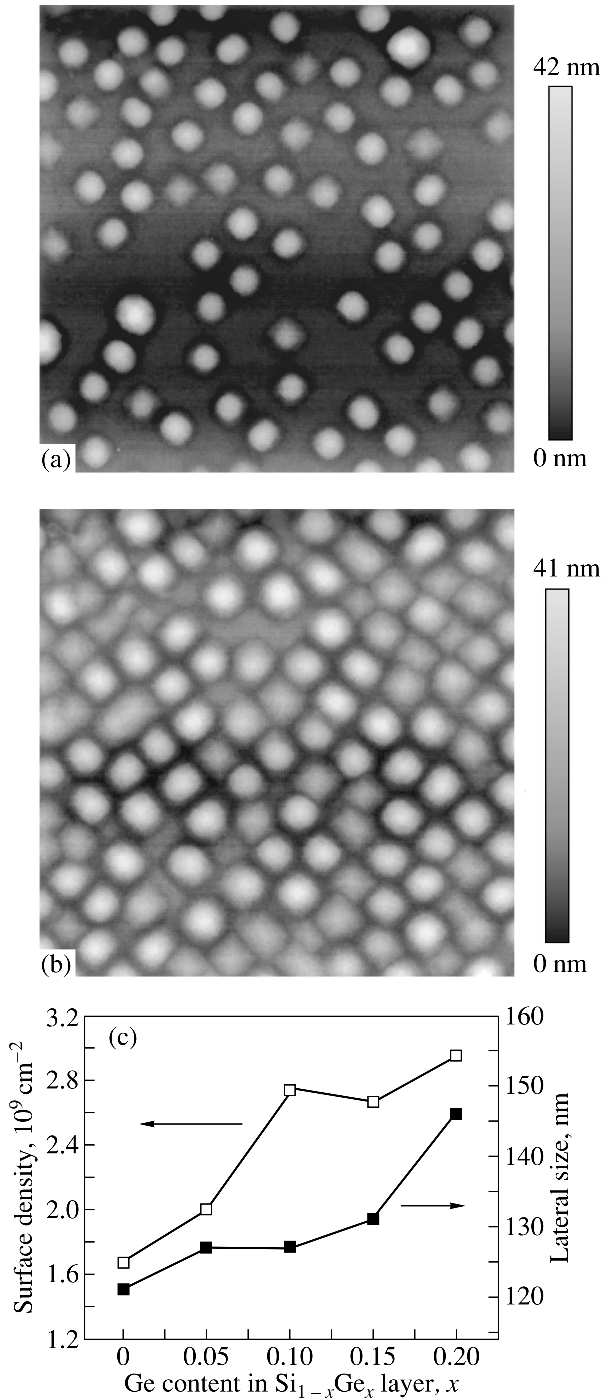

Fig. 1. AFM images of islands grown on a predeposited $Si_{1-x}Ge_x$ layer with Ge content (a) $x = 0$ and (b) 10%. The equivalent thickness of pure Ge deposited onto the layer was 9 ML. Scan dimensions are 2×2 μm^2. (c) Surface density and average lateral dimension of islands vs. Ge content in the $Si_{1-x}Ge_x$ layer.

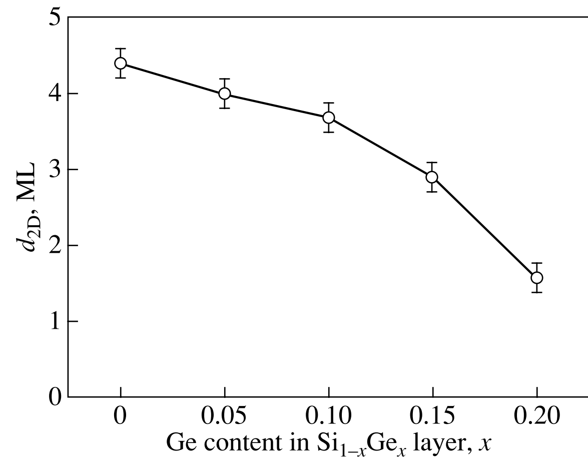

Fig. 2. Critical Ge layer thickness d_{2D} as a function of Ge content in the $Si_{1-x}Ge_x$ layer.

of a $Si_{0.8}Ge_{0.2}$ layer. Note that, according to AFM studies, the surfaces of the structures remained planar after GeSi deposition. Therefore, we believe that the increased surface roughness strongly reduces the surface diffusion length and finally causes an increase in the surface density of islands.

In our opinion, the increased surface density of islands and their more uniform distribution over the surface are responsible for the fact that it is possible to deposit Ge on the $Si_{1-x}Ge_x$ layer by 2–3 ML more than on a Si buffer before the onset of formation of dislocation islands.

In addition to the growth of the surface density, it is also found that islands increase in size with Ge content in the $Si_{1-x}Ge_x$ layer (Fig. 1c). The simultaneous increase in the surface density and dimensions of islands signifies that more atoms contribute to the formation of islands, since the total volume of islands rises. We suggest that an additional flow of atoms into the islands is due to a reduction in the wetting-layer thickness. Some Ge atoms are released during the reduction and participate in the formation of islands. In order to verify this hypothesis, we experimentally determined the critical thickness d_{2D} for the two-dimensional growth of Ge on a $Si_{1-x}Ge_x$ layer as a function of x. The critical density for the 2D–3D transition was measured using reflection high-energy electron diffraction (RHEED). We found that, as the Ge content in the $Si_{1-x}Ge_x$ layer increases, the thickness d_{2D} decreases (Fig. 2) from 4.4 ± 0.2 ML in the case of a Si buffer layer to 1.6 ± 0.2 ML when Ge is deposited on $Si_{0.8}Ge_{0.2}$.Thus, the thickness of the wetting layer is also reduced with increasing Ge content in the $Si_{1-x}Ge_x$ layer, since it cannot exceed the critical thickness for planar growth of a Ge film. This reduction could be confirmed by studying the PL of samples grown with and without a predeposited SiGe layer. It is found that, in the case of islands grown on a SiGe layer, PL signals originating from the wetting layer are shifted towards higher energies as compared to the case of a sample without a predeposited SiGe layer. There are two possible reasons for this behavior: first, the increased wetting

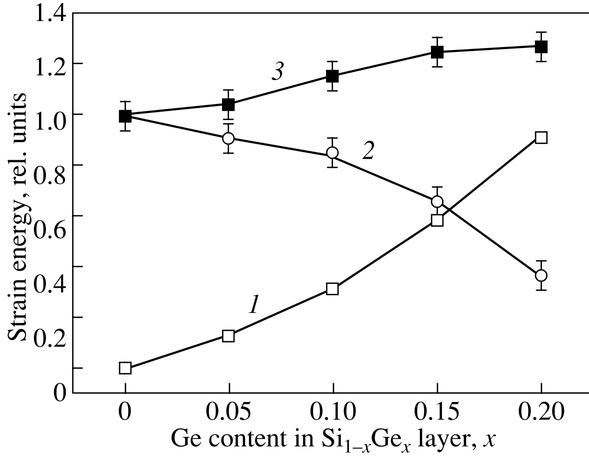

Fig. 3. (*1*, *2*) Elastic energies accumulated in (*1*) the $Si_{1-x}Ge_x$ layer (E_{SiGe}) and (*2*) pure Ge layer of critical thickness (E_{Ge}) and (*3*) their sum (E_{tot}) as functions of Ge content in the $Si_{1-x}Ge_x$ layer. All energies are normalized to the elastic energy of a Ge layer of critical thickness grown on a Si buffer layer ($d_{2D} = 4.4 \pm 0.2$ ML).

layer thickness and, second, the increased Si content in the wetting layer. Since samples were grown under exactly the same conditions, we associate this shift with the decrease in the wetting layer thickness, which leads to a shift of the hole energy level towards the top of the Si valence band due to confinement effects and, thus, to an increased PL intensity.

Segregation of Ge, which takes place under the growth conditions we uses, can also decrease $d_{2D}(x)$ (Fig. 2). However, the Ge segregation can cause no more than one additional Ge monolayer to appear on the surface of the $Si_{1-x}Ge_x$ layer. Since the increase in d_{2D} is as large as 2.8 ± 0.4 ML when Ge is grown on a predeposited $Si_{0.8}Ge_{0.2}$ layer, the Ge segregation by itself cannot account for the observed decrease in d_{2D}.

Another possible reason for the reduction in d_{2D} is the additional elastic energy accumulated in the $Si_{1-x}Ge_x$ layer. The elastic energies of the $Si_{1-x}Ge_x$ layer and the Ge film were each calculated using the well-known formula from the theory of elasticity:

$$E = 2G\varepsilon^2 d\frac{1+\nu}{1-\nu}, \quad (1)$$

where G is the shear modulus, ν is Poisson's ratio, ε is either the xx or yy component of the strain tensor, and d is either the $Si_{1-x}Ge_x$ layer thickness (10 nm in our case) or the critical thickness d_{2D} of the Ge film. The elastic energy of the $Si_{1-x}Ge_x$ layer was calculated with inclusion of Ge segregation. The total elastic energy E_{tot} accumulated in the structure just before the onset of island formation was calculated by summing the elastic energy of the $Si_{1-x}Ge_x$ layer (E_{SiGe}) and the elastic energy of the Ge layer of critical thickness d_{2D} (E_{Ge}):

$$E_{tot} = E_{SiGe} + E_{Ge}. \quad (2)$$

The results of our calculations are presented in Fig. 3 in units of the elastic energy of a Ge layer of thickness $d_{2D} = 4.4 \pm 0.2$ ML, which corresponds to the growth of Ge on a Si buffer layer. It is clear that the total elastic energy accumulated in the structure before the transition from the 2D to 3D growth is almost constant and increases only slightly with the Ge content in the $Si_{1-x}Ge_x$ layer. The small increase in E_{tot} may be due to relaxation associated with augmented surface roughness.

The increased sizes of islands grown on a predeposited SiGe layer can originate not only from an additional flow of Ge atoms due to the reduction in the wetting layer thickness but also from the enhanced Si diffusion into the islands. It was shown in [6] that the Si content in an island increases with island size. X-ray diffraction analysis showed that the average Ge content in the islands decreases from 52 ± 3 to $41 \pm 3\%$ as the Ge content in the $Si_{1-x}Ge_x$ layer increases from $x = 0$ to 15%. This fact may seem strange, as the fraction of Ge atoms involved in bulk diffusion from the sublayer to the islands should increase, thereby increasing the Ge content in the islands. Apparently, it is Si atoms that predominantly diffuse into the islands and reduce the elastic stresses by creating a SiGe solution. The experimentally observed reduction in the thickness of the Ge wetting layer also decreases the barrier to Si diffusion from the $Si_{1-x}Ge_x$ layer into the islands. As a result, the Si content in the islands grows with increasing Ge content in the $Si_{1-x}Ge_x$ layer; this fact, combined with the reduction in the wetting layer thickness, enables us to explain the experimentally observed increase of the islands in size.

Because of the increase in the island size and in their surface density, the fraction of the surface occupied by the islands grows and neighboring islands start to effectively interact with each other; therefore, a correlation appears in the relative positions of the islands. The direction of ordering is close to ⟨100⟩. Because of the anisotropy of the elastic properties, the stresses caused by islands on the surface decay with distance from an island much faster along the direction ⟨110⟩ than along ⟨100⟩ [6]. The degree of island ordering was studied using the autocorrelation function of the surface [7]. The autocorrelation function was found to exhibit three peaks along the ⟨110⟩ direction, which indicates a strong short-range correlation in the relative positions of islands up to the third nearest neighbor island.

4. CONCLUSIONS

In the present work, the growth of self-assembled Ge(Si) islands on a strained $Si_{1-x}Ge_x$ layer ($0\% < x < 20\%$) has been studied. The size and the surface density

of islands have been found to increase with the Ge content in the $Si_{1-x}Ge_x$ layer. The augmentation of surface roughness resulting from deposition of the $Si_{1-x}Ge_x$ layer leads to an increased surface density of islands. The island size increases because of the higher Si content in the islands, which is due to enhanced Si diffusion from the $Si_{1-x}Ge_x$ layer into the islands as a result of the experimentally observed decrease in the wetting layer thickness. The significant reduction of the wetting layer in thickness in the case of Ge deposited on a $Si_{1-x}Ge_x$ layer is associated with the elastic energy accumulated in the $Si_{1-x}Ge_x$ layer. The increase in the surface fraction occupied by islands due to an increase in the island size and in their surface density leads to enhanced ordering of the relative positions of islands. The ordering of the islands has been studied by analyzing the surface autocorrelation function.

ACKNOWLEDGMENTS

This work was supported by the Russian Foundation for Basic Research (project nos. 02-02-16792, 02-02-17846a), INTAS (NANO grant no. 01-444), and the BRHE program.

REFERENCES

1. B. Voigtländer, Surf. Sci. Rep. **43**, 127 (2001).
2. U. Denker, M. Stoffel, O. G. Schmidt, and H. Sigg, Appl. Phys. Lett. **82**, 454 (2003).
3. B. Cho, T. Schwartz-Selinger, K. Ohmori, and D. G. Cahill, Phys. Rev. B **66**, 195 407 (2002).
4. P. Sutter and M. G. Lagally, Phys. Rev. Lett. **84**, 4637 (2000).
5. N. V. Vostokov, S. A. Gusev, Yu. N. Drozdov, Z. F. Krasil'nik, D. N. Lobanov, N. Mesters, M. Miura, L. D. Moldavskaya, A. V. Novikov, J. Pascual, V. V. Postnikov, Y. Shiraki, V. A. Yakhimchuk, N. Usami, and M. Ya. Valakh, Phys. Low-Dimens. Semicond. Struct., No. 3/4, 295 (2001).
6. M. Meixner, E. Schöll, M. Schmidbauer, H. Raidt, and R. Köler, Phys. Rev. B **64**, 245307 (2001).
7. Christian Teichert, Phys. Rep. **365**, 335 (2002).

Translated by G. Tsydynzhapov

Physics of the Solid State, Vol. 47, No. 1, 2005, pp. 30–33. Translated from Fizika Tverdogo Tela, Vol. 47, No. 1, 2005, pp. 33–36.
Original Russian Text Copyright © 2005 by Shegai, Berezovsky, Nikiforov, Ul'yanov.

PROCEEDINGS OF THE CONFERENCE "NANOPHOTONICS 2004"
(Nizhni Novgorod, Russia, May 2–6, 2004)

Photoconductivity of Si/Ge/SiO$_x$ and Si/Ge/Si Structures with Germanium Quantum Dots

O. A. Shegai, A. Yu. Berezovsky, A. I. Nikiforov, and V. V. Ul'yanov

Joint Institute of Semiconductor Physics, Siberian Division, Russian Academy of Sciences, pr. Lavrent'eva 13, Novosibirsk, 630090 Russia

e-mail: shegai@thermo.isp.nsc.ru

Abstract—A nonmonotonic dependence of the lateral photoconductivity (PC) on the interband light intensity is observed in Si/Ge/Si and Si/Ge/SiO$_x$ structures with self-organized germanium quantum dots (QDs): in addition to a stepped increase in PC, a stepped decrease in PC is also observed. The effect of temperature and drive field on these features of the PC for both types of structures with a maximum nominal thickness of the Ge layer (N_{Ge}) is studied. The results obtained are discussed in the context of percolation theory for nonequilibrium carriers localized in different regions of the structure: electrons in the silicon matrix and holes in QDs. *© 2005 Pleiades Publishing, Inc.*

1. INTRODUCTION

Studying the mechanisms of interband photoconductivity (PC) in Si/Ge structures with self-organized Ge quantum dots (QDs) is important, since these structures can serve as a basis for constructing novel photoelectric devices [1]. In these structures, in contrast to bulk semiconductors, the variation of the interband PC with increasing illumination intensity has a threshold character related to the nonequilibrium-carrier (electron) transfer via disordered localized states [2]. At relatively small values of N_{Ge} (when the distance between QDs is greater than the QD base size), the current flows via electron states localized between the QDs. These states appear in the presence of spatial relaxation of stresses around the QDs [2]. The contribution to the PC related to nonequilibrium holes, localized mainly in the states in QDs, is small. The QD size increases with N_{Ge}, and the electron localization region decreases. This means that the contribution of hole transfer via the QD states to the PC can be comparable to that of electron transfer. This study is devoted to the observation of this effect. We studied Si/Ge/Si structures and Si/Ge/ SiO$_x$ structures with QDs at large values of N_{Ge}. We note that, in Si/Ge/SiO$_x$ structures, there was no wetting layer and the QD concentration was higher. Measurements show that, in addition to a stepped increase in PC studied earlier [2], a stepped decrease in PC is observed in structures with QDs. The kinetics of formation of these features and their behavior with varying temperature and driving field are studied in detail.

2. EXPERIMENTAL RESULTS AND DISCUSSION

The synthesis of Si/Ge/Si structures with QDs is described in [1]. Si/Ge/SiO$_x$ structures with germanium QDs were prepared by molecular-beam epitaxy. A buffer Si layer ~50-nm thick was grown on a Si(001) substrate, and then the buffer layer surface was exposed to oxidation. Next, for each of the structures, a Ge layer with N_{Ge} = 0, 0.3, 0.5, and 1 nm, respectively, was grown and subsequently covered by a silicon layer about 10-nm thick. The presence of self-organized QDs was confirmed by structural studies, which showed that the typical size of QD bases was 8–10 nm, the QD height was 2–2.5 nm, and the QD concentration was ~10^{12} cm^{-2}. For measurements of the PC, samples about 2×4 mm in size were cut from a washer and linear indium contacts were deposited on the surface along the short side of the structure so that the distance between them was about 2 mm.

For the Si/Ge/SiO$_x$ structures with QDs (N_{Ge} = 0.3, 0.5 nm) at T = 4.2 K, a stepped increase in PC was observed. An increase in the driving field produced a shift of the step to smaller illumination intensities, just as for structures grown on a Si sublayer [2, 3].

Figure 1 shows the PC as a function of the illumination intensity I for a structure with N_{Ge} = 1 nm (sample 4) at various temperatures. In this figure, we see that a PC step appears above T = 18.6 K, which is substantially higher than the temperature (T = 4.2 K) at which a similar I dependence of the PC was observed earlier for Si/Ge/Si structures with Ge QDs [2, 3]. An increase in temperature results in a shift of the step to higher illumination intensities (Fig. 1a). As the temperature is increased further, a region of a stepped decrease

1063-7834/05/4701-0030$26.00 © 2005 Pleiades Publishing, Inc.

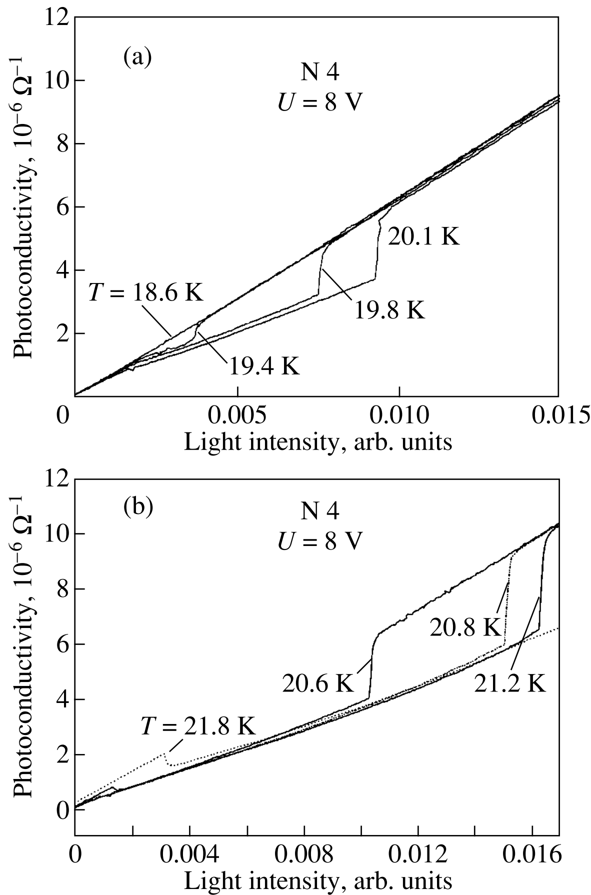

Fig. 1. Appearance of (a) a step and (b) a dip on the PC dependence on interband illumination intensity with increasing measurement temperature for a Si/Ge/SiO$_x$ structure with QDs (the nominal Ge layer thickness is 1 nm) for $U = 8$ V.

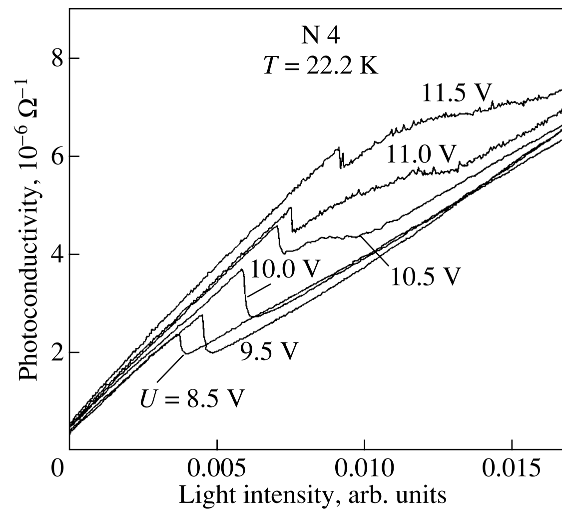

Fig. 2. Effect of the driving field on the position of the stepped decrease in PC for a Si/Ge/SiO$_x$ structure with QDs (the nominal Ge layer thickness is 1 nm) at $T = 22.2$ K and $U = 8.5$–11.5 V.

appears on the PC curve (Fig. 1b) and then the observed features disappear. Figure 2 shows the effect of the driving field on the position of the stepped decrease in PC. Analysis showed that the observed feature is linearly displaced to higher values of I with increasing U. Likewise, the driving field affects the position of a jump on the PC curve (Fig. 3).

In Fig. 4, the PC dependence on I for Si/Ge/Si structures with QDs (samples 2–7 with $N_{Ge} = 11$ ML) are shown for $U = 12$ V at different temperatures. It is seen that, as the temperature increases, the step is displaced to lower values of I and the step amplitude decreases. Figure 5 shows the driving-field dependences at 20 K, where, in addition to a step, a stepped decrease appears on the PC curves as U increases above 4 V. Starting from $U = 4.5$ V, both steps are shifted to smaller values of I with an increase in the driving field. Thus, for structures of both types (Si/Ge/SiO$_x$ and Si/Ge/Si) with Ge QDs, a stepped increase and a stepped decrease are observed on the PC curves; however, their positions depend differently on the temperature and on driving field.

3. DISCUSSION

Our analysis of the results obtained is based a model that we suggested earlier for describing the nonequilibrium-carrier transfer via states localized in different regions of the structure, namely, the transfer of electrons in the Si matrix and holes in Ge QDs. The population of these states increases with the intensity of interband illumination. For the structures investigated, the features in the PC appear when the percolation threshold is reached for nonequilibrium carriers in localized states.

The QD size increases with N_{Ge}, and the neighboring QDs begin to overlap. An increase in the overlap of QDs decreases the percolation threshold for holes. For electrons, the effect is opposite; namely, with increasing N_{Ge}, the size of the localization region for electrons decreases and the percolation threshold increases. The mechanism of electron localization also changes with increasing N_{Ge}. At low values of N_{Ge}, this mechanism is related to relaxation of stresses around QDs, and at high values of N_{Ge}, electrons are confined by the QD barriers (Si/Ge heterointerfaces).

The described features of PC were not observed at low temperatures ($T = 4.2$ K). The reason for this is that the intensity of the available source of interband light was not sufficient for nonequilibrium carriers to attain the percolation level. Since the Ge layer thickness is maximum in the structures considered, the relief is also maximum. If the temperature increases by a factor of approximately 5, the percolation of nonequilibrium carriers becomes possible. The electron and hole con-

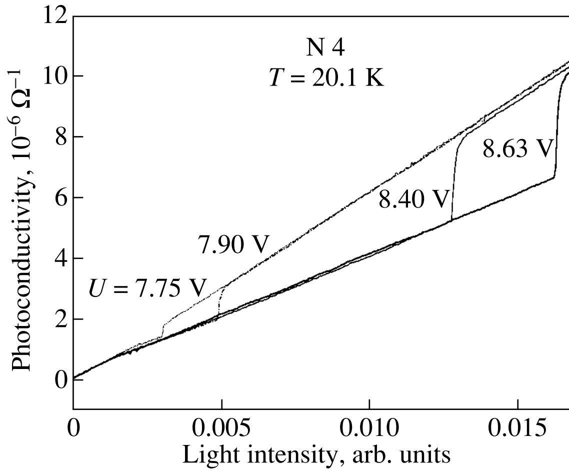

Fig. 3. Effect of the driving field on the position of the step on the PC curves for a Si/Ge/SiO_x structure with QDs (the nominal Ge layer thickness is 1 nm) at $T = 20.1$ K and $U = 7.75$–8.63 V.

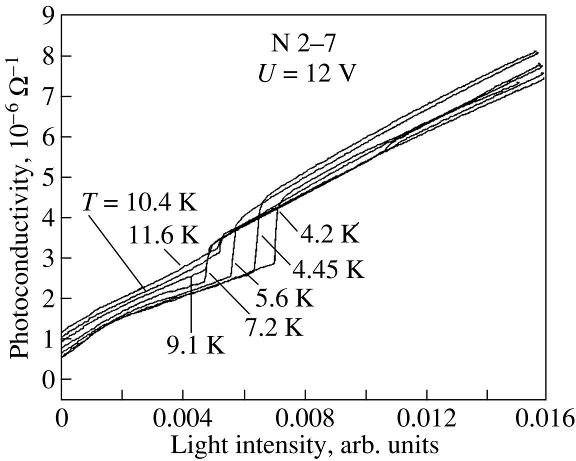

Fig. 4. Effect of temperature on the step position on PC curves for a Si/Ge/Si structure with QDs ($N_{Ge} = 11$ ML) for $U = 12$ V.

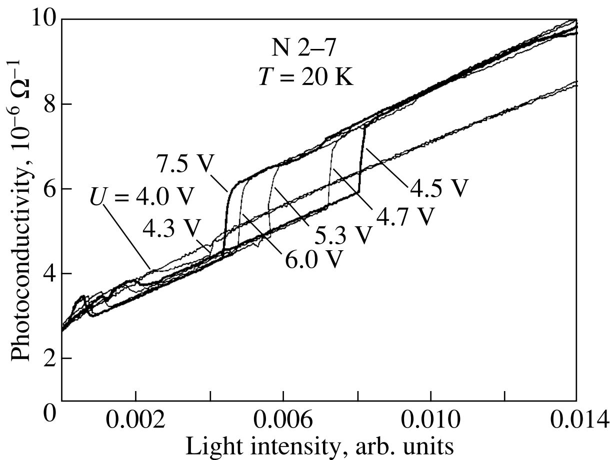

Fig. 5. Effect of the driving field on the position of the step on PC curves for a Si/Ge/Si structure with QDs ($N_{Ge} = 11$ ML) at $T = 20$ K and $U = 4.0$–7.5 V.

duction in the structures considered can be described in the terms of the continuum problem in percolation theory through "white" and "black" regions [4]. In addition, it is necessary to take into account the Coulomb interaction, which lowers the barriers separating the white and black regions, thus increasing the recombination rate. Accordingly, the number of carriers decreases, which is manifested in the experiment by a falling region on the PC curve. We assume that, in the figures, the conductivity due to electrons above the percolation threshold is greater than the electron conductivity below the threshold. In this case, a stepped decrease in the PC signal is due to the fact that holes localized in QDs attain the percolation level, and a stepped PC increase occurs, as also assumed in [2], because the electrons localized in the Si matrix attain the percolation level. The recombination at the Si/Ge heterointerface decreases the population of localized states by nonequilibrium electrons (i.e., a specific lowering of the electronic temperature occurs). A greater illumination intensity is needed for electrons to reach the percolation level again.

For a Si/Ge/SiO_x structure, we assume that the shift of both observed features to higher illumination intensities with an increase in temperature (Fig. 1) is related to a decrease in the population of localized states by nonequilibrium charge carriers, which can be thermally excited above the percolation threshold and then recombine. The behavior of these features with increasing driving field (Figs. 2, 3) is explained by depopulation of the localized states because of the increased rate of carrier tunneling across the Si/Ge heterointerface with subsequent recombination.

In the Si/Ge/Si structures with QDs, the QD concentration is approximately one order of magnitude smaller than in the Si/Ge/SiO_x structures. Therefore, the characteristic extent of localized electron states is greater. A fraction of holes in the Ge wetting layer are localized between QDs and form excitons. The behavior of the PC features for the Si/Ge/Si structures with QDs is determined by the presence of excitons. An increase in the temperature and driving field results in an increase in the population of localized states due to the destruction of excitons, and the electrons reach the percolation level at lower illumination intensities.

4. CONCLUSIONS

Thus, in Si/Ge/Si and Si/Ge/SiO_x structures with self-organized QDs, we have observed a stepwise increase or decrease in the PC signal, depending on the intensity of interband light. As the driving field and temperature increase, the observed features shift to higher illumination intensities for the Si/Ge/SiO_x structures and in the opposite direction for the Si/Ge/Si structures. The results have been analyzed using percolation theory for nonequilibrium carriers localized in different regions of the structure.

ACKNOWLEDGMENTS

This study was supported by the Russian Foundation for Basic Research, project nos. 03-02-16466 and 03-02-16468.

REFERENCES

1. O. P. Pchelyakov, Yu. B. Bolkhovityanov, A. V. Dvurechenskiĭ, L. V. Sokolov, A. I. Nikiforov, A. I. Yakimov, and B. Voigtländer, Fiz. Tekh. Poluprovodn. (St. Petersburg) **34**, 1281 (2000) [Semiconductors **34**, 1229 (2000)].
2. O. A. Shegai, V. A. Markov, A. I. Nikiforov, A. S. Shaimuratova, and K. S. Zhuravlev, Phys. Low-Dimens. Semicond. Struct., No. 1/2, 261 (2002).
3. O. A. Shegai, K. S. Zhuravlev, V. A. Markov, A. I . Nikiforov, and A. Sh. Shaĭmuratova, Izv. Ross. Akad. Nauk, Ser. Fiz. **67**, 192 (2003).
4. B. I. Shklovskiĭ and A. L. Éfros, *Electronic Properties of Doped Semiconductors* (Nauka, Moscow, 1979; Springer, New York, 1984).

Translated by I. Zvyagin

Physics of the Solid State, Vol. 47, No. 1, 2005, pp. 34–37. Translated from Fizika Tverdogo Tela, Vol. 47, No. 1, 2005, pp. 37–40.
Original Russian Text Copyright © 2005 by Yakimov, Dvurechenskiĭ, Kirienko, Nikiforov.

PROCEEDINGS OF THE CONFERENCE "NANOPHOTONICS 2004"
(Nizhni Novgorod, Russia, May 2–6, 2004)

Ge/Si Photodiodes and Phototransistors with Embedded Arrays of Germanium Quantum Dots for Fiber-Optic Communication Lines

A. I. Yakimov, A. V. Dvurechenskiĭ, V. V. Kirienko, and A. I. Nikiforov

Institute of Semiconductor Physics, Siberian Division, Russian Academy of Sciences, pr. Akademika Lavrent'eva 13, Novosibirsk, 630090 Russia

e-mail: yakimov@isp.nsc.ru

Abstract—Photodetectors based on Ge/Si multilayer heterostructures with germanium quantum dots are fabricated for use in fiber-optic communication lines operating in the wavelength range 1.30–1.55 μm. These photodetectors can be embedded in an array of photonic circuit elements on a single silicon chip. The sheet density of germanium quantum dots falls in the range from 0.3×10^{12} to 1.0×10^{12} cm^{-2}, and their lateral size is approximately equal to 10 nm. The heterostructures are grown by molecular-beam epitaxy. For a reverse bias of 1 V, the dark current density reaches 2×10^{-5} A/cm^2. This value is the lowest in the data on dark current densities available in the literature for Ge/Si photodetectors at room temperature. The quantum efficiency of photodiodes and phototransistors subjected to illumination from the side of the plane of the *p–n* junctions is found to be 3% at a wavelength of 1.3 μm. It is demonstrated that the maximum quantum efficiency is achieved for edge-illuminated waveguide structures and can be as high as 21 and 16% at wavelengths of 1.3 and 1.5 μm, respectively.
© 2005 Pleiades Publishing, Inc.

1. INTRODUCTION

The design of fiber-optic communication lines is one of the most important directions in the development of highly efficient methods for transmitting information in television and telephone networks, the Internet, and optical computers. Fiber-optic communication lines consist of a transmitter, a photoreceiver, cross points, and optical fibers. The photoreceiver makes it possible to detect optical radiation, to convert optical signals into electric signals, and to provide subsequent amplification of the electric signals. The optical fibers used in fiber-optic communication lines are predominantly produced from silica. High-purity silica is characterized by the absorption spectrum with three transparency windows at wavelengths of 0.85, 1.30, and 1.55 μm. The near-atmospheric transparency window lies in the same wavelength range. Currently, it is universally accepted that the near-IR wavelength range 1.30–1.55 μm is of the utmost importance in using fiber-optic communication lines.

At present, the high cost of optical transmitters and detectors operating in the near-IR spectral range has hindered widespread use of fiber-optic communication lines. It can be expected that the changeover to silicon-compatible technology for fabricating photonic elements of fiber-optic communication lines will result in a considerable decrease in the cost of these elements. In turn, this should lead to a monolithic integration of all components (including elements used in radio-amplifier and bias electronics) into a simple, reliable, and easily reproducible optoelectronic integrated circuit [1]. However, silicon is transparent to photon radiation at wavelengths longer than 1.1 μm. At the same time, germanium photodetectors are characterized by a high sensitivity in the range of wavelengths $\lambda \sim 1.5$ μm. In this respect, there arises a problem associated with the preparation of Ge/Si heterostructures that will be photosensitive in the telecommunication wavelength range 1.30–1.55 μm at room temperature. From the standpoint of the incorporation of Ge/Si heterojunctions into a silicon VLSI circuit, Ge/Si heterostructures with coherently embedded germanium nanoclusters (quantum dots) are of particular interest, because elastically strained germanium layers in these heterostructures can be overgrown with structurally perfect silicon layers on which, subsequently, it is possible to produce other elements of the VLSI circuit. Moreover, it is this system that has already been used to fabricate light-emitting diodes operating in the wavelength range 1.3–1.5 μm at room temperature with a quantum efficiency of approximately 0.015% [2].

In this work, we fabricated Ge/Si photodetectors operating in the near-IR spectral range and containing embedded layers of germanium nanoclusters as an active element. These layers of germanium nanoclusters were grown by molecular-beam epitaxy. The mean lateral size of germanium nanoclusters was approxi-

mately equal to 10 nm, their sheet density fell in the range from 0.3×10^{12} to 1.0×10^{12} cm^{-2} depending on the growth conditions, and the number of germanium layers in heterostructures varied from 12 to 36. In some cases, the density of germanium nanoislands was increased. For this purpose, the germanium nanoclusters were grown through the Volmer–Weber mechanism on a preliminarily oxidized silicon surface [3]. The image of an array of germanium nanoclusters formed at a temperature of 650°C on an oxidized Si(001) surface after the deposition of a germanium layer with a thickness of 3 ML is displayed in Fig. 1. According to Raman spectroscopy, the germanium content in nanoislands was approximately equal to 100% in the case when the germanium layers were grown at a low temperature (300°C) and decreased to 65% when the growth temperature increased to 650°C. The photoluminescence spectra of germanium nanoislands at T = 4.2 K exhibited maxima in the wavelength range of 1.5 μm. Photodetectors were fabricated in the form of *p–i–n* photodiodes or *n–p–n* bipolar phototransistors with a base containing an embedded Ge/Si multilayer heterostructure with germanium self-assembled nanoislands [4]. The photodetectors were produced either in the form of conventional vertical devices with illumination from the side of the *p–n* junction (or the Ge/Si heterojunction) or in the form of edge-illuminated lateral waveguides on silicon-on-insulator substrates [5].

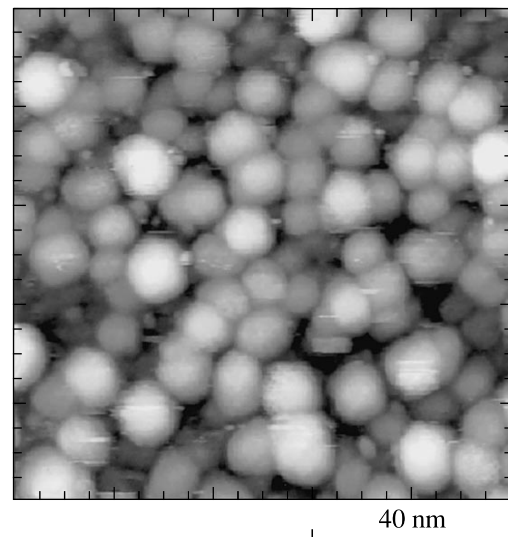

Fig. 1. STM image of an array of germanium nanoislands on the oxidized Si(001) surface. The deposition temperature of germanium is 650°C. The mean germanium coverage is 3 ML.

2. PHOTODIODES FOR ILLUMINATION FROM THE SIDE OF THE PLANE OF THE *p–n* JUNCTION

Initially, n^+–i–p^+ photodiodes based on Ge/Si multilayer heterostructures with 30 layers of germanium quantum dots were grown on KÉM-0.01 *n*-type substrates and were then illuminated from the side of the plane of the *p–n* junction. The dark current density in this device is virtually independent of the diode area and, at a reverse bias of 1 V, is found to be equal to 2×10^{-5} A/cm^2. This value is the lowest in the data on dark current densities reported thus far in the literature for Ge/Si photodetectors at room temperature. In the near-IR spectral range, the photodiodes are photosensitive up to wavelengths of 1.6–1.7 μm. For normal incidence of light on the photodiode, the quantum efficiency increases with an increase in the reverse bias U and reaches a maximum value of 3% for $U > 2$ V at a wavelength of 1.3 μm (Fig. 2). The observed increase in the quantum efficiency of photodiodes in an electric field can be explained as follows. It is known that the Ge/Si heterojunction belongs to type-II heterojunctions, because the lowest lying energy states of electrons and holes are localized in the conduction bands of silicon and germanium, respectively [6]. The absorption of photons whose energies are less than the band gap of silicon leads to a transition of electrons from the valence band of germanium to the conduction band of silicon. As a result, the conduction band of silicon contains free electrons, whereas the germanium nanoislands involve holes. Since the holes are localized in germanium quantum dots, the dominant contribution to the photocurrent in weak electric fields is made only by electrons. At high voltages, holes can easily tunnel from the states localized in germanium quantum dots to the valence band of silicon and, thus, contribute to the photocurrent. It is evident that the photoresponse reaches saturation in sufficiently strong electric fields when all the photoholes involved can leave the germanium quantum dots.

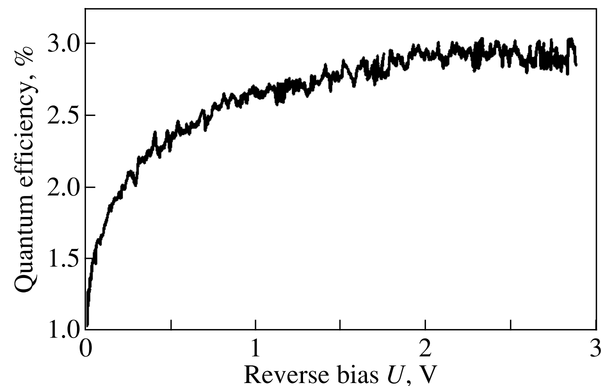

Fig. 2. Dependence of the quantum efficiency of the p^+–i–n^+ photodiode on the reverse bias at a wavelength of 1.3 μm for normal incidence of light.

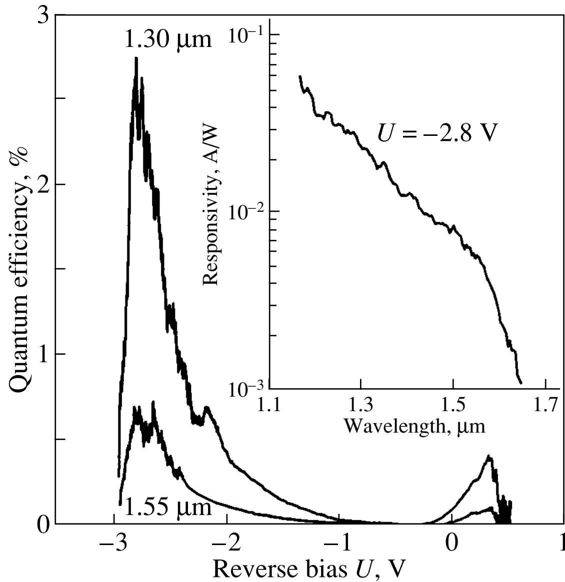

Fig. 3. Dependences of the quantum efficiency of the phototransistor on the reverse bias. The inset shows the spectral characteristic of the photoresponse at a reverse bias U = –2.8 V.

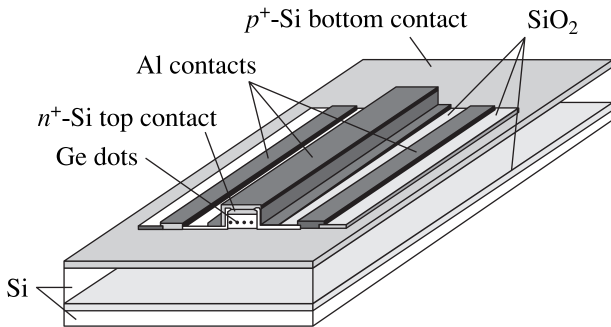

Fig. 4. Schematic drawing of the lateral photodetector fabricated on a silicon-on-insulator substrate.

3. THE n^+–p–n^+ BIPOLAR PHOTOTRANSISTOR FOR ILLUMINATION FROM THE SIDE OF THE PLANE OF THE p–n JUNCTION

As an alternative to the near-IR photodetector, we designed and fabricated n^+–p–n^+ bipolar phototransistors based on Ge/Si multilayer heterostructures in which 12 layers of germanium nanoclusters embedded in the p-Si region play the role of a floating base. The concentration of dopants (As, Sb) in the n^+-Si silicon regions was approximately equal to 10^{18} cm^{-3}, and the boron concentration in the p layer was 5×10^{16} cm^{-3}. The operation of this device is based on the decrease in the potential barrier for electrons between the n^+-Si heavily doped regions upon photogeneration of holes in germanium quantum dots due to interband optical transitions and a localized positive charge induced in these regions. The decrease in the potential barrier under illumination results in an increase in the injection current flowing from the emitter to the collector, i.e., in the generation of the photocurrent governed by the positive charge of the base. The phototransistors were also illuminated from the side of the plane of the p–n junction.

The spectral characteristic of the photoresponse and the dependence of the quantum efficiency on the reverse bias for one of these devices are shown in Fig. 3. The asymmetry of the photocurrent with respect to the applied bias is associated with the difference between the concentrations of dopants in the emitter and in the collector. In this case, the induced emission of holes from germanium nanoclusters to the valence band of silicon in an electric field brings about a decrease in the positive charge of the phototransistor base and, consequently, a decrease in the quantum efficiency of phototransformation at high voltages. It was found that the maximum quantum efficiency of the phototransistor at a wavelength of 1.3 μm is approximately equal to 3%, as is the case with p^+–i–n^+ photodiodes.

4. THE n^+–i–p^+ Ge/Si WAVEGUIDE PHOTODIODE

A further increase in the quantum efficiency was achieved for a waveguide photodetector whose operation is based on the effect of multiple internal reflection of light from the waveguide walls. Since the light rays should propagate along the plane of the integrated circuit on which all necessary elements of the fiber-optic communication line are assembled, this design of the device completely satisfies the requirement that the photodetector must be illuminated from the edge side [1]. The photosensitive layers were grown through molecular-beam epitaxy on silicon-on-insulator substrates in the form of lateral waveguides with illumination of the waveguide edge in the chip plane. The width of the waveguides was equal to 50 μm, and their length varied from 100 μm to 5 mm. The photodetectors were fabricated in the form of n^+–i–p^+ silicon photodiodes with 36 layers of germanium nanoislands embedded in the base region and separated by silicon interlayers 30 nm thick. This device combines a vertical photodiode and a lateral waveguide (Fig. 4). The silicon-on-insulator wafers were manufactured using the SMART CUT technique (Wafer World Inc.). The thickness of the cutoff silicon layer of the silicon-on-insulator structure was equal to 280 nm, and the thickness of the buried oxide layer was 380 nm. The upper silicon layer had the (100) orientation. Before performing molecular-beam epitaxy, the silicon layer was thinned down to 250 nm through thermal oxidation with subsequent removal of the oxide in a solution of hydrofluoric acid.

The dependences of the quantum efficiency η of the waveguide on the reverse bias at wavelengths of 1.30 and 1.55 μm for a waveguide length L = 4 mm are plot-

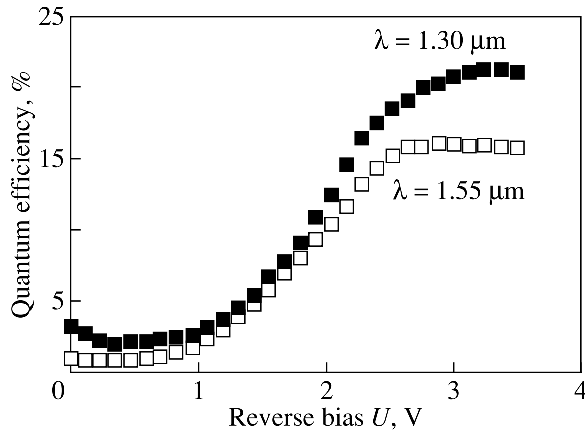

Fig. 5. Dependences of the quantum efficiency of the waveguide on the reverse bias at wavelengths of 1.30 and 1.55 μm for a waveguide length $L = 4$ mm.

ted in Fig. 5. It turned out that the maximum quantum efficiency is achieved for the structures with a waveguide length $L < 3$ mm at a reverse bias $U > 3$ V and can be as high as 21 and 16% at wavelengths of 1.30 and 1.55 μm, respectively. As can be seen from Fig. 5, the quantum efficiency of long waveguides reaches saturation. Most likely, this implies that the light penetrating through the photodetector edge and then passing along the germanium layers is completely absorbed.

5. CONCLUSIONS

Thus, we developed a technique for fabricating *p*–*i*–*n* silicon photodiodes and *n*–*p*–*n* silicon phototransistors with embedded arrays of germanium quantum dots for use in fiber-optic communication lines operating in the near-IR range (1.3–1.5 μm). In these devices, the sheet density of germanium quantum dots is of the order of 10^{12} cm^{-2} and their lateral size is less than 10 nm. For normal incidence of light on the photodetectors, the quantum efficiency can be as high as 3%. However, the use of waveguide photodetectors whose operation is based on the effect of multiple internal reflection and which were fabricated on silicon-on-insulator substrates made it possible to increase the quantum efficiency to 21 and 16% at wavelengths of 1.30 and 1.55 μm, respectively.

ACKNOWLEDGMENTS

This work was supported by the Council on Grants from the President of the Russian Federation for the Support of Young Doctors of Sciences (project no. MD-28.2003.02) and the International Association of Assistance for the Promotion of Cooperation with Scientists from the New Independent States of the Former Soviet Union (project no. INTAS 03-51-5051).

REFERENCES

1. H. Presting, Thin Solid Films **321**, 186 (1998).
2. W.-H. Chang, A. T. Chou, W. Y. Chen, H. S. Chang, T. M. Hsu, Z. Pei, P. S. Chen, S. W. Lee, L. S. Lai, S. C. Lu, and M.-J. Tsai, Appl. Phys. Lett. **83**, 2958 (2003).
3. A. I. Nikiforov, V. V. Ul'yanov, O. P. Pchelyakov, S. A. Teys, and A. K. Gutakovskiĭ, Fiz. Tverd. Tela (St. Petersburg) **46**, 80 (2004) [Phys. Solid State **46**, 77 (2004)].
4. A. I. Yakimov, A. V. Dvurechenskiĭ, A. I. Nikiforov, S. V. Chaĭkovskiĭ, and S. A. Teys, Fiz. Tekh. Poluprovodn. (St. Petersburg) **37**, 1383 (2003) [Semiconductors **37**, 1345 (2003)].
5. M. El Kurdi, P. Boucaud, S. Sauvage, G. Fishman, O. Kermarrec, Y. Campidelli, D. Bensahel, G. Saint-Girons, G. Patriarche, and I. Sagnes, Physica E (Amsterdam) **16**, 523 (2003).
6. A. I. Yakimov, N. P. Stepina, A. V. Dvurechenskii, A. I. Nikiforov, and A. V. Nenashev, Phys. Rev. B **63**, 045312 (2001).

Translated by O. Borovik-Romanova

Physics of the Solid State, Vol. 47, No. 1, 2005, pp. 38–41. Translated from Fizika Tverdogo Tela, Vol. 47, No. 1, 2005, pp. 41–43.
Original Russian Text Copyright © 2005 by Vostokov, Krasil'nik, Lobanov, Novikov, Shaleev, Yablonsky.

PROCEEDINGS OF THE CONFERENCE "NANOPHOTONICS 2004"
(Nizhni Novgorod, Russia, May 2–6, 2004)

Influence of the Germanium Deposition Rate on the Growth and Photoluminescence of Ge(Si)/Si(001) Self-Assembled Islands

N. V. Vostokov, Z. F. Krasil'nik, D. N. Lobanov, A. V. Novikov, M. V. Shaleev, and A. N. Yablonsky

Institute for Physics of Microstructures, Russian Academy of Sciences, Nizhni Novgorod, 603950 Russia

e-mail: shaleev@ipm.sci-nnov.ru

Abstract—The growth and photoluminescence of Ge(Si)/Si(001) self-assembled islands are investigated over a wide range of germanium deposition rates v_{Ge} = 0.1–0.75 Å/s at a constant growth temperature T_g = 600°C. Examination of the surface of the grown structures with an atomic force microscope revealed that, for all the germanium deposition rates used in the experiments, the dominant island species are dome islands. It is found that an increase in the deposition rate v_{Ge} leads to a decrease in the lateral size of the self-assembled islands and an increase in their surface density. The decrease in the lateral size is associated both with the increase in the germanium content in the self-assembled islands and with the increase in the fraction of the surface occupied by these islands. The observed shift in the position of the photoluminescence peak toward the low-energy range is also explained by the increase in the germanium content in the islands with an increase in the deposition rate v_{Ge}. *© 2005 Pleiades Publishing, Inc.*

1. INTRODUCTION

The formation of three-dimensional self-assembled islands due to the mismatch between the lattice parameters of germanium and silicon has been experimentally observed over wide ranges of growth temperatures and rates of deposition of germanium layers onto the Si(001) surface [1–3]. Recent investigations have demonstrated that the growth of Ge(Si)/Si(001) self-assembled islands at deposition temperatures of germanium $T_g \geq 600$°C begins with the formation of pyramidal islands on the surface of the structure under observation [1, 4]. An increase in the amount of deposited germanium leads to an increase in the size of these islands without changing their shape. After the pyramidal islands during growth reach a critical volume, they transform into dome islands [5], in which the angle between the lateral faces and the base is greater than that observed in the pyramidal islands. For the most part, the growth of dome islands occurs at the expense of an increase in their height, whereas the island size in the growth plane remains virtually unchanged. For growth temperatures $T_g \geq 600$°C and equivalent thicknesses of deposited germanium layers $d_{Ge} > 7$ ML (1 ML ≈ 0.14 nm), the dominant island species formed on the surface of the structure are dome nanoislands. A decrease in the deposition temperature of germanium layers in the range below 600°C brings about the formation of hut islands on the surface of the studied structure [6, 7], i.e., the formation of pyramidal quantum dots with a rectangular base extended along the [100] or [010] direction. At growth temperatures $T_g \leq 550$°C, the surface of the structure under investigation contains only hut islands, whereas dome islands are absent. Such a drastic change in the surface morphology in a narrow range of growth temperatures can be explained by the considerable increase in the surface density of islands with a decrease in the deposition temperature of germanium layers [8]. Since the surface density of islands is relatively high and the deposition temperature of germanium layers is rather low, the pyramidal islands can fall short of the critical size required for their transformation into dome islands.

In this work, we investigated how the surface density of islands grown at a germanium deposition temperature T_g = 600°C affects the surface morphology. The surface density of islands was controlled by varying the germanium deposition rate. Moreover, we analyzed the influence of the germanium deposition rate on the optical properties of the structures containing islands grown at a temperature of 600°C.

2. SAMPLE PREPARATION AND EXPERIMENTAL TECHNIQUE

The structures to be studied were grown on Si(001) substrates through molecular-beam epitaxy from solid sources. The structures intended for examination of the surface morphology consisted of a 150- to 200-nm-thick silicon buffer layer and a germanium layer with

1063-7834/05/4701-0038$26.00 © 2005 Pleiades Publishing, Inc.

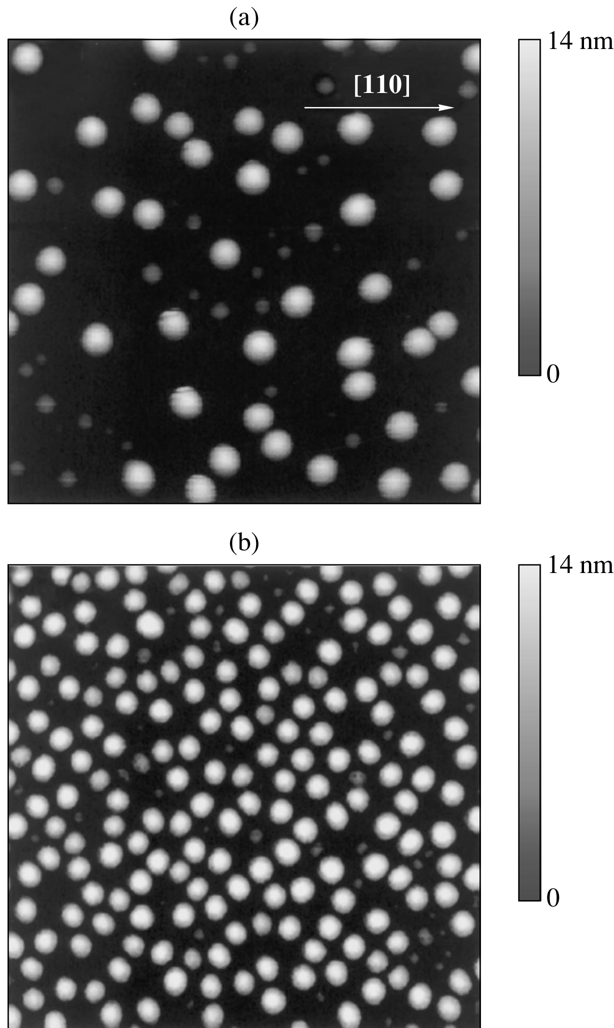

Fig. 1. AFM images of the surface of the structures grown at deposition rates v_{Ge} = (a) 0.1 and (b) 0.3 Å/s. The scanned area is 1 × 1 μm.

an equivalent thickness d_{Ge} = 7–8 ML. The germanium layer was grown at a temperature T_g = 600°C and at a germanium deposition rate v_{Ge} ranging from 0.1 to 0.75 Å/s. After the deposition of germanium, the structures used in optical observations were capped with a silicon cladding layer. The surface morphology of the structures thus prepared was investigated using a Solver P4 atomic force microscope (AFM) operating in a noncontact mode. The photoluminescence spectra were recorded on a BOMEM DA3.36 Fourier-transform spectrometer equipped with a cooled InSb detector. Optical pumping was performed using an Ar^+ laser (the 514.5-nm line).

3. RESULTS AND DISCUSSION

The AFM examination of the Ge(Si)/Si(001) self-assembled islands grown at the deposition temperature T_g = 600°C revealed that, for all germanium deposition rates in the range v_{Ge} = 0.1–0.75 Å/s, the surface of the structure under observation contains two types of islands, namely, pyramidal and dome islands (Fig. 1). It should be noted that the dome islands are dominant on the surface. The AFM images of the surface of the structures grown at germanium deposition rates v_{Ge} = 0.1 and 0.3 Å/s are displayed in Fig. 1. It is in this range of deposition rates (0.1–0.3 Å/s) that the changes in the island parameters are most pronounced (Fig. 1). As the deposition rate v_{Ge} increases from 0.1 to 0.3 Å/s, the surface density of dome islands increases by a factor of approximately 5 (from 4.4×10^9 to 2.2×10^{10} cm^{-2}), whereas their lateral size decreases by approximately 30% (from 90 to 63 nm) (Fig. 2). With a further increase in the germanium deposition rate (to 0.75 Å/s), the surface density and the lateral size of islands change insignificantly and gradually reach their steady-state values: the surface density becomes equal to 2.6×10^{10} cm^{-2}, and the lateral size falls in the range 60–70 nm.

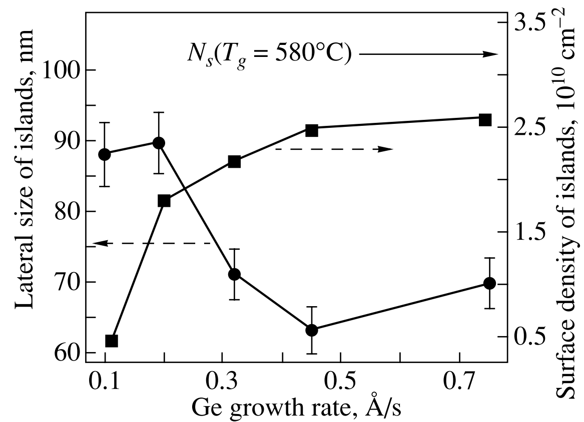

Fig. 2. Dependences of the surface density and the mean lateral size of islands on the growth rate of germanium layers.

An analysis of the surface density of self-assembled islands as a function of the germanium deposition rate v_{Ge} demonstrated that the maximum surface density obtained at T_g = 600°C is approximately 1.3 times less than the surface density of islands in the structures grown at T_g = 580°C (Fig. 2), i.e., at the temperature corresponding to the formation of hut islands on the surface of the structure. It is assumed that hut islands are not formed on the surface of the structures grown at T_g = 600°C even at high rates of deposition of germanium layers due to a lower surface density of islands in these structures.

The observed decrease in the lateral size of dome islands with an increase in the germanium deposition rate can be explained as resulting from the fact that the island composition depends on the germanium deposition rate. For a constant thickness of deposited germanium layers, an increase in the growth rate leads to a

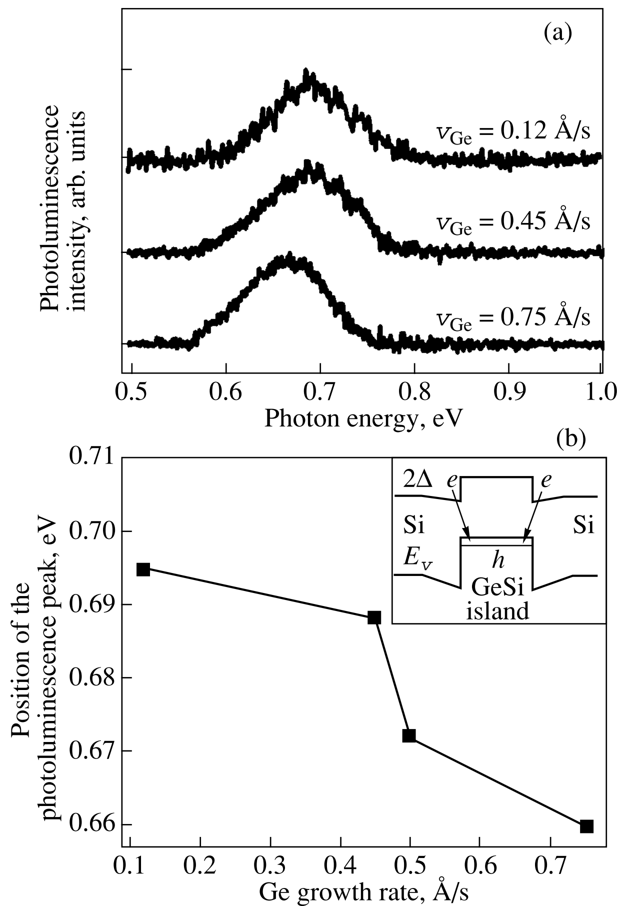

Fig. 3. (a) Photoluminescence spectra of the structures with islands formed at different growth rates of germanium layers. (b) Dependence of the position of the photoluminescence peak attributed to islands on the growth rate v_{Ge}. Photoluminescence spectra were recorded using an InSb detector at $T = 4$ K.

decrease in the time required for the complete formation of islands and, hence, to a decrease in the time it takes for silicon to diffuse into growing islands. A decrease in the deposition time of a germanium layer by approximately one order of magnitude with an increase in the deposition rate v_{Ge} from 0.1 to 0.75 Å/s can lead to an increase in the mean germanium content in the islands. According to the results of theoretical [5] and experimental [9] studies of Ge(Si)/Si(001) islands, an increase in the fraction of germanium in pyramidal and dome islands is accompanied by a decrease in the island size. Therefore, the increase in the germanium content in islands with an increase in the germanium deposition rate can be one of the possible reasons for the experimentally observed decrease in the lateral size of dome islands.

Another reason for the change in the lateral size of dome islands could be the increase in the fraction of the surface occupied by the islands as the deposition rate v_{Ge} increases (Fig. 1). Floro *et al.* [10] showed that, in the case where the islands occupy a sufficiently large fraction of the surface of the grown structures, elastic interactions between these islands can also lead to a decrease in the critical size of pyramidal islands and, hence, to a decrease in the lateral size of dome islands.

An analysis of the photoluminescence spectra of the grown structures revealed that the low-energy portions of the spectra of all the samples under investigation contain a broad photoluminescence peak (Fig. 3a). This photoluminescence peak is associated with the indirect optical transition between a hole located in an island and an electron of silicon at the type-II heteroboundary with the island [11] (see inset to Fig. 3b).

A comparison of the photoluminescence spectra of the structures grown at different deposition rates of germanium layers shows that, with an increase in the growth rate, the photoluminescence peak attributed to the islands shifts toward the low-energy range. In the case where the germanium deposition rate v_{Ge} increases from 0.1 to 0.75 Å/s, the shift in the position of the photoluminescence peak is approximately equal to 35 meV (Fig. 3b). This shift of the photoluminescence peak associated with the formation of islands is explained by the increase in the germanium content in the islands as the growth rate of germanium layers increases. As was noted above, an increase in the deposition rate v_{Ge} can result in an increase in the fraction of germanium in the islands due to the decrease in the time required for silicon to diffuse from the buffer layer into growing islands. An increase in the mean germanium content in the islands is accompanied by an increase in the gap between the valence bands of silicon and the island. In turn, this leads to a decrease in the energy of the indirect optical transition (see inset to Fig. 3b) [9] and, consequently, to the experimentally observed shift in the position of the photoluminescence peak associated with the islands toward the low-energy range as the deposition rate of germanium increases.

4. CONCLUSIONS

Thus, the growth and photoluminescence of Ge(Si)/Si(001) self-assembled islands grown at a temperature of 600°C were investigated as a function of the germanium deposition rate. It was demonstrated that, for all the germanium deposition rates used in the experiments (0.1–0.75 Å/s), the dominant island species are dome islands, even though their surface density increases significantly with an increase in the growth rate. The inference was drawn that the decrease in the lateral size of self-assembled islands with an increase in the deposition rate of germanium layers is caused by both the increase in the germanium content in these islands and by the increase in the fraction of the surface occupied by them. The observed shift in the position of the photoluminescence peak associated with the self-assembled islands toward the low-energy range with an increase in the germanium deposition rate was also

explained as resulting from the increase in the germanium content in the islands.

ACKNOWLEDGMENTS

This work was supported by the Russian Foundation for Basic Research (project no. 02-02-16792), the International Association of Assistance for the Promotion of Cooperation with Scientists from the New Independent States of the Former Soviet Union (project no. INTAS NANO 01-444), and the Ministry of Industry, Science, and Technology of the Russian Federation.

REFERENCES

1. T. I. Kamins, E. C. Carr, R. S. Williams, and S. J. Rosner, J. Appl. Phys. **81**, 211 (1997).
2. O. P. Pchelyakov, Yu. B. Bolkhovityanov, A. V. Dvurechenskiĭ, L. V. Sokolov, A. I. Nikiforov, A. I. Yakimov, and B. Voigtländer, Fiz. Tekh. Poluprovodn. (St. Petersburg) **34**, 1281 (2000) [Semiconductors **34**, 1229 (2000)].
3. M. W. Dashiell, U. Denker, C. Muller, G. Costantini, C. Manzano, K. Kern, and O. G. Schmidt, Appl. Phys. Lett. **80**, 1279 (2002).
4. A. V. Novikov, B. A. Andreev, N. V. Vostokov, Yu. N. Drozdov, Z. F. Krasil'nik, D. N. Lobanov, L. D. Moldavskaya, A. N. Yablonskiy, M. Miura, N. Usami, Y. Shiraki, M. Ya. Valakh, N. Mesters, and J. Pascual, Mater. Sci. Eng. B **89**, 62 (2002).
5. F. M. Ross, J. Tersoff, and R. M. Tromp, Phys. Rev. Lett. **80**, 984 (1998).
6. Y.-W. Mo, D. E. Savage, B. S. Swartzentruber, and M. G. Lagally, Phys. Rev. Lett. **65**, 1020 (1990).
7. O. G. Schmidt, C. Lange, and K. Eberl, Phys. Status Solidi B **215**, 319 (1999).
8. N. V. Vostokov, Z. F. Krasil'nik, D. N. Lobanov, A. V. Novikov, M. V. Shaleev, and A. N. Yablonskiĭ, Fiz. Tverd. Tela (St. Petersburg) **46** (1), 63 (2004) [Phys. Solid State **46**, 60 (2004)].
9. N. V. Vostokov, Yu. N. Drozdov, Z. F. Krasil'nik, D. N. Lobanov, A. V. Novikov, and A. N. Yablonskiĭ, Pis'ma Zh. Éksp. Teor. Fiz. **76**, 425 (2002) [JETP Lett. **76**, 365 (2002)].
10. J. A. Floro, G. A. Lucadamo, E. Chason, L. B. Freund, M. Sinclair, R. D. Twesten, and R. Q. Hwang, Phys. Rev. Lett. **80**, 4717 (1998).
11. V. Ya. Aleshkin, N. A. Bekin, N. G. Kalugin, Z. F. Krasil'nik, A. V. Novikov, V. V. Postnikov, and H. Seyringer, Pis'ma Zh. Éksp. Teor. Fiz. **67**, 46 (1998) [JETP Lett. **67**, 48 (1998)].

Translated by O. Borovik-Romanova

Physics of the Solid State, Vol. 47, No. 1, 2005, pp. 42–45. Translated from Fizika Tverdogo Tela, Vol. 47, No. 1, 2005, pp. 44–46.
Original Russian Text Copyright © 2005 by Vostokov, Drozdov, Krasil'nik, Kuznetsov, Novikov, Perevoshchikov, Shaleev.

PROCEEDINGS OF THE CONFERENCE "NANOPHOTONICS 2004"
(Nizhni Novgorod, Russia, May 2–6, 2004)

$Si_{1-x}Ge_x$/Si(001) Relaxed Buffer Layers Grown by Chemical Vapor Deposition at Atmospheric Pressure

N. V. Vostokov*, Yu. N. Drozdov*, Z. F. Krasil'nik*, O. A. Kuznetsov, A. V. Novikov*, V. A. Perevoshchikov**, and M. V. Shaleev***

** Institute for Physics of Microstructures, Russian Academy of Sciences, Nizhni Novgorod, 603950 Russia*

e-mail: anov@ipm.sci-nnov.ru

*** Research Physicotechnical Institute, Nizhni Novgorod State University, pr. Gagarina 23/5, Nizhni Novgorod, 603950 Russia*

Abstract—Relaxed step-graded buffer layers of $Si_{1-x}Ge_x$/Si(001) heterostructures with a low density of threading dislocations are grown through chemical vapor deposition at atmospheric pressure. The surface of the $Si_{1-x}Ge_x$/Si(001) ($x \sim 25\%$) buffer layers is subjected to chemical mechanical polishing. As a result, the surface roughness of the layers is decreased to values comparable to the surface roughness of the Si(001) initial substrates. It is demonstrated that $Si_{1-x}Ge_x$/Si(001) buffer layers with a low density of threading dislocations and a small surface roughness can be used as artificial substrates for growing SiGe/Si heterostructures of different types through molecular-beam epitaxy. © *2005 Pleiades Publishing, Inc.*

1. INTRODUCTION

The use of SiGe heterostructures in modern semiconductor technology provides a means for considerably improving the characteristics of already existing silicon-based devices and opens up possibilities for the design of new optoelectronic devices compatible with silicon technology. The acute problem associated with the design of the majority of devices based on SiGe heterostructures is to form a temperature-stable relaxed buffer layer from a $Si_{1-x}Ge_x$ heterostructure with a low density of threading dislocations (less than 10^6 cm^{-2}) and a small surface roughness [1]. One of the methods currently employed is to grow SiGe buffer layers of high quality through chemical vapor deposition [2]. Chemical vapor deposition provides growth of SiGe heterostructures at high deposition rates (10 μm/h or higher). This is especially important for the growth of SiGe step-graded buffer layers, in which the gradient of the germanium content does not exceed 10% per micrometer and whose total thickness reaches several micrometers. However, since the growth rate substantially decreases with a decrease in the temperature of the substrate, the use of chemical vapor deposition becomes efficient only at high growth temperatures. The growth of buffer layers at high temperatures can lead to a considerable increase in the surface roughness due to the crossover from two-dimensional growth to three-dimensional growth of the SiGe layer [3] and the development of a characteristic crosshatch pattern of the irregularities associated with the presence of a two-dimensional network of misfit dislocations in the structure [4]. The development of the surface roughness of the buffer layer has an adverse effect on the transport properties of the structures formed on this layer and hampers the use of lithography. Recently, Sawano *et al.* [5] proposed to use chemical mechanical polishing of the surface of SiGe buffer layers to decrease the surface roughness.

In this paper, we report experimental results obtained for chemical vapor deposition of $Si_{1-x}Ge_x$/Si(001) relaxed step-graded buffer layers with a low density of threading dislocations. It is shown that chemical mechanical polishing of the buffer layers leads to a substantial decrease in the surface roughness. The $Si_{1-x}Ge_x$/Si(001) buffer layers thus prepared can be used as artificial substrates for growing SiGe heterostructures of different types through molecular-beam epitaxy.

2. SAMPLE PREPARATION AND EXPERIMENTAL TECHNIQUE

Structures with $Si_{1-x}Ge_x$ buffer layers were grown on Si(001) substrates through hydride chemical vapor deposition under atmospheric pressure with the use of germane GeH_4 and silane SiH_4. The growth of the structures was carried out in a horizontal metallic water-cooled reactor equipped with a straight-channel graphite heater [6]. After preliminary chemical treatment, the silicon substrates were annealed in the reactor

1063-7834/05/4701-0042$26.00 © 2005 Pleiades Publishing, Inc.

in a flow of hydrogen at a temperature $T \sim 1200°C$. Then, a silicon buffer layer ~2 μm thick was deposited on the substrate. The $Si_{1-x}Ge_x$ step-graded buffer layers were grown at temperatures of 1025–920°C. The gradient of the germanium content was varied from 5 to 10% per micrometer. The germanium content in the growing layer was increased by decreasing the growth temperature and varying the ratio between the GeH_4 and SiH_4 fluxes. The growth rate was governed by the germanium content in the buffer layer and varied from 2 to 4 nm/s. The maximum germanium content in the buffer layers ranged from 5 to 45% for a total layer thickness varying from 2 to 7 μm. In order to decrease the surface roughness, the SiGe buffer layers were subjected to chemical mechanical polishing with a special solution consisting of hydrogen peroxide, glycerol, and Aerosil [7]. The thickness of the removed layer could be changed by varying the composition of the solution, the pressure applied to the structure, and the polishing time. This thickness was determined using x-ray diffraction analysis with weighing of the samples prior to and after polishing.

Then, SiGe/Si test structures were grown by molecular-beam epitaxy from solid sources on the relaxed buffer layers subjected to chemical mechanical polishing. Germanium and silicon were evaporated with the use of electron beam evaporators. The growth rates of SiGe layers varied in the range 0.01–0.10 nm/s. The density of threading dislocations in the buffer layers was determined by selective etching. X-ray diffraction analysis of the grown structures was carried out on a DRON-4 double-crystal diffractometer. The surface morphology of the structures was examined with the use of a Solver P4 atomic force microscope (AFM).

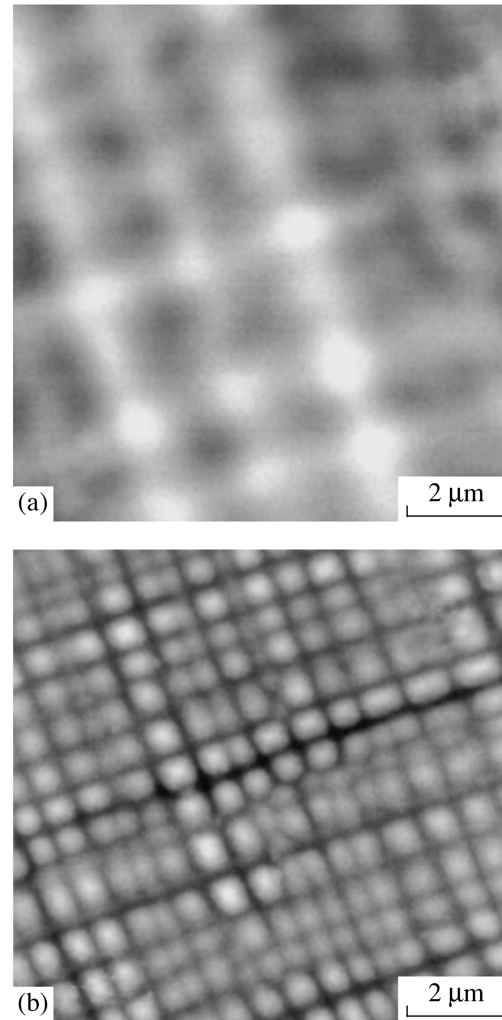

Fig. 1. AFM images of the surface of the $Si_{1-x}Ge_x$ buffer layers with a maximum germanium content x = (a) 20 and (b) 45%. The largest difference between the heights of the surface asperities: (a) 40 and (b) 200 nm.

3. RESULTS AND DISCUSSION

The ω–2Θ x-ray diffraction patterns of the SiGe step-graded buffer layers contain a peak attributed to the silicon substrate and peaks assigned to $Si_{1-x}Ge_x$ layers with different germanium contents. According to the x-ray diffraction analysis, the relaxation of elastic stresses in individual layers of the structures reached 90–100%. In $Si_{1-x}Ge_x$ buffer layers with a maximum germanium content $x < 30\%$, the density of threading dislocations, which was determined by selective etching, did not exceed 10^6 cm^{-2}. As was shown by Schaffler [1], the threading dislocations at these densities have no noticeable effect on the mobility of charge carriers in SiGe/Si heterostructures.

Examination of the SiGe buffer layers with atomic force microscopy revealed a characteristic crosshatch pattern of irregularities on the surface of the structure (Fig. 1). This pattern is associated with the existence of a two-dimensional network of misfit dislocations in the structure [8]. An increase in the maximum germanium content in the structure leads to an increase in the number density of misfit dislocations, which is necessary for relaxation of elastic stresses in the SiGe layer. As a result, the increase in the germanium content in the buffer layers is accompanied by a decrease in the period of the two-dimensional crosshatch network of irregularities and an increase in their amplitude (Fig. 1). In turn, this leads to an increase in the surface roughness of the structure. The root-mean-square roughness of the surface of the buffer layers, which was determined from the AFM images, increases from ~3 nm for buffer layers with a maximum germanium content $x \leq 10\%$ to 6–10 nm for structures with a maximum germanium content $x \sim 25\%$ (Fig. 2). It should be noted that these values are approximately one order of magnitude larger than the surface roughnesses of the Si(001) initial substrates and the silicon buffer layer grown on the Si(001) substrate through molecular-beam epitaxy

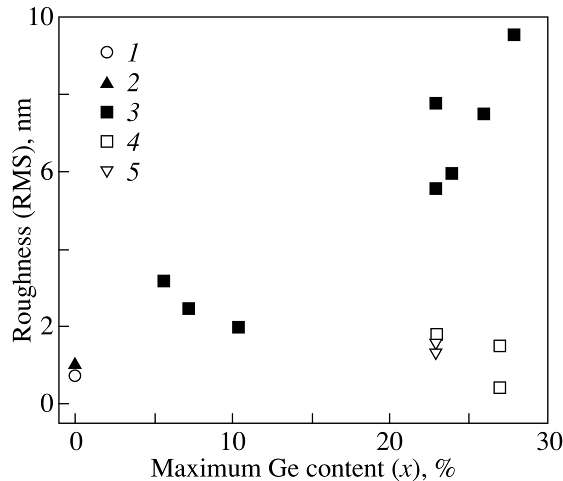

Fig. 2. Surface roughness of the SiGe structures as a function of the maximum germanium content in the buffer layer: (*1*) Si(001) substrate, (*2*) silicon buffer layer grown on a Si(001) substrate through molecular-beam epitaxy, (*3*) SiGe buffer layers grown by chemical vapor deposition, (*4*) SiGe buffer layers after chemical mechanical polishing, and (*5*) SiGe/Si structures grown by molecular-beam epitaxy on a SiGe buffer layers subjected to chemical mechanical polishing. The surface roughness was determined from AFM images 10 × 10 μm in size.

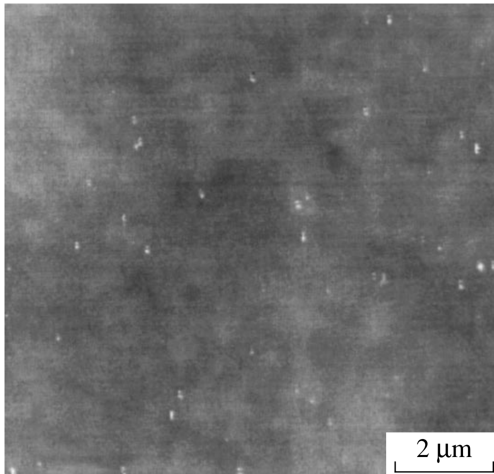

Fig. 3. AFM image of the surface of the $Si_{1-x}Ge_x$ buffer layer with the maximum germanium content x ~ 25% after chemical mechanical polishing. The largest difference between the heights of the surface asperities is 10 nm.

(Fig. 2). The large surface roughnesses of the SiGe/Si step-graded buffer layers can be explained by the high growth temperatures (T > 900°C) used in chemical vapor deposition.

In order to decrease the surface roughness, the structures were subjected to chemical mechanical polishing. We optimized the conditions of chemical mechanical polishing, which allowed us to obtain $Si_{1-x}Ge_x$ relaxed buffer layers with a maximum germanium content x ~ 25% and a small surface roughness. A comparison of the AFM images of the surfaces of the buffer layers prior to and after chemical mechanical polishing showed that, under optimum conditions, the polishing results in complete removal of the surface irregularities associated with the network of misfit dislocations (Figs. 1, 3). After chemical mechanical polishing, the surface roughness of buffer layers with a maximum germanium content $x < 30\%$ decreases by approximately one order of magnitude and becomes comparable to the surface roughness of the Si(001) initial substrates (Fig. 2).

The structures thus prepared with $Si_{1-x}Ge_x$/Si(001) relaxed step-graded buffer layers subjected to chemical mechanical polishing were used as artificial substrates for growing SiGe/Si heterostructures through molecular-beam epitaxy. In order to remove the contaminants introduced upon chemical mechanical polishing, the buffer layers were sequentially treated in organic and inorganic reagents prior to the growth. The final cleaning was achieved by annealing the structure at a temperature of 800°C in the growth chamber of the molecular-beam epitaxy apparatus. We grew test structures with an unstrained SiGe layer and a SiGe/Si lattice in which the composition and thicknesses of the layers were chosen in such a way as to ensure the mutual compensation of elastic stresses in one period of the structure. The growth temperature of the structures was equal to 600°C. The AFM investigations of the surface of the grown structures demonstrated that preliminary annealing of the buffer layers at a temperature of 800°C does to lead to repeated formation of the surface irregularities associated with the network of misfit dislocations. The surface roughness of the SiGe/Si heterostructures grown by molecular-beam epitaxy on SiGe buffer layers is comparable to the surface roughness of the Si(001) initial substrates (Fig. 2). The x-ray diffraction investigations showed a high degree of perfection of the structures grown by molecular-beam epitaxy.

ACKNOWLEDGMENTS

This work was supported by the Ministry of Industry, Science, and Technology of the Russian Federation; the Russian Foundation for Basic Research, (project no. 02-02-16792); and the BRHE program, (project no. Y1 P-01-05).

REFERENCES

1. F. Schaffler, Semicond. Sci. Technol. **12**, 1515 (1997).

2. D. J. Paul, A. Ahmed, N. Griffin, M. Pepper, A. C. Churchill, D. J. Robbins, and D. J. Wallis, Thin Solid Films **321**, 181 (1998).
3. H. Sunamura, Y. Shiraki, and S. Fukatsu, Appl. Phys. Lett. **66**, 953 (1995).
4. J. L. Liu, S. Tong, Y. H. Luo, J. Wan, and K. L. Wang, Appl. Phys. Lett. **79**, 3431 (2001).
5. K. Sawano, K. Kawaguchi, T. Ueno, S. Koh, K. Nakagawa, and Y. Shiraki, Mater. Sci. Eng. B **89**, 406 (2002).
6. O. A. Kuznetsov, L. K. Orlov, Yu. N. Drozdov, V. M. Vorotyntsev, M. G. Mil'vidskiĭ, V. I. Vdovin, R. Carles, and G. Landa, Fiz. Tekh. Poluprovodn. (St. Petersburg) **27**, 1591 (1993) [Semiconductors **27**, 878 (1993)].
7. V. A. Perevoshchikov and V. D. Skupov, *Specific Features of Abrasive and Chemical Treatment of Semiconductor Surfaces* (Nizhegor. Gos. Univ., Nizhni Novgorod, 1992) [in Russian].
8. M. A. Lutz, R. M. Feenstra, F. K. LeGoues, P. M. Money, and J. O. Chu, Appl. Phys. Lett. **66**, 724 (1995).

Translated by N. Korovin

Physics of the Solid State, Vol. 47, No. 1, 2005, pp. 46–48. Translated from Fizika Tverdogo Tela, Vol. 47, No. 1, 2005, pp. 47–49.
Original Russian Text Copyright © 2005 by Antonov, Aleshkin, Gavrilenko, Krasil'nik, Novikov, Uskova, Shaleev.

PROCEEDINGS OF THE CONFERENCE "NANOPHOTONICS 2004"
(Nizhni Novgorod, Russia, May 2–6, 2004)

Negative Photoconductivity of Selectively Doped SiGe/Si : B Heterostructures with a Two-Dimensional Hole Gas in the Middle-Infrared Range

A. V. Antonov*, V. Ya. Aleshkin*, V. I. Gavrilenko*, Z. F. Krasil'nik*, A. V. Novikov*, E. A. Uskova, and M. V. Shaleev***

** Institute for Physics of Microstructures, Russian Academy of Sciences, Nizhni Novgorod, 603950 Russia*
e-mail: aav@ipm.sci-nnov.ru
*** Research Physicotechnical Institute, Nizhni Novgorod State University, pr. Gagarina 23/5, Nizhni Novgorod, 603950 Russia*

Abstract—The spectra of lateral photoconductivity in selectively doped SiGe/Si : B heterostructures with a two-dimensional hole gas are analyzed. It is revealed that the lateral photoconductivity spectra of these heterostructures exhibit two signals opposite in sign. The positive signal of the photoconductivity is associated with the impurity photoconductivity in silicon layers of the heterostructures. The negative signal of the photoconductivity is assigned to the transitions of holes from the SiGe quantum well to long-lived states in silicon barriers. The position of the negative photoconductivity signal depends on the composition of the quantum well, and the energy of the low-frequency edge of this signal is in close agreement with the calculated band offset between the quantum-confinement level of holes in the quantum well and the valence band edge in the barrier.
© *2005 Pleiades Publishing, Inc.*

1. INTRODUCTION

In recent years, considerable interest has been expressed by researchers in the optical properties of SiGe nanostructures. Owing to the compatibility of these nanostructures with silicon technology, optoelectronic devices based on SiGe heterostructures with quantum wells and quantum dots can be integrated with signal processing circuits on a single chip. In this respect, investigation into the physical phenomena underlying the operation of SiGe photodetectors in different spectral ranges is of particular importance. A number of papers concerned with the study of absorption and photoconductivity in the middle-infrared range are discussed in [1–3]. Single and multiple quantum-well photodetectors operating in the middle-infrared range are described in [4, 5]. However, for the most part, these (and other) works have been reduced to an investigation of vertical charge transfer under the condition where the photoresponse is caused by the photoexcitation of charge carriers from a quantum well into barriers and the concentration of charge carriers contributing to the electric current increases. In this work, we studied the lateral photoconductivity spectra of selectively doped SiGe/Si : B heterostructures with a two-dimensional hole gas. The negative photoresponse observed in the middle-infrared range can be used to characterize SiGe heterostructures with quantum wells.

2. SAMPLE PREPARATION AND EXPERIMENTAL TECHNIQUE

The SiGe/Si : B heterostructures to be studied were grown through molecular-beam epitaxy on Si(100) substrates that were lightly doped with boron. The heterostructures contained a $Si_{1-x}Ge_x$ single quantum well in which the germanium content was varied from 12 to 30 at. %. The quantum-well width d_{QW} decreased from 25 to 10 nm with an increase in the germanium content and did not exceed the critical thickness of the epitaxially grown GeSi layer on the Si(001) substrate. Boron-doped silicon layers were located on both sides of the quantum well at a distance of 20 nm. The surface concentration of boron in the doped silicon layers was approximately equal to 4×10^{12} cm^{-2}. Strip ohmic contacts separated by a distance of 3 to 4 mm were deposited on the surface of a square sample. The lateral photoconductivity was measured on a BOMEM DA3.36 Fourier-transform spectrometer with a KBr beam splitter. A globar was used as a radiation source. The samples were placed in a light guide insert in a storage helium Dewar vessel.

3. RESULTS AND DISCUSSION

The measured dependences of the electrical resistance of the $Si_{1-x}Ge_x$/Si : B heterostructures on the reciprocal of the temperature are plotted in Fig. 1. At temperatures $T > 35$ K, boron impurities in the substrate

and in the doped silicon layers are ionized and the electrical resistance of the heterostructure is determined by free-carrier conduction. At low temperatures ($T < 35$ K), holes in bulk Si : B are frozen at acceptors. Since the quantum-well depth in the heterostructures under investigation is greater than the ionization energy of boron impurities (46 meV), the holes from the doped layers fill the quantum well and form a two-dimensional hole gas. Therefore, the electrical conductivity in the quantum well at low temperatures is virtually independent of temperature (Fig. 1). At a temperature of 4.2 K, the two-dimensional hole concentration, which was experimentally determined from the Hall effect, increases with an increase in the germanium content in the quantum well and ranges from 3×10^{11} to 10^{12} cm^{-2}. The hole mobilities, which were also obtained from measurements of the Hall effect, depend on the germanium content in the quantum well and are equal to 5500, 1500, and 300 cm^2/(V s) for $x = 0.12$, 0.21, and 0.30 at 4.2 K, respectively.

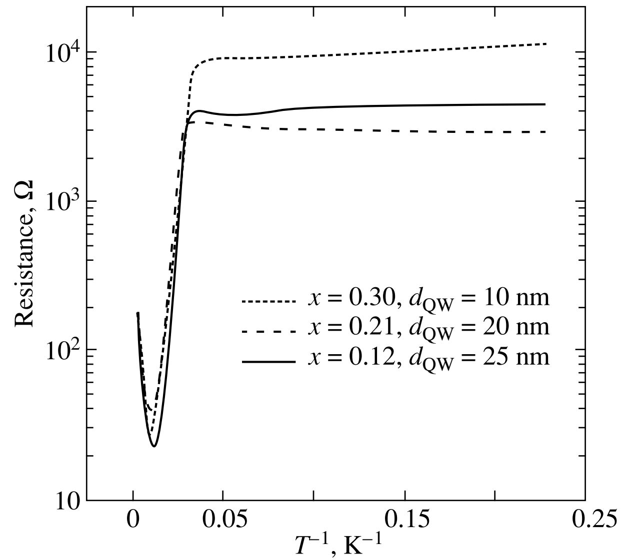

Fig. 1. Dependences of the electrical resistance of $Si_{1-x}Ge_x$/Si : B heterostructures with a two-dimensional hole gas on the reciprocal of the temperature.

The experimental photoconductivity spectra of the heterostructures with quantum wells are depicted in Fig. 2. For comparison, this figure also shows the photoconductivity spectrum of a Si : B ($x = 0$) bulk sample. As can be seen from the measured spectra, the photoconductivity spectrum of the heterostructures with quantum wells exhibits two signals of different origins. The first signal is represented by the impurity band associated with the photoionization of boron acceptors in silicon.

The characteristic features in the spectrum of the impurity photoconductivity in the Si : B bulk sample also clearly manifest themselves in the spectra of all the heterostructures with quantum wells and correspond to the photoresponse of the silicon barriers and the substrate. Apart from the band attributed to boron impurities, the photoconductivity spectra of the SiGe/Si : B heterostructures contain a broad band whose position depends on the germanium content in the quantum well. The intensity ratio of these two bands depends on the bias voltage applied to the sample. At a relatively low bias voltage (approximately 1 V), the intensity of the band associated with the photoconductivity of the quantum well is higher than that of the band assigned to the ionization of boron impurities in the silicon layers. However, with an increase in the bias voltage, the intensity of the band corresponding to impurities increases and, at high bias voltages, becomes higher than the intensity of the band attributed to the quantum well.

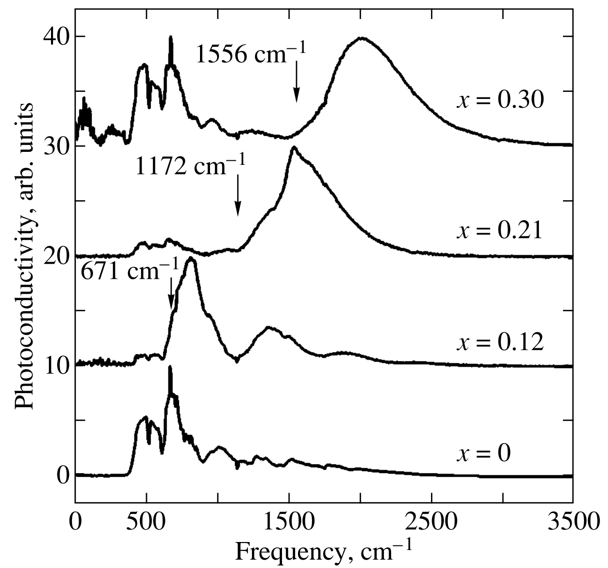

Fig. 2. Photoconductivity spectra of bulk Si : B ($x = 0$) and SiGe/Si structures with different germanium contents in quantum wells at a temperature of 4.2 K. Arrows and numbers near the curves indicate the calculated positions and energies of the transition of holes from the valence band of the SiGe quantum well to the valence band of silicon, respectively.

The photoconductivity spectrum of the Si : B bulk sample (Fig. 2) is characterized by clearly pronounced oscillations. Similar oscillations (phonon replicas) were observed earlier by Bannaya *et al.* [6]. The period of these oscillations is determined by the energy of optical phonons in silicon (~60 meV). Furthermore, similar oscillations are also clearly seen in the photoconductivity spectrum of the heterostructure with $Si_{1-x}Ge_x$ quantum wells at a germanium content $x =$ 0.12. The minimum observed in the photoconductivity spectrum at a frequency of 1200 cm^{-1} can be hypothetically associated with the absorption of light by oxygen in silicon.

As the germanium content increases, the band assigned to the quantum well in the photoconductivity spectrum shifts toward the high-energy range. In Fig. 2,

the arrows indicate the calculated positions of the quantum-confinement level in the quantum well for each sample. The calculations were performed using a 6×6 Hamiltonian. This Hamiltonian describes the subbands of heavy, light, and spin-split-off holes. It can be seen that the calculated energies are in good agreement with the energies of the low-frequency edge of the photoconductivity band.

Moreover, it was found that the photoconductivity signal associated with the quantum well (the characteristic relaxation time $\tau \sim 1$ ms) is more inertial than the photoconductivity signal of boron impurities in silicon ($\tau \sim 10$ μs). It should also be noted that the photoconductivity attributed to the quantum well is negative in sign; i.e., the electrical resistance of the sample increases under exposure to light. The opposite effect is observed for impurity photoconductivity; more precisely, the electrical resistance of the sample decreases upon generation of excess charge carriers that contribute to the electric current. It is interesting that, in the photoconductivity spectra of the heterostructure samples with quantum wells (Fig. 2), both of the photoconductivity signals have the same sign. This can be explained by the phase error introduced during data processing by the Fourier-transform spectrometer.

In our opinion, the high-frequency band in the photoconductivity spectra of the selectively doped SiGe/Si : B heterostructures with a two-dimensional hole gas should be assigned to the transitions of holes from the quantum well to long-lived states in the silicon barriers. A similar negative photoconductivity was revealed by Yakimov *et al.* [7] upon interband excitation of SiGe/Si heterostructures with quantum dots. The capture of holes in barrier states dominates over their return to the quantum well, and the long lifetime of holes in the silicon barrier can be governed by the tunneling processes. Therefore, the photoexcitation of holes leads to a decrease in their concentration in the quantum well, i.e., to a decrease in the electric current and the appearance of the negative photoconductivity signal.

4. CONCLUSIONS

Thus, in this work, we investigated the lateral photoconductivity in selectively doped SiGe/Si : B heterostructures with a two-dimensional hole gas. It was found that the mobility of the two-dimensional hole gas decreases as the hole concentration and the germanium content in quantum wells increase. The hole mobility determined from the measurements of the Hall effect at a temperature of 4.2 K in the heterostructure with a low germanium content ($x = 0.12$) in the quantum well is higher than 5×10^3 cm^2/(V s). The measured spectra of lateral photoconductivity in the heterostructures under investigation exhibit two signals of different origins. The positive signal of the photoconductivity is associated with the impurity photoconductivity in silicon layers of the heterostructures. The position of this signal does not depend on the parameters of the $Si_{1-x}Ge_x$ quantum well. The second signal of the photoconductivity is negative in sign, and its position depends on the composition of the quantum well. The energy of the low-frequency edge of the negative photoconductivity signal is in good agreement with the calculated energy of the quantum-confinement level of holes in the quantum well. The negative photoconductivity signal is assigned to the transitions of holes from the quantum well to long-lived states in silicon barriers. These transitions lead to a decrease in the concentration of charge carriers in the two-dimensional conducting channel and, consequently, to an increase in the electrical resistance of the heterostructure.

ACKNOWLEDGMENTS

This work was supported by the International Science and Technology Center (ISTC) (project no. 2206); the Russian Foundation for Basic Research (project nos. 02-02-16792, 03-02-16808); the Federal Program of the Ministry of Industry, Science, and Technology of the Russian Federation; and the Russian Federal Program "Integration."

REFERENCES

1. T. Fromherz, E. Koppensteiner, M. Helm, G. Bauer, J. F. Nützel, and G. Abstreiter, Phys. Rev. B **50** (20), 15073 (1994).
2. T. Fromherz, P. Kruck, M. Helm, G. Bauer, J. F. Nützel, and G. Abstreiter, Appl. Phys. Lett. **68** (25), 3611 (1996).
3. E. Dekel, E. Ehrenfreund, D. Gershoni, P. Boucaud, I. Sagnes, and Y. Campidelli, Phys. Rev. B **56** (24), 15734 (1997).
4. R. P. G. Karunasiri, J. S. Park, and K. L. Wang, Appl. Phys. Lett. **59** (20), 2588 (1991).
5. D. Krapf, B. Adoram, J. Shappir, A. Sa'ar, S. G. Thomas, J. L. Liu, and K. L. Wang, Appl. Phys. Lett. **78** (4), 495 (2001).
6. V. F. Bannaya, E. M. Gershenzon, Yu. P. Ladyzhinskiĭ, and T. G. Fuks, Fiz. Tekh. Poluprovodn. (Leningrad) **7** (6), 1092 (1973) [Sov. Phys. Semicond. **7**, 741 (1973)].
7. A. I. Yakimov, A. V. Dvurechenskii, A. I. Nikiforov, O. P. Pchelyakov, and A. V. Nenashev, Phys. Rev. B **62** (24), R16283 (2000).

Translated by O. Borovik-Romanova

Physics of the Solid State, Vol. 47, No. 1, 2005, pp. 49–53. Translated from Fizika Tverdogo Tela, Vol. 47, No. 1, 2005, pp. 50–53.
Original Russian Text Copyright © 2005 by Yakunin, Al'shanskiĭ, Arapov, Neverov, Harus, Shelushinina, Kuznetsov, de Visser, Ponomarenko.

PROCEEDINGS OF THE CONFERENCE
"NANOPHOTONICS 2004"
(Nizhni Novgorod, Russia, May 2–6, 2004)

Galvanomagnetic Study of the Quantum-Well Valence Band of Germanium in the $Ge_{1-x}Si_x$/Ge/$Ge_{1-x}Si_x$ Potential Well

M. V. Yakunin*, G. A. Al'shanskiĭ*, Yu. G. Arapov*, V. N. Neverov*, G. I. Harus*, N. G. Shelushinina*, O. A. Kuznetsov, A. de Visser***, and L. Ponomarenko*****

** Institute of Metal Physics, Ural Division, Russian Academy of Sciences, ul. S. Kovalevskoĭ 18, Yekaterinburg, 620219 Russia*

e-mail: yakunin@imp.uran.ru

*** Research Physicotechnical Institute, Nizhni Novgorod State University, pr. Gagarina 23/5, Nizhni Novgorod, 603600 Russia*

**** Van der Waals–Zeeman Institute, University of Amsterdam, 1018 XE Amsterdam, The Netherlands*

Abstract—The structure of the quantum-well valence band in a Ge(111) two-dimensional layer is calculated by the self-consistent method. It is shown that the effective mass characterizing the motion of holes along the germanium layer is almost one order of magnitude smaller than the mass for the motion of heavy holes along the [111] direction in a bulk material (this mass is responsible for the formation of quantum-well levels). This creates a unique situation in which a large number of subbands appear to be populated at moderate values of the layer thickness d_w and the hole concentration p_s. The depopulation of two or more upper subbands in a 38-nm-thick germanium layer at a hole concentration $p_s = 5 \times 10^{15}$ m^{-2} is revealed from the results of measuring the magnetoresistance in a strong magnetic field aligned parallel to the germanium layers. The destruction of the quantum Hall state at a filling factor $\nu = 1$ indicates that the two lower subbands merge together in a self-formed potential profile of the double quantum well. It is demonstrated that, in a quasi-two-dimensional hole gas, the latter effect should be sensitive to the layer strain. © *2005 Pleiades Publishing, Inc.*

1. INTRODUCTION

Upon addition of one more degree of freedom to the two-dimensional motion of charge carriers in a layer, there arise favorable conditions for the occurrence of new physical phenomena in semiconductor heterosystems. For example, these conditions can either bring about the formation of new electronic phases in a multicomponent system residing in the quantum Hall state or extend the range of existence of the phases formed in a two-dimensional layer [1].

Such a crossover can be most efficiently accomplished by the following two methods. The first method consists in providing the possibility of populating upper quantum-well subbands. In particular, Sergio *et al.* [2] demonstrated that the population of at least eight subbands can be achieved in a wide parabolic potential well filled with electrons in which two- and three-dimensional states coexist. Gusev *et al.* [3] revealed a new collective state. It was found that collective states in a hole gas are more readily generated than those in an electron gas due to the greater mass of the holes [4].

The second method involves the fabrication of a system composed of interrelated two-dimensional layers in which new phenomena of the physics of multicomponent systems can manifest themselves owing to the formation of interlayer correlated states [1, 5]. It should be noted that the hole systems are more promising due to the greater mass of the holes, because, in this case, the interlayer tunneling that hinders the formation of interlayer correlated states is suppressed [6].

In this work, we investigated the magnetotransport phenomena in a quasi-two-dimensional hole gas in a germanium layer under conditions where a large number of subbands are populated. The system under consideration was doped selectively. This brought about a bending of the potential well bottom and the formation of a double-quantum-well profile. In turn, this resulted in separation of the hole gas into two two-dimensional sublayers in germanium layers of large thickness.

2. OBJECTS OF INVESTIGATION

The measurements were performed for a series of $Ge_{1-x}Si_x$/Ge/$Ge_{1-x}Si_x$ ($x \approx 0.1$) quantum wells grown on a (111) substrate. The central region of the $Ge_{1-x}Si_x$ barriers was doped with boron. The samples to be studied had different thicknesses d_w of the germanium layer and different hole gas densities p_s in this layer. The parameters of the samples are given in the table.

The quantum Hall effect was observed when the magnetic field was applied perpendicularly to the ger-

1063-7834/05/4701-0049$26.00 © 2005 Pleiades Publishing, Inc.

Parameters of the studied samples

Sample no.	d_w, nm	p_s, 10^{15} m^{-2}
578	8	1.4
1006	12.5	4.9
1123	23	3.4
1124, 1125	22	2.8
475a2	38	5
476b4	38	5.8

manium layers (Fig. 1). This effect was thoroughly analyzed in a number of our previous works (see, for example, [7]). This paper reports on the results of investigations performed for thicker layers and data on the magnetoresistance of the same samples in a magnetic field aligned parallel to the layers.

3. RESULTS AND DISCUSSION

The specific features of the quantum Hall effect at the filling factor $\nu = 1$ (i.e., the plateau at the Hall resistance $R_{xy} = 25.8$ kΩ and the corresponding minimum of the longitudinal magnetoresistance ρ_{xx}) are not observed for germanium layers with a thickness of greater than ~30 nm and are well pronounced for thinner layers. This behavior is associated with the formation of a double quantum well (see below).

The results of the measurements in a parallel magnetic field are presented in Fig. 2. For convenience of comparative analysis, the results obtained for different samples are normalized to the resistance ρ_0 in a zero magnetic field.

The parallel magnetic field has virtually no effect on the magnetoresistance of germanium layers with the smallest thickness (see the data in Fig. 2 for sample 578 with a layer thickness $d_w \approx 8$ nm). The results of the calculations (Fig. 3) clearly demonstrate that only one hole quantum-well subband is populated in this sample. Samples with thicker germanium layers possess a strong negative magnetoresistance (up to 40% of the zero-field resistance ρ_0). It is worth noting that the negative magnetoresistance of germanium layers with a moderate thickness ($d_w \approx 20$ nm) is described by a smooth curve, whereas the negative magnetoresistance of layers with the largest thickness (~40 nm; samples 475a2, 476b4) is characterized by a monotonic curve with local features [8]. These features are clearly seen after subtracting the monotonic background, which was simulated by a fourth-degree polynomial (see inset to Fig. 2). The experiments performed in tilted magnetic fields showed that the above features manifest themselves in a narrow range of tilt angles in the vicinity of the magnetic field aligned parallel to the germanium layers when Shubnikov–de Haas oscillations have already disappeared.

The quantum-well structure of the valence band in the Ge(111) layer was calculated by self-consistently solving a system of Schrödinger equations (on the basis of the Luttinger Hamiltonian with due regard for the exchange–correlation energy [9]) and Poisson equations. The main features of the calculated valence band structure can be summarized as follows (Figs. 3, 4).

(1) The subbands in the Ge(111) layer have a relatively simple structure. Although the shape of the subbands differs significantly from parabolic, they do not contain additional extrema. This is inconsistent both with the predictions made for an infinitely deep poten-

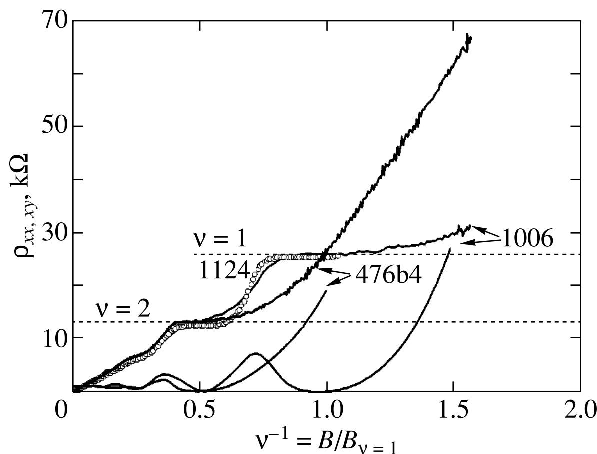

Fig. 1. Quantum Hall effect in germanium layers with thicknesses $d_w < 30$ nm (samples 1006, 1124) and $d_w > 30$ nm (sample 476b4).

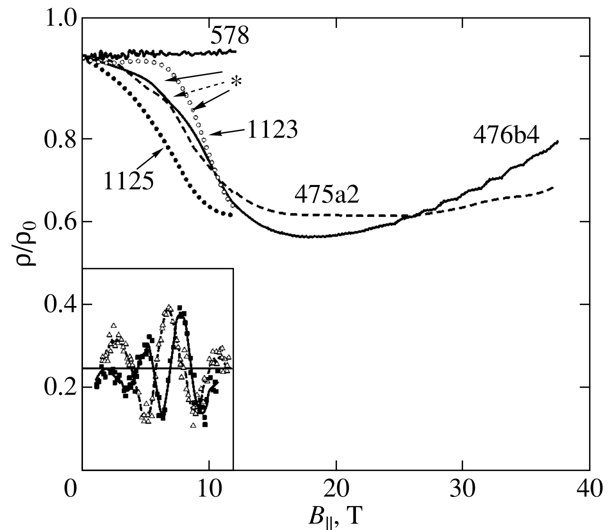

Fig. 2. Magnetoresistances of different samples in a parallel magnetic field at $T = 1.6$ K. The asterisk indicates the local features in the magnetoresistance of samples 475a2 and 476b4. The inset shows the magnetoresistances of samples 475a2 and 476b4 after subtracting the monotonic component.

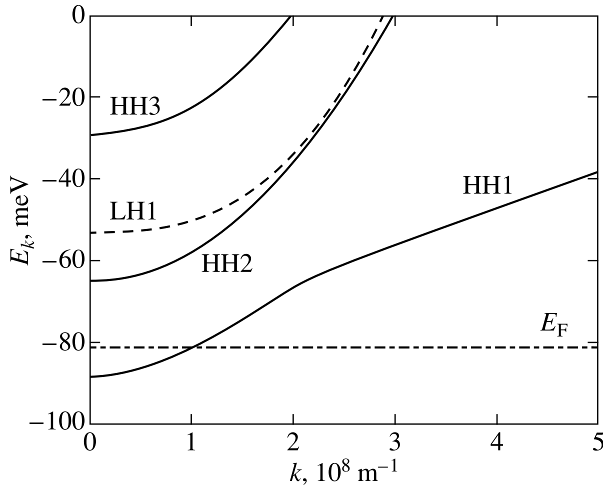

Fig. 3. Structure of the valence band in an 8-nm-thick germanium layer.

tial well [10] and with the results of the valence band calculations performed for a GaAs(100) layer (see, for example, [11]) but agrees with the results of the calculations performed by Winkler *et al.* [12] for Ge(100) layers.

(2) The energy dispersion $E_i(k_{\in(111)})$ for the extreme hole subband is characterized by a rather small effective mass m/m_0 = 0.053–0.062, which is close to the light-hole mass $m_{LH\langle 111\rangle}/m_0$ = 0.040 in bulk germanium [13]. The small effective mass is due to a considerable mixing of heavy- and light-hole bulk states in the wave function of the subband at $k_{\parallel} \neq 0$, whereas the states in the extreme subband at $k_{\parallel}$ = 0 correspond to heavy holes. Herein lies a radical difference between the valence and conduction bands. Actually, in the conduction band, the character of the wave functions in the subband remains almost unchanged even though $k_{\parallel}$ is varied, whereas the mass of electrons in the subbands is equal to the bulk mass and increases with an increase in $k_{\parallel}$, thus reflecting only an insignificant nonparabolicity due to the influence of the nearest bands. A combination of small masses of the holes for motion along the layer with large bulk masses of the heavy germanium holes, $m_{HH\langle 111\rangle}/m_0$ = 0.50 [13] (this mass is responsible for the formation of quantum-well levels), creates a unique situation where a large number of subbands are populated at moderate values of the hole concentration and the layer thickness.

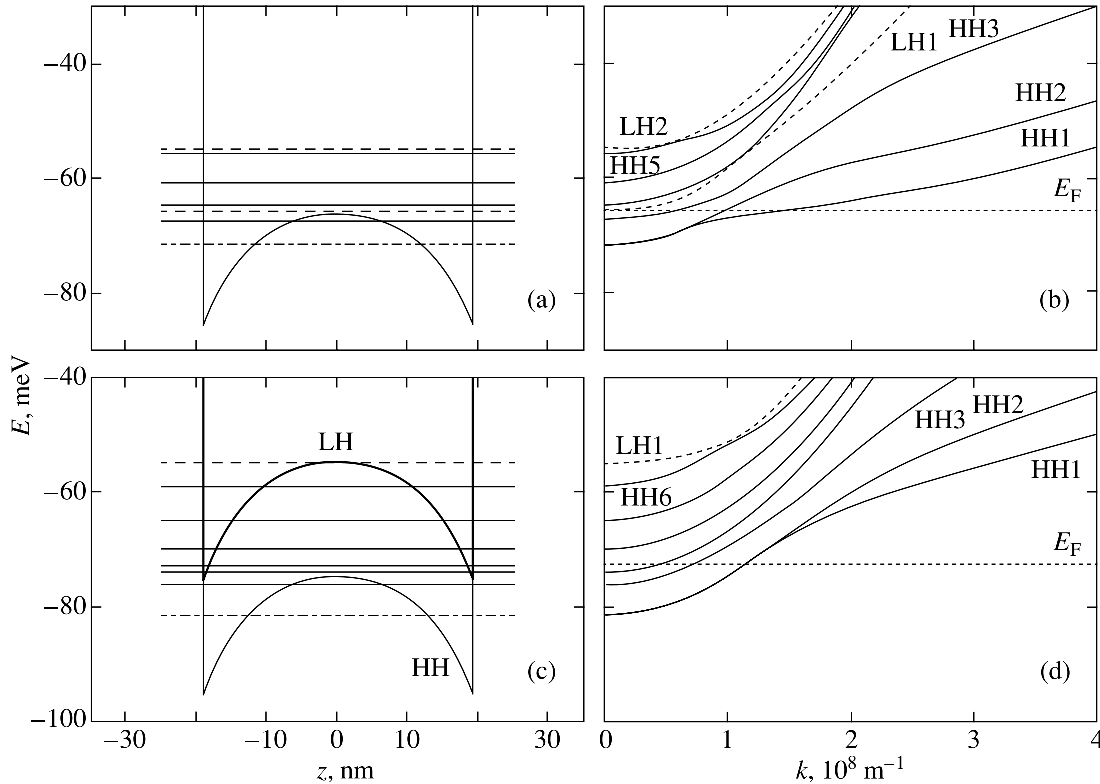

Fig. 4. Calculated valence band structure for sample 475a2. The energy increases deep into the valence band. The potential profiles and energy levels are calculated (a) without regard for the strain and (c) at the strain parameter ζ = 10 meV. The structures of the corresponding subbands and the Fermi levels are calculated (b) without regard for the strain and (d) at the strain parameter ζ = 10 meV.

According to the performed calculations, the fact that the specific features revealed in the quantum Hall effect disappear at the filling factor $\nu = 1$ in thick germanium layers can be explained by merging the two extreme subbands HH1 and HH2 in the self-formed double-quantum-well potential (Fig. 4a), but only in the case where the layer strain is taken into account. It can be seen from Figs. 4b and 4d that the two extreme subbands merge together only at small values of $k_{||}$ and diverge from each other with an increase in $k_{||}$. This is yet another specific feature in the quantum-well spectrum of the degenerate valence band. If two levels of the electron gas in the double quantum well were to coincide with each other at $k_{||} = 0$, their subbands would remain virtually merged with an increase in $k_{||}$ over the entire range of energies. In an unstrained germanium layer at energies in the vicinity of the Fermi level, these subbands are rather widely separated (Fig. 4b) and the gap at the Fermi level should bring about the formation of a quantum Hall state at the filling factor $\nu = 1$. However, the layer strain extends the range in which the subbands merge together and the subbands at a strain parameter $\zeta = 10$ meV remain merged at the Fermi level (Fig. 4d). Since the gap at the Fermi level is absent, the Landau levels of both subbands (i.e., in two sublayers) coincide in pairs and only even features of the quantum Hall effect should manifest themselves for the germanium layer as a whole (this is actually observed in the experiment).

The above splitting of the hole subbands stems from the fact that the fractions of the states of light holes, which are admixed to levels of symmetric and antisymmetric states, are different at energies close to and above the barrier in the double quantum well. The germanium layers in the $Ge_{1-x}Si_x$ alloy are uniaxially stretched along the growth direction due to the smaller lattice spacing. This leads to a shift of the light-hole subbands deep into the valence band. As a consequence, the nonparabolicity range of heavy-hole subbands is shifted to high energies and the range in which the HH1 and HH2 subbands merge together increases and reaches the Fermi level at $k_{||} = k_F$. Therefore, in the absence of strains in samples 475a2 and 476b4, there should exist a gap of ~2 meV at the Fermi level. At liquid-helium temperatures, this would reliably provide the formation of a quantum Hall state at the filling factor $\nu = 1$. However, for a strain parameter (half the strained gap) $\zeta > \sim 6$ meV, the range in which the subbands merge together reaches k_F. In this case, the state at the Fermi level appears to be either doubly degenerate or quadruply degenerate with allowance made for the spin. In the magnetic field, the levels remain doubly degenerate after spin splitting and only even quantum Hall states manifest themselves in the experiment. The interlayer correlation effects additionally contribute to the destruction of quantum Hall states at the filling factor $\nu = 1$ [1, 5, 14].

The results of the calculations demonstrate that, apart from the two extreme merged subbands, one or two higher lying subbands are populated in a 38-nm-wide potential well at a hole concentration $p_s \approx 5 \times 10^{15}$ m^{-2} (Fig. 4). We believe that the population of these upper subbands is responsible for the local features observed in the magnetoresistance $\rho(B_{||})$ of samples 475a2 and 476b4. Owing to the upward diamagnetic shift of the subbands, the Fermi level intersects them sequentially and each intersection manifests itself as a feature in the magnetoresistance due to the change in the density of states at the Fermi level and the suppression of intersubband scattering. The observed local features of the magnetoresistance (two, at the minimum) suggest that at least two upper subbands are populated in a zero magnetic field.

It should be noted that samples 1123 and 1124 with germanium layers of moderate thickness (~20 nm) also have a negative magnetoresistance of the same type and magnitude but without local features. This indicates that only one subband is depopulated in the parallel magnetic field. A decrease in the resistance $\rho(B_{||})$ of sample 1123 is observed in magnetic fields stronger than those for sample 1125 (Fig. 1). Since the former sample is characterized by a higher hole concentration and a wider potential well, the above difference can be explained by the fact that, for sample 1123 in a zero magnetic field, the Fermi level is located deeper in this upper subband.

In conclusion, we note that the possibility of populating many subbands in the studied samples suggests that this hole heterosystem is promising for the search for correlated states at ultralow temperatures.

ACKNOWLEDGMENTS

This work was supported by the Russian Foundation for Basic Research (project nos. 02-02-16401, 04-02-614) and the Russian Academy of Sciences within the program “Physics of Solid-State Nanostructures.”

REFERENCES

1. S. M. Girvin and A. H. MacDonald, *Perspectives in Quantum Hall Effects*, Ed. by S. Das Sarma and Aron Pinczuk (Wiley, New York, 1997), Chap. 5.
2. C. S. Sergio, G. M. Gusev, J. R. Leite, E. B. Olshanetskii, A. A. Bykov, N. T. Moshegov, A. K. Bakarov, A. I. Toropov, D. K. Maude, O. Estibals, and J. C. Portal, Phys. Rev. B **64**, 115314 (2001).
3. G. M. Gusev, A. A. Quivy, T. E. Lamas, J. R. Leite, A. K. Bakarov, A. I. Toropov, O. Estibals, and J. C. Portal, Phys. Rev. B **65**, 205316 (2002).
4. G. M. Gusev, A. A. Quivy, T. E. Lamas, J. R. Leite, O. Estibals, and J. C. Portal, *Workbook of International Conference EP2DS-15* (Nara, Japan, 2003), pp. 366, 762.

5. J. P. Eisenstein, *Perspectives in Quantum Hall Effects*, Ed. by S. Das Sarma and Aron Pinczuk (Wiley, New York, 1997), Chap. 2.
6. E. Tutuc, S. Melinte, E. P. De Poortrere, R. Pillarisetty, and M. Shayegan, Phys. Rev. Lett. **91**, 076802 (2003); W. R. Clarke, A. P. Macolich, A. R. Hamilton, M. Y. Simmons, M. Perrer, and D. A. Ritchie, *Workbook of International Conference EP2DS-15* (Nara, Japan, 2003), p. 187.
7. Yu. G. Arapov, V. N. Neverov, G. I. Harus, N. G. Shelushinina, M. V. Yakunin, and O. A. Kuznetsov, Zh. Éksp. Teor. Fiz. **123**, 137 (2003) [JETP **96**, 118 (2003)]; Nanotechnology **11**, 351 (2000); Fiz. Tekh. Poluprovodn. (St. Petersburg) **32**, 721 (1998) [Semiconductors **32**, 649 (1998)].
8. M. V. Yakunin, G. A. Alshanskii, Yu. G. Arapov, G. I. Harus, V. N. Neverov, N. G. Shelushinina, O. A. Kuznetsov, B. N. Zvonkov, E. A. Uskova, L. Ponomarenko, and A. de Visser, *Workbook of International Conference EP2DS-15* (Nara, Japan, 2003), p. 493; Physica E (Amsterdam) **22**, 68 (2004).
9. P. A. Bobbert, H. Wieldraaijer, R. van der Weide, M. Kemerink, P. M. Koenraad, and J. H. Wolter, Phys. Rev. B **56**, 3664 (1997).
10. M. I. D'yakonov and A. V. Khaetskiĭ, Zh. Éksp. Teor. Fiz. **82**, 1584 (1982) [Sov. Phys. JETP **55**, 917 (1982)].
11. U. Ekenberg and M. Altarelli, Phys. Rev. B **32**, 3712 (1985).
12. R. Winkler, M. Merkler, T. Darnhofer, and U. Rossler, Phys. Rev. B **53**, 10858 (1996).
13. J. C. Hensel and K. Suzuki, Phys. Rev. B **9** (10), 4219 (1974).
14. G. S. Boebinger, H. W. Jiang, L. N. Pfeifer, and K. W. West, Phys. Rev. Lett. **64**, 1793 (1990).

Translated by O. Borovik-Romanova

Physics of the Solid State, Vol. 47, No. 1, 2005, pp. 5–8. Translated from Fizika Tverdogo Tela, Vol. 47, No. 1, 2005, pp. 9–12.
Original Russian Text Copyright © 2005 by Steinman.

PROCEEDINGS OF THE CONFERENCE "NANOPHOTONICS 2004"
(Nizhni Novgorod, Russia, May 2–6, 2004)

Oxygen-Induced Modification of Dislocation Luminescence Centers in Silicon

E. A. Steinman

Institute of Solid State Physics, Russian Academy of Sciences, Chernogolovka, Moscow oblast, 142432 Russia
e-mail: steinman@issp.ac.ru

Abstract—Prospects for using the long-wavelength dislocation luminescence line *D*1 in silicon-based light-emitting diodes are considered. The standard spectral position of this line at 807 meV, rather than being canonic, depends on the morphology of the dislocation structure and the impurity environment of an individual dislocation. Data on the spectral distribution of luminescence intensity in the region of the *D*1 line have been analyzed in terms of the concentration of interstitial oxygen in a sample, plastic deformation parameters, and thermal treatment. The results obtained suggest that oxygen exerts a dominant effect on the spectral position of line *D*1 and luminescence intensity in its vicinity. It is shown that the probable structure of recombination centers can be described in terms of the donor–acceptor pair model, in which oxygen complexes serve as donors and the acceptors are structural defects in the dislocation core. © *2005 Pleiades Publishing, Inc.*

The increasing interest in light-emitting diodes (LEDs) has stimulated studies of the optical properties of silicon-based materials [1]. The most intriguing among the various approaches to the problem of silicon application for LED production is the use of deep states associated with impurities and structural defects. Even the very first attempt to fabricate a silicon LED with radiative recombination occurring at dislocation states resulted in the production of room-temperature luminescence [2].

It is customarily believed that dislocation photoluminescence (DPL) in silicon can be identified with four main lines, *D*1–*D*4 [3], peaking at 807, 873, 935, and 997 meV, respectively. Of particular interest from the standpoint of LED applications is the *D*1 line, because its energy coincides with the window of the highest transparency in fiber-optic communications and lies in the region of silicon transparency. In addition, line *D*1 features the best temperature stability. Note also that dislocation luminescence centers are extremely stable with respect to thermal treatment of a sample and, therefore, suffer practically no degradation. Despite the fairly lengthy investigation of the centers accounting for DPL, the microscopic nature of the long-wavelength lines remains largely unclear. Possible candidates for the sources of lines *D*1 and *D*2 have been proposed to be geometric features in the dislocation lines (kinks or steps) [4], the deformation potential [5], impurity–dislocation complexes [6], and dislocation crossing points [7, 8]. None of these models, however, provides an exhaustive description of the experimental behavior of the long-wavelength DPL lines. The present communication analyzes the available data and reports on additional studies performed to refine the role played by oxygen in the formation of DPL centers.

A gradual increase in dislocation density through an increase in the degree of plastic strain brings about a redistribution of the DPL spectral intensity into the region of the *D*1 line [9]. The relatively narrow *D*1 line, with a half-width on the order of 5–10 meV, transforms into a broad band (with a half-width of about 80 meV) consisting of several unresolved lines. Here and in what follows, the *D*1 band is taken to mean the spectral region of 750–850 meV. In Fz-Si, the spectral intensity is largely concentrated in the long-wavelength wing of *D*1. By contrast, in Cz-Si with dislocations, the short-wavelength *D*1 wing is more strongly pronounced and high-temperature annealing shifts the maximum of the broad band away from *D*1 toward higher energies [10]. Figure 1 presents typical DPL spectra obtained in different conditions. We readily see that, at comparatively low dislocation densities ($N_D \sim 10^6$ cm^{-2}), the spectrum is dominated by the narrow *D*1 and *D*2 lines with a half-width of the order of 5 meV. As N_D in crystals with a low interstitial oxygen content ($[O_i] \sim 10^{16}$ cm^{-3}) is increased to 10^8 cm^{-2} or more, the long-wavelength wing of the *D*1 band becomes stronger, whereas in crystals with a high oxygen content $[O_i] \sim 10^{18}$ cm^{-3}) the maximum of the DPL band is shifted shortward. It was shown in [11] that subjecting a Fz-Si sample preliminarily strained at 900°C to annealing at 450°C increases the long-wavelength wing of the *D*1 line peaking at about 780 meV in intensity. Because annealing at 450°C stimulates the formation of oxygen complexes exhibiting donor action, so-called thermal donors (TDs), the new DPL line was assigned to recombination at centers including TDs and acceptor dislocation states. A study of the temperature quenching of *D*1 and of the line at 780 meV, as well as of passivation by

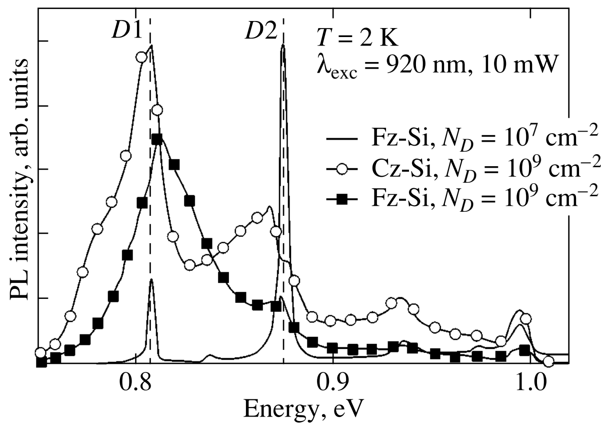

Fig. 1. DPL spectra obtained on Fz-Si samples with two different dislocation densities and on Cz-Si with a high dislocation density. Dashed lines identify the standard positions of the $D1$ and $D2$ lines.

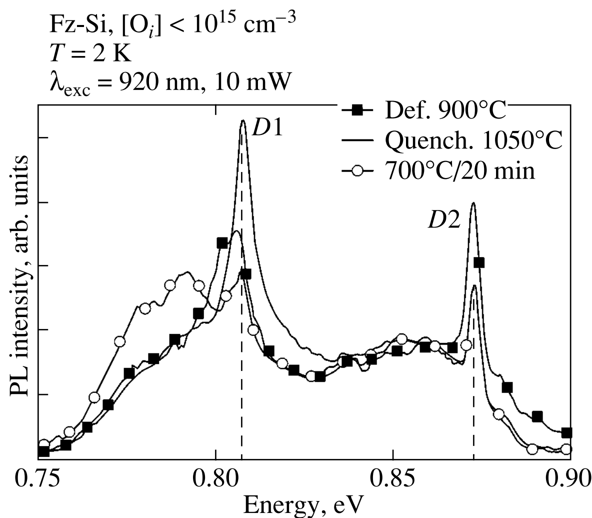

Fig. 2. DPL spectrum of a silicon sample with a low oxygen concentration obtained after deformation at 900°C, and its variation after quenching from 1050°C and subsequent annealing at 700°C. Dashed lines indicate the standard positions of the $D1$ and $D2$ lines. The spectra are normalized against integrated intensity.

atomic hydrogen, provided evidence supporting this assumption. Although the concentration $[O_i]$ in Fz-Si is not high enough for effective TD formation, it appears reasonable to assume that, near a dislocation, this concentration is substantially higher because of the pickup of oxygen by a moving dislocation [12].

Additional annealing of Cz-Si samples with dislocations was found to cause a more pronounced effect on the DPL lines [13]. In this case, the part played by oxygen diffusion to dislocations obviously increases. Indeed, it is known that extended defects are capable of accumulating impurity atoms because of the energy in the impurity–dislocation system being lower. In particular, silicon with dislocations typically exhibits an exponential decrease in the interstitial-oxygen concentration $[O_i]$ after thermal treatment at elevated temperatures [14]; this decrease occurs several orders of magnitude faster than it does in dislocation-free crystals. Precipitation of oxygen on dislocations is corroborated by the increase in the starting stress required to break away a dislocation [15]. One may conceive of a temperature at which inverse dissolution of precipitates is possible. This is indeed supported by the increase in the concentration $[O_i]$ in the course of annealing at a high temperature [16]. Hence, "evaporation" of oxygen from dislocations should bring about a decrease in the starting stress. It was shown in [17] that the temperature dependence of the starting dislocation stress in silicon has a break near 1100°C, which was interpreted as resulting from the dislocations breaking away from the oxygen atmosphere. A study of the variation of the PL spectra of plastically deformed silicon samples with annealing temperature and subsequent quenching also revealed that, starting from the quenching temperature of 1000°C, the $D1$ and $D2$ lines narrow [18] and the structureless background decreases simultaneously in intensity. Thus, one observes a correlation between the mechanical and optical studies of the properties of oxygen-decorated dislocations.

The reversible change of the PL intensity distribution near the $D1$ line observed to occur under annealing and quenching suggests the formation of impurity–dislocation complexes acting as recombination centers, in which oxygen plays the role of a dominant impurity. Thus, by introducing dislocations through plastic deformation of a sample, we obtain a set of dislocations decorated by oxygen to various degrees; so the PL spectrum of such a sample should represent a superposition of several PL bands. Conversely, annealing at a high temperature followed by quenching should bring about a partial freeing of dislocations from oxygen. Figure 2 illustrates the effect of quenching from 1050°C and subsequent annealing at 700°C on the DPL spectrum of a Fz-Si sample with a concentration $[O_i] \sim 10^{15}$ cm^{-3} that was previously deformed at 900°C. Quenching is seen to reduce the relative contribution of the long-wavelength wing. Subsequent annealing at 700°C gives rise to a sharp redistribution of the intensity to enhance the long-wavelength wing, which suggests reverse diffusion of oxygen atoms to the dislocations and the formation of oxygen–dislocation complexes. In addition to the redistribution of spectral intensity, quenching noticeably reduces the total PL intensity. A possible cause of this could be an increase in the defect concentration and, as a consequence, a decrease in the lifetime. Therefore, the spectra in Fig. 2 are normalized to the integrated PL intensity. Figure 3 shows the effect of post-quenching isochronous annealing on DPL in Fz-Si, which consists in a reverse increase in PL intensity. We see accelerated growth of

the long-wavelength wing of the $D1$ line, which indicates an enhancement of recombination via the oxygen–dislocation complexes.

Unlike Fz-Si, plastic deformation of samples with a high concentration [O_i] effected at a high temperature and a low rate[1] immediately produces a DPL band with a maximum shifted toward shorter wavelengths (Fig. 4). In this case, quenching also favors the appearance of the standard $D1$ line with a long-wavelength wing in the DPL spectrum. Here, we actually witness reconstruction of the local oxygen concentration in the vicinity of a dislocation, which can be attained only by annealing in samples with a low oxygen concentration (Fz-Si). Subsequent annealing restores, however, the original band with a shortward-shifted maximum (Fig. 4). We may assume that the short time of the prequenching annealing does not allow the restoration of a spatially uniform distribution of interstitial oxygen, with the result that reverse diffusion of oxygen to a dislocation takes place faster than in the original sample. The process of oxygen gettering by dislocations is, on the whole, not monotonic. It was shown in [19] that the rate of oxygen pickup near a dislocation is governed by parameters such as the local and volume-averaged concentration [O_i], the diffusion coefficient, and the rate of oxygen precipitation on the dislocation itself.

Figure 5 plots the dependence of this shifted band on pump power [20]. We see that increasing the pump power by a factor of 40 shifts the DPL band maximum to higher frequencies by more than 10 meV, with a further increase in the excitation power no longer being efficient. This indicates that the DPL band in Cz-Si may also derive from donor–acceptor-type recombination. The 100-mW pump power is apparently high enough to excite the nearest neighbor donor–acceptor pairs, so that a further increase in power up to 190 mW can neither boost the PL intensity nor shift the maximum.

Thus, our results show that oxygen plays a dominant role in DPL center formation. The recombination model proposed in [11] for the 778-meV band does not contradict the results obtained on Cz-Si samples, in which the main DPL peak is shifted shortward of $D1$. It is known that among TDs there are a number of oxygen clusters that contain two to ten oxygen atoms and have similar donor-level ground state energies of around 70 meV [21]. Taking all this into account, the fitting of the calculated curve to an experimental spectrum performed in [11] yielded an energy of ~360 meV for the acceptor state. The energy of the photon emitted in recombination at a donor–acceptor pair (considered without inclusion of the van der Waals term and phonon participation) is [22]

$$E(r) = E_g - (E_A + E_D) + e^2/\varepsilon r,$$

[1] A low deformation rate is understood to be the relative change of sample dimensions in a time of the order of 10^{-3} min.

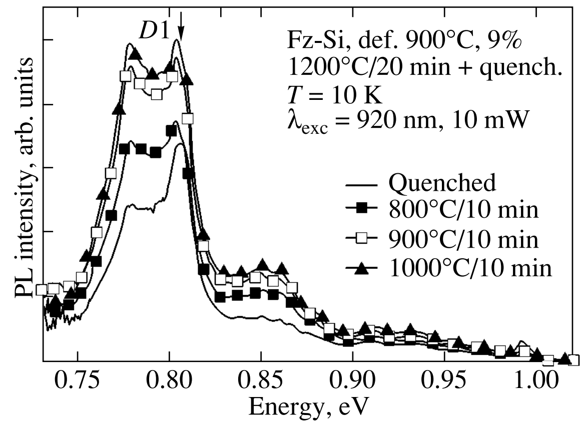

Fig. 3. DPL spectra of Fz-Si obtained after quenching from 1200°C and subsequent isochronous annealing.

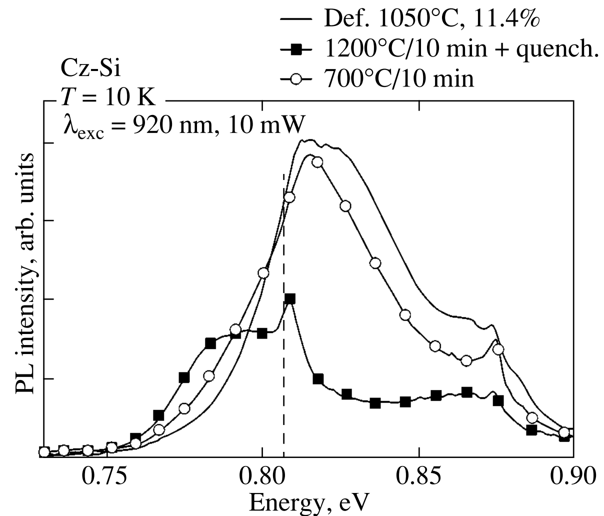

Fig. 4. DPL spectra of Cz-Si obtained after deformation, quenching, and subsequent annealing.

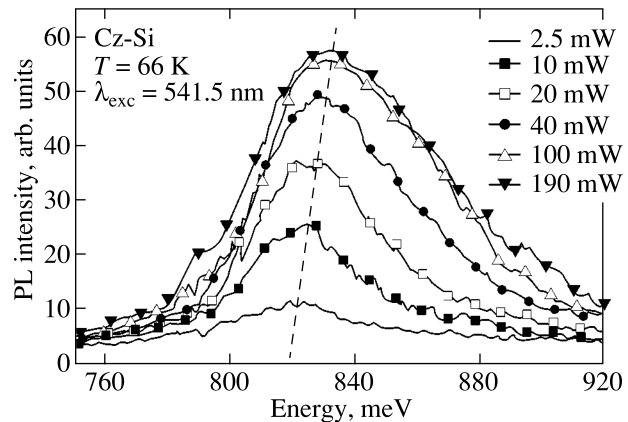

Fig. 5. Shift of the DPL band maximum with increasing pump power.

where E_g is the width of the indirect band gap in Si; E_A and E_D are the donor and acceptor ionization energies, respectively; r is the distance between the donor and acceptor; and ε is the low-frequency dielectric constant. Therefore, the Coulomb term for a photon energy of 830 meV (the maximum of the DPL band in Cz-Si) should be 95 meV, which corresponds to a donor–acceptor distance of ~1.5 nm [22]. This figure appears reasonable. Thus, the model of donor–acceptor recombination permits adequate description of the spectral distribution of intensity in the long-wavelength DPL wing.

To sum up, we have analyzed experimental data on the dependence of the DPL band position on oxygen concentration near a dislocation and shown that the experimental data can be consistently described by assuming donor–acceptor-type recombination in which oxygen clusters act as donors and the part of the acceptor is played by the dislocation defect responsible for the $D1$ line.

ACKNOWLEDGMENTS

This study was supported by INTAS (grant no. 01-0194) and the RAS program "New Materials."

REFERENCES

1. L. Pavesi, J. Phys.: Condens. Matter **15**, R1169 (2003).
2. V. V. Kveder, E. A. Steinman, S. A. Shevchenko, and H. G. Grimmeiss, Phys. Rev. B **51** (16), 10520 (1995).
3. N. A. Drozdov, A. A. Patrin, and V. D. Tkachev, Pis'ma Zh. Éksp. Teor. Fiz. **23**, 651 (1976) [JETP Lett. **23**, 597 (1976)].
4. M. Suezawa, Y. Sasaki, and K. Sumino, Phys. Status Solidi A **79**, 173 (1983).
5. Yu. Lelikov, Yu. Rebane, S. Ruvimov, D. Tarhin, A. Sitnikova, and Yu. Shreter, in *Proceedings of the 10th International Conference on Defects in Semiconductors*, Ed. by G. Davies, G. G. De Leo, and M. Stavola (Trans. Tech., Zurich, 1992); Mater. Sci. Forum **83–87**, 1321 (1992).
6. V. Higgs, E. C. Lightowlers, C. E. Norman, and P. C. Kightley, in *Proceedings of the 10th International Conference on Defects in Semiconductors*, Ed. by G. Davies, G. G. De Leo, and M. Stavola (Trans. Tech., Zurich, 1992); Mater. Sci. Forum **83–87**, 1309 (1992).
7. T. Sekiguchi and K. Sumino, J. Appl. Phys. **79**, 3253 (1996).
8. E. A. Steinman, V. I. Vdovin, T. G. Yugova, V. S. Avrutin, and N. F. Izyumskaya, Semicond. Sci. Technol. **14** (6), 582 (1999).
9. E. A. Steinman, V. V. Kveder, V. I. Vdovin, and H. G. Grimmeiss, Solid State Phenom. **69–70**, 23 (1999).
10. S. Pizzini, M. Guzzi, E. Grilli, and G. Borionetti, J. Phys.: Condens. Matter **12**, 10131 (2000).
11. E. A. Steinman and H. G. Grimmeiss, Semicond. Sci. Technol. **13**, 124 (1998).
12. O. V. Kononchuk, V. I. Orlov, O. V. Feklisova, E. B. Yakimov, and N. A. Yarykin, Fiz. Tekh. Poluprovodn. (St. Petersburg) **30** (2), 256 (1996) [Semiconductors **30**, 143 (1996)].
13. Yu. A. Osip'yan, A. M. Rtishchev, and E. A. Steinman, Fiz. Tverd. Tela (Leningrad) **26**, 1772 (1984) [Sov. Phys. Solid State **26**, 1072 (1984)].
14. I. Yonenaga and K. Sumino, in *Proceedings of Yamada IX Conference on Dislocations in Solids*, Ed. by H. Suzuki *et al.* (Univ. Tokyo Press, Tokyo, 1985), p. 385.
15. K. Sumino and H. Harada, Philos. Mag. A **44**, 1319 (1981).
16. I. Yonenaga and K. Sumino, J. Appl. Phys. **80** (2), 734 (1996).
17. B. Ya. Farber and V. I. Nikitenko, Phys. Status Solidi A **73**, k141 (1982).
18. A. N. Izotov, Yu. A. Osip'yan, and E. A. Steinman, Fiz. Tverd. Tela (Leningrad) **28**, 1172 (1986) [Sov. Phys. Solid State **28**, 655 (1986)].
19. S. Sekader, A. Giannattasio, R. J. Falster, and P. R. Wilshaw, Solid State Commun. **95–96**, 43 (2004).
20. A. J. Kenyon, E. A. Steinman, C. W. Pitt, D. E. Hole, and V. I. Vdovin, J. Phys.: Condens. Matter **15** (39), S2843 (2003).
21. M. Suesawa and K. Sumino, Phys. Status Solidi A **85**, 469 (1984).
22. U. O. Ziemelis and R. R. Parsons, Can. J. Phys. **59**, 784 (1981).

Translated by G. Skrebtsov

Physics of the Solid State, Vol. 47, No. 1, 2005, pp. 54–57. Translated from Fizika Tverdogo Tela, Vol. 47, No. 1, 2005, pp. 54–57.
Original Russian Text Copyright © 2005 by Valakh, Holiney, Dzhagan, Krasil'nik, Lytvyn, Lobanov, Milekhin, Nikiforov, Novikov, Pchelyakov, Yukhymchuk.

PROCEEDINGS OF THE CONFERENCE
"NANOPHOTONICS 2004"
(Nizhni Novgorod, Russia, May 2–6, 2004)

Raman Spectroscopy and Electroreflectance Studies of Self-Assembled SiGe Nanoislands Grown at Various Temperatures

M. Ya. Valakh*, R. Yu. Holiney*, V. N. Dzhagan*, Z. F. Krasil'nik, O. S. Lytvyn*, D. N. Lobanov**, A. G. Milekhin***, A. I. Nikiforov***, A. V. Novikov**, O. P. Pchelyakov***, and V. A. Yukhymchuk***

**Institute of Semiconductor Physics, National Academy of Sciences of Ukraine, pr. Nauki 45, Kiev, 03028 Ukraine*
e-mail: yukhum@isp.kiev.ua
***Institute of the Physics of Microstructures, Russian Academy of Sciences, Nizhni Novgorod, 603950 Russia*
****Institute of Semiconductor Physics, Siberian Division, Russian Academy of Sciences, pr. Akademika Lavrent'eva 13, Novosibirsk, 630090 Russia*

Abstract—SiGe nanoislands grown in a silicon matrix at temperatures of 300 to 600°C are studied using Raman spectroscopy and electroreflectance. For islands grown at relatively low temperatures (300–500°C), phonon bands are observed to have a doublet structure. It is shown that changes in the percentage composition, size, and shape of nanoislands and, hence, in the elastic stresses (depending on the growth temperature of the structures) have a significant effect on the energies of optical electronic interband transitions in the islands. As a consequence, the resonance conditions for Raman scattering also change. It is found that interdiffusion from the silicon substrate and the cover layer (determining the mixed composition of SiGe islands) is of importance even at low growth temperatures of nanostructures (300–400°C). *© 2005 Pleiades Publishing, Inc.*

1. INTRODUCTION

Semiconductor structures several nanometers in size typically exhibit quantum confinement effects. By varying the geometrical dimensions and configuration of nanometer-sized objects, one can control the properties of the crystal structure, primarily the energy spectra of carriers and phonons. Nanostructures can form in different ways, for example, through self-assembly of growing nanoislands via the Stranski–Krastanow mechanism [1]. Among semiconductor nanostructures, arrays of Ge and SiGe quantum dots (QDs) are of special interest [2], because they are employed in near-infrared optoelectronics and are compatible with silicon technology. In order to develop perfect devices, one needs information on the optical and electronic properties of QDs, which depend on various factors, such as their size, shape, density, homogeneity of spatial distribution, stresses, and percentage composition. These characteristics of QDs are significantly affected by interdiffusion during their growth, which is of importance not only for Si/Ge systems but also for QDs based on III–V and II–VI compound semiconductors.

As shown in [3], the percentage composition and stresses in QDs can be determined using Raman scattering. In most relevant studies, Raman scattering was used to investigate SiGe QDs produced at high temperatures (600–750°C) [2, 4, 5]. In this work, we studied SiGe QDs grown at lower temperatures (300–600°C).

2. EXPERIMENTAL TECHNIQUE

The structures under study were grown, using molecular-beam epitaxy (MBE), on a Si(001) substrate covered with a preliminarily grown buffer Si layer. After 8-ML-thick germanium was deposited on the buffer layer, the formed islands were covered with a 50-nm-thick Si layer. MBE was performed at substrate temperatures varied in the range 300–600°C from sample to sample. Raman spectra were taken with a DFS-24 spectrometer at room temperature using various lines of an Ar^+ laser for laser excitation. Electroreflectance spectra were measured in the range 1.8–3.7 eV at room temperature using the conventional electrolytic method. The modulating-voltage amplitude was 1 V, which corresponds to weak-field conditions. Therefore, the Aspnes formulas can be used to calculate the direct-transition energies [6].

3. RESULTS AND DISCUSSION

Figure 1 shows Raman spectra of SiGe nanoislands grown at temperatures of 300 to 600°C. These spectra exhibit specific features that differentiate them from the spectra taken by us from islands grown at higher temperatures (650–750°C) [5]. First, the bands corresponding to Ge–Ge and Si–Ge vibrations have a doublet structure. Second, resonance enhancement of the scattering intensity is observed. Third, there is a low-fre-

quency band (inset to Fig. 1) associated with interaction between acoustic phonons and electronic states localized within islands [7].

The high-frequency component of the Ge–Ge doublet for islands grown at a temperature of 300°C is located at 315 cm^{-1}. For an almost pure germanium island, such a high frequency indicates significant elastic compression caused by a 4% lattice mismatch between the island and the silicon substrate. As the island growth temperature increases to 400°C (let alone to 500°C), the high-frequency component of the Ge–Ge doublet in the Raman spectrum shifts to lower frequencies (see table). This shift can be due to a decreased stress in islands or an increased Si content in them. The change in stress can be associated with a decrease in the lattice mismatch between $Si_{1-x}Ge_x$ islands and the Si substrate and (or) relaxation through an increase in the ratio of the island height to its lateral dimensions (h/L). Our atomic-force microscopy (AFM) studies showed that, in the case where 8-ML-thick germanium was deposited at temperatures of 450 to 580°C and then not covered with silicon, the islands were hut clusters (Fig. 2a). Scanning tunneling microscopy studies have shown that, at lower temperatures of epitaxial growth (300–450°C), islands are also hut clusters [8, 9]. Since the ratio h/L cannot significantly change with increasing the temperature of epitaxial growth (and, in addition, the relaxation in silicon-covered islands is hindered by the cover layer), we arrive at the conclusion that the decrease in elastic stresses in islands is most likely caused by the increased Si content in them due to interdiffusion. This conclusion is also in agreement with electroreflectance measurements.

It is known [10] that, in unstressed $Si_{1-x}Ge_x$ solid solutions, the energies of direct transitions E_0(Si–Ge) and E_1(Si–Ge) increase as x decreases, with $E_0(x)$ varying most significantly. The transition energy E_0'(Si–Ge) varies with x only very slightly [10]. As follows from our experimental data, the direct-transition energy E_0(Si–Ge) increases monotonically with growth temperature despite the decreased stresses in islands (see table), which suggests that the Si content in the islands increases. The fact that interdiffusion in islands is noticeable at such low temperatures is also supported by photoluminescence data [9].

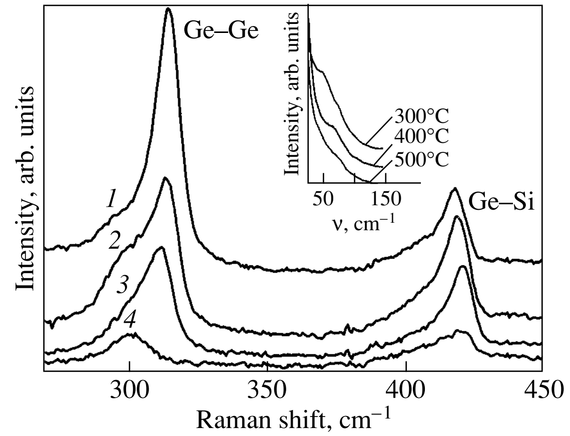

Fig. 1. Raman spectra of SiGe nanoislands grown at temperatures of (1) 300, (2) 400, (3) 500, and (4) 600°C. The inset shows the low-frequency region of the Raman spectra. Laser excitation was provided by the 514.5-nm line of an Ar^+ laser.

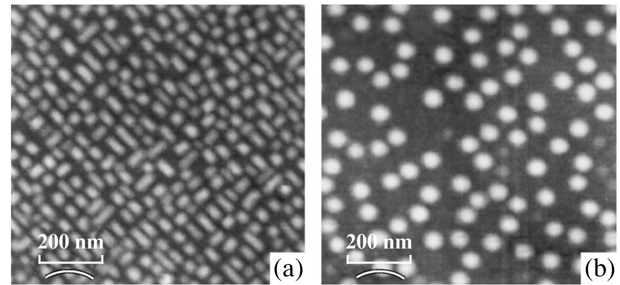

Fig. 2. AFM images of SiGe nanoislands grown at temperatures of (a) 500 and (b) 600°C.

We estimated the composition of islands forming at temperatures of 300 to 500°C under the assumption that the decreased stress in islands is due to Si diffusion into them. The x dependence of the frequency position of the Ge–Ge vibration band in the Raman spectrum is given by [11]

$$\omega_{GeGe} = 280.8 + 19.37x. \quad (1)$$

Including the dependence on elastic strain [12], we obtain

$$\omega_{GeGe} = 280.8 + 19.37x - 400\varepsilon(x), \quad (2)$$

Experimental values of the frequencies of Ge–Ge and Si–Ge Raman bands, composition x, elastic strain ε, and direct-transition energies E_0(Si–Ge), E_1(Si–Ge), and E_0'(Si–Ge)

T, °C	ν_{GeGe}, cm^{-1}	ν_{SiGe}, cm^{-1}	x_{Ge}	$\varepsilon_{\parallel}$	E_0(Si–Ge), eV	E_1(Si–Ge), eV	E_0'(Si–Ge), eV
300	315.0	418.6	0.98	–0.041	1.97	2.46	3.07
400	314.3	419.0	0.96	0.039	2.11	2.42	3.10
500	311.9	420.4	0.87	0.035	2.16	2.34	3.14
600	300.5	419.9	0.56	0.021	–	–	–

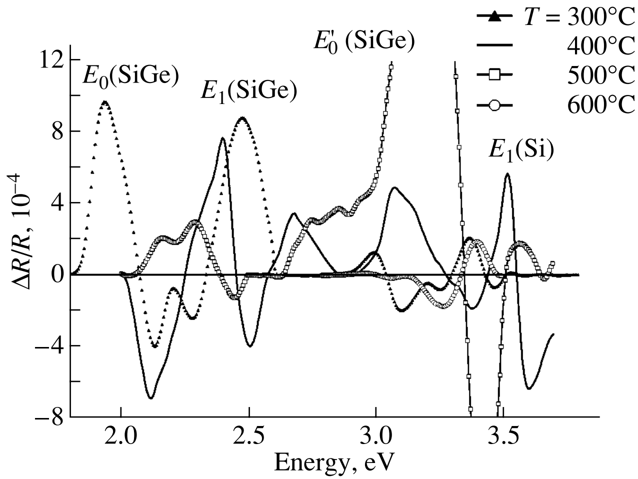

Fig. 3. Electroreflectance spectra of SiGe nanoislands grown at various temperatures.

where $\varepsilon(x) = (a_{SiGe}(x) - a_{Si})/a_{Si}$, with a_{SiGe} and a_{Si} being the lattice parameters of the islands and substrate, respectively. The results obtained (see table) suggest that Si diffusion into islands occurs even at low temperatures of epitaxial growth (300–500°C).

AFM studies of islands grown at 600°C and not covered with silicon showed that such islands have the form of pyramids and domes (Fig. 2b). Stress relaxation in them occurs through increasing both the Si content and the h/L ratio. Therefore, we used the $\omega_{GeGe}(x, \varepsilon)$ and $\omega_{SiGe}(x, \varepsilon)$ dependences to determine the content x and elastic strain ε in islands. Since the island density at a growth temperature of 600°C is an order of magnitude lower than that at 500°C (Fig. 2) and the Si content in islands is significantly higher, we can neglect the contribution from the interface between a SiGe island and the Si cover layer to Raman scattering. The frequency of the Si–Ge band for the solid solutions at hand in the range $0.25 \le x \le 0.9$ is closely fitted by

$$\omega_{SiGe} = 387 + 81(1-x) - 78(1-x)^2 - 575\varepsilon. \quad (3)$$

By solving the set of equations (2) and (3), we obtain $x = 0.56$ and $\varepsilon = -0.021$. For these values of x and ε, the direct-transition energy E_1(Si–Ge) for islands is much higher than the exciting photon energy (2.41 eV); therefore, the resonance condition for Raman scattering ceases to be satisfied. As a consequence, the Ge–Ge band intensity in the Raman spectrum decreases by approximately one order of magnitude in comparison with that for islands grown at 300°C.

The doublet structure of the Ge–Ge and Si–Ge bands can be caused by a difference in the shape of the islands, TO–LO phonon splitting at $\mathbf{k} = 0$ due to internal stresses in islands, or a change in the phonon frequency $\omega(\mathbf{k})$ at $\mathbf{k} \neq 0$ due to confinement effects. Let us discuss these causes further.

The difference in elastic stress between variously shaped islands even with the same composition can indeed result in different positions of a Raman band. However, for samples with nanoislands grown at relatively high temperatures (600–750°C), the doublet structure of Raman bands was not spectrally resolved even in the case where there were definitely two different shapes of islands [5]. For this reason, we determined the ensemble averages of the composition and stress for nanoislands. The doublet structure of the Ge–Ge and Si–Ge Raman bands is observed for structures grown at lower temperatures (300–500°C). If germanium is deposited to a nominal thickness of less than 8 ML at these temperatures, only hut clusters with rectangular rather than square bases form. In this case, the ratio of height to lateral dimension is direction-dependent, which results in an asymmetric stress distribution in islands and may manifest itself in Raman spectra as a doublet structure. However, the spacing between the frequency positions of the Raman doublet components is so large (7 to 10 cm^{-1}) that the elastic strain in different directions must differ by a factor of 2, which is unlikely.

Another cause of the doublet structure of Raman bands might be the breakdown of the selection rules for Raman scattering and the appearance of both the LO- and TO-phonon modes because of splitting of the F_{2g} phonon at $\mathbf{k} = 0$ under internal stresses in islands. However, our measurements of polarized Raman spectra showed that the intensities of both components of Ge–Ge vibrations vary in proportion to the polarization vectors of the incident and scattered light. This fact also contradicts the assumption that the doublet structure of Raman bands is due to LO–TO phonon splitting at $\mathbf{k} \neq 0$.

Finally, the low-frequency shoulder in the Ge–Ge Raman band can be due to size effects; the phonon frequency changes because nonzero phonon wave vectors other than $\mathbf{k} = 0$ become involved in Raman scattering. As shown in [13], in structures a few lattice parameters in size, a change of one or two monolayers in height can have a significant effect on the phonon frequency involved in Raman scattering because of the changed phonon wave vector. Calculations within a linear-chain model [13] showed that a change of 4 ML in height produces a frequency spacing of ~7 cm^{-1} between the corresponding Raman bands, which agrees with our experimental results. Furthermore, this assumption allows one to explain the shift of the Ge–Ge band to lower frequencies observed by us as the exciting photon energy was increased.

By measuring electroreflectance spectra, we determined the electronic transition energies for the samples under study. In the energy region up to 3.0 eV, the electroreflectance spectra for nanoislands grown at 300°C reveal two direct transitions, E_0 and E_1 [10, 14], with energies of 1.97 and 2.46 eV, respectively (Fig. 3). As the island growth temperature increases, the transition

energy E_0 increases slightly, which is due to the predominant effect of the increased Si content in nanoislands (see table). However, the transition energy E_1 decreases despite the increase in the Si content in the nanoislands. This behavior of the transition energy E_1 is associated with the competing effects of the stresses and composition. For islands grown at 400 and 500°C, the low-frequency shift due to a decrease in stress dominates over the high-frequency shift due to a decrease in x. Since the electroreflectance spectrum intensity was very low for islands grown at 600°C, we could not reliably estimate the transition energies and did not present them in the table.

As mentioned above, the observed changes in the direct-transition energy E_1(Si–Ge) manifest themselves in the Raman spectra. Indeed, the high intensity of the Ge–Ge and Si–Ge vibration bands for islands grown at temperatures of 300 to 500°C is due to a resonance enhancement of Raman scattering, because the exciting photon energy (2.41 eV) is close to the direct-transition energy E_1(Si–Ge).

ACKNOWLEDGMENTS

This study was supported by INTAS, NANO grant no. 01-444.

REFERENCES

1. V. A. Shchukin, N. N. Ledentsov, P. S. Kop'ev, and D. Bimberg, Phys. Rev. Lett. **75**, 2968 (1995).
2. K. Brunner, Rep. Prog. Phys. **65**, 27 (2002).
3. J. C. Tsang, P. M. Mooney, F. Dasol, and J. O. Chu, J. Appl. Phys. **75**, 8098 (1994).
4. J. L. Liu, J. Wan, Z. M. Jiang, A. Khitun, K. L. Wang, and D. P. Yu, J. Appl. Phys. **92**, 6804 (2002).
5. Z. F. Krasil'nik, P. M. Lytvyn, D. N. Lobanov, N. Mestres, A. V. Novikov, J. Pascual, M. Ya. Valakh, and V. A. Yukhymchuk, Nanotechnology **13**, 81 (2002).
6. D. E. Aspnes, Surf. Sci. **37**, 418 (1973).
7. A. G. Milekhin, A. I. Nikiforov, O. P. Pchelyakov, S. Schulze, and D. R. T. Zahn, Nanotechnology **13**, 55 (2002).
8. O. P. Pchelyakov, Yu. B. Bolkhovityanov, A. V. Dvurechenskiĭ, L. V. Sokolov, A. I. Nikiforov, A. I. Yakimov, and B. Voigtländer, Fiz. Tekh. Poluprovodn. (St. Petersburg) **34**, 1281 (2000) [Semiconductors **34**, 1229 (2000)].
9. M. W. Dashiell, U. Denker, C. Muller, G. Costantini, C. Manzano, K. Kern, and O. G. Schmidt, Appl. Phys. Lett. **80**, 1279 (2002).
10. J. S. Kline, F. H. Pollak, and M. Cardona, Helv. Phys. Acta **41**, 968 (1968).
11. H. K. Shin, D. J. Lockwood, and J.-M. Baribeau, Solid State Commun. **114**, 505 (2000).
12. P. H. Tan, K. Brunner, D. Bougeard, and G. Abstreiter, Phys. Rev. B **68**, 125302 (2003).
13. M. A. Araújo Silva, E. Riberio, P. A. Schulz, F. Cerdeira, and J. C. Bean, Phys. Rev. B **53**, 15871 (1996).
14. T. P. Pearsall, F. H. Pollak, J. C. Bean, and R. Hull, Phys. Rev. B **33**, 6821 (1986).

Translated by Yu. Epifanov

Physics of the Solid State, Vol. 47, No. 1, 2005, pp. 58–62. Translated from Fizika Tverdogo Tela, Vol. 47, No. 1, 2005, pp. 58–62.
Original Russian Text Copyright © 2005 by Cirlin, Tonkikh, Ptitsyn, Dubrovskiĭ, Masalov, Evtikhiev, Denisov, Ustinov, Werner.

PROCEEDINGS OF THE CONFERENCE "NANOPHOTONICS 2004"
(Nizhni Novgorod, Russia, May 2–6, 2004)

Influence of Antimony on the Morphology and Properties of an Array of Ge/Si(100) Quantum Dots

G. E. Cirlin[1, 2, 3], A. A. Tonkikh[1, 2, 3], V. E. Ptitsyn[1], V. G. Dubrovskiĭ[2], S. A. Masalov[2], V. P. Evtikhiev[2], D. V. Denisov[2], V. M. Ustinov[2], and P. Werner[3]

[1] *Institute of Analytical Instrumentation, Russian Academy of Sciences, Rizhskiĭ pr. 26, St. Petersburg, 198103 Russia*
e-mail: cirlin@beam.ioffe.rssi.ru
[2] *Ioffe Physicotechnical Institute, Russian Academy of Sciences, Politekhnicheskaya ul. 26, St. Petersburg, 194021 Russia*
[3] *Max Planck Institut für Mikrostrukturphysik, Halle (Saale), 06120 Germany*

Abstract—The morphological features of the quantum-dot formation in the (Ge,Sb)/Si system during molecular-beam epitaxy are studied using reflection high-energy electron diffraction and atomic-force microscopy. It is found that islands obtained by simultaneous sputtering of Ge and Sb have a higher density and are more homogeneous than in the case of sputtering of pure Ge. The regularities in the island formation are discussed in terms of the theory of island formation in systems with lattice mismatch. The field-emission properties of the grown structures are studied using a scanning electron microscope. The reduced brightness of (Ge,Sb)/Si nanostructures is estimated to be $B \sim 10^5$ A/(cm^2 sr V), which is an order of magnitude higher than the brightness of Schottky cathodes. © *2005 Pleiades Publishing, Inc.*

1. INTRODUCTION

Silicon is a basic material for use in the modern semiconductor industry; microelectronic devices are made primarily by using planar silicon technology. However, other applications of silicon-based structures are now also being intensively developed. Various Ge/Si materials hold promise for the development of light-emitting devices based on Si substrates. Germanium can be embedded in a Si matrix in the form of nanoislands, which form during molecular-beam epitaxy (MBE). It is commonly believed that, in this case, holes are localized in the germanium and electrons are located in the adjacent Si layer due to Coulomb attraction. Such structures are sources of recombination radiation, which is observed in photoluminescence spectra in the range 1.5–1.9 μm [1]. In multilayer structures with Ge quantum dots (QDs) embedded in a Si matrix, an array of nanoislands connected due to tunneling can be produced with the formation of a miniband for electrons [2]. In this case, the radiative recombination times can be significantly shorter than those in bulk silicon. Arrays of Ge nanoislands on Si substrates are also used in multiprobe field emitters [3]. For applications in instruments, arrays of nanoislands should be as uniform as possible, which calls for further investigation into this area. It is known that, in general, MBE-grown Ge islands form two phases on the (100) silicon surface. The phases differ in shape and size and are called hut and dome phases [4]. When grown through MBE on a substrate at temperatures of 550 to 600°C, both phases commonly coexist, with the consequence that the islands range widely in size. In this paper, we propose a technique that allows one to suppress the formation of dome clusters at temperatures of 550 to 600°C and to produce Ge islands that are more uniform in size and have a higher density.

2. EXPERIMENT

Growth experiments were conducted on a Riber Siva-45 and a Riber Supra MBE setup. Electron-beam evaporators were used as sources of Si and Ge atomic beams. The atomic beams were controlled by two quadrupole mass spectrometers tuned to masses of 28 and 74, respectively, and by quartz gauges. Prior to growth, a silicon surface was chemically treated by the RCA method. We used *p*- and *n*-Si(100) substrates with resistivities of 2–20 and 0.001–0.01 Ω cm, respectively. The surface oxide layer was removed from a Si substrate directly in the growth chamber, and then a 100-nm-thick buffer silicon layer was deposited, followed by deposition of a Ge layer with an equivalent thickness of 0.75 to 1.0 nm. The substrate temperature T_s was varied from 500 to 600°C. For a number of samples, the substrates were exposed to a Sb beam during the deposition of germanium, and for the other samples, only Ge was deposited on the Si substrates. The Ge growth rate was varied from 0.002 to 0.02 nm/s. The temperature of the Sb_4 source was kept fixed (450°C), which corresponded to an effective deposition rate of 0.2 ML/s (1 ML = 6.8×10^{14} cm^{-2}) on a cold substrate. Reflection high-

energy electron diffraction (RHEED) patterns showed that Ge islands formed in all samples. The as-grown samples were cooled rapidly to room temperature and removed from the vacuum chamber. The morphology of the structures was studied by atomic-force microscopy (AFM) in the noncontacting operation mode using an atmospheric microscope (Digital Instruments Inc.). The field-emission properties of Ge/Si nanostructures were studied using an LS SPM Omicron high-vacuum scanning tunneling microscope (STM).

3. RESULTS AND DISCUSSION

3.1. Morphological Characteristics of an Array of Ge/Si Quantum Dots

In order to investigate the dependence of the morphology of a Ge/Si QD array on the growth parameters, several series of samples, differing in Ge growth rate and substrate temperature, were grown in the presence and in the absence of antimony. Figure 1 shows a typical RHEED pattern taken from the Si(100) surface along the [01$\bar{1}$] direction at the instant of time at which the effective thickness of a deposited Ge layer was 0.7 nm. The substrate temperature was 550°C in this case. The observed bright sharp spots indicate the formation of three-dimensional islands on the substrate surface. In order to precisely determine the time the transition from two-dimensional to three-dimensional island growth occurs, we investigated the dynamics of the (01) reflection intensity in the *A*–*A*1 cross section (Fig. 1) using a technique described in [5]. It should be noted that, for all samples obtained in the presence of both Sb and Ge beams, the formation of three-dimensional islands started earlier than in the case of the deposition of pure germanium (all other growth conditions being equal), whereas the opposite situation was observed in [6], where Si(100) substrates were heavily misoriented and where a 0.5- to 1.0-ML-thick antimony layer was preliminarily deposited. The samples prepared in the presence and in the absence of a Sb beam differ significantly in morphology. As an example, Fig. 2a shows an AFM image of a Si(100) surface with Ge islands grown at a rate V_{gr} = 0.02 nm/s with T_s = 550°C. The islands are seen to have rectangular or square bases; they are typical hut clusters [3]. Figure 2b shows an AFM image of a Si(100) surface with Ge islands grown under the same growth conditions, except that the substrate surface was exposed to an antimony beam during the deposition of germanium. We see that there are evident distinctions. First, the hut phase of Ge islands disappears altogether in the presence of antimony. Second, the mean island dimensions increase: the base of the pyramid is D^* = 40 nm, and the height is H = 3 nm. The pyramid faces are {106} planes. Such islands do not belong to the dome phase, because RHEED patterns do not reveal a multifaceted structure of their faces. This conclusion is also confirmed by AFM data. The Fourier transform of an AFM image (Fig. 2b) indicates that pyramids (Ge islands) are

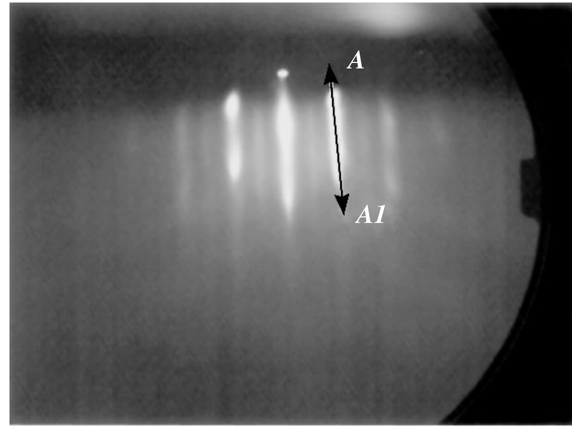

Fig. 1. RHEED pattern from a Si surface covered with germanium 0.7-nm thick.

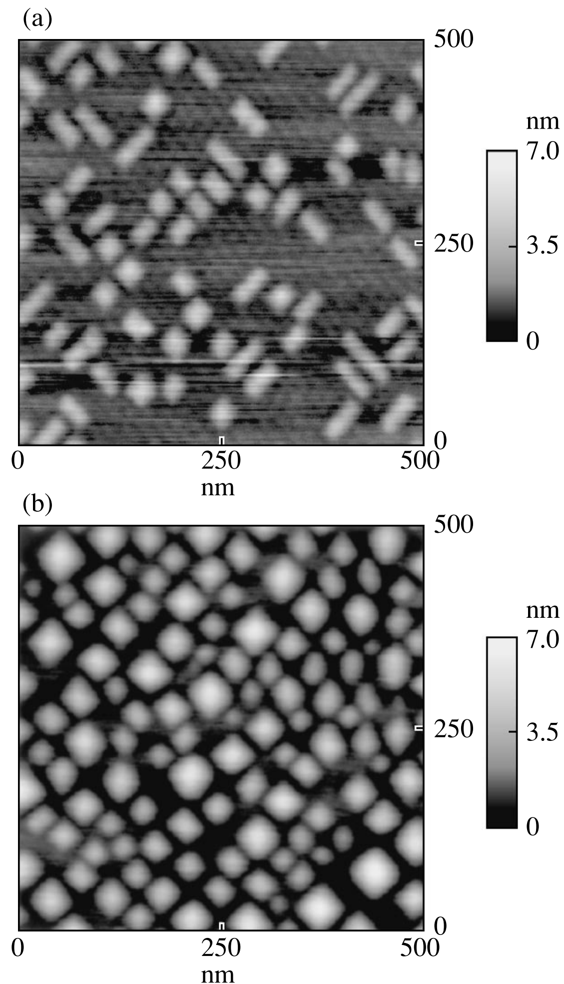

Fig. 2. AFM image of 0.85-nm-thick germanium (a) on a Si surface (Ge was deposited at a substrate temperature of 550°C at a rate of 0.02 nm/s) and (b) on a Si(100) surface (Ge was deposited in combination with Sb at a substrate temperature of 550°C at a rate of 0.02 nm/s).

Morphological characteristics of Ge/Si QD arrays obtained under various growth conditions

Sample no.	T_s, °C	Germanium		The presence of Sb	Hut clusters				Dome clusters			Pyramidal clusters			Total surface density, 10^{10} cm^{-2}
		thickness	V_{gr}, nm/s		rectangular base, nm		square base, nm	surface density, 10^{10} cm^{-2}	D^*, nm	H, nm	surface density, 10^8 cm^{-2}	D^*, nm	H, nm	surface density, 10^{10} cm^{-2}	
					X	Y									
1	500	0.85	0.002	–	97.0	17.0	23.2	8	53	15	6	–	–	–	8
2	500	0.85	0.004	–	73.8	17.2	22.0	11	47	16	4	–	–	–	11
3	500	0.85	0.008	–	52.5	14.0	18.0	15	–	–	–	–	–	–	15
4	500	0.85	0.015	–	42.2	13.7	19.5	18	–	–	–	–	–	–	18
5	550	0.85	0.002	–	75.5	22.3	27.0	2.1	64.5	9.3	20	–	–	–	2.3
6	550	0.85	0.005	–	57.0	25.0	23.7	4.1	57.2	7.4	32	–	–	–	4.4
7	550	0.85	0.01	–	63.0	22.7	34.0	–	–	–	–	–	–	–	2.8
8	550	0.85	0.02	–	64.0	26.3	35.7	–	–	–	–	–	–	–	3.3
9	600	0.75	0.02	–	–	–	–	–	73.5	10	50	–	–	–	0.5
10	500	0.7	0.02	+	–	–	–	–	–	–	–	17.3	1.2	22	22
11	550	0.85	0.002	+	–	–	–	–	–	–	–	24.0	2.6	14	14
12	550	0.85	0.02	+	–	–	–	–	–	–	–	40.0	3.1	5.2	5.2
13	550	1	0.02	+	–	–	–	–	–	–	–	45.3	4.0	5.6	5.6
14	600	0.75	0.02	+	–	–	–	–	–	–	–	40.6	1.5	1.3	1.3

ordered in real space along the ⟨010⟩ crystallographic directions [7].

The data on the grown samples are listed in the table and suggest the following conclusions:

(1) In all cases where the substrate surface was exposed to a Sb beam during the deposition of germanium, the density of the Ge island array was higher than in the samples grown without Sb. This result correlates with the RHEED data, according to which the effective thickness of the wetting layer is smaller in the case of simultaneous deposition of Ge and Sb.

(2) By increasing the Ge deposition rate and by deposing Sb and Ge simultaneously, one can suppress the formation of dome clusters on the Si surface and obtain a fairly dense array of clusters that are uniform in size.

(3) When pure germanium is deposited, the formation of either hut clusters with {105} faces or hut and dome clusters is observed. In the presence of Sb, clusters with {106} faces are formed. In the latter case, the typical lateral cluster size is less than one-half the characteristic size of dome clusters forming at the same effective thickness and surface temperature in the absence of Sb.

The results obtained can be interpreted in terms of a kinetic model developed in [8] for the formation of stressed islands in a heteroepitaxial system with lattice mismatch. According to theory, the quasi-steady-state lateral island dimension L_R (at a fixed ratio of the island height to the lateral dimension) can be written as [8]

$$L_R \propto \frac{(\Delta E_{\mathrm{surf}})^{3/2} D^{1/2}(T)}{(\Delta E_{\mathrm{elast}})^{1/2} T V^{1/2}}, \tag{1}$$

where D is the diffusion coefficient; T is the surface temperature; V is the beam velocity relative to the surface; and ΔE_{surf} and $\Delta E_{\mathrm{elast}}$ are the changes in the surface and elastic energies per unit area, respectively, due to the formation of islands.

The kinetic model predicts an increase in the island surface density and a decrease in the island size with an increase in the deposition rate at a constant surface temperature and a fixed effective thickness of the deposited layer. In the system under study, an increase in the growth rate causes an increase in the number of centers of fluctuating cluster nucleation. However, the characteristic size up to which clusters can grow before the Ge source is switched off is fairly small and dome clusters do not form. The Sb impurity causes both the energetic and kinetic properties of the system to change [9]. First, the atomic surface diffusion length decreases; therefore, the cluster growth rate also decreases as compared with its value in the case of deposition of pure Ge. Second, the activation barrier for cluster nucleation decreases; therefore, with all other factors being equal, this effect causes an increase in the number of clusters, a decrease in their mean size, and a decrease in the critical thickness for island formation.

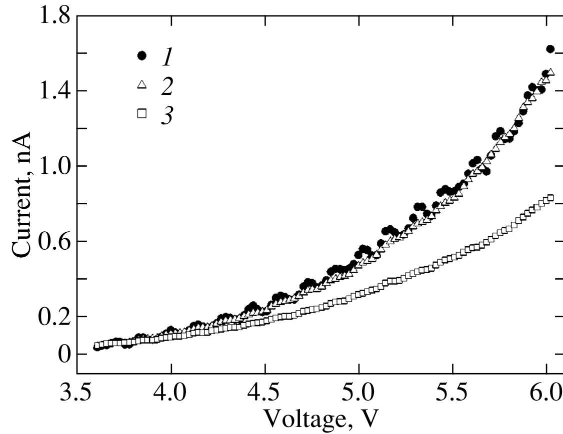

Fig. 3. Current–voltage characteristics of Ge/Si nanostructures. Scanned areas: (*1*) Ge wetting layer, (*2*) Ge wetting layer plus Ge QDs, and (*3*) a single Ge QD.

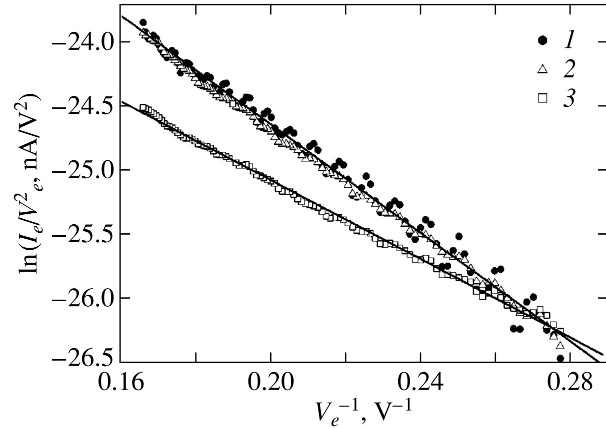

Fig. 4. Current-voltage characteristics of Ge/Si nanostructures drawn in Fowler–Nordheim coordinates. The curve notation is the same as in Fig. 3.

3.2. Field-Emission Properties

In order to develop field emitters based on nanostructures, a number of conditions must be satisfied, the main one of which is the presence of an array of uniformly distributed equal-sized nanoislands [10]. We studied the field-emission properties of an array of Ge/Si QDs using a sample whose morphological characteristics were similar to those of sample 14 (see table) and which was grown on an n^+Si(100) substrate. The surface density of crystalline Ge nanostructures was $\sim 1 \times 10^{10}$ cm^{-2}. For this density, in studying the field-emission properties of a chosen microscopic region, two characteristic directions of spatial scanning with the STM probe can be distinguished: (i) the direction along which the probe moves over the "smooth" substrate surface and (ii) the direction along which the probe moves predominantly over the tops of Ge nanocrystals.

By properly limiting the size of a scanned area, we can measure the field-emitted current from the top of a single QD.

To measure the current–voltage relation, a sawtooth voltage was applied between the probe and the substrate varying from a certain initial value V_0 (close to zero) to a maximum value V_m. The probe was moved in steps within the chosen microscopic area, and the emission current I_e was measured as a function of voltage V_e for each fixed position of the probe. Note that, in measuring the *I–V* relation, the probe could be either at a positive or a negative potential, whereas the surface under study was always kept at a zero potential (because of the specific design features of the STM of the LS SPM setup). Therefore, when the probe is at a positive potential, the surface spot under study is an electron emitter. Conversely, the STM probe becomes an electron emitter when the potential V_e is negative. The measured *I–V* relations are shown in Figs. 3 and 4.

In our experimental conditions, the only mechanism for electron emission from the surface of Ge/Si nanostructures is electron tunneling through a potential barrier at the interface between the surface spot under study and the probe tip. However, the dimensionality and the shape of the potential barrier, as well as the thickness of the vacuum gap, are unknown variables. Therefore, in order to interpret the experimental data on the $I_e(V_e)$ relation, we must first investigate the validity of the one-dimensional potential barrier approximation, which is one of the basic approximations of the Fowler–Nordheim (F–N) phenomenological theory of field emission [11]. According to the F–N theory, for a one-dimensional potential barrier (with inclusion of the effect of image force), the $I_e(V_e)$ function is exponential and takes the form of a linear function in V_e^{-1} versus $\ln(I_e/V_e^2)$ coordinates. Note that the F–N theory has been supported by numerous experiments performed on metallic emitting tips, with the emission current varying by over more than six orders of magnitude [11]. For semiconductor emitters, the F–N theory agrees with experiment on the initial portion of the *I–V* curve for emission currents varying by over two to three orders of magnitude [12].

It is seen from Figs. 3 and 4 that the experimental data can be closely fitted by either an exponential or a straight line (in the corresponding coordinates). Therefore, we can use the F–N relation

$$I_e/S_e \approx \frac{1.537 \times 10^{-6} \beta^2 V_e^2}{\varphi t^2(y)} \times \exp\left(-\frac{6.83 \times 10^7 \varphi^{3/2}}{\beta V_e} \nu(y)\right), \quad (2)$$

where S_e is the area of the emitting surface (in cm^2); φ is the work function (in eV); β is a geometrical factor or a

field factor (in cm^{-1}); V_e is in volts; and $t(y)$ and $\nu(y)$ are tabulated functions of the argument $y = 3.79 \times 10^{-4}\beta^{1/2}V_e^{1/2}\varphi^{-1}$, which are used to interpret the data obtained and, in particular, to estimate the emission current density and the reduced brightness B of the electron emitter. With Eq. (2) and the data presented in Fig. 4, we obtain the following estimates for electron emission from the surface of a single Ge island:

$$\ln\left\{\frac{1.537 \times 10^{-6}\beta^2 S_e}{\varphi t^2(y)}\right\} \cong -15.3,$$

$$\left(\frac{6.83 \times 10^7 \varphi^{3/2}}{\beta}\nu(y)\right) \cong 22.$$

Putting $\varphi_{Ge} \approx 4.8$ eV [13], $t(y) = t(0.5) \approx 1.044$, and $\nu(y) \approx \nu(0.5) \approx 0.7$ and using the above estimates, we find that the field-emission current density and the brightness of the Ge emitter vary within the following limits as V_e is varied from V_0 to V_m:

$$10^4 \le I_e/S_e \le 2.5 \times 10^5 \text{ A/cm}^2,$$

$$3 \times 10^4 \le B \le 5 \times 10^5 \text{ A/(cm}^2 \text{ sr V)}.$$

The above numerical estimates for the field-emission current density agree well with field-emission data on emitting semiconductor tips (including Ge emitters) [12]. As for the estimates of the reduced brightness, they far exceed the maximum values (~10^4 A/(cm^2 sr V) [14]) currently reached for so-called Schottky cathodes, which are widely used in scanning electron microscopes and electron lithography devices. The result obtained can be explained by the fact that, in our experiments, the factor β is significantly higher (by approximately two orders of magnitude) than the factor β for Schottky cathodes used in the instruments mentioned above.

4. CONCLUSIONS

An array of Ge(Sb) islands on a Si surface is a novel phase of the Ge/Si heteroepitaxial system, which exhibits important properties, such as islands that are uniform in shape (there are only pyramidal islands with square bases on the Si surface, and their faces are not multifaceted) and a significantly increased surface density of islands. In certain cases, islands are ordered along the $\langle 010 \rangle$ crystallographic directions and form a two-dimensional network on a Ge wetting layer. The techniques proposed for producing an array of islands that are uniform in shape can be employed to develop silicon-based devices. For example, the nanostructures in question can be used to develop electron emitters with an extremely high brightness [up to ~10^6 A/(cm^2 sr V)]. We also note that, by optimizing the growth parameters, a light-emitting diode has been fabricated on the basis of multilayer structures with Ge/Si quantum dots operating at room temperature [15].

ACKNOWLEDGMENTS

This study was supported in part by the Ministry of Science and Education of the Russian Federation, the Russian Academy of Sciences, and the Russian Foundation for Basic Research. One of the authors (G.E.C.) is grateful to the Alexander von Humboldt Stiftung, and another author (A.A.T.) is grateful to the DFG.

REFERENCES

1. N. V. Vostokov, Z. F. Krasil'nik, D. N. Lobanov, A. V. Novikov, M. V. Shaleev, and A. N. Yablonskiĭ, Fiz. Tverd. Tela (St. Petersburg) **46**, 63 (2004) [Phys. Solid State **46**, 60 (2004)].
2. N. D. Zakharov, V. G. Talalaev, P. Werner, A. A. Tonkikh, and G. E. Cirlin, Appl. Phys. Lett. **83**, 3084 (2003).
3. V. N. Tondare, B. I. Birajdar, N. Pradeep, D. S. Joag, A. Lobo, and S. K. Kulkarni, Appl. Phys. Lett. **77**, 2394 (2000).
4. O. P. Pchelyakov, Yu. B. Bolkhovityanov, A. V. Dvurechenskiĭ, L. V. Sokolov, A. I. Nikiforov, A. I. Yakimov, and B. Voigtländer, Fiz. Tekh. Poluprovodn. (St. Petersburg) **34**, 1281 (2000) [Semiconductors **34**, 1229 (2000)].
5. G. E. Cirlin, N. P. Korneeva, V. N. Demidov, N. K. Polyakov, V. N. Petrov, and N. N. Ledentsov, Fiz. Tekh. Poluprovodn. (St. Petersburg) **31**, 1230 (1997) [Semiconductors **31**, 1057 (1997)].
6. I. Berbezier, A. Ronda, A. Portavoce, and N. Motta, Appl. Phys. Lett. **83**, 4833 (2003).
7. A. A. Tonkikh, G. E. Cirlin, V. G. Dubrovskiĭ, V. M. Ustinov, and P. Werner, Fiz. Tekh. Poluprovodn. (St. Petersburg) **38**, 1239 (2004) [Semiconductors **38**, 1202 (2004)].
8. V. G. Dubrovskii, G. E. Cirlin, and V. M. Ustinov, Phys. Rev. B **68**, 075409 (2003).
9. C. S. Peng, Q. Huang, W. Q. Cheng, J. M. Zhou, Y. H. Zhang, T. T. Sheng, and C. H. Tung, Appl. Phys. Lett. **72**, 2541 (1998).
10. D. Temple, Mater. Sci. Eng. R **24**, 185 (1999).
11. A. Modinos, *Field, Thermionic and Secondary Electron Emission Spectroscopy* (Plenum, New York, 1984; Nauka, Moscow, 1990).
12. R. Fischer and H. Neumann, Fortschr. Phys. **14**, 603 (1966); *Autoelectronic Emission of Semiconductors* (Nauka, Moscow, 1971).
13. V. S. Fomenko, *Emission Properties of Materials: Handbook* (Naukova Dumka, Kiev, 1981) [in Russian].
14. M. J. Fransen, M. H. F. Overwijk, and P. Kruit, Appl. Surf. Sci. **146**, 357 (1999).
15. V. G. Talalaev, G. E. Cirlin, A. A. Tonkikh, N. D. Zakharov, and P. Werner, Phys. Status Solidi A **198**, R4 (2003).

Translated by Yu. Epifanov

Physics of the Solid State, Vol. 47, No. 1, 2005, pp. 63–66. Translated from Fizika Tverdogo Tela, Vol. 47, No. 1, 2005, pp. 63–66.
Original Russian Text Copyright © 2005 by Pchelyakov, Dvurechenskiĭ, Nikiforov, Pakhanov, Sokolov, Chikichev, Yakimov.

PROCEEDINGS OF THE CONFERENCE "NANOPHOTONICS 2004"
(Nizhni Novgorod, Russia, May 2–6, 2004)

Si–Ge–GaAs Nanoheterostructures for Photovoltaic Cells

O. P. Pchelyakov, A. V. Dvurechenskiĭ, A. I. Nikiforov, N. A. Pakhanov, L. V. Sokolov, S. I. Chikichev, and A. I. Yakimov

Institute of Semiconductor Physics, Siberian Division, Russian Academy of Sciences, pr. Akademika Lavrent'eva 13, Novosibirsk, 630090 Russia
e-mail: pch@isp.nsc.ru

Abstract—Synthesis from molecular beams in an ultrahigh vacuum is a promising method for producing multilayer semiconducting thin-film structures for high-efficiency conversion of heat and solar energies into electricity, where cascade converters with complex optimized chemical compositions and alloying profiles are necessary. Until recently, nanotechnologies of heterostructures, such as quantum wells, superlattices, and quantum dots, were not applied for photovoltaic conversion. The state of the art of technologies in this field is analyzed.
© 2005 Pleiades Publishing, Inc.

1. INTRODUCTION

Increasing the physical and economic efficiencies of power installations based on semiconductor photovoltaic cells (PCs) is a challenge in condensed-matter physics, transfer phenomena, power engineering, computational mathematics, and physical chemistry from not only a fundamental but also an applied standpoint. This problem can be solved by making PCs from cascade multilayer heterostructures with InAs–GaAs–AlAs films, as well as from phosphorus- and nitrogen-containing compounds and nanoheterostructures with superlattices and quantum dots (QDs) [1–3]. The first GaAlAs/GaAs-based solar cells were fabricated at the Ioffe Physicotechnical Institute by using liquid-phase epitaxy [4]. Molecular-beam epitaxy (MBE) in an ultrahigh vacuum is also a promising method for producing multilayer semiconductor thin-film compositions for high-efficiency conversion of thermal and solar energies into electricity. High-precision technologies, such as MBE, are especially important for the creation of cascade thin-film PCs that have complex optimized chemical compositions and alloy profiles of heterostructures. Until recently, nanotechnologies related to the formation of heterostructures containing quantum dots, superlattices, and QDs were not applied for photovoltaic conversion. In this work, we analyze the state of the art of technologies in this field.

2. HETEROSTRUCTURES BASED ON III–V COMPOUNDS

Group III–V semiconductor compounds with phosphorus or nitrogen have a unique combination of physical and chemical properties, which makes them promising for high-efficiency opto- and microelectronic devices. At present, semiconductor heterostructures based on compounds of Group III and V elements (Al, Ga, In; N, P, As) are used as cascade solar-energy converters in systems with and without light concentrators. The efficiency of multilayer InGaAsP/GaAsN/GaAs solar-energy converters is expected to be as high as 40%, which is twice the efficiency of modern silicon solar batteries.

The idea of a multistage SC was proposed in 1955 [4]; however, it could only be realized in the 1980s owing to the appearance of MOCVD and molecular epitaxy, which made it possible to produce thin AlGaAs/GaAs layers connected by tunnel heterojunctions. However, the predicted conversion efficiency, which is close to 30%, could not be achieved because of the difficulties encountered in the production of perfect tunnel diodes and problems related to the oxidation of AlGaAs layers [5]. Perfect and stable tunnel diodes were fabricated later in the form of double heterostructures (DHs), where a p^+–n^+ tunneling junction was placed between thin broad-band p^+ and n^+ layers. Further progress came from the substitution of InGaP for AlGaAs in the top *p–n* junction, which made it possible to create a monolithic double-junction SC having an area of 4 cm^2 and an efficiency of 30.3% [6]. $In_{0.5}Ga_{0.5}P$ was found to be the best material for the top junction in the SC, since it has a band gap E_g = 1.9 eV (which is close to the optimum value for a pair with GaAs, where E_g = 1.42 eV) and does not undergo oxidation. The double structure of the top *p–n* junction made from $In_{0.5}Ga_{0.5}P$ and GaAs has a theoretical limit of 34%. The lattice parameters of these materials and the generated photoelectric currents in them can be matched, and the top and bottom *p–n* junctions can be connected by a tunnel diode. Based on experimental and theoretical studies, researchers optimized the layer thicknesses (for matching the photocurrents) and doping levels, thus designing cascade SCs [7]. The main problems in reaching a high efficiency were caused by poor electro-

1063-7834/05/4701-0063$26.00 © 2005 Pleiades Publishing, Inc.

physical properties of the heteroepitaxial layers; therefore, there is a need to improve these properties and the quality of the tunnel diodes. A critical parameter for the tunnel diodes is the peak current required to decrease the SC series resistance. Let us enumerate the main factors restricting SC efficiency:

(1) ohmic losses induced by contact and spreading resistances;

(2) carrier recombination at the outer surface and layer interfaces;

(3) carrier recombination in the bulk of a SC;

(4) lattice-parameter mismatch in layers;

(5) lattice defects in layers and at interfaces;

(6) incomplete accumulation of photoexcited carriers;

(7) insufficient using of the operating region of the solar spectrum.

3. HETEROSTRUCTURES FOR PHOTOELECTRIC CONVERTERS ON GERMANIUM AND SILICON SUBSTRATES

At present, InGaP/GaAs heterostructures for SCs are grown on GaAs and Ge substrates and are applied in the power supply systems of spacecrafts. However, their wide application is hindered by the high cost of single-crystal GaAs and Ge substrates and by the fact that the density of these materials is twice that of silicon. Despite these disadvantages, such converters are successfully applied as power supplies in spacecrafts and mobile ground-based systems. The transition to germanium substrates has resulted from the lower cost and higher strength of Ge as compared to GaAs. However, to further decrease the cost of SCs based on Group III and V materials, it is necessary to use cheaper large-area Si substrates. This problem is one of the current challenges in photovoltaic conversion. In this case, the basic materials-science problem is to match the lattice parameters of a film and a substrate, whose mismatch is a few percent. New approaches to solving this problem have been developed and realized at the Institute of Semiconductor Physics (ISP, Siberian Division of the RAS). These methods are based on suppressing the formation of antiphase domains in GaAs and Ge layers [8] and on using so-called artificial substrates with buffers made of GeSi solid solutions and low-temperature silicon [9, 10].

The dislocation structure of Ge_xSi_{1-x}/Si(001) solid-solution films has been studied for 15 years. The characteristic density of threading dislocations (TDs) in $Ge_{0.3}Si_{0.7}$ layers is too high for application (10^8–10^9 cm^{-2}). The typical growth temperature of such heterostructures is 550°C. A high density of TDs in such heterostructures is caused by a high density of short misfit dislocations, each of which is connected with the layer surface by a couple of segments (threading dislocations). Even at the very beginning of plastic relaxation (less than 1%), the TD density in such a sample is 10^7 cm^{-2}, which is equal to the density of nucleating misfit dislocations. By the end of plastic relaxation, the TD density increases to 10^8 cm^{-2}.

To overcome the disadvantages of conventional methods, we studied the growth of GeSi solid-solution films on Si substrates with buffers deposited by low-temperature (300–350°C) molecular-beam epitaxy. In this case, a low-temperature sublayer, which is saturated with point defects and serves as a source of vacancies and interstices, activates nonconservative processes of dislocation motion and annihilation upon subsequent growth of a solid-solution layer [9, 10]. It has been shown that, at compositions of up to $x \sim 0.3$, the density of threading dislocations in Ge_xSi_{1-x}/Si(001) heterostructures can be reduced to 10^6 cm^{-2}. Heterostructures with a two-step composition have been grown that have record thin relaxed films with a germanium content of 0.38–0.61 on the surface and a total thickness of 600–750 nm.

4. NANOTECHNOLOGIES IN PHOTOVOLTAIC CONVERSION

A new important trend in increasing the efficiency of SCs and heat photogenerators is the application of nanoheterostructures, such as quantum-well superlattices and QD systems [3, 11–13]. Such structures based on Ge–Si and III–V compounds have been developed at the ISP [13–18]. To date, the electronic properties of semiconducting QDs have been extensively studied; QDs represent the limiting case of low-dimensional systems, namely, zero-dimensional systems consisting of a set of atomic nanoclusters in a semiconducting matrix [19, 20]. Due to the discreteness of the energy spectrum of such clusters, they can be considered to be artificial analogs of atoms, although the clusters contain a large number of particles. The properties of such "atoms" can be changed by varying the quantum-dot size, shape, and composition using various technologies. Therefore, periodic structures consisting of many layers with ordered ensembles of artificial atoms can have properties of artificial crystals.

Since the atomic clusters are nanometer-sized, possible applications of the traditional lithography-related methods for producing structures are substantially limited and new approaches are required. The idea of using morphological surface changes during the growth of unmatched heteroepitaxial systems proved successful for forming an array of atomic nanoclusters when a transition takes place from two-dimensional to three-dimensional growth via the Stranski–Krastanow mechanism. For the Ge/Si system, this idea was first realized in 1992; as a result, one-electron effects were revealed in the new class of nanostructures [21, 22]. This process of creation of artificial atoms, which was called self-organization, has been shown to explain the formation of an array of nanoclusters with a rather uniform size distribution [19, 20]. Self-assembling arrays of nanoclusters, nanoislands, or QDs have only recently been

applied in light converters and photodetectors; nevertheless, this approach is believed to be promising.

5. OPTICAL PROPERTIES OF STRUCTURES WITH QUANTUM DOTS

The specific features of structures with QDs are, first, the possibility of controlling the spectral photoresponse band by preliminarily filling the discrete states with the required transition energy and, second, the presence of lateral quantization in zero-dimensional systems, which lifts the forbiddenness of optical transitions polarized in the plane of a photodetector and, hence, enables light absorption under normal photon incidence. Moreover, the photoexcited-carrier lifetime in QDs is expected to increase strongly because of the so-called phonon bottleneck effect [23].

5.1. IR Absorption

Photon absorption in the IR spectral region in Ge/Si multilayer heterostructures with self-assembling QDs was studied in [24, 25]. In both cases, islands had a base of ~40–50 nm and a height of 2–4 nm. The island density was 10^8 cm^{-2}. In [24], the Ge islands were doped with boron in order to fill the ground state of QDs by holes. The absorption spectra contained a broad (~100-meV-wide) line in the wavelength range 5–6 μm. The intensity of this line decreased strongly in going to light polarized normal to the layer plane, and this line was explained as being due to transitions between the two lowest transverse-quantization levels of heavy holes in QDs.

To activate optical transitions inside undoped QDs, the authors of [25] applied additional illumination. The photoinduced absorption polarized parallel to the layer plane had an asymmetrical maximum near 4.2 μm and was related to hole transitions from the ground state of QDs to the extended states of the valence band. The absorption cross section determined in [25] is unusually high (2×10^{-13} cm^2): it is at least an order of magnitude higher than the well-known photoionization cross sections for local centers in Si [26] and three orders of magnitude higher than this quantity for InAs/GaAs QDs [27]. These data indicate that the Ge/Si system is promising for application in IR detectors and photoelectric converters.

5.2. Photoconductivity

The authors of [28, 29] were the first to detect a photoelectric current in Ge/Si heterostructures with self-assembling QDs generated by photons with energies smaller than the silicon band gap. The possibility of designing a QD-based photodetector that can be adjusted to the near and middle infrared regions was demonstrated in [30]. The photodetector consisted of a silicon pin diode whose base contained a two-dimensional array of Ge nanoclusters. The mean lateral QD size was 15 nm, and the QD height was 1.5 nm. No photoresponse was detected in a sample with a continuous 6-ML-thick Ge film.

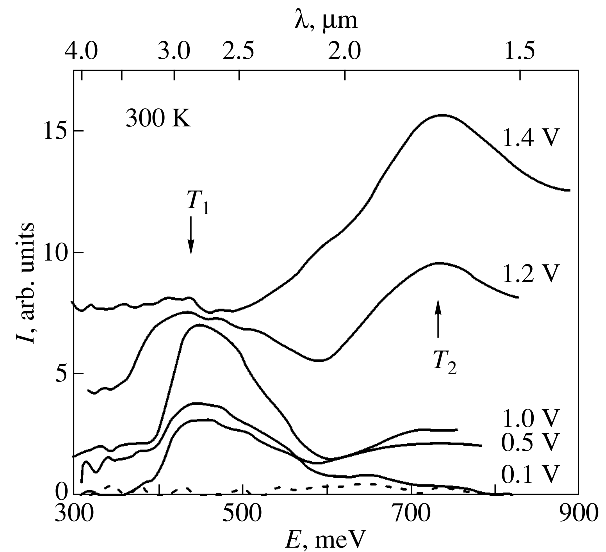

Photocurrent spectra for a silicon pin diode with Ge quantum dots recorded at different reverse biases. The dashed line corresponds to the absence of photocurrent in the structure with a continuous Ge layer.

Photocurrent spectra recorded at different reverse biases are shown in the figure. At energies lower than the fundamental absorption edge in silicon (~1.12 eV), two maxima are observed at wavelengths of 1.7 and 2.9 μm (arrows T_2 and T_1, respectively) for a structure with QDs. The intensities of both maxima depend strongly on the reverse bias, and both dependences correlate with each other.

The authors of [13] reported on the creation of SCs with germanium QDs located in the region of a space charge near a *p*–*n* junction in silicon. The quantum yield and the conversion efficiency of a SC were observed to increase. Those authors were the first to conclude that nanotechnology can also be used effectively for the creation of SCs in other photovoltaic devices. In [31], examples of the creation of SCs in the form of a pin diode with self-assembled germanium QDs in silicon are described. It was shown in [31] that the addition of QDs in *p*-silicon increases the quantum efficiency of a SC near 1.45 μm and that the effect increases with the number of germanium QD layers. A high efficiency of separation of electron–hole pairs using a built-in electric field was demonstrated, and the collection of carriers was shown to be possible without noticeable recombination at QDs and interfaces.

6. CONCLUSIONS

Silicon-based nanostructures with germanium QDs are a new class of materials for photovoltaic conversion. In various scientific centers, researchers have started to study such structures to apply them in solar

batteries and heat photogenerators. Reported studies on the electric and optical properties of arrays of Ge islands in Si allow one to conclude that arrays of artificial atoms form with a discrete energy spectrum, which manifests itself up to room temperature. The main factors determining the spectrum of states are the quantum confinement and Coulomb interaction of carriers. A new factor that appears in a QD array and distinguishes it from a single QD is Coulomb interaction between islands. The photoexcitation rate and capture cross section of holes have been determined as functions of the energy-level depth. The cross sections have been found to be a few orders of magnitude greater than their well-known values in Si. The possibility of designing a photodetector with germanium QDs that can be adjusted to the near and middle infrared regions has been experimentally demonstrated. Self-assembling arrays of nanoclusters, nanoislands, or QDs have been only recently applied in light converters and photodetectors; nevertheless, the first experimental results allow one to conclude that nanotechnology can be used to advantage in this important field of photoelectronics.

ACKNOWLEDGMENTS

This work was supported by the Russian Foundation for Basic Research (project nos. 03-02-16506, 03-02-16468, 03-02-16085), the interindustry scientific and technical program "Physics of Solid-State Nanostructures" (project no. 98-1100), the program of support for leading scientific schools of the Russian Federation (no. NSh-533-2003-2), and the program "Russian Universities: Fundamental Studies" (grant no. 4103).

REFERENCES

1. V. M. Andreev, in *Photovoltaic and Photoactive Materials: Properties, Technology, and Applications*, Ed. by J. M. Marshall and D. Dimova-Malinovska (Kluwer Academic, Dordrecht, 2002), p. 131.
2. J. F. Geisz and D. J. Friedman, Semicond. Sci. Technol. **17**, 769 (2002).
3. V. Aroutiounian, S. Petrosyan, and A. Khachatryan, J. Appl. Phys. **89** (4), 2268 (2001).
4. E. D. Jackson, in *Transactions of Conference on the Use of Solar Energy* (Univ. of Arizona Press, Tucson, 1955), Vol. 5, p. 122.
5. K. Ando, C. Amano, H. Sugiura, M. Yamaguchi, and A. Saletes, Jpn. J. Appl. Phys. **26** (1987).
6. E. Takamoto, H. Ikeda, and M. Kurita, Appl. Phys. Lett. **70** (3), 381 (1997).
7. M. B. Kagan, M. M. Koltun, A. P. Landsman, and T. L. Lyubashevskaya, Geliotekhnika, No. 1, 7 (1968).
8. A. K. Gutakovsky, A. V. Katkov, M. I. Katkov, O. P. Pchelyakov, and M. A. Revenko, J. Cryst. Growth **201**, 232 (1999).
9. Yu. B. Bolkhovityanov, O. P. Pchelyakov, and S. I. Chikichev, Usp. Fiz. Nauk **171**, 689 (2001) [Phys. Usp. **44**, 655 (2001)].
10. Yu. B. Bolkhovityanov, A. S. Deryabin, A. K. Gutakovskii, M. A. Revenko, and L. V. Sokolov, Thin Solid Films (2004) (in press).
11. K. M. Yu and M. Yamaguchi, Sol. Energy Mater. Sol. Cells **60**, 19 (2000).
12. M. A. Green, Mater. Sci. Eng. B **74**, 118 (2000).
13. J. Konle, H. Presting, H. Kibbel, and F. Banhard, Mater. Sci. Eng. B **89**, 160 (2002).
14. A. I. Yakimov, A. V. Dvurechenskiĭ, A. I. Nikiforov, S. V. Chaĭkovskiĭ, and S. A. Teys, Fiz. Tekh. Poluprovodn. (St. Petersburg) **37** (11), 1383 (2003) [Semiconductors **37**, 1345 (2003)].
15. O. P. Pchelyakov, Yu. B. Bolkhovityanov, A. V. Dvurechenskiĭ, L. V. Sokolov, A. I. Nikiforov, A. I. Yakimov, and B. Voigtländer, Fiz. Tekh. Poluprovodn. (St. Petersburg) **34** (11), 1281 (2000) [Semiconductors **34**, 1229 (2000)].
16. A. I. Yakimov, A. V. Dvurechenskii, and A. I. Nikiforov, Thin Solid Films **380** (1–2), 82 (2001).
17. A. I. Yakimov, N. P. Stepina, A. V. Dvurechenskii, A. I. Nikiforov, and A. V. Nenashev, Phys. Rev. B **63**, 045312 (2001).
18. O. P. Pchelyakov, A. I. Toropov, V. P. Popov, A. V. Latyshev, L. V. Litvin, Yu. V. Nastaushev, and A. L. Aseev, Proc. SPIE **490**, 247 (2002).
19. L. Jacak, P. Hawrylak, and A. Wojs, *Quantum Dots* (Springer, Berlin, 1998).
20. N. N. Ledentsov, V. M. Ustinov, V. A. Shchukin, P. S. Kop'ev, Zh. I. Alferov, and D. Bimberg, Fiz. Tekh. Poluprovodn. (St. Petersburg) **32** (4), 385 (1998) [Semiconductors **32**, 343 (1998)].
21. A. I. Yakimov, V. A. Markov, A. V. Dvurechenskii, and O. P. Pchelyakov, Philos. Mag. B **65** (4), 701 (1992).
22. A. I. Yakimov, V. A. Markov, A. V. Dvurechenskii, and O. P. Pchelyakov, J. Phys.: Condens. Matter **6**, 2573 (1994).
23. M. Sugawara, K. Mukai, and H. Shoji, Appl. Phys. Lett. **71** (19), 2791 (1997).
24. J. L. Liu, W. G. Wu, A. Balandin, G. L. Jin, and K. L. Wang, Appl. Phys. Lett. **74** (2), 185 (1999).
25. P. Boucaud, V. Le Thanh, S. Sauvage, D. Debarre, and D. Bouchier, Appl. Phys. Lett. **74** (3), 401 (1999).
26. D. K. Schreder, in *Charge-Coupled Devices*, Ed. by D. F. Barbe (Springer, Heidelberg, 1980; Mir, Moscow, 1982).
27. S. Sauvage, P. Boucaud, J.-M. Gerard, and V. Thierry-Mieg, Phys. Rev. B **58** (12), 10562 (1998).
28. G. Abstreiter, P. Schittenhelm, C. Engel, E. Silveira, A. Zrenner, D. Meertens, and W. Jager, Semicond. Sci. Technol. **11**, 1521 (1996).
29. P. Schittenhelm, C. Engel, F. Findeis, G. Abstreiter, A. A. Darhyber, G. Bauer, A. O. Kosogov, and P. Werner, J. Vac. Sci. Technol. B **16** (3), 1575 (1998).
30. A. I. Yakimov, A. V. Dvurechenskii, Yu. Yu. Proskuryakov, A. I. Nikiforov, O. P. Pchelyakov, S. A. Teys, and A. K. Gutakovskii, Appl. Phys. Lett. **75** (6), 1413 (1999).
31. A. Alguno, N. Usami, T. Ujihara, K. Fujiwara, G. Sazaki, K. Nakajima, and Y. Shiraki, Appl. Phys. Lett. **83** (6), 1258 (2003).

Translated by K. Shakhlevich

Physics of the Solid State, Vol. 47, No. 1, 2005, pp. 67–70. Translated from Fizika Tverdogo Tela, Vol. 47, No. 1, 2005, pp. 67–69.
Original Russian Text Copyright © 2005 by Nikiforov, Ul'yanov, Pchelyakov, Teys, Gutakovsky.

PROCEEDINGS OF THE CONFERENCE "NANOPHOTONICS 2004"
(Nizhni Novgorod, Russia, May 2–6, 2004)

Formation of Ultrasmall Germanium Nanoislands with a High Density on an Atomically Clean Surface of Silicon Oxide

A. I. Nikiforov, V. V. Ul'yanov, O. P. Pchelyakov, S. A. Teys, and A. K. Gutakovsky

Institute of Semiconductor Physics, Siberian Division, Russian Academy of Sciences, pr. Akademika Lavrent'eva 13, Novosibirsk, 630090 Russia

e-mail: nikif@isp.nsc.ru

Abstract—The experimental results of an investigation into the initial stages of growth of a germanium film on an atomically clean oxidized silicon surface are reported. It is shown that the growth of the germanium film in this system occurs through the Volmer–Weber mechanism. Elastically strained nanoislands with a lateral size of less than 10 nm and a density of 2×10^{12} cm^{-2} are formed on the oxidized silicon surface. In germanium films with a thickness greater than 5 monolayers (ML), there also arise completely relaxed germanium nanoislands with a lateral size of up to 200 nm and a density of 1.5×10^9 cm^{-2}. *© 2005 Pleiades Publishing, Inc.*

1. INTRODUCTION

In recent years, investigating the phenomenon of self-assembling of nanoislands has attracted particular research attention primarily for finding practical applications for this process. In this respect, the Si(100) surface with 10- to 100-nm dislocation-free germanium nanoislands that arise after the formation of a continuous germanium film is of considerable interest [1]. Researchers have succeeded in decreasing the size of these nanoislands to values at which quantum confinement effects manifest themselves up to room temperature [2]. Silicon-based structures with germanium quantum dots are extensively used in optoelectronics over a wide spectral range, namely, from the IR range [3] to the wavelengths used in fiber-optic communication lines [4]. In our previous work [4], we managed to decrease the sizes of germanium nanoislands and to increase their density by using a preliminarily oxidized silicon surface for growing the nanoislands.

The size of the germanium nanoislands decreases with a decrease in the temperature of germanium deposition. The minimum size (15 nm) was achieved for germanium nanoislands grown on a clean silicon surface. In order to decrease the size of germanium nanoislands and increase their density, the nanoislands were grown on an atomically clean oxidized silicon surface, which was prepared directly in a molecular-beam epitaxy apparatus. It has long been known that an oxide layer can be grown on a silicon surface under ultrahigh vacuum. Lander and Morrison [5] were the first to demonstrate that the appropriate conditions for etching and growing an oxide film can be determined by varying the oxygen pressure and temperature. This technique was further advanced quite recently, when the formation of an ultrathin oxide layer was combined with the growth of a silicon epitaxial film [6]. The growth of germanium nanoislands on a preliminarily oxidized silicon surface makes it possible to decrease the size and increase the density of germanium nanoislands significantly. Shklyaev *et al.* [7] and Barski *et al.* [8] showed that, when the nanoislands are grown on an oxidized Si(111) surface, their lateral sizes are less than 10 nm and the density is higher than 10^{12} cm^{-2}. The oxidation conditions have a substantial effect on the formation of germanium nanoislands and, moreover, play a critical role in further overgrowth of the nanoislands with a silicon layer. Since the oxide layer is sufficiently thick, it is impossible to grow a silicon epitaxial film with a permissible degree of imperfection. In this connection, the oxidation conditions must be controlled carefully. In a molecular-beam epitaxy apparatus, careful control can be most conveniently exercised by using reflection high-energy electron diffraction (RHEED), which provides layer-by-layer monitoring of both oxidation [9] and subsequent growth of germanium and silicon layers.

2. SAMPLE PREPARATION AND EXPERIMENTAL TECHNIQUE

The synthesis was carried out in a Katun'-S apparatus for molecular-beam epitaxy. Silicon was evaporated from an electron beam evaporator. The germanium flux was produced by either the electron beam evaporator or an effusion cell equipped with a boron nitride crucible. Dopants (Sb, B) were evaporated from effusion cells. The analytical section of the chamber consisted of a

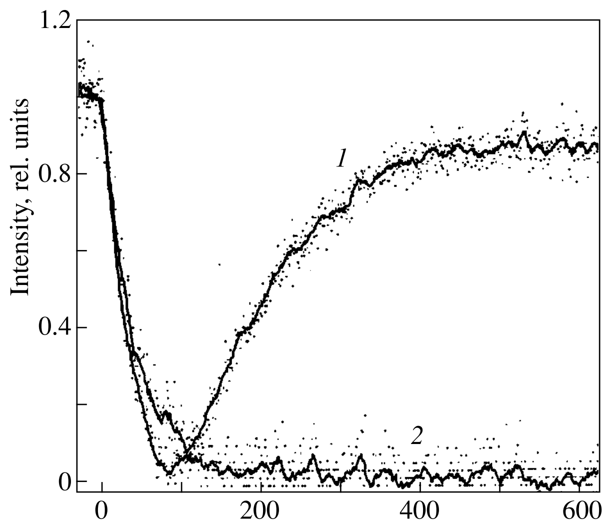

Fig. 1. Relative changes in the intensity of the (*1*) specular and (*2*) superstructure reflections during oxidation of the Si(100) surface at a temperature of 400°C and an oxygen pressure of 2×10^{-5} Pa.

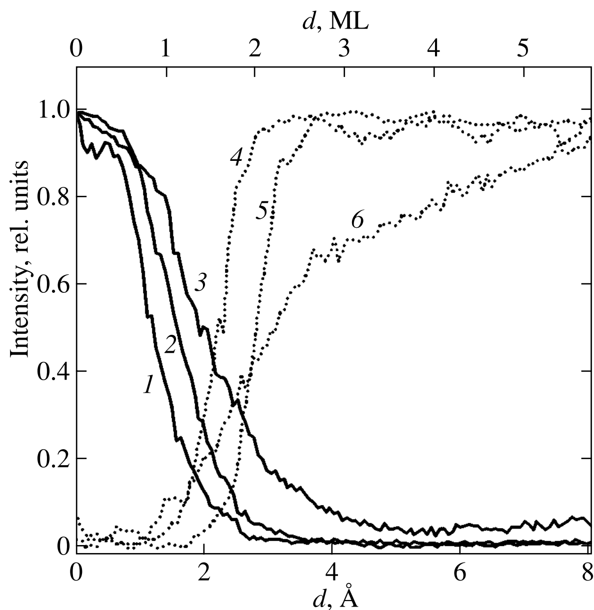

Fig. 2. Relative changes in the intensity of the (*1–3*) specular and (*4–6*) 3D reflections during the growth of a germanium film on the oxidized Si(100) surface at different substrate temperatures T_s = (*1*, *4*) 550, (*2*, *5*) 500, and (*3*, *6*) 450°C.

quadrupole mass spectrometer, a quartz crystal monitor, and a reflection high-energy electron diffractometer (electron energy, 20 kV). The diffraction patterns were recorded with a CCD camera during the growth of germanium films. The diffraction image was entered into a personal computer. Software was used to observe and record the diffraction pattern at a rate of 10 images per second. The growth rate of germanium films was 10 monolayers (ML) per minute. The temperature of the substrate was varied from room temperature to 700°C. The substrates were prepared in the form of a Si(100) plate in which the misorientation angle was less than 0.5°. Oxidation was performed in the molecular-beam epitaxy apparatus under an oxygen pressure up to 10^{-4} Pa in the chamber and at a substrate temperature ranging from 400 to 600°C. After the oxygen was pumped out of the chamber, germanium was deposited on the oxidized silicon surface.

3. RESULTS AND DISCUSSION

The intensities of reflections of the RHEED pattern were measured in the course of oxidation. The changes in the intensity of the specular reflection proved highly informative. Figure 1 shows the relative changes in the intensity of the specular and (2 × 1) superstructure reflections during oxidation of the Si(100) surface at a substrate temperature of 400°C and an oxygen pressure of 2×10^{-5} Pa. The minimum in the intensity of the specular reflection corresponds to the maximum roughness of the surface, i.e., to a surface covered with an oxide layer 0.5 ML thick. Then, the intensity of the specular reflection increases and tends to a stationary value. The formation of the second and subsequent oxide layers does not lead to variations in the intensity of the specular reflection, because the surface morphology remains unchanged. The superstructure reflection disappears almost entirely for a film thickness of 0.5 ML with no further variation.

The growth of the germanium film was controlled using the RHEED pattern, i.e., by recording both qualitative variations in the structure and surface morphology of the growing film and quantitative information on the elastic strain of the surface unit cell [10]. The initial stage of growth of the germanium film on the oxidized silicon surface was analyzed using the measured changes in the intensities of the specular reflection and three-dimensional diffraction reflection (3D reflection). These quantities are very sensitive to variations in the surface roughness. The appearance of the 3D reflection indicates the presence of three-dimensional objects on the surface under investigation. Figure 2 shows the characteristic changes in the intensities of the reflections during the growth of the germanium film on the oxidized Si(100) surface. The intensities of these reflections change even after the deposition of one monolayer, and no oscillations of the intensity of the specular reflection are observed. This implies that there is no stage of formation of a wetting layer during the growth of the germanium film. Upon deposition of the first monolayer, an adsorption germanium layer is formed on the SiO_2 surface. After deposition of the second monolayer, the adsorption germanium layer transforms into three-dimensional nanoislands. Therefore, in contrast to the growth of films through the Stranski–

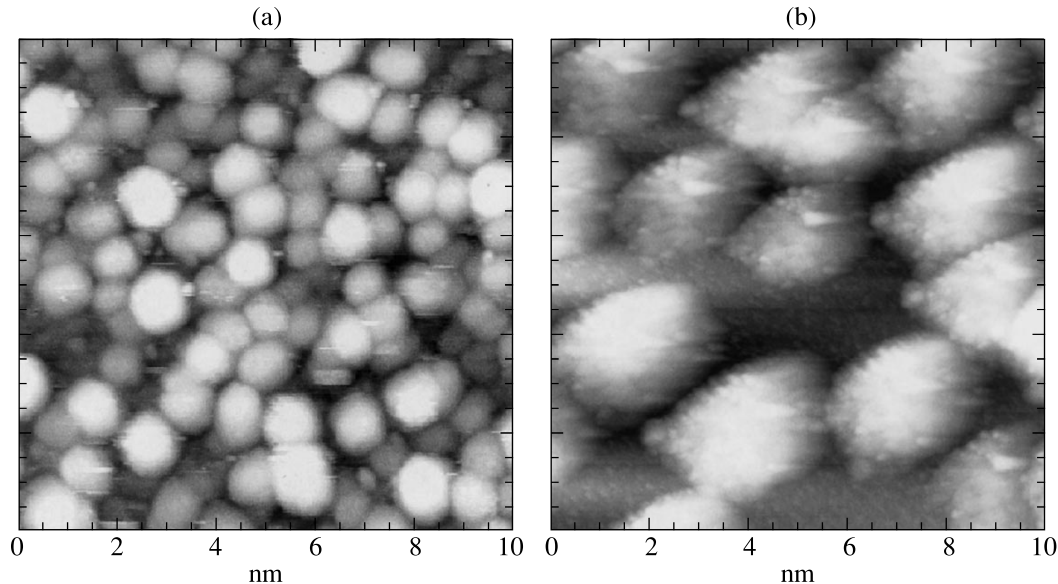

Fig. 3. STM image of the array of germanium nanoislands on the silicon oxide surface. d_{Ge} = (a) 0.3 and (b) 0.7 nm.

Krastanov mechanism, which is observed on a clean silicon surface, the growth of a germanium film on an oxidized silicon surface occurs through the Volmer–Weber mechanism.

The size and density of the germanium nanoislands depend on the thickness of the deposited germanium layer. Figure 3 displays *ex situ* scanning tunnel microscope (STM) images of an array of germanium nanoislands on the surface of silicon oxide after the deposition of germanium layers with thicknesses of 0.3 and 0.7 nm at a substrate temperature of 650°C. In germanium films with a thickness of up to 5 ML, there arise nanoislands with a base of less than 10 nm and a density of higher than 1×10^{12} cm^{-2}. An increase in the effective thickness of the deposited germanium layer leads to the formation of small-sized nanoislands and nanoislands with a larger size and a substantially lower density. The lateral size of the latter nanoislands reaches 200 nm, and their density is 1.5×10^9 cm^{-2}. Taking into account the change in the size of the surface unit cell, which was established in our recent work [11], we can draw the conclusion that the large-sized germanium nanoislands are relaxed and have a lattice parameter equal to the lattice parameter of bulk germanium. This can also be judged from the moiré fringes in the electron microscope image.

It should be noted that the shape of the germanium nanoislands is close to spherical with no faceting. A similar shape was observed by Shklyaev *et al.* [7], who performed *in situ* STM investigations of germanium nanoislands on the Si(111) surface. It seems likely that the shape of the germanium nanoislands depends primarily on the presence or absence of an oxide layer on the silicon surface rather than on the substrate orientation and the thickness of the oxide layer. The size and density of small nanoislands vary insignificantly when the germanium film has a thickness corresponding to the formation of large-sized nanoislands (Fig. 3b). Consequently, the germanium nanoislands on the oxidized Si(100) surface are characterized by a bimodal distribution over the sizes and density for a germanium film with a thickness greater than 1 nm. This is also confirmed by electron microscopy.

4. CONCLUSIONS

Thus, the results obtained in this work demonstrate that, in contrast to the growth of films through the Stranski–Krastanov mechanism, which is observed in the Ge/Si(100) system, the growth of germanium films on an oxidized silicon surface occurs through the Volmer–Weber mechanism. This manifests itself in the absence of a wetting layer prior to the formation of three-dimensional nanoislands. For a germanium film with a thickness of less than 5 ML, the nanoislands have a lateral size of less than 10 nm and a density of 2×10^{12} cm^{-2}. For greater thicknesses of the germanium film, there also arise nanoislands with a lateral size of up to 200 nm and a density of 1.5×10^9 cm^{-2}. The latter nanoislands are completely relaxed.

ACKNOWLEDGMENTS

This work was supported by the Russian Foundation for Basic Research (project nos. 03-02-16468, 03-02-16506) and the International Association of Assistance for the Promotion of Cooperation with Scientists from the New Independent States of the Former Soviet Union (project no. INTAS 03-51-5051).

REFERENCES

1. D. J. Eaglesham and M. Cerullo, Phys. Rev. Lett. **64**, 1943 (1990).
2. A. I. Yakimov, A. V. Dvurechenskii, A. I. Nikiforov, and O. P. Pchelyakov, Thin Solid Films **336**, 332 (1998).
3. A. I. Yakimov, A. V. Dvurechenskii, A. I. Nikiforov, and Yu. Yu. Proskuryakov, J. Appl. Phys. **89**, 5676 (2001).
4. A. I. Yakimov, A. V. Dvurechenskiĭ, A. I. Nikiforov, S. V. Chaĭkovskiĭ, and S. A. Teys, Fiz. Tekh. Poluprovodn. (St. Petersburg) **37**, 1383 (2003) [Semiconductors **37**, 1345 (2003)].
5. J. J. Lander and J. Morrison, J. Appl. Phys. **33**, 2098 (1962).
6. Y. Wei, M. Wallace, and A. C. Seabaugh, J. Appl. Phys. **81**, 6415 (1997).
7. A. A. Shklyaev, M. Shibata, and M. Ichikawa, Phys. Rev. B **62** (43), 1540 (2000).
8. A. Barski, M. Derivaz, J. L. Rouviere, and D. Buttard, Appl. Phys. Lett. **77**, 3541 (2000).
9. H. Watanabe and T. Baba, Appl. Phys. Lett. **74**, 3284 (1999).
10. A. I. Nikiforov, V. A. Cherepanov, O. P. Pchelyakov, A. V. Dvurechenskii, and A. I. Yakimov, Thin Solid Films **380**, 158 (2000).
11. A. I. Nikiforov, V. V. Ul'yanov, O. P. Pchelyakov, S. A. Teys, and A. K. Gutakovskiĭ, Fiz. Tverd. Tela (St. Petersburg) **46**, 80 (2004) [Phys. Solid State **46**, 77 (2004)].

Translated by N. Korovin

Physics of the Solid State, Vol. 47, No. 1, 2005, pp. 71–75. Translated from Fizika Tverdogo Tela, Vol. 47, No. 1, 2005, pp. 70–73.
Original Russian Text Copyright © 2005 by Burbaev, Kurbatov, Rzaev, Pogosov, Sibel'din, Tsvetkov, Lichtenberger, Schäffler, Leitao, Sobolev, Carmo.

PROCEEDINGS OF THE CONFERENCE "NANOPHOTONICS 2004"

(Nizhni Novgorod, Russia, May 2–6, 2004)

Morphological Transformation of a Germanium Layer Grown on a Silicon Surface by Molecular-Beam Epitaxy at Low Temperatures

T. M. Burbaev*, V. A. Kurbatov*, M. M. Rzaev*, A. O. Pogosov*, N. N. Sibel'din*, V. A. Tsvetkov*, H. Lichtenberger, F. Schäffler**, J. P. Leitao***, N. A. Sobolev***, and M. C. Carmo*****

** Lebedev Physical Institute, Russian Academy of Sciences, Leninskiĭ pr. 53, Moscow, 119991 Russia*

e-mail: burbaev@mail1.lebedev.ru

*** Insitut für Halbleiter- und Festkörperphysik, Johannes Kepler Universität, Linz, Austria*

**** Department of Physics, University of Aveiro, Aveiro, Portugal*

Abstract—Multilayer Si/Ge nanostructures with germanium layers of different thicknesses are grown by molecular-beam epitaxy at low temperatures (<350°C) and studied using photoluminescence and atomic force microscopy. It is found that the germanium layer undergoes a morphological transformation when its thickness becomes equal to approximately five monolayers: an island relief transforms into a smooth undulating relief.
© 2005 Pleiades Publishing, Inc.

1. INTRODUCTION

It is known that Si/Ge structures with three-dimensional quantum dots grown through the Stranski–Krastanov mechanism at temperatures of molecular-beam epitaxy T_g = 600–700°C, as a rule, belong to type-II heterostructures [1–4]. The probability of exciton recombination occurring in these structures is relatively low, because this process is indirect in both real and reciprocal k spaces [5]. It seems likely that the prospects for using these structures as emitters (in particular, in the spectral range 1.3–1.6 μm, which is of practical importance) are not favorable. However, in a number of recent works, it has been shown that there exist Si/Ge structures grown at high (T_g = 600°C) [6] and low (T_g = 250–300°C) [7–9] temperatures in which two-dimensional quantum dots are formed through a mechanism different from the Stranski–Krastanov mechanism. According to transmission electron microscopy, these quantum dots are two-dimensional disk-shaped islands with a lateral size of approximately 10 nm [6, 9]. The small size of these dots removes the forbiddenness from the indirect recombination in the k space due to the uncertainty relation. Moreover, as was shown by Makarov *et al.* [6], these objects can be type-I structures and hold promise for use in fabricating emitters.

In this work, we studied Si/Ge nanostructures with two-dimensional and three-dimensional nanoislands grown at low temperatures (T_g < 350°C). At low temperatures T_g, germanium and silicon in adjacent layers are mixed only slightly. Owing to the high germanium content in quantum dots in these nanostructures, their emission spectra are shifted toward the low-energy range with respect to the spectra of the nanostructures grown at high temperatures. This shift can often be necessary for applications. Note also that these objects have been investigated to a lesser extent. In order to reveal the specific features in the formation of a germanium wetting layer and germanium islands on a silicon surface at low temperatures of molecular-beam epitaxy, Si/Ge nanostructures were studied using atomic force microscopy (AFM), photoluminescence (PL), and reflection high-energy electron diffraction (RHEED).

2. SAMPLE PREPARATION AND EXPERIMENTAL TECHNIQUE

The Si/Ge nanostructures used in our experiments were grown on Si(001) substrates through molecular-beam epitaxy on Riber SIVA-45 and Katun' apparatuses. As a rule, the nanostructures consisted of four or five germanium layers separated by silicon barriers. The thickness of silicon layers was equal to 25 nm, and the thickness of germanium layers was varied from 2 to 12 monolayers (ML). For observations with an atomic force microscope, the upper germanium layer in a number of samples was not covered with silicon. The growth temperatures of germanium and silicon layers

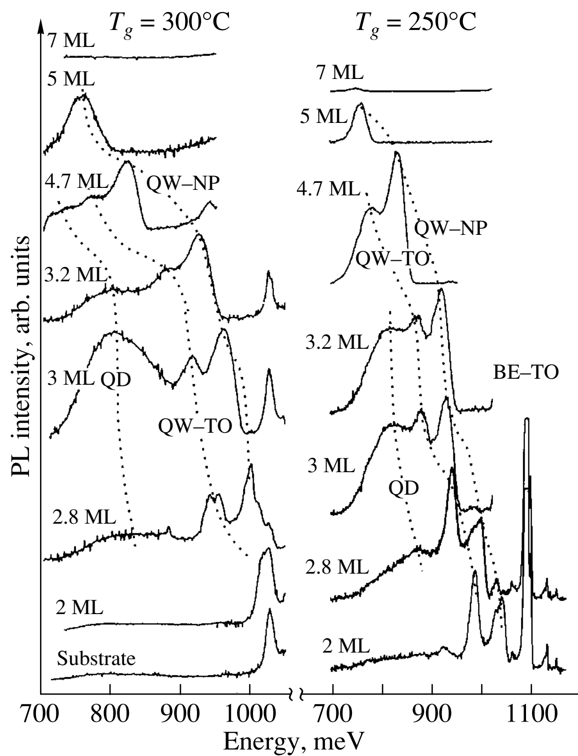

Fig. 1. Evolution of the photoluminescence spectra of the Si/Ge multilayer nanostructures with an increase in the thickness of germanium layers (the thickness is given in monolayers). $T = 2$ K, $\lambda = 0.66$ μm. Designations: QW–TO and QW–NP are the phonon (silicon) and zero-phonon lines of the quantum-well emission, respectively; QD is the line of the quantum-dot emission; and BE–TO is the phonon line of emission of bound excitons.

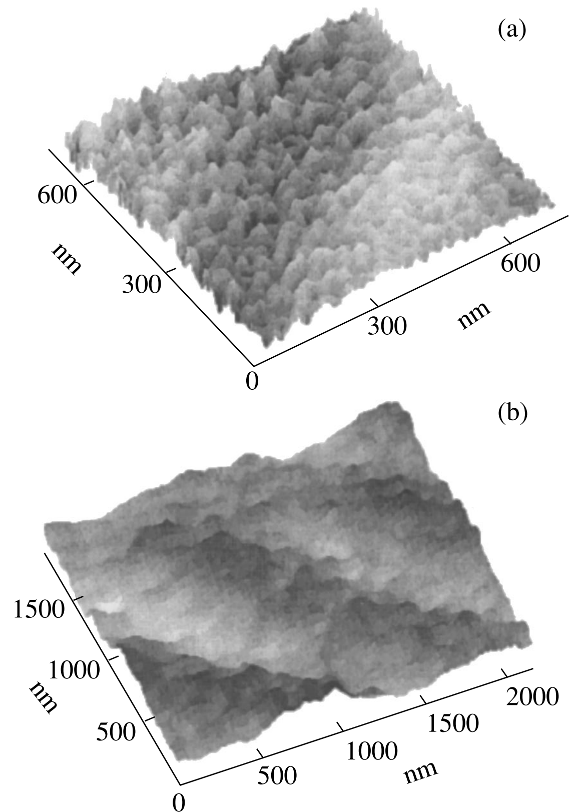

Fig. 2. AFM images of the surfaces of the structures grown at temperatures (a) $T_g = 250$–300°C with a germanium layer thickness of 3 ML and (b) $T_g = 250$°C with a germanium layer thickness of 5 ML.

were equal to 250–300 and 300–450°C, respectively. The deposition rate of germanium layers fell in the range 0.005–0.01 nm/s. Several nanostructures were grown on the Katun' apparatus at temperatures ranging from 300 to 350°C. The number of germanium layers and the thicknesses of germanium and silicon layers were different in these nanostructures.

The morphology of germanium layers was examined using a SOLVER P-47 atomic force microscope. The photoluminescence spectra were measured at temperatures of 2 and 5 K and at wavelengths of exciting radiation $\lambda = 0.66$ and 0.488 μm. The emission was recorded with a germanium *p–i–n* photodiode cooled with liquid nitrogen.

3. RESULTS AND DISCUSSION

Figure 1 shows the photoluminescence spectra of multilayer nanostructures of two series ($T_g = 250$ and 300°C) with different thicknesses of the germanium layers.

The photoluminescence spectra contain two emission lines (namely, the phonon line and the zero-phonon line) associated with the formation of a wetting layer and the emission line attributed to quantum dots. The spectra are cut in the low-energy range (at ~0.7 eV) because of the spectral limitations of the germanium photodetector.

A comparison of the photoluminescence spectra obtained in this work with the corresponding spectra of nanostructures grown at higher temperatures [2–4] revealed that, in our case, the emission of quantum dots exhibits unusual behavior. This emission is clearly observed even at a germanium layer thickness of 2.8 ML. The emission intensity reaches a maximum at a germanium layer thickness of 3 ML and sharply decreases (as compared to the intensity of emission of the wetting layer) with a further increase in the germanium coverage. In the case of nanostructures grown at high temperatures of molecular-beam epitaxy, the emission of two-dimensional layers vanishes against the background of an increasing intensity of the island emission with an increase in the layer thickness. It should also be noted that, in our spectra, the phonon replicas of the emission line associated with the quantum dots are either weakly pronounced or not observed altogether. This suggests that the studied nanostructures can undergo quasi-direct transitions. An analysis

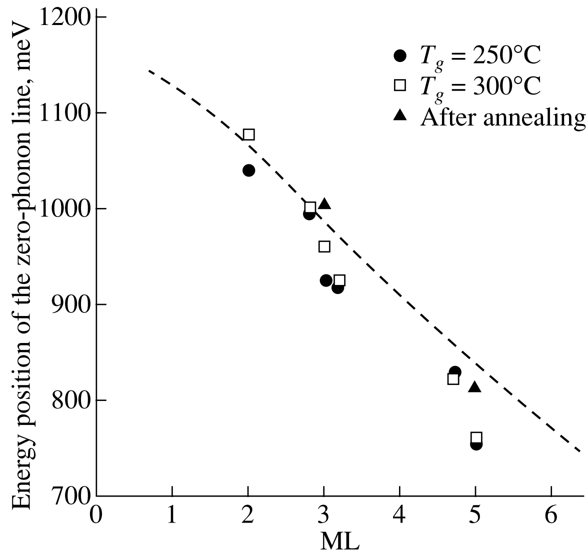

Fig. 3. Dependence of the energy position of the zero-phonon emission line assigned to the germanium quantum wells in silicon on the thickness of germanium layers (the thickness is given in monolayers). The dashed line corresponds to the results of the calculation according to the data taken from [11].

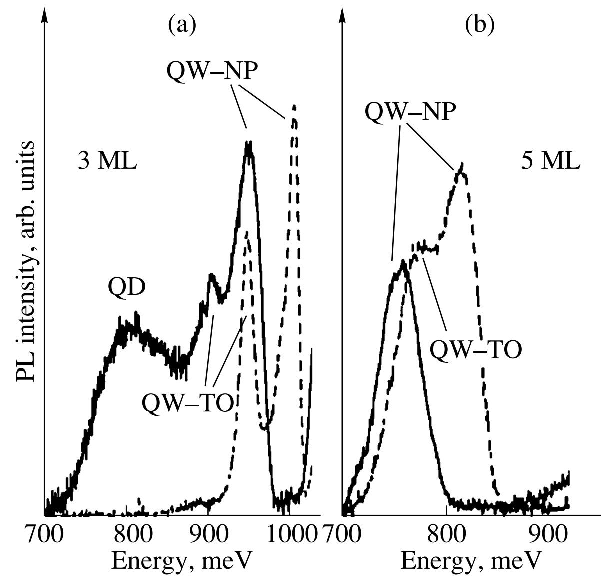

Fig. 4. Evolution of the photoluminescence spectra of the nanostructures grown at temperatures T_g = (a) 250 and (b) 300°C upon annealing (a) at 500°C for 2 min and (b) at 400°C for 2 min. The solid and dashed lines indicate the spectra measured before and after annealing, respectively.

of the RHEED patterns measured during the growth of nanostructures demonstrated that the three-dimensional structures manifest themselves only when the thickness of the germanium layer becomes greater than 7 ML.

The characteristic AFM image of the surface of the structures grown at T_g = 250–300°C with a germanium layer thickness of 3 ML is displayed in Fig. 2a. It can be seen that the surface morphology of the structures with a germanium coverage of less than 5 ML is characterized by a small-sized island relief. An increase in the layer thickness to 5 ML leads to a substantial smoothing of the surface (Fig. 2b). The smoothing of the surface relief is accompanied by a drastic decrease in the intensity of the emission associated with the nanoislands (Fig. 1). In the case where the thickness of the germanium layer reaches 10–12 ML, islands somewhat larger in size than those formed at the initial growth stage are again observed in the AFM images. A similar morphological transformation of the germanium layers grown at T_g = 300°C on the silicon surface was revealed in our previous work [10]. Note that the smoothing of the surface of these structures is more pronounced.

The energy positions of the zero-phonon emission lines assigned to the quantum wells and the results of the theoretical calculation carried out by Vescan *et al.* [11] are compared in Fig. 3. It can be seen from the experimental data that, beginning with a layer thickness of 3 ML, the germanium coverage exceeds the mean thickness of germanium layers. This indicates that the two-dimensional germanium layer on the silicon surface is not a continuous layer (the two-dimensionality of the germanium layer is confirmed by the photoluminescence spectra and the RHEED patterns).

Short-term annealing (120 s) of the nanostructures at temperatures of 400–500°C results in the formation of a continuous layer and its smoothing (Figs. 3, 4).

The photoluminescence spectra of the nanostructures grown at temperature T_g = 300°C (Fig. 5a) exhibit an unusual feature, namely, a narrow line at an energy of 1080 meV, whose position remains unchanged even though the technological thickness of the germanium layer is varied. Figure 5b shows the photoluminescence spectrum measured under optimum conditions of observation (the temperature is somewhat higher than the liquid-helium temperature, the spectrum is excited by radiation of an argon laser, and the thickness of germanium layers in the nanostructure is equal to 5 ML). A similar line was observed earlier in [8, 10]. This line arises at a germanium layer thickness of 3.2 ML when the intensity of the emission associated with the islands begins to decrease, reaches a maximum at a layer thickness of 5 ML, and disappears with a further increase in the thickness of germanium layers. For nanostructures grown at T_g = 250°C, this line is not observed in the spectra. In order to investigate the behavior of this line under changes in the growth temperature, we prepared several nanostructures (on the Katun' apparatus) at temperatures T_g = 300–350°C. Examination of these nanostructures revealed that the number of germanium layers and the thickness of the silicon barriers between

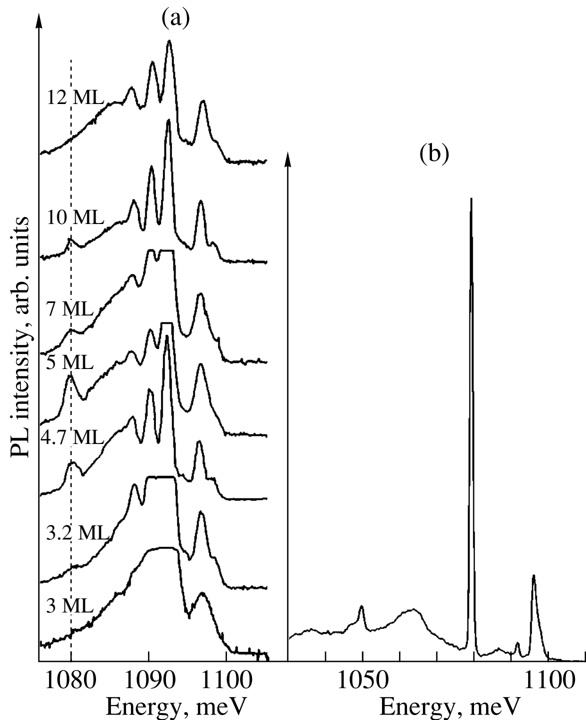

Fig. 5. (a) Dependence of the intensity of the photoluminescence line at an energy of 1080 meV on the thickness of the germanium layer. (b) Photoluminescence spectrum with the line at 1080 meV under optimum conditions of observation (5 ML, $T = 5$ K, $\lambda = 0.488$ μm).

the germanium layers do not affect the characteristics of the line of interest. Elucidation of the origin of the photoluminescence line at an energy of 1080 meV calls for further investigation. Despite the clear correlation with the morphological transformation of the germanium layer, the extremely narrow spectral width (~1 meV) of this line complicates its interpretation as a line of the emission associated with the quantum well, especially as the line is observed simultaneously with the emission of the wetting layer under conditions where this layer is not continuous. Note that, according to Thonke *et al.* [12], the narrow lines in this spectral range can be attributed to radiation-induced defects in silicon doped with boron.

4. CONCLUSIONS

Thus, the results of the above investigation into the properties of nanostructures grown through molecular-beam epitaxy at temperatures ranging from 250 to 300°C can be summarized as follows. At the initial growth stage, the two-dimensional germanium layer (3–5 ML) is not continuous. This is confirmed by comparing the photoluminescence spectra measured before and after annealing with the results of theoretical calculations. When the thickness of germanium layers does not exceed 3 ML, there arise small-sized amorphous islands. These islands manifest themselves in the photoluminescence spectra and are observed in the AFM images but cannot be identified as three-dimensional species according to the RHEED patterns. As follows from the RHEED data, three-dimensional nanostructures are formed beginning with a layer thickness exceeding 7 ML. In the range 3–5 ML, the surface undergoes a structural transformation; i.e., the small-sized (50 nm) island relief transforms into a smooth undulating relief. This leads to a drastic decrease in the intensity of the quantum-dot emission. Moreover, the morphological transformation of the surface into an undulating relief is accompanied by the appearance of a photoluminescence line at an energy of 1080 meV. This line disappears after annealing or with an increase in the thickness of the germanium layer when the surface is overgrown with islands according to the Stranski–Krastanov mechanism.

ACKNOWLEDGMENTS

This work was supported by the International Association of Assistance for the Promotion of Cooperation with Scientists from the New Independent States of the Former Soviet Union (project no. INTAS 03-51-5015), the Russian Foundation for Basic Research (project nos. 03-02-20007, 03-02-17191), the Presidium of the Russian Academy of Sciences within the program "Low-Dimensional Quantum Structures," and the Portuguese Science and Technology Foundation (FCT) (project no. 41574/2001).

REFERENCES

1. O. P. Pchelyakov, Yu. B. Bolkhovityanov, A. V. Dvurechenskiĭ, L. V. Sokolov, A. I. Nikiforov, A. I. Yakimov, and B. Voigtländer, Fiz. Tekh. Poluprovodn. (St. Petersburg) **34** (11), 1281 (2000) [Semiconductors **34**, 1229 (2000)].

2. G. Abstreiter, P. Schittenhelm, C. Engel, E. Silveira, A. Zrenner, D. Meertens, and W. Jäger, Semicond. Sci. Technol. **11**, 1521 (1996).

3. P. Schittenhelm, C. Engel, F. Findeis, G. Abstreiter, A. A. Darhuber, G. Bauer, A. O. Kosogov, and P. Werner, J. Vac. Sci. Technol. B **16** (3), 1575 (1998).

4. O. G. Schmidt, C. Lange, and K. Eberl, Appl. Phys. Lett. **75**, 1905 (1999).

5. A. V. Dvurechenskiĭ and A. I. Yakimov, Fiz. Tekh. Poluprovodn. (St. Petersburg) **35** (9), 1143 (2001) [Semiconductors **35**, 1095 (2001)].

6. A. G. Makarov, N. N. Ledentsov, A. F. Tsatsul'nikov, G. E. Cirlin, V. A. Egorov, N. D. Zakharov, and P. Werner, Fiz. Tekh. Poluprovodn. (St. Petersburg) **37** (2), 219 (2003) [Semiconductors **37**, 210 (2003)].

7. V. A. Markov, H. H. Cheng, Chin-ta Chia, A. I. Nikiforov, V. A. Cherepanov, O. P. Pchelyakov, K. S. Zhurav-

lev, A. B. Talochkin, E. McGlynn, and M. O. Henry, Thin Solid Films **369**, 79 (2000).

8. T. M. Burbaev, T. N. Zavaritskaya, V. A. Kurbatov, N. N. Mel'nik, V. A. Tsvetkov, K. S. Zhuravlev, V. A. Markov, and A. I. Nikiforov, Fiz. Tekh. Poluprovodn. (St. Petersburg) **35** (8), 979 (2001) [Semiconductors **35**, 941 (2001)].
9. M. M. Rzaev, T. M. Burbaev, V. A. Kurbatov, N. N. Melnik, M. Mühlberger, A. O. Pogosov, F. Schäffler, N. N. Sibeldin, V. A. Tsvetkov, P. Werner, N. D. Zakharov, and T. N. Zavaritskaya, Phys. Status Solidi C **0**, 1262 (2003).
10. T. M. Burbaev, V. A. Kurbatov, A. O. Pogosov, M. M. Rzaev, N. N. Sibel'din, and V. A. Tsvetkov, Fiz. Tverd. Tela (St. Petersburg) **46** (1), 74 (2004) [Phys. Solid State **46**, 71 (2004)].
11. L. Vescan, M. Gorlin, T. Stoica, P. Gartner, K. Grimm, O. Chrieten, E. Matveeva, C. Dieker, and B. Holländer, Appl. Phys. A **71**, 423 (2000).
12. K. Thonke, J. Weber, J. Wagner, and R. Sauer, Physica B (Amsterdam) **116**, 252 (1983).

Translated by O. Borovik-Romanova

Physics of the Solid State, Vol. 47, No. 1, 2005, pp. 76–81. Translated from Fizika Tverdogo Tela, Vol. 47, No. 1, 2005, pp. 74–79.
Original Russian Text Copyright © 2005 by Aleshkin, Antonov, Veksler, Gavrilenko, Erofeeva, Ikonnikov, Kozlov, Kuznetsov, Spirin.

PROCEEDINGS OF THE CONFERENCE
"NANOPHOTONICS 2004"
(Nizhni Novgorod, Russia, May 2–6, 2004)

Shallow Acceptor Levels in Ge/GeSi Heterostructures with Quantum Wells in a Magnetic Field

V. Ya. Aleshkin*, A. V. Antonov*, D. B. Veksler*, V. I. Gavrilenko*, I. V. Erofeeva*, A. V. Ikonnikov*, D. V. Kozlov*, O. A. Kuznetsov, and K. E. Spirin***

**Institute for Physics of Microstructures, Russian Academy of Sciences, Nizhni Novgorod, 603950 Russia*

e-mail: dvkoz@ipm.sci-nnov.ru

***Research Physicotechnical Institute, Lobachevskiĭ State University, pr. Gagarina 23/5, Nizhni Novgorod, 603950 Russia*

Abstract—Shallow acceptors in Ge/GeSi heterostructures with quantum wells are studied theoretically and experimentally in the presence of a magnetic field. It is shown that, in addition to the cyclotron resonance lines, magnetoabsorption spectra reveal transitions from the acceptor ground state to excited states related to Landau levels from the first and second confinement subbands, as well as the resonances caused by ionization of A^+ centers. © *2005 Pleiades Publishing, Inc.*

1. INTRODUCTION

In recent years, there have been numerous studies on shallow acceptors in Ge/GeSi heterostructures with quantum wells (QWs) [1–5]. In these structures, due to the built-in strain and quantum confinement, the subbands of light and heavy holes are split; therefore, the hole effective masses decrease. Accordingly, the binding energies of shallow acceptors become appreciably smaller than those in bulk Ge, in contrast to donors, whose binding energy increases as compared to the bulk case because of additional confinement of the wave function by the QW potential. Previously, we described a new experimental method of studying shallow impurities in semiconductors by measuring the differential impurity magnetoabsorption in the terahertz range for modulated interband photoexcitation of charge carriers [6–8]. In the present study, this method is used to determine the types of shallow acceptor centers that contribute to the observed magnetoabsorption in the terahertz range in Ge/GeSi heterostructures. It is known that, in the energy spectrum of a shallow impurity center in a QW, there are states related to different confinement subbands [9]. If a magnetic field is applied normal to the layer plane of the heterostructure, the electron and hole confinement subbands are split into series of Landau levels. In the case of donors, the levels belonging to different confinement subbands do not interact with one another. For acceptors, the situation is more complicated: a "mixing" of motion along the growth direction of the structure with transverse motion in the Luttinger Hamiltonian results in an interaction of hole states belonging to different confinement subbands. We note that, if the Hamiltonian that describes the carrier motion in a quantum well in the presence of a magnetic field is axially symmetric, the carrier states are degenerate with respect to the projection of the angular momentum onto the symmetry axis (see, for example, [10]). If an impurity ion is introduced, this degeneracy is lifted and a set of discrete impurity states appears. In this case, a very complicated pattern of lines related to transitions between such states can be observed in the impurity magnetoabsorption spectrum. In order to provide a detailed description of impurity transitions in Ge/GeSi heterostructures with QWs in a magnetic field and to interpret the experimental results, we developed a numerical method based on expanding the acceptor wave function in terms of the wave functions of holes in a QW in the absence of a magnetic field.

2. EXPERIMENTAL

In what follows, we present the results of a study of magnetoabsorption spectra in the submillimeter region for two $Ge/Ge_{1-x}Si_x$ heterostructures grown on lightly doped Ge(111) substrates by gas-transport epitaxy. Both structures consisted of 162 Ge QWs separated by GeSi barriers. The structures had the following parameters: $x = 0.12$, $d_{Ge} = 200$ Å, $d_{GeSi} = 260$ Å, and $\varepsilon_{xx} = 2.2 \times 10^{-3}$ (structure 306) and $x = 0.09$, $d_{Ge} = 350$ Å, $d_{GeSi} = 150$ Å, and $\varepsilon_{xx} = 4.4 \times 10^{-4}$ (structure 308). For both structures, the total thickness exceeded the critical thickness, so the elastic stress relaxed at the substrate–heterostructure interface. As a result, the Ge layers were biaxially stretched (ε_{xx} is a biaxial elastic strain measured by x-ray diffraction) and the GeSi layers were biaxially compressed. The structures were not intentionally doped; the concentration of residual

1063-7834/05/4701-0076$26.00 © 2005 Pleiades Publishing, Inc.

acceptors was about 10^{14} cm^{-3} [1]. In order to prevent interference from microwave radiation in the samples, the substrates were polished to form a wedge with an angle of 2°. The samples were placed at the center of a superconducting solenoid in a cryomagnetic cell introduced into a helium transport STG-40 dewar vessel. Absorption spectra were measured at $T = 4.2$ K at a constant radiation frequency with magnetic field scanning. Backward-wave tubes were used as radiation sources covering the frequency range from 300 to 1250 GHz. Free carriers in a sample were generated by radiation from a gallium arsenide light-emitting diode ($\lambda \approx 0.9$ μm). The radiation transmitted through the structure was detected by an n-InSb crystal. Most measurements were performed using radiation modulation with a 1-kHz meander and a standard locked-in detection circuit. Measurements with time resolution of the signal were also performed using pulsed optical excitation. In this case, the pulse signal was recorded as a function of the magnetic field using a TDS3034B "Tektronix" multichannel digital oscillograph.

3. METHOD OF CALCULATION

To calculate the spectrum of a shallow acceptor, we have to solve the effective-mass equation with the Hamiltonian written as a sum of the kinetic energy (the magnetic field–dependent Luttinger Hamiltonian), the potential energy of a hole in the QW, and a term describing the strain and the energy of Coulomb interaction with the charged acceptor. The magnetic field was assumed to be directed along the z axis, which was chosen to coincide with the growth axis of the structure.

The effective-mass equation was written in the two-dimensional-momentum representation. The acceptor wave function in the momentum representation is

$$\Psi_k^{(s)}(\mathbf{k}, z) = \int \Psi_\rho^{(s)}(\boldsymbol{\rho}, z)\exp(-i\mathbf{k}\boldsymbol{\rho})d^2\boldsymbol{\rho}, \qquad (1)$$

where $s = 1, \ldots, 4$ is the number of the hole wave function component. In this representation, the Hamiltonian describing the motion of a hole in the QW in the presence of a magnetic field takes the form

$$H_L = \begin{pmatrix} F & H & I & 0 \\ H^* & G & 0 & I \\ I^* & 0 & G & -H \\ 0 & I^* & -H^* & F \end{pmatrix}, \qquad (2)$$

where

$$F = \hbar^2\frac{(\gamma_1(z)+\gamma_3(z))(\hat{k}_x^2+\hat{k}_y^2)+\hat{k}_z(\gamma_1(z)-2\gamma_3(z))\hat{k}_z}{2m_0} + \frac{d(z)}{\sqrt{3}}(\varepsilon_{zz}-\varepsilon_{xx}) \pm \frac{3\hbar eB\kappa}{4m_0c} + V(z), \qquad (3)$$

$$G = \hbar^2\frac{(\gamma_1(z)-\gamma_3(z))(\hat{k}_x^2+\hat{k}_y^2)+\hat{k}_z(\gamma_1(z)+2\gamma_3(z))\hat{k}_z}{2m_0} - \frac{d(z)}{\sqrt{3}}(\varepsilon_{zz}-\varepsilon_{xx}) \pm \frac{\hbar eB\kappa}{4m_0c} + V(z), \qquad (4)$$

$$H = \hbar^2\frac{-i\frac{1}{\sqrt{3}}\{(2\gamma_2+\gamma_3)\hat{k}_z\}(\hat{k}_x-i\hat{k}_y) + i\sqrt{\frac{2}{3}}(\gamma_2-\gamma_3)(\hat{k}_x+i\hat{k}_y)^2}{2m_0}, \qquad (5)$$

$$I = \hbar^2\frac{\frac{(\gamma_2+2\gamma_3)}{\sqrt{3}}(\hat{k}_x-i\hat{k}_y)^2 + \sqrt{\frac{2}{3}}\{(\gamma_2-\gamma_3)\hat{k}_z\}(\hat{k}_x+i\hat{k}_y)}{2m_0}. \qquad (6)$$

Here, $\hat{k}_x = k_x + i\frac{eB}{2\hbar c}\frac{\partial}{\partial k_y}$, $\hat{k}_y = k_y - i\frac{eB}{2\hbar c}\frac{\partial}{\partial k_x}$, and $\hat{k}_z = -i\frac{\partial}{\partial z}$; γ_1, γ_2, γ_3, and κ are the Luttinger parameters, which depend on the material; d is the deformation potential constant for the valence band; ε_{ij} are the strain tensor components; m_0 is the free electron mass; B is the magnetic field; and V is the QW potential. The vector potential was chosen as $\mathbf{A} = \frac{1}{2}[\mathbf{B}\times\mathbf{r}]$, and the braces denote the anticommutator $\{\gamma_3 k_z\} = \gamma_3 k_z + k_z\gamma_3$.

In the momentum representation, the Coulomb potential operator, which is a diagonal matrix, has an integral form,

$$\hat{V}^{(s,s)}(k,z) = -\frac{e^2}{\chi}\int_0^\infty dk'\int_0^{2\pi} d\beta\Psi_k^{(s)}(k',\beta,z) \times \frac{\exp(-|z|\sqrt{(k'-k)^2+2k'k(1-\cos\beta)})}{\sqrt{(k'-k)^2+2k'k(1-\cos\beta)}}, \qquad (7)$$

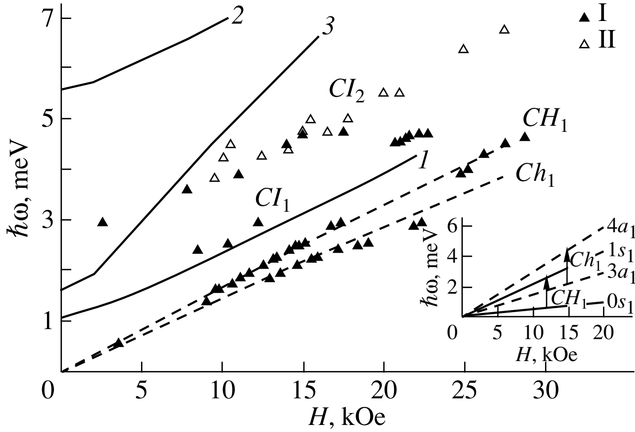

Fig. 1. (I) Summarized data on the positions of the observed magnetoabsorption spectral lines for the $Ge/Ge_{0.88}Si_{0.12}$ structure 306 (d_{Ge} = 200 Å) and the calculated energies of optical transitions between the states of an acceptor placed at the center of the GeSi barrier (solid lines *1–3*) and Landau levels of holes in a quantum well (dashed CH_1 and Ch_1 lines). (II) Data from photoconductivity measurements. The inset shows the hole Landau levels, transitions between which correspond to the CH_1 and Ch_1 lines; solid lines represent the lowest Landau level corresponding to the projection of the angular momentum onto the z axis $J = -3/2$ ($0s_1$, following the classification developed in [5]) and the lowest level with $J = -1/2$ ($1s_1$ [5]); dashed lines represent the lowest Landau level for holes with $J = +3/2$ ($3a_1$, following the classification developed in [5]) and the lowest Landau level of holes with $J = +5/2$ ($4a_1$ [4]).

where β is the angle between the vectors **k** and **k**', χ is the permittivity of the semiconductor, and e is the elementary charge.

As in [3], we use the axial approximation, i.e., we disregard the anisotropy of the hole dispersion law in the QW plane. To this aim, in the off-diagonal elements of the Luttinger Hamiltonian given by Eqs. (5) and (6), we omit the terms proportional to (γ_2–γ_3). In the axial approximation, the projection of the total angular momentum J onto the normal to the QW plane is conserved. Therefore, the dependence of the acceptor wave function $\Psi_k^{(s)}(\mathbf{k}, z)$ on the direction of the wave vector **k** specified by the angle β has a simple form,

$$\Psi_k^{(s)}(k, \beta, z) = \Psi_k^{(s)}(k, z)\exp\left[i\beta\left(J + s - \frac{5}{2}\right)\right]. \quad (8)$$

We search for the acceptor wave function in the form of an expansion in terms of the wave functions of holes in the QW in the absence of a magnetic field and an impurity ion. Substituting this expansion into the effective-mass equation with the Hamiltonian (2) and Coulomb potential (7), we obtain an integrodifferential equation for the expansion coefficients. Following [3], we solved this equation by replacing the derivatives by finite differences and the integral over k' in Eq. (7) by a discrete sum that was truncated at values of k' much greater than the inverse Bohr radius.

4. RESULTS AND DISCUSSION

In Fig. 1, we summarize the data on the positions of the observed magnetoabsorption spectral lines in structure 306. The CH_1 and Ch_1 lines were observed for the first time in [11–13]; they are related to the $0s_1 \longrightarrow 1s_1$ and $3a_1 \longrightarrow 4a_1$ cyclotron transitions between the lower Landau levels for holes (see inset to Fig. 1). Various Ge/GeSi samples exhibit up to three magnetoabsorption lines to the left of the main cyclotron resonance (CR) line CH_1 (i.e., on the side of lower magnetic fields). These lines are related to transitions involving shallow impurities (acceptors), which is also confirmed by polarization measurements [6–8]. It is seen in Fig. 1 that the positions of the CI_1 and CI_2 lines are not extrapolated to the origin, in contrast to the CR lines. Observation of the magnetoabsorption of shallow acceptors using modulated interband illumination becomes possible due to carriers captured by ionized impurities, which are always present in the sample due to partial compensation of the majority impurities (acceptors) by donors (see, e.g., [1]). The CI_1 line in sample 306a was observed for the first time in [11–13]; however, because of the strong overlap with the CH_1 line, its spectral position was not determined with sufficient accuracy. We succeeded in narrowing the lines and improving the spectral resolution by decreasing the interband illumination intensity [14]. In Fig. 1, in addition to the magnetoabsorption data, we show the positions of the CI_2 line, which were determined from the spectral measurements of the submillimeter photoconductivity using a backward-wave tube [4] and Fourier spectroscopy [1]. Earlier, we attributed this line either to the photoionization of A^+ centers or to the $1s \longrightarrow 2p_+$ transition for neutral acceptors (A^0 centers) located in the barrier. It is known that the binding energy of a neutral impurity is maximum and minimum at the center of the QW and at the center of the barrier, respectively. In the case of a homogeneously doped structure, the absorption (or photoconductivity) spectra exhibit two peaks corresponding to impurities located at the QW center (high-frequency peak) and at the center of the barrier (low-frequency peak) (for donors in GaAs/AlGaAs, this structure was discussed, for example, in [15]). We note that, when the impurity ion is moved into the barrier, the localized states of holes with energies below the bottom of the confinement subband are conserved. Such acceptor states are formed from the QW free-hole states. Typical acceptor binding energies in Ge/GeSi heterostructures are 7–8 meV at the QW center and 2 meV at the center of the barrier [8]; i.e., the transitions involving the acceptors located at the QW center lie outside the photon energy range that can be studied using a backward-wave tube (such transitions were observed when measuring the photoconductivity using a Fourier spectrometer [1]). For sample 306a, we observed for the first time two impurity magnetoabsorption lines, CI_1 and CI_2, in the “low-frequency” range; therefore, we were able to distinguish between

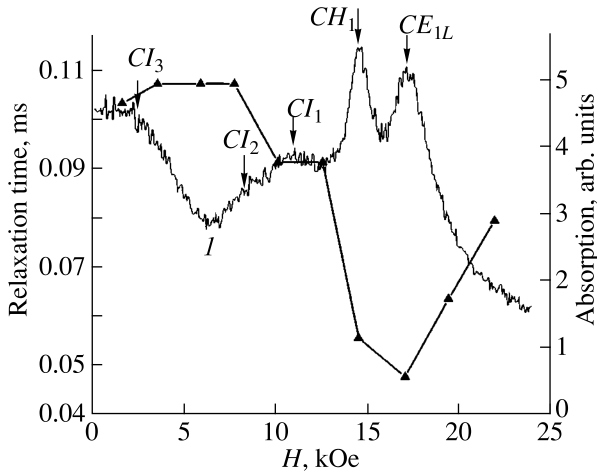

Fig. 2. (*1*) Typical magnetoabsorption spectrum in $Ge/Ge_{0.91}Si_{0.09}$ heterostructure 308 (d_{Ge} = 350 Å). Dots correspond to the relaxation times obtained from oscillograms of the magnetoabsorption signal under pulsed illumination.

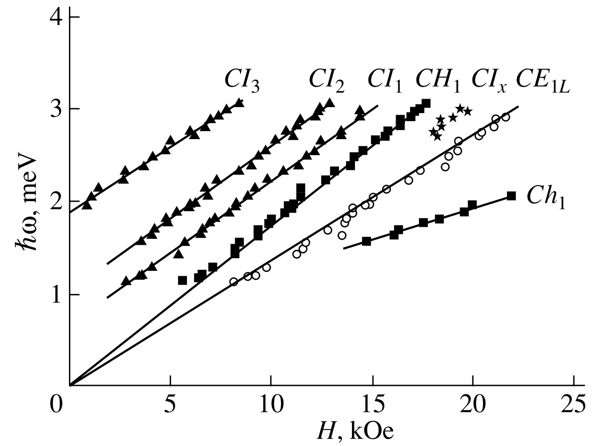

Fig. 3. Summarized data on the positions of the observed magnetoabsorption spectral lines for Ge/GeSi heterostructure 308. CH_1 and Ch_1 are the cyclotron resonance lines, and CI_1 and CI_3 are the impurity magnetoabsorption lines.

the absorption by A^+ centers and A^0 centers located in the barrier.

To interpret the observed magnetoabsorption lines in Ge/GeSi heterostructures, we calculated the energies of acceptor states corresponding to definite values of the projection of the total angular momentum J onto the growth axis of the structure. The acceptor ground-state level in a magnetic field splits into two states with projections ±3/2, of which the lower (ground) state has projection $J = –3/2$. It was shown in [5] (where a different expansion of the acceptor wave functions was used, namely, in terms of the eigenfunctions of holes in a magnetic field, i.e., the functions corresponding to Landau levels) that the spectra of impurity absorption are dominated by the transitions from the ground state (related to the lowest Landau level $0s_1$) to states with projection $J = –1/2$ and that only one of them (that to the state related to the first Landau level $1s_1$) survives in high magnetic fields; i.e., the $1s \longrightarrow 2p_+$ transition occurs. Therefore, in what follows, we restrict ourselves to detailed analysis of the transitions from the ground state to the states with $J = –1/2$.

Figure 1 shows the calculated energies of the $0s_1 \longrightarrow 1s_1$ and $3a_1 \longrightarrow 4a_1$ cyclotron transitions (CH_1 and Ch_1 resonances) (dashed lines) and impurity transitions from the ground-state level of an acceptor placed at the center of the quantum barrier ($J = –3/2$) to excited states corresponding to $J = –1/2$ (solid lines) in heterostructure 306. Lines *1* and *2* correspond to the transitions to the acceptor states related to the first Landau levels in the first and second confinement subbands ($1s_1$, $1a_2$), i.e., to transitions of the $1s \longrightarrow 2p_+$ type. Line *3* corresponds to the transition to the acceptor state corresponding to the second Landau level in the first confinement subband $2s_1$, i.e., to a transition of the type $1s \longrightarrow 3p_+$. We see that the calculated energies of cyclotron transitions agree well with the positions of the CH_1 and Ch_1 lines obtained experimentally. The position of the impurity magnetoabsorption line CI_1 is in reasonable agreement with curve *1* calculated for transitions of the $1s \longrightarrow 2p_+$ type within the first confinement subband for an impurity located at the center of the GeSi barrier. It is possible that the observed differences (experimental points lie somewhat higher than curve *1*) are due to the dispersion of transition energies because of a uniform distribution of the residual impurities over the structure. Thus, it seems that the CI_1 line corresponds to the excitation of A^0 centers located in the barrier. At the same time, our calculations show that the CI_2 line cannot be associated with transitions between the levels in the spectrum of a neutral acceptor. The first estimates of the binding energies of A^+ centers (i.e., neutral acceptors with an additional hole, located in the QW) obtained by the variational method give $E_+ \approx 2$ meV [16]. This value is somewhat lower than the extrapolated spectral position of the CI_2 line as $H \longrightarrow 0$ (Fig. 1). We may assume that A^+ centers, as well as D^- centers, have no excited bound states [17]; hence, the observed optical transitions must occur for $\hbar\omega \geq E_+$. Thus, the CI_2 line is, apparently, related to the excitation of A^+ centers.

A typical magnetoabsorption spectrum for structure 308 with a wider QW is shown in Fig. 2. We succeeded in observing three lines of impurity magnetoabsorption, CI_1–CI_3 [6–8] (the CE_{1L} line is related to electron CR in the $1L$ valley [18]); the data on the positions of the observed lines are summarized in Fig. 3. By analogy with sample 306, two impurity lines may be associated with the $1s \longrightarrow 2p_+$ transition for A^0 centers in the barriers (CI_1 or CI_2) and with the photoionization of

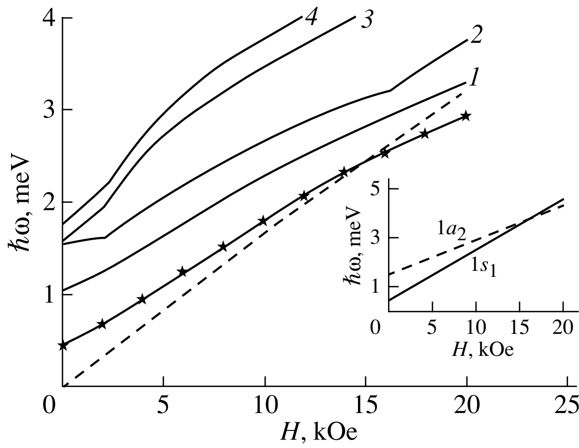

Fig. 4. Transitions from the ground-state acceptor level (J = –3/2) in $Ge/Ge_{0.91}Si_{0.09}$ heterostructure 308 (d_{Ge} = 350 Å) to the excited states corresponding to J = –1/2. Solid lines represent the transitions involving an impurity placed at the center of the quantum barrier. The asterisk line represents the $1s \longrightarrow 2p_+$ transition in the spectrum of a hole bound to an impurity ion in the neighboring well. The dashed line represents the cyclotron resonance of holes. The inset shows two Landau levels corresponding to projection J = –1/2; the solid line is for the lowest level related to the first confinement subband ($1s_1$, following the classification developed in [5]); and the dashed line is for the lowest level related to the second confinement subband ($1a_2$ [5]).

A^+ centers (CI_3). In [6–8], we assumed that the third line may be due to transitions between acceptor excited states, which can be populated under nonequilibrium conditions in the presence of interband illumination. For this to occur, it is necessary that the carrier interband recombination lifetime be comparable to the characteristic times of relaxation from the excited states, which are approximately equal to 10^{-8}–10^{-7} s [19]. However, our measurements of magnetoabsorption with time resolution have shown that the typical relaxation times for all impurity lines are about 10^{-4} s (Fig. 2). Hence, all observable impurity lines are related to transitions from the ground states of shallow acceptor centers.

Figure 4 shows the calculated energies of the $0s_1 \longrightarrow 1s_1$ cyclotron transition corresponding to the CH_1 line in Fig. 3 (dashed line) and impurity transitions from the ground state to states with J = –1/2 for an acceptor placed at the center of the quantum barrier in heterostructure 308 (solid lines). Lines *1* and *2* correspond to transitions to the states of the first Landau level (a transition of the $1s \longrightarrow 2p_+$ type) of different (first and second) confinement subbands. Thus, a small confinement energy (as compared to that in sample 306 with a narrower QW) results in the appearance of a doublet $1s \longrightarrow 2p_+$ transition. Although we did not calculate the transition matrix elements in this study, we may assume that the intensities of these transitions are comparable because of the strong hybridization of the states. It is seen in the inset to Fig. 4 that, in a magnetic field of about 16 kOe, there is a crossing of the first Landau levels $1s_1$ and $1a_2$ corresponding to the first and second confinement subbands (the crossing is a consequence of the strong nonparabolicity of the dispersion law for holes in a quantum well). In Fig. 4, we see that this results in the anticrossing of impurity levels related to these Landau levels with J = –1/2. Thus, for H < 16 kOe, line *1* corresponds to a transition to a state of the $2p_+$ type that virtually belongs to the first confinement subband and, for H > 16 kOe, to a state that belongs to the second subband. Lines *3* and *4* correspond to transitions to the states related to the second Landau level in the first and second confinement subbands, respectively. Finally, the asterisk line corresponds to the $1s \longrightarrow 2p_+$ transition for an exotic shallow neutral center (which was not discussed earlier) consisting of an acceptor located at the QW center that has captured a hole from a neighboring QW.

From comparing our experimental data with the results of the calculations for sample 308, it follows that the positions of the observed CI_1 and CI_2 lines (Fig. 3) qualitatively agree with calculated curves *1* and *2* in Fig. 4. Due to a rather strong overlap of the CI_1 and CI_2 lines (Fig. 2, [8, Fig. 1]), calculations of the absorption spectra are needed for a more detailed comparison between theory and experiment. As to the CI_3 line, its position is extrapolated to a quantum energy of about 2 meV as $H \longrightarrow 0$, which is in good agreement with the ionization energy of A^+ centers in the QW (as is the case in sample 306) [16]. On the other hand, the position of the CI_3 line in sample 308 agrees fairly well with curves *3* and *4* calculated for transitions of the type $1s \longrightarrow 3p_+$. Obviously, in order to determine the origin of the CI_3 line in this sample, it is necessary to calculate the matrix elements for the corresponding transitions.

In this study, we observed for the first time a new magnetoabsorption line, CI_x (Fig. 3), which appears on the right-hand wing of the hole CR line CH_1 as the frequency is increased. The performed calculations show that this new line can be related to the $1s \longrightarrow 2p_+$ transition in a very shallow neutral acceptor at the QW center with a hole bound to it in a neighboring QW. In principle, such bound states can appear under nonequilibrium conditions of optical excitation of free carriers, with subsequent capture by ionized impurities in heterostructures with QWs. It is seen in Fig. 4 that initially (at low magnetic fields) the energy of such a transition only slightly exceeds the energy of the cyclotron transition $0s_1 \longrightarrow 1s_1$ and, possibly, it cannot be resolved in the absorption spectrum against the background of the neighboring lines CI_1 and CH_1 (the distances from the transition energy to the CR energies are smaller than the spectral line widths). However, as the magnetic field is increased further, the energy of this transition varies sublinearly with magnetic field (cf. curve *1* in Fig. 4),

due to the above-mentioned crossing of the $1s_1$ and $1a_2$ Landau levels belonging to the first and second confinement subbands, and becomes smaller than the energy of the cyclotron transition (Fig. 4). The CI_1 line, which lies only 0.15 meV above the hole CR line CH_1 and is observed in sample 307 (having a somewhat wider QW, with d_{Ge} = 300 Å, and narrower CR and impurity magnetoabsorption lines than those in sample 306), is probably related to the excitation of such very shallow acceptors [8].

ACKNOWLEDGMENTS

The authors thank M.D. Moldavskaya for her longstanding cooperation, which laid the grounds for the present study, and V.L. Vaks, Yu.N. Drozdov, A.N. Panin, and E.A. Uskova for their help in preparing the experiments.

This study was supported by the Russian Foundation for Basic Research (projects nos. 03-02-16808, 04-02-17178), the Russian Academy of Sciences, the Ministry of Education and Science of the Russian Federation, and the federal program "Integration" (project no. B0039/2102).

REFERENCES

1. V. Ya. Aleshkin, V. I. Gavrilenko, I. V. Erofeeva, A. L. Korotkov, Z. F. Krasil'nik, O. A. Kuznetsov, M. D. Moldavskaya, V. V. Nikonorov, and L. V. Paramonov, Pis'ma Zh. Éksp. Teor. Fiz. **65**, 196 (1997) [JETP Lett. **65**, 209 (1997)].
2. V. Ya. Aleshkin, V. I. Gavrilenko, I. V. Erofeeva, D. V. Kozlov, A. L. Korotkov, O. A. Kuznetsov, and M. D. Moldavskaya, Phys. Status Solidi B **210**, 649 (1998).
3. V. Ya. Aleshkin, B. A. Andreev, V. I. Gavrilenko, I. V. Erofeeva, D. V. Kozlov, and O. A. Kuznetsov, Fiz. Tekh. Poluprovodn. (St. Petersburg) **34**, 582 (2000) [Semiconductors **34**, 563 (2000)].
4. V. Ya. Aleshkin, B. A. Andreev, V. I. Gavrilenko, I. V. Erofeeva, D. V. Kozlov, O. A. Kuznetsov, M. D. Moldavskaya, and A. V. Novikov, Physica E (Amsterdam) **7** (3–4), 608 (2000).
5. V. Ya. Aleshkin, V. I. Gavrilenko, D. B. Veksler, and L. Reggian, Phys. Rev. B **66**, 155336 (2002).
6. V. Ya. Aleshkin, D. B. Veksler, V. I. Gavrilenko, I. V. Erofeeva, A. V. Ikonnikov, D. V. Kozlov, and O. A. Kuznetsov, in *Proceedings of Meeting on Nanophotonics* (Inst. Fiziki Mikrostruktur Ross. Akad. Nauk, Nizhni Novgorod, 2003), p. 248.
7. V. Ya. Aleshkin, I. V. Erofeeva, V. I. Gavrilenko, A. V. Ikonnikov, D. B. Kozlov, O. A. Kuznetsov, and D. B. Veksler, in *Proceedings of 11th International Symposium on Nanostructures: Physics and Technology* (St. Petersburg, Russia, 2003), p. 214.
8. V. Ya. Aleshkin, A. V. Antonov, D. B. Veksler, V. I. Gavrilenko, I. V. Erofeeva, A. V. Ikonnikov, D. V. Kozlov, and O. A. Kuznetsov, Fiz. Tverd. Tela (St. Petersburg) **46** (1), 126 (2004) [Phys. Solid State **46**, 125 (2004)].
9. V. Ya. Aleshkin, B. A. Andreev, V. I. Gavrilenko, I. V. Erofeeva, D. V. Kozlov, and O. A. Kuznetsov, Nanotechnology **11** (4), 348 (2000).
10. L. D. Landau and E. M. Lifshitz, *Course of Theoretical Physics*, Vol. 3: *Quantum Mechanics: Non-Relativistic Theory*, 4th ed. (Nauka, Moscow, 1987; Oxford Univ. Press, Oxford, 1980).
11. V. Ya. Aleshkin, D. B. Veksler, V. L. Vaks, V. I. Gavrilenko, I. V. Erofeeva, O. A. Kuznetsov, M. D. Moldavskaya, J. Leotin, and F. Yang, in *Proceedings of Meeting on Nanophotonics* (Inst. Fiziki Mikrostruktur Ross. Akad. Nauk, Nizhni Novgorod, 1999), p. 114.
12. V. Ya. Aleshkin, V. I. Gavrilenko, I. V. Erofeeva, O. A. Kuznetsov, M. D. Moldavskaya, V. L. Vaks, and D. B. Veksler, in *Proceedings of 6th International Symposium on Nanostructures: Physics and Technology* (St. Petersburg, Russia, 1999), p. 356.
13. V. Ya. Aleshkin, D. B. Veksler, V. L. Vaks, V. I. Gavrilenko, I. V. Erofeeva, O. A. Kuznetsov, M. D. Moldavskaya, F. Yang, M. Goiran, and J. Leotin, Izv. Ross. Akad. Nauk, Ser. Fiz. **64**, 308 (2000).
14. V. Ya. Aleshkin, A. V. Antonov, D. B. Veksler, V. I. Gavrilenko, I. V. Erofeeva, A. V. Ikonnikov, D. V. Kozlov, O. A. Kuznetsov, and K. E. Spirin, in *Proceedings of Meeting on Nanophotonics* (Inst. Fiziki Mikrostruktur Ross. Akad. Nauk, Nizhni Novgorod, 2004), p. 129.
15. S. Huant, W. Knap, R. Stepniewski, G. Martinez, V. Thierry-Mied, and B. Etienne, in *High Magnetic Fields in Semiconductor Physics II*, Ed. by G. Landwehr (Springer, Berlin, 1989), Springer Ser. Solid-State Sci., Vol. 87, p. 293.
16. V. Ya. Aleshkin, V. I. Gavrilenko, and D. V. Kozlov, in *Proceedings of Meeting on Nanophotonics* (Inst. Fiziki Mikrostruktur Ross. Akad. Nauk, Nizhni Novgorod, 2003), p. 318.
17. A. B. Dzyubenko, Phys. Lett. A **165**, 357 (1992).
18. V. Ya. Aleshkin, D. B. Veksler, V. I. Gavrilenko, I. V. Erofeeva, A. V. Ikonnikov, D. V. Kozlov, and O. A. Kuznetsov, Fiz. Tverd. Tela (St. Petersburg) **46** (1), 131 (2004) [Phys. Solid State **46**, 130 (2004)].
19. S. V. Meshkov and É. I. Rashba, Zh. Éksp. Teor. Fiz. **76** (6), 2206 (1979) [Sov. Phys. JETP **49**, 1115 (1979)].

Translated by I. Zvyagin

Physics of the Solid State, Vol. 47, No. 1, 2005, pp. 82–85. Translated from Fizika Tverdogo Tela, Vol. 47, No. 1, 2005, pp. 80–82.
Original Russian Text Copyright © 2005 by Shamirzaev, Seksenbaev, Zhuravlev, Nikiforov, Ul'yanov, Pchelyakov.

PROCEEDINGS OF THE CONFERENCE "NANOPHOTONICS 2004"
(Nizhni Novgorod, Russia, May 2–6, 2004)

Photoluminescence of Germanium Quantum Dots Grown in Silicon on a SiO_2 Submonolayer

T. S. Shamirzaev, M. S. Seksenbaev, K. S. Zhuravlev, A. I. Nikiforov, V. V. Ul'yanov, and O. P. Pchelyakov

Institute of Semiconductor Physics, Siberian Division, Russian Academy of Sciences, ul. Akademika Lavrent'eva 13, Novosibirsk, 630090 Russia

e-mail: timur@thermo.isp.nsc.ru

Abstract—The photoluminescence of quantum dots in $Si/Ge/SiO_2/Si$ and Si/Ge/Si structures is investigated as a function of temperature. The low activation energies for the temperature quenching of photoluminescence of germanium quantum dots in both structures are explained in terms of the thermally stimulated capture of holes from quantum dots to the energy levels of defects localized in their vicinity. © *2005 Pleiades Publishing, Inc.*

1. INTRODUCTION

Structures with Si/Ge-based quantum dots have attracted the attention of researchers owing to their possible integration into modern silicon technology [1, 2]. It is known that the formation of quantum dots in semiconductors with different lattice parameters occurs through the Stranski–Krastanov mechanism. In the case when germanium layers are grown on silicon, a germanium wetting layer with a thickness of approximately 4 ML is initially formed on the silicon surface and then germanium islands grow on the wetting layer [3]. Recent investigations have revealed that the growth of germanium quantum dots on an oxidized surface proceeds according to the Volmer–Weber mechanism without the formation of a wetting layer [4]. At present, it has been established that the quantum dots in the $Si/Ge/SiO_2/Si$ system are characterized by a smaller size and a considerably higher density than those in the Si/Ge/Si system [4, 5]. The structural properties of these objects were investigated by Milekhin *et al.* [6]. However, the electronic structure and recombination of charge carriers in these quantum dots have not been studied yet.

The purpose of this work was to perform a comparative study of the charge carrier recombination in quantum dots in Si/Ge/Si and $Si/Ge/SiO_2/Si$ systems. The results obtained are in agreement with the conclusions drawn earlier by Nikiforov *et al.* [4], according to which the presence of a SiO_2 layer in the structure stimulates the growth of germanium quantum dots without the formation of a wetting layer. The low activation energies for quenching of photoluminescence (PL) observed with an increase in the temperature indicate a transfer of holes from the quantum-well levels not to the valence band of silicon but to the energy levels of a defect localized in the vicinity of the quantum dots.

2. SAMPLE PREPARATION AND EXPERIMENTAL TECHNIQUE

The structure to be studied was grown on a Si(100) substrate through molecular-beam epitaxy at a substrate temperature of 550°C. Immediately before the formation of a layer of germanium quantum dots, the surface of the silicon substrate was oxidized in an oxygen atmosphere in the growth chamber at a pressure $P = 10^{-4}$ Pa and a temperature of 500°C for 10 min. The thickness of the SiO_2 layer thus formed on the silicon surface was equal to 1–2 ML. Then, a germanium layer with a thickness of 3 ML was deposited on the SiO_2 layer. The germanium layers were grown at a substrate temperature of 550°C. Moreover, a structure with a thin SiO_2 layer that was not covered with a germanium layer and a structure with germanium quantum dots in the silicon matrix without preliminary oxidation of the silicon surface were grown for comparison. The latter structure was grown on the Si(100) substrate at a temperature of 700°C and contained five pairs of germanium and silicon layers, with a germanium layer thickness of 8 ML. The photoluminescence was excited by radiation from an argon laser at wavelength $\lambda = 488$ nm with a power density of 10 W/cm^2, was analyzed using a double grating monochromator, and was recorded by a cooled germanium *p–i–n* diode in a synchronous detection mode. The measurements were carried out in the temperature range $T = 5$–125 K.

3. RESULTS AND DISCUSSION

Figures 1 and 2 show the photoluminescence spectra of the structures with germanium quantum dots formed on the unoxidized and oxidized silicon surfaces and also the spectrum of the structure with a thin SiO_2 layer not covered with a germanium layer. All the spectra

shown in these figures were measured at a temperature of 5 K. It can be seen that the photoluminescence spectra of all the structures with germanium quantum dots contain a line with the maximum at an energy $h\nu = 1.1$ eV due to the recombination of excitons in bulk silicon. Moreover, the spectra of the structures with germanium quantum dots exhibit a line with the maximum at an energy $h\nu = 0.8$ eV (this line is denoted by the letter *T*). The absence of line *T* in the photoluminescence spectrum of the $Si/SiO_2/Si$ structure indicates that this line can be attributed to the recombination in germanium quantum dots. In the high-energy range, the photoluminescence spectrum of the $Si/Ge/SiO_2/Si$ structure contains two lines with maxima at energies $h\nu = 1.08$ and 1.06 eV. These lines are denoted by numerals *1* and *2*, respectively, and can be associated either with the two-phonon replicas of the exciton lines or with the band–impurity transitions in the silicon matrix [7]. The refinement of the nature of these lines would require an additional investigation, which is beyond the scope of our present work. Furthermore, the photoluminescence spectrum of the structure with germanium quantum dots grown without preliminary oxidation of the silicon surface is characterized by two lines with maxima at energies $h\nu = 0.94$ and 1.02 eV due to the recombination of excitons in the wetting layer. These lines are not observed in the photoluminescence spectra of the structure with germanium quantum dots formed on the oxidized silicon surface. These findings are in good agreement with the data obtained earlier by high-energy electron diffraction during the growth of the structure in [4], according to which the wetting layer is absent. As the temperature of the measurement increases, line *T* in the photoluminescence spectra of the structure with quantum dots formed on the unoxidized silicon surface is split into two lines with maxima at energies $h\nu_A$ = 0.779 eV (line *A*) and $h\nu_B$ = 0.829 eV (line *B*), as is shown in Fig. 3. These spectra were approximated by two Gaussian curves, and the results obtained were used to construct the temperature dependences of the integrated intensity of lines *A* and *B* (Fig. 4). The activation energies for temperature quenching of photoluminescence were determined to be E_A = 126 meV for line *A* and E_B = 66 meV for line *B*. It should be noted that our data are close to the activation energies for quenching of photoluminescence in quantum dots observed by Wan *et al.* [8].

Since the shape of line *T* in the photoluminescence spectra of the structure with quantum dots formed on the oxidized silicon surface changes with an increase in the temperature, this line can also be represented as the sum of two lines. However, we failed to decompose line *T* into components, because the photoluminescence spectra measured at elevated temperatures exhibit intense lines with maxima at energies $h\nu = 0.76$ and 0.74 eV, which are attributed to the recombination at the levels of defects in silicon with the participation of oxygen [7, 9, 10]. The activation energy of temperature

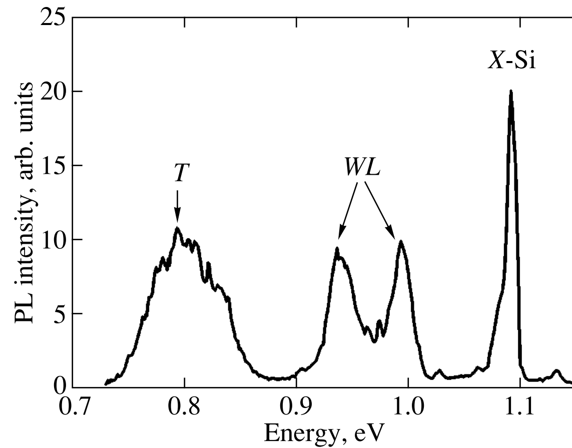

Fig. 1. Photoluminescence spectrum of the structure with Si/Ge/Si quantum dots at a temperature of 5 K.

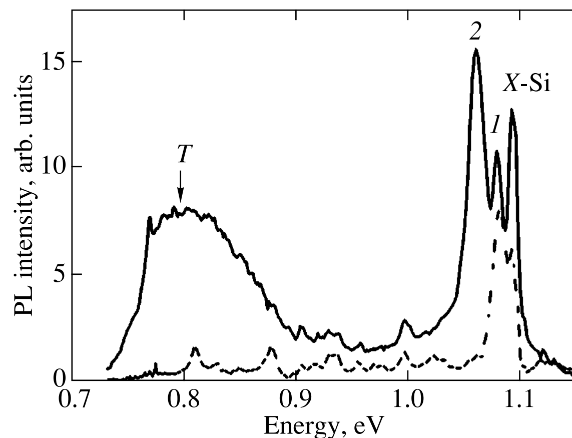

Fig. 2. Photoluminescence spectra of the structure with $Si/Ge/SiO_2/Si$ quantum dots (solid line) and the $Si/SiO_2/Si$ structure (dashed line) at a temperature of 5 K.

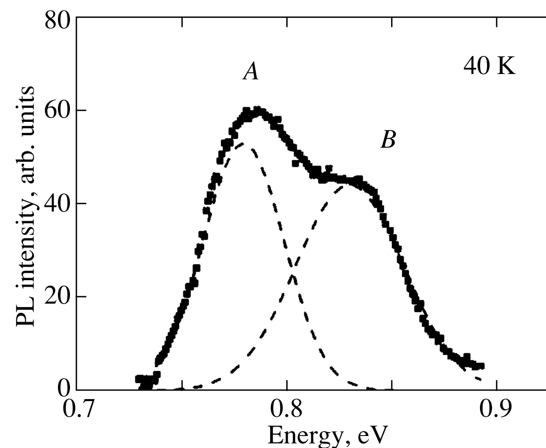

Fig. 3. Approximation of the photoluminescence spectrum of the structure with Si/Ge/Si quantum dots by two Gaussian curves.

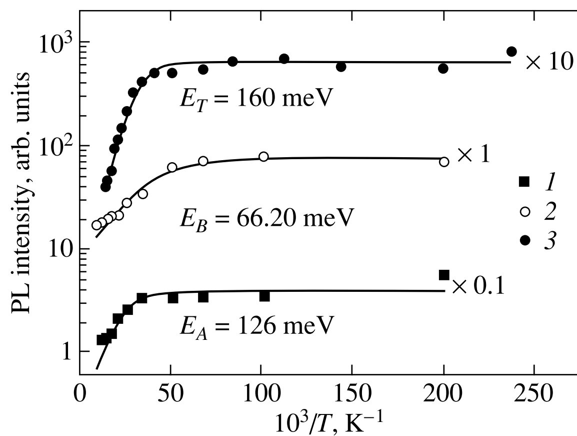

Fig. 4. Temperature dependences of the integrated intensity of (*1*) line *A* and (*2*) line *B* for the structure with Si/Ge/Si quantum dots and (*3*) line *T* for the structure with $Si/Ge/SiO_2/Si$ quantum dots.

quenching for line T (E_T) of the structure with quantum dots on the oxidized silicon surface is equal to 160 meV.

The differences between the energies at the maxima of lines *A* and *B* (50 meV) and the activation energies of their temperature quenching (60 meV) are close to each other. This allows us to assume that the origin of these lines is associated with the recombination of excitons in quantum dots of different sizes; consequently, the quantum dots in the structure under investigation are characterized by a bimodal size distribution.

It is believed that the temperature quenching of photoluminescence in Si/Ge/Si quantum dots is caused by the ejection of charge carriers from the quantum-well levels of holes into the silicon matrix [8]. In this case, the activation energy for temperature quenching of photoluminescence in quantum dots should be equal to the energy of localization of a hole in a quantum dot. According to the energy conservation law, the sum of the energy of hole localization and the energy at the maximum of the photoluminescence in quantum dots must be equal to the band gap of the silicon matrix (1.17 eV) minus the energy of electron localization and the binding energy of the exciton in the quantum dot. However, it is easy to see that this condition is not satisfied for any of the observed lines. Furthermore, the characteristic energies of hole localization, which are calculated for Ge/Si quantum dots, lie in the range 300–400 meV [11]. This is in agreement with the energy position of line *T* in the photoluminescence spectra of both structures (namely, Si/Ge/Si and $Si/Ge/SiO_2/Si$)[1] but disagrees greatly with our data on the activation energy for temperature quenching of photoluminescence in quantum dots. In our opinion, the difference between the activation energy for temperature quenching of photoluminescence in quantum dots and the calculated energies of hole localization is associated with the fact that an increase in the temperature leads to a transfer of holes from the quantum-well levels not to the valence band of silicon but to the energy levels of a defects localized in the vicinity of the quantum dots. In this case, the difference between the activation energy for temperature quenching of photoluminescence and the energy of localization of holes at the quantum-well levels is equal to the energy at the level of the defect, which amounts to approximately 200 meV. The small difference in the activation energies for temperature quenching of photoluminescence in Si/Ge/Si and $Si/Ge/SiO_2/Si$ quantum dots can be explained by the fact that the introduction of oxygen into silicon brings about a change in the energy level of the defect. According to this model, the use of a silicon matrix free of defects should sharply increase the activation energy for temperature quenching of photoluminescence in quantum dots. This effect was actually observed by Cirlin *et al.* [12], who revealed photoluminescence of quantum dots at room temperature. In this case, the activation energy is of the order of 300–400 meV.

[1] Since the exciton binding energy and the energy of electron localization in quantum dots are considerably less than the energy of hole localization, the main contribution to the difference between the band gap and the energy position of the line attributed to the recombination in quantum dots (1170 – 800 = 370 meV) is made by the energy of hole localization in the quantum dots.

4. CONCLUSIONS

Thus, we investigated the photoluminescence of quantum dots in Si/Ge/Si and $Si/Ge/SiO_2/Si$ structures. It was demonstrated that the photoluminescence spectra of $Si/Ge/SiO_2/Si$ quantum dots do not exhibit lines of exciton recombination in the wetting layer. It was revealed that the activation energy for temperature quenching of photoluminescence in quantum dots is several hundreds of millielectron-volts lower than the energy of hole localization in quantum dots. The results obtained were explained in terms of the thermally stimulated capture of holes from quantum dots to the energy levels of defects localized in the vicinity of the quantum dots.

ACKNOWLEDGMENTS

This work was partly supported by the International Association of Assistance for the Promotion of Cooperation with Scientists from the New Independent States of the Former Soviet Union (project no. INTAS 01-0444) and by the Russian Foundation for Basic Research (project no. 03-02-16468).

REFERENCES

1. O. P. Pchelyakov, Yu. B. Bolkhovityanov, A. V. Dvurechenskiĭ, L. V. Sokolov, A. I. Nikiforov, A. I. Yakimov, and B. Voigtländer, Fiz. Tekh. Poluprovodn. (St. Petersburg) **34**, 1281 (2000) [Semiconductors **34**, 1229 (2000)].

2. A. I. Yakimov, V. A. Markov, A. V. Dvurechenskiĭ, and O. P. Pchelyakov, Pis'ma Zh. Éksp. Teor. Fiz. **63**, 423 (1996) [JETP Lett. **63**, 444 (1996)].
3. T. M. Burbaev, T. N. Zavaritskaya, V. A. Kurbatov, N. N. Mel'nik, V. A. Tsvetkov, K. S. Zhuravlev, V. A. Markov, and A. I. Nikiforov, Fiz. Tekh. Poluprovodn. (St. Petersburg) **35**, 979 (2001) [Semiconductors **35**, 941 (2001)].
4. A. I. Nikiforov, V. V. Ul'yanov, O. P. Pchelyakov, S. A. Teys, and A. K. Gutakovskiĭ, Fiz. Tverd. Tela (St. Petersburg) **46**, 80 (2004) [Phys. Solid State **46**, 77 (2004)].
5. A. A. Shklyaev and M. Ichikawa, Surf. Sci. **514**, 19 (2002).
6. A. G. Milekhin, A. I. Nikiforov, M. Yu. Ladanov, O. P. Pchelyakov, S. Shultze, and D. R. T. Zahn, Fiz. Tverd. Tela (St. Petersburg) **46**, 94 (2004) [Phys. Solid State **46**, 92 (2004)].
7. G. Davies, Phys. Rep. **176**, 83 (1989).
8. J. Wan, Y. H. Luo, Z. M. Jiang, G. Jin, J. L. Liu, and Kang L. Wang, Appl. Phys. Lett. **79**, 1980 (2001).
9. J. Wagner, A. Dornen, and R. Sauer, Phys. Rev. B **31**, 5561 (1985).
10. A. Dornen, G. Pensl, and R. Sauer, Phys. Rev. B **35**, 9318 (1987).
11. A. V. Dvurechenskiĭ, A. V. Nenashev, and A. I. Yakimov, Izv. Ross. Akad. Nauk, Ser. Fiz. **66**, 156 (2002).
12. G. E. Cirlin, V. G. Talalaev, N. D. Zahkarov, V. A. Egorov, and P. Werner, Phys. Status Solidi B **232**, R1 (2002).

Translated by O. Moskalev

Physics of the Solid State, Vol. 47, No. 1, 2005, pp. 86–88. Translated from Fizika Tverdogo Tela, Vol. 47, No. 1, 2005, pp. 83–85.
Original Russian Text Copyright © 2005 by Andreev, Krasil'nik, Yablonsky, Kuznetsov, Gregorkiewicz, Klik.

PROCEEDINGS OF THE CONFERENCE "NANOPHOTONICS 2004"
(Nizhni Novgorod, Russia, May 2–6, 2004)

Erbium Photoluminescence Excitation Spectroscopy in Si : Er Epitaxial Structures

B. A. Andreev*, Z. F. Krasil'nik*, A. N. Yablonsky*, V. P. Kuznetsov, T. Gregorkiewicz***, and M. A. J. Klik*****

**Institute of the Physics of Microstructures, Russian Academy of Sciences, Nizhni Novgorod, 603950 Russia*
e-mail: yablonsk@ipm.sci-nnov.ru

*** Physicotechnical Institute, Lobachevskiĭ Nizhni Novgorod State University, pr. Gagarina 23/5, Nizhni Novgorod, 603950 Russia*

****Van der Waals–Zeeman Institute, University of Amsterdam, Valckenierstaat 65, NL-1018XE Amsterdam, The Netherlands*

Abstract—Excitation spectra of erbium photoluminescence in Si : Er epitaxial structures are studied within a broad pump wavelength range (λ_{ex} = 780–1500 nm). All the structures studied reveal a fairly strong erbium photoluminescence signal at photon energies substantially smaller than the silicon band-gap width (λ = 1060 nm) with no exciton generation. A possible mechanism of erbium ion excitation in silicon without exciton involvement is discussed. © *2005 Pleiades Publishing, Inc.*

1. INTRODUCTION

Erbium-doped silicon is presently attracting considerable attention because the wavelength of the $^4I_{13/2} \longrightarrow {}^4I_{15/2}$ radiating transition in the Er^{3+} ion 4f shell falls into the spectral region of maximum transparency of quartz fiber-optic communication lines ($\lambda \approx$ 1.54 μm). Sublimation molecular beam epitaxy (SMBE) [1] offers the possibility of producing uniformly and selectively doped Si : Er structures with a high lattice quality, which exhibit intense erbium photo- and electroluminescence at a wavelength of 1.54 μm [2].

It is known that the mechanism of erbium ion excitation in silicon involving the electron subsystem of the semiconductor is substantially more efficient than direct optical excitation of Er ions in insulating matrices [3, 4]. However, it is customarily assumed that energy transfer through the electron subsystem of silicon is a complex multistage process involving impurity levels in the silicon band gap and is not fully understood. This stimulated our study of the excitation spectra of the erbium photoluminescence (PL) in SMBE-grown Si : Er structures with different types of optically active erbium centers.

2. EXPERIMENTAL

Homogeneously and selectively erbium-doped silicon structures were SMBE grown on [100]-oriented p-type silicon substrates with a resistivity ρ ~10–20 Ω cm. A Si : Er crystalline source was used to obtain erbium-doped silicon layers. Undoped silicon layers in multilayer structures were produced with a second source, silicon with a low impurity concentration (down to 10^{15} cm^{-3}). The thickness of the epitaxial structures studied ranged from 0.8 to 5.5 μm. The structure growth temperature was varied from 500 to 600°C. SIMS measurements showed the structures grown to contain up to 5×10^{18} cm^{-3} Er atoms, 5×10^{19} cm^{-3} O atoms, and 4×10^{18} to 1×10^{19} cm^{-3} C atoms.

An optical parametric oscillator (OPO) pumped by a Nd : YAG pulsed laser was employed to study the PL excitation spectra of the Si : Er/Si structures in the near IR range (780–1500 nm). The pump power pulses were 5-ns long at a pulse repetition frequency of 20 Hz, and the maximum pulse energy was 7 mJ at a wavelength of 780 nm. Thus, the maximum pulse power was as high as 10^6 W. PL signals were measured with a grating spectrometer, a nitrogen-cooled germanium detector (Edinburgh Instruments), and a digital oscillograph (TDS 3032, Tektronix). The samples under study were cooled to 10 K in a closed-cycle cryostat (Oxford Instruments).

3. RESULTS AND DISCUSSION

We studied excitation spectra of the erbium PL for a series of SMBE-grown Si : Er structures within a broad pump wavelength range (λ_{ex} = 780–1500 nm). All of the structures studied showed a fairly high erbium PL signal at pump photon energies substantially smaller than the silicon band-gap width (λ = 1060 nm) (Fig. 1). Furthermore, at high pump power levels, a sharp rise in the erbium PL intensity was observed at pump wave-

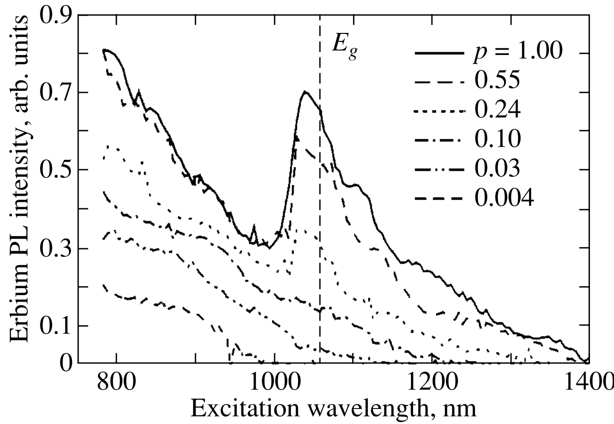

Fig. 1. Erbium PL excitation spectra (λ_{ex} = 1540 nm) in a Si : Er structure taken at different pump power levels $p = P/P_{max}$ at T = 10 K.

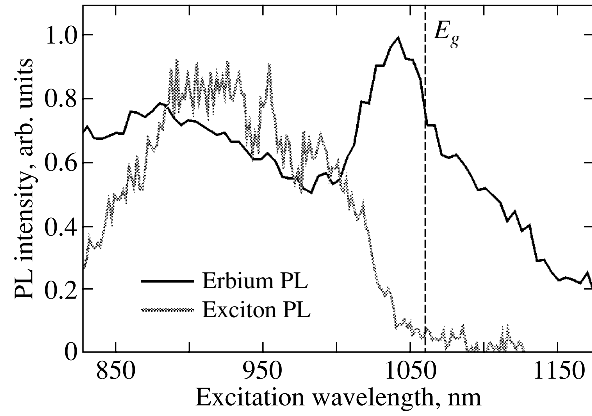

Fig. 2. Excitation spectra of the erbium and exciton PL in a Si : Er structure.

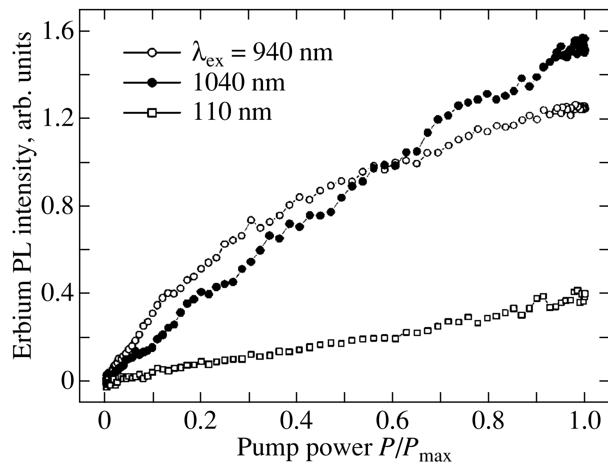

Fig. 3. Erbium PL intensity plotted vs. pump power for pump photon energies above (λ_{ex} = 940 nm), near (λ_{ex} = 1040 nm), and below (λ_{ex} = 1100 nm) the silicon band-gap width.

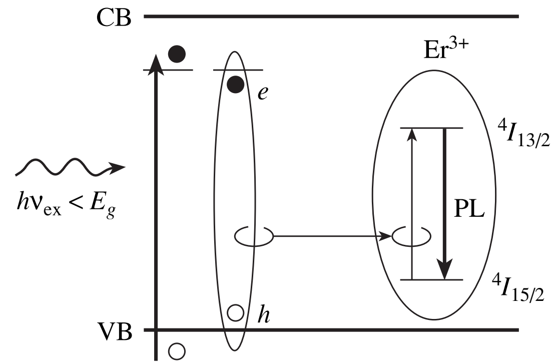

Fig. 4. Schematic level diagram for the proposed erbium ion excitation mechanism in the Si : Er structures for $h\nu_{ex} < E_g$.

lengths in the range 1000–1050 nm, which corresponds to the interband absorption edge in bulk silicon.

According to the universally accepted model, excitation of erbium PL in Si : Er structures requires interband pumping (absorption of a photon with energy in excess of the silicon band-gap width). This stimulates the generation of electron–hole pairs, their binding into excitons, exciton binding to erbium impurity complexes, and subsequent nonradiative recombination of the bound excitons followed by energy transfer to the erbium ions [5]. To establish the mechanism of erbium ion excitation at photon energies less than the silicon band-gap width, we also studied excitation spectra of the excitonic PL. This PL signal derives from radiative recombination of the excitons bound to shallow impurity centers, primarily in the substrate of the Si : Er/Si structures, and permits determination of the efficiency of generation of electron–hole pairs (excitons) in the structure as a function of pump wavelength. As is evident from Fig. 2, within the range 1000–1050 nm, the exciton PL intensity drops sharply with increasing pump wavelength. There is no exciton PL signal at pump power levels below E_g (λ_{ex} > 1060 nm). The decay of the exciton PL intensity indicates a decrease in exciton generation efficiency in the Si : Er structures within the given spectral region and suggests that the excitation of erbium ions for $h\nu_{ex} < E_g$ apparently does not involve excitons.

It should be noted that for λ_{ex} > 1060 nm the structures become practically transparent for the pump radiation. In part, this implies a very high efficiency of erbium PL excitation in this spectral region, because in these conditions only a small fraction of the pump

power is absorbed in the sample and contributes to PL excitation.

Note also that the excitation of erbium PL for $h\nu_{ex} < E_g$ manifests itself more strongly at high pump power levels. This is convincingly seen when one compares the graphs relating erbium PL intensity to pump power obtained at pump energies above (λ_{ex} = 940 nm) and below (λ_{ex} = 1100 nm) the silicon band-gap width (Fig. 3). As follows from these graphs, the erbium PL intensity produced by interband excitation (940 nm) grows faster at low pump powers and saturates partially at a high power level, whereas at λ_{ex} = 1100 nm this relation remains linear throughout the interval studied.

4. CONCLUSIONS

The above experimental data suggest that for $h\nu_{ex} < E_g$ the pump radiation is apparently absorbed in the Si : Er epitaxial layer. The excitation of the erbium PL in these conditions may be due to the presence of impurity (defect) levels in the silicon band gap that are associated with erbium ions and form in the course of growth of the Si : Er epitaxial layer. In this case, absorption of a photon with an energy less than the band-gap width may give rise to electron excitation from the valence band directly to these impurity levels and their subsequent nonradiative recombination with valence band holes, with a transfer of energy to the internal shell of the erbium ions. The proposed model of excitation of the erbium PL is shown schematically in Fig. 4. The high efficiency of this mechanism can be assigned to the absence of electron–hole pair generation in the structures for $h\nu_{ex} < E_g$, because interaction with free carriers is a major cause of nonradiative de-excitation of erbium ions in silicon. The decrease in Auger de-excitation may also account for the increase in erbium PL intensity with pump wavelength in the range 1000–1030 nm with a simultaneous decrease in the exciton PL intensity.

ACKNOWLEDGMENTS

This study was supported by the Russian Foundation for Basic Research (project no. 02-02-16773), INTAS (project nos. 01-0468, 01-0194), and NWO (project no. 047-009-013).

REFERENCES

1. B. A. Andreev, A. Yu. Andreev, H. Ellmer, H. Hutter, Z. F. Krasilnik, V. P. Kuznetsov, S. Lanzerstorfer, L. Palmetshofer, K. Piplits, R. A. Rubtsova, N. S. Sokolov, V. B. Shmagin, M. V. Stepikhova, and E. A. Uskova, J. Cryst. Growth **201–202**, 534 (1999).
2. Z. F. Krasilnik, V. Ya. Aleshkin, B. A. Andreev, O. B. Gusev, W. Jantsch, L. V. Krasilnikova, D. I. Kryzhkov, V. P. Kuznetsov, V. G. Shengurov, V. B. Shmagin, N. A. Sobolev, M. V. Stepikhova, and A. N. Yablonsky, in *Towards the First Silicon Laser*, Ed. by L. Pavesi, S. Gaponenko, and L. Dal Negro (Kluwer Academic, Dordercht, 2003), pp. 445–454.
3. F. Priolo, G. Franzo, S. Coffa, and A. Carnera, Phys. Rev. B **57** (8), 4443 (1998).
4. O. B. Gusev, M. S. Bresler, P. E. Pak, I. N. Yassievich, M. Forcales, N. Q. Vinh, and T. Gregorkiewicz, Phys. Rev. B **64**, 075302 (2001).
5. M. S. Bresler, O. B. Gusev, B. P. Zakharchenya, and I. N. Yassievich, Fiz. Tverd. Tela (St. Petersburg) **38** (5), 1474 (1996) [Phys. Solid State **38**, 813 (1996)].

Translated by G. Skrebtsov

Physics of the Solid State, Vol. 47, No. 1, 2005, pp. 89–92. Translated from Fizika Tverdogo Tela, Vol. 47, No. 1, 2005, pp. 86–89.
Original Russian Text Copyright © 2005 by Shengurov, Pavlov, Svetlov, Chalkov, Shilyaev, Stepikhova, Krasil'nikova, Drozdov, Krasil'nik.

PROCEEDINGS OF THE CONFERENCE
"NANOPHOTONICS 2004"
(Nizhni Novgorod, Russia, May 2–6, 2004)

Heteroepitaxy of Erbium-Doped Silicon Layers on Sapphire Substrates

V. G. Shengurov*, D. A. Pavlov*, S. P. Svetlov*, V. Yu. Chalkov*, P. A. Shilyaev*, M. V. Stepikhova, L. V. Krasil'nikova**, Yu. N. Drozdov**, and Z. F. Krasil'nik****

** Research Physicotechnical Institute, Nizhni Novgorod State University, pr. Gagarina 23/5, Nizhni Novgorod, 603600 Russia*

e-mail: svetlov@phys.unn.ru

*** Institute for Physics of Microstructures, Russian Academy of Sciences, Nizhni Novgorod, 603950 Russia*

Abstract—The possibility of using sublimation molecular-beam epitaxy as an efficient method for growing erbium-doped silicon layers on sapphire substrates for optoelectronic applications is analyzed. The advantage of this method is that the erbium-doped silicon layers can be grown at relatively low temperatures. The use of sublimation molecular-beam epitaxy makes it possible to grow silicon layers of good crystal quality. It is demonstrated that the growth temperature affects not only the structure of silicon-on-sapphire layers but also the crystallographic orientation of these layers. The electrical and luminescence properties of the erbium-doped silicon layers are discussed. It is revealed that structures of this type exhibit intense erbium photoluminescence at a wavelength of 1.54 μm. © *2005 Pleiades Publishing, Inc.*

1. INTRODUCTION

The design of silicon-on-insulator devices and structures, including heteroepitaxial silicon films on sapphire, is a promising direction in modern micro- and nanoelectronics. The advantages of such structures are their high radiation and thermal resistances and a low power consumption of integrated circuits [1]. The possibility of fabricating multifunctional microprocessor circuits on sapphire substrates and the general tendency toward an increase in the level of integration call for designing of optoelectronic circuits. In this respect, silicon-based structures doped with rare-earth elements are of considerable interest [2].

The purpose of this work was to investigate the possibility of using sublimation molecular-beam epitaxy as an efficient method for growing erbium-doped silicon-on-sapphire layers emitting at a wavelength of 1.54 μm.

In contrast to the vapor-phase crystallization method, which has been extensively employed in recent years for growing silicon-on-sapphire structures [3], the sublimation molecular-beam epitaxy method being developed in this work makes it possible to use low-temperature growth conditions. This allows one to minimize the adverse effect associated with the difference between the coefficients of thermal expansion of silicon and sapphire [4] and, consequently, to reduce compressive stresses in heteroepitaxial layers. In this work, we demonstrated the possibility of using sublimation molecular-beam epitaxy for growing Si : Er layers on sapphire substrates with a high degree of structural perfection, analyzed the influence of the growth conditions on the structure and electrical parameters of the erbium-doped silicon-on-sapphire layers, and investigated their luminescence properties.

2. SAMPLE PREPARATION AND EXPERIMENTAL TECHNIQUE

Epitaxial silicon layers were grown through sublimation molecular-beam epitaxy according to a procedure similar to that described in our earlier work [5]. Sapphire plates 35 × 35 mm in size and 0.5 mm in thickness with the $(1\bar{1}02)$ orientation were used as substrates. Prior to deposition of silicon layers, the sapphire plates were annealed immediately in the growth chamber at a temperature of 1400°C for 30 min. The fluxes of silicon and erbium atoms were produced by heating a sublimation source, which was cut in the form of a rectangular bar from a silicon ingot doped with erbium during the course of growth. The source was heated to a temperature of ~1330°C upon passage of an electric current. In a number of experiments, a thin undoped silicon buffer layer on a sapphire substrate was grown from a KÉF-15 silicon source. The thickness of this layer fell in the range 0.1–0.7 μm. The deposition rate of silicon layers was equal to 0.08–0.10 nm/s. The substrate temperature T_s varied from 550 to 730°C and was measured accurate to within ±20°C with the use of a VIMP-015 optical pyrometer. The pressure of residual gases during the growth of sil-

1063-7834/05/4701-0089$26.00 © 2005 Pleiades Publishing, Inc.

Growth conditions and structural analysis data for heteroepitaxial silicon layers on sapphire substrates

Sample no.	Growth conditions		d, μm	Layer orientation	$\Delta\omega_{1/2}$, deg
	T_s, °C	t, min			
12-42	730	20	0.30	(100)	0.44
12-52	730	20	0.30	(100)	0.36
12-54	730	15	0.25	(100)	0.38
12-59	730	30	0.40	(100)	0.32
12-62	730	30	0.4	(100)	0.33
12-39	600	120	0.75	(100)	0.62
12-35	600	20	0.50	(100)	0.58
12-27	600	20	0.27	(100)	0.49
12-60	730	15	0.70	(100)	0.33
	600	60	0.45		
12-64	730	5	0.3	(100)	0.5
	600	55			
12-66	730	10	0.55	(110)	0.39
	600	25			
	550	25			

icon layers did not exceed 1×10^{-7} Torr. The thickness of the silicon layers grown varied in the range from 0.25 to 0.75 μm. This thickness was measured on an MII-4 interferometer from the step formed on the substrate after part of the silicon layer was etched.

The structure of silicon-on-sapphire layers was analyzed using reflection high-energy electron diffraction (RHEED) and x-ray diffraction. The RHEED patterns were recorded on an ÉMR-102 electron diffractometer at a glancing angle of incidence (accelerating voltage, 100 kV). The x-ray diffraction patterns were measured on a DRON-4 diffractometer [CuK_{α_1} radiation, Ge(400) monochromator]. The surface morphology was examined by atomic force microscopy (AFM) with an Accurex TMX-2100 instrument. The concentration distributions of charge carriers were measured using electrochemical capacitance–voltage profiling.

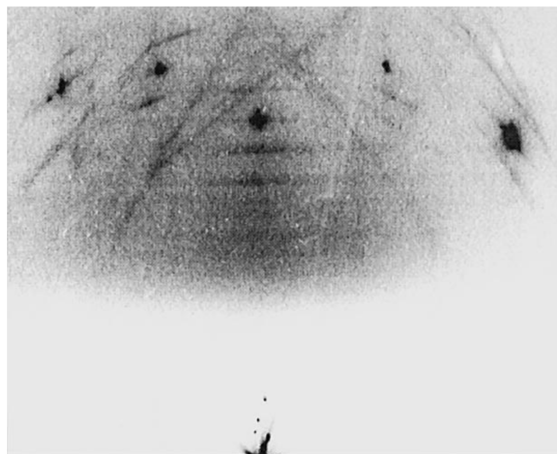

Fig. 1. RHEED pattern of the silicon-on-sapphire structure.

The photoluminescence (PL) spectra were recorded on a BOMEM DA3 Fourier spectrometer with a spectral resolution reaching 1 cm^{-1}. The photoluminescence was excited with an argon laser at a wavelength of 514.5 nm and a power of ~270 mW. The spectra were measured with a cooled North-Coast EO-817A germanium detector at temperatures of 77 and 300 K.

3. RESULTS AND DISCUSSION

3.1. Structure of the Grown Layers

Let us consider the structural features of silicon-on-sapphire layers and the influence of the growth temperature on their structure. The growth conditions and structural analysis data are listed in the table. As was noted in our previous work [6], the RHEED patterns of the silicon layers grown on substrates annealed at a high temperature (1400°C) contain Kikuchi lines and Kikuchi bands (Fig. 1). This suggests that the surface region of the silicon layer is characterized by a high degree of structural perfection. An increase in the growth temperature leads to an increase in the sharpness of the observed Kikuchi patterns. This directly indicates improvement of the silicon-on-sapphire structure.

It is found that the silicon layers grown at a high temperature (730°C) are characterized by a high degree of structural perfection. According to the x-ray diffraction data, the full width at half-maximum of the rocking curve is determined to be $\Delta\omega_{1/2}$ = 0.32°–0.44°. A decrease in the growth temperature results in deterioration of the silicon-on-sapphire structure. As can be seen from the table, the values of $\Delta\omega_{1/2}$ for the silicon layers grown at a temperature of 600°C lie in the range 0.5°–0.7°. In this case, it is of interest to analyze the data on the crystallographic orientation of the silicon-on-sapphire layers. The silicon layers with the (100) orientation are formed at a substrate temperature T_s = 600°C and above. However, a decrease in the substrate temperature to 550°C leads to the formation of silicon layers containing crystal blocks with both the (100) and (110) orientations. It is worth noting that the silicon layers thus formed have a single-crystal structure: the RHEED patterns of the surfaces of these layers and also the silicon layers grown at higher temperatures involve only Kikuchi lines. According to the AFM data, the silicon layers have a sufficiently smooth surface (Fig. 2).

In some cases, the epitaxial silicon layers were grown at two growth temperatures: the first portion of the silicon layer (approximately one-fourth of the layer thickness) was grown at a high temperature (730°C), and the second portion was obtained at a lower temperature (600°C). It should be noted that these layers (samples 12-60, 12-64) retain a rather high degree of struc-

tural perfection. However, a further decrease in the growth temperature of the second portion of the silicon layer, for example, to 550°C (sample 12-66), resulted in a change in the crystallographic orientation from (100) to (110), as in the case considered above.

3.2. Distribution of Impurities in Silicon-on-Sapphire Structure

The concentration distribution of charge carriers over the thickness of the erbium-doped silicon layer (sample 12-60) is depicted in Fig 3a. It can be seen from this figure that the silicon layer predominantly has *p*-type conductivity, which is not characteristic of Si : Er homoepitaxial layers grown under similar conditions [7]. In order to elucidate the origin of this discrepancy, we studied a phosphorus-doped silicon layer grown on a sapphire substrate. Figure 3b shows the concentration distribution of charge carriers over the thickness of the phosphorus-doped silicon layer. As can be seen from Fig. 3b, the concentration distribution of charge carriers is nonuniform over the layer thickness: the silicon layer possesses *p*-type conductivity at the boundary with the substrate and in the surface region and *n*-type conductivity in the central region. In our opinion, such a distribution can be explained as follows. Aluminum atoms are accumulated on the sapphire surface upon preepitaxial high-temperature annealing of the substrate. During the growth of the silicon layers, one part of these atoms is incorporated into the growing layer and another part of the atoms is rejected by the growth surface. These processes lead to the formation of the regions with *p*-type conductivity. It can be assumed that this mechanism is also responsible for the type of conduction in erbium-doped silicon-on-sapphire layers.

3.3. Photoluminescence Properties of Silicon-on-Sapphire Structures

The results obtained in the study of the photoluminescence in the erbium-doped silicon-on-sapphire structures are presented in Fig. 4. It can be seen that the photoluminescence spectra measured at a temperature of 77 K are characterized by a rather intense signal at a wavelength of 1.54 μm. Judging from the positions and widths of the spectral lines, this signal is typical of radiative transitions in the rare-earth ion ($^4I_{13/2} \longrightarrow {^4I_{15/2}}$ transitions in the 4*f* shell of the Er^{3+} ion). The strongest photoluminescence signal in this range is observed for sample 12-60, whose spectrum has a fine structure of lines with a half-width of ~10 cm^{-1}. The spectrum of this sample is similar to the photoluminescence spectra of Si : Er layers with a high oxygen content. In particular, it is possible to distinguish a group of lines associated with the Er^{3+} oxygen-containing centers (Er–O1,2 centers), which were originally revealed in the materials prepared by ion implantation [8].

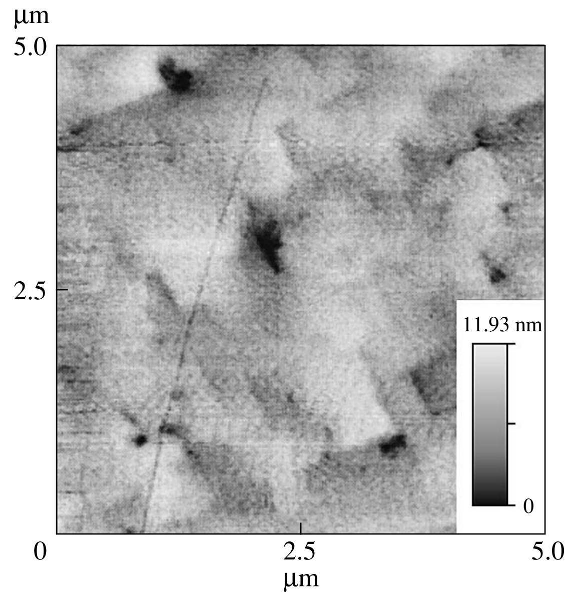

Fig. 2. AFM image of the surface of a silicon layer grown on the sapphire substrate at a substrate temperature T_s = 600°C.

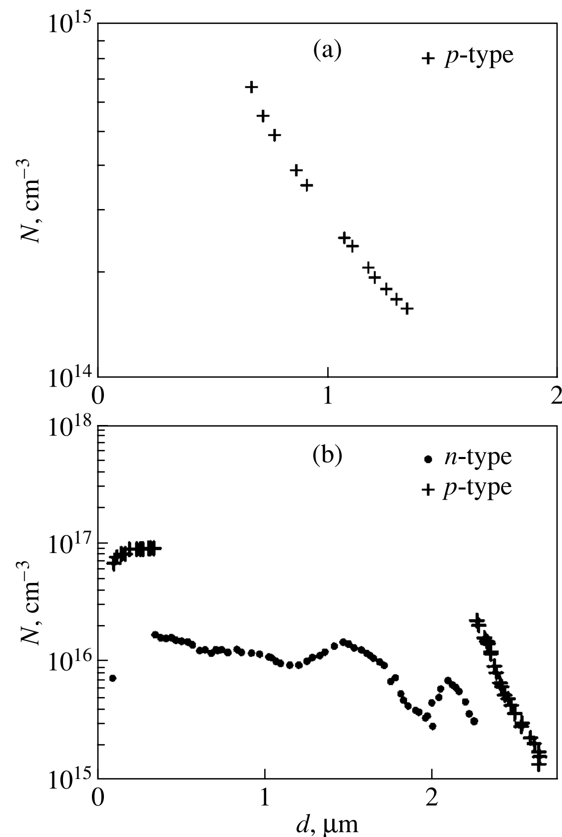

Fig. 3. Concentration distributions of charge carriers over the thickness of (a) erbium-doped silicon layers and (b) phosphorus-doped silicon layers on sapphire substrates.

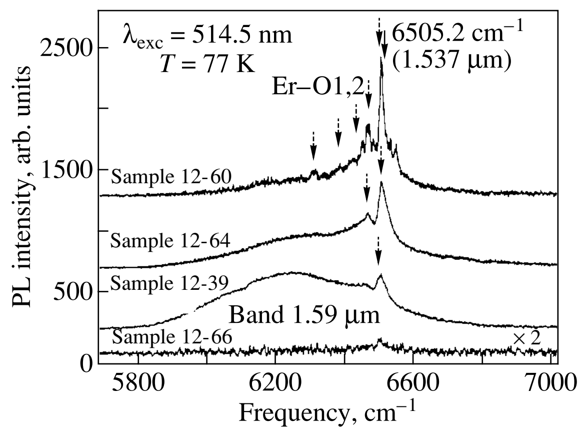

Fig. 4. Photoluminescence spectra of the silicon-on-sapphire structures. Arrows indicate the positions of the luminescence lines attributed to the dominant optically active centers involving Er^{3+} ions.

The deterioration of the structural perfection of the silicon-on-sapphire layers (see table) results in a considerable broadening of the photoluminescence band observed at a wavelength of 1.54 μm. It is evident that this broadening is caused by the stresses arising in the layers. Moreover, apart from the photoluminescence signal assigned to the rare-earth impurities, the spectrum contains a second luminescence band with the maximum at a wavelength of 1.59 μm. With due regard for its width and shape, this band can be attributed to either the defect complexes formed in the silicon layer or the complexes of impurity centers, for example, centers involving carbon and oxygen atoms [9]. Note that the photoluminescence band with the maximum at a wavelength of 1.59 μm is also observed in the spectra of silicon-on-sapphire structures containing a layer that was not doped with erbium. The intensity of photoluminescence in the silicon-on-sapphire layers decreases significantly with an increase in the temperature. As a result, it becomes almost impossible to record the photoluminescence at 300 K.

4. CONCLUSIONS

Thus, we demonstrated that structurally perfect erbium-doped silicon-on-sapphire layers, which exhibit a rather intense luminescence at a wavelength of 1.54 μm, can be grown through sublimation molecular-beam epitaxy at relatively low temperatures (600–700°C). It was shown that the growth temperature affects the degree of structural perfection of silicon-on-sapphire layers. In turn, the structure of silicon-on-sapphire layers has an effect on the photoluminescence response.

ACKNOWLEDGMENTS

This work was supported by the Russian Foundation for Basic Research (project no. 04-02-17120) and the International Association of Assistance for the Promotion of Cooperation with Scientists from the New Independent States of the Former Soviet Union (project no. INTAS 03-51-6486).

REFERENCES

1. S. Cristoloveanu, Rep. Prog. Phys. **50** (3), 327 (1987).
2. N. A. Sobolev, Fiz. Tekh. Poluprovodn. (St. Petersburg) **29**, 1153 (1995) [Semiconductors **29**, 595 (1995)].
3. V. S. Pankov and M. B. Tsybul'nikov, *Epitaxial Silicon Layers on Dielectric Substrates and Devices on Their Base* (Énergiya, Moscow, 1979) [in Russian].
4. E. D. Richmond, J. G. Pelligrino, M. E. Twigg, S. Qadri, and M. T. Duffy, Thin Solid Films **192**, 287 (1990).
5. S. P. Svetlov, V. Yu. Chalkov, and V. G. Shengurov, Prib. Tekh. Éksp., No. 4, 141 (2000) [Instrum. Exp. Tech. **43**, 564 (2000)].
6. S. P. Svetlov, V. Yu. Chalkov, V. G. Shengurov, Yu. N. Drozdov, Z. F. Krasil'nik, L. V. Krasil'nikova, M. V. Stepikhova, D. A. Pavlov, T. V. Pavlova, P. A. Shilyaev, and A. F. Khokhlov, Izv. Vyssh. Uchebn. Zaved., Mater. Élektron. Tekh. **2**, 27 (2003).
7. V. B. Shmagin, B. A. Andreev, A. V. Antonov, Z. F. Krasil'nik, M. V. Stepikhova, V. P. Kuznetsov, E. A. Uskova, and R. A. Rubtsova, Izv. Akad. Nauk, Ser. Fiz. **65** (2), 276 (2001).
8. H. Przybylinska, W. Jantsch, Yu. Suprun-Belevitch, M. Stepikhova, L. Palmetshofer, G. Hendorfer, A. Kozanecki, R. J. Wilson, and B. J. Sealy, Phys. Rev. B **54**, 2532 (1996).
9. W. Kuerner, R. Sauer, A. Doerner, and K. Thonke, Phys. Rev. B **39** (18), 13327 (1989).

Translated by O. Borovik-Romanova

Physics of the Solid State, Vol. 47, No. 1, 2005, pp. 9–12. Translated from Fizika Tverdogo Tela, Vol. 47, No. 1, 2005, pp. 13–16.
Original Russian Text Copyright © 2005 by Krivelevich, Makoviĭchuk, Selyukov.

PROCEEDINGS OF THE CONFERENCE "NANOPHOTONICS 2004"
(Nizhni Novgorod, Russia, May 2–6, 2004)

Excitation and De-excitation Cross Sections for Light-Emitting Nanoclusters in Rare Earth–Doped Silicon

S. A. Krivelevich, M. I. Makoviĭchuk, and R. V. Selyukov

Institute of Microelectronics and Informatics, Russian Academy of Sciences, ul. Universitetskaya 21, Yaroslavl, 150007 Russia

e-mail: sel@imras.yar.ru

Abstract—The excitation and de-excitation cross sections of light-emitting nanoclusters in rare earth–doped silicon are calculated. Two processes of de-excitation are considered: emission of a photon by the center and transfer of the cluster energy to a scattered electron. The cross sections of these two processes are shown to be large. Therefore, de-excitation has a significant effect on the concentration of excited rare-earth centers in silicon. © *2005 Pleiades Publishing, Inc.*

1. INTRODUCTION

Silicon-based light-emitting structures can be produced by doping silicon with rare-earth (RE) elements [1–4]. In these structures, luminescence is due to electron transitions between spin–orbit split 4*f* states of the RE atom entering an optically active center. The emitted light with such wavelengths is absorbed only weakly by silicon. Therefore, these structures can be used in systems with optical coupling between the components of an integrated circuit.

In RE-doped silicon, the electroluminescence intensity is the highest for reverse-biased *p*–*n* junctions. In this case, optically active centers are excited through the impact mechanism during hot-carrier scattering. However, scattering can also cause de-excitation of already excited centers. Therefore, we need to know the dependences of the cross sections of these processes on applied electric field. The excitation cross section of these centers was calculated in [5–7]. The main objective of this paper is to calculate the de-excitation cross sections in the structures under study.

2. CALCULATION OF THE EXCITATION AND DE-EXCITATION CROSS SECTIONS

Let us consider the process of de-excitation of centers. This process can occur through photon emission by the RE atom or energy transfer to a scattered electron. In both cases, the process has no threshold. Therefore, de-excitation can be caused by electrons with any energy and we should calculate the cross sections of the corresponding processes using the general scattering theory. In the case of nonradiative de-excitation, we invoke the principle of detailed balance as applied to scattering processes [8]:

$$\frac{d\sigma_{\rm dw}}{k'^2 d\Omega} = \frac{d\sigma_{\rm ex}}{k^2 d\Omega}, \quad (1)$$

where k and k' are the wave vectors of the incident and scattered electrons, respectively; $d\sigma_{\rm dw}/d\Omega$ is the differential cross section of nonradiative de-excitation; and $d\sigma_{\rm ex}/d\Omega$ is the differential cross section of the process that is reversed in time with respect to the former process. It can be easily seen that this process is impact excitation in which the wave vectors of the incident and scattered electrons are interchanged.

In order to calculate the differential cross section of excitation, we should estimate the average electron energy $\langle E\rangle$ in the space-charge region of the reverse-biased *p*–*n* junction. For this purpose, we need to solve the balance equation for this energy, which has the form

$$\frac{d\langle E\rangle}{dt} = -\alpha(E)\sqrt{\frac{2\langle E\rangle}{m^*}}I - \frac{\langle E_p\rangle}{\lambda}\sqrt{\frac{2\langle E\rangle}{m^*}} + ev_{\rm d}E. \quad (2)$$

In the right-hand side of Eq. (2), the first term is the energy loss due to ionization of the host atoms (m^* is the effective electron mass; $\alpha(E)$ is the impact ionization coefficient, depending on the electric field strength E; I is the ionization energy). The second term is the energy loss due to electron scattering by longitudinal optical phonons ($\langle E_p\rangle$ is the average optical-phonon energy, λ is the electron mean free path associated with optical-phonon scattering). Finally, the third term takes into account the electron gas heating by an electric field ($v_{\rm d}$ is the electron drift velocity).

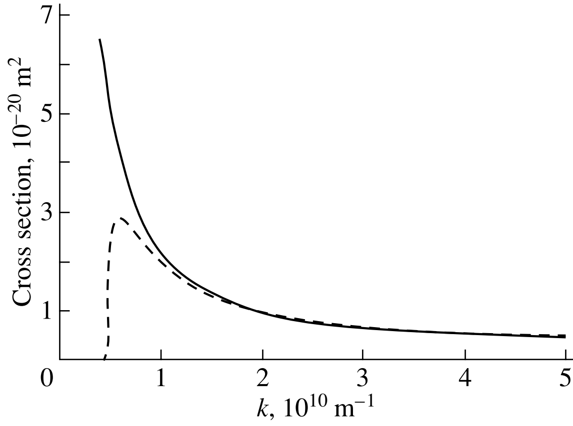

Fig. 1. Dependence of the cross sections of excitation (dashed curve) and nonradiative de-excitation (solid curve) of an erbium atom on electron wave vector.

The steady-state solution to Eq. (2) describes the dependence of the average energy on the electric field strength:

$$\langle E \rangle = \frac{m^* v_d^2}{2} e^2 E^2 (\alpha(E) I + \langle E_p \rangle / \lambda)^{-2}. \quad (3)$$

On the other hand, the average energy can be found using the distribution function

$$\langle E \rangle = \int_0^{2\pi} \int_0^{\pi} \int_0^{\infty} E(k) f(k, \theta, \phi, E) k^2 \sin(\theta) dk d\theta d\phi. \quad (4)$$

Here, $f(k, \theta, \phi, E)$ is the nonequilibrium distribution function of electrons. To a first approximation, this function for a semiconductor in an electric field can be found to be

$$f = f_0 + \frac{f_0}{k_B T_e} (\mathbf{v}, e\mathbf{E}) \tau. \quad (5)$$

Here, $\mathbf{v}$ is the electron velocity, τ is the relaxation time, k_B is the Boltzmann constant, T_e is the electron gas temperature, and f_0 is the Maxwell distribution function

$$f_0 = \left(\frac{\hbar^2}{2\pi m^* k_B T_e} \right)^{3/2} \exp\left(-\frac{\hbar^2 k^2}{2m^* k_B T_e} \right). \quad (6)$$

The dependence of the electronic temperature on applied electric field can be found by equating expressions (3) and (4). Estimates show that the average electron energy for a reverse-biased *p–n* junction is high enough for the Born approximation to be used in calculating the differential cross section for excitation [8]. We substitute $d\sigma_{ex}/d\Omega$ thus calculated into Eq. (1) and find $d\sigma_{dw}$ to be

$$d\sigma_{dw} = \frac{e^2 m^{*2}}{2\pi \hbar^4 (k\varepsilon\varepsilon_0)^2} \frac{dq}{q^3} \sum_{i=1}^{\infty} \frac{q^{2i}}{(i!)^2} \overline{M}_{i\alpha\beta}. \quad (7)$$

Here, q is the magnitude of the difference between the wave vectors of the scattered and incident electrons (wave-vector transfer); $M_{i\alpha\beta}$ is the square of the modulus of the atomic multipole moment matrix element; and the subscripts β and α label the excited and ground states of the atom, respectively.

Since the wave-vector transfer is comparatively small, we can keep only the first two terms in Eq. (7) and write

$$d\sigma_{dw} = \frac{e^2 m^{*2}}{2\pi \hbar^4 (k\varepsilon\varepsilon_0)^2} M_{1\alpha\beta} \frac{dq}{q} + \frac{e^2 m^{*2}}{8\pi \hbar^4 (k\varepsilon\varepsilon_0)^2} M_{2\alpha\beta} q dq. \quad (8)$$

Integrating over all possible values of q gives

$$\sigma_{dw}(k) = \frac{e^2 m^{*2}}{2\pi \hbar^4 (k\varepsilon\varepsilon_0)^2} M_{1\alpha\beta} \ln\left(\frac{q_{max}}{q_{min}} \right) + \frac{e^2 m^{*2}}{16\pi \hbar^4 (k\varepsilon\varepsilon_0)^2} M_{2\alpha\beta} (q_{max}^2 - q_{min}^2), \quad (9)$$

where q_{max} and q_{min} are the maximum and minimum values of q, respectively; from the conservation energy for the atom plus incident electron system, they can be found to be

$$q_{max} = \sqrt{k^2 + \frac{2m^* E_{\alpha\beta}}{\hbar^2}} + k, \quad (10)$$

$$q_{min} = \sqrt{k^2 + \frac{2m^* E_{\alpha\beta}}{\hbar^2}} - k. \quad (11)$$

Here, $E_{\alpha\beta}$ is the difference between the energies of the first excited and ground states of the RE atom. The wave-vector dependences of the cross sections of excitation and nonradiative de-excitation are shown in Fig. 1.

Experimentally, the value of σ_{dw} averaged over k is measured. This quantity is defined as

$$\sigma_{dw} = \int_0^{2\pi} \int_0^{\pi} \int_0^{\infty} \sigma_{dw}(k) f(k, \theta, \phi) k^2 \sin(\theta) dk d\theta d\phi. \quad (12)$$

The field dependences of σ_{ex} and σ_{dw} found using Eq. (12) are shown in Figs. 2 and 3. (The integration of the excitation cross section over k was performed not from zero but rather from the threshold value dictated by the excitation energy of the center.)

Now, let us consider radiative de-excitation of the optically active center. In this case, the energy transferred by an electron to the atom goes solely into an increase in kinetic energy of the latter and can be neglected. Therefore, we can treat the process as a transition stimulated in the two-level system by the perturb-

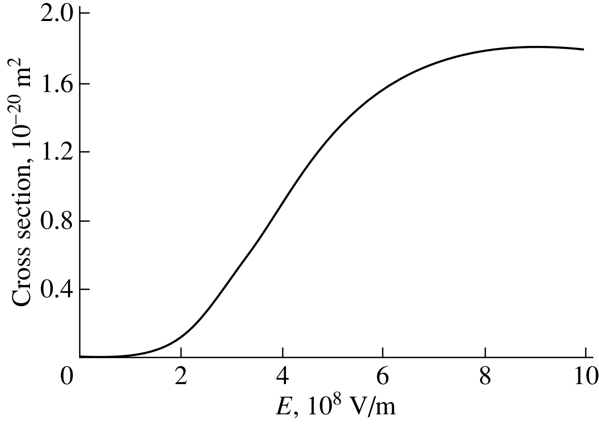

Fig. 2. Dependence of the excitation cross section of an erbium atom on electric field strength.

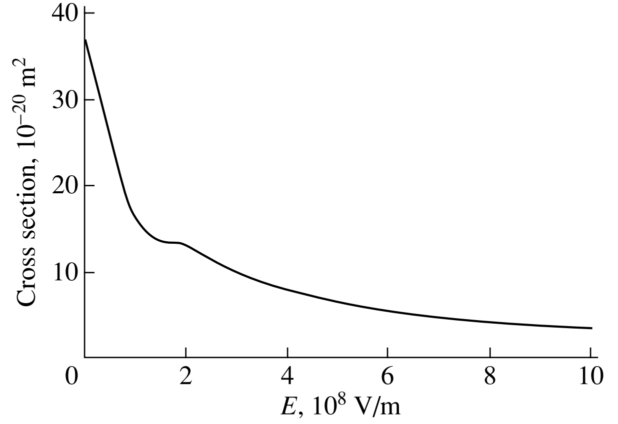

Fig. 3. Field dependence of the nonradiative de-excitation cross section of an erbium atom.

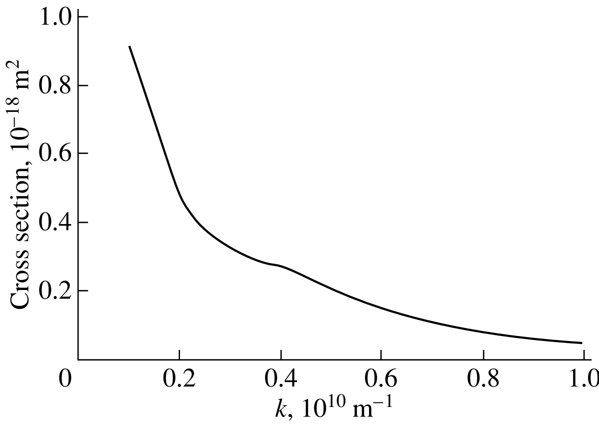

Fig. 4. Dependence of the radiative de-excitation cross section of an erbium atom on electron wave vector.

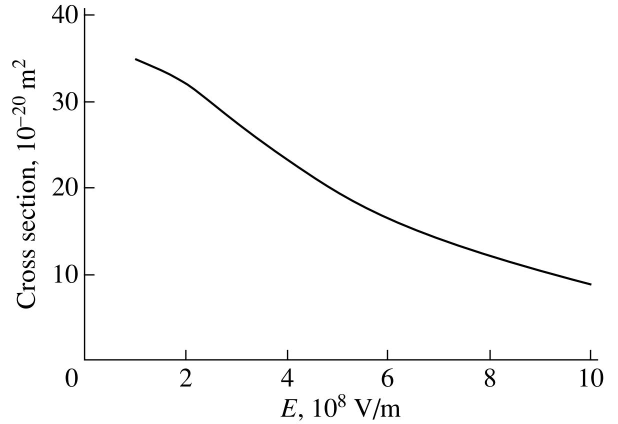

Fig. 5. Field dependence of the radiative de-excitation cross section of an erbium atom.

ing field produced by the incident electron. The probability of a stimulated transition in the atom is given by (see, e.g., [9])

$$P_{\alpha\beta} = \left(\frac{2\pi}{\hbar}\right)^2 |E(\omega_{\alpha\beta}) M_{1\alpha\beta}|^2, \qquad (13)$$

where $\omega_{\alpha\beta} = \dfrac{E_{\alpha\beta}}{\hbar}$ is the transition frequency in the system and $E(\omega_{\alpha\beta})$ is the Fourier transform of the electric field produced by the electron:

$$E(\omega_{\alpha\beta}) = \frac{1}{2\pi}\int_{-\infty}^{+\infty} \frac{e}{4\pi\varepsilon\varepsilon_0} \exp(-i\omega_{\alpha\beta} t) \times \int_V \frac{|\Psi|^2}{r^2} \cos\theta \, dV dt. \qquad (14)$$

Here, Ψ is the wave function of the scattered electron and θ is the angle between the directions of the dipole moment and the electric field. Integration in the second integral is performed over all space.

In calculating the radiative de-excitation cross section, we take into account that the electron scattering is elastic and that there are many fairly hot electrons in the structure under study. Therefore, we can employ a quasi-classical expression for the elastic-scattering cross section [9] and the probability multiplication theorem. Thus, the total cross section is equal to the product of the elastic-scattering cross section and the transition probability and has the form

$$\sigma_{de} = \left(\frac{m^* a^2 Z e^2}{\varepsilon\varepsilon_0 \hbar^2}\right) \frac{1}{3\pi} \frac{1}{\xi} \left[7 - \frac{7 + 9\xi + 3\xi^2}{(1+\xi)^3}\right] P_{\alpha\beta}, \qquad (15)$$

where $\xi = (2ka)^2$ and a is the radius of the center.

The field dependence of this cross section can be found in much the same way as in the preceding case. The results are presented in Figs. 4 and 5.

3. CONCLUSIONS

De-excitation has been shown to have a significant effect on the concentration of excited centers, because its cross section is comparatively large. Therefore, one might expect that the proportion of such centers will be small in reverse-biased structures. This demonstrates the need to seek ways to decrease the de-excitation effect.

REFERENCES

1. N. A. Sobolev, Fiz. Tekh. Poluprovodn. (St. Petersburg) **29**, 1153 (1995) [Semiconductors **29**, 595 (1995)].
2. M. S. Bresler, T. Gregorkevich, O. B. Gusev, N. A. Sobolev, E. I. Terukov, I. N. Yassievich, and B. P. Zakharchenya, Fiz. Tverd. Tela (St. Petersburg) **41** (5), 851 (1999) [Phys. Solid State **41**, 770 (1999)].
3. V. F. Masterov, F. S. Nasredinov, P. P. Seregin, V. Kh. Kudoyarova, A. N. Kuznetsov, and E. I. Terukov, Pis'ma Zh. Tekh. Fiz. **22** (23), 25 (1996) [Tech. Phys. Lett. **22**, 960 (1996)].
4. V. F. Masterov, F. S. Nasredinov, P. P. Seregin, E. I. Terukov, and M. M. Mezdrogina, Fiz. Tekh. Poluprovodn. (St. Petersburg) **32** (6), 708 (1998) [Semiconductors **32**, 636 (1998)].
5. V. F. Masterov and L. G. Gerchikov, Fiz. Tekh. Poluprovodn. (St. Petersburg) **33** (6), 664 (1999) [Semiconductors **33**, 616 (1999)].
6. I. N. Yassievich and L. C. Kimerling, Semicond. Sci. Technol. **8**, 718 (1993).
7. S. A. Krivelevich, M. I. Makoviĭchuk, and R. V. Selyukov, in *Abstracts of Sixth Russian Conference of the Physics of Semiconductors* (St. Petersburg, 2003), p. 207.
8. L. D. Landau and E. M. Lifshitz, *Course of Theoretical Physics*, Vol. 3: *Quantum Mechanics: Non-Relativistic Theory*, 3rd ed. (Nauka, Moscow, 1979; Pergamon, New York, 1977).
9. D. I. Blokhintsev, *Principles of Quantum Mechanics* (Nauka, Moscow, 1983) [in Russian].

Translated by Yu. Epifanov

Physics of the Solid State, Vol. 47, No. 1, 2005, pp. 93–97. Translated from Fizika Tverdogo Tela, Vol. 47, No. 1, 2005, pp. 90–94.
Original Russian Text Copyright © 2005 by Krasil'nikova, Stepikhova, Yu. Drozdov, M. Drozdov, Krasil'nik, Shengurov, Chalkov, Svetlov, Gusev.

PROCEEDINGS OF THE CONFERENCE "NANOPHOTONICS 2004"
(Nizhni Novgorod, Russia, May 2–6, 2004)

Analysis of the Gain and Luminescence Properties of $Si/Si_{1-x}Ge_x$: Er/Si Heterostructures Produced by Sublimation Molecular-Beam Epitaxy in a Gas Phase

L. V. Krasil'nikova*, M. V. Stepikhova*, Yu. N. Drozdov*, M. N. Drozdov*, Z. F. Krasil'nik*, V. G. Shengurov, V. Yu. Chalkov**, S. P. Svetlov**, and O. B. Gusev*****

** Institute of the Physics of Microstructures, Russian Academy of Sciences, Nizhni Novgorod, 603950 Russia*
e-mail: luda@ipm.sci-nnov.ru
*** Physicotechnical Institute, Nizhni Novgorod State University, pr. Gagarina 23/5, Nizhni Novgorod, 603950 Russia*
**** Ioffe Physicotechnical Institute, Russian Academy of Sciences, Politekhnicheskaya ul. 26, St. Petersburg, 194021 Russia*

Abstract—$Si/Si_{1-x}Ge_x$: Er/Si structures grown by sublimation molecular-beam epitaxy (SMBE) in a gas phase are studied. These structures are considered possible structures for realizing a Si/Er-based laser. It is shown that SMBE in a gas phase can be applied to create effective light-emitting structures that generate an intense luminescence signal at a wavelength of 1.54 μm. The structures and chemical compositions of the $Si/Si_{1-x}Ge_x$: Er/Si structures, whose parameters are close to those calculated for creating laser-type structures, are examined, and their photoluminescence (PL) spectra and kinetics are studied at 4.2 and 77 K. It is shown that the fraction of Er^{3+} optically active centers in the $Si_{1-x}Ge_x$: Er layers thus grown reaches ~10% of the total erbium-impurity concentration. The optical gains in the active $Si_{1-x}Ge_x$: Er layers at $x = 0.1$ and 0.02 are estimated to be ~0.03 and ~0.2 cm^{-1}, respectively. The gain in structures of this type can be significantly increased via the intentional formation of isolated Er^{3+} optically active centers whose PL spectra have a characteristic fine structure. *© 2005 Pleiades Publishing, Inc.*

1. INTRODUCTION

The significant interest expressed in structures based on erbium-doped silicon mostly stems from the possible creation of optoelectronic devices operating in an optical range near 1.54 μm [1]. The radiative transition of Er^{3+} ion at this wavelength coincides with the spectral window of a quartz fiber, which opens up wide prospects for the use of Si : Er structures in modern systems of fiber-optic communications. Searching for conditions for the production of laser-type structures and the development of a technology for their production are of particular importance in this field.

Earlier [2, 3], we demonstrated the advantages of sublimation molecular-beam epitaxy (SMBE) for growing high-efficiency light-emitting structures based on erbium-doped silicon. Si/Si : Er structures produced by this method exhibit record narrow luminescence spectral lines, which implies a high optical gain. It was shown in [2] that the optical gain should reach 30 cm^{-1} in Si : Er layers whose photoluminescence (PL) response spectrum mainly contains a spectral line of isolated centers of the rare-earth ion with a line half-width of 0.1 cm^{-1} (10 μeV [4]).

A necessary condition for the operation of a Si : Er laser is the development of effective waveguide structures that can provide radiation localization in an active layer. One possible variant of such structures is a $Si/Si_{1-x}Ge_x$: Er/Si heterostructure with an active $Si_{1-x}Ge_x$: Er waveguide layer. To estimate the optimum parameters of the $Si_{1-x}Ge_x$: Er layers, we calculate the total gains in $Si/Si_{1-x}Ge_x$: Er/Si structures depending on the thickness $d_{Si_{1-x}Ge_x:Er}$ and the germanium content x in the $Si_{1-x}Ge_x$: Er layer (Fig. 1). For the calculations, we assumed that the gain g in the active $Si_{1-x}Ge_x$: Er layers is the same as in Si : Er layers and is equal to ~30 cm^{-1}. The coefficient of optical limitation of an electromagnetic wave was calculated from the formula

$$\Gamma = \frac{(n_1^2 - n_2^2)d^2k_0^2}{2 + (n_1^2 - n_2^2)d^2k_0^2}. \quad (1)$$

Here, n_1 and n_2 are the refractive indices of the active $Si_{1-x}Ge_x$: Er layer and the limiting Si layers, respectively; d is the thickness of the active $Si_{1-x}Ge_x$: Er layer; $k_0 = 2\pi/\lambda$; and λ is the radiation wavelength. As is seen from the calculation results (Fig. 1), the total

1063-7834/05/4701-0093$26.00 © 2005 Pleiades Publishing, Inc.

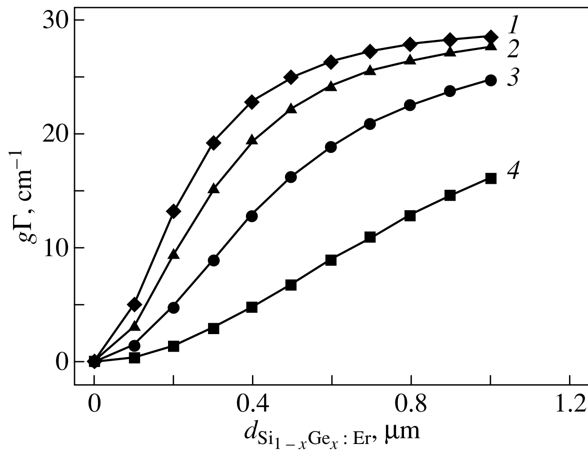

Fig. 1. Dependence of the total gain $g\Gamma$ in the $Si/Si_{1-x}Ge_x$: Er/Si structures on the thickness $d_{Si_{1-x}Ge_x:Er}$) of the $Si_{1-x}Ge_x$: Er active layer for various values of the Ge content x: (*1*) 0.6, (*2*) 0.4, (*3*) 0.2, and (*4*) 0.08. In the calculation, the optical gain g in the $Si_{1-x}Ge_x$: Er active layer was taken to be 30 cm^{-1}.

gains in such structures are maximum for sufficiently thick $Si_{1-x}Ge_x$: Er layers (thicker than 0.5 μm) and high germanium contents in them; these factors can obviously hinder the growth of perfect structures. At large thicknesses and high Ge contents, the grown $Si_{1-x}Ge_x$ heteroepitaxial layers are, as a rule, metastable and elastic stresses relax in the $Si_{1-x}Ge_x$ layers on silicon because of their different lattice parameters (compared to silicon). However, the problem of the effect of these processes on the luminescence properties of erbium rare-earth ions remains unsolved.

The goal of this work is to study the PL properties of $Si/Si_{1-x}Ge_x$: Er/Si structures developed for a silicon-based laser. The structures were grown by SMBE in a gas phase; this method (which is an SMBE modification) was designed especially for growing SiGe : Er solid-solution layers. We estimate the concentrations of optically active erbium-ion centers and the gains of these structures.

2. EXPERIMENTAL

The $Si/Si_{1-x}Ge_x$: Er/Si structures were grown by SMBE in a germane (GeH_4) atmosphere. A distinguishing feature of this technique is germanium supply to a growing layer due to the pyrolysis of GeH_4 on the surface of a silicon substrate heated with an electric current (this technique is described in detail in [5]). As in the case of the standard SMBE method, layers were doped with a rare-earth impurity using two types of source: erbium-doped polycrystalline silicon and Er metallic plates. The growth conditions and the parameters of characteristic $Si/Si_{1-x}Ge_x$: Er/Si structures are given in the table. The structural parameters and the elemental compositions of the grown $Si_{1-x}Ge_x$: Er epitaxial layers were examined with x-ray diffraction and secondary-ion mass spectrometry. The PL properties of the structures were measured at 4.2 K on a BOMEM DA3 Fourier spectrometer with a spectral resolution of ~0.5 cm^{-1}. A PL signal was excited by radiation from an Ar^+ laser with a wavelength of 514.5 nm and was recorded with a cooled North-Coast EO-817A germanium photodetector. The exciting radiation power was varied from 2 to 380 mW. The PL time dependences were measured with a pulse semiconductor laser radiating at a wavelength of 659 nm and with a germanium photodetector used for signal recording. The PL kinetics was measured at $T = 77$ K at the wavelength corresponding to the maximum erbium-photoluminescence signal, and the time resolution of the recording circuit was 5 μs.

3. RESULTS AND DISCUSSION

When optically excited, the epitaxial $Si/Si_{1-x}Ge_x$: Er/Si structures generate an effective PL signal at 1.54 μm, which is related to intracenter transitions in the 4*f* shell of the rare-earth ion Er^{3+} ($^4I_{13/2} \longrightarrow {}^4I_{15/2}$ transitions). The PL response of the structures under study at 4.2 K is shown in Fig. 2. The PL intensities of the most effective $Si/Si_{1-x}Ge_x$: Er/Si structures turn out to be comparable to the PL intensity of uniformly doped Si : Er layers. For comparison, Fig. 2 also shows the PL spectrum of a Si/Si : Er structure (sample 37) recorded under the

Growth conditions and the parameters of $Si/Si_{1-x}Ge_x$: Er/Si structures

Sample no.	Substrate	T_{gr}, °C	x, %	$d_{SiGe:Er}$, nm	RES, %	Er source	[Er], cm^{-3}	d_{Si}, nm
10-110	KDB-02 (100)	500	9.74	500	57	Poly-Si : Er	2×10^{18}	210
10-90	KDB-02 (100)	500	8.73	500	100	"	3×10^{18}	520
10-71	KÉS-0.01 (111)	500	1.9	150	–	Metallic Er/O_2^+ implant.	2.2×10^{17}	350
37	KDB-10 (100)	500	0	0	–	Poly-Si : Er	5×10^{18}	1800

Note: T_{gr} is the growth temperature; $d_{SiGe:Er}$ is the thickness of the $Si_{1-x}Ge_x$: Er layers; RES is the residual elastic stress determined by x-ray diffraction; and d_{Si} is the thickness of the outer Si layer. For sample 37, the thickness d_{Si} corresponds to that of the Si : Er layer (Si/Si : Er structure). Sample 10-71 was additionally implanted by oxygen ions.

same conditions; the estimated internal quantum efficiency of this structure is ~20% [2]. As is seen, the PL signal of the $Si_{1-x}Ge_x$: Er layers mainly contains a peak with a maximum at a wavelength of 6507 cm^{-1} and a line width of ~30 cm^{-1}. The line shape and width indicate that this peak can be caused by erbium-ion optically active centers in SiO_2-like precipitates, whose formation has also been observed in Si : Er layers under certain growth conditions [2]. Note that we did not detect any influence from elastic-stress relaxation on the PL properties despite the large thicknesses of the $Si_{1-x}Ge_x$: Er layers and the high Ge concentration in them (Fig. 2). Moreover, the PL intensity in partly relaxed $Si_{1-x}Ge_x$: Er layers was higher than that in a highly stressed structure (the residual elastic stresses are given in the table).

Let us estimate the concentration of Er^{3+} ion optically active centers in the heterostructures under study. To this end, we analyze the dependence of the erbium PL intensity on the exciting radiation power. As a rule, the PL intensity in the Si : Er structures is saturated at a high pumping power. Figure 3 shows the dependences of the PL intensities of the $Si/Si_{1-x}Ge_x$: Er/Si structures on the exciting radiation power. The $I_{PL}(P)$ dependences obtained are described well by the well-known expression [6]

$$I_{PL} \propto abP/(1+bP), \quad (2)$$

where P is the exciting radiation power. The parameter a determines the PL saturation level at high pumping powers ($I_{PL} \propto a$ at $bP \gg 1$) and depends directly on the concentration of Er^{3+} optically active centers. The parameter b characterizes the increase in the PL intensity for weak pumping ($I_{PL} \propto abP$ at $bP \ll 1$). The solid lines in Fig. 3 show the fitting dependences calculated by Eq. (2) with the following parameters: $a = 32.2 \times 10^4$, 21.2×10^4, 20.9×10^4, and 1.22×10^4 arb. units for curves *1–4*, respectively, and b = 0.036, 0.006, 0.004, and 0.011 mW^{-1} for curves *1–4*, respectively. The coefficients b obtained as a result of fitting are an order of magnitude smaller than those determined for Si : Er layers [7]. Indeed, as seen from Fig. 3, the PL intensity in the structures under study is weakly saturated with increasing excitation power. If the Er^{3+} ions are excited through the exciton mechanism, then the weak increase in $I_{PL}(P)$ in the $Si/Si_{1-x}Ge_x$: Er/Si structures can obviously be explained by a significant contribution of alternative recombination channels to the processes of excitation and de-excitation of the Er ions. These channels can be nonradiative recombination channels (which decrease the total lifetime of the erbium ions in the excited state) or can serve as competing channels during the excitation of rare-earth ions. In the case where the PL signal increases slowly with pumping power and does not level off, which is observed in the $Si/Si_{1-x}Ge_x$: Er/Si structures under study, the coefficient b in Eq. (2) is independent of the concentration of

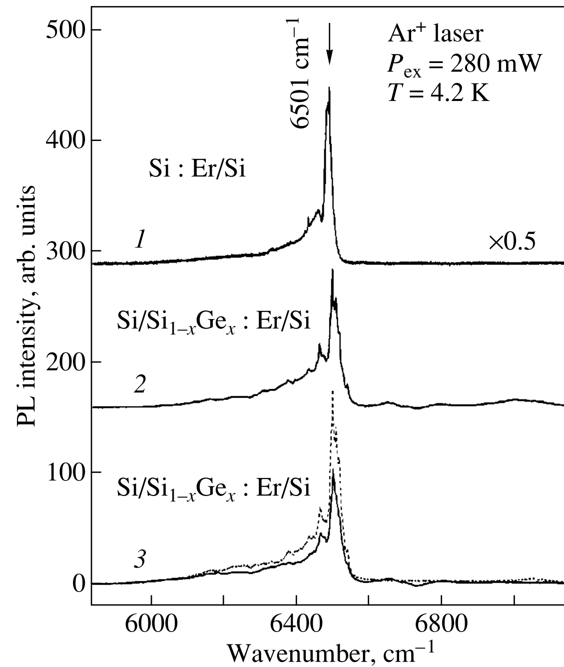

Fig. 2. PL spectra of Si : Er/Si and $Si/Si_{1-x}Ge_x$: Er/Si structures recorded under the same experimental conditions: samples (*1*) 37, (*2*) 10-110, and (*3*) 10-90. The dashed line shows the PL spectrum of sample 10-90 annealed at T = 800°C for 30 min. Annealing leads to stress relaxation in the $Si_{1-x}Ge_x$: Er layer (according to x-ray diffraction data, the RES after annealing is 50%), which results in an increased PL intensity.

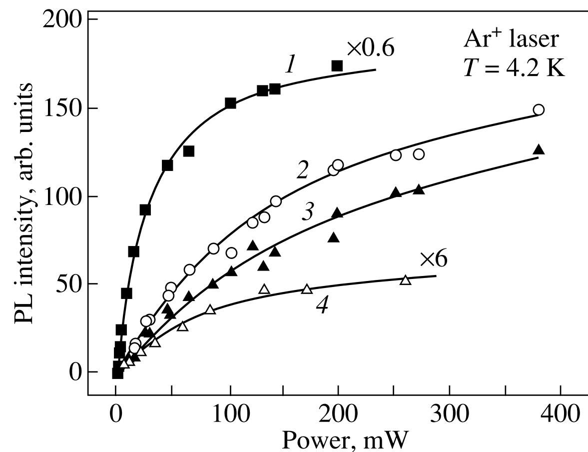

Fig. 3. Dependences of the PL intensities of the Si : Er/Si and $Si/Si_{1-x}Ge_x$: Er/Si structures on the exciting radiation power: samples (*1*) 37, (*2*) 10-110, (*3*) 10-90, and (*4*) 10-71.

erbium-ion optically active centers N_0^E and is specified by the concentration of the alternative channels. Therefore, using the model described in [7], we can determine the concentration of the alternative recombination

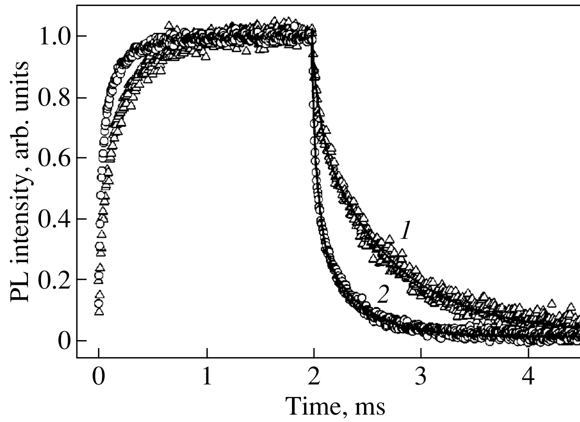

Fig. 4. Oscillograms of the erbium PL signals generated by samples (*1*) 10-90 and (*2*) 10-110.

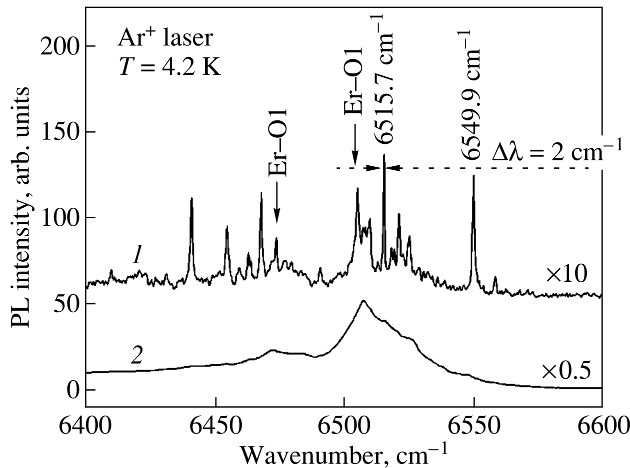

Fig. 5. PL spectra of epitaxial $Si/Si_{1-x}Ge_x$: Er/Si structures: samples (*1*) 10-71 and (*2*) 10-90. The arrows show the PL lines of basic Er^{3+} optically active centers identified in the fine structure of the PL spectrum of sample 10-71.

channels N_0^A involved in the excitation of the Er^{3+} ions in the $Si/Si_{1-x}Ge_x$: Er/Si structures. For the structure exhibiting the highest PL intensity (sample 10-110), this concentration is 3×10^{18} cm^{-3}. Therefore, under the condition $N_0^A \gg N_0^E$, the concentration of optically active Er^{3+} ions in these structures is estimated to be $\sim 3 \times 10^{17}$ cm^{-3}, which is ~10% of the total erbium-impurity concentration.

The processes of nonradiative recombination in the $Si/Si_{1-x}Ge_x$: Er/Si structures give rise to specific features in the PL time dependences (Fig. 4). The solid lines in Fig. 4 show the fitting functions $I_{PL} = I_{PL}(0) + A_1\exp(-(t-t_0)/\tau_1) + A_2\exp(-(t-t_0)/\tau_2)$. Oscillograms of erbium PL signals from each structure studied contain a fast component with a time constant $\tau_1 = 0.06$ ms, whose contribution depends on the lattice perfection and is obviously related to the participation of nonradiative channels in the de-excitation of the Er ions. The time constants τ_2 of the $Si/Si_{1-x}Ge_x$: Er/Si structures are close to the characteristic values of the radiative lifetime of an Er^{3+} ion in the excited state, which are 1 ms for most semiconductors [8]. The total lifetime of an erbium ion in the excited state is specified by the contributions of the exponential components (coefficients A_1, A_2) to the PL decay kinetics. For a relaxed structure (sample 10-110), the total lifetime of the erbium ion is determined by the time constant τ_1 and is equal to 0.06 ms. The PL kinetics of a structure with a stressed $Si_{1-x}Ge_x$: Er layer (sample 10-90) is dominated by the slow component τ_2, and, in this case, the total lifetime of the erbium ion is ~0.7 ms.

Let us estimate the optical gain in the structures under study in the same way as was done in [9] for Si : Er layers. The gain can be calculated from the formula

$$g = N_0^E \frac{\lambda^4}{4\pi n^2 c \tau_r \Delta\lambda}, \qquad (3)$$

where $\lambda = 1.54$ μm, τ_r is the radiative lifetime of the erbium ion in the excited state, n is the refractive index of the medium, c is the velocity of light in vacuum, $\Delta\lambda$ is the full width at half-maximum of the PL line, and N_0^E is the concentration of optically active Er^{3+} ions. Using the values obtained for the concentration of optically active Er^{3+} ions ($N_0^E \sim 3 \times 10^{17}$ cm^{-3}), the lifetime ($\tau_r \sim 1$ ms), and the linewidth, ~30 cm^{-1} ($\Delta\lambda \sim 7.5$ nm), we find that the gain is equal to 0.03 cm^{-1} for the sample exhibiting the maximum PL intensity (sample 10-110).

As is seen from Eq. (3), the gain in the laser structures to be developed can be increased by decreasing the PL linewidth. It is known that, in SMBE-grown Si : Er layers, erbium centers generating narrow luminescence lines form at high growth temperatures (~560–580°C) or as a result of postgrowth annealing [2]. For $Si_{1-x}Ge_x$: Er layers, however, these processes can have a different character. Additional codoping (e.g., by oxygen ions) can also be applied. Figure 5 shows the PL spectrum of a $Si/Si_{1-x}Ge_x$: Er/Si structure grown from a metallic erbium source (sample 10-71). The sample was additionally implanted by 150-keV oxygen ions to a dose of 5×10^{15} cm^{-2} and then vacuum-annealed at 800°C for 30 min. The study of the PL spectrum of this sample revealed Er^{3+} optically active centers that had a characteristic fine structure of the spectrum, for example, the well-known oxygen-containing center Er–O1 [10]. The most intense PL lines of the erbium centers in this sample are at 6515.7 and 6549.9 cm^{-1}. The width of the lines dominating in the PL spectrum is $\Delta\lambda \sim 2$ cm^{-1}. In this case, the substantial decrease in the linewidth results in an increase in

the gain g by an order of magnitude; the gain is estimated to be ~0.2 cm^{-1}.

4. CONCLUSIONS

We have shown that SMBE in a germane atmosphere can be used to produce effective light-emitting epitaxial $Si/Si_{1-x}Ge_x$: Er/Si structures. The PL intensity of such structures is comparable to the PL intensity of uniformly doped Si : Er layers, whose internal quantum efficiency is known to reach ~20%. The concentration of optically active Er^{3+} centers in the $Si_{1-x}Ge_x$: Er layers under study has been estimated to be ~10% of the total erbium-impurity concentration. The optical gain in the structures produced is 0.03–0.20 cm^{-1}, and the gain is maximum in the $Si/Si_{1-x}Ge_x$: Er/Si samples whose PL spectrum has a fine structure.

ACKNOWLEDGMENTS

This work was supported by the Russian Foundation for Basic Research (project nos. 02-02-16773, 04-02-17120) and INTAS (project nos. NANO-01-0444, 03-51-6486).

REFERENCES

1. *Silicon-Based Optoelectronics*, Ed. by S. Coffa and L. Tsybeskov; MRS Bull. **23** (4), 16 (1998).
2. Z. F. Krasilnik, V. Ya. Aleshkin, B. A. Andreev, O. B. Gusev, W. Jantsch, L. V. Krasilnikova, D. I. Kryzhkov, V. P. Kuznetsov, V. G. Shengurov, V. B. Shmagin, N. A. Sobolev, M. V. Stepikhova, and A. N. Yablonsky, in *Towards the First Silicon Laser*, Ed. by L. Pavesi, S. Gaponenko, and L. Dal Negro (Kluwer Academic, Dordercht, 2003), NATO Sci. Ser. II: Math. Phys. Chem., Vol. 93, p. 445.
3. B. Andreev, V. Chalkov, O. Gusev, A. Emel'yanov, Z. Krasil'nik, V. Kuznetsov, P. Pak, V. Shabanov, V. Shengurov, V. Shmagin, N. Sobolev, M. Stepikhova, and S. Svetlov, Nanotechnology **13**, 97 (2002).
4. N. Q. Vinh, H. Przybylinska, Z. F. Krasil'nik, and T. Gregorkiewicz, Phys. Rev. Lett. **90** (6), 066401 (2003).
5. S. P. Svetlov, V. G. Shengurov, V. Yu. Chalkov, Z. F. Krasil'nik, B. A. Andreev, and Yu. N. Drozdov, Izv. Ross. Akad. Nauk, Ser. Fiz. **65** (2), 203 (2001).
6. R. Serna, Jung H. Shin, M. Lohmeier, E. Vlieg, A. Polman, and P. F. A. Alkemade, J. Appl. Phys. **79** (5), 2658 (1996).
7. B. A. Andreev, Z. F. Krasil'nik, V. P. Kuznetsov, A. O. Soldatkin, M. S. Bresler, O. B. Gusev, and I. N. Yassievich, Fiz. Tverd. Tela (St. Petersburg) **43** (6), 979 (2001) [Phys. Solid State **43**, 1012 (2001)].
8. P. B. Klein and G. S. Pomrenke, Electron. Lett. **24** (24), 1502 (1988).
9. V. Ya. Aleshkin, B. A. Andreev, and Z. F. Krasil'nik, in *Proceedings of Meeting on Nanophotonics-2002* (Inst. Fiziki Mikrostruktur Ross. Akad. Nauk, Nizhni Novgorod, 2002), p. 289.
10. H. Przybylinska, W. Jantsch, Yu. Suprun-Belevitch, M. Stepikhova, L. Palmetshofer, G. Hendorfer, A. Kozanecki, R. J. Wilson, and B. J. Sealy, Phys. Rev. B **54** (4), 2532 (1996).

Translated by K. Shakhlevich

Physics of the Solid State, Vol. 47, No. 1, 2005, pp. 98–101. Translated from Fizika Tverdogo Tela, Vol. 47, No. 1, 2005, pp. 95–98.
Original Russian Text Copyright © 2005 by Remizov, Shmagin, Antonov, Kuznetsov, Krasil'nik.

PROCEEDINGS OF THE CONFERENCE "NANOPHOTONICS 2004"
(Nizhni Novgorod, Russia, May 2–6, 2004)

Effective Excitation Cross Section and Lifetime of Er^{3+} Ions in Si : Er Light-Emitting Diodes Fabricated by Sublimation Molecular-Beam Epitaxy

D. Yu. Remizov, V. B. Shmagin, A. V. Antonov, V. P. Kuznetsov, and Z. F. Krasil'nik

Institute for Physics of Microstructures, Russian Academy of Sciences, Nizhni Novgorod, 603950 Russia
e-mail: remizov@ipm.sci-nnov.ru

Abstract—A series of Si : Er electroluminescent diode structures is fabricated by sublimation molecular-beam epitaxy. The diode structures efficiently emit at a wavelength of 1.5 μm under conditions of *p*–*n* junction breakdown at room temperature. The effective cross section of excitation of Er^{3+} ions with hot carriers heated by the electric field of a reverse-biased *p*–*n* junction and the lifetime of Er^{3+} ions in the first excited state $^4I_{13/2}$ are determined for structures that emit in a mixed breakdown mode and are characterized by the maximum intensity and excitation efficiency of the Er^{3+} electroluminescence. © *2005 Pleiades Publishing, Inc.*

1. INTRODUCTION

In recent years, sublimation molecular-beam epitaxy, which successfully combines the high growth rate with good crystal quality of grown layers [1], has proved itself to be an original and very promising method for fabricating light-emitting structures based on silicon doped with erbium. This method has made it possible to prepare various Si : Er materials, such as uniformly doped light-emitting structures with a Si : Er layer thickness of up to 4 μm, multilayer periodic structures (… Si/Si : Er/Si …) that are characterized by a high quantum efficiency and intense photoluminescence at a wavelength $\lambda \sim 1.5$ μm, and electroluminescent diode structures that efficiently emit at 1.5 μm under conditions of *p*–*n* junction breakdown at room temperature [2–5].

Earlier [5], we investigated how the mechanism of breakdown of a space-charge region affects the electroluminescent properties of Si : Er/Si light-emitting diodes fabricated through sublimation molecular-beam epitaxy. It was demonstrated that, at room temperature, the intensity and excitation efficiency of the Er^{3+} electroluminescence in diodes operating in a nearly mixed breakdown mode ($U_{br}^{77} \approx U_{br}^{300}$, where U_{br}^{77} and U_{br}^{300} are the breakdown voltages at temperatures of 77 and 300 K, respectively) are higher than those of diodes operating in tunneling ($U_{br}^{77} > U_{br}^{300}$) or avalanche ($U_{br}^{77} < U_{br}^{300}$) breakdown modes. In the present work, diodes operating in a mixed breakdown mode with an insignificant predominance of the tunnel component in the breakdown current were fabricated by sublimation molecular-beam epitaxy. We studied the kinetics of rise in the Er^{3+} electroluminescence in these diodes for the first time and determined the effective excitation cross section and the lifetime of Er^{3+} ions in the first excited state $^4I_{13/2}$.

2. SAMPLE PREPARATION AND EXPERIMENTAL TECHNIQUE

For our experiments, light-emitting diode structures were grown through sublimation molecular-beam epitaxy on *p*-Si : B substrates with the (100) orientation and a resistivity of 15 Ω cm. The structures contained a 0.1-μm-thick p^+-Si buffer layer with a carrier concentration of 5×10^{18} cm^{-3}. The characteristics of *n*-Si : Er layers were as follows: the thickness was approximately equal to 1 μm, the carrier concentration varied from $\sim 4 \times 10^{17}$ to 7×10^{17} cm^{-3}, the growth temperature was ~520°C, and the Er concentration ranged from $\sim 1 \times 10^{18}$ to 2×10^{18} cm^{-3}. The light-emitting diodes were fabricated according to the standard mesa technology (mesa area, 2.5 mm^2; 70% of the area was free for emission escape).

The electroluminescence spectra were recorded in the wavelength range 1.0–1.6 μm at a resolution of 6 nm with an MDR-23 grating monochromator and an InGaAs IR photodetector cooled to liquid-nitrogen temperature. The electroluminescence spectra were excited and measured using a pulse modulation of the pump current (pulse duration, 4 ms; pulse frequency, ~40 Hz; amplitude, up to 500 mA) and a synchronous accumulation of signals. The time measurements were performed on a BORDO 110 digital oscilloscope with a bandwidth of 0–200 MHz and a faster InGaAs IR photodetector (time response, ~15 μs) operating at room temperature. The broadband of the optical channel used in the time measurements was determined by the broadband (1.5–2.5 μm) of the optical interference filter in the short-wavelength range and the broadband of the InGaAs photodetector in the long-wavelength range. The current–voltage characteristics of the diodes were measured in a pulsed mode. The breakdown voltage U_{br} was determined by extrapolating a straight-line

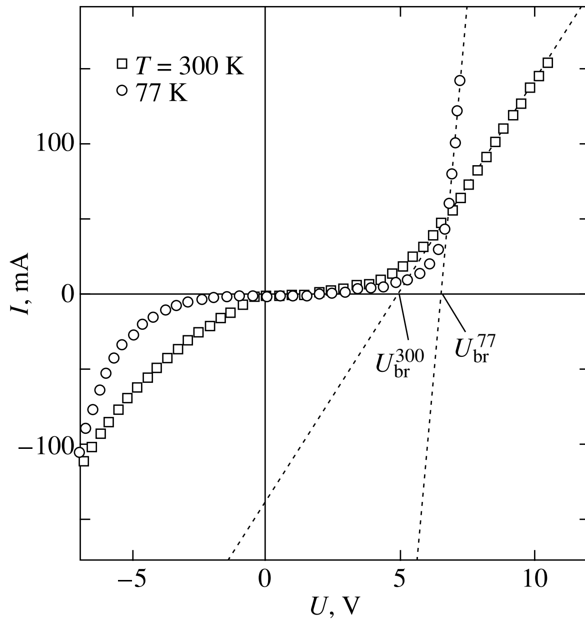

Fig. 1. Current–voltage characteristics of the Si : Er/Si diode fabricated by sublimation molecular-beam epitaxy. Measurement temperature: $T = 77$ and 300 K. Dotted lines show the extrapolation of the straight-line portions of the reverse branches in the current–voltage characteristics to the intersection with the voltage axis. Arrows indicate the breakdown voltages.

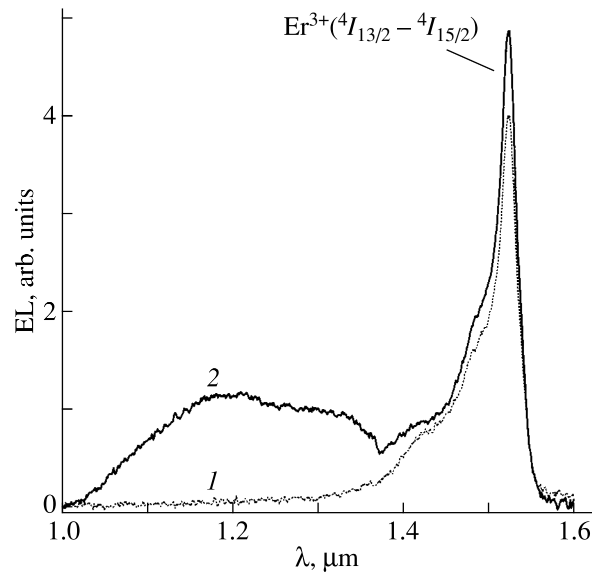

Fig. 2. Electroluminescence spectra of the Si : Er/Si diode (fabricated by sublimation molecular-beam epitaxy) under conditions of *p–n* junction breakdown (*1*) with and (*2*) without an optical filter. $T = 300$ K. The pump current density is equal to 8 F/cm^2. The transition in the 4*f* shell of the Er^{3+} ion is identified.

portion of the reverse branch of the current–voltage characteristic to the intersection with the voltage axis.

3. RESULTS AND DISCUSSION

The current–voltage characteristics and the electroluminescence spectra of one of the diodes fabricated through sublimation molecular-beam epitaxy are shown in Figs. 1 and 2, respectively. The breakdown voltages are determined to be $U_{br}^{300} \approx 5.0$ V and $U_{br}^{77} \approx 6.6$ V. These values suggest a mixed mechanism of breakdown with an insignificant predominance of the tunnel component in the breakdown current. The different slopes of the reverse branches in the current–voltage characteristics of the diode at temperatures $T = 77$ and 300 K are associated with the temperature dependence of the carrier mobility in the substrate. The electroluminescence spectrum is typical of diodes with a mixed breakdown and contains a rather narrow line of the erbium electroluminescence ($^4I_{13/2} \longrightarrow {^4I_{15/2}}$ transition in the 4*f* shell of the Er^{3+} ion) and a broad band of the so-called “hot” electroluminescence due to the intraband radiative relaxation of carriers heated in the electric field of the space-charge region [6]. A comparison of the electroluminescence spectra measured with and without the optical filter shows that the filter effectively cuts off the hot electroluminescence band. The use of the filter allowed us to perform time measurements without a monochromator and, thus, to increase considerably the signal-to-noise ratio of the recorded signal.

The effective excitation cross section and the lifetime of Er^{3+} ions in the excited state were determined by measuring the kinetics of rise in the Er^{3+} electroluminescence upon pulse modulation of the pump current. In the framework of the two-level model, the balance equation determining the excitation and de-excitation of Er^{3+} ions and its solution, which describes the rise in the electroluminescence intensity (EL) (after the pump current is switched on, can be written in the following form [7]:

$$\frac{dN^*}{dt} = \frac{\sigma j}{q}(N - N^*) - \frac{N^*}{\tau}, \tag{1}$$

$$N^* = N\frac{\sigma\tau j/q}{1 + \sigma\tau j/q}\left[1 - \exp\left(-\frac{t}{\tau_{on}}\right)\right]. \tag{2}$$

Here, N and N^* are the total concentration of Er^{3+} ions and their concentration in the $^4I_{13/2}$ excited state, respectively; σ is the effective excitation cross section of Er^{3+} ions; τ is the lifetime of Er^{3+} ions in the excited state; j is the pump current density; q is the elementary

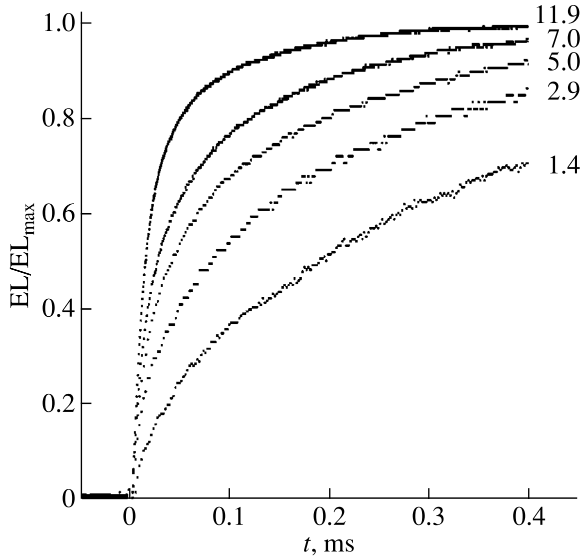

Fig. 3. Curves of the electroluminescence intensity rise after switching on the pump current. The curves are normalized to the steady-state value of the electroluminescence intensity. The temperature is 300 K. Numbers near curves indicate the pump current densities (in A/cm^2).

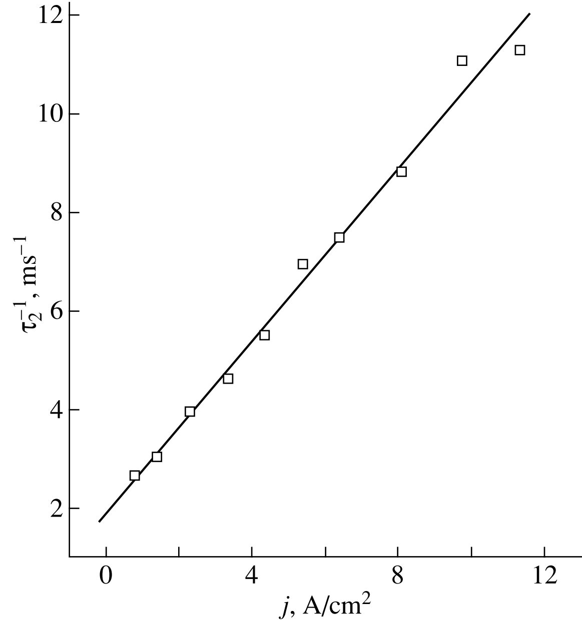

Fig. 4. Dependence of the reciprocal rise time of the Er^{3+} electroluminescence intensity on the pump current density. Points are the experimental data. The straight line corresponds to the approximation of the experimental data by relationship (3).

charge; and τ_{on} is the time of rise in the electroluminescence intensity. The time τ_{on} is given by the expression

$$\frac{1}{\tau_{on}} = \frac{\sigma j}{q} + \frac{1}{\tau}. \tag{3}$$

Since the intensity of the Er^{3+} electroluminescence satisfies the relationship EL $\sim N^*/\tau_{rad}$ (where τ_{rad} is the radiative lifetime of Er^{3+} ions in the excited state), expression (2) can be rewritten in a form more convenient for describing the results of kinetic measurements:

$$\mathrm{EL} = \mathrm{EL}_{max}\frac{\sigma\tau j/q}{1+\sigma\tau j/q}\left[1-\exp\left(-\frac{t}{\tau_{on}}\right)\right], \tag{4}$$

where EL_{max} is the maximum electroluminescence intensity corresponding to the transition of all Er^{3+} ions to the excited state. The dependence of the steady-state value of the erbium electroluminescence intensity (at $t \longrightarrow \infty$) on the pump current density is described by the relationship

$$\mathrm{EL} = \mathrm{EL}_{max}\frac{\sigma\tau j/q}{1+\sigma\tau j/q}. \tag{5}$$

The rise curves EL(t) normalized to the steady-state value of the electroluminescence intensity EL($t \longrightarrow \infty$) at different pump current densities are plotted in Fig. 3. It can be seen from Fig. 3 that, in accordance with expression (3), the rise time τ_{on} decreases with an increase in the pump current density. The rise curves EL(t) can be theoretically described by the expression

$$\mathrm{EL}(t) = A_0 + A_1\left[1-\exp\left(1\frac{t}{\tau_1}\right)\right] + A_2\left[1-\exp\left(-\frac{t}{\tau_2}\right)\right]. \tag{6}$$

Here, the first term is a constant determined by the signal-forming circuit; and the second and third terms describe the rise in the hot and erbium electroluminescence intensities, respectively. Since the rise time of the hot electroluminescence is approximately equal to 200 ns [8], the constant τ_1 in our experiments is determined by the response time of the detector and is approximately equal to 15 μs. Removing the filter from the optical scheme of the experiment does not affect the rise times τ_1 and τ_2 but leads to a change in the ratio between the amplitudes A_1 and A_2, so that the amplitude A_1 of the fast component increases. This confirms our assumption that the fast component of the rise curve EL(t) is associated with the rise in the hot electroluminescence intensity.

Figure 4 shows the dependence of the reciprocal rise time of the Er^{3+} electroluminescence intensity on the pump current density. The approximation of the experimental results by relationship (3) leads to the following effective excitation cross section and lifetime of Er^{3+} ions: $\sigma = 1.4 \times 10^{-16}$ cm^2 and $\tau = 540$ μs.

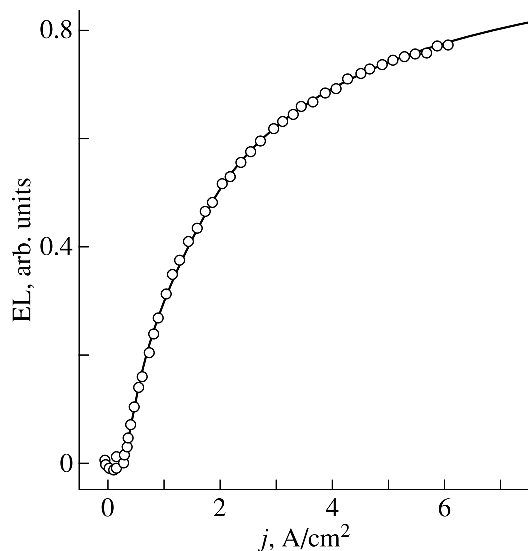

Fig. 5. Dependence of the Er^{3+} electroluminescence intensity on the pump current density. Points are the experimental data. The straight line corresponds to the approximation of the experimental data by relationship (5).

The product $\sigma\tau$ of dividing the effective excitation cross section by the lifetime of Er^{3+} ions in the excited state can be independently obtained from the experimental dependence of the steady-state value of the erbium electroluminescence intensity on the pump current density. Figure 5 depicts the dependence of the erbium electroluminescence intensity on the pump current density and its approximation by relationship (5) for the same diode. As can be seen from Fig. 5, the experimental data are adequately described by relationship (5). The aforementioned product is estimated as $\sigma\tau = 6.9 \times 10^{-20}$ cm^2 s. This result is in good agreement with the data of kinetic measurements. Actually, direct multiplication of the quantities σ and τ determined from the kinetic data gives the product $\sigma\tau = 7.6 \times 10^{-20}$ cm^2 s.

4. CONCLUSIONS

Thus, Si : Er light-emitting diodes with the mixed or nearly mixed mechanism of breakdown of a space-charge region and the impact mechanism of Er^{3+} ion excitation were fabricated by sublimation molecular-beam epitaxy. The excitation efficiency of the erbium electroluminescence in these diodes is only insignificantly lower than that in implantation light-emitting diodes with the avalanche mechanism of breakdown ($\sigma = 2.3 \times 10^{-16}$ cm^2, $\tau = 380$ μs [9]). This is in agreement with the inference made previously that the excitation efficiency of the erbium electroluminescence increases with an increase in the avalanche component in the breakdown current in diodes [5]. Moreover, the fabricated diodes substantially surpass light-emitting diodes with the tunneling mechanism of breakdown in terms of both the excitation cross section and the lifetime of the excited state ($\sigma = 6 \times 10^{-17}$ cm^2, $\tau = 100$ μs [7]). The shorter lifetime of Er^{3+} ions in tunnel diodes is most likely associated with the higher doping level (as compared to avalanche and mixed diodes) and, hence, with the higher concentration of defects.

ACKNOWLEDGMENTS

This work was supported by the Russian Foundation for Basic Research (project nos. 02-02-16773, 04-02-17120) and the International Association of Assistance for the Promotion of Cooperation with Scientists from the New Independent States of the Former Soviet Union (project no. INTAS 03-51-6468).

REFERENCES

1. V. P. Kuznetsov and R. A. Rubtsova, Fiz. Tekh. Poluprovodn. (St. Petersburg) **34**, 519 (2000) [Semiconductors **34**, 502 (2000)].
2. B. Andreev, V. Chalkov, O. Gusev, A. Emel'yanov, Z. Krasil'nik, V. Kuznetsov, P. Pak, V. Shabanov, V. Shengurov, V. Shmagin, N. Sobolev, M. Stepikhova, and S. Svetlov, Nanotechnology **13** (1), 97 (2002).
3. Z. F. Krasil'nik, V. Ya. Aleshkin, B. A. Andreev, O. B. Gusev, W. Jantsch, L. V. Krasilnikova, D. I. Kryzhkov, V. P. Kuznetsov, V. G. Shengurov, V. B. Shmagin, N. A. Sobolev, M. V. Stepikhova, and A. N. Yablonsky, in *Towards the First Silicon Laser*, Ed. by L. Pavesi, S. Gaponenko, and L. Dal Negro (Kluwer Academic, Dordrecht, 2003), p. 445.
4. B. A. Andreev, T. Gregorkevich, Z. F. Krasil'nik, V. P. Kuznetsov, D. I. Kuritsyn, M. V. Stepikhova, V. G. Shengurov, V. B. Shmagin, A. N. Yablonskiĭ, and W. Jantsch, Izv. Akad. Nauk, Ser. Fiz. **67** (2), 273 (2003).
5. V. B. Shmagin, D. Yu. Remizov, Z. F. Krasil'nik, V. P. Kuznetsov, V. N. Shabanov, L. V. Krasil'nikova, D. I. Kryzhkov, and M. N. Drozdov, Fiz. Tverd. Tela (St. Petersburg) **46** (1), 110 (2004) [Phys. Solid State **46**, 109 (2004)].
6. F. G. Chynoweth and K. G. McKay, Phys. Rev. **102** (2), 369 (1956).
7. S. Coffa, G. Franzo, and F. Priolo, Appl. Phys. Lett. **69** (14), 2077 (1996).
8. W.-X. Ni, C.-X. Du, K. B. Joelsson, G. Pozina, and G. V. Hansson, J. Lumin. **80** (1–4), 309 (1999).
9. N. A. Sobolev, Yu. A. Nikolaev, A. M. Emel'yanov, K. F. Shtel'makh, P. E. Khakuashev, and M. A. Trishhenkov, J. Lumin. **80** (1–4), 315 (1999).

Translated by O. Borovik-Romanova